AN EXPERIMENTAL ROCK MECHANICS INVESTIGATION INTO SHEAR DISCONTINUITIES AND THEIR INFLUENCE IN THE HYDROCARBON RESERVOIR ENVIRONMENT

by

BRIAN RONALD CRAWFORD

BSc Geology

(University of Glasgow)

MSc (DIC) Structural Geology and Rock Mechanics

(Imperial College, London University)

Thesis presented for the degree of Doctor of Philosophy

at

The Department of Petroleum Engineering,

Heriot-Watt University,

Edinburgh, UK.

1995

PAGE NUMBERING AS ORIGINAL

"If our eye could penetrate the earth and see its interior from pole to pole, from where we stand to the antipodes, we would glimpse with horror a mass terrifyingly riddled with fissures and caverns."

Thomas Burnet,

Telluris Theoria Sacra

Amsterdam. Wolters, 1694, p.38.

TABLE OF CONTENTS

			Page
		TABLE OF CONTENTS	i
		LIST OF TABLES	iv
		LIST OF FIGURES	vi
		ACKNOWLEDGEMENTS	xvii
		ABSTRACT	xviii
		INTRODUCTION	xix
CHAPTER 1:		BRITTLE SHEAR FRACTURING IN ROCK: AN OVERVIEW	1
	1.1:	INTRODUCTION	1
	1.2:	DEFORMATION MECHANISMS AND LOCALISATION	2
	1.3:	MACROSCOPIC STRENGTH CRITERIA	9
	1.4:	FRACTURE MECHANICS	30
	1.5:	EXPERIMENTAL STUDIES OF SHEAR FAULTING	37
CHAPTER 2:		THE IMPORTANCE OF SHEAR DISCONTINUITIES IN HYDROCARBON RESERVOIRS: A CRITIQUE	48
	2.1:	INTRODUCTION	48
	2.2:	FAULT SIZE POPULATIONS	49
	2.3:	FAULT SEALING POTENTIAL	59
		2.3.1: Mechanisms of Fault Seal	61
		2.3.2: Fault-related Diagenesis	65
		2.3.3: Shale Smears	69
		2.3.4: Granulation Seams	74
		2.3.5: Fault Seal Capacity In The North Sea	84
	2.4:	DEFORMABILITY	90
		2.4.1: Production-related Seismicity	90
		2.4.2: Bedding-parallel Shear	105
CHAPTER 3:		DIRECT SHEAR EXPERIMENTATION: RIG DESIGN AND RESULTS	122
	3.1:	INTRODUCTION	122
	3.2:	DIRECT SHEAR RIG DESIGN	122
	3.3:	TEST SPECIMENS AND EXPERIMENTAL METHODOLOGY	129
	3.4:	EXPERIMENTAL RESULTS	132
		3.4.1: Sliding Surface Morphology	132
		3.4.2: Force-Displacement Curves	138
		3.4.3: Theoretical Analysis of Contact Area Variation With Sliding Displacement	152
		3.4.4: Stress-Displacement Curves	155

Page

3.5: EMPIRICAL EXPRESSIONS FOR FRICTIONAL STRENGTH 155
3.5.1 Maximum Friction Plots 167
3.5.2 Variable Friction Plots 171
3.5.3 Shear Stress - Normal Stress Plots 173
3.6: DISCUSSION 180

CHAPTER 4: COUPLED PERMEABILIY-MICROSEISMICS MEASUREMENT DURING TRIAXIAL COMPRESSION TESTING: EQUIPMENT DEVELOPMENT 183

4.1: INTRODUCTION 183
4.2: STRESS APPLICATION 188
4.3: PERMEABILITY MEASUREMENT 194
4.3.1: The Pulse-Decay Permeability Method 194
4.4: MICROSEISMIC MONITORING 198
4.4.1: Acoustic Emission Characteristics 200
4.4.2: The LOCAN-320 AE Monitoring Unit 204

CHAPTER 5: COUPLED PERMEABILITY - MICROSEISMICS MEASUREMENT DURING TRIAXIAL COMPRESSION TESTING: RESULTS 211

5.1: INTRODUCTION 211
5.2: EXPERIMENTAL METHODOLOGY 212
5.3: STRENGTH RESULTS 217
5.4: PERMEABILITY RESULTS 224
5.4.1: Permeability Data 227
5.4.2: Discussion 234
5.5: MICROSEISMIC RESULTS 239
5.5.1: Definition of a Fractal Set 240
5.5.2: Fractal Damage Mechanics 246
5.5.3: Acoustic Emission Data 255
5.5.4: Discussion 263

CHAPTER 6: ARTIFICIAL FAULT GOUGE GENERATED UNDER DIRECT SHEAR AND TRIAXIAL COMPRESSION CONDITIONS: RESULTS 268

6.1: INTRODUCTION 268
6.2: PARTICLE SIZE DISTRIBUTIONS 268
6.2.1: Normal 269
6.2.2: Log-Normal 270
6.2.3: Rosin-Rammler 270
6.2.4: Graphical Representation of Data 272
6.2.5: Fractal Fragmentation 276
6.3: EXPERIMENTAL SIZE DISTRIBUTION DETERMINATION 280
6.3.1: Sieving 281

6.3.2: Laser Sizing 282
6.4: DIRECT SHEAR RESULTS 288
6.4.1: Sieving Results 289
6.4.2: Malvern Results 295
6.4.3: Frictional Strength Correlations and Surface Energy Considerations 305
6.5: TRIAXIAL COMPRESSION DEBRIS 317
6.5.1: Shear Band Permeability Estimation 318
6.5.2: Malvern Results 328
6.5.3: Sealing Potential Correlation 335

CHAPTER 7: EXPERIMENTAL CONCLUSIONS AND FURTHERANCE OF WORK 339

7.1: CONCLUSIONS 339
7.1.1: Direct Shear Experimentation 339
7.1.2: Triaxial Compression Experimentation 341
7.1.3: Experimental Fault Gouge Analyses 343
7.2: FURTHER WORK 346
7.2.1: Direct Shear Experimentation 346
7.2.2: Triaxial Compression Experimentation 347
7.2.3: Experimental Fault Gouge Analyses 347

REFERENCES 348
APPENDIX I 370
APPENDIX II 383

LIST OF TABLES

Table		Page
1.5.1	Summary of studies of localisation of deformation	39
2.2.1	Equivalent values of the fractal dimensions of various fault "size" attributes for a typical 1D fault displacement population	55
2.3.4.1	Terms in the published literature synonymous with "granulation seam"	76
3.3.1	Specimen lithologies, pre-shear discontinuity descriptions and test variables for direct shear experimental programme	133
3.5.1	Frictional Strength Criteria	163
3.5.2	Typical values of variable friction coefficient, for a range of rock types	166
3.5.1.1	Maximum friction data for direct shear tests under constant normal displacement control	168
3.5.3.1	Frictional sliding constants for direct shear data	179
4.4.1	A qualitative comparison of the capabilities of laboratoy shear testing apparatus	184
5.2.1	Geological, poroperm and rock mechanical characteristics of the Clashach test sandstone	214
5.2.2	Initial confining pressures for dynamic failure and frictional-sliding, and final confining pressures for re-shearing	218
5.4.1.1	Tabulated permeability and associated absolute errors, stress states and displacements for the seven Clashach triaxial compression experiments	232
6.2.5.1	Fractal dimensions of a variety of fragmented objects	278
6.3.1.1	Comparison of U.S.Tyler and B.S.Sieve Series	283
6.4.1	Recovered experimental direct shear fault gouge weights	290
6.4.2	Direct shear specimen percentage mineral contents	290
6.4.1.1	Direct shear fault gouge distribution characteristics by sieving	291

6.4.1.2 Behaviour of the distribution parameter, n, for various fragmentation methods 291

6.4.2.1 Particle size distribution constants derived from laser sizing, for direct shear-generated fault gouge 303

6.4.3.1 Harmonic means and specific surface areas for laser-sized direct shear debris distributions, plus shear fracture energies for those samples exhibiting slip-weakening 308

6.5.1.1 Experimental details for shear band thickness calibration specimens #23R and #24R 321

6.5.1.2 Stress, strain and permeability values for shear bands induced under triaxial compression 321

6.5.2.1 Tabulated Rosin-Rammler constants for laser-sized gouge distributions 331

LIST OF FIGURES

Figure		Page
1.2.1	Mode of failure transitions in rock	4
1.2.2	Flow diagram illustrating the inter-relationships between lithological and environmental controls with material processes during rock deformation	4
1.2.3	Review of fracture processes	8
1.3.1	Limits to the dependence of differential stress at shear failure in compression on confining pressure for a wide range of igneous rocks	13
1.3.2	The Coulomb criterion for shear failure, depicted as a linear Mohr envelope	13
1.3.3	Andersonian fault classification	17
1.3.4	Schematic open crack in compression showing initial extension directions	23
1.3.5	The Griffith parabolic failure envelope	24
1.3.6	The combined Griffith-Coulomb failure envelope	24
1.3.7	Tensile failure conditions	29
1.3.8	Stress conditions for failure in the negative quadrants of the Griffith failure envelope	31
1.3.9	Mohr's stress circles representing tensile, shear and hybrid tension/ shear fractures	31
1.4.1	The three basic plane modes of distortion at a crack tip	33
1.4.2	Co-ordinate frames for analyses of linearly elastic crack tip stress fields	33

Figure Page

1.5.1 Generalised delineation of four stages in the complete load-displacement curve of a rock in compression, and corresponding changes in various physical properties 42

1.5.2 Curves of stress versus axial strain, lateral strain and volumetric strain for a brittle rock in a compressive test to failure 42

1.5.3 Schematic diagram showing the propagation of tensile cracks from the edges of a shear crack in a brittle material 46

1.5.4 Observed fracture types from experimental growth of shear fractures .. 46

2.2.1 Line sampled displacement population curves from a 2D seismic survey in the North Sea 53

2.2.2 Composite log-log frequency distribution plot of fracture lengths per unit area of 2D observation plane 53

2.2.3 Schematic map showing the positions of randomly distributed barriers (faults) with a power-law length population 57

2.2.4 2D scheme for approximating streamline lengths 57

2.2.5 Normalised permeability values computed using the statistical streamline technique for a variety of power-law size distributions 60

2.3.1.1 Summary of controls on fault sealing 62

2.3.1.2 Plot of sealing capacity of different types of fault seal 62

2.3.2.1 "Pump" and "valve" models for fluid outflows following shallow crustal earthquakes 67

2.3.2.2 Schematic model of the seismic valving mechanism for fluid transport up faults 67

2.3.3.1 Schematic of a shale smear simple zone analogy 71

2.3.3.2 Schematic of the strained volume of rock associated with normal fault slip 71

2.3.3.3 Histogram showing the types of shale smear for the full range of Shale Smear Factor values 73
2.3.4.1 Series of block diagrams showing the sequential development from a single deformation band to a slip surface 77
2.3.4.2 Schematic depicting the relationships between cataclastic slip bands, cataclastic slip zones and slip surfaces 77
2.3.4.3 General microstructural characteristics in an idealised fault zone 79
2.3.4.4 Mohr stress diagrams for faults that strain soften and strain harden 79
2.3.4.5 Stress-strain path during failure of a strain-hardening fault 81
2.3.4.6 Successive Mohr stress circles and failure envelopes for a fault with rapid transient increase in pore pressure during failure 81
2.3.5.1 Fault-related seal classification 86
2.3.5.2 Parameters contributing to fault seal 88
2.4.1.1 Examples of induced changes in stress that can trigger failure in different faulting environments 92
2.4.1.2 Mohr stress circle for pore pressure induced fault slip 92
2.4.1.3 Schematic maps describing the application of the concepts of "barriers" and "asperities" to explain the seismicity in the Codgell oil field 97
2.4.1.4 Measured surface deformations at Wilmington oil field near Long Beach, California 99
2.4.1.5 Number of earthquakes recorded per year and decline in average reservoir pressure in two gas fields 99
2.4.1.6 Schematic cross-section summarising surface deformation and faulting associated with fluid withdrawal 102
2.4.1.7 Calculated change in horizontal normal stress,due to fluid extraction 102
2.4.2.1 Folding styles 107
2.4.2.2 Schematic of the sliding of an overthrust block on a horizontal plane 110

2.4.2.3 Schematic of the shear stress that resists buckling by the flexural slip mechanism induced by the buckling stress 110

2.4.2.4 Crystal fibres on a flexural slip bedding plane indicating opening as well as differential bedding slip 110

2.4.2.5 Bedding slip "squeezing" in the walls of an excavation with associated upward heave and buckling in the invert 114

2.4.2.6 Profile along rib faces showing progressive extrusion of individual soft layers. Differential shearing of pillars 114

2.4.2.7 Shear failure of massive roof rock under inferred horizontal compression, followed by violent shear failure along "cymoidal" fractures that increase in dip downwards 117

2.4.2.8 Relation of common types of rib failures to lithology of roof rocks, Utah 117

2.4.2.9 F.E. model of a producing oil reservoir indicating induced bedding-parallel shear slippage 120

3.1.1 Schematic model of an interbedded rockmass with discontinuities, consisting of two lithologies, two faults, a joint set and bedding-planes. 123

3.2.1 End view of the direct shear rig parallel to the direction of sliding 125

3.2.2 Side view of the direct shear rig perpendicular to the direction of sliding 126

3.2.3 Scaled schematic of the direct shear rig, showing details of the control system and hydraulics 128

3.4.1.1 Schematic cross-sections illustrating macroscopic specimen deformation on direct shear of red sandstone, fissile mudrock, carbonaceous siltstone and heterolithic sandstone/ siltstone lithologies 139

3.4.1.2 Photomicrograph of laboratory direct shear specimen showing slickenslides, slickenlines and slickensteps 140

Figure Page

3.4.2.1 Schematic diagrams of a typical friction experiment and typical frictional force as a function of rider displacement results 141

3.4.2.2 Undrained direct shear results with intact and fractured samples of Lyons sandstone 141

3.4.2.3 Controlled normal stress and controlled normal displacement direct shearing modes 143

3.4.2.4 (a) Idealised relationship between dilation, shear and normal stress with shear displacement for CNS conditions, and (b) typical pattern of asperity failure under CNS conditions 145

3.4.2.5 Load-displacement curves for direct shear specimens 3,5 & 6 148

3.4.2.6 Load-displacement curves for direct shear specimens 8 & 9 149

3.4.2.7 Load-displacement curves for direct shear specimens 11, 12 & 14 150

3.4.2.8 Load-displacement curves for direct shear specimens S1, S2, S3 & S4 . 151

3.4.3.1 Geometry for the determination of the area of overlap of two circles with varying centre displacement 153

3.4.4.1 Displacement-stress plots for direct shear specimens #3, #5 & #6 156

3.4.4.2 Displacement-stress plots for direct shear specimens #8 & #9 157

3.4.4.3 Displacement-stress plots for direct shear specimens #11, #12 & #14 ... 158

3.4.4.4 Displacement-stress plots for direct shear specimens S1, S2, S3 & S4 .. 159

3.5.1.1 Maximum friction plot for direct shear data 170

3.5.2.1 Variable friction versus normal stress plots for the direct shear test data . 172

3.5.3.1 Frictional strength envelopes for direct shear specimens #3, #5 & #6 174

3.5.3.2 Frictional strength envelopes for direct shear specimens #8 & #9 175

3.5.3.3 Frictional strength envelopes for direct shear specimens #11, #12 & #14 176

3.5.3.4 Frictional strength envelopes for direct shear specimens S1, S2, S3 & S4 177

4.1.1 Schematic representation of coupled permeability - microseismics experimental testing facility, peripheral to the triaxial compression configuration 185

4.1.2 Overview of the triaxial compression system 187

4.2.1 Applied stress convention in the triaxial compression test 189

4.2.2 Block diagram of triaxial test arrangement 189

4.2.3 Principles of operation of the basic closed loop electro-hydraulic servo-system 193

4.4.1.1 Conventional parameters used to describe an AE signal 201

4.4.2.1 PAC-supplied calibration curve for the AE transducer used in this study 207

4.4.2.2 Scale drawing showing components of AE waveguide 209

4.4.2.3 Triaxial cell with waveguide and mounted AE transducer, sitting within stiff compression rig 210

5.2.1 Schematic of experimental programme for triaxial compression testing .. 215

5.3.1 Axial load-displacement curves for seven Clashach sandstone specimens deformed under different confining pressures 219

5.3.2 Mohr stress circle plots for Clashach sandstone with Coulomb and Griffith fracture strength envelopes 221

5.3.3 Mohr stress circle plots for Clashach sandstone with Coulomb-type frictional strength envelopes 221

5.3.4 Clashach sandstone triaxial compression specimens 225

5.3.5 Calculated and measured induced fault surface areas versus confining pressure operative at macroscopic fracture 225

5.4.1.1 (a) Axial permeability versus axial microstrain plots for seven Clashach specimens, and (b) percentage permeability reduction versus percentage specimen shortening 228

5.4.1.2 Axial permeability versus (a) hydrostatic stress and resolved normal stress post-dynamic failure, and (b) resolved normal stress post-frictional sliding and re-shearing 233

5.4.2.1 Schematic illustration of faulted core with shear band inclined to axial flow direction 236

5.4.2.2 (a) Inverse linear correlation between geometric constant and resolved normal stress and (b) linear correlation between axial permeability and geometric constant 238

5.5.1.1 Cantor Dust 243

5.5.1.2 Sierpinski Carpet 243

5.5.1.3 Mengor Sponge 243

5.5.2.1 Idealised synoptic model of damage development in a heterogeneous brittle solid under compression 249

5.5.2.2 Dependence of crack velocity and event rate on measured stress intensity KI from double torsion tensile experiments carried out in water at room temperature 252

5.5.2.3 Variation in b-value (and inferred crack-length distribution exponent, D) with stress intensity and crack tip "humidity" for a variety of crystalline rocks 252

5.5.2.4 Synoptic model of the evolution of seismic b-values predicted by Fig. 5.5.2.3 254

6.2.5.1 Self-similar gouge of cubic particles with $D = \log 6/\log 2 = 2.58$ 279

6.3.2.1 Schematic illustration of the optical configuration employed for laser particle sizing 284

6.3.2.2 Properties of scattered light for large and small particles 284

6.4.1.1 Influence of lithology on averaged (a) distribution and (b) absolute size Rosin-Rammler constants, of sieved direct shear debris 294

6.4.1.2 Schematic representation of the micromechanics of fault gouge comminution associated with macroscopic shearing of (a) quartzose granular and (b) phyllosilicate-rich rocks 297

6.4.2.1 Distribution functions for red sandstones #3, #5 & #6 299

6.4.2.2 Distribution functions for fissile mudstones #8 & #9 300

6.4.2.3 Distribution functions for carbonaceous siltstones #11, #12 & #14 301

6.4.2.4 Distribution functions for heterolithics S1, S2, S3 & S4 302

6.4.3.1 Empirical correlation between coefficient of sliding friction and inferred fractal dimension 306

6.4.3.2 Empirical correlation between inferred fractal dimension and specific surface area 306

6.4.3.3 Empirical correlation between coefficient of sliding friction and specific surface area 309

6.4.3.4 Stress and slip distributions near a crack tip with a breakdown zone in which the deformation behaviour is governed by the slip-weakening relation 312

6.4.3.5 Transformation of post-failure data from an initially intact triaxial compression test to infer the shear stress versus relative slip relation used in the slip-weakening model 312

6.4.3.6 Empirical correlation between shear fracture energy and specific surface area 316

6.4.3.7 Empirical correlation between shear fracture energy and inferred fractal dimension 316

6.4.3.8 Empirical correlation between shear fracture energy and the coefficient of sliding friction 316

6.5.1.1 Axial stress versus strain curves for Clashach specimens #23R & #24R 320

Figure Page

6.5.1.2 Thin-section photomicrographs of shear bands from Clashach specimens (a) #23R and (b) #24R 322

6.5.1.3 Shear band thickness/slip ratios versus resolved normal stress across the shear plane 325

6.5.1.4 Influence of resolved normal stress on (a) shear band permeability and (b) fault seaing potential 327

6.5.1.5 Influence of angular shear strain on (a) shear band permeability and (b) fault seaing potential 327

6.5.2.1 Straight-line graphical representations of the Rosin-Rammler function for laser-sized fault gouge distributions (a) 300mm-range lens (b) 45mm-range lens 330

6.5.2.2 Clashach fault gouge "coefficient of variation" versus (a) resolved normal stress and (b) angular shear strain 333

6.5.3.1 Empirical correlation between the Rosin-Rammler "coefficient of variation" and (a) shear band permeability and (b) fault sealing potential 336

6.5.3.2 Empirical correlation between shear band permeability and fault gouge specific surface area 336

AI.1 Red sandstone direct shear specimen #3 sliding surfaces i

AI.2 Red sandstone direct shear specimen #5 sliding surfaces ii

AI.3 Red sandstone direct shear specimen #6 sliding surfaces iii

AI.4 Fissile mudstone direct shear specimen #8 sliding surfaces iv

AI.5 Fissile mudstone direct shear specimen #9 sliding surfaces v

AI.6 Carbonaceous siltstone direct shear specimen #11 sliding surfaces vi

AI.7 Carbonaceous siltstone direct shear specimen #12 sliding surfaces vii

AI.8 Carbonaceous siltstone direct shear specimen #14 sliding surfaces viii

AI.9 Heterolithic direct shear specimen S1 sliding surfaces ix

AI.10 Heterolithic direct shear specimen S2 sliding surfaces x

Figure Page

AI.11 Heterolithic direct shear specimen S3 sliding surfaces..... xi

AI.12 Heterolithic direct shear specimen S4 sliding surfaces..... xii

AII.1 Temporal variation in stress, event rate, b-value and *D* for Clashach specimen #15 i

AII.2 Temporal variation in stress, event rate, b-value and *D* for Clashach specimen #16 ii

AII.3 Temporal variation in stress, event rate, b-value and *D* for Clashach specimen #18 iii

AII.4 Temporal variation in stress, event rate, b-value and *D* for Clashach specimen #19 iv

AII.5 Temporal variation in stress, event rate, b-value and *D* for Clashach specimen #20 v

AII.6 Temporal variation in stress, event rate, b-value and *D* for Clashach specimen #21 vi

AII.7 Temporal variation in stress, event rate, b-value and *D* for Clashach specimen #22 vii

AII.8 Stress, event rate, b-value and *D* versus axial microstrain for Clashach specimen #15 viii

AII.9 Stress, event rate, b-value and *D* versus axial microstrain for Clashach specimen #16 ix

AII.10 Stress, event rate, b-value and *D* versus axial microstrain for Clashach specimen #18 x

AII.11 Stress, event rate, b-value and *D* versus axial microstrain for Clashach specimen #19 xi

AII.12 Stress, event rate, b-value and *D* versus axial microstrain for Clashach specimen #20 xii

AII.13 Stress, event rate, b-value and D versus axial microstrain for Clashach specimen #21 xiii

AII.14 Stress, event rate, b-value and D versus axial microstrain for Clashach specimen #22 xiv

ACKNOWLEDGEMENTS

This thesis is dedicated to the memory of Patrick Bradshaw. I wish to acknowledge the guidance of my supervisor Prof.B.G.D.Smart, and to thank him for instilling in this "geologist" an appreciation and delight in hydraulics, engineering instrumentation and control.

This thesis has greatly benefited from the craft and learning of the following experts, whose contributions are appreciatively acknowledged: Prof.B.G.D.Smart for design of the direct shear rig and development of the pulse-decay permeameter system; Dr.I.G.Main for discussion of acoustic emission statistics, his fractal damage mechanics model, and self-organised criticality; Dr.B.T.Ngwenya for performing XRD analyses of the direct shear fault gouge; Dr.K.W.McGregor for instruction on operation of the direct shear rig; Mr.P.W.H.Olden for provision of a finite element model of reservoir deformation by bedding-parallel shear slippage.

Contributions from Petroleum Engineering MEng students C.McMeekin (pulse decay permeability, 1991) and C.Burnside (acoustic emission and micfrofracturing, 1992) whose theses proved invaluable to this study, are recognised and appreciated.

For stimulating discussion and constructive criticism, I wish to extend heartfelt thanks to all of my colleagues in the Rock Mechanics Research Group, including Dr.J.M.Somerville, Mr.J.S.Harper, Ms.S.A.Hamilton and Mr.P.W.H.Olden.

For adroit technical support, Messrs. J.Carlin and A.Winters (Strathclyde University) and Messrs. D.McLaughlin and C.Macleod (Heriot-Watt University) are thanked.

For assistance with typing and for continued support, Ms.J.L.Sewell's contribution is particularly acknowledged, and finally, for friendship and encouragement I must thank Dr.R.A.Farquhar and Mr.T.Manzocchi.

ABSTRACT

Shear fractures are defined in terms of the mechanism and homogeneity of deformation, macroscopic strength criteria and fracture mechanics parameters. The significance of shear discontinuities (encompassing both faults and planes of weakness reactivated in shear) within the hydrocarbon reservoir environment is emphasised with regard to both petrophysical properties (sealing potential) and controls on reservoir deformation, and an experimental rock mechanics programme has been undertaken to study fundamental aspects of their frictional strength and permeability. The design of a new direct shear rig is described, and initial results presented from a suite of experiments conducted under constant normal displacement control, analogous to ultra-stiff wall rock conditions. Load-displacement data for a variety of sedimentary lithologies, is analysed in terms of the mechanism of frictional sliding, with slip on induced wear debris (fault gouge) being found to conform to a simple linear strength law. A coupled permeability measurement and microseismics monitoring facility, for studying the influence of microstructural deformation on fluid flow under varying triaxially compressive stress states, is described. Data is presented for discrete failure and frictional sliding tests on a homogeneous sandstone. A method for estimating induced shear band permeability from axial core plug measurements is outlined. Computed permeability reductions range from 2.5 to 3.5 orders of magnitude, with shear band sealing exhibiting an order of magnitue increase with increasing resolved normal stress and angular shear strain. Acoustic emission is described using an existing fractal damage mechanics theory for fault nucleation, and suggests a condition of self-organised criticality during frictional sliding. Collected fault gouge from the direct shear and triaxial compression specimen suites has been analysed using both sieving and laser particle-sizing methods. Measured cumulative weight distributions are described using the Rosin-Rammler exponential function, implying fractal size-scaling. Correlations are presented between distribution constants and: (i) frictional resistance (coefficient of sliding friction and shear fracture energy) from direct shear testing; (ii) fluid flow (permeability and sealing potential) from triaxial compression testing. Such relations may reflect that portion of the total strain energy allocated to the creation of new surface area.

INTRODUCTION

The common reservoir engineering concept of a naturally fractured reservoir envisages a "sugar-cube" geometry in which the fractures are of infinite extent, constant aperture and regular spacing, and furthermore, the classification "naturally fractured" usually refers to those reservoirs in which open joints provide the major proportion of the effective permeability for fluid production. Whilst volumetrically, tectonic features generally contribute very little to the total porosity of a reservoir, the matrix porosity between tectonic surfaces is only effective porosity if these discontinuities do not possess reduced permeability characteristics. Although developments in probe permeametry have enabled quantification of sedimentary heterogeneity down to the lamina-scale, no parallel advance has been evident in similarly quantifying the flow characteristics of tectonic discontinuities which overprint the stratigraphy. To fully incorporate fault architecture into reservoir simulation model gridblocks, reliable predictions of their size population, spatial distribution, geometry and hydraulic characteristics are a prerequisite. However, although structural geological observations reveal small-scale faulting to be common in high porosity reservoir sandstones, the petrophysical properties and sealing characteristics of such tectonic surfaces remain surprisingly the least quantified of the above physical attributes. Also, reservoir deformation accommodated by slippage on shear discontinuities associated with production-related transients in *in situ* stress, is postulated to have major detrimental repercussions with respect to such phenomena as induced-seismicity and well casing-failure. In particular, the mechanism of bedding-parallel shear is highlighted, in which flexure above a compacting and subsiding reservoir generates excess shear stresses in the overburden, that can result in horizontal shear failure and slippage along weak lithologies such as shale intercalations.

Accordingly, an experimental rock mechanics programme has been undertaken expressly to study pertinent fundamental properties of shear discontinuities, including specifically frictional resistance and permeability. This study has focused in particular on the development and proving of laboratory equipment and techniques.

In Chapter 1, fundamental properties of brittle deformation are discussed, and shear fracturing defined in terms of the mechanism and homogeneity of deformation, macroscopic strength criteria and fracture mechanics parameters. In Chapter 2, the significance of shear discontinuities within the hydrocarbon reservoir environment is emphasised with regard to both petrophysical properties resulting in sealing behaviour and thus reservoir compartmentalisation, and control on production-related reservoir deformation. In Chapter 3, the design of a new servo-hydraulic direct shear rig is outlined. Initial load-displacement data generated by a variety of sedimentary lithologies, sheared under optimum frictional wear conditions corresponding to maximum suppression of discontinuity-normal dilation, is expressed in terms of a frictional strength law. In Chapter 4, a combined liquid permeameter and microseismics monitoring system, peripheral to a conventional rock mechanics servo-hydraulic triaxial compression configuration, is detailed, capable of quantifying fluid flow potential associated with microstructural deformation resulting from applied stress states. In Chapter 5, strength, acoustic emission and permeability results for compressive triaxial stresses ranging from hydrostatic to dynamic failure to frictional sliding conditions, are presented. Acoustic emission is quantified in terms of an existing fractal damage mechanics model, and a means of estimating shear band permeability from transient whole core measurements is outlined. In Chapter 6, experimentally-generated frictional wear products (fault gouge) resulting from both the direct shear and triaxial compression test programmes, are analysed using conventonal sieve and laser particle-sizing techniques. Small particle statistical parameters are used to describe the debris distributions, and are correlated with both frictional resistance and fluid flow. In Chapter 7, general experimental conclusions and recommendations for continuation of related research are elaborated.

1. BRITTLE SHEAR FRACTURING IN ROCK: AN OVERVIEW

1.1 INTRODUCTION

In this introductory chapter, brittle rock deformation and the various processes leading ultimately to shear localisation resulting in the formation of shear bands commonly referred to as faults, are reviewed. Macroscopic strength criteria representing both theoretical and empirical relationships between principal stresses on shear failure are contrasted with fracture mechanics theory describing the relationships between crack tip stresses and propagation modes. Both approaches are finally reconciled via a discussion of fracture criteria in the light of experimental results, which show that macroscopic shear fractures form by the coalescence of tensile microcracks.

In this chapter 1, primary attention is focused on assessing the formation and growth of shear *fractures* in rock material from the microscale to the macroscale (faulting). An important distinction thus exists between this chapter and the succeeding chapter 2, which deals with the role of shear *discontinuities*, specifically in the hydrocarbon reservoir environment. In the latter chapter, not only shear fracturing as discussed in chapter 1 is indicated (both tectonic shear fractures and "anthroprogenic" ones induced due to production-related stress changes) but also activation of pre-existing planar features in shear, such as joints and bedding planes. Thus in this instance, shear discontinuities is used as an "umbrella-term" encompassing both shear fractures (faults) formed by strain localisation and the coalescence of microcracks, as well as subsequent shearing of existing planes of weakness, resulting from a transient in the ambient physical conditions.

Throughout this thesis work fractures will be described as "shear fractures" (equivalent to "faults") if they exhibit shear displacement, and as "joints" if they are dilational features which exhibit no shear. Obviously this study is overwhelmingly concerned with the former fracture type, and will only touch on jointing when it serves to highlight important differences between the two fracture types such as mode of genesis, physical properties etc. A cautionary note is made at this stage regarding the increasing tendency in rock mechanics literature of referring to all planar discontinuities in the rockmass as "joints"

irrespective of their mode of displacement. Such a trend is not adhered to in this discussion.

1.2 DEFORMATION MECHANISMS AND LOCALISATION

For a full assessment of the way in which a rock has been deformed, both experimentally and tectonically *in situ*, two concepts are essential for a complete description:

(i) deformation mechanism(s) and,

(ii) the degree of homogeneity of the deformation (Rutter, 1986[1]).

Three fundamental deformation mechanisms can operate in rocks:

(i) Cataclasis, in which crystal structure remains undistorted but grains or groups of grains become cracked and the fragments may exhibit frictional sliding with respect to one-another. The process necessarily involves dilatancy and as such is pressure sensitive.

(ii) Intracrystalline plasticity, in which grains become internally distorted through dislocation motion or deformation twinning.

(iii) Flow by diffusive mass transfer (pressure solution), in which shape change of the deforming aggregate is achieved by stress induced diffusion of matter away from interfaces sustaining high normal stresses, with the same or different phases being re precipitated at potentially dilatant sites.

Whilst (ii) and (iii) can be constant volume processes and hence are relatively pressure insensitive, both are sensitive to temperature and deformation rate relative to (i).

Deformation can be heterogeneous due to localisation into a band (a brittle fault or ductile shear zone) in an otherwise homogeneously deforming (or rigid) body. Each of the above fundamental mechanisms can result in localised or distributed rock deformation depending on rock type and physical conditions as well as strain magnitude, localisation sometimes developing after a certain degree of homogeneous flow. With "brittleness"

being unequivocally associated with microcrack formation, and "ductility" defined as the capacity for more or less uniformly distributed flow, the former is therefore essentially a mechanistic concept defined at the microscopic level, whilst the latter must be defined at the macroscopic level and is independent of deformation mechanism. For example, in the earliest experimental studies on the "brittle to ductile transition" the transition from localised cataclasis (brittle faulting) to ductility due to distributed microcracking (cataclastic flow) was observed with increasing confining pressure at constant temperature. Ductility due to intracrystalline plasticity (deformation by the movement of dislocations or the twinning of crystals) on the other hand could be achieved experimentally by the application of yet higher confining pressures, or higher temperatures, or both. Rutter was particularly concerned by the restricted use of the term "ductility" which he felt was increasingly being identified purely with deformation by intracrystalline plasticity and thus being made mechanism dependent, to the exclusion of cataclastic flow processes. Also, it was stressed that cataclastic flow (cataclasis without localisation) which may involve microfracturing of every grain in the rock or may fragment the rock into cm-sized to sub-micron-sized pieces, can accommodate folding via small movements on homogeneously distributed bounding cracks. Thus in the above example both brittleness and ductility occur together and the scale of observation needs to be indicated, in this instance brittle on the grain scale, macroscopically ductile.

In order to avoid any confusion with regard to the nomenclature of mode of failure transitions in rocks, Rutter produced a simple diagrammatic representation showing some interrelationships between descriptions of mode of failure, expressed according to dominant deformation mechanism and degree of observed localisation (Fig.1.2.1). Deformation mechanisms are grouped into those involving dilatancy (cataclasis) and those NOT involving volume change (termed crystal-plastic) and combining flow by dislocation motion and by diffusive mass transfer. Various transitions between the modes of failure are shown, depending on combinations of changes in temperature, confining pressure, pore fluid pressure, strain and strain rate.

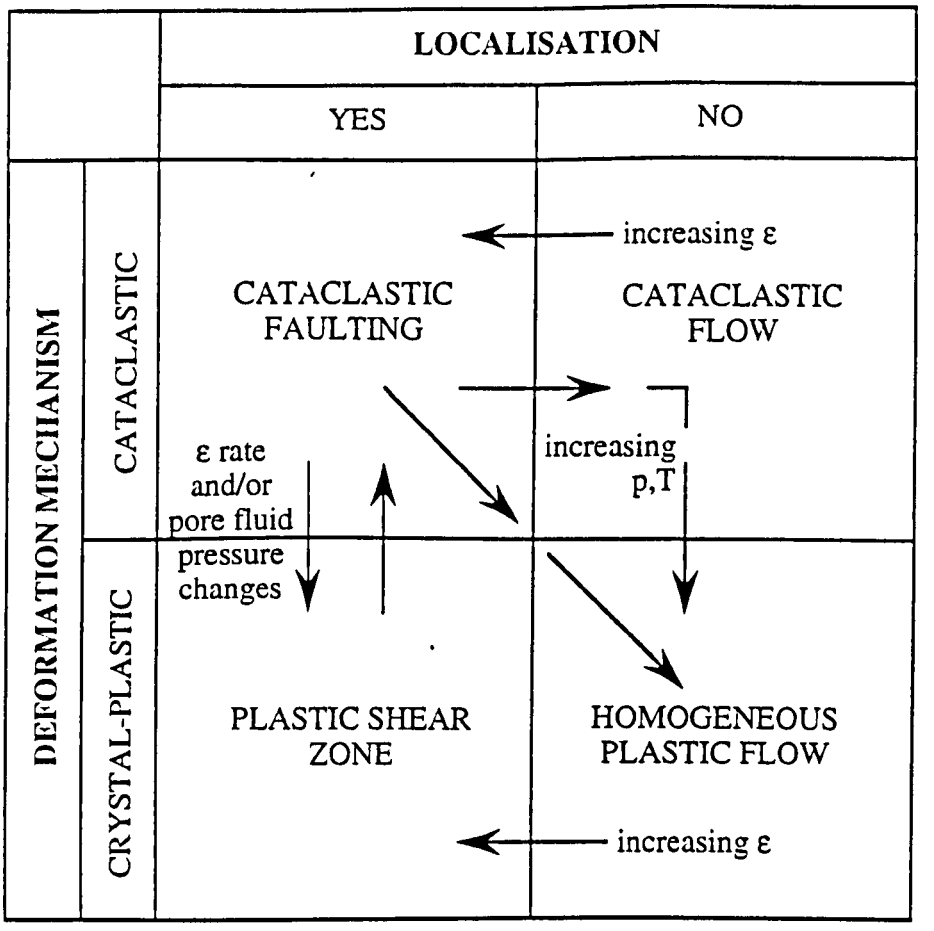

Fig.1.2.1 Mode of failure transitions in rock, after Rutter[1].

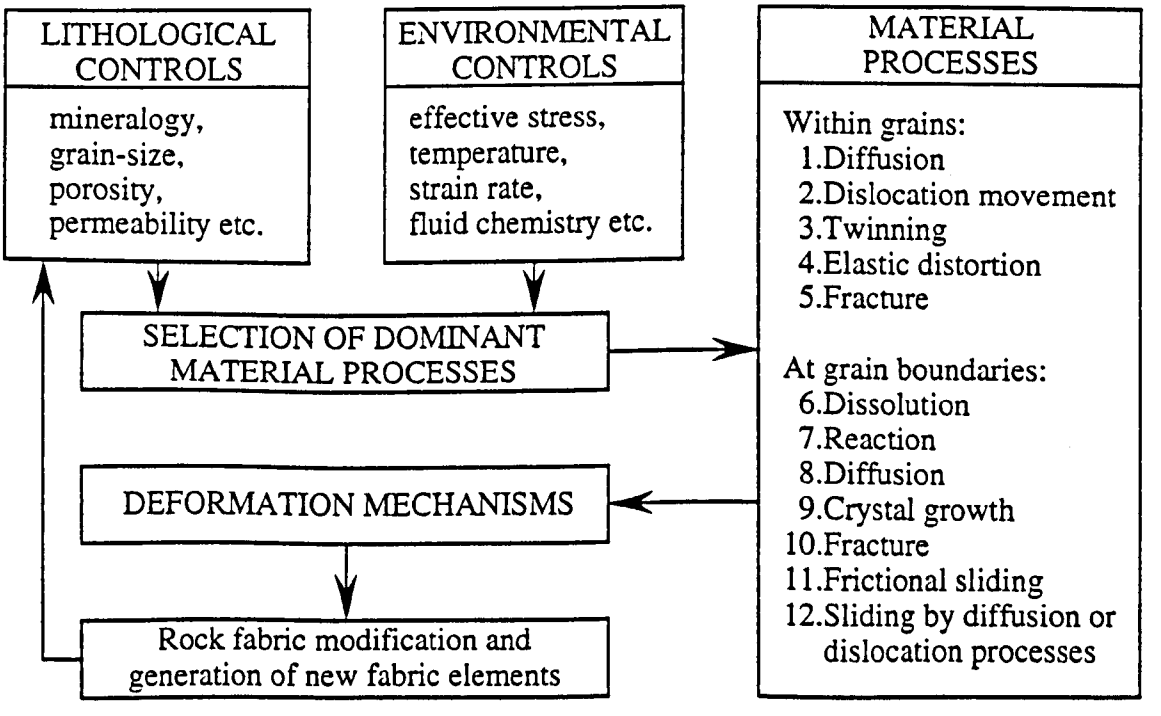

Fig.1.2.2 Flow diagram illustrating the inter-relationships between lithological and environmental controls with material processes during rock deformation, after Knipe[2].

Knipe (1989)[2] writes that the response of a rock to deformation is a function of a large number of environmental and lithological variables. Fig.1.2.2 lists these variables and outlines the ways in which these factors combine to activate a dominant set of material processes. The combined material processes operative in a rock under specific environmental conditions will control the deformation mechanisms which operate and thus the resultant microstructures which evolve. Knipe separates brittle deformation processes into:

(i) frictional grain-boundary sliding where fracture does not dominate the deformation and,

(ii) fracture processes.

Knipe writes that deformation by frictional grain-boundary sliding leaves individual grains essentially undeformed. with instead grains acting as rigid bodies and sliding past each other. In this respect, sliding commences when the cohesion and frictional resistance between grains is overcome, and therefore the initiation of sliding is critically dependent upon the amount and strength of cement bridges between the grains. Frictional grain-boundary sliding is a pressure sensitive mode of deformation, enhanced by low confining pressures and high fluid pressures (low effective stresses) and as such is prevalent in partially or unlithified sediments (Maltman, 1984[3]) and in fault zones containing incohesive gouges (Wang, 1986[4]). Intergranular frictional sliding has the potential to involve complex volume changes, where high fluid pressures and fluid influxes promote significant dilation and even fluidisation and liquefaction of the aggregate (c.f. soft sediment deformation structures) however late stage fluid losses may eliminate the grain-scale transient dilation. Large volume losses are also possible in clays and muds subjected to this deformation process, associated with preferred mineral alignment within the grain framework due to porosity collapse on fluid expulsion. Such deformation processes are cited as being responsible for faulting in partially lithified sediments recovered from DSDP cores. Knipe (1986)[5] proposes that fluid migration coupled with frictional grain-boundary sliding (resulting from fluid overpressuring or the regional

stress field) could induce a migrating wavefront of deformation in which the following sequential process migrates through partially lithified sediments:

dilation + fluid influx →
disaggregation + displacement →
collapse + grain alignment Eqn.1.2.1

Knipe regards this process involving the migration of fluid "packets" and pressure waves as being of potential importance in the evolution of bedding fabrics formed during compaction and in the alignment of clay particles in fault and shear zones.

Fracture processes are concerned with the nucleation, propagation and displacement along new surfaces created during deformation, Knipe (1989)[2] highlighting the fact that integration of the fracture mechanics approach, which defines the conditions and processes associated with single crack or fault propagation, has been of seminal importance in the interpretation of failure modes and conditions in rock. Some important applications of fracture mechanics theory, specifically to shear discontinuities in rock, will briefly be discussed in section 1.4. Fracture processes (in which fracturing dominates the deformation) also incorporate (or indeed are synonymous with) cataclasis, where fragmentation of material together with rotation and associated grain-boundary sliding and dilation, dominate faulting at high crustal levels producing fault gouges and breccias.

The simple classification of fracture mechanisms given below emphasises the range of pre-failure processes which influence or control the propagation of fractures: (i) Elastic strain accumulation, where the elastic strain energy associated with a stress concentration at a crack tip controls propagation. A number of theories are based on quantification of this stress intensity factor to predict conditions needed for crack extension at tips with different geometries and under different loads (see section 1.4). Developed fractures tend to follow microstructural weaknesses in the material and as such may be transgranular utilising cleavage orientations or intergranular in which case grain-boundaries are exploited. Thus the frequency, orientation, shape, aspect ratio and distribution of pre-

existing cracks, flaws, grain-boundary voids and pores can all influence the amount of strain capable of accumulating in a rock prior to failure by catastrophic fracture propagation; (ii) Crystal-plastic processes, can contribute to the fracture processes when dense dislocation tangles or high twin densities develop to inhibit further deformation by crystal plasticity and induce rapid work-hardening leading to fracture. Also, in polycrystalline aggregates juxtaposition of different mineral phases with different crystal structure orientations and thus different operating slip systems gives rise to strain incompatibility which can induce void formation along grain boundaries especially at triple points. Steady increase in the density of such features can eventually lead to failure; (iii) Diffusion processes, can lead to the development of voids at tensile grain-boundaries or triple points by the concentration of point defects or vacancies. Also, diffusion of impurities to grain-boundaries can result in their "embrittlement" and lead to failure; (iv) Phase transformations and reactions, by creating products with a different volume to the reactants can induce stress concentrations in an aggregate, resulting in void formation and leading ultimately to failure; (v) Fluid processes, have a fundamental role in fracture processes on two counts, mechanical and chemical. The former arise where fluid pressure causes hydraulic fracture with the effective stress exceeding the strength of the material. The latter involves the control of fracture propagation by the corrosion and reaction taking place at the crack tip leading to sub-critical crack growth (see section 1.4).

Whilst elastic strain energy accumulation is the main process associated with fast fracture propagation (brittle failure) all the above mechanisms may be involved in sub-critical crack growth at lower propagation velocities below the critical stress level needed for catastrophic failure (Fig.1.2.3).

Figure 1.2.3(a) illustrates the range of pre-failure processes that may be operative during fluid-absent deformation under different strain rate conditions. The broad arrow represents migration of the failure line position associated with an increase in temperature or confining pressure. Figure 1.2.3(b) shows the possibility of additional slow crack growth processes such as stress corrosion in an aqueous environment. The broad arrow indicates the movement direction of the failure line during an increase in the stress

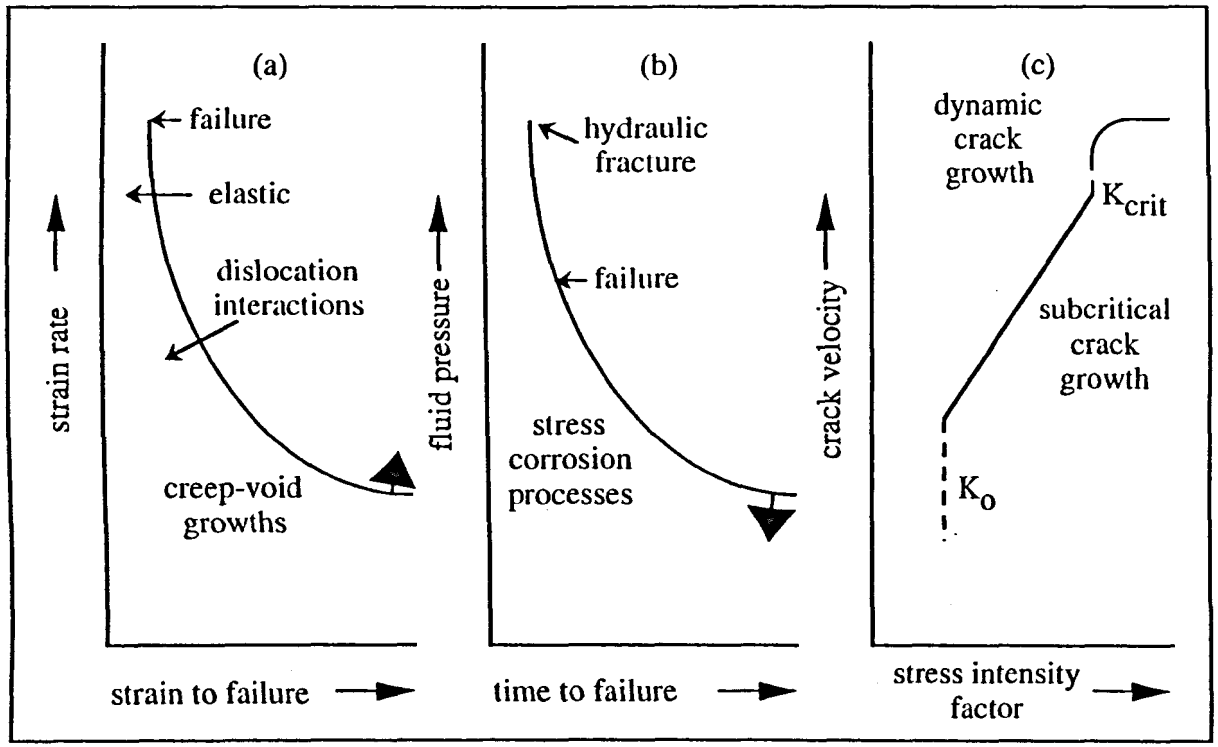

Fig.1.2.3 Review of fracture processes: (a) Range of pre-failure processes potentially operative during fluid-absent deformation under different strain rate conditions; (b) illustrating the possibility of additional slow crack growth processes such as stress corrosion in a fluid-rich environment; (c) fracture mechanisms associated with different crack velocities and stress intensity factors, after Knipe[2] (see text for details).

intensity factor and/or alteration in the fluid chemistry towards a more corrosive composition. Figure 1.2.3(c) shows the fracture mechanisms associated with different crack velocities and stress intensity factors. The stress intensity factor, K, equivalent to the driving force behind crack propagation, describes the stress field at the crack tip and is dependent on the loading conditions and material properties (see section 1.4). K magnitude ranges from K_o, below which sub-critical crack growth ceases, to K_{crit}, at which critical level the crack propagates catastrophically to approach the velocity of sound in the medium.

1.3 MACROSCOPIC STRENGTH CRITERIA

In section 1.2 above, an attempt is made to understand shear fracturing in rock in terms of both the mechanism and the homogeneity of deformation. In section 1.4 below fracture mechanics theory describes the conditions under which an individual crack will propagate in an elastic medium. It is a continuum mechanics approach in which the crack is idealised as a mathematically flat and narrow slit in a linear elastic medium. It seeks to analyse the stress field around the crack and then to formulate a fracture criterion based on certain critical parameters of the stress field. The macroscopic strength is thus related to the theoretical, intrinsic strength (that is the strength required to break the bonds across a lattice plane) of the material through the relationship between the applied stresses and the crack-tip stresses. However only in one special case, that of tensile fracture of a homogeneous elastic material, do these theories also predict the macroscopic strength. Thus in describing the strength of rock under general stress conditions, we are still forced to use criteria which are empirical or semi-empirical in nature. Such macroscopic fracture criteria had been well established by the beginning of the twentieth century (Coulomb, 1773[6], Mohr, 1900[7]) and thus pre-date the theoretical framework underlying fracture mechanics. A very brief summary of macroscopic strength criteria will be given below as many rock mechanics texts give detailed descriptions of these (see in particular the excellent account given in Jaeger & Cook, 1979[8], pages 95-106). In particular, attention will be focused on the Griffith criterion (as it possesses the attractive feature of combining both tensile and shear failure in a single criterion) to gain an understanding of

how the various fracture types (both shear and tensile) develop, and how their formation may be interpreted in terms of crustal stress and fluid pressure conditions.

There is no universal simple law governing the level of stress at which a specific lithology fractures as this level probably depends on the mode of fracture (tensile or shear) and also involves all principal stress components. To express the failure conditions in the most general way, an appropriate function is sought experimentally which has the three principal stresses, $\sigma_1 > \sigma_2 > \sigma_3$ as variables, which takes on a certain fixed value for any combination of the principal stresses at which fracture occurs. This condition, often written in the form:

$$\sigma_1 = f(\sigma_2, \sigma_3) \quad \ldots\ldots\ldots \quad \text{Eqn.1.3.1}$$

is known as a "failure criterion". The function, f, includes at least one variable characteristic of the material. However, the assumption cannot be made that a particular failure criterion, f, will necessarily apply to more than one particular mode of fracture, unless it can be shown that the underlying physical mechanisms are the same. In particular, it is possible that extension and shear fractures may be controlled by different criteria of failure. One such criterion, which experiment shows is generally adequate, is that tensile failure will occur with parting on a plane normal to the least principal stress, when that stress is tensile and exceeds some value T, the tensile strength, (Jaeger & Cook, page 90) thus:

$$\sigma_3 = -T \quad \ldots\ldots\ldots \quad \text{Eqn.1.3.2}$$

The accurate determination of the uniaxial tensile strength is notoriously difficult, both because of the experimental problem of achieving a macroscopically uniform tensile stress, and because of the inherently large scatter in the tensile strength of most rocks. Consequently, there is a general preference for obtaining T from an indirect test such as

the Brazilian disk method which gives more consistent results, although this approach rests on certain assumptions about stress distribution (see the discussion in section 6.3.1). The range of combinations of principal stresses over which the preceding conclusion (Eqn.1.3.2) can be tested is severely limited because of the narrow range of confining pressures in the triaxial test in which clearly internal extensile fractures can occur. With increasing confining pressure, a transition is soon made to shear fracturing, but even before the transition, complications arise concerning intrusion fractures in which the macroscopic stress field is perturbed by loading on the crack faces as the fracture propagates. In such a case Eqn.1.3.2 is no longer valid. This non-applicability is most obvious for the extension fractures that occur when all the principal stresses are compressive, and a similar exception probably should be made for the "axial-splitting" type of extension fracturing that occurs in uniaxial compression or at very low confining pressure, although difficulties may again stem from uncertainty about the true stress distribution (Paterson, 1978[9], pages23-24).

The failure stresses in the case of shear fracturing are known in much greater detail than those for extension fracturing, as measurement of the former comprises the bulk of triaxial testing carried out on many rock types and over a very wide range of confining pressures. It is found that the maximum differential stress, $\sigma_1 - \sigma_3$, preceding a brittle shear failure always depends markedly on the confining pressure. For some rock types, a linear relationship between principal stresses on failure is experimentally observed:

$$\sigma_1 = \sigma_o + k.\sigma_3 \quad \ldots\ldots\ldots \quad \text{Eqn.1.3.3}$$

Here, σ_o is the uniaxial compressive strength, and k is a constant known as the triaxial stress factor. However, for other lithologies a markedly non-linear relationship is evident (Fig.1.3.1). For triaxial compression tests in which each specimen fails in shear, usually only one shear plane is evident, although occasionally specimens exhibit two conjugate shear planes with opposite senses of shear. The acute angle (2θ) between them, which is

often considerably less than 90°, is bisected by the σ_1 direction. When the rock exhibits a linear relationship between principal stresses at failure, the angle 2θ is constant for all values of confining pressure, σ_3, however if the rock exhibits a curved relationship between these stresses, this angle 2θ is not constant, but increases as the confining pressure is increased. Two main concepts possess the capability to describe these different experimental relationships, namely the Coulomb and Griffith criteria. In section 6.3.1 the applicability of the Coulomb criterion is contrasted with that of the Griffith criterion for experimental triaxial compression data, however a brief summary of each theory will be given below with particular emphasis on their applicability to natural fracturing.

The Coulomb criterion (Coulomb, 1773[6]) remains the simplest and most widely reported of all the failure criteria, both theoretical and empirical. Coulomb had made extensive researches into friction (see section 4.5) and he suggested in connection with shear failure of rocks that the shear stress tending to cause failure across a plane is resisted by the cohesion (adherence) of the material and by a constant times the normal stress across the plane:

$$|\tau| - \mu\sigma_n = \tau_o \quad \ldots\ldots\ldots \quad \text{Eqn.1.3.4}$$

The constant τ_o may be regarded as the inherent shear strength of the material, and the constant μ, by analogy with "true" frictional sliding (see the definition of μ_s in Eqn.4.5.5) as a coefficient of internal friction of the material. Since the sign of the shear stress only affects the direction of sliding, only $|\tau|$ appears in the criterion. Introducing the angle of internal friction, ϕ^o:

$$\mu = \tan\phi \quad \ldots\ldots\ldots \quad \text{Eqn.1.3.5}$$

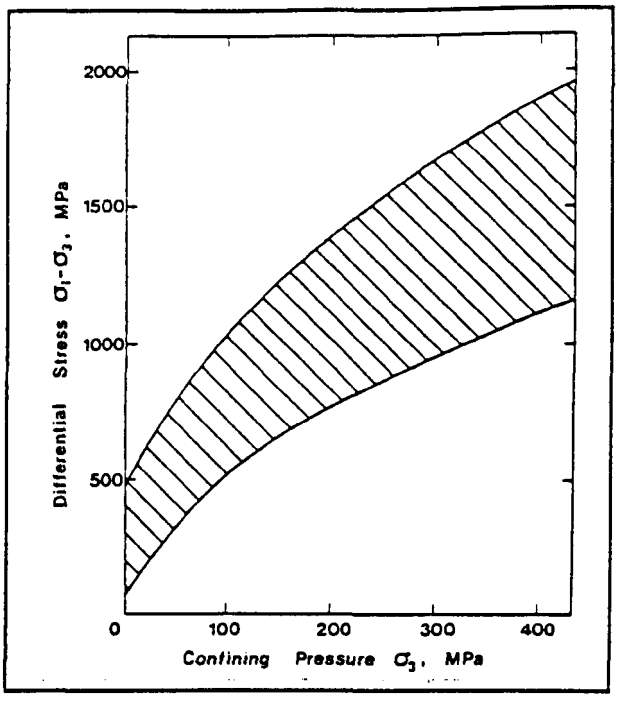

Fig.1.3.1 Limits to the dependence of differential stress at shear failure in compression on confining pressure for a wide range of igneous rocks, after Paterson[9].

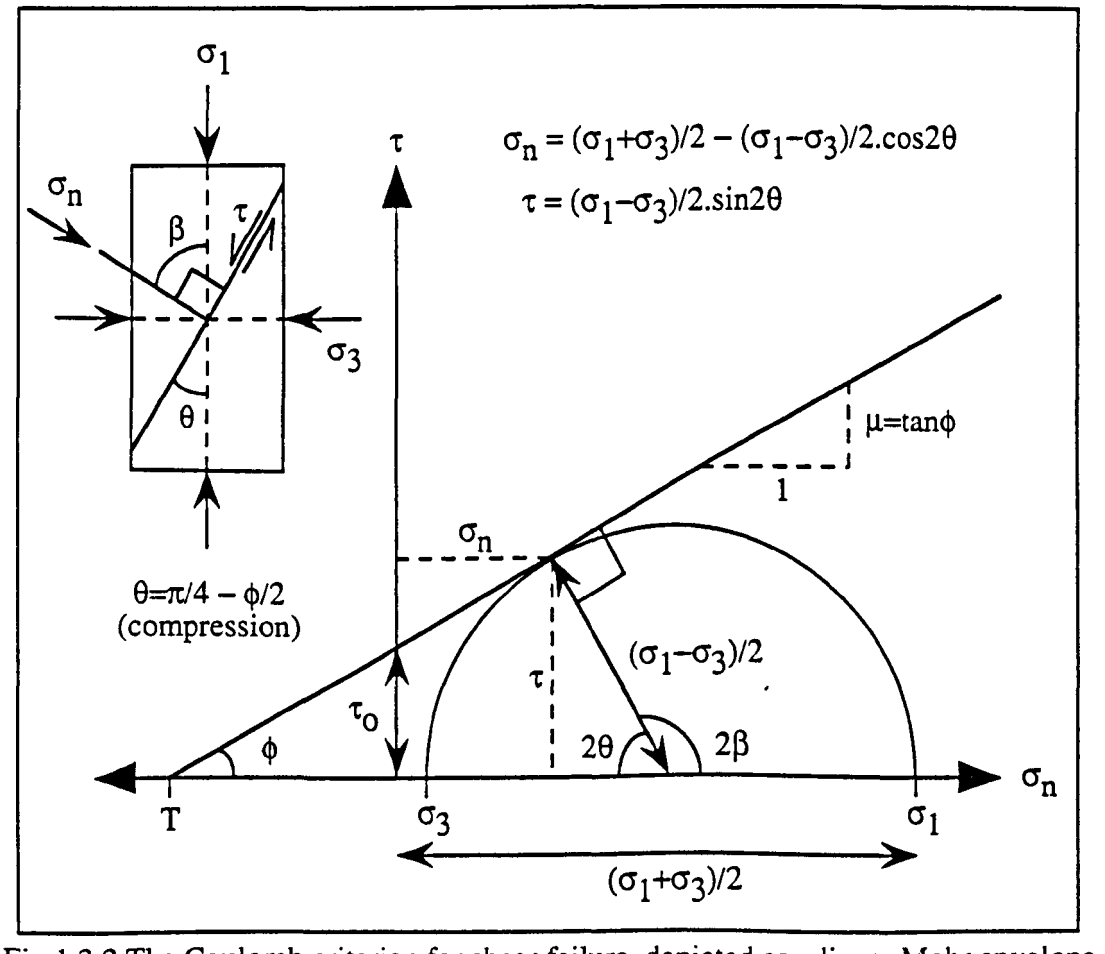

Fig.1.3.2 The Coulomb criterion for shear failure, depicted as a linear Mohr envelope

In this simple 2-D case, the intermediate principal stress, σ_2 (which is assumed to act parallel to the strike of the shear plane and at right-angles to the direction of shear) has, in theory, no influence upon failure. Whilst there are many methods of representing the variation of stress in 2-D that of the Mohr circle diagram is by far the most important and widely used (Mohr, 1900[7], 1914[10]). Using this method, particular combinations of σ_1 and σ_3 giving rise to shear failure are represented as Mohr circles in σ_n versus τ stress-space. The curve which is tangent to a series of such Mohr circles represents the failure conditions for that material under test. Thus, a linear relationship between principal stresses at failure, if represented by a series of Mohr circles, will exhibit a linear shear failure envelope with the equation of the Coulomb criterion (Eqn.1.3.3) as shown in Fig.1.3.2. From this construction it follows that:

$$(\sigma_1 - \sigma_3)/2 = [(\sigma_1 + \sigma_3)/2 + \tau_o(1/\tan\phi)]\sin\phi \quad \ldots\ldots\ldots \quad \text{Eqn.1.3.6}$$

Eqn.1.3.6 can be rearranged to fit the linear form of Eqn.1.3.3:

$$\sigma_1 = [(2\tau_o\cos\phi)/(1 - \sin\phi) + \sigma_3\{(1 + \sin\phi)/(1 - \sin\phi)\}] \quad \ldots\ldots\ldots \quad \text{Eqn.1.3.7}$$

Hence, from Eqn.1.3.7 it is apparent that the Coulomb criterion satisfies triaxial compression data for rock types with a linear relationship between principal stresses at failure. Further, from Eqn.1.3.7 it follows that:

$$k = (1 + \sin\phi)/(1 - \sin\phi) \quad \ldots\ldots\ldots \quad \text{Eqn.1.3.8}$$

$$\sigma_o = 2\tau_o.k\text{^}1/2 \quad \ldots\ldots\ldots \quad \text{Eqn.1.3.9}$$

Interestingly, the uniaxial compressive strength is related to both the cohesion and the angle of internal friction. An important feature of the Coulomb criterion is that the angle

θ between the shear fracture plane and the axis of the maximum principal stress (θ = fault^σ_1) can be predicted. To do this it is necessary to express the failure criterion as given in Eqn.1.3.4 in terms of the principal stresses, as depicted graphically in Fig.1.3.2. This expression is then differentiated with respect to θ and the optimum conditions for shear failure obtained. It can be shown that for optimum shear conditions:

$$\pm\theta = (45^o - \phi/2) \quad \text{.....} \quad \text{Eqn.1.3.10}$$

$$2\theta = 90^o - \phi \quad \text{.....} \quad \text{Eqn.1.3.11}$$

In Eqn.1.3.11 (minus sign for compression, plus sign for tension) 2θ is the acute angle between conjugate shear planes. This angle is represented graphically by the acute angle a tangent line to the linear envelope makes with the normal stress axis. A shortcoming of the Coulomb criterion lies in its prediction of the magnitude of the tensile strength, T, which from Fig.1.3.2 is:

$$T = \tau_o/\tan\phi \quad \text{.....} \quad \text{Eqn.1.3.12}$$

For angles of $\phi<45^o$, that is for most sedimentary rocks, it follows that the predicted tensile strength is greater than the cohesive strength, however this prediction is at variance with empirical experience which frequently shows tensile strength to be around half the magnitude of the cohesion.

Jaegar & Cook (page 425) note that, "all the phenomena of brittle fracture studied.....on a laboratory scale appear to be reproduced on a geological scale. Faults are geological fractures of rock in which there is relative displacement in the plane of fracture. They are thus shear fractures.....and Griggs and Handin 1960)[11] and others have used the term "fault" for shear fractures both on the laboratory and geological scale." Geological faulting was discussed by Anderson (1951)[12] on the basis of the Coulomb and Mohr theories of shear fracture and classified according to the relative magnitudes of the

principal stresses, $\sigma_1 > \sigma_2 > \sigma_3$. Anderson based his classification on the general observation that in many areas of the world, especially in those of low topographic relief, it an be inferred from studies of joints, faults and dykes, that the axes of principal stress are close to the horizontal or vertical. Anderson postulated a "standard state" of stress in the Earth's crust, equivalent to a hydrostatic state in that the magnitudes of the horizontal stresses at any specific depth in the crust, are equal to that of the vertical geostatic stress induced at that depth by gravitational loading. Based on the Coulomb and Mohr theories, fracture takes place in one or both of a pair of conjugate planes which pass through the direction of σ_2 and are equally inclined at angles $<45^o$ to the direction of σ_1. Since the surface of the earth is a free surface, one of the principal stresses at the surface must be normal to it, so it is reasonable to assume that one principal stress is vertical at moderate depths. Anderson postulated that the magnitudes of the horizontal stresses, relative to that of the vertical geostatic stress, could change in one of three ways and (if the changes in the magnitudes of the stresses were sufficient) could result in fault formation. The three cases (depicted in Fig.1.3.3) are:

(i) both horizontal stresses decrease in magnitude, but not by the same amount
(ii) both horizontal stresses increase in magnitude, but not by the same amount
(iii) one horizontal stress increases in magnitude whilst the other horizontal principal stress decreases in magnitude

Such variations in horizontal stress lead to the triaxial stress states illustrated in Fig.1.3.3 which, if the magnitude of the differential stresses is sufficiently large, will result in the three main types of faults, normal, thrust (reverse) and strike-slip (wrench).Whilst Anderson did not specify the magnitude of the stress changes required to initiate these three types of "Andersonian" faults, Sibson (1973)[13] estimated the relative magnitudes of the differential stress $(\sigma_1 - \sigma_3)$ required to cause slip on these faults subsequent to their initiation at: thrust: normal: strike-slip = 4: 1.6: 1. The above Andersonian classification of faults is applicable to the initiation of idealised, perfectly planar discontinuities that develop in geological environments where one of the principal stresses acts vertically and the others in the horizontal plane. However, it may be inferred from many geological

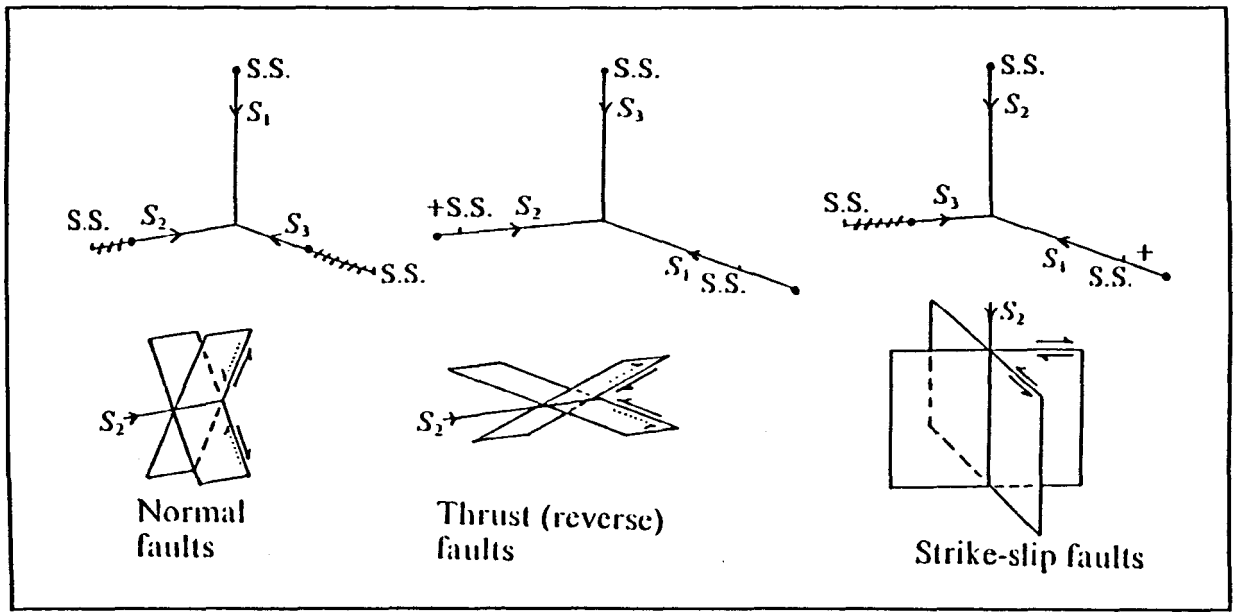

Fig.1.3.3 Andersonian fault classification showing the three possible ways in which the "standard state" (SS) may be varied, producing the three corresponding fault-types- normal, thrust (reverse) and strike-slip, after Price & Cosgrove[26].

structures that the axes of principal stress are inclined away from the vertical and horizontal (for example asymmetric folds imply an axis of principal compression inclined to the horizontal).

Broadly speaking, two different approaches have been taken in the development of a theory of brittle failure to predict macroscopic fracture stress. The first, *empirical* approach advocates criteria of failure consistent with observed failure conditions under particular experimental configurations but whose applicability is intended to extend to more general stress states. The Coulomb and Mohr criteria are thus failure theories in this sense. Although they are discussed in physical terms such as limits on stresses on particular planes, they do not attempt to address the physical mechanisms of failure and are therefore best regarded as empirical. Their main role is to provide a basis for calculating failure conditions in practical situations. The second approach attempts to build up physical models of brittle fracture which are amenable to *theoretical* treatment, so that, whilst a degree of empiricism is still involved, the models aim to contribute to the physical understanding of the fracture process. The Griffith theory, and those approaches based on it, are the best-known in this second group.

An excellent overview of the Griffith-type theories of brittle failure can be found in Paterson[9], pages51-70. One of the most significant advances in the theory of fracture was the proposal made by Griffith in 1920[14] that the strength of brittle materials is governed by the initial presence of small cracks or "flaws". To calculate the tensile strength, Griffith introduced an approach which in effect uses surface energy as a measure of the local cohesive strength of the material. This failure criterion, based on the principle that the potential energy of a system will tend to a minimum, is that the crack will propagate if in doing so the sum of the following three terms is zero or negative:

(i) the surface energy of the newly created crack

(ii) the change in the elastic strain energy of the body

(iii) the change in the potential energy of the loading system

Since, in the absence of any other changes, this sum represents the change in the Gibbs potential, the energy criterion is equivalent to requiring the Gibbs potential to be minimised, and it is therefore sometimes referred to as the "thermodynamic criterion of failure". In the case of an applied uniaxial macroscopic tensile stress, σ_t, the energy criterion predicts failure at the stress:

$$\sigma_t = T = [\beta(E\gamma/c)]^{1/2} \quad \text{.....} \quad \text{Eqn.1.3.13}$$

- σ_t: maximum applied tensile stress
- T: measured macroscopic tensile strength
- β: numerical constant of the order of unity
- E: Young's modulus of material
- γ: surface energy of crack
- 2c: crack length = major diameter of elliptical cross-section (minor diameter assumed negligibly small)

Griffith demonstrated that the maximum tensile "tip" stress can become sufficiently large so that it equals the atomic bonding strength and so permits the "critical" crack to propagate, when the applied σ_t equals Eqn.1.3.13. The exact value of β depends on the assumptions made in calculating the local elastic stress distribution around the crack. If plane strain is assumed, $\beta = 2/[\pi(1 - \nu^2)]$ where ν is Poisson's ratio; if generalised plane stress is assumed, $\beta = 2/\pi$; for penny-shaped ellipsoidal cracks (c.f. Sneddon, 1946[15]) $\beta = \pi/[2(1 - \nu^2)]$. It is implicit that the crack is normal to the applied stress. If there is a random distribution of crack orientations, each with given length 2c, the crack that will first begin to extend when the stress satisfies Eqn.1.3.13, will be the one whose major axis lies normal to the direction of applied stress. It is possible to argue from atomic bonding theory (see for example Scholz, 1990[16], pages1-3) that the theoretical tensile strength of ideal brittle solids is approximately T = E/10. For many strong rocks, E=100GPa so that T=10 000MPa! Griffith suggested that the vast discrepancy between theoretical and observed material tensile strengths was the direct result of the intense

local stress concentrations which developed at the tips of microscopic flaws. Using reasonable values for the physical constants in Eqn.1.3.13, he obtained values for the critical stress, σ_t, which were in good agreement with the measured values of tensile strength, T, for large specimens of glass. He also prepared "fibres" of glass free from flaws and surface imperfections, and found that the tensile strengths of such specimens were as much as 4500MPa, in reasonable agreement with the theoretical atomic bond strength.

In the application of Griffith's energy hypothesis in deriving a formula for the uniaxial tensile strength, it is implicit that the crack will spread in its own plane. This assumption permits a unique calculation of the energy changes resulting from extension of the crack. However, in applying this theory to more complicated stress states and in particular to compressive stress states, two difficulties arise:

(i) it can no longer be assumed that the crack will spread in its own plane
(ii) if the crack is of negligible width, it will tend to close under predominantly compressive conditions, and it can no longer be considered that the crack faces are not loaded

Griffith (1924)[17] avoided the first problem by changing to a critical maximum local tensile stress criterion of failure, and the second by considering only open cracks. This Griffith theory for a biaxially stressed body with randomly orientated cracks of a given length proceeds in the following steps (see full details in Jaeger & Cook pages 277-280):

(i) from an elastic stress distribution around an elliptical cavity with free faces, the maximum tensile stress component is obtained for an arbitrary orientation of the cavity with respect to the applied stresses
(ii) the cavity orientation is determined for which this maximum local tensile stress is greatest, and the applied stresses are then calculated for a critical value of the maximum local tensile stress thus obtained

(iii) the critical value of the local tensile stress is obtained from the uniaxial test and is expressed in terms of the uniaxial tensile strength

Griffith considered the 2-D problem of propagation of cracks in a sheet subjected to biaxial compression. In it he assumed that randomly orientated, elliptical microcracks in such a sheet were so spaced that the stress field associated with each did not interfere with that of its neighbour (the cracks were isolated). Griffith showed that even when the applied stresses are compressive, the "tip" stresses associated with each flaw would be tensile and that these tip stresses would be a maximum for elliptical cavity orientation at which the failure is initiated, θ, given by:

$$\cos 2\theta = 1/2[(\sigma_1 - \sigma_3)/(\sigma_1 + \sigma_3)] \quad \ldots\ldots\ldots \quad \text{Eqn.1.3.14}$$

Here θ is the angle between the major axis of ellipse and the maximum principal stress σ_1. However, since the maximum local tensile stress does not occur exactly at the end of the major axis and is not normal to the major axis, the cracking will develop in an orientation inclined to the major axis of the ellipse and more nearly parallel to the maximum macroscopic principal stress, σ_1 (see Jaeger & Cook, pages 342-345 for a fuller account). This tendency for a crack to propagate out of its own plane under predominantly compressive conditions (Fig.1.3.4) has been demonstrated experimentally by Brace & Bombolakis (1963)[18]. The above procedure leads to the macroscopic criterion of failure, generally known simply as the (plane) Griffith criterion and expressed in terms of the biaxial principal stresses σ_1, σ_3 (compression positive) and the magnitude of the uniaxial tensile strength, T, as:

$$(\sigma_1 - \sigma_3)^2 - 8T(\sigma_1 + \sigma_3) = 0 \quad \text{if } \sigma_1 > -3\sigma_3 \quad \ldots\ldots\ldots \quad \text{Eqn.1.3.15}$$

$$\sigma_3 = -T \quad \text{if } \sigma_1 < -3\sigma_3 \quad \ldots\ldots\ldots \quad \text{Eqn.1.3.16}$$

The condition of $\sigma_1 > -3\sigma_3$ defines the stress states of "predominantly compressive character". Whilst the above equations were formulated by Griffith for biaxially compressive macroscopic stresses, Orowan (1949)[19] argued that the Griffith criterion as above can be applied to general states of stress because normal or shear stresses acting on the plane perpendicular to the edge of the crack will not appreciably influence the failure condition. For this reason, the Griffith criterion for biaxial stresses, and often without any supporting argument, has been applied directly to the analysis of conventional triaxial tests, in the form of Eqn.1.3.15 and Eqn.1.3.16.

Murrell (1958)[20] expressed this non-linear relationship between principal stresses at failure as a Mohr's envelope (Fig.1.3.5) with the parabolic equation:

$$\tau^2 = 4T(\sigma_n + T) \quad \ldots\ldots\ldots \quad \text{Eqn.1.3.17}$$

For the tensile fracture portion of this shear failure envelope, the most critically orientated crack is normal to σ_3. For the shear portion, it is inclined at an angle θ to the σ_1 direction. This criterion is based on a microscopic failure mechanism and has the attractive feature of combining both tensile and shear failure in a single criterion. It predicts a cohesive strength as defined for the Coulomb shear failure criterion, of $\tau_0 = 2T$ which is in good agreement with experiment. This follows because $\tau = \tau_0 = 2T$ in Eqn.1.3.17 when $\sigma_n = 0$. It also predicts a uniaxial compressive strength value, $\sigma_0 = 8T$ from Eqn.1.3.15 by setting $\sigma_3 = 0$, which, though smaller than generally observed, is also of the correct order. Like the Coulomb criterion, the plane Griffith also predicts that σ_2 exerts no influence on macroscopic strength.

Murrell (1963[21], 1965[22]) made an alternative suggestion to Orowan, that the biaxial criterion of Griffith can be generalised in or "extended" to triaxial stress, as a paraboloid of equation:

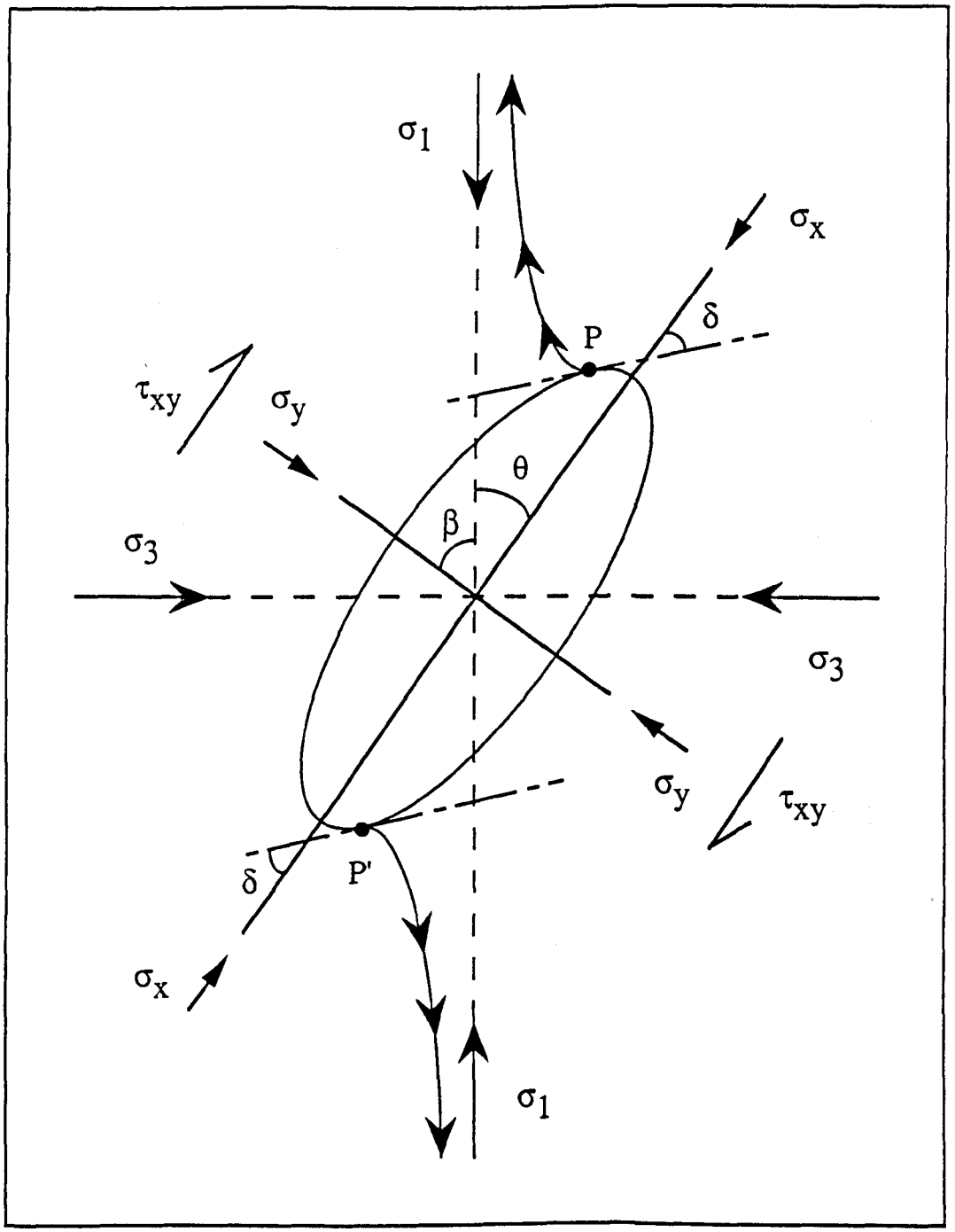

Fig.1.3.4 Schematic open crack in compression showing the positions P & P' of maximum tangential tension and the directions of initial crack extension, modified from Jaeger & Cook[8].

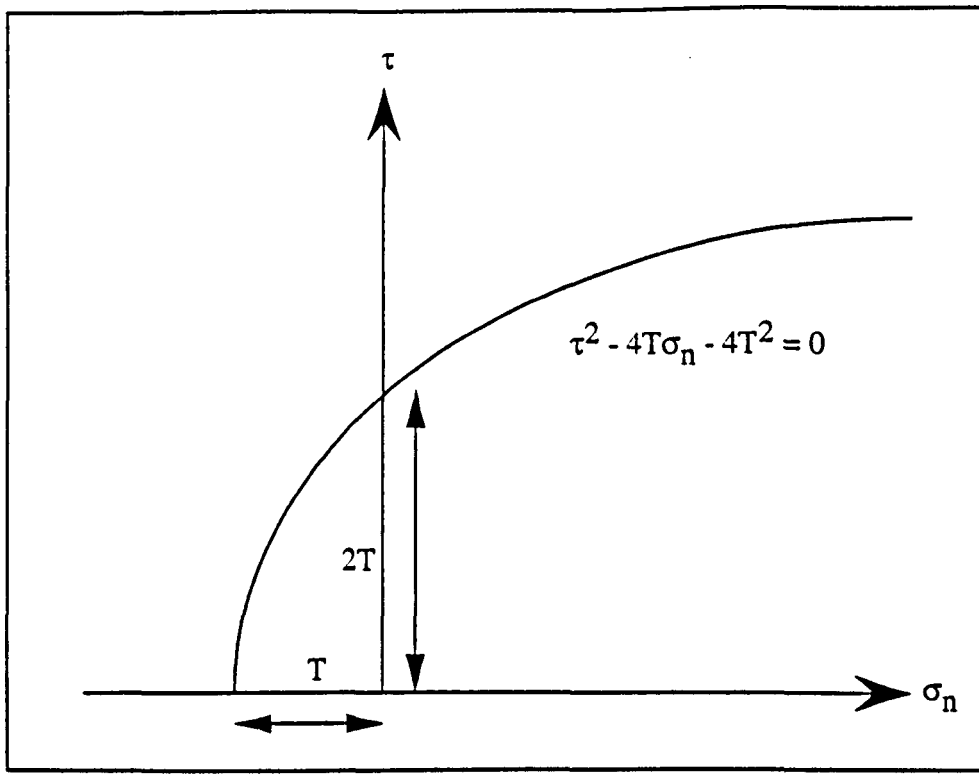

Fig. 1.3.5 The Griffith parabolic failure envelope

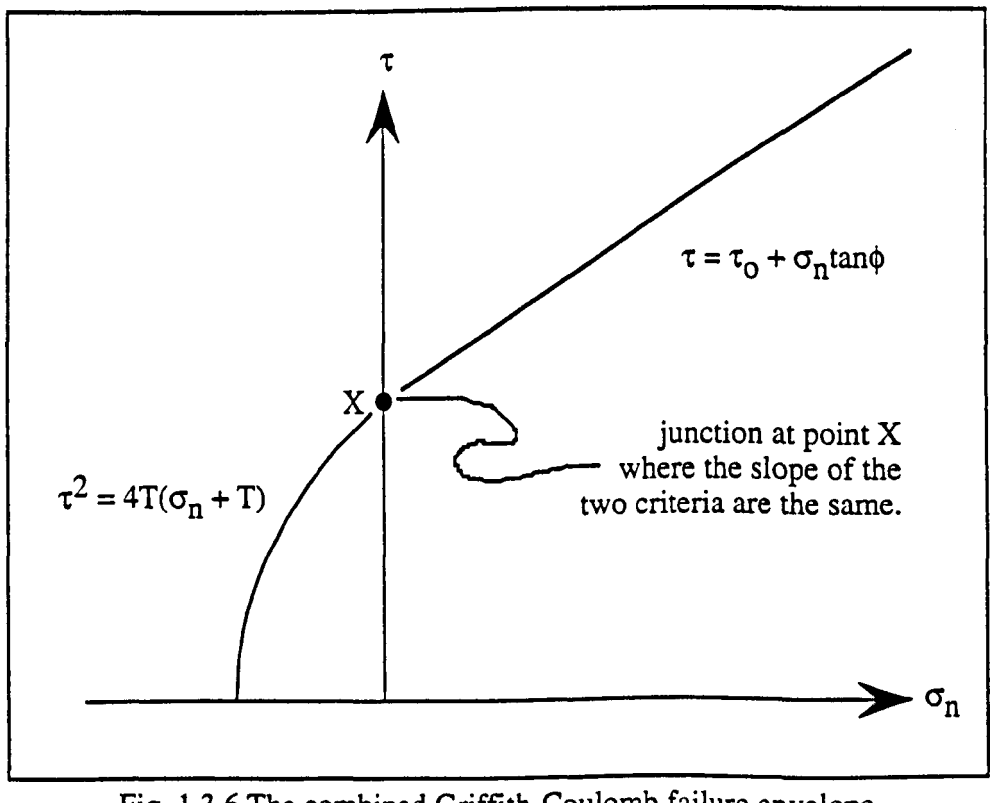

Fig. 1.3.6 The combined Griffith-Coulomb failure envelope

$$(\sigma_1 - \sigma_3)^2 + (\sigma_3 - \sigma_1)^2 + (\sigma_1 - \sigma_2)^2 - 24T(\sigma_1 + \sigma_2 + \sigma_3) = 0 \quad \text{.....} \quad \text{Eqn.1.3.18}$$

This paraboloid is truncated by the planes $\sigma_1 = -T$, $\sigma_2 = -T$, $\sigma_3 = -T$ (for fuller details of Murrell's extension of the Griffith criterion see Jaeger & Cook, pages103-106). This criterion has the features that it gives the more realistic value of 12 for the ratio of σ_0 to T, that it introduces σ_2, and that it is symmetric with respect to the three principal stress axes, however there appears to be no reason for selecting this triaxial criterion except on empirical grounds.

The theory leading to the plane Griffith criteria of Eqn.1.3.15 and Eqn.1.3.16 neglects the fact that cracks may be expected to close under sufficiently high compressive stresses. Also, on closure, it may be expected that frictional forces will operate between the closed surfaces. In experiments under moderate confining pressure it is likely that many of the cracks in a rock will close under the action of an applied stress component normal to the plane. An indication of this closure is the increase in velocity of sound waves with applied hydrostatic pressure, an increase which flattens out at high pressures (see section 1.5). After closure the crack faces will exert a normal force on each other and, since the only relative displacement of crack faces during spreading of the crack is then sliding, a tangential loading will also be introduced on the crack faces. Addressing these effects under the assumption of uniform distribution of forces on the crack faces, McLintock and Walsh (1962)[23] calculated the conditions for crack extension under biaxial stress for a model similar to Griffith's, except that the cracks were assumed to close under a certain value, σ_c, of the macroscopic normal stress component perpendicular to the crack. This theory, known as the "modified Griffith theory" (see Jaeger & Cook pages 280-282) was extended by Murrell & Digby (1970)[24] to a general three-dimensional problem with closed cracks. Griffith[17] derived his criterion for failure under 2-D stresses at infinity by studying in detail the variation of the tangential stress in the surface of a flat elliptical

crack with major and minor semi-axes. The principal stresses, σ_1 and σ_3, are taken to be inclined at $(\pi/2+\beta)$ and β to the maximum principal stress direction, but it is also convenient to use their components in crack coordinates, σ_x and σ_y (see Fig.1.3.4). McLintock & Walsh[23] assumed that a normal stress σ_c at infinity is necessary to close the crack. They then assumed that the normal stress across the surface of the closed crack is $\sigma_n = \sigma_y - \sigma_c$ and that a frictional force $\tau_f = \mu.\sigma_n$ resists sliding across the surface. These frictional sliding stresses were then superimposed on the stress field around the flaw (from the solution derived by Griffith) to arrive at a relationship between principal stresses at failure. In both biaxial and triaxial cases, when the cracks are closed, the initiation of failure is governed by the criterion:

$$[(1 + \mu^2)^{1/2} - \mu].(\sigma_1 - \sigma_3) = \alpha'T(1 + \sigma_c/T)^{1/2} + 2\mu(\sigma_3 - \sigma_c) \quad \text{.....} \quad \text{Eqn.1.3.19}$$

or the equivalent Mohr envelope:

$$\tau = \alpha'/2T(1 + \sigma_c/T)^{1/2} + \mu(\sigma_n - \sigma_c) \quad \text{.....} \quad \text{Eqn.1.3.20}$$

In these expressions, σ_1 and σ_3 are the greatest and least principal stresses (compression positive) τ and σ_n are the maximum shear stress and the normal stress on the plane of the crack at which failure is initiated, that is the plane containing the intermediate principal stress axis and inclined at the angle θ to the σ_1 axis where $\tan 2\theta = 1/\mu$, μ is the coefficient of friction on the crack faces and σ_c is the critical macroscopic compressive stress perpendicular to the crack required to close it. In the general triaxial case (Murrell & Digby[24]) the constant α' is a complicated function of Poisson's ratio, ν, and the crack aspect ratio. For the penny-shaped crack it reduces to $\alpha' = 2(2 - \nu)$. In the biaxial case (McLintock & Walsh[23]) $\alpha' = 4$. In both these biaxal and triaxial cases, again the predicted criterion of failure is independent of σ_2. In contrast to the parabolic form of the criterion for open cracks (Eqn.1.3.17) the criterion for closed cracks (Eqn.1.3.20) is linear, and therefore has the same form as the Coulomb criterion, with a cohesion, τ_o, of:

$$\tau_o = \alpha'/2T(1 + \sigma_c/T)^{1/2} - \mu\sigma_c \quad \ldots\ldots\ldots \quad \text{Eqn.1.3.21}$$

The coefficient of internal friction, $\tan\phi$, is equal to the coefficient of friction, μ, of the closed cracks. If the cracks or "flaws" correspond to long narrow notches which close under very low normal stresses, then σ_c becomes negligibly small so that Eqn.1.3.19 and Eqn.1.3.20 become respectively:

$$[(1 + \mu^2)^{1/2} - \mu].(\sigma_1 - \sigma_3) = \alpha'T + 2\mu\sigma_3 \quad \ldots\ldots\ldots \quad \text{Eqn.1.3.22}$$

$$\tau = (\alpha'T)/2 + \mu\sigma_n \quad \ldots\ldots\ldots \quad \text{Eqn.1.3.23}$$

These equations, representing a linear relationship between principal stresses at failure and the corresponding Mohr envelope, differ only from the Coulomb criterion in that the cohesive strength, τ_o, is equal to $(\alpha'T)/2$ or $2T$ in the biaxial case. This led Brace (1960)[25] to suggest that this formed the physical basis of the Coulomb criterion. Thus the question of which of the two criteria discussed here (Coulomb or Griffith) best fits experimental data, is partly resolved by McLintock & Walsh[23] whose analysis suggests that each represents an end member in a continuum of failure conditions. Crack closure will not take place in a tensile stress field, so that the form of the envelope in tension will be determined by Eqn.1.3.17, so that the form of the complete envelope will most likely be as shown in Fig.1.3.6, where the junction between the two criteria occurs where the slopes of each are identical.

In the preceding section 1.3 on macroscopic strength criteria, emphasis has been placed on the development of shear failure, when the least principal stress, σ_3, has been compressive (positive). However, under some crustal conditions, it is possible for the pore pressure, p, to be greater in magnitude than the least principal stress, so that the least effective stress, σ_3', is tensile (negative). Depending upon the magnitude of the least principal stress, σ_3, and also upon the value of the differential stress $(\sigma_1 - \sigma_3)$ both

expressed relative to the tensile strength of the rock, T, Price & Cosgrove (1990[26], pages 29-34) suggest that failure can occur in one of two ways:

(i) if $(\sigma_3 - p) > T$ and also $(\sigma_1 - \sigma_3) < 4T$ failure will occur in tension and one or more fracture planes willl develop perpendicular to the axis of the least principal compressive stress as the result of hydraulic fracturing

(ii) if $0.8T < (\sigma_3 - p) < T$ and also $4T < (\sigma_1 - \sigma_3) < 5.5T$ hybrid extension and shear forms of failure may occur

The above crucial stress conditions are derived in the following manner. The first condition for tensile failure merely implies that the least effective principal stress must attain a magnitude sufficiently great to overcome the inherent resistance of the rock to fail in tension. The second is based on the geometry of the parabolic failure envelope predicted by the Griffith criterion. From Fig.1.3.7 it can be inferred that stress circles which touch the failure envelope at the coordinates (-T, 0) cannot have a diameter greater than 4T. Mohr circles with diameters greater than 4T must touch the envelope at some other coordinate, and so will give rise to some form of failure in shear rather than in tension (see Eqn.1.3.15 and Eqn.1.3.16). For the second type of failure, that of hybrid extension and shear, consider the stress condition when $(\sigma_1 - \sigma_3)$ exceeds 4T by a small amount, and when the least effective stress is tensile and relatively large, but smaller in magnitude than the tensile strength of the rock (as shown in Fig.1.3.8). Here, the appropriate Mohr stress circles touch the failure envelope in the tensile (negative) sector. Mohr's hypothesis suggests that the Coulomb condition for predicting the angle θ between the failure surface and the axis of maximum principal stress (see Eqn.1.3.10 and Eqn.1.3.11) can be extended to non-linear failure envelopes. Accordingly, he suggested that if, at the point where the stress circle touches the failure envelope, a tangent is drawn to the envelope, then the acute angle which a line drawn perpendicular to that tangent makes with the normal stress axis defines the angle 2θ between conjugate shear surfaces. Mohr's empirically-based suggestion was later demonstrated by Griffith to be analytically valid. For the stress and failure conditions shown in Fig.1.3.8, it is obvious that the

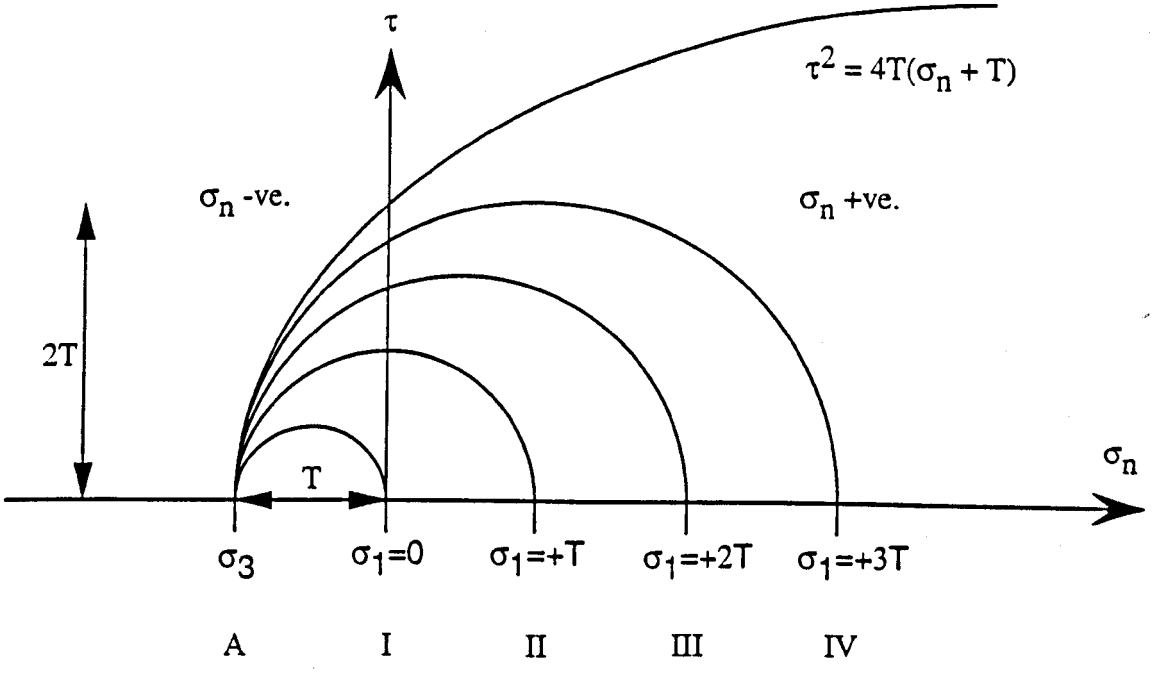

$(\sigma_3 - p) > T$

$(\sigma_1 - \sigma_3) < 4T$

— Hydraulic fracturing tensile failure

$A\ (\sigma_n, \tau) = (-\sigma_3, 0) = (T, 0)$

I, II, III, IV all touch failure envelope at A (T, 0)

For IV, $(\sigma_1 - \sigma_3) = 3T - (-T) = 4T$

For $\sigma_1 > 3T$, $(\sigma_1 - \sigma_3) > 4T$, $\therefore$ Mohr stress circle impinges on failure envelope at some other point than A, where $\sigma_n \neq T$, $\tau \neq 0$

Fig. 1.3.7 Tensile failure conditions

normal stress acting across the fracture plane will be tensile resulting in dilation, with however, a shear stress acting along it so that shear displacement will also occur. Consequently, the failure plane will be a hybrid extension/shear fracture. It follows from the geometry of the failure envelope that should conjugate hybrid failure planes develop, the acute angle between the planes will be less than 45°. This relationship is based wholly on the theoretical prediction of the Griffith law, which unlike the Coulomb or Mohr theories, possesses the attractive feature of combining both tensile and shear failure in a single criterion, and has not been verified experimentally due to the extreme difficulty in conducting such tests (production and characterisation of hybrid extension/shear fractures in the laboratory perhaps representing an informative area for future research). However, other predictions from the Griffith criterion concerned with tensile failure and shear failure with σ_3 compressive, have been verified experimentally. Moreover, field evidence demonstrates that such hybrid faults have developed under geological conditions, where although it may be argued that such features formed in extension and were subsequently reactivated in shear, evidence from vein-filling growth fibres, which track relative displacement of the fracture walls, provide positive proof. A summary of the three fracture types, distinguished in terms of crustal stress and fluid pressure conditions operative at the time of fracture formation, is given in Fig.1.3.9.

1.4 FRACTURE MECHANICS

In essence, fracture mechanics concerns the study of stress concentrations caused by sharp-tipped flaws and the conditions for propagation of these flaws. Fracture mechanics largely derives from the work of Griffith (1920)[14] and Irwin (1958)[27] in which the importance of the crack as stress concentrator was recognised as being fundamental in controlling brittle fracture. A brief summary of the main aspects of fracture mechanics theory is presented here so as to aid understanding of some of the terms and concepts discussed in section 1.5 dealing with the formation and growth of shear fractures. However, an excellent and comprehensive review of fracture mechanics theory and application relating specifically to rock deformation, is given in the treatise "Fracture Mechanics of Rock" edited by Atkinson (1987). This summary is drawn in part from the

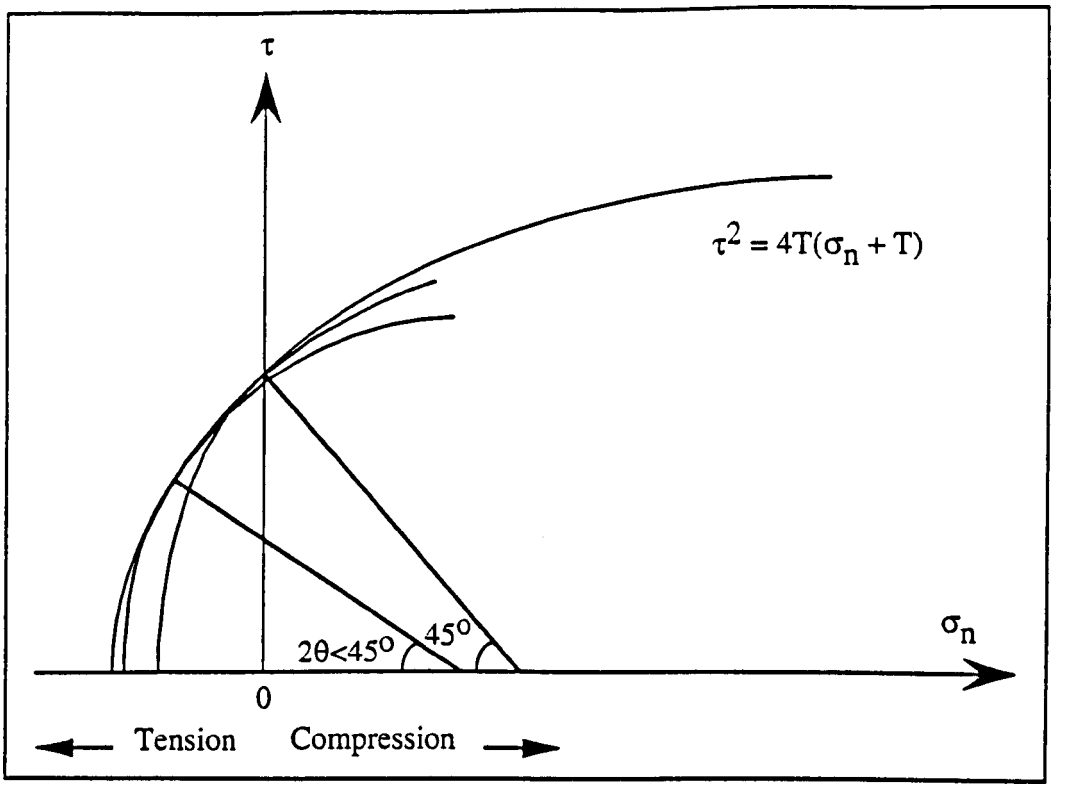

Fig. 1.3.8 Stress conditions for failure in the negative quadrants of the Griffith failure envelope, and the predicted angle (2θ) between conjugate hybrid extension/shear fractures (after Price & Cosgrove[26].)

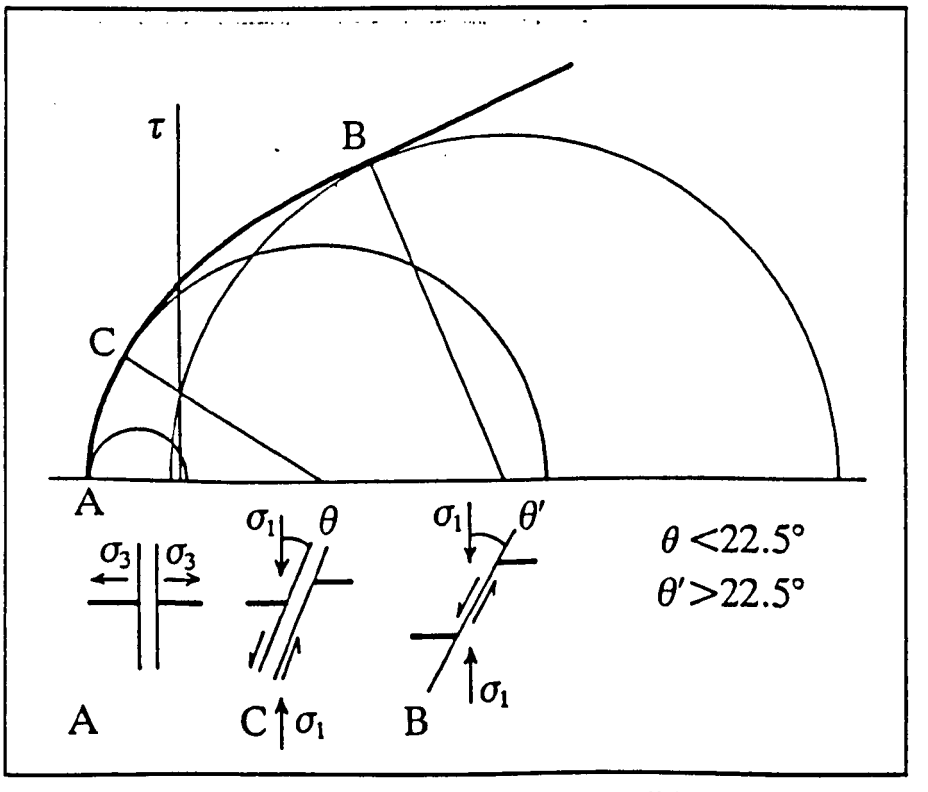

Fig.1.3.9 Mohr's stress circles representing rock stress conditions giving rise to: A tensile failure; B. shear failure; C. hybrid tension/shear fractures. The sense of movement exhibited by the failure planes and their orientation with respect to the axes of greatest and least principal stress are also shown (after Price & Cosgrove[26].)

chapter "Introduction to Fracture Mechanics and its Geophysical Applications" (Atkinson, 1987[28]) opening the above volume.

Underlying the basis of fracture mechanics is the notion that a criterion based on plausible physical grounds or experimental evidence is used to determine whether a crack or discontinuity will propagate or heal. Fracture mechanics has been defined as, "the fracture of materials in terms of the laws of applied mechanics and the macroscopic properties of materials. It provides a quantitative treatment, based on stress analysis, which relates fracture strength to the applied load and structural geometry of a component containing defects" (Irwin & de Wit, 1983)[29]. The defect is usually modelled as a crack, but it could be a pore or other non-linear defect. The influence of applied loads on crack extension can be described in terms of certain parameters which characterise the stress and strain intensity near the crack tip. Starting with the concept of an ideal flat, perfectly sharp crack of zero thickness, there are three basic modes of crack tip displacement (Fig.1.4.1) termed: Mode I, tensile; Mode II, in-plane shear; Mode III, anti-plane shear. These basic plane modes of distortion around the crack tip are defined with respect to a reference plane that is normal to a straight-line crack edge. In problems concerning crack loading the superposition of these three basic modes is sufficient to describe the most general case of crack tip deformation and stress field. If Cartesian coordinates are assumed then on the plane $y = 0$: for Mode I, $\sigma_x \neq 0$, $\sigma_y \neq \sigma_z \neq 0$, $\tau_{xy} = 0$; for Mode II, $\tau_{xy} \neq 0$, $\sigma_y = 0$; for Mode III, $\tau_{yz} \neq 0$, $\sigma_y = 0$, $\tau_{xy} = 0$ (Fig.1.4.2).

Stress intensity analysis aims to give a measure of the real forces applied to a crack tip, which will determine whether it will grow or remain stable. These cannot be deduced merely from the external loading conditions. The stress distribution in the crack tip region is analysed on the assumption that a classical linear theory of elasticity applies, which is valid provided that any region of non-linear behaviour is negligibly small compared with the length of the crack and the dimensions of the cracked body. Fig.1.4.2 shows the stress components in the crack tip stress field. In a homogeneous linearly elastic medium, the stresses near the crack tip are proportional to $r^{-1/2}$, where r is the distance measured from the crack. The coefficient of the $r^{-1/2}$ term in the stress is termed the "stress intensity

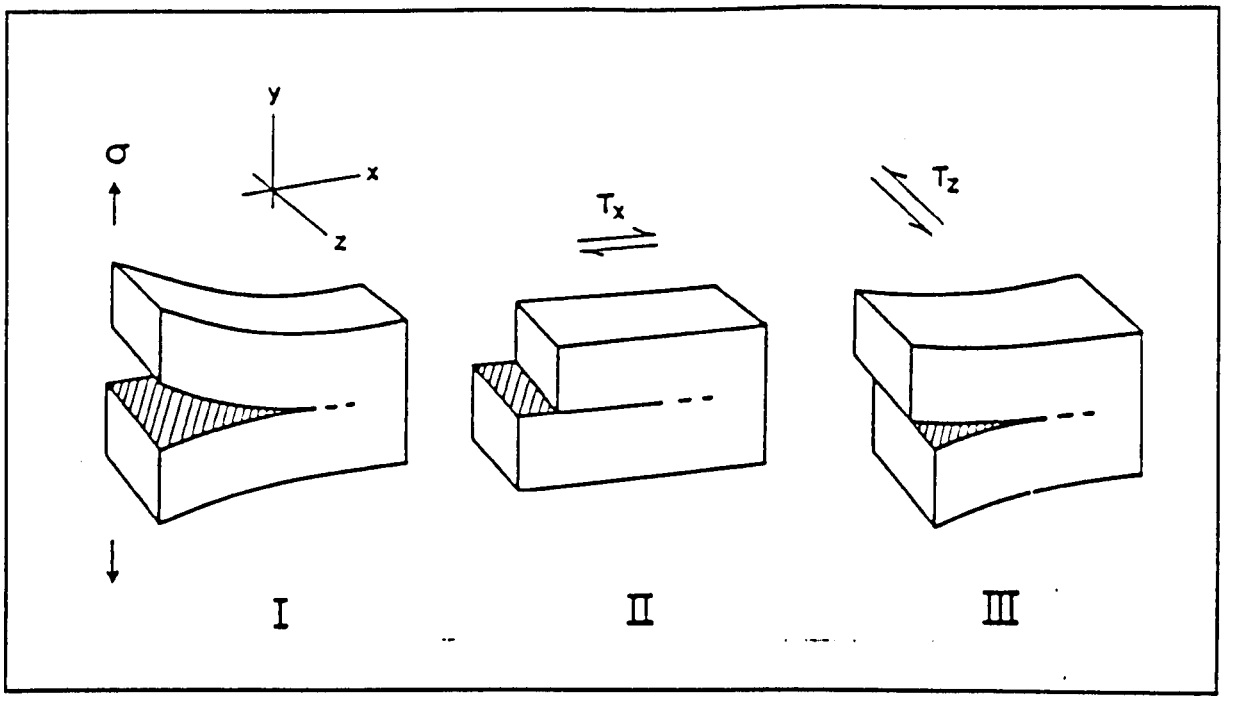

Fig.1.4.1 The three basic plane modes of distortion at a crack tip (Atkinson[28].)

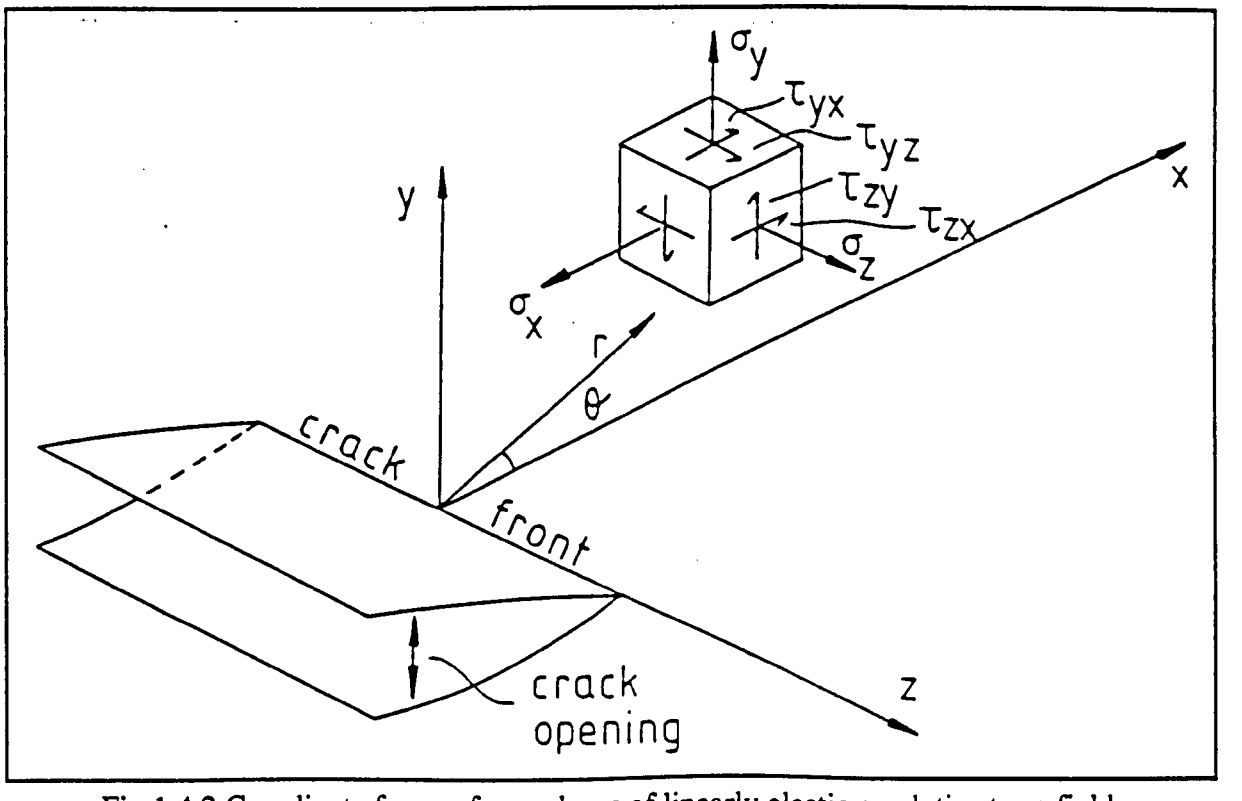

Fig.1.4.2 Coordinate frames for analyses of linearly elastic crack tip stress fields (Atkinson[28].)

factor" and it depends on such factors as the applied load, the shape of the body and the crack length. The stress intensity factor, K, is thus the magnitude of the crack tip stress field for a particular mode in a homogeneous linear elastic material. As a simple demonstration, for the values of the σ_{yy} stress component in Mode I at points near the crack tip within the material in the plane of the crack, the elastic solution is:

$$\sigma_{yy} = \sigma.(c/2r)^{1/2} \quad ..... \quad \text{Eqn.1.4.1}$$

2c: crack length.

r: distance from the crack tip.

σ: macroscopic stress applied normal to the crack.

(Eqn.1.4.1) can be written in the form:

$$\sigma_{yy} = K_I / (2\pi r)^{1/2} \quad ..... \quad \text{Eqn.1.4.2}$$

K_I: $\sigma.(\pi c)^{1/2}$.

The factor $1/(2\pi r)^{1/2}$ is the distribution function along the r-axis and $K_I = \sigma.(\pi c)^{1/2}$ is the scaling factor or stress intensity factor. Full expressions for all the components of stress and displacement at all points in the reference plane in each of the three basic modes of distortion can be found in the extensive literature. The dimensions of K are stress $\times$ (crack length)$^{1/2}$, that is Pa$\times$ (m)$^{1/2}$ or N/m$^{1.5}$.

Thus, for a particular loading on a specimen of particular shape, the mechanical situation around a crack tip can be described in terms of stress intensity factors and the basic distortion modes. With regard to what aspect of this local situation around the crack tip determines when the crack will begin to spread under the action of increasing the external loading, the simplest view is that the crack will begin to spread when a certain critical

intensity of loading is reached at its tip, as measured by the stress intensity factors. That is, the failure criterion is expressed in terms of "critical stress intensity factors". These factors are material parameters, depending on the type of material, its particular physical condition of grain-size, strain-hardening etc. and the conditions of temperature and pressure. They are designated K_{IC}, K_{IIC} and K_{IIIC}. When K reaches K_C, catastrophic crack growth is assumed to occur. The material property K_{IC} is also called the "plane strain fracture toughness". Practical procedures for determining the critical K_C parameters for various materials have been extensively developed and codified (see ISRM "Suggested Methods for Determining The Fracture Toughness of Rock", 1988[30]).

Instead of considering crack tip stresses, an alternative fracture mechanics approach to crack extension is to examine the "crack extension force" or "strain energy release rate", G, which is the loss of energy per unit of new crack separation area formed during an increment of crack extension. Note that G is a rate with respect to crack length and not with respect to time. For fracture in each of the three fundamental modes of crack tip displacement, the crack extension force for plane strain and assuming linear elasticity is given by:

$$G_I = K_I^2(1-\nu^2)/E \quad \text{.....} \quad \text{Eqn.1.4.3}$$

$$G_{II} = K_{II}^2(1-\nu^2)/E \quad \text{.....} \quad \text{Eqn.1.4.4}$$

$$G_{III} = K_{III}^2/2\mu = K_{III}^2(1+\nu)/E \quad \text{.....} \quad \text{Eqn.1.4.5}$$

- ν: Poisson's ratio.
- E: Young's modulus.
- μ: Shear modulus.

For plane stress, the factor $(1-\nu^2)$ in Eqn.'s 1.4.3, 1.4.4 and1.4.5 is replaced by unity.

Thus a key concept in the widespread use of fracture mechanics is that extension of a fracture will occur once a critical value of stress intensity factor, K_C, or crack extension force, G_C, has been reached or exceeded. Once K_C or G_C has been reached. crack propagation is known as "fast/catastrophic fracture" because its speed can approach that of sound in the medium, provided that the crack is isolated and its walls are traction free.

Classical fracture mechanics deals with a single, ideal atomically sharp crack. This is a suitable representation for single crystals or at a microscopic level in polycrystalline materials, extensive electron optical studies supporting the assertion that brittle cracks in such materials are in fact atomically sharp and do propagate by the sequential rupturing of bonds. However, at a more macroscopic level of study, real polycrystalline polyphase materials such as rocks and ceramics show more complex behaviour. For sequential loading of a blunt machined notch in rock, initially a few microcracks will form, but the system behaviour will remain linear. On further loading, microcracking intensity will increase, and behaviour in the crack tip region will become non-linear. Finally, macrocrack extension will occur due to microcrack linkage in this non-linear zone, known as the "process zone". The macrocrack propagates by taking with it a "damage cloud" contained in the process zone. In some materials the process zone may be small with respect to the dimensions of the cracked body and hence a fracture mechanics analysis assuming linear elasticity (linear elastic fracture mechanics, LEFM) will still be valid. However, if the process zone size becomes large, then non-linear fracture mechanics analyses are required, such as the "J-integral" (for details of the J-integral and its application to problems involving shear cracks in geophysics such as faults and earthquakes, see Li, 1987[31]). In fracture mechanics literature, the term process zone is often given a more general meaning encompassing any zone of non-linear behaviour at a crack tip, where for example plasticity as opposed to microcracking could be the means by which the non-linearity is obtained.

For decades engineers have successfully used the critical stress intensity factor/critical strain energy release rate approach to predict catastrophic crack propagation in metals, ceramics, glasses and rocks. However, in systems subjected to long-term loading, this

classical approach breaks down, especially if high temperatures or reactive environments are present. This is because significant rates of crack extension can occur at values of K, G that may be substantially lower than K_C, G_C. This phenomenon is known as "subcritical crack growth". It was first observed in glass, but has subsequently been observed in experiments on most engineering materials including rocks and minerals. Subcritical crack growth can be due to several competing mechanisms, of which the most familiar is "stress corrosion" or "hydrolytic weakening". A particular mechanism will be dominant under specific ranges of environmental and material variables, hence as the range of these variables in the earth's crust is enormous, it might be expected that different mechanisms will contribute to subcritical crack growth in different parts of the crust and in the same part at different times. Stress corrosion crack growth occurs because the chemical action of an environmental agent, such as water, weakens the strained bonds at crack tips and so facilitates crack propagation. It occurs at crack velocities which decrease as K is lowered to some threshold value K_O, below which no crack propagation is observed. Well-known trimodal behaviour for subcritical crack growth studies on glass, shows three distinct regions on a stress intensity factor versus crack velocity diagram, for tensile crack growth by stress corrosion (see Fig.1.2.3):

Region 1: crack growth velocity controlled by rate of stress corrosion reactions at crack tips.

Region 2: crack growth velocity controlled by the rate of transport of reactive species to crack tips.

Region 3: crack growth mainly controlled by mechanical rupture, being relatively insensitive to the chemical environment.

K_O marks the lower bound to Region 1 whilst K_{IC} marks the upper bound to Region 3.

1.5 EXPERIMENTAL STUDIES OF SHEAR FAULTING

Santarelli and Brown (1989)[32] in a study of the formation and propagation of surfaces of discontinuity in rocks (brittle failure) to examine the possibility of predicting the behaviour of rocks around model underground excavations, compiled a summary table of

experimental studies on the localisation of shear deformation (Table 1.5.1). As shown in this table, several indirect techniques have been used to study the onset of localisation. A large number of strain gauges bonded to a specimen can measure detailed surface deformations, although the glue used could be construed as being disruptive to such studies, therefore optical methods such as slit diffractometry are preferred. The most common of these is holographic interferometry which allows the compilation of complete surface strain maps and has been employed in uniaxial, biaxial and triaxial experimentation. Sonic techniques have also been used, including both passive and active microseismics. Acoustic emission monitoring records the high frequency elastic vibrations emitted by propagating microcracks under deformation, with source location via acoustic tomography providing important information on their location. Active microseismics measures the velocity and attenuation of artificially transmitted elastic waves (compressional "P-waves" and/or shear "S-waves") which are highly sensitive to the presence of cracks. Direct microscopic observation requires that specimens are deformed stably through the post-failure region under servo-controlled displacement control, to achieve stable crack propagation. For optical examination, samples may be injected with a dyed resin prior to specimen unloading and sample thin-sectioning. Alternatively electron microscopy has been used to study the sizes, shapes, orientations and distribution/localisation of microcracks. From Table 1.5.1 it is evident that pre-failure localisation of strain occurs at a hardening stage prior to peak strength, $\sigma_{localisation}/\sigma_{peak}$ varying from 60 to 99% for the rock types considered. Lithology dependency aside, scatter in localisation ratios are partly the result of sensitivity to the various measuring techniques employed, and the fact that early localisation can be produced by poor specimen end-preparation.

Whilst Table 1.5.1 and the above microstructural observations refer primarily to igneous rock types with their characteristic interlocking crystalline textures, Hallbauer, Wagner and Cook (1973)[33] performed triaxial compression tests on specimens of a fine-grained argillaceous quartzite. Careful macroscopic and microscopic studies were conducted on longitudinal sections from different specimens stopped at predetermined points along the

Author(s)	Lithology	Test Type	Measuring Technique	Localisation Ratio (%)
Scholz, 1968	granite	U	AE location	92
Freidman, Perkins &	granite	U	microscope	99
Green, 1970	limestone	U	microscope	99
Thill, 1972	marble	T	velocity	95
Brady, 1974	marble	T	microscope	95
	granite	T	microscope	95
Rao & Ramana, 1974	pyroxenite	U	velocity	78
	dunite	U	velocity	75
	serpentinite	U	velocity	76
Hadley, 1975	granite	T	strain gauge	90
	gabbro	T	strain gauge	90
Liu & Livanos, 1976	granite	U	slit diffractometry	92
Lockner, Walsh & Byerlee, 1977	granite	T	velocity	85
Sobolev, Spetzler & Salov, 1978	granite	B	velocity holographic - interferometry microscope	80
Soga, Mizutani, Spetzler & Martin, 1978	granite	T	velocity holographic - interferometry	60
Kranz, 1979	granite	U	microscope	≥87
Wong, 1982	granite	T	microscope	99
Yanagidani, Ehara, Nishizawa & Kusonose, 1985	granite	U	AE location strain gauge	≥83

Table 1.5.1 Summary of studies of localisation of deformation (for full references cited above see Santarelli and Brown[32]). Type of test: U=uniaxial; B=biaxial; T=triaxial. Localisation ratio=stress at onset of localisation/peak strength (%).

complete stress-strain curve, enabling microcrack development and fracture growth to be related to deformation. Whilst usually in triaxial tests the confining pressure is applied via hydraulic fluid acting on an impermeable jacket of negligible stiffness, so that radial expansion and specimen dilation is not resisted locally nor on average by increasing confinement, the *in situ* situation in which the specimen would be surrounded by more rock would be expected to have much greater lateral resistance, thus increasing the value of the least principal stress. This would tend to inhibit failure and focus fracture into a limited volume, so to simulate natural deformation more closely Hallbauer *et al* jacketed the specimens in 1mm-thick copper tubing, and used a special sealed triaxial cell with limited fluid volume. The copper tubing provided resistance to local lateral expansion of specimen circumference, whilst the sealed cell stiffness caused confining pressure to increase as 11000MPa $\times \varepsilon_{lateral}$, tending to suppress dilation. Three progressive regions of damage development were discerned on the complete stress-strain curve from thin-section study:

(i) $0.6\sigma_{max}$ to $0.95\sigma_{max}$: The first visible structural damage appears as elongated microcracks distributed at random but concentrated in the central portion of the specimen with their long axes tending parallel to the direction of maximum principal stress.

(ii) $0.95\sigma_{max}$ to σ_{max}: Towards the end of this region there is pronounced increase in microcracking which tends to coalesce along a plane in the central portion of the specimen. At the point of maximum stress, σ_{max}, a macroscopic fracture plane develops in the central portion of the specimen, which grows towards the ends of the specimen by the step-wise joining of microcracks. Initially there is little or no movement on this fracture plane.

(iii) $\varepsilon \geq \varepsilon$ at σ_{max}: In this region the fracture plane extends towards the ends of the specimen where its direction changes so as to allow relative movement to take place across its surface between the two halves of the specimen, and a rapid drop in the resistance of the specimen to the applied load occurs.

Following specimen unloading and sectioning, measurements on the microcracks showed them to be on average about 300μm long and 3μm wide (presumably they were substantially wider whilst under stress). The ratio between the volume of these stress-free microcracks and the corresponding inelastic volumetric dilatancy at those positions on the stress-strain curve to which the specimens were loaded, proved to be remarkably constant at about 16 to 19%.

It is now widely accepted that, in the brittle field, the stress-strain behaviour of a rock in compression can be divided into several stages prior to macroscopic fracture. The basis of such a scheme was first proposed by Brace (1964)[34] and built upon by Brace *et al* (1966)[35] and has been consolidated by intensive laboratory experimentation, as outlined in summary by Paterson[9], pages112-160) providing a synoptic view of brittle behaviour with failure being recognised as the culmination of progressive development of cracking. Based on the synthesis of such experimental studies as provided by Paterson, a generalised demarcation of four distinct stages in the complete load-displacement curve of a rock in a compression test, and the corresponding courses of change in various physical properties, is shown graphically in Fig.1.5.1. The main stages distinguished are:

Stage I: a "settling-down" phase

Stage II: a nearly perfect linearly elastic phase

Stage III: a phase of microfracture development and dilatancy involving stable microcrack propagation

Stage IV: a phase of unstable development in the pattern of microcracking involving local weakening and leading to the growth of a macroscopic fracture

The nature of the pre-failure deformation may be understood by examining all the strain components. In Fig.1.5.2 axial, lateral and volumetric strain versus stress are plotted for a typical uniaxial compression test. On initial loading (phase I) the stress-axial strain curve is concave upwards and the rock undergoes more volume compaction than expected from solid elasticity. This behaviour is caused by the closing of preexisting cracks, primarily those orientated at a high angle to the applied axial stress, and is largely suppressed in

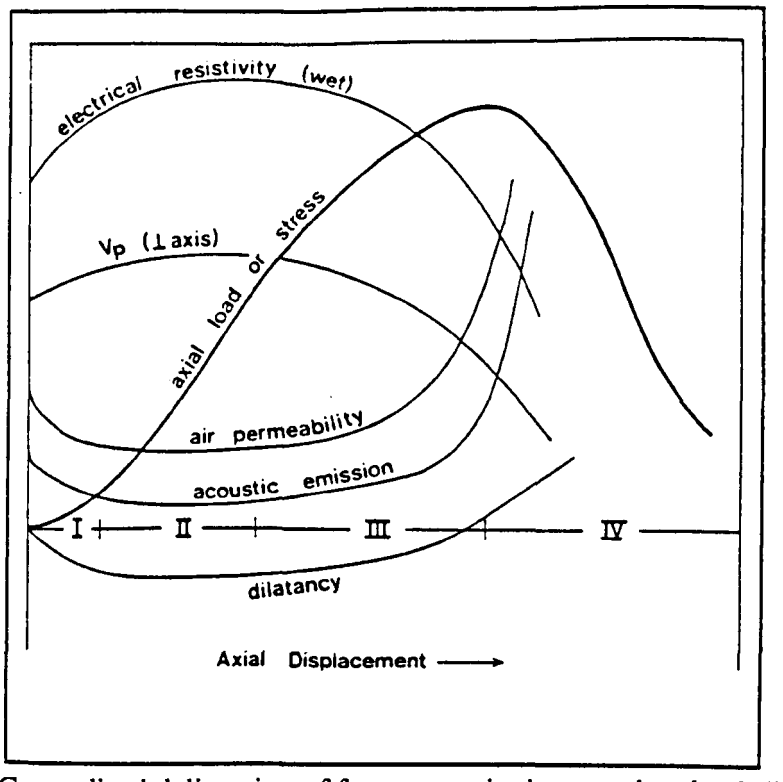

Fig.1.5.1 Generalised delineation of four stages in the complete load-displacement curve of a rock in compression, and corresponding changes in various physical properties (Paterson[9].)

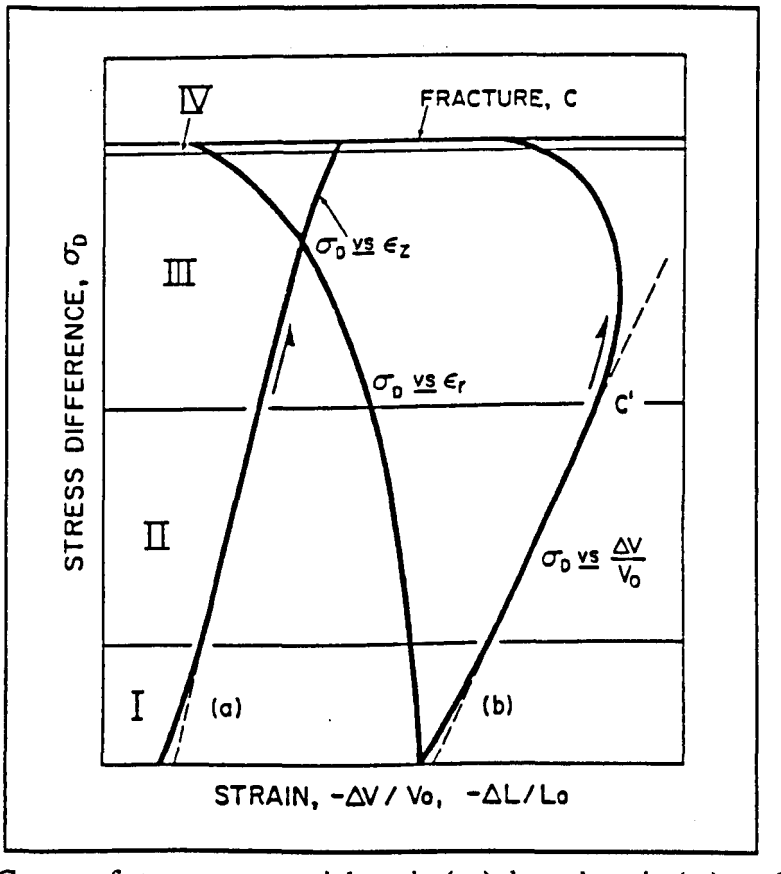

Fig.1.5.2 Curves of stress versus axial strain (ε_z), lateral strain (ε_r), and volumetric strain ($\Delta V/V$) for a brittle rock in a compressive test to failure (Scholz[16].)

triaxial compression tests (although it does occur in tests performed under relatively low confinement) as the confining pressure closes such cracks prior to application of a deviatoric stress. This process is observed to be more or less completely reversible, that is non-linearly elastic in its macroscopic effect. In more porous rocks, irreversible pore collapse may also be expected to contribute in this stage, especially in uniaxial compression, however this effect will not be restricted to stage I. After such cracks orientated at a high angle to the maximum principal compressive stress have largely closed, the rock deforms in a nearly linear elastic manner, according to its intrinsic elastic constants (phase II). This stage is thought to involve predominantly the elastic deformation of both constituent grains and pore space, however acoustic emission and hysteresis detected in this stage indicates that some irreversible processes are occurring. Some sliding on pre-existing cracks has been suggested (Bieniawski, 1967[36]) relating the shape of the hysteresis loop to the frictional resistance to such sliding, with reference to the theory of Walsh (1965)[37] however microscopical studies have failed to provide evidence of shear crack activity, so that the explanation for hysteresis must remain somewhat conjectural although whatever is occurring is probably premonitory to the developments in stage III. The sensitivity with which non-linearity in the stress-strain curve can be detected of course influences the extent attributed to stage II, but it is evident that this extent also varies considerably with rock type and confining pressure. At an axial stress magnitude commonly found to be around half the peak failure stress, the rock specimen is observed to dilate relative to what would be expected from linear elasticity (stage III). This dilation is accompanied by a decrease in the axial modulus, but is primarily due to nonelastic lateral expansion (Fig.1.5.2).

This rheological property in which volume dilation occurs as a result of application of a deviatoric stress, is known as dilatancy. Prior to the work of Brace *et al* [35] dilatancy was known primarily only as a property of granular material, however, following their work, it can be interpreted with regard to rock material, as resulting from the development of pervasive microcracking within the rock with a concomitant increase in void space. The AE that occurs during compressive failure experimentation confirms this interpretation of the strain data, AE beginning at the onset of dilatancy, with activity accelerating in

proportion to the rate of dilatancy throughout stage III. In stage III, departures from perfectly elastic behaviour are clearly in evidence from dilatancy, increased AE, decreased velocity of elastic waves, and other changes such as those observed in electrical resistivity and air permeability (detailed in chapter 7 of Paterson[9]) resulting from proliferation and propagation of large numbers of microcracks distributed fairly uniformly throughout the specimen. From elastic wave velocity and microscopical studies it is apparent that these cracks develop predominantly parallel to the maximum principal compressive stress direction, however Paterson notes that generalisations regarding the details of this development, such as whether microcracks mainly propagate from smaller preexisting ones or whether the nucleation of new ones commonly predominates, are at present unresolved, with observations to date indicating that a considerable variety of behaviour exists at the microscopic level. However, an important general characteristic is that the propagation of such microcracks is a stable process, with cracks only extending by limited amounts in response to given stress increments, without, at this stage, continuing to extend to form macroscopic fractures.

Stage IV is distinguished from stage III due to an often observed localisation in both deformation and AE in this stage. As the concentration of cracking increases, there develops a linking up (coalescence) of microcracks which leads to the growth of the macroscopic fracture, either of the axial splitting or of the shear type. Although it appears that in some cases the microcracks continue to be predominantly axial in orientation, whilst in others an increasing proportion come to be of inclined or "shear" character, at least in the macroscopic shear failure case, crack linkage is probably generally a subsequent development to the local concentration of microcracking in a band of inelastic deformation (see optical holography studies of anelastic deformation as a precursor to failure, by Sobolev *et al* [38], 1978). However, it appears that much remains to be done to elucidate the details of this failure progression, and its dependence on lithology.

Hadizadeh & Rutter (1983)[39] investigated experimentally the low temperature brittle-to-ductile transition in a fine-grained orthoquartzite (Oughtibridge Ganister with 98% quartz content) using both mechanical and microstructural characteristics. At relatively low

pressures shear orientated grain-boundary cracks formed both pre- and post-peak strength, loosening the microstructure to the point at which axial transgranular cracks developed, followed by fault zone localisation. At relatively high pressures fault zone localisation was suppressed by friction, and cataclastic flow was observed to occur by the formation of ultracataclasite shear zones around each grain boundary, with rhomb-shaped, relatively intact grain cores surviving to high (>20%) strains. Microstructural studies of deformation in the brittle regime showed that faulting, which only developed well past the peak in the stress-strain curve, was preceded by a pervasive loosening of the microstructure. Following their interpretation, from about half of the ultimate stress level, microcracks grow around grain boundaries from pore space notches, so that most of the cracks grow in highly shear stressed orientations, guided by what is presumably the relative weakness of the grain boundary, leading to the development of a cellular arrangement of microcracks bounding single grains or clusters of several grains. Interestingly, peak strength did not apparently appear to be associated with any particular microstructural peculiarity, but was thought to be due to displacement weakening through sliding on grain-boundary microcracks. The main conclusion from Hadizadeh & Rutter's study was, however, that only when the grains are sufficiently loosened to the extent that a large proportion are freed from their neighbours (at $\approx 1\%$ permanent strain) do axially orientated transgranular cracks develop, leading soon after to fault localisation. Thus the loosening of the microstructure by grain-boundary crack growth is probably a precursor to higher strain deformation at all confining pressures. They contend that natural zones of intense cataclasis (fault zones) often develop microstructures comparable with those seen in the above described experiments.

Finally, one of the most basic problems with regard to fault formation, which was anticipated in Fig.1.3.4, is that although rock, both in the laboratory and *in situ*, is macroscopically observed to fail in compression by the formation of shear fractures (faults) inclined at an acute angle, θ, to the σ_1 direction, analytical and experimental experience shows that it is impossible for a shear crack in an isotropic elastic medium to grow in its own plane (Scholz[16], pages26-27). Instead, the propagation of a shear crack

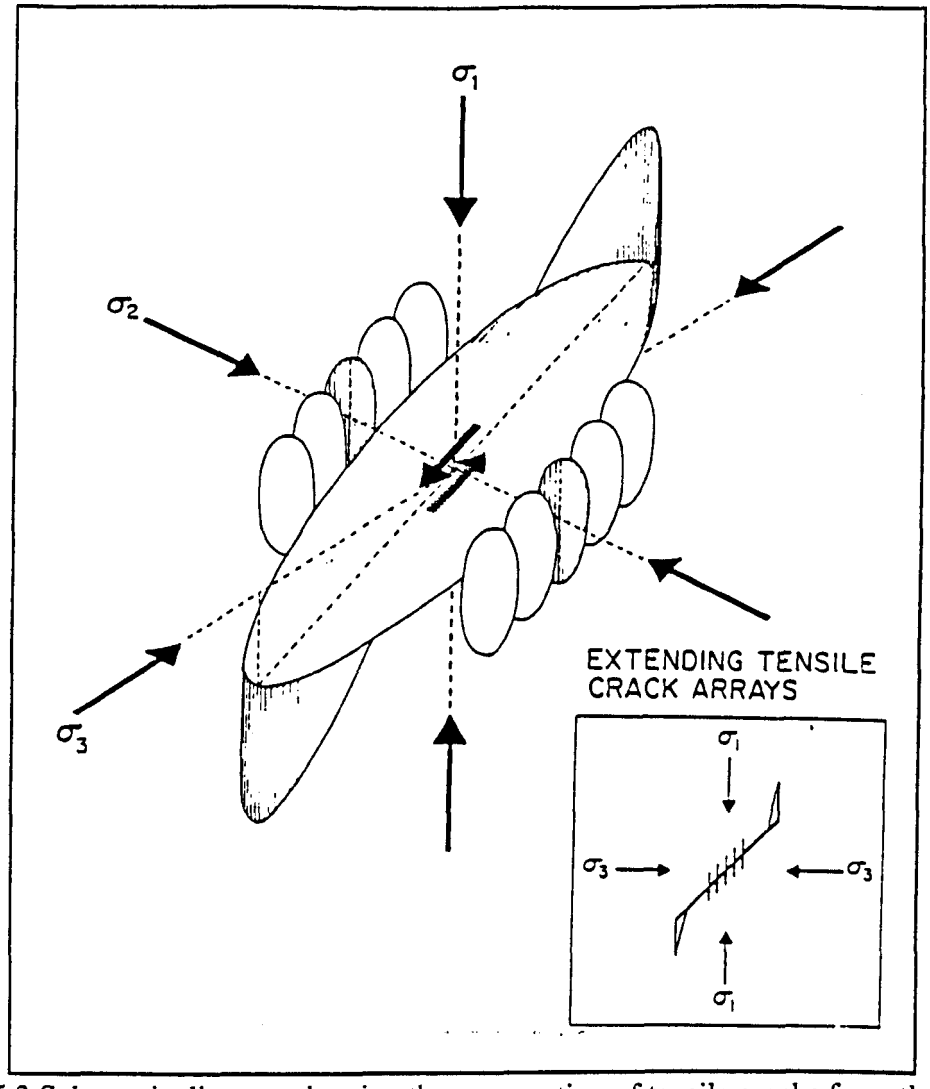

Fig.1.5.3 Schematic diagram showing the propagation of tensile cracks from the edges of a shear crack in a brittle material (Scholz[16].)

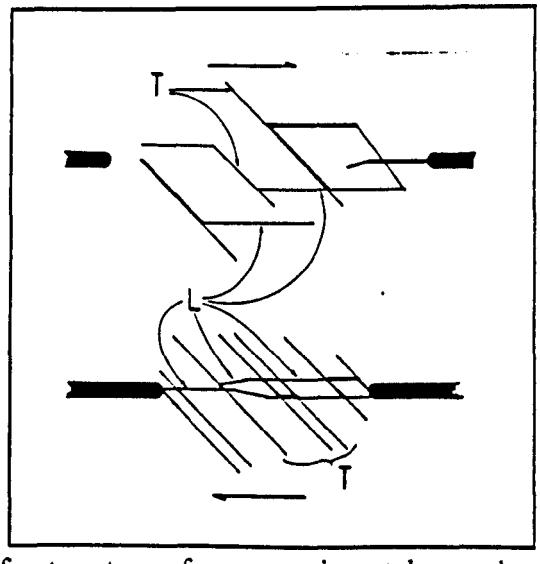

Fig.1.5.4 Observed fracture types from experimental growth of shear fractures: T. oblique tensile fractures; L. linking fractures. T fractures for first in response to the initial stress field, followed by L fractures as the deformation increases (Cox & Scholz[40].)

inclined to σ_1, occurs by the generation of Mode I cracks parallel to σ_1, as shown in Fig.1.5.3. The upper and lower tips of this crack, which are in a Mode II configuration, grow by propagation of single Mode I cracks in the axial direction (as in the experiments of Brace & Bombolakis[18]) whilst the lateral edges, which are in Mode III, generate an array of Mode I axial cracks (as in the torsional experiments of Cox & Scholz, 1988[40]). Part of the answer to the problem was found by Cox & Scholz who observed that although the initial cracks that propagated from a Mode III crack were as shown in Fig.1.5.3, further shearing resulted in the array of Mode I cracks being broken through by cracks parallel to the shear plane, which formed a shear process zone, the first stage in forming a fault (Fig.1.5.4).

2. THE IMPORTANCE OF SHEAR DISCONTINUITIES IN HYDROCARBON RESERVOIRS: A CRITIQUE

2.1 INTRODUCTION

In the province of hydrocarbon reservoir fields, shear discontinuities can exert major influences on scales ranging from far-field, major tectonic basin-bounding faults, down to near-wellbore structures associated with failure zones resulting from imbalances between the uncontrollable factors of earth stresses, rock strength and pore pressure, and the controllable factors of wellbore fluid pressure, and mud chemical composition. In addition, shear discontinuities can be beneficial, for example in their role as important structural oil and gas traps, or indeed disadvantageous, for example when acting to compartmentalise reservoir horizons, resulting in an increase in the complexity of required production technology.

In petroleum engineering terms, distinction is made between predominantly matrix permeability reservoirs and naturally fractured reservoirs, the latter being regarded as particularly attractive potential economic targets in exploratory ventures. With regard to naturally fractured reservoirs, reservoir engineers usually make two assumptions (Aguilera, 1980[41]):

(i) the fractures have a negligible storage capacity and are only channels of high permeability that allow fluids to flow

(ii) the matrix has an important storage capacity, but a very small permeability

Both assumptions can, however, be misleading when applied to the production development of naturally fractured reservoirs. With regard to the first presumption, many reservoirs that produce at high initial rates decline drastically after a short period of time, due to the producible oil being stored in the fracture system, so that consequently it is important to estimate oil-in-place reasonably within the fracture network. With regard to the second assumption, if the permeability of the matrix is very low, then the oil bleed-off from the matrix into the fractures will be very slow and only the oil originally within the

fractures will be produced over a reasonable timescale, so that if the matrix has a reasonable permeability, then the storage capacity of the matrix becomes of paramount importance. Thus the storage capacity of naturally fractured reservoirs can vary extensively, depending on the degree of fracturing in the formation and the value of the porosity, the greater the value of primary porosity the greater the success of naturally fractured reservoirs.

This philosophy outlined above serves to highlight the industry's general understanding of fractured reservoirs, envisaging them as intact rockmass transected by a network of open, dilatant fracture conduits analogous perhaps to jointing in a granite. To supplement the "traditional" industry visualisation of fractured reservoirs as regularly jointed rockmasses, in this second chapter a critique of the role of shear fractures in hydrocarbon reservoirs is given, concentrating on their control over *in situ* fluid flow, and on overall deformability resulting from production-related transients in effective stress. In chapter 4 of this thesis work experimental investigations into the frictional strength of shear discontinuities deformed under constant normal displacement boundary conditions more appropriate to sliding occurring within reservoirs is addressed, whilst in Chapter 6 the sealing potential of experimentally induced shear fractures similar to naturally occurring granulation seams is quantified under triaxial stress conditions.

2.2 FAULT SIZE POPULATIONS

Amongst the outstanding problems of reservoir characterisation is that of the quantitative incorporation of sub-seismic heterogeneities (heterogeneities below the limits of exploration seismic resolution) into reservoir simulation model gridblocks. In particular, sub-seismic faults represent one type of heterogeneity for which reliable assessment methods are a particular prerequisite. The principal questions to be addressed in assessing the likely effects of sub-seismic faults on reservoir formation permeability (Heath *et al*, 1994[42]) concern:

(i) the size population of sub-seismic faults

(ii) the hydraulic nature of the faults

(iii) the likely effects of a particular fault population of specified hydraulic character on a particular reservoir sequence

(iv) how the effects of the faults can be expressed in terms of the effective permeabilities of simulator gridblocks

Whilst prediction of sub-seismic sealing faults has shown considerable advance in recent years (Childs *et al,* 1990[43], Heffer & Bevan, 1990[44], Yielding *et al,* 1992[45], Walsh *et al* 1994[46]) much greater uncertainty is attached to the actual spatial distributions of such fault populations. The fluid flow potential of faults, according to Heath *et al* [42], can be considered as being either hydraulically active or passive. Hydraulically active faults are defined as, "those in which the fault surfaces or fault zones have a permeability, or transmissibility, different from those of the host rocks," so that such faults may be either sealing, or may channnelise fluid flow. The various mechanisms of fault sealing are considered in section 2.3 below.

Hydraulically passive fault surfaces are defined as, "those in which the effect of the faults is limited to the geometric effects of variable fault offsets on the juxtapositions across the fault surfaces of permeable and impermeable host rock units." As such, these effects are strongly sequence dependent, and may decrease or indeed increase connectivity (Knott, 1993[47]). Realistic input of fault geometries and properties in simulation studies should be followed by calculation of the differences between effective permeabilities of unfaulted matrix volumes and their faulted equivalents. Heath *et al* [42] report on investigations into the hydraulic effects of populations of impermeable sub-seismic faults in lithologically homogeneous sandstone reservoir formations. Thus they do not consider the role of faults as seals in the sense of hydraulically isolating a volume of fluid, but consider faults only as sealing surfaces, or impermeable barriers or baffles, which increase the tortuosity of a flow path within a connected volume of fluid, but are not necessarily capable of supporting large pressure differences. Instead, they have attempted to incorporate fault population statistics in an effort to assess their likely hydraulic impact. Prior to a brief outline of Heath *et al* 's results, a short description of fault size population systematics will be given with special regard to results obtained from hydrocarbon reservoirs.

Fault size populations have been demonstrated to be fractal or scale invariant systems (see section 6.5.1) over a range of scales from mm to km of fault displacement (references 43 to 46 and Marrett & Allmendinger, 1991[48]). A scale invariant set has the same relative numbers of large and small elements at all scales between the upper and lower fractal limits, and is expressed by a power law distribution where the number of objects "N" of size "s" or greater is given by:

$$N = a.s^{-D} \quad \ldots\ldots\ldots \quad \text{Eqn.2.2.1}$$

a : a variable dependent on sample size

D : the fractal dimension of the set

Eqn.2.2.1 can be expressed as a straightline curve on a plot of log(N) versus log(s)which is the customary way to plot fault population data:

$$\log(N) = \log(a) - D.\log(s) \quad \ldots\ldots\ldots \quad \text{Eqn.2.2.2}$$

where "a" is a function of fault density for a sample of given size. Walsh *et al* [46] provide a succinct summary of the various fault population databases utilised in the literature. An example dataset might be fault throws encountered on a sample line across a map. By taking account of the sampled line length, the ordinate can be linearly scaled to cumulative fault density (usually referred to as "CUMFD") with units of number of faults per km of sample line length, and when areas or volumes are sampled the ordinate can be scaled to express fault densities in terms of the fault trace length per square km of sampled horizon (km/km^2) or the fault surface area per cubic km of sampled volume (km^2/km^3). Population curves derived from seismic data have an additional left hand shallow segment (Fig.2.2.1) at displacements below the limits of seismic resolution (approximately 20msecs TWTT for many seismic datasets, Heath *et al* [42], which for

typical North Sea datasets corresponds to fault displacements of around 30m) whilst multi-line sampling can give rise to an additional steep right-hand segment (Fig.2.2.1). The fractal relationship has been shown to exist for faults sampled on scales represented by regional seismic, 3D oilfield seismic, coalmine plans and outcrop. Whilst faults exist on all such scales, it is uncommon for any one method of data acquisition to include fault sizes spanning more than two orders of magnitude, hence the need for extrapolation to fault sizes not represented in the dataset. Specifically, for practical purposes, interest in the power law (fractal) relationship lies in the fact that if data from seismically imaged faults establishes a part of a straight line curve for a given range of fault sizes, then the numbers, or density of faults of a different size range can be estimated with some confidence.

Heffer & Bevan[44] produced a composite frequency distribution of fracture lengths per unit area of 2-dimensional observation plane, compiled from in-house seismic maps, outcrop surveys from the North Sea and North America, and from the literature on all scales of fracture throughout the world. In total 30 datasets were included, and whilst the collection was not exhaustive, neither were any encountered datasets omitted. Fig.2.2.2 shows the overall composite log-log plot, which defines a common trend with a slope of approximately -3 across a wide range of scales, despite the data deriving from many different structural and lithological settings. Moreover, on examining the internal structure of the plot, it is evident that each elemental data set has a characteristic form which asymptotically approaches the -3 trend at larger fracture lengths in the range under consideration, but which falls significantly below the trend at smaller lengths (an explanation of this departure in terms of truncation errors is provided by Heffer & Bevan). One concept which is consistent with the observed composite dataset is that larger fractures form by the coalescence of juxtaposed smaller fractures (Allegre *et al* , 1982[49]). With increasing strain accumulation in a rock volume, smaller cracks appearing more or less at random, grow in density, clusters of these smaller fractures joining to form larger fractures. At the percolation threshold, one large fracture crosses the whole region of rock to generally relieve the strain (for comments on potential explanations and

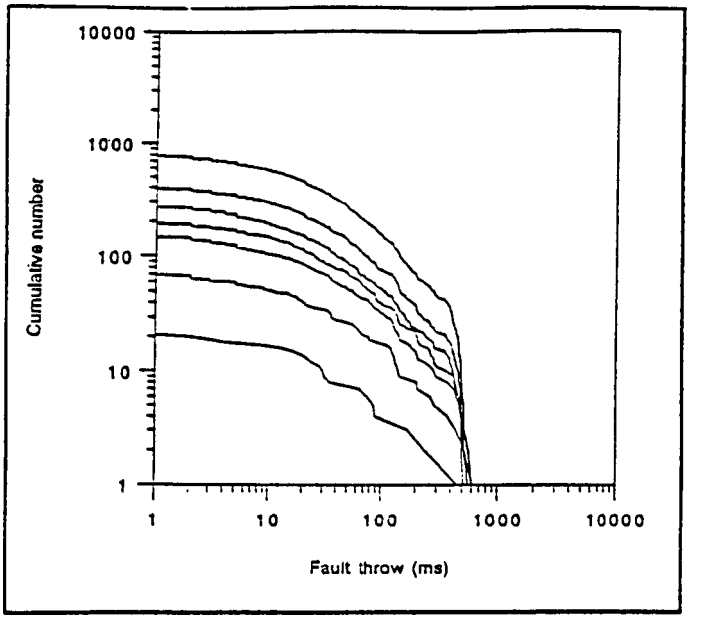

Fig.2.2.1 Line sampled displacement population curves from a 2D seismic survey of an 1800km^2 area in the North Sea showing (from top) multi-line samples for every line (n = 56, with line spacing of 1km) every 2nd, 3rd, 4th, 5th and 10th lines and a single line sample (bottom) after Walsh *et al* [46].

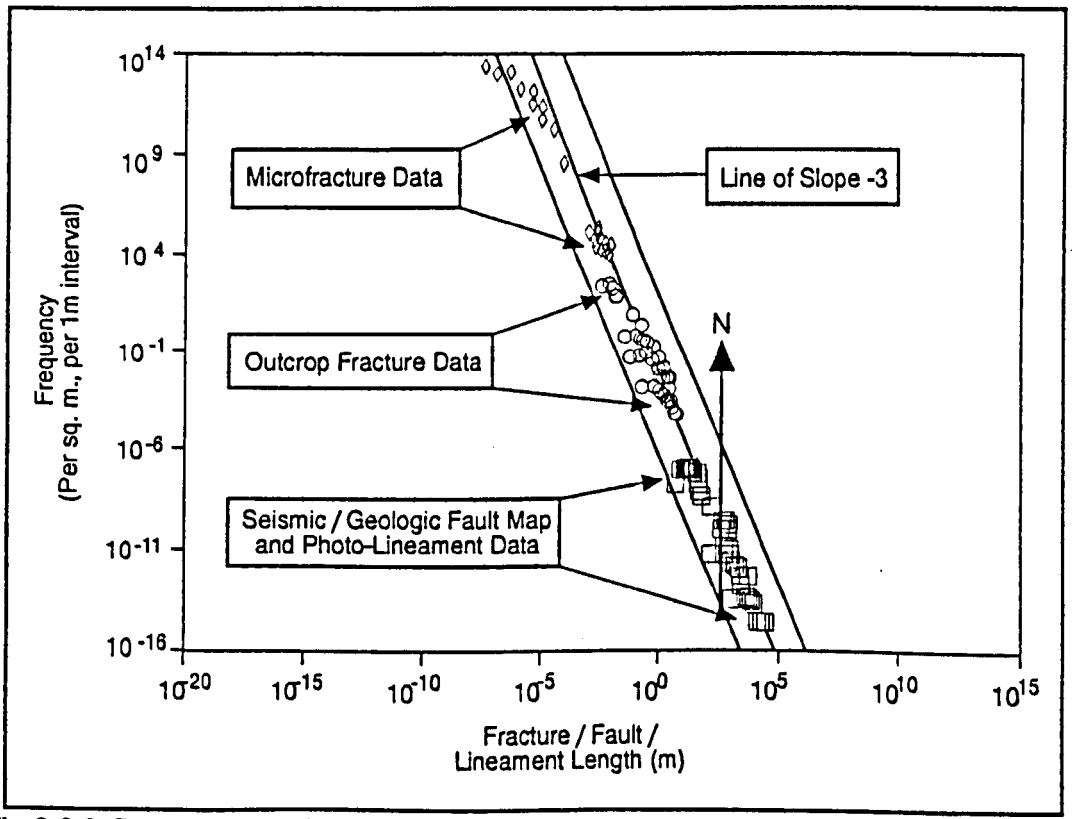

Fig.2.2.2 Composite log-log frequency distribution plot of fracture lengths per unit area of 2D observation plane (from seismic maps, outcrop faces etc.) after Heffer & Bevan [44].

related theories for the exponent of -3 proposed for the length distributions can be found in Heffer & Bevan[44]).

A minor complication in the reporting of fault size population statistics arises from the way in which fault "size" is expressed, because this influences the numerical value of the fractal dimension. Fault size can be measured by either 1D, 2D or 3D sampling with the sampling method determining the attributes that can be used to characterise size, however as the relationships between these various attributes are known it is possible to convert the numerical value of the fractal dimension for one fault size attribute to that for another attribute. Measured values of fractal dimension for 1D displacement populations range between 0.5 and 1.0, the higher values of D indicating higher numbers of small faults relative to larger faults than in populations with lower fractal dimensions. If the fractal dimension for displacement is 0.67 say, a typical value, then the fractal dimension for the other attributes will be as shown in Table 2.2.1. These relationships are comprehensively explained in Yielding *et al* [45].

Heath *et al* [42] argue that the problem of estimating the effect on the horizontal permeability (k_h) of sub-seismic sealing faults is comparable with that of estimating the effect of shales on the vertical permeability (k_v), and that for this reason much of the work directed at shales should be applicable to faults (Haldorsen & Lake, 1984[50], Begg & King, 1985[51]). Major differences between the modelling of shales as opposed to faults include:

(i) size populations of faults (power law) are better constrained than size populations of shales (nonpower-law, dependent on depositional environment)

(ii) hydraulic characteristics of shales are more predictable than those of faults

However, with regard to realistic predictions of spatial distributions, the use of shale density maps to provide a basis for analysing spatial variation in k_v supports the use of a similar technique for assessing the effects of faults on k_h. A typical North Sea fault density is 0.2faults/km (1D) for fault displacements >30m, or 0.08faults traces/km^2 (2D)

Size Attribute	Sampling Dimension	Fractal Dimension (D)
Displacement (d)	1D	0.67
Max. Displacement (d_m)	2D	1.33
Trace Length (l)	2D	2.0
Max. Displacement (D)	3D	2.0
Max. Dimension (L)	3D	3.0
Fault Surface Area (A)	3D	1.5

Table 2.2.1 Equivalent values for the fractal dimensions of various fault "size" attributes for a typical 1D fault displacement population, for which the fractal dimension of "d" is 0.67 and the relationship between "D" and "L" is given by D = cL^1.5 (see text for details). The fractal dimension, D, is equal to the negative of the slope of the population curve, after Walsh *et al* [46].

for trace lengths >3km, with approximate ranges of 0.03 - 3 (1D) and 0.01 - 1 (2D). Expressing fault density in terms of fault trace length/km^2 (i.e. km/km^2) with a resolution limit as above, a typical North Sea value would be 0.2 with extreme values ranging from 0.03 - 3, that is numerically identical to the 1D values. The 3D density equivalent to these typical 1D and 2D values is about 0.2km^2/km^3.

The main objective of Heath *et al* 's study was to compare the values of k_e (the effective permeability of a scaled-up heterogeneous volume) given by statistical and by numerical methods for a rock volume containing a fault population, in order to assess the validity of a simple statistical method through comparison with a more complex numerical one. The numerical simulation technique incorporated routines developed for permeability up-scaling or homogenisation (Holden et al, 1990[52]) into a system designed for the calculation of effective permeabilities. The aim of the upscaling was to calculate k_e, the permeability of a homogeneous volume having the same effect on flow as a volume of the same size with matrix permeability, k, but containing a population of fault surfaces with zero transmissibilities. The simulation technique provides an estimate of the effective permeability by solving Darcy's law and using conservation of mass in one phase incompressible flow through a 3D block (the block consists of orthorhombic cells). The boundary conditions to flow are constant pressure on the inflow and outflow sides, and no-flow through the other sides of the block, with the pressure in each cell being estimated by a standard finite-difference method. The simulation system requires a list of barrier sizes and centre positions generated according to a pre-defined distribution of size, for example by a power-law relationship. A variety of 2D and 3D models (see for example Fig.2.2.3) were run for a range of barrier size distributions (regular, random and power law) and densities (by simply adding more faults to a dataset) for which the principal findings were:

(i) for the same type of fault-size distribution (regular, random or power-law) there is an approximately linear decrease in effective permeability with increasing fault density

(ii) there are significant decreases in k_e even at fault densities which are modest in relation to observed fault densities

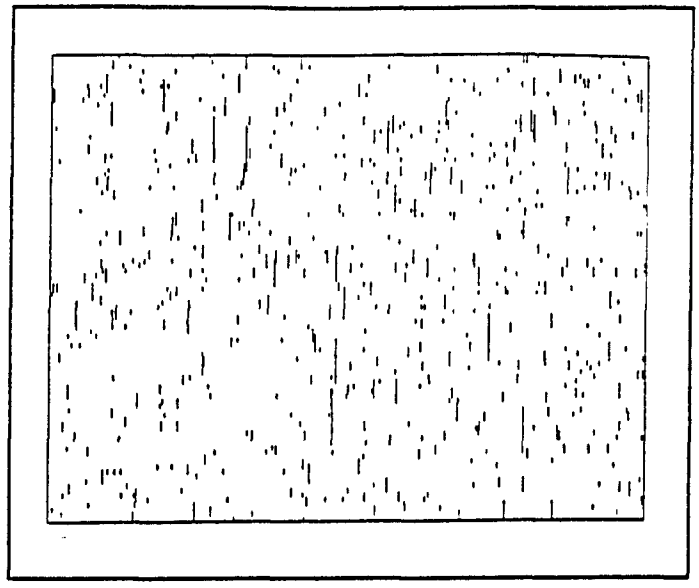

Fig.2.2.3 Schematic map showing the positions of randomly distributed barriers (faults) with a power-law length population, after Heath *et al* [42].

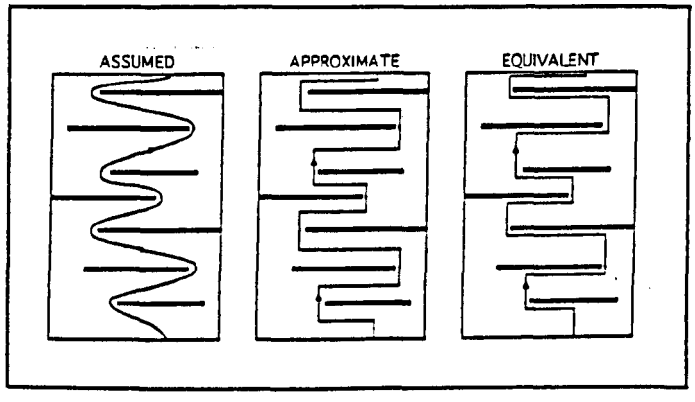

Fig.2.2.4 2D scheme for approximating streamline lengths, after Heath *et al* [42].

The statistical simulation method employed by Heath *et al* [42] borrowed from recent developments in the determination of the effects of discontinuous shales on single-phase vertical permeability (Haldorsen & Lake[50], Begg & King[51]). Since discontinuous barriers represented by impermeable vertical faults might well be expected to have a similar effect on k_h as do shales on k_v, statistical simulation techniques might provide a simple alternative to the numerical simulation of fault systems. Heath *et al* [42] estimated the impact of faults on k_h using a slightly modified version of the "statistical streamline" technique developed by Begg & King[51], which is itself a development of the method described by Haldorsen & Lake[50]. The modification is introduced to take account of the power-law size distributions of faults, for reasons fully explained in Heath *et al* [42]. The statistical streamline technique is based on the premise that the presence of barriers increases the tortuosity of flow paths within a rock volume. Tortuosity estimates (that is the increase in the length of streamlines due to the presence of permeability barriers) can be simply made using an approximation of average streamline length through, or across, a volume or area of interest (Fig.2.2.4). The approximation is valid for barriers with a regular size distribution and requires only a knowledge of the density of the barriers and of the mean barrier length, L, and width, W, (the assumption is made that the faults are square plates with L=W). However, incorporation of mean lengths and densities can lead to significant errors when applied to barriers with many small faults relative to large ones (that is negative exponential and power law expressions) resulting in the impact of large barriers being underestimated. In such cases a better approximation of the extension to the streamline length is obtained by calculating on a fault by fault basis, with such explicit incorporation of fault sizes being found to increase the tortuosity significantly more than the use of mean fault sizes. The consequence of using mean as opposed to explicit fault sizes is evident in the observed reduction of k_e/k ratios by $\approx 100\%$ at higher fault densities (k_e refers to the faulted volume effective permeability, k refers to the unfaulted volume matrix permeability).

Results from both the numerical and the statistical simulations were found to be closely comparable for power-law size distributions of barriers (faults) in both 2D and 3D, from which Heath *et al* concluded that acceptable results can be obtained for fault populations by using the simple statistical method. Having established the validity of the modified statistical streamline technique for assessing the effect of populations of sealing faults on k_e, the method was used to quantify these effects for realistic ranges of fault densities and population slopes, for both 3D (Fig.2.2.5a) and 2D (Fig.2.2.5b) cases. The results indicate that :

(i) for realistic values of fault densities, populations of sub-seismic sealing faults have a significant impact on effective permeabilities, with k_e/k values ranging down to ≈ 0.001 for the 2D model at high densities.

(ii) for the same population exponents and fault densities, k_e values for 2D models are lower than those for 3D models, consistent with conclusions drawn from statistical simulation of shale sequences

(iii) k_e appears more sensitive to variation in fault densities than to variation in the power law exponent, due mainly, according to Heath *et al*, to the greater impact on flow of larger faults than to the more numerous smaller ones, so that k_e shows a wide range because of the wide range in likely fault densities.

2.3 FAULT SEALING POTENTIAL

Faulting forms one of the foremost controls on the distribution, size and internal structure of hydrocarbon reservoirs. Whilst the role of fault zones in providing both a pathway for secondary hydrocarbon migration and a seal to hydrocarbon accumulations has long been recognised, very little attention has been focused on the processes contributing to the production of fault rocks, and their possible influences on sealing properties. Whilst section 2.2 above concentrated on the influence of fault size populations on reservoir formation permeability, in this section the finite hydraulic nature of the fault zones themselves will be considered.

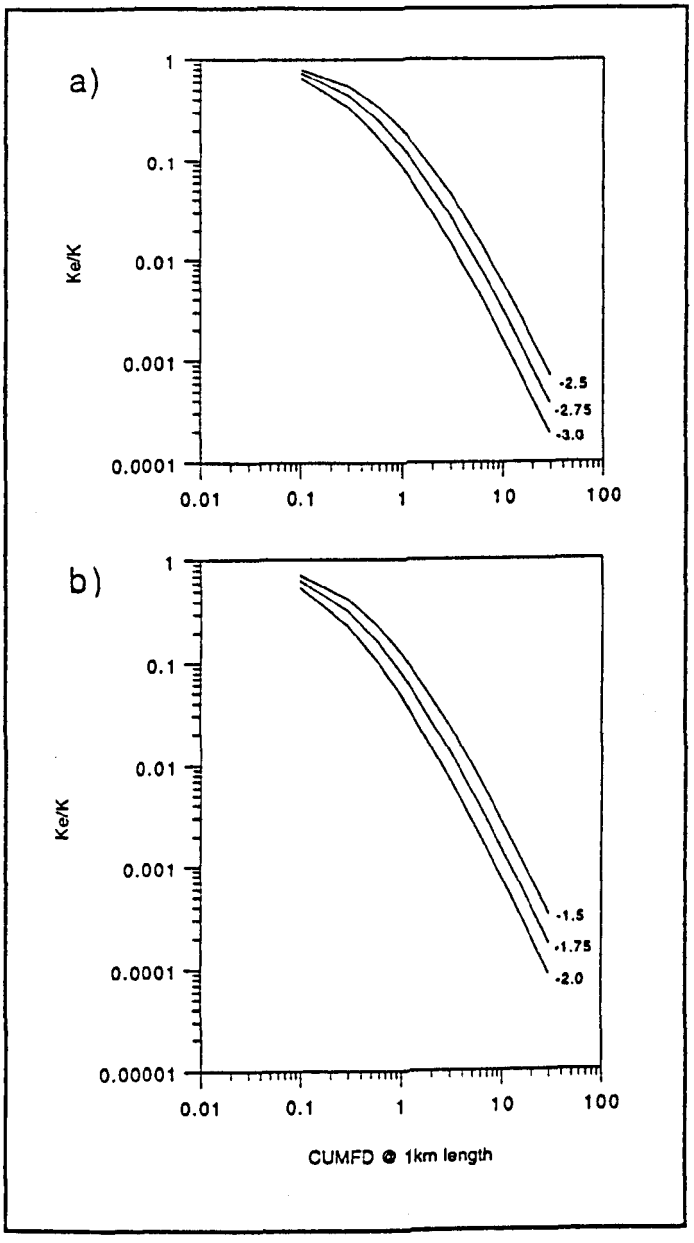

Fig.2.2.5 k_e/k values computed using the statistical streamline technique for a variety of power-law size distributions, with a range of exponents and fault densities, for both 3D (a) and 2D (b) models, after Heath *et al* [42].

2.3.1 Mechanisms of Fault Seal

Whilst intuitively the understanding of fault seal potential is crucial to the assessment of the migration and trapping of hydrocarbons, with the effectiveness of the seal depending upon the poroperm characteristics of the fault zone which in turn are controlled by the microfabrics present, Knipe (1992)[53] shrewdly addresses the actual physical processes (predominantly those of deformation) effecting microfabric evolution and thus seal development in fault zones. Sealing is defined by Knipe as, "the reduction in the flow potential or permeability across a barrier provided by an adjacent medium juxtaposed either stratigraphically or by faulting." For hydrocarbon sealing to occur, it is necessary for the buoyancy forces associated with the density difference between water and hydrocarbon to be matched or exceeded by the capillary or displacement pressure of the seal (Hubbert, 1953[54]) with the height of a hydrocarbon column (z) which can be supported at a sealing medium being dependent on (Fig.2.3.1.1):

(i) the difference between the displacement pressure characteristics of the sealing medium and the reservoir formation
(ii) the water/oil density difference
(iii) the hydrostatic and hydrodynamic conditions

An approach to analyses of the interrelationships between these variables and the sealing capacity or height of the associated hydrocarbon column, is to measure the capillary pressure of core material in the laboratory in order to calculate the heights of hydrocarbon columns that may be present at depth (in conjunction with data on water and hydrocarbon properties). For example, Watts (1987)[55] used the following equation to estimate the trapped column height, z:

$$z = Pd_m I_h / [(P_w - P_h) g I_m \cos\phi] \quad \text{.....} \quad \text{Eqn.2.3.1.1}$$

Pd_m: mercury/air entry (or displacement) pressure

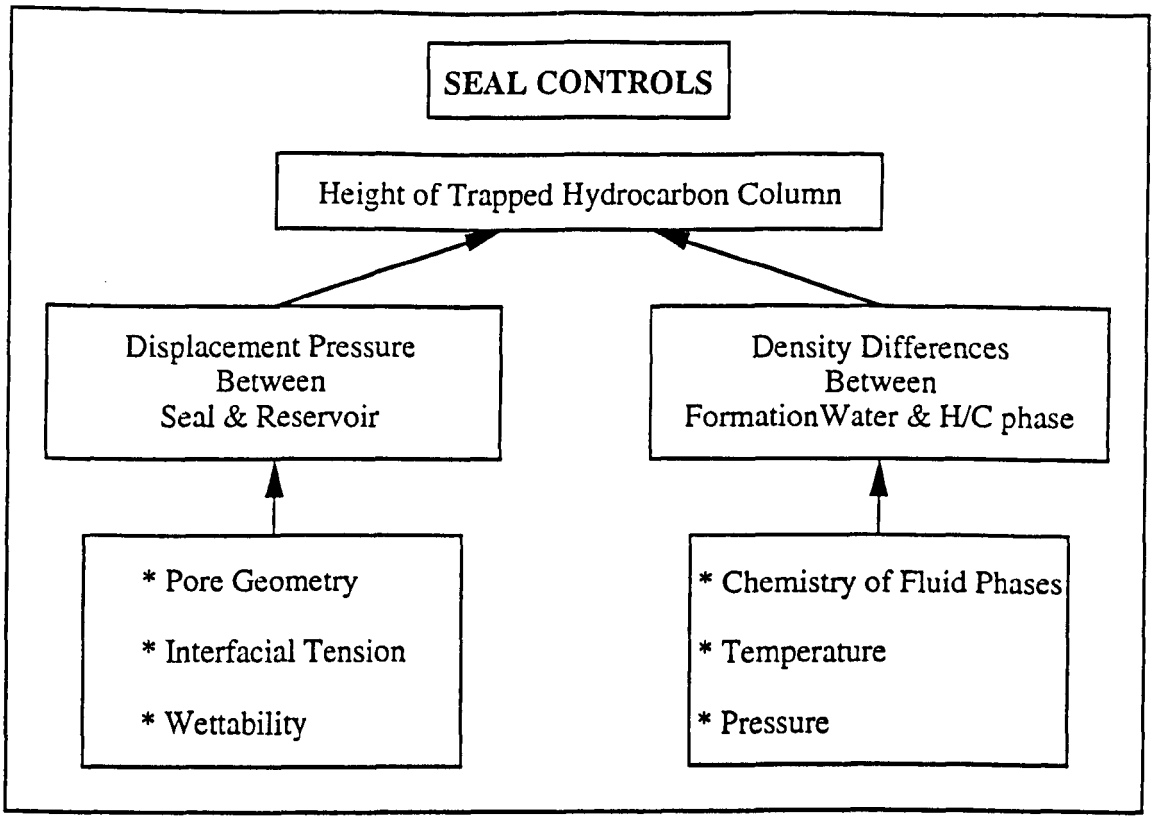

Fig.2.3.1.1 Summary of controls on fault sealing, after Knipe [53].

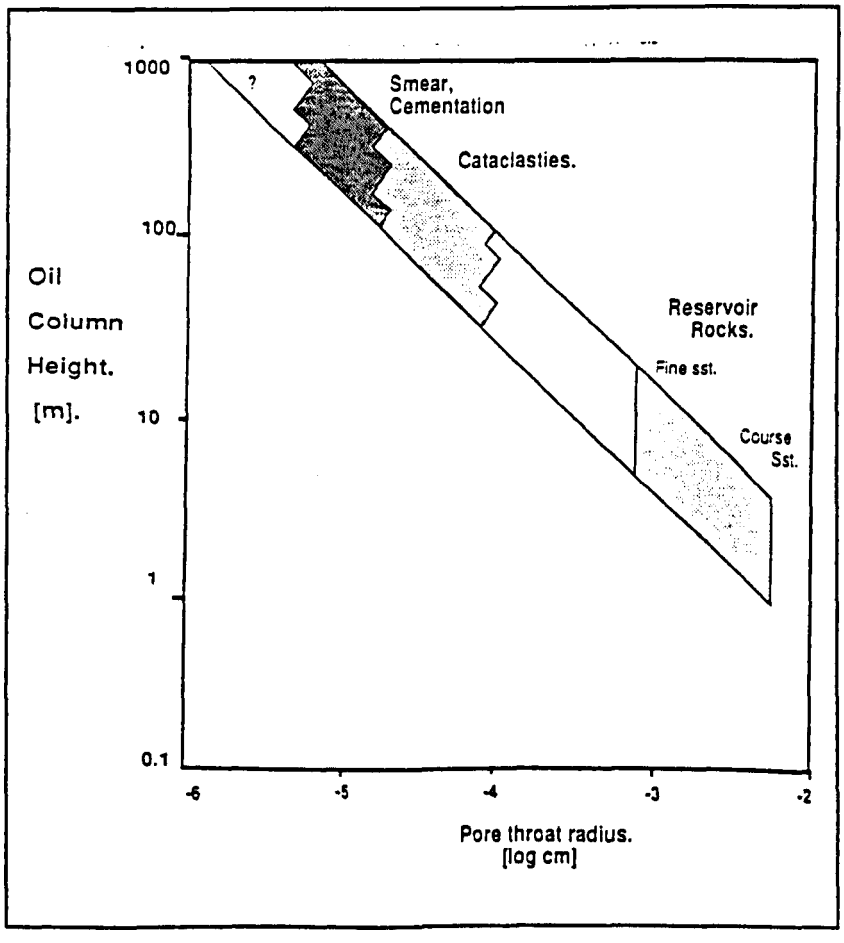

Fig.2.3.1.2 Plot of sealing capacity of different types of fault seal, after Knipe [53].

I_h: hydrocarbon/formation water interfacial tension

P_w: formation water density

P_h: hydrocarbon density

g: gravitational acceleration

I_m: mercury/air interfacial tension

ϕ: mercury/air contact angle

It is also possible to present the height of trapped hydrocarbons, z, in terms of the pore geometry, Berg (1975)[56]:

$$z = 2I_h(r_t^{-1} - r_p^{-1})/[g(P_w - P_h)] \quad \text{.....} \quad \text{Eqn.2.3.1.2}$$

With r_t being the pore throat radius in the seal and r_p the average pore radius in the reservoir, from Eqn.2.3.1.2 it is evident that these textural parameters are fundamental to the sealing process. Thus the factors which influence the evolution of grain-size, shape and sorting, together with the characteristics of the cement phases present, are fundamental to the pore and pore throat sizes, the permeability of the sealing medium and thus to its sealing properties.

Knipe's[53] approach is to quantify these parameters through laboratory measurement on fault zone material, thus providing data to enable estimation of the sealing capacity of fault zones. The types of seal developed under different faulting conditions reflect the range of microfabrics present in the fault zones, sealing capacity being a product of the evolution of porosity, permeability and pore geometry during fault rock evolution. As microfabric evolution and seal development reflect the range of deformation processes operative within the fault zone, Knipe categorises the different seals which can develop on the basis of their different deformation mechanism paths, through comparison of the different microstructural features which characterise each of these deformation mechanisms. The deformation mechanisms which can operate within fault zones depend

on the interaction of the material properties (mineralogy, texture, porosity, permeability) and the environmental conditions (effective stress, temperature). Rock deformation mechanisms can be divided into three categories, based on the recognition of distinguishing microstructural features: frictional sliding, fracture processes and cataclastic flow; diffusive mass transfer (pressure solution); crystal plastic processes, which are reviewed in greater detail in section 1.2. As the microstructural changes associated with each mechanism are different, the type of sealing arising from the operation of each also differs, so that establishing the deformation mechanisms operating in different faults is therefore critical to the assessment of seal development. Based on the above methodology, Knipe groups fault seals into three broad categories:

(i) Porosity collapse seals. Changes in the permeability, porosity and sealing potential within the fault zone are induced by changes in the pore volume, shape and size by grain refinement and rearrangement associated with frictional sliding and/or the cataclasis, dissolution, alteration and plastic deformation of grains/fragments within the fault zone. Shale smear seals would fall in this category.

(ii) Cement seals. Changes in the permeability, porosity and sealing potential arising from the growth of new phases within and adjacent to fault zones. Asphalt/tar impregnations are included as cement seals here.

(iii) Juxtaposition seals. Seals produced by the juxtaposition of two lithologies with different capillary pressures. In this case seal characteristics are largely independent of the faulting processes and the fault only serves to juxtapose the two lithologies with either different pore geometries and/or fluid pressures.

Whilst the sealing properties of a single fault may in part be due to all these factors if the range of conditions and lithologies involved are large, different types of fault rock and hence different characteristic seals are likely to develop in different situations, so that information from the fault rock microstructure analyses (grain size, shape, sorting, pore geometry etc.) can be used to estimate the sealing capacity of the zone. The sealing capacities of the three categories listed above, or the equivalent hydrocarbon column

heights which these seals could support, were calculated by Knipe, using Eqn.2.3.1.2. Values for the pore size and pore throat diameters were based on those measured from mercury injection tests, and from SEM and TEM micrographs, whilst the values of the other important variables influencing the sealing capacity (formation water and hydrocarbon densities, the hydrocarbon interfacial tension) enclosed the range commonly encountered in reservoirs. The results of these estimates of sealing capacity are shown schematically in Fig.2.3.1.2, and indicate that the most effective seals are those with the smallest pore throats. The distribution of seals along faults is known as a fundamental control on their trapping potential. With this in mind, Knipe also discusses briefly the factors most likely to cause the seal type to vary, not only between different faults, but also along individual faults, including:

(i) the distribution of lithologies intersecting the fault planes
(ii) the propagation and displacement mechanisms of the faults (their deformation mechanism histories)
(iii) the nature of the fluid flow along the fault
(iv) the fault plane geometry

Whilst the above analysis of faulting processes provides a useful framework for categorising fault seal on the basis of deformation mechanisms, in the literature relating to hydrocarbon reservoir degradation, three principal fault seal types are recognised: (i) diagenetic/cement seals; (ii) clay smear seals; (iii) cataclastic seals. A brief review of each type will be given below, concentrating on (iii), as cataclastic shear bands generated experimentally as part of this thesis work are described in chapter six (see section 6.4).

2.3.2 Fault-related Diagenesis

Fault zones are often cited as simple barriers/seals or conversely as permeable migration pathways/conduits for sub-surface fluids such as brines and hydrocarbons, with cataclasis and diffusive mass transfer being the most important deformation mechanisms which induce complex textural changes in the vicinity of fault zones. Whilst the dilational nature of cataclastic fracturing increases the porosity and permeability of the fault zones

to promote fluid flow, however intense fracturing and grain-size reduction reduce the size of inter-granular pore space, leading to permeability reduction. Low rates of cementation and pressure solution may produce low strength contacts between clasts in a gouge, so that, under such conditions, some strain may be accommodated by sliding along the edges of the clasts, enabling inter-granular pore-spaces to open and close during macroscopic fault displacement (Knipe[53]). The influx of fluid into dilational pore spaces aids the mass transport of material in solution which may lead to the precipitation of porosity occluding cements within the fault zone. The material involved in the mass transfer process may be provided by the action of pressure solution which also leads to a reduction in porosity and permeability due to chemical-induced grain compaction.

The precipitation of cements along and adjacent to a fault zone, resulting in changes in porosity and permeability controlling the sealing capacity, can be induced by changes in the fluid pressure and temperature experienced by fluids during the faulting process. Sibson (1981)[57] first presented a detailed analysis of the fluid pressure cycles associated with faulting. Models were presented (Sibson, 1990[58]) for the behaviour of faults as "valves" which control the channelling of fluids in fault zones and as "pumps" which cause expulsion of accumulated fluids. Direct evidence that channel flow of aqueous fluids accompanies shallow crustal faulting comes from the observation of transitory surface effusions following some moderate to large earthquakes in consolidated rocks, and the textural characteristics of the hydrothermal vein systems often found associated with ancient exhumed faults. Such phenomena were considered in relation to two alternative models. In the first, the transitory post-seismic flow can be readily interpreted in terms of the "dilatancy/fluid diffusion" hypothesis with fluid expulsion resulting from the collapse of a broad network of pre-failure dilatant fractures enclosing rigid crustal blocks, in response to the decrease in deviatoric stress accompanying slip. Essentially the fault/fracture system is acting as a "pump" with aqueous fluids being slowly drawn into the dilatant fracture system as elastic strain accumulates, to be rapidly expelled in a pulse every time slip occurs on the main fault as shown schematically in Fig.2.3.2.1(a). In the second, diametrically opposed model, the fault/fracture system functions as a self-sealing "valve" on a fluid reservoir, as shown in Fig.2.3.2.1(b). In such a model, it is the slow

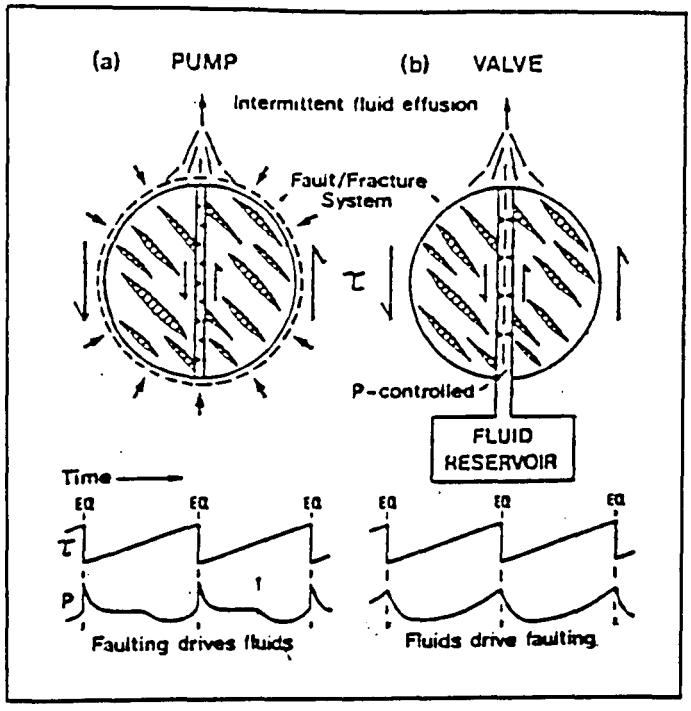

Fig.2.3.2.1 "Pump" (a) and "valve" (b) models for fluid outflows following shallow crustal earthquakes (EQ), after Sibson [57].

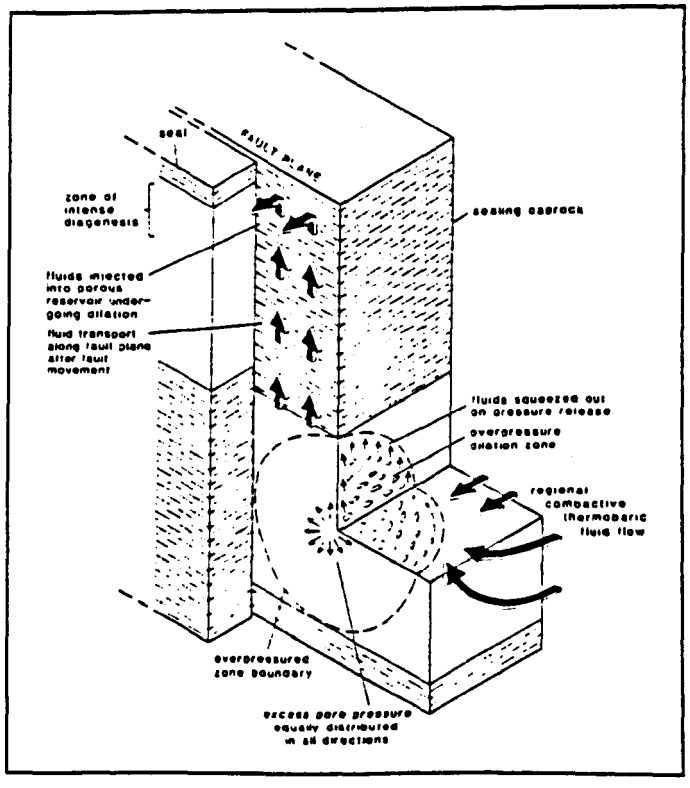

Fig.2.3.2.2 Schematic model of the seismic valving mechanism for fluid transport up faults, after Burley *et al* [59].

build-up of fluid pressure that periodically induces fault slip, rather than the other way around. Once failure has occurred (in accordance with the effective stress law, $\tau=\tau_0+\mu(\sigma_n-p)$) freshly created fracture permeability on the fault and allied fractures allows fluids to escape, so that pressure in the reservoir drops, progressive deposition of hydrothermal minerals re-seals the fracture system, and the whole cycle may be repeated.

Seismic valving was propounded by Burley *et al* (1989)[59] as an elegant mechanism for explaining the timing of diagenesis in the Tartan field and adjacent Witch Ground Graben (UK North Sea) as constrained from combined cathodoluminescence microscopy and fluid inclusion studies of successive cement generations. The sequence of mineral cements was found to be cyclical, such cyclicity suggesting multiple injection of similar pore fluids, explainable through repeated movement of similar pore fluids along fault conduits. A mechanism involving inflation of pores and microfracturing in mudrocks juxtaposed against the sealing faults that delineate the Tartan structure is envisaged as the main process involved in the emplacement of fluids in the Tartan reservoir (Fig.2.3.2.2). Dilation and microfracturing result simply from overpressure induced by a compactional thermobaric drive. As the fluid pressure in the mudrocks juxtaposed against the sealing faults gradually rises, frictional resistance on the fault plane decreases until the point is reached where the rising shear stress exceeds the frictional resistance. The ensuing rapid release of shear stress as failure occurs relaxes the inflated pores and microfractures within the dilatant zone. Pore fluids are rapidly expelled along the direction of least resistance, fluid transport from the collapsing dilatant zone thus taking place along the main fault plane and adjacent parallel fractures. After fluid escape, pressure in the dilatant zone drops, the fault re-seals and the thermobaric drive restarts the process. Thus in this model, it is the gradual build-up of overpressure that periodically induces fault failure.

Sibson also emphasised the role of dilation sites created along the fault zones during the displacement events (e.g. dilational jogs, see Sibson, 1985[60]) as locations where rapid fluid influx and pressure drops can induce preferential precipitation. Knipe[53] notes that the dilation magnitude together with the fluid pressure and permeability changes during faulting events, will all influence the volume of cement produced, for example in fault

zones where both dilation and fluid pressure changes are large, very rapid precipitation can result with the production of a breccia composed of rock fragments floating in cement (termed implosion breccias by Sibson, 1986[61]). Implosion breccias are related to the collapse of the wall rock into dilation sites generated by the slip events. In contrast, for slip events in which fault zone dilation at the time of precipitation is suppressed, so that cataclastic fragments remain in contact to provide a load-bearing framework, cement precipitation will create overgrowths within the pores of the cataclasite. Irrespective of the detailed mechanism of cement generation involved, Knipe[53] considers the reduction in both porosity and permeability through cementation to be large, with for example 20% initial porosity sandstones typically showing reductions to <1%, with attendant permeability diminishment of over an order of magnitude.

2.3.3 Shale Smears

"Shale smear" is a general term used to describe a shale or clay layer intervening between sandstone units juxtaposed across a fault, in the manner of fault-plane "fillings" rather than fault gouges (Smith, 1980[62]). Whilst early descriptions of shale smears (for example Weber *et al* , 1978[63]) are of occurrences on growth faults, the examples described by Lindsay *et al* , 1991[64] are the result of tectonic faulting of lithified sediments. They examined the nature and systematics of shale smears in working quarries exposing Westphalian sandstone/shale sequences offset by faults of up to 15m throw. The smears occurred on sandstone/sandstone fault surfaces, some extending from footwall to hangingwall cut-offs of the shale source layer. The smears hydraulically separate sandstone units in footwall and hangingwall which, in the absence of shale smearing, would be expected to be hydraulically connected across the fault. Three distinct types of shale smear were recognised, and named according to the proposed mechanism of their formation: (i) abrasion smear; (ii) shear zone smear; (iii) injection smear.

Abrasion smears were found to be the most common and occurred as uniform, wafer-thin (<1mm) films or veneers on sandstone fracture surfaces. Surface markings such as striae and tool marks from embedded breccia clasts were commonly observed. Relative movement of shale past a sandstone surface leaves a thin veneer of shale on the sandstone

surface in much the same way as a film of abraded material builds up on and smoothes the surface of sandpaper or some other abrasive. As soon as a continuous veneer is formed little or no further abrasion takes place and the thickness of the veneer is not progressively increased. Whether or not a shale veneer is present will depend less on the thickness of the source shale layer, than on the amount of subsequent movement on the juxtaposed sandstone surfaces and on their roughnesses (formation and preservation of abrasion smears is favoured by sandstone fault surfaces which are rough on the mm scale, but smooth on the cm and larger scales).

A shear zone smear can form by offset of a shale layer on a plastic shear zone comparable with the zones of simple shear in igneous and metamorphic rocks in which they are often the predominant displacement structures (Ramsay, 1980[65]). Shear zones are essentially faults in which continuity of layers is maintained within the shear zone, but individual layers are thinned, extended and rotated within the zone. Faults in soft sediments frequently show this continuous displacement geometry, whilst displacement on tectonic faults in lithified sediments may be partly accommodated by continuous and partly by discontinuous displacement - the ideal single shear fracture (discontinuous) and the ideal shear zone (continuous) are simply the end members of a spectrum of displacement geometries in which the total displacement is the sum of the two components. The geometry of such shear zones is illustrated schematically in Fig.2.3.3.1 in which the relationship between shear zone displacement (d), shear zone thickness (T_{zone}) and shear strain (γ) are shown. The thickness of a displaced layer within a shear zone (i.e. the smear thickness) decreases as a function of the shear strain (Ramsay & Huber, 1983[66]) and is given by:

$$T_{smear} = T_{original}(\sin\alpha'/\sin\alpha) \quad \ldots\ldots\ldots \quad \text{Eqn.2.3.3.1}$$

where $T_{original}$ and T_{smear} are respectively the shale layer thicknesses outside and inside the shear zone and α and α' are the angles between the layer and the shear zone outside and inside the shear zone respectively (Fig.2.3.3.1).

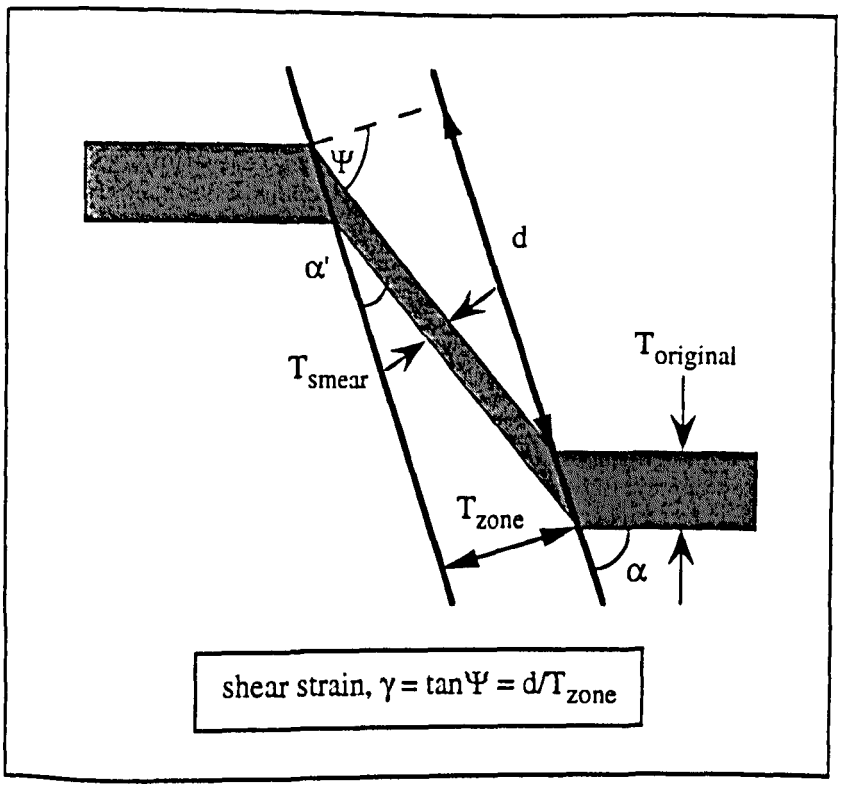

Fig.2.3.3.1 Schematic of a shale smear simple shear zone analogy (see text for details).

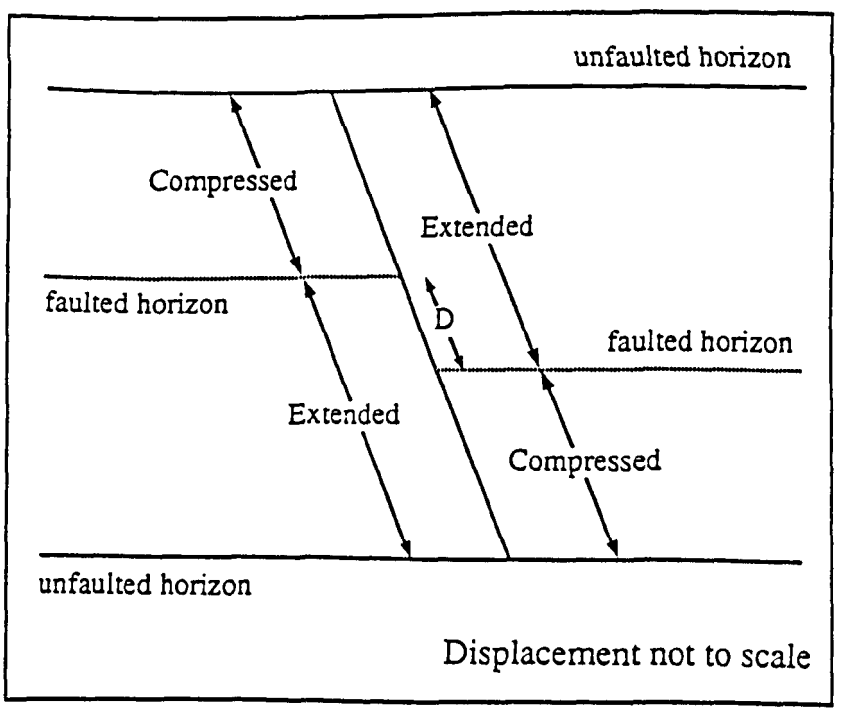

Fig.2.3.3.2 Schematic of the strained volume of rock associated with normal fault slip, after Lindsay *et al* [64].

Injection smears are hypothesised to arise from the concept that variable displacement along faults requires volume decrease adjacent to the fault on one side and dilation on the other side (Barnett *et al* , 1987[67]) as shown schematically in Fig.2.3.3.2. Such changes are preferentially accommodated by shale layers which are thinned on one side and thickened on the other side of the fault. So long as the throw is less than the shale layer vertical thickness, flow of shale is possible across the shale/shale interface, however when the footwall and hangingwall cutoffs of the shale layer are no longer juxtaposed, the same pressure gradient exists to drive shale from one side of the fault to the other along the fault surface. The mechanism is favoured by the presence of plastic clays which in the outcrops studied by Lindsay *et al* [64] characteristically occurred as seatearths in coal bearing sequences.

Lindsay *et al* defined the ratio of fault throw to vertical thickness of the offset shale layer (known as the Shale Smear Factor, SSF) as a robust measure to examine the continuity of shale smears. Their data indicated that continuous smears are to be expected for SSF values of 9 or less but may also occur with SSF values of up to 50 (Fig.2.3.3.3). This overlap in SSF values for incomplete and complete smears reflects the variety of mechanisms and controls involved.

Weber *et al* [63] performed a series of ring-shear tests of sand/clay systems to simulate faulting and clay smear emplacement in a deltaic sandstone-shale sequence. The ring-shear apparatus consisted of a ring-shaped container, the upper half of which was fixed whilst the lower half rotated (Mandl *et al* , 1977[68], see description in section 3.3.5). The clay bands were sheared off under various simulated overburden pressures along a median slip plane, and formed a single continuous multi-layered clay gouge along the shear zone, which proved to be an effective seal to vertical water flow when tested. These experimental results were then compared with field observations of syndepositional normal faulting of a clastic Tertiary deltaic sequence in the opencast lignite mines of Frechen, West Germany. The actual mechanism of clay emplacement was considered

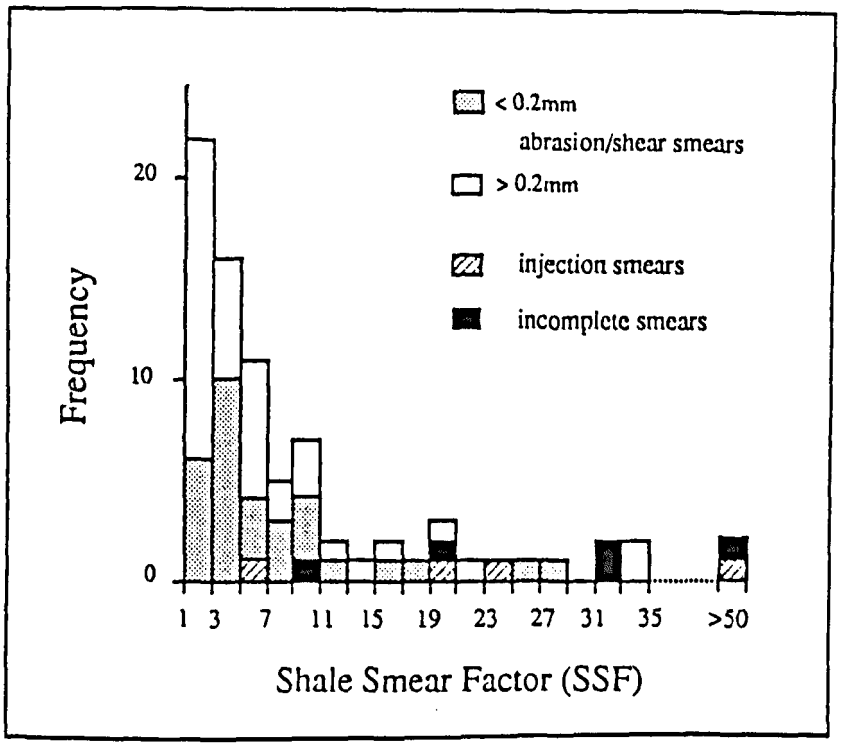

Fig.2.3.3.3 Histogram showing the types of shale smear for the full range of Shale Smear Factor (SSF) values, after Lindsay *et al* [64].

probably to be more effective than in the laboratory model, involving a larger amount of material being squeezed into the fault zone. Clay gouges within the field shear zones decreased in thickness away from the source beds, and individual clay gouges from separate source beds coalesced to form one multilayered clay gouge. Thicker shale source beds provided longer more continuous clay gouges than thinner ones.

2.3.4 Granulation Seams

Volumetrically, planar tectonic features contribute very little to the total porosity of an aquifer or hydrocarbon reservoir (see discussion in section 2.1) with the matrix porosity being orders of magnitude more important, however matrix porosity between tectonic surfaces is only effective porosity when these surfaces do not have reduced permeability characteristics. Whilst the fluid flow characteristics of small-scale sedimentary features and architecture have received considerable attention, especially with the development of probe permeametry, the fluid flow characteristics of tectonic surfaces acting as baffles as opposed to conduits has been largely ignored. Thus whilst the sealing characteristics of tectonic surfaces have a crucial influence on the overall large scale flow characteristics of porous media, surprisingly little work has focused on the micromechanics of the sealing mechanism. Chapter 7 of this thesis work attempts to address this interesting topic, through direct quantification of the effective sealing potential of experimentally produced shear fractures induced under various triaxial stress states, and the relationships between permeability modification and the nature of the shear debris (artificial fault gouge) generated.

Fluid flow retardation is associated with various tectonic features (for example pressure solution seams) however granulation seams are a particularly important type of permeability barrier. They occur as conjugate sets within high porosity sandstones which form some of the most productive hydrocarbon reservoirs in the North Sea. Though their displacement is small and width limited on individual seams (both generally <10mm) they act as extremely effective permeability barriers and are thus one of the most significant types of planar heterogeneity in many massive sandstone hydrocarbon reservoirs, with otherwise excellent fluid sweep potential. In many of these fields,

intersecting granulation seams in three dimensions serve to compartmentalise the reservoir, such that blocks can often have quite different physico-chemical features (for example diagenetic histories through differential flow rates of formation fluids), poroperm characteristics and can even lack hydrocarbons.

Cataclasis leads to zones of grain rearrangement and comminution which have been referred to by a plethora of terms as summarised in Table 2.3.4.1. As the terms listed in this table were applied to specific cases, rather than being intended for general usage, they tend to be mutually conflicting, and fail to concur with all recorded observations. In light of this rather confusing current terminology, partly genetic, partly descriptive, the term "granulation seam" will be adopted here for such structures, as although perhaps no more apt than the others, it seems to have achieved more widespread usage in the current literature. The nature of faulting in porous sandstones is typically as that described for faults in the Navajo and Entrada sandstones of SE Utah (see Aydin 1978[70], Aydin & Johnson, 1978[76] and Aydin & Reches, 1982[77]). Both sandstones are friable, composed primarily of quartz and feldspar, and possess porosities of around 25%. Three forms of faults are recognised in these sandstones (Fig.2.3.4.1): (i) deformation bands; (ii) zones of deformation bands; (iii) slip surfaces. Each form occurs in dip-slip, strike-slip and oblique-slip orientations. Small faults occur as deformation bands, about 1mm-thick, in which pores collapse and sand grains fracture and along which there are shear displacements of the order of a few mm's to cm's (a). Two or more adjacent deformation bands (b) that share the same strike and dip form a zone of deformation bands (c). A zone becomes thicker by the addition of new bands side-by-side. Slip surfaces, pervasive surfaces of discontinuity in displacement, form at either edge of zones of highly concentrated deformation bands, and can accommodate large displacements in then order of several or tens of metres (d). Such subdivisions (Fig.2.3.4.2) were also found applicable in the high porosity aeolian sandstones (Lower Permian Penrith Sandstone Formation) at outcrop in NW England and SW Scotland, by Fowles & Burley (1994)[78].

With regard to their mechanism of formation, it is well documented in the references listed in Table2.3.4.1 that cataclasis is the primary deformation mechanism, involving

Term	Author
Braided Shear Fracture	Engelder (1974) [69]
Deformation Band	Aydin (1978) [70]
Granulation Seam	Pittman (1981) [71]
Microfaults/Gouge Zones	Jamison & Stearns (1982) [72]
Shear Fault	Blenkinsop & Rutter (1986) [73]
Granulated Fault Strands	Underhill & Woodcock (1987) [74]
Tabular Compaction Zones	Kulander *et al* (1990) [75]

Table 2.3.4.1 Terms in the published literature synonymous with "granulation seam".

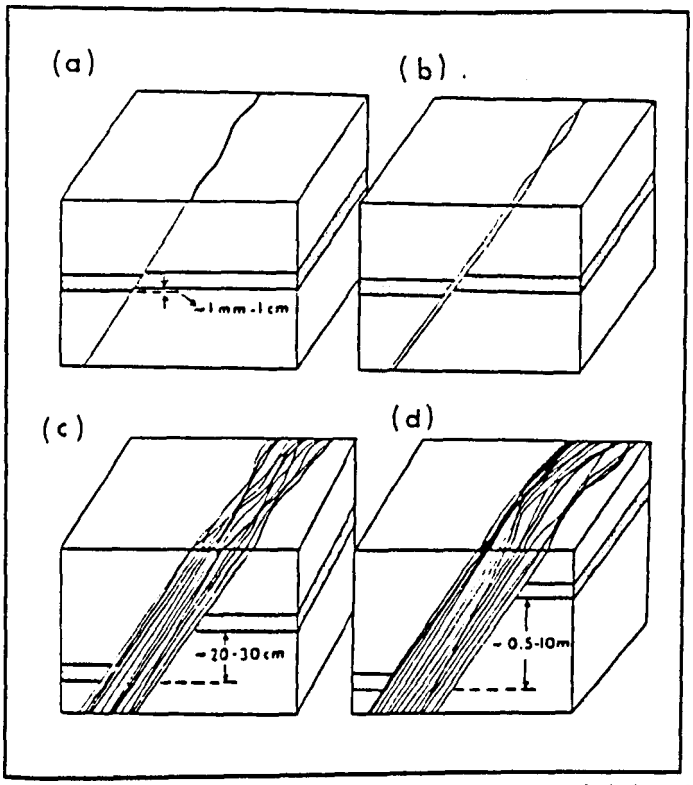

Fig.2.3.4.1 Series of block diagrams showing the sequential development from a single deformation band to a slip surface (see text for details) after Aydin & Johnson [76].

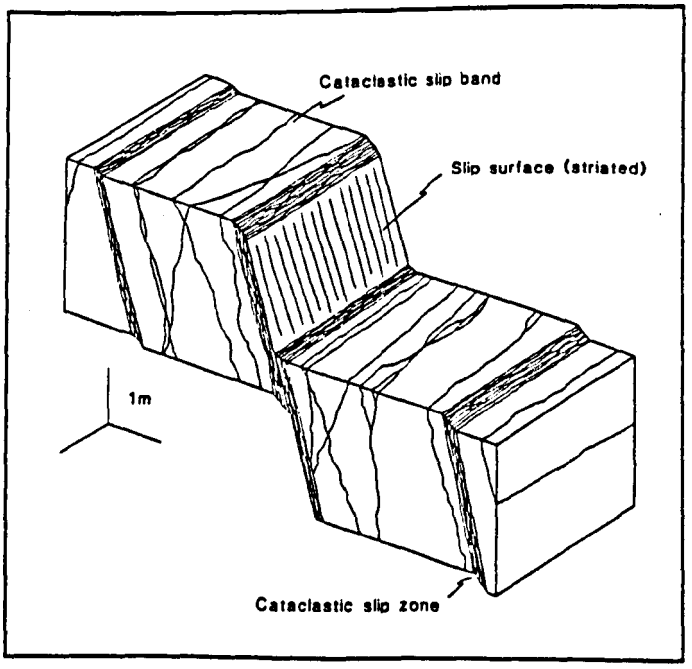

Fig.2.3.4.2 Schematic depicting the relationships between cataclastic slip bands, cataclastic slip zones and slip surfaces, after Fowles & Burley [78].

both grain fragmentation and rigid body rotation. Underhill & Woodcock (1987)[74] present an interpretation of the faulting mechanism associated with granulation seams within New Red aeolian sandstones outcropping on the Isle of Arran. Thin-sections cut across such faults in Arran show a three-fold subdivision similar to that described by Aydin[70], based on differing microstructure (Fig.2.3.4.3). The host sandstone consists of rounded, loosely packed grains with iron oxide coatings and a grain-contact cement, and possesses high porosity and interconnected porespace suggesting high permeability. The outer zone of the fault is generally 0.75 - 0.5mm in width, and consists of predominantly well-sorted, unfractured grains showing tighter packing due to rupture of the grain-contact cement, so that porosity is reduced. The inner fault zone is generally <5mm in width and is characterised by poor sorting and low porosity, with a few large rounded grains sitting in a fine-grained matrix of spalled grain fragments, overgrowths and cement. Such microstructural observations provided Underhill & Woodcock[74] with an interpretation of the faulting mechanism, suggestive of the idea that the unusual character of faults in high porosity sandstones was the direct result of strain hardening of each fault after only a small increment of slip.

Consider theoretical Mohr circle plots (Fig.2.3.4.4) to compare the more general case of a rock that strain softens at failure, as shown in Fig.2.3.4.4(a), with one in which strain softening occurs as in Fig.2.3.4.4(b). For strain softening of a host rock with failure envelope A (for fracture) the resulting fault zone would have a failure envelope B (for friction) with similar friction angle and a lowered cohesive strength, so that when the ambient stress field builds up again, the stress circle will impinge on envelope B before A, so that failure occurs preferentially along the already faulted zone (representing a planar band of weakness). In contrast, a strain hardened fault must be represented by a frictional failure envelope that lies outside that of the host rock fracture envelope A in the stress range of interest, Underhill & Woodcock suggesting two mechanisms by which this scenario could occur: (i) through an increase in the cohesive strength during failure with or without a change in friction angle, as shown by friction envelope C in Fig.2.3.4.4(b); (ii) through an increase in friction angle during failure with or without a change in

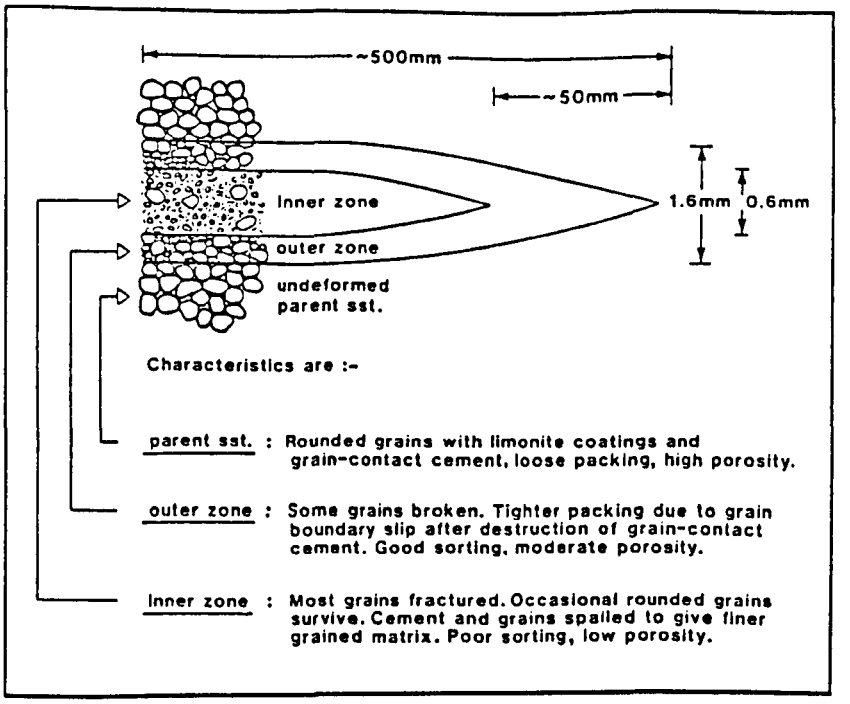

Fig.2.3.4.3 General microstrucutural characteristics in an idealised fault zone, after Underhill & Woodcock [74].

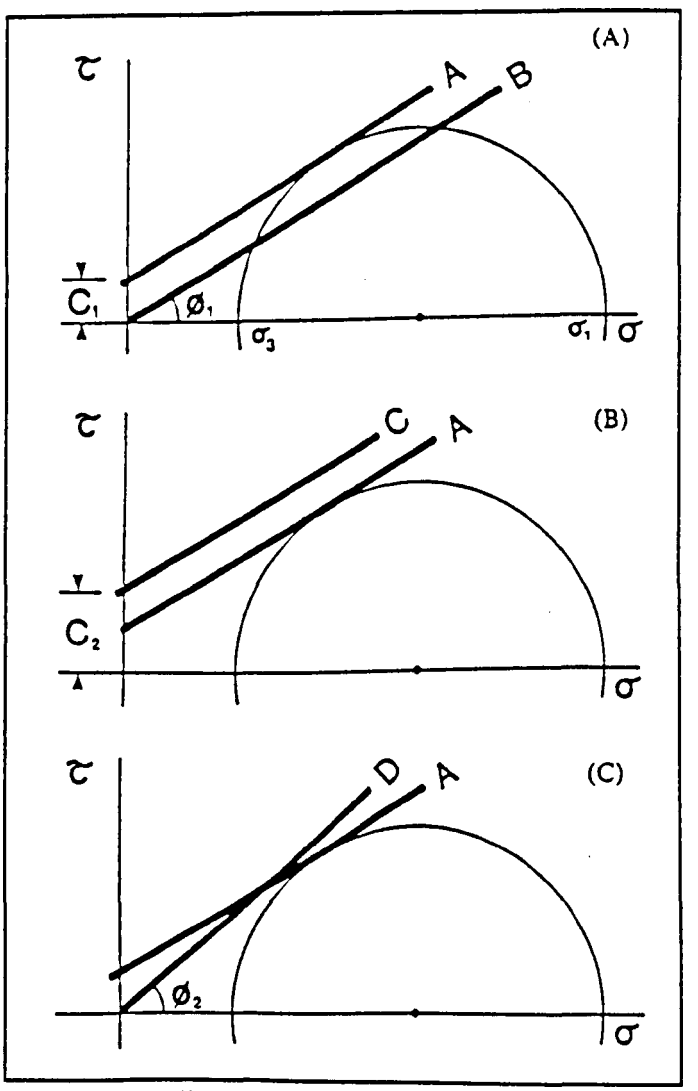

Fig.2.3.4.4 Mohr stress diagrams for faults that (a) strain soften and (b, c) strain harden (see text for details) after Underhill & Woodcock [74].

cohesive strength, as shown by friction envelope D in Fig.2.3.4.4(c). For both scenarios renewed failure would occur in virgin host rock rather than on the pre-existing fault.

Underhill & Woodcock investigated theoretically which of the above two effects is the more likely for the high porosity Arran sandstones, applying soil mechanics principles to the fault zone. Assessment of the mechanical processes operating along such a fault suggested that, immediately after slip, it has a lower cohesion but higher friction angle than the host rock, cohesion being lost throughout the fault mainly by progressive rupturing of the weak grain-contact cement, friction angle increasing in the outer zone through tightening of grain packing and in the inner zone through intensifying interlocking as a result of both increasing angularity and poorer sorting. It is also possible (though unproved *in situ*) that minor recementation of grain-contacts along the fault could occur between slip increments, causing some recovery of cohesive strength and further enhancing fault hardening. Also, uniform coarse sands show a high rate of granulation during slip due to the low number of grain-contacts per unit volume with correspondingly high grain-contact stress concentrations As grain size and sorting decrease, grain-contact stresses rapidly fall so that granulation rate also decreases, perhaps explaining why a few large grains may survive within the inner zone of a fault once they are surrounded by fine material.

Following Underhill & Woodcock, in Fig.2.3.4.5 curve A represents a typical stress-strain profile for a rock or dense uncemented sand that strain softens, whereas curve B represents a loose-packed sand that strain hardens. For uncemented sands that are not granulating, curves A and B converge at a packing density (the "critical state") at which the sand can deform continuously without further porosity change (c.f. superplastic flow) as detailed in Lamb & Whitman (1969)[79]. Curves C, D and E represent the stress-strain behaviour of progressively finer, more poorly sorted sediment. The postulated stress-strain path for a high-porosity weakly-cemented sandstone initially follows curve A with, at strain "a" the grain-contact cement commencing fracture, resulting in collapse of the grain framework. The newly formed fault zone will initially strain soften due to progressive loss of cohesion and transient lower friction angle, so that a texture like that

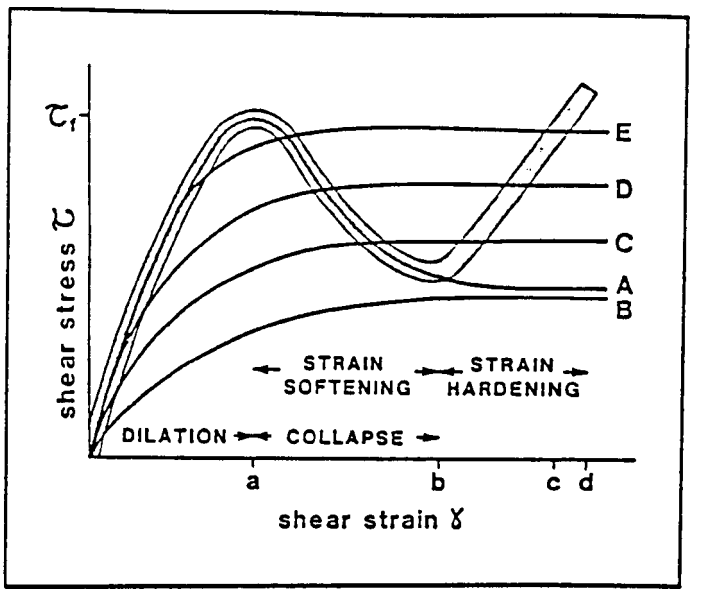

Fig.2.3.4.5 Stress-strain path during failure of a strain-hardening fault, (see text for details) after Underhill & Woodcock [74].

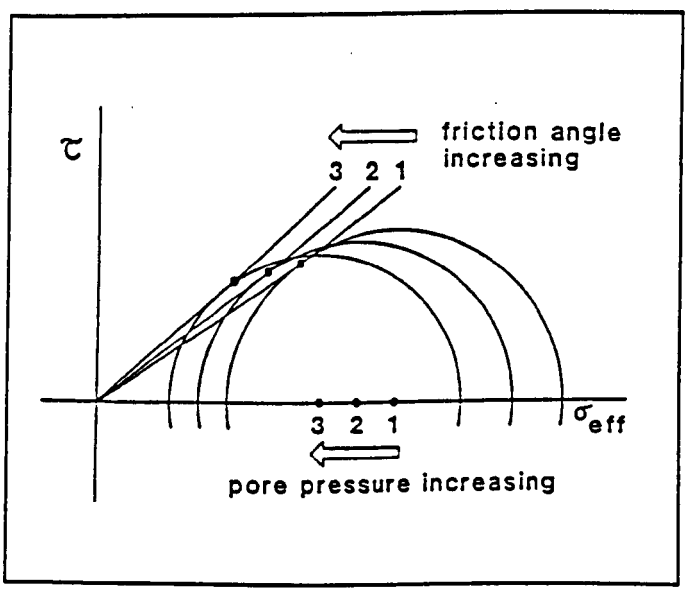

Fig.2.3.4.6 Successive Mohr stress circles and failure envelopes (1, 2, 3) for a fault with rapid transient increase in pore pressure during failure (see text for details) after Underhill & Woodcock [74].

of the outer fault zone (Fig.2.3.4.3) develops. The fault is postulated to behave as though it were an uncemented sand so that its deformation path would follow curve A, were it not for the depth of burial being sufficient for ambient stress magnitudes to induce grain fracture. In this case, when the grain framework can collapse no further (at strain "b") grains start to fracture, initially at a high rate but decreasing as grain-size decreases. Friction angle increases and the stress-strain path is driven up again by the strain hardening effect, crossing curves C, D and E at a strain appropriate to the grain-size at the time. Finally, the fault zone locks at strain "d" as it strain hardens to a point at which its frictional resistance exceeds the shear stress along it.

An obvious problem with this stress-strain path, as noted by Underhill & Woodcock, is that the locked-up stress must exceed the initial failure stress, (T_f in Fig.2.3.4.5) if net strain hardening has occurred. Two possible explanations were proposed. The first is that stress overshoot does not in fact occur, the fault locking up when the frictional resistance reaches the initial host rock failure (fracture) stress at strain "c". The second is that apparent stress overshoot occurs because of transient pore pressure increase along the fault. In the latter case, it is possible for the shear stress on the fault to remain constant or even to decrease, but still promote slip due to the effective normal stress being lowered by the increasing pore pressure. On a Mohr circle plot (Fig.2.3.4.6) this situation can be represented by successive stress circles being driven to the left to track a series of failure envelopes with increasing friction angle. After failure, the excess pore pressure dissipates and the stress circle moves to the right, well away from the failure envelopes. Whilst long-term abnormal pore pressures seem unlikely in these porous and permeable sandstones, transient high pore pressures along the faults seem likely during slip. Pore fluid has to escape from both the outer and inner zones of the fault as porosity decreases, its escape being progressively slowed, especially in the inner zone, by decreasing permeability, suggesting transient overpressuring of the fault zone as a plausible cause of apparent stress overshoot.

Aydin & Johnson (1983)[80] also studied the mechanisms and mechanics of faulting in porous rocks, in terms of a theory of deformation of elasto-plastic, time-independent

materials developed in a series of papers by Rice, Rudnicki and Cleary (Rice, 1975[81], Rudnicki & Rice, 1975[82], Cleary & Rudnicki, 1976[83], Cleary, 1976[84], Rudnicki, 1977[85], Rice, 1979[86]) and by Eshelby (1957)[87], which generalised plasticity theory such that it can describe localised deformation in idealised plastic or brittle materials. The tendency for strain to localise in porous rocks can be understood in terms of "bifurcation" in the macroscopic constitutive relations (see for example Vardoulakis *et al*, 1980[88]). Mathematically speaking, here "bifurcation" refers to loss of uniqueness of the boundary solution as a result of considering the shear band as a zone in which there is localisation of strain leading to a macroscopic instability of the material. Aydin & Johnson[80] observed that slip surfaces in the Entrada and Navajo sandstones occurred within well-developed zones of deformation bands, representing extremely localised, large deformation. They interpreted the formation of such slip surfaces in terms of instability represented by Rudnicki's[85] "runaway instability" and by Rice's[86] "Eshelby line" describing interaction between the inelastic properties of the material, in this case the fault zone, and the "softness" of the loading system, in this case the matrix. In effect, the relatively soft matrix behaves much as a "soft" loading machine used in testing rocks in which a rock specimen (analogous to the fault material) fails violently as strain energy is released from the loading machine. As the material within a fault zone is stiffer than the surrounding sandstone matrix, as described by Underhill & Woodcock[74], the stresses within the zone are higher than the far-field stresses, so that the surrounding sandstone can be deforming elastically under relatively low far-field stresses, whereas the stresses within the zone can be sufficiently high for the strains to become extremely large, field observation by Aydin & Johnson[80] showing these large strains being accommodated along a discrete surface or discontinuity.

A comprehensive summary of production-related properties of granulation seams (specifically permeability and porosity reduction) is given by Kulander *et al* (1990)[75]. The concept of permeability reduction in a fault zone is based on a limited set of permeability measurements (Pittman, 1981[71], Harper & Moftah, 1985[89], Nelson, 1985[90]) made perpendicular and parallel to a gouge zone in sandstone, indicating dramatic

variation in percentage reduction of gouge zone compared to matrix permeability, both within an individual formation (11 to 95%) and between formations (11 to 99%). Such wide variations in the percentage of permeability reduction is almost certainly a function of varying host rock composition, grain size and porosity, combined with variations in the degree of granulation involved. Apparent porosity reductions as observed in thin-section have been reported frequently (Aydin[70], Pittman[71], Jamison & Stearns, 1982[72], Nelson[90], Underhill & Woodcock[74]) however due to the very small grain-sizes involved, estimates of porosity from thin-section point-counting techniques should be treated with caution. Aydin[70] used a statistical approach to determine the average porosity reduction in a series of gouge zones in sandstone. By calculating the difference in the average porosity of two populations of plugs, one with and one without gouge zones, the average porosity reduction associated with granulation of the host rock was determined at around 60 to 75%. As an alternative to thin-section analysis and the Aydin statistical approach, Kulander *et al* [75] examined the porosity reduction in a more rigorous manner through Computerised Axial Tomography (CAT) scanning techniques, and found an average porosity reduction of 46% for a whole core sample with a single inclined granulation seam.

2.3.5 Fault Seal Capacity In the North Sea

The majority of North Sea structural traps require that at least one fault be a sealing fault. The typical trap in the North Sea is a tilted fault block with at least one fault sealing the hydrocarbon column. Faults can act as pressure barriers to subsurface fluids during the production life of a field or as differential migration barriers to hydrocarbons over geological time, so that an understanding of the probability of a fault acting as a differential migration barrier is critical for prospects relying on fault seal. The probability of a fault acting as a pressure barrier is important in field development and production where fault bounded compartments may not be in pressure communication because of sealing faults. Knott [47] examined over 400 faults from 101 exploration targets and 25 oil and gas fields in a regional study of fault seal in the North Sea. The faults cut clastic successions from a variety of depositional environments (marine, paralic and nonmarine) from both Brent Group and Rotliegendes Group stratigraphies. The emphasis of the study

was on fault-related seals that act as pressure or migration barriers over geological time, with one of the objectives being the determination of those parameters most important in controlling fault seals, especially where reservoir is juxtaposed against reservoir (empirical understanding of such controls is a prerequisite for fault seal prediction).

Knott classified fault related seals according to the following definitions (Fig.2.3.5.1):

(i) Juxtaposition fault. The fault forms an essential trapping element to an isolated hydrocarbon accumulation and sealing occurs due to abutment of the reservoir lithology against a sealing lithology

(ii) Partially sealing fault. The fault separates reservoir compartments with different hydrocarbon-water contacts in a single pool with no pressure drawdown between adjacent compartments during the production life of the field and over a range of pressure intervals

(iii) Temporary sealing fault. The fault may act as a temporary pressure barrier during production but not over geologic time, therefore no initial change occurs in elevation of the hydrocarbon water contact across the fault

For partially sealing faults, seal is provided mainly by the fault plane itself, due to, for instance, mechanical and chemical reduction of porosity and permeability of the reservoir rock within the fault zone, although a component of juxtaposition seal may also be present. For temporary sealing faults, seal may occur across the upper part of the fault due to juxtaposition and across the remainder of the fault by a combination of juxtaposition and membrane seal (the capacity of the latter in this case being insufficient to support differential hydrocarbon column heights across the fault over geological time). Knott analysed only the fault-related seals within classes (i) and (ii) as above, that is those faults (juxtaposition and partially-sealing) sealing over geological time, as primary interest lay in determination of those parameters controlling fault seal in exploration targets, and in faulted segments of fields with different hydrocarbon/water contacts (although some of the observations may well be applicable to temporary sealing faults).

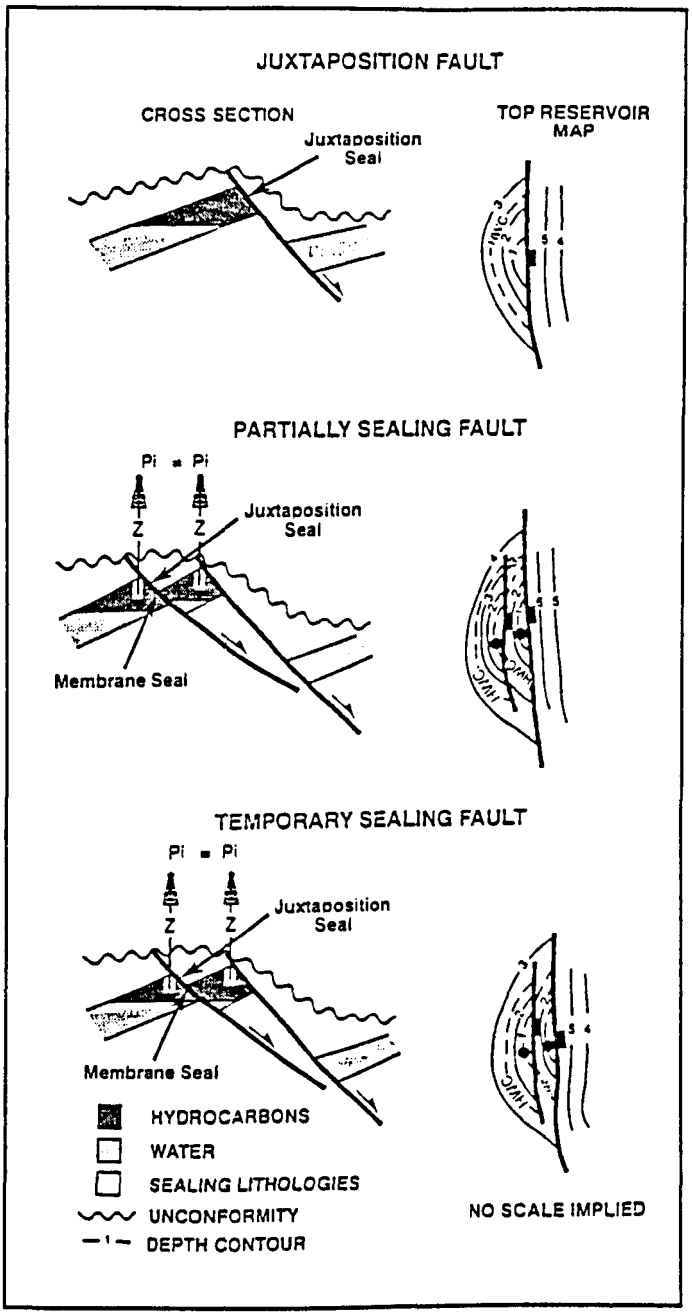

Fig.2.3.5.1 Fault-related seal classification (see text for details) after Knott [47].

In Knott's analysis, a fault was determined to be sealing *sensu stricto* (that is membrane sealing along the fault plane) from pressure data, geochemistry, hydrocarbon type, hydrocarbon-water contacts and production data where available. The importance of differentiating between geometries and mechanisms was also stressed, for example whilst a juxtaposition fault is a geometrical effect which may seal by that mechanism, the actual sealing may be provided by, for example, clay smear. A purely geometric subdivision was also employed, based on the relation between fault throw and reservoir interval thickness:

(i) Extrareservoir fault. A fault which completely offsets the reservoir interval against a sealing lithology

(ii) Intrareservoir fault. A fault which only partly offsets the reservoir interval, or throws one reservoir interval against another

Whilst the sealing mechanism in the former is generally by juxtaposition, in the latter the sealing mechanism can be either membrane seal (clay smear, cataclasis, or cementation along the fault plane) or juxtaposition. This geometric definition was deemed necessary because the North Sea reservoirs under consideration (Brent Group and Rotliegendes Group) are generally overlain and underlain by sealing lithologies at least as thick as the reservoir intervals, so that a useful first-order distinction exists where extrareservoir faults are more likely to provide juxtaposition seal than intrareservoir faults. Knott recognised the following parameters as important contributors to fault seal (see Fig.2.3.5.2):

(i) Fault orientation. Fault trend may influence sealing, for example in strike-slip systems reverse faults are considered more likely to seal than normal faults due to greater shear stress for fault displacement in the former

(ii) Burial depth. With increasing confining pressure, faulting mechanisms favourable to fault seal (such as cataclasis) are more pronounced, also diagenetic reactions that reduce porosity and permeability also increase with depth (however sealing due to clay smear is more likely at shallow depths where mud is undercompacted

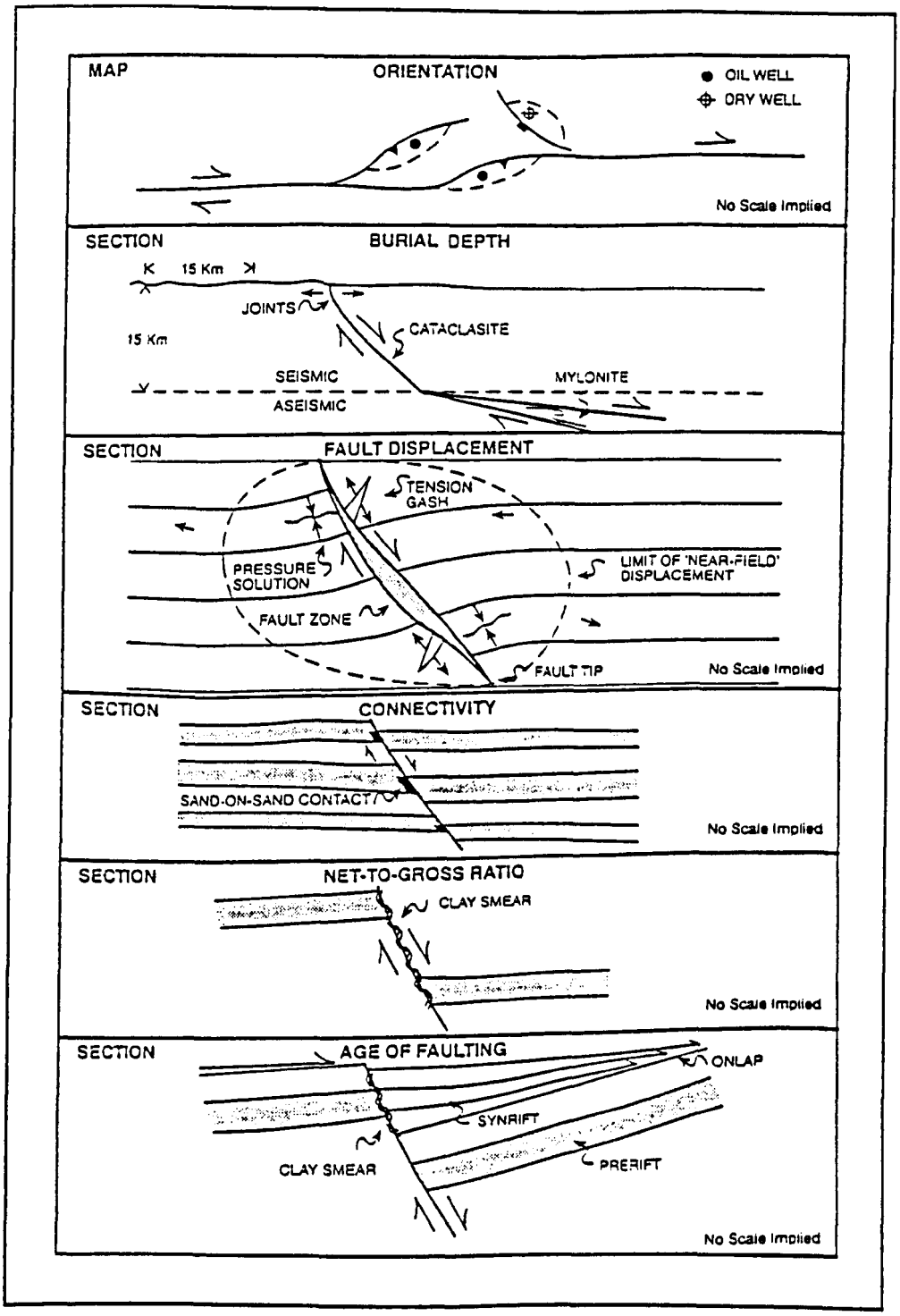

Fig.2.3.5.2 Parameters contributing to fault seal (see text for details) after Knott [47].

(iii) Fault displacement. For a particular lithology the larger the fault throw the wider the fault zone and the greater the mechanical reduction in porosity and permeability due to cataclasis. With varying fault displacement, zones of extension (tension gashes) and contraction (pressure solution) form, with fault seal being less likely in zones where open fractures are present

(iv) Net-to-gross ratio (N/G). Defined as the thickness of the net reservoir divided by the overall thickness of the interval in question, the percentage and distribution of nonreservoir rocks in a succession indicates the likelihood of ductile smear or injection (membrane seal) of these lithologies along the fault zone. The N/G also indicates the probability that there are sandstone to sandstone contacts across the fault (not necessarily of the same unit)

(v) Connectivity. Juxtaposition of reservoir against nonreservoir across a fault produces a juxtaposition seal. Defined by Knott as, "the fraction of net sand in the reservoir interval in geometric contact across the fault" a complete analysis of the role of connectivity requires an accurate picture of the stratigraphy on either side of the fault for its entire length. Sand-on-sand contacts across faults where there is no membrane seal or clay smear are unlikely to provide seal

(vi) Age of faulting. Syndepositional faulting usually favours membrane sealing as muds are generally undercompacted, exhibiting greater ductility, and are therefore more likely to smear than shales in pre-rift sections which are more likely to be indurated (hardened)

Knott plotted parameters including fault strike and throw, reservoir thickness and depth, N/G, porosity and net sand connectivity against seal performance to define trends and correlations to predict fault seal characteristics. In summary, a correlation was evident (although not statistically significant) between fault orientation and sealing, sealing was found proportional to fault throw normalised as a fraction of the reservoir thickness, and the great majority of faults with throws greater than the thickness of the reservoir interval were sealing faults. Knott concluded that the most useful parameters in fault seal prediction are fault displacement, N/G and net sand connectivity.

2.4 DEFORMABILITY

In an assessment of the effects of shear discontinuities in the hydrocarbon reservoir environment, fault population statistics (section 2.2) and sealing potential (section 2.3) have been discussed in terms of their relative influence on hydrocarbon structural entrapment and pore fluid migration. However, whilst the above effects represent (with the exception of the seismic pumping/valving phenomena) largely "passive" controls on fluid flow, current rock mechanics philosophy also predicts a "reactive" role for shear discontinuities, due to the response of pre-existing fractures and indeed the formation of new fractures resulting from transients in the *in situ* stress field associated with production. In section 2.4 the role of shear discontinuities in controlling overall reservoir deformation resulting from temporal variations in specifically pore fluid pressure are assessed. In section 2.4.1 the phenomenon of reservoir seismicity due to induced fault formation and reactivation is discussed, whilst in section 2.4.2 induced shear slippage on planes of sedimentary heterogeneity, as an important contributing mechanism for strain accommodation within a deforming reservoir, is reviewed.

2.4.1 Production-related Seismicity

In recent years it has become increasingly apparent that some of man's engineering activities can have a measurable influence on the way in which crustal stresses are released in earthquakes. Increases in seismic activity have resulted from: impoundment of reservoirs behind high dams; large-scale surface quarrying; deep underground mining; the injection of fluids under high pressure into the ground in solution mining, waste disposal, geothermal power generation, and secondary oil recovery; the removal of fluids in hydrocarbon recovery; the after-effects of large underground explosions. A number of adjectives have been used to describe this type of seismicity - "man-made", "induced", "artificial" and "triggered".

Engineering works can influence the *in situ* stress regime through changes in solid (elastic) stress or fluid (pore) pressure. The orientation of the principal stresses in nature varies with the tectonic environment, with the minimum principal stress, σ_3, vertical in

regions of thrust faulting, the maximum principal stress, σ_1, vertical in regions of normal faulting and the intermediate principal stress, σ_2, vertical in regions of strike-slip faulting, so that the triggering effect of the induced elastic stress will be greatest in regions where the induced stress adds to the tectonic shear stress by increasing the radius of the Mohr circle representing σ_1 and σ_3, either by increasing σ_1 or decreasing σ_3. Thus an increase in vertical stress from the elastic load of a dam impounded reservoir will have the greatest impact in regions of normal faulting where the vertical stress is the maximum, whereas a decrease in vertical stress due to the removal of surface load in quarrying operations will have the greatest impact in regions of thrust faulting, where the vertical stress is the minimum. Increasing pore pressure (for example by fluid injection) whilst not changing the radius of the Mohr stress circle, translates the circle to the left on a Mohr diagram, and thus always moves the circle towards the failure envelope, regardless of the tectonic stress environment.

In terms of this simple representation of failure, earthquakes are triggered when one of the following situations occurs (Simpson, 1986[91]): (i) the pre-existing stress conditions on a fault are such that the magnitude of the induced stresses are sufficient to produce failure; (ii) the triggering source acts to drive the natural stress condition closer to the failure envelope either (a) by a purely elastic effect increasing the differential stress (increasing the diameter of the Mohr circle) or (b) through increased pore pressure, decreasing the effective stress (translating the Mohr circle towards the failure envelope) or (c) a combined elastic and pore pressure effect. In Fig.2.4.1.1, comparison is made between the influence of isolated changes in elastic stress decrease (a) for mining and increase (b) for "dry" reservoir impoundment (zero pore pressure effects), isolated changes in pore pressure (c) for fluid injection, and combined elastic and pore pressure effects (d) for "wet" reservoir impoundment (significant pore pressure effects).

With regard to hydrocarbon reservoirs, very few oilfields have been monitored by standard microseismic techniques, but of those which have, there is substantial evidence of induced fracturing. This takes the form of microearthquakes of magnitude, M>3 on the local Richter scale, corresponding to slip on faults up to a scale of a few hundred metres,

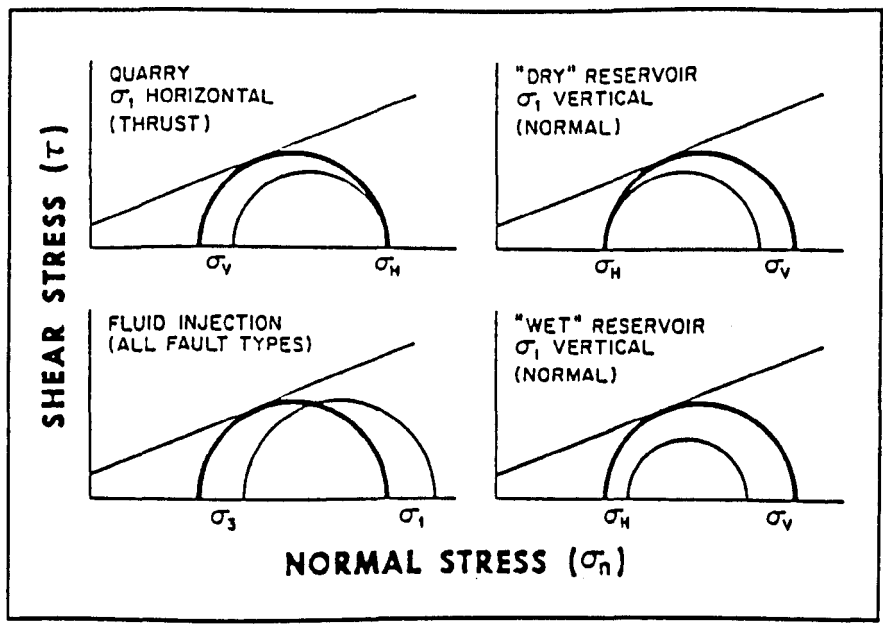

Fig.2.4.1.1 Examples of induced changes in stress that can trigger failure in different faulting environments (see text for details) after Simpson [91].

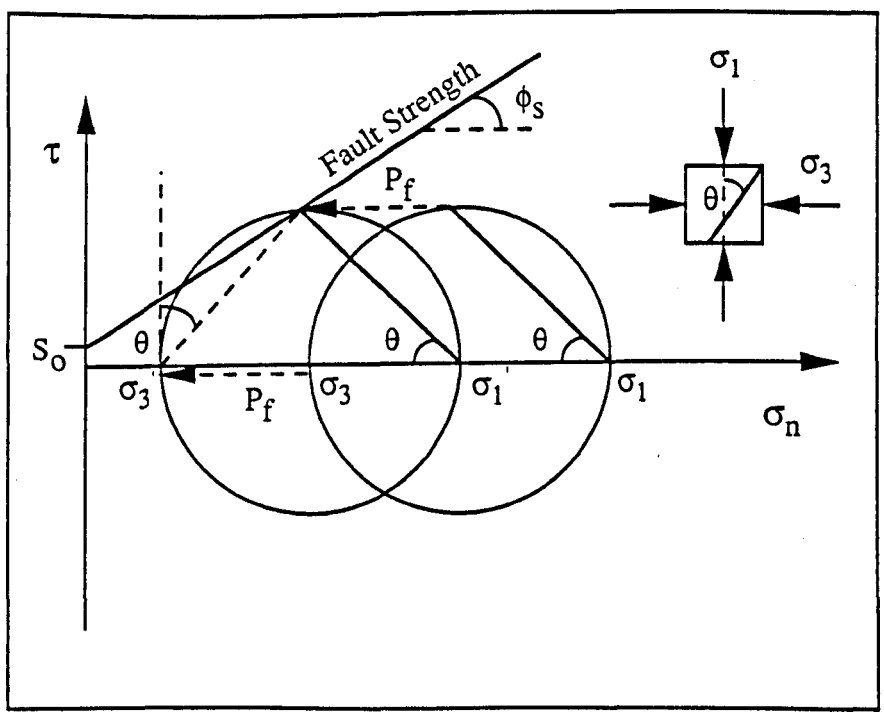

Fig.2.4.1.2 Mohr stress circle for pore pressure induced fault slip.

at depths in the range 1-6km. The evidence for induced seismicity in the North Sea is mainly based on "felt reports" of tremor experienced by operators on exploration or production platforms (Marrow, 1989[92]). The noise level offshore means that earthquakes of magnitude, M<2-3 cannot be recorded unambiguously, however the short duration of the tremors felt on platforms, and the fact that they are felt at all, implies that the microearthquakes are shallow (2-3km depth) with M>3, similar to examples cited below from Europe and the USA. Examples of induced microearthquakes in hydrocarbon provinces have been recorded where water injection to improve oil recovery was responsible, and also from fields where pressure drawdown as a direct result of production was the trigger. Both cases can be adequately modelled by the poroelastic effect, based on the concept of effective stress, each being discussed separately below.

Fluid injection: The injection of fluids under high pressure into the crust has provided some of the best-documented and best-understood cases of triggered seismicity. Since the injected fluid represents a relatively small mass and cannot substantially alter the elastic stresses, the major influence on the stress field is by increasing the pore pressure within the formation into which the fluids are injected. The resultant changes in strength can be expressed in terms of the excess of the injection pressure over the pre-existing formation pressure. A controlled field experiment was conducted at an oil field in Rangely, Colorado (Raleigh *et al* , 1972[93], 1976[94]) where fluid injection during secondary oil recovery had triggered minor seismicity. In this experiment, it was possible to measure all of the parameters necessary to establish the connection between the injection and the induced seismicity. A dense array of seismometers was used to accurately determine the locations and focal parameters of the induced earthquakes, hydrofracturing was used to measure the state of stress in the rock at the depth of injection, injection pressures were both measured and controlled, and laboratory tests provided estimates of the strength of the rock into which the injection took place. Thus Raleigh *et al* [93] were able to combine the stress estimates, fault plane orientations and the frictional properties of Weber sandstone to show that a pore pressure of approximately 26MPa (an increase of 9MPa from the original formation pressure of 17MPa) would be sufficient to induce slip. In

Raleigh *et al* [94], seismicity was shown to be controllable by raising and lowering the pore pressure about the predicted value of 26MPa.

Shear fractures obey the effective stress principle in that internal fluid pore pressure within the fracture directly counteracts the strengthening effect of the external normal stress applied across the slip plane. To calculate the fluid pressure required to cause a fault or joint to slip, it is necessary to quantify the amount by which the Mohr circle corresponding to the current state of stress has to travel to the left to bring the normal and shear stress on the fault plane to the limiting condition represented by the criterion of failure (Fig.2.4.1.2). This calculation is slightly more complicated than for the case of unfractured rock, because in addition to initial stresses and strength parameters, the orientation of the fault plane (θ with respect to the σ_1-direction) needs to be considered. If the initial stresses are σ_3 and σ_1, then the pore fluid pressure, P_f, that will produce fault slip is (Goodman, 1989[95]):

$$P_f = \frac{S_o}{\tan\phi_s} + \sigma_3 + (\sigma_1 - \sigma_3)\left(\sin^2\theta - \frac{\sin\theta\cos\theta}{\tan\phi_s}\right) \quad \text{.....} \quad \text{Eqn.2.4.1.1}$$

From Eqn.2.4.1.1 it is evident that initial crustal stresses, fault orientation and frictional strength properties of the fault plane (cohesion, S_o, and angle of sliding friction, ϕ_s) are required in order to predict the likelihood of triggering earthquakes from fluid injection. This simple application of the effective stress principal has been shown to satisfactorily explain the occurrence of earthquakes due to water injection in a deep waste disposal well near Denver, Colorado (Healy *et al*, 1968[96]) and in the Rangely oilfield, western Colorado (Raleigh *et al* [93, 94]).

Davis & Penington (1989)[97] examined a sequence of induced earthquakes that occurred at the Codgell oil field, West Texas, from about 1974 to 1982. The earthquakes occurred within an array of injecting wells which surrounded the perimeter of the field and which decreased in radius during the life of the injection project. Whilst from the above

discussion (Eqn.2.4.1.1) it is evident that significant increases in field fluid pressures due to injection can result in the occurrence of significant triggered earthquakes (the largest of the Denver earthquakes exceeded M>5) Davis & Penington noted that, however, high fluid pressures do not necessarily result in earthquakes, pointing out that numerous examples of injection sites were present in Texas where induced failure should have occurred by any reasonable failure law, but that no earthquakes had been observed. Thus, although the lowering of effective rock strength from injection is clearly the predominant mechanism controlling failure in many sites, other mechanisms may also contribute. In particular, they highlighted the mechanism whereby slip along one section of a fault may load stress onto nearby locked portions of a fault, a process considered significant for major plate boundary faults, but generally overlooked as a cause of small-scale intraplate triggered earthquakes. They examined the sequence of earthquakes recorded at Codgell in terms of two failure models. In the first model, seismic failure occurred when and where fluid pressures exceeded some critical value as given by Eqn.2.4.1.1. In the second model, earthquakes occurred at the edges of low fluid pressure areas where stresses had been transferred as a result of aseismic deformation in adjacent high fluid pressure regions.

Fluid pressures may affect the behaviour of faults in two ways:

(i) Increase in pore pressure lowers the effective strength of faults (Hubbert & Rubey, 1959[98])

(ii) Increase in pore pressure can alter the mode of deformation from seismic stick-slip to aseismic creep (Byerlee & Brace, 1972[99])

From Eqn.2.4.1.1, for the Codgell oil field with S_o = 4MPa, μ_s = 0.8 (ϕ_s = 39°), σ_1 = 47MPa and σ_3 = 28MPa, Davis & Penington[97] calculated that an injection pressure of P_f = 6MPa should be sufficient to induce failure, however injection pressures at Codgell had exceeded 38MPa since 1960, and indeed, for these values, 877 of the 2420 projects in Texas which injected at shallow depths should be in failure, whereas only the Codgell

field was known to be seismically active. The obvious conclusion was that shear failure probably occurs in many of these fields, but that it occurs either as aseismic creep, or as earthquakes below the detection threshold for the area.

Davis & Penington compared the critical pore pressure model with the stress loading model for seismicity, by calculating the fluid pressure history in the Codgell field using equations for fluid flow in an areally infinite aquifer, giving deviations from initial fluid pressures at any time and at any point in the reservoir through addition of the effects of all the injecting and all the producing wells. Thus with information on both the seismic and the fluid pressure histories at the Codgell field, they could test the hypothesis concerning the importance of stress loading in controlling earthquakes, through comparison of predictions made by two models of deformation in which (a) the effects of stress loading are negligible, and (b) one in which stress loading from aseismic failure controls the location and timing of earthquakes (in (a) only the fluid pressures are important in controlling deformation in the field, in (b) both fluid pressures and loading stresses control deformation). The stress loading model (b) was also related to the concepts of "barriers" and "asperities" used to describe the effects of fault heterogeneity on earthquake behaviour (the term barrier referring to a high strength section of a fault resisting deformation, the term asperity to a high stress region which eventually fails, producing seismicity) as shown schematically in Fig.2.4.1.3.

In conclusion, Davis & Penington noted that, with regard to the critical pore pressure model, there are many sites in Texas where any reasonable analysis of injection pressures, principal stresses and rock strength suggests that failure should occur, but no earthquakes are observed, suggesting that failure at these sites occurs aseismically or as earthquakes below the detection threshold. Stress loading from aseismic injection-induced failure may play a critical role in controlling triggered seismicity in some cases, with shear stress increases in regions of failure being of sufficient magnitude to initiate earthquakes in some instances. Evidence suggests that stress loading plays a role in the timing and location of injection-induced earthquakes in the Codgell oilfield, where if

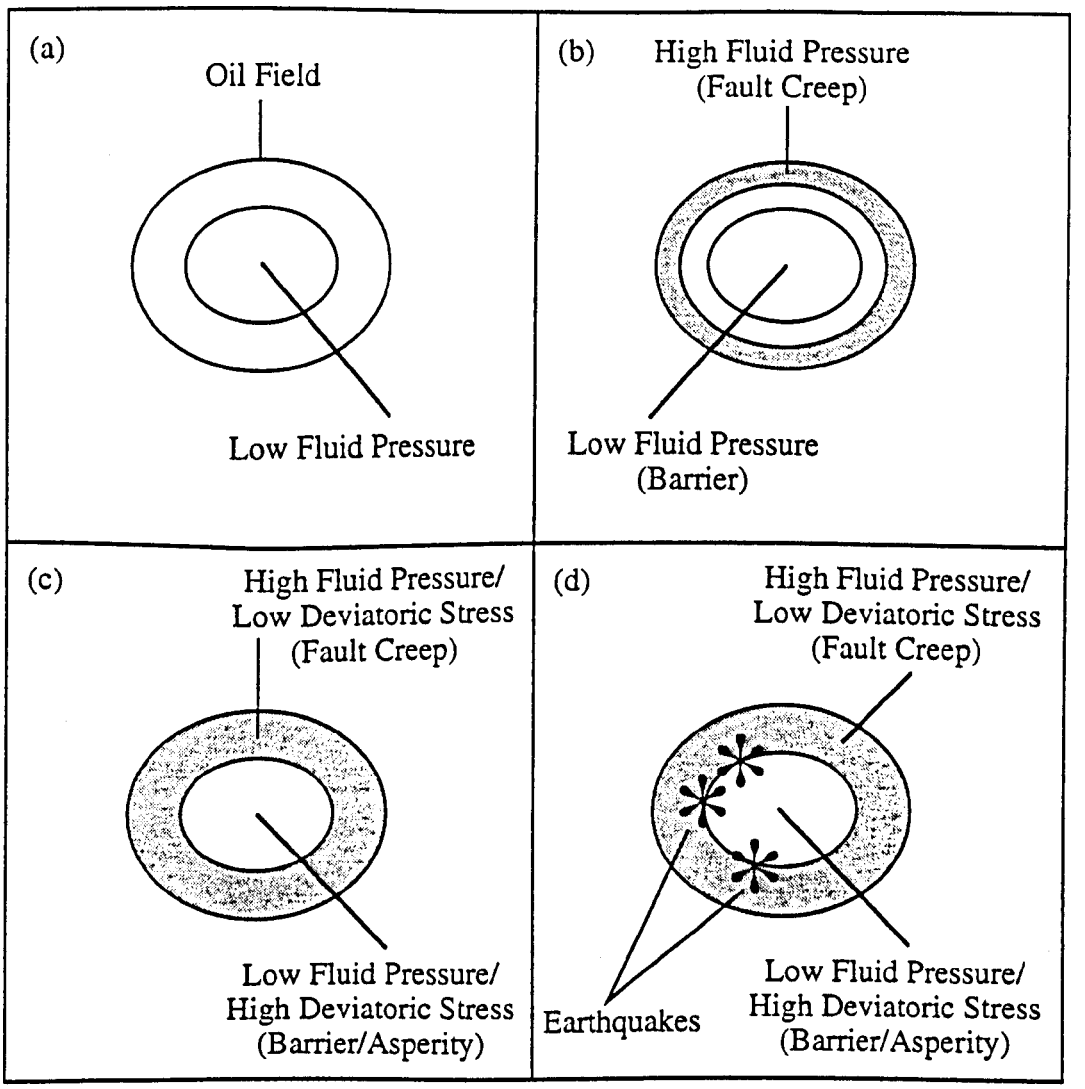

Fig.2.4.1.3 Schematic maps describing the application of the concepts of "barriers" and "asperities" to explain the seismicity in the Codgell oil field (see text for details). (a) Production but no injection, Mohr's circle moves away from failure as fluid pressure decreases. (b) Continued production with injection around the periphery. Aseismic failure occurs along the periphery of the field while the low fluid pressure areas remain barriers to deformation. (c) As injection progresses inward, aseismic failure continues. Stress loading from aseismic failure on the edge of the field increases deviatoric stress within the barriers (high strength regions) which develop into asperities (high stress regions). (d) The regions of highest stress fail seismically because of their high strength and large deviatoric stresses,
after Davis & Pennington [97].

fluid pressures alone controlled seismicity, then earthquakes should occur in the regions of highest fluid pressure, which is not observed. Combined with the observation that adjacent large-volume high pressure fields do not exhibit seismicity, these discrepancies can be resolved using a model in which stress loading is accounted for, although data was not conclusive enough to clearly choose one model over another.

Fluid withdrawal: As discussed above, earthquakes induced by injection of fluids into the subsurface are thought to result from increased pore pressures that decrease effective normal stresses and allow faults to slip at ambient levels of shear stress. Thus it at first appears paradoxical that faulting and seismicity have also been attributed to fluid extraction in a number of localities, as the fact that fluid extraction decreases pore pressure, by the same argument suggests that extraction should increase the effective confining stress and inhibit fault slip. Yet the evidence for induced earthquakes related directly to both increased pore pressures resulting from fluid injection, and to subsidence and horizontal deformation resulting from fluid extraction, is compelling.

Whilst the classic case of injection-induced seismicity occurred at the Rangely oil field, Colorado, as discussed above, numerous well-documented examples of seismicity and ground subsidence triggered by fluid extraction are recorded in the literature (Yerkes & Castle, 1976[100]). A summary of important observations associated with such phenomena can be found in Segall (1989)[101], as described below. Earthquakes empirically associated with fluid extraction occurred at the Wilmington oil field in Long Beach, California (Kovach, 1974[102]) where seismicity and spectacular surface deformation accompanied oil production, subsidence between 1936 and 1966 reaching 9m and horizontal displacements 3.7m. A profile of the horizontal strain as given in Fig.2.4.1.4 shows that the central subsiding region contracted by as much as 1.2% whereas the flanks of the subsiding region extended by a few tenths of one percent. Six shallow earthquakes (M2.4 to 3.3) occurred within the oil field between 1947 and 1955 when the rate of subsidence was greatest, generated by slip on bedding planes (see section 2.4.2 below) at depths of 470m to 520m, which sheared off tens to hundreds of wells over several square kilometres. Virtually all of the compaction that caused the surface subsidence was

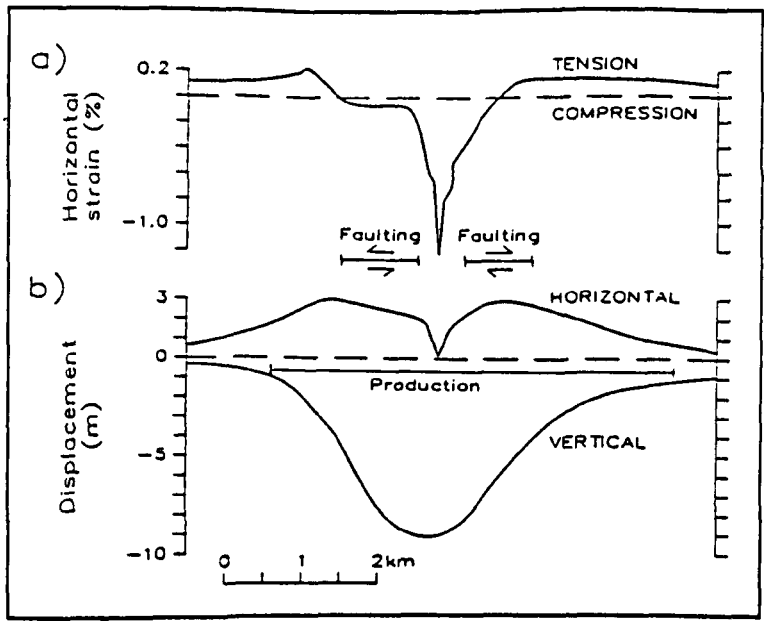

Fig.2.4.1.4 Measured surface deformations at Wilmington oil field near Long Beach, California (a) Horizontal strain change. (b) radial displacement (inward +ve.) between 1937 and 1962, and vertical displacement (downward -ve.) between 1928 and 1962. Note limits of producing zone and location of bedding plane faults, after Segall [101].

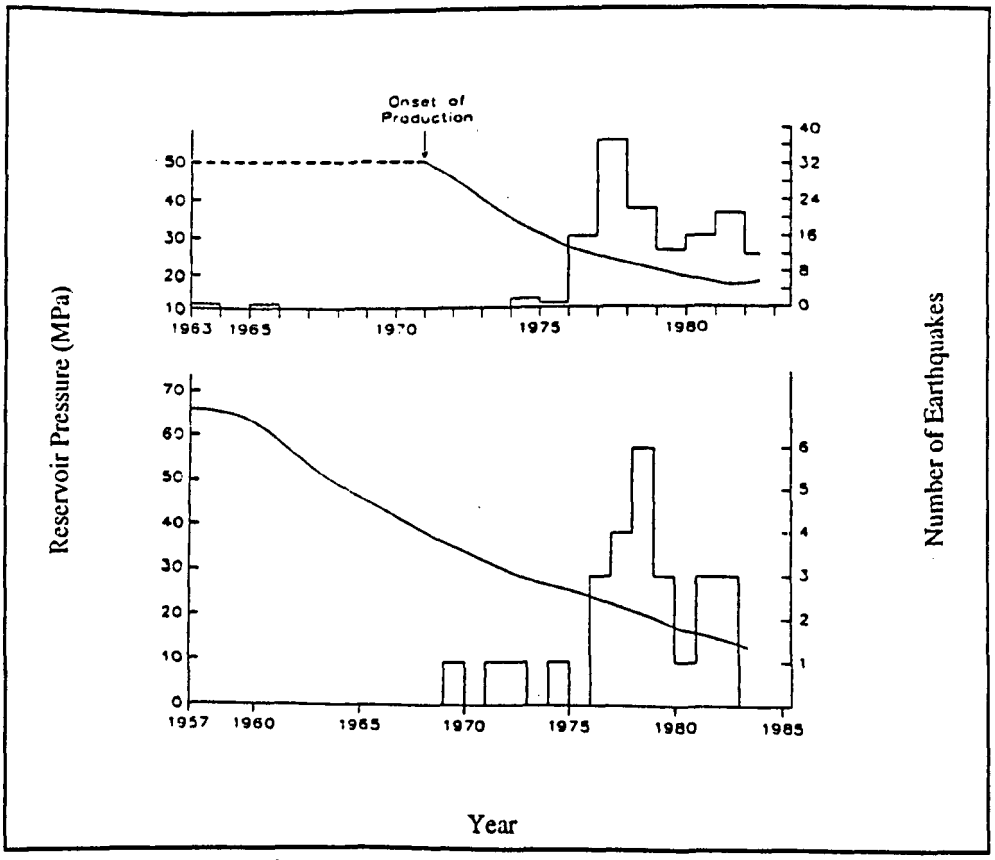

Fig.2.4.1.5 Number of earthquakes recorded per year and decline in average reservoir pressure in two gas fields. (a) Strachan oil field in Alberta, Canada. (b) Pau basin gas field, France, after Segall [101].

localised in the producing beds at depths of 650m to 1050m, several hundred metres below the slip surfaces. The faults were located near the centre of subsidence (Fig.2.4.1.4) within the area that contracted horizontally at the Earth's surface. During the 1920's, a series of earthquakes were felt near the Goose Creek oil field in south Texas, where oil production caused the field to subside by as much as 1m between 1917 and 1925 (Pratt & Johnson, 1926[103]). The earthquakes occurred on normal faults that reached the surface along the margins of the subsiding field, recurrent slip on these faults dropping the oil field relative to the surroundings by as much as 0.4m.

Active aseismic reverse faulting has been recognised within the Buena Vista Hills oil field, California, where the 2.6km-long Buena Vista Hills fault, dipping 25°N, slipped at a rate of ≈2cm/yr between 1932 and 1959 (Howard, 1968[104]). Slip on the fault sheared wells, produced a surficial scarp, and buckled oil, gas and water pipelines. The fault is located in a region of substantial subsidence and horizontal contraction.

The Rocky Mountain House seismic zone in Alberta, Canada, is located near several major gas fields, where gas production from lower Palaeozoic carbonates at depths of 3 to 5km began in 1971 (Wetmiller, 1986[105]). By 1976 the average reservoir pressure had dropped by 25MPa and the rate of seismicity ($M \leq 3.4$) had increased dramatically, as shown in Fig.2.4.1.5(a). Wetmiller used a local seismic network to obtain improved hypocentres and to better define the association of gasfields with seismicity, and found that all of the 67 events located during the experiment occurred within a 5km-diameter by 1km-thick area located immediately below the payzone, a composite focal mechanism indicating reverse faulting with nearly horizontal , E-W trending P-axis.

Grasso & Wittlinger (1989)[106], Feigner & Grasso (1990)[107] and Grasso & Feigner (1990)[108] recorded nearly 800 earthquakes with $M \leq 4.2$ clustering in a small volume around an active gas field in the Pau basin in the foreland of the western Pyrenees. The gas reservoir is a 500m thick sequence of Cretaceous and Upper Jurassic limestones that form a broad anticline at depths of 3.2 to 5.5km. The pore pressure in the reservoir has decreased by 50MPa since the onset of exploitation, as illustrated in Fig.2.4.1.5(b), with

earthquakes beginning in 1969 when the reservoir formation pressure had decreased by ≈30MPa. Repeated levelling showed a maximum subsidence of only ≈5cm between 1887 and 1967. The epicentres of 95% of the well-located events and all those of the M>3 events were found to lie within the boundaries of the gas field, most events were shallow, having focal depths of 2.5 to 5.0km, and more than 85% of the better located events concentrated above the top of the reservoir, <10% being located within the reservoir itself. Composite focal mechanisms constructed from clusters of events suggests that P-axes are subhorizontal and crudely radially distributed towards the gas reservoir.

Whilst the field observations described above are relatively unambiguous, the mechanics of extraction-induced faulting and seismicity are less evident. Segall[101] summarised these observations in a schematic cross-section shown in Fig.2.4.1.6. Extraction of pore fluids causes subsidence with accompanying horizontal contraction of the centre of the subsiding region and lesser extension of the flanks. Both normal and reverse faults may accompany extraction. As at the Goose Creek field, normal faults may develop at the margins of the subsiding region, and reverse faults in the central contracting region. At Wilmington, Buena Vista Hills and Pau, the reverse faulting is localised above the producing layers whilst at Rocky Mountain House the seismicity is below the reservoir.

Segall (1985)[109] proposed that all the observations of subsidence, faulting and seismicity described above, resulting from production-related fluid withdrawal, can be understood through consideration of the stress changes caused by fluid extraction. For a linear, isotropic, poroelastic solid (Biot, 1941[110], Rice & Cleary, 1976[111]) the solid strains, ε_{ij}, are taken to be linear functions of the solid stresses, σ_{ij}, and the change in fluid mass content per unit volume, Δm, where:

$$2\mu\varepsilon_{ij} = \sigma_{ij} - \frac{\nu_u}{1+\nu_u}\sigma_{kk}\delta_{ij} + \frac{2\mu B}{3\rho}\Delta m\,\delta_{ij} \qquad \text{.....} \qquad \text{Eqn.2.4.1.2}$$

μ: shear modulus

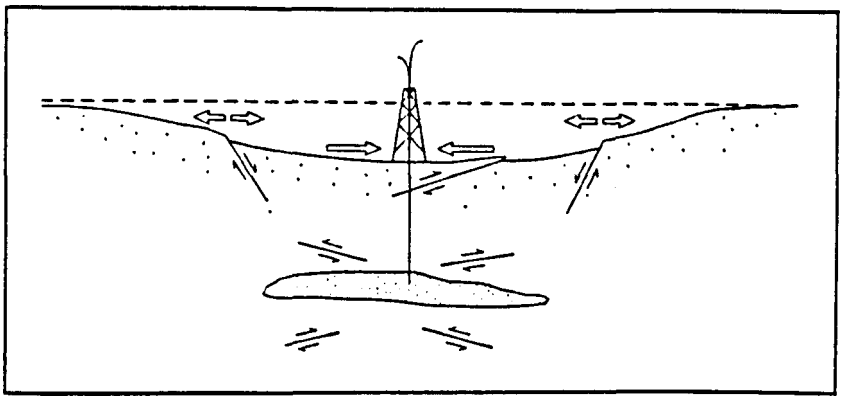

Fig.2.4.1.6 Schematic cross-section summarising surface deformation and faulting associated with fluid withdrawal (open arrows indicate horizontal strain at earth's surface) after Segall [101].

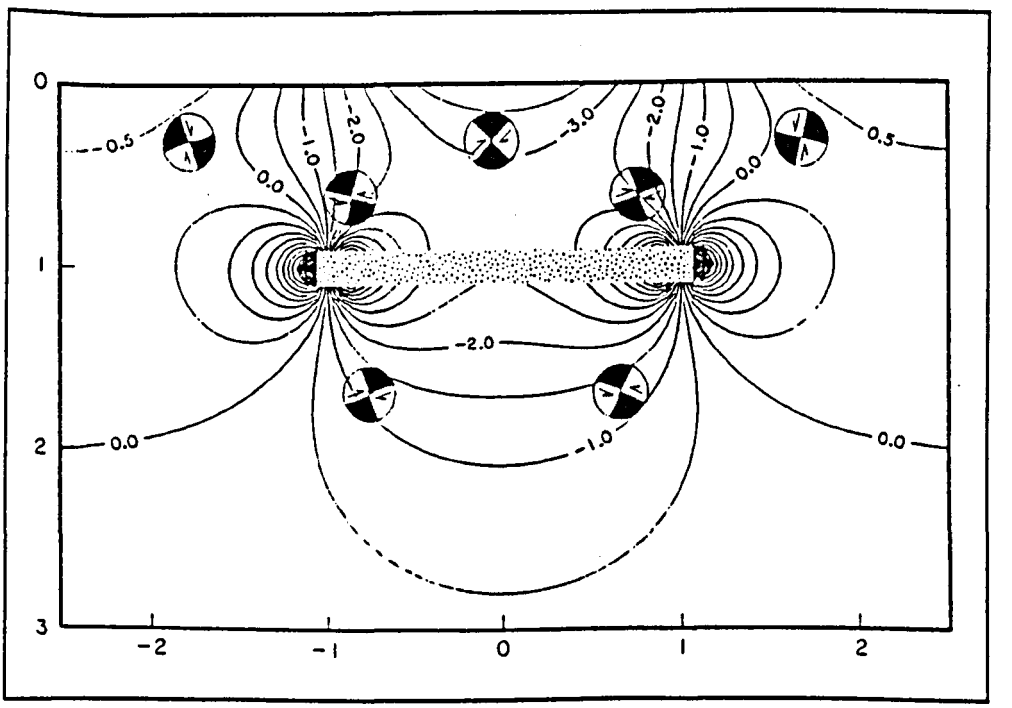

Fig.2.4.1.7 Calculated change in horizontal normal stress, σ_{yy}, due to fluid extraction (relative tension positive). Simulated focal mechanisms indicate planes of maximum shear stress and sense of shear on those planes, after Segall [101].

ν_u: undrained Poisson's ratio

B: Skempton's pore pressure coefficient

ρ: fluid density

Undrained conditions refer to deformation in which no pore fluid flow occurs. To understand deformation induced by fluid extraction, it is useful to use Eqn.2.4.1.2 to express the solid volumetric strain, ε_{kk}, in terms of the mean stress, σ_{kk}, and change in fluid mass per unit volume, Δm:

$$\varepsilon_{kk} = \frac{\sigma_{kk}}{3K_u} + \frac{B\Delta m}{\rho} \quad \text{.....} \quad \text{Eqn.2.4.1.3}$$

Eqn.2.4.1.3 has a simple and important physical interpretation, stating that the solid volumetric strain is composed of two parts, an undrained elastic component under conditions of no pore-fluid flow, $\sigma_{kk}/3K_u$ (where K_u is the undrained bulk modulus) and a component resulting from changes in the amount of fluid in the pores of the rock, $B\Delta m/\rho$. For relatively incompressible fluids, such as oil and water, the latter component is very nearly equal to $B\Delta v$, where Δv is the change in pore fluid volume per unit solid volume. In this case, B is therefore the ratio of solid volume change to change in pore fluid volume. The range of B is restricted to $0 \leq B \leq 1$, with water-saturated soils yielding $B \approx 1$, and diverse rocktypes ranging from sandstones to granites giving B from 0.5 to 0.9 (Rice & Cleary). For example, if water is uniformly withdrawn from a rock with B=0.8, the volumetric contraction of the rock is 80% of the volume of extracted water. Thus from Eqn.2.4.1.3 extraction of pore fluids results in localised contraction of the reservoir rocks, stressing and deforming the surrounding rock mass. Segall[109], used a theoretical method, based on Biot's[110] constitutive theory for fluid-infiltrated elastic media, to calculate the change in stresses acting in the focal region resulting from fluid extraction in the overlying oil fields. Stress and deformation changes resulting from the withdrawal of

fluid from a permeable layer embedded in a fluid-infiltrated, impermeable half-space were calculated. With the form of the governing equations which express stress equilibrium and continuity of pore-fluid mass being dependent on the choice of free variables, which are in turn dependent on the boundary conditions, Segall[109] adopted displacement and pore fluid mass as the most suitable free variables. If fluid production is from permeable layers imbedded in relatively impermeable surroundings, then $\Delta m \approx 0$ outside the producing zone. Given the net flux of fluid out of the reservoir, it is possible to solve for $\Delta m(x, t)$ and thus to calculate the displacements and stresses.

Previously, Geertsma (1973)[112] computed displacements and stresses for a uniform pressure decrease in a thin disk-shaped reservoir, using a similar analytical method to that of Segall[109], although the former was concerned with the effects of fluid withdrawal on land subsidence, and not with faulting and seismicity. The important result is that, because of the mechanical coupling between stress and pore pressure, there are undrained pore pressure changes outside the reservoir even when there are no changes in fluid content at these points, that is stresses are generated even when there are no changes in pore fluid content, σ_{ij} at x being in general non-zero when Δm at x vanishes. Also, the stresses, unlike the displacements, scale with the shear modulus, μ, so that if the rock is stiff, large stresses may be generated without massive subsidence.

As a simple example to illustrate the basic physical process, Segall[101] considered the stress and deformation resulting from fluid withdrawal from a flat permeable layer of thickness, T, small compared to the depth, D, embedded in an otherwise impermeable half-space, with for simplicity the assumptions of uniform $\Delta m(t)$ over the entire reservoir layer, and plane-strain conditions (no-strain in the z-direction). The resultant change in horizontal stress, σ_{yy}, and the orientation of the planes of maximum shear stress (as shown by simulated focal mechanisms) are illustrated in Fig.2.4.1.7. The rock above and below the producing layer is compressed horizontally, whereas the rock on the flanks goes through relative tension (or decrease in compression). Significant stress changes extend both above and below the producing layer. Faults slip when the total shear stress (the sum of the ambient and induced stresses) overcomes the frictional resistance,

favoured slip planes therefore depending on the orientation and magnitude of the ambient stress field (only the component of stress induced by extraction was considered by Segall as the ambient stress field will vary from site to site). Orientation of the planes of maximum shear from simulation, predict reverse faulting above and below the producing zone and normal faulting on its flanks, qualitatively consistent with observations from the producing field operations described above. Note that the substantial decrease in pressure within the reservoir inhibits frictional slip within the reservoir rocks themselves. Thus the stress pattern given in Fig.2.4.1.7 can be understood in a straightforward manner:

(i) fluid extraction causes the reservoir rock to contract

(ii) contraction in the vertical direction is accommodated by subsidence of the free surface

(iii) contraction in the horizontal direction is resisted by the surrounding rocks which are pulled in toward the centre of the reservoir

(iv) strata above and below the reservoir is driven into horizontal compression as a result of (iii)

(v) rock far away from the reservoir is displaced less than rock immediately above and below the reservoir, causing the flanking regions to extend

2.4.2 Bedding-parallel Shear

In this section the role of bedding planes as frictional interfaces (planar shear discontinuities) will be reviewed, and their potential influence as an important deformation phenomenon in hydrocarbon reservoirs assessed. Particularly in fluvially deposited arenite rockmasses, initial size, shape and spatial distribution of detrital grains deposited in an environment controlled by current and gravity, will control the sedimentary layering of the material. Grading and composition, in particular the formation of bedding planes containing clay layers, have first order influence on the primary anisotropy of the rockmass. Thus a functional fabric formed by vectorial depositional processes and the resulting preferred dimensional orientation of components controls the development of primary anisotropy (Moelle & Chappell, 1985[113]).

The concept of bedding planes as planes of weakness has been recognised within the discipline of structural geology for many years. Practically all fault surfaces change their orientation when they pass through layers of different rock lithology, often showing a "staircase-like" form in cross-section. The part of a fault which passes at a relatively high angle through a lithological unit is known as a "ramp" and the section which is sub-parallel or parallel to the lithology is known as a "flat". The terms ramp and flat are mostly used in descriptions of low-angle overthrust faults where the hangingwall has moved upwards over the footwall, but as descriptions they can be applied to differently inclined sectors of any inclined fault surface. They are generally used irrespective of the actual geometric orientation of the lithological layering and, for example, a flat can be steeply inclined where the lithology is steeply inclined. Ramps and flats are connected to rock "competence" (Ramsay & Huber, 1987[114], page 507). In geology, the term competence is used to describe the differences in rock properties which lead to mechanical instability, those rocks which flow more easily than their neighbours being described as the least competent members, those that are stiffer than their neighbours being termed the most competent rocks. Thus although the term competence is therefore rather vaguely defined in an exact rheological way, it does give a very useful comparative description of the components of a layered system, which can be employed in the field to give some idea of the contrast of the components of a deformed layered system. Ramps are found in the more competent layers in a succession (massive limestone, conglomerate, sandstone) whereas flats are found in the incompetent layers (evaporites, shales, marls, brittle coal horizons).

In rocks which are well-bedded or show a regular planar lamination, the strains set up during the folding process are often controlled by simple shear parallel to the planar structure (Ramsay & Huber, pp.445-446). If the simple shear displacement is distributed continuously throughout the structure then the fold so formed is termed a flexural flow fold, as shown in Fig.2.4.2.1(a), whereas if the shear is discontinuous the fold is termed a flexural slip fold as shown in Fig.2.4.2.1(b). Flexural flow folds are generally formed

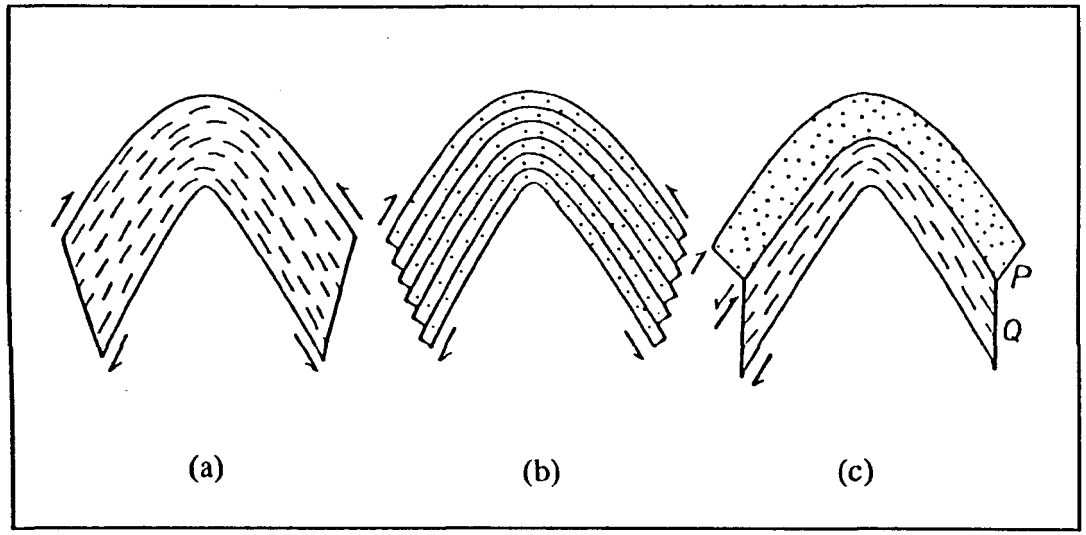

Fig. 2.4.2.1 Folding styles. (a) Flexural flow fold. (b) Flexural slip fold. (c) Types of flexural fold developed in interlayered competent (P) and incompetent (Q) strata. Arrows indicate direction and sense of layer parallel slip, after Ramsay & Huber [114].

where the rocks have an initially penetrative and fairly uniform planar fabric, such as is found in shales, whereas flexural slip folds occur where a number of distinct lithological layers are separated by well marked bedding surfaces, for example in the Upper Carboniferous turbidite sequences of North Devon, where extremely well-developed chevron folds ("zig-zag-style" folds with narrow angular hinge zones and straight limbs) are evident (Ramsay, 1974[115]). As the displacements in flexural folds are always parallel to the bedding or lamination surfaces there is no tendency for the orthogonal thickness across the layer to change, so that such folds always show a concentric or parallel form. Thus shear on surfaces parallel to the layer as the layer folds is known as flexural slip if the surfaces of shear are discrete with a finite thickness, or flexural flow if deformation takes place at the granular scale with no discrete surfaces of slip. A fundamental feature of this fold deformation type is that there is no distortion in the plane of the folded layer. Flexural folds develop in layers with high mechanical anisotropy commonly due to a layer-parallel mineral fabric or banding, and analogous structures can be formed by compressing a pack of paper sheets parallel to the layering. As the pack buckles the individual sheets slide over each other. The maximum amount of slip occurs on the limbs at the inflection points and decreases towards the hinge where slip is zero, strain markers within flexural flow folds showing that the maximum strain occurs at the inflection points of the limbs and that no strain occurs at the hinge. A feature of this strain distribution is that one of the lines of finite longitudinal strain is always parallel to the layering, and it follows that when the structure develops as a flexural flow fold, there will be no strain on the bedding planes. In a flexural flow fold where the slip planes are very closely spaced, strain will be uniformly distributed across the folded layer, whereas in a flexural slip fold, as in a sequence of sandstone or limestone units, the layer-parallel shearing would not be uniformly distributed throughout the sequence of layers, but would be concentrated on the bedding planes. One of the most common features associated with flexural slip folding are the slip-parallel lineations developed on the layer surfaces, which are frequently orientated sub-perpendicular to the fold hinge, and generally die out towards it where the slip between beds is zero. Detailed field studies of turbiditic sequences shows that flexural slip occurs on discrete "movement horizons" between rock "packets" in which the beds have welded contacts. Stair-stepping displacements of sedimentary dykes

and early-formed quartz veins show that the movement horizons generally have a decimetre to metre spacing and are marked by bedding-parallel quartz veins, from 1mm to several cm thick, which can be used to identify movement horizons in the absence of displaced markers (Tanner, 1989[116]). They consist of several sheets of quartz fibres which each carry a slickenfibre lineation, and which together preserve a record of the displacements on an individual surface. Based on laboratory direct shear testing, Krahn & Morgenstern (1979[117]) noted that the frictional resistance along a limestone bedding plane was much greater than along a limestone flexural slip surface, which they interpreted as being due to flexural slip folding having reduced the roughness along certain bedding planes to values much less than those produced by shearing undeformed bedding planes.

Insights into the mechanics of bedding-parallel shear associated with both tectonic thrusting and flexural folding, can be gained through application of poroelastic theory and the effective stress law. Since their earliest recognition, overthrusts have presented a mechanical paradox with regard to their mode of emplacement, as the force required to propel sheets of specific observed lengths is frequently many times greater than the crushing strength that the rock column can support. Hubbert & Rubey[98] stressed the importance of pore fluid pressure in the mechanics of sliding large rock masses with particular reference to low-angle overthrusts. Following an excellent summary of their work in Jaeger & Cook[8], consider the sliding of a block OABC of height, h, and length, ℓ, on the horizontal plane CB on which the coefficient of friction is, μ. If the bulk density of the fluid filled rock is, ρ, then the vertical stress, σ_x, at depth x is, $\sigma_x = \rho g x$. The pore pressure, p, at depth x is taken to be, $p = \lambda\sigma_x = \lambda\rho g x$ (where λ is the ratio of hydrostatic to lithostatic load, $\approx \rho_{fluid}/\rho_{rock}$) so that $\sigma_x' = \sigma_x - p = (1 - \lambda)\rho g x$ is the effective stress. The problem is thus, for a block pushed to the right by stresses, σ_y (as shown in Fig.2.4.2.2) which are taken to be the maximum possible stresses so that the material is at the point of failure at every point of OC, to determine the greatest length, ℓ, that can be transported in this way. For a Coulomb-type intact rock failure criterion, written in terms of effective stresses as, $\sigma_y' = \sigma_o + k\sigma_x'$ (see Eqn.1.3.3) Hubbert & Rubey[98] showed that:

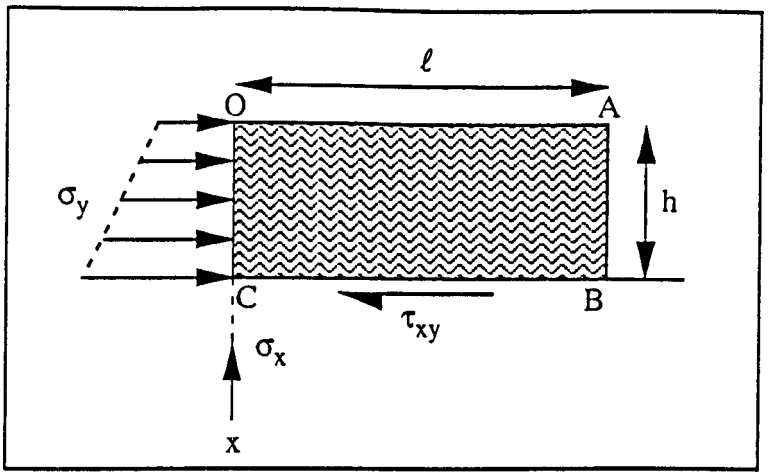

Fig.2.4.2.2 Schematic of the sliding of an overthrust block on a horizontal plane (see text for details) after Jaeger & Cook [8].

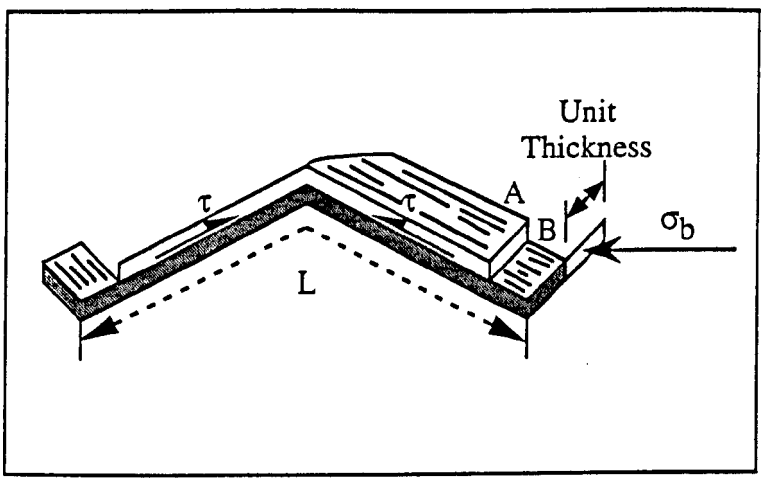

Fig.2.4.2.3 Schematic of the shear stress, τ, that resists buckling by the flexural slip mechanism induced by the buckling stress, σ_b, after Price & Cosgrove [26].

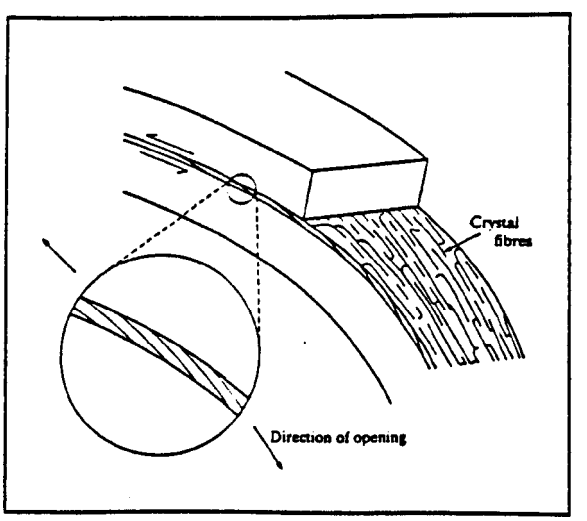

Fig.2.4.2.4 Crystal fibres on a flexural slip bedding plane indicating opening as well as differential bedding slip, after Price & Cosgrove [26].

$$\ell = \frac{2h\sigma_o + \rho g h^2[k + \lambda(1-k)]}{2\sigma_o + 2\mu(1-\lambda)\rho g h} \quad \ldots\ldots\ldots \quad \text{Eqn.2.4.2.1}$$

For overpressured horizons, $\lambda > (\rho_{fluid}/\rho_{rock} \approx 0.4)$ Hubbert & Rubey thus showed numerically that values of ℓ calculated from Eqn.2.4.2.1 are an order of magnitude larger than those predicted in the absence of pore pressure. For a second scenario, that of a block sliding down an inclined slope, a similar effective stress approach can demonstrate that for $\lambda \neq 0$, sliding is possible at angles of slope inclination less than the angle of sliding friction.

Price & Cosgrove[26] (pp.366-370) present a theoretical analysis of the mechanical effects of fluid pressure in a rock mass on the flexural folding phenomenon, based on the following conceptual model. Consider the shear stresses which develop along the bedding planes which bound a competent layer resisting buckling by the flexural slip mechanism (Fig.2.4.2.3). These shear stresses may develop because of strain resulting from inter-layer cohesion and also as a result of the frictional resistance to slip between layers, inherent in flexural slip folding. By neglecting the other factors which influence fold initiation and development (the internal stresses and strains incurred by flexuring of the competent layers, and gravity, that is the body-weight of the units) the maximum role which such bedding-parallel shear stresses play in flexural folding can be considered.

From Fig.2.4.2.3, for a unit distance parallel to the fold axis, the buckling force, F_b, is given by $F_b = \sigma_b.a$, where, a, is the layer thickness, and σ_b, is the buckling stress. The shearing force, F_s, which resists movement of bed A over bed B is given by $F_s = \tau.L$, where, L, is the arc length of the bed which will determine the wavelength of the fold, and τ, is the average shear stress acting parallel to the bedding. For the assumption of the layer-parallel, frictional sliding, shearing stress, τ, being the only factor causing resistance to buckling then, in folding, $F_b = F_s$, so that, $(L/a) = (\sigma_b/\tau)$ or the ratio of the buckling to shearing stresses is directly proportional to the slenderness ratio of the folded

bed. For the realistic assumptions of L/a = 100, and σ_b = 100MPa (less than the failure strength of most competent sedimentary rocks under low confining pressure, that is at shallow depth) Price & Cosgrove showed that τ should have a magnitude of around 1MPa. For slip on a non-cohesive boundary, $\tau = \mu_s.\sigma_n'$, where μ_s is the coefficient of sliding friction (assumed to have a representative value of 0.5) and σ_n' is the effective normal stress, it follows that for τ = 1MPa, the effective vertical stress ($\sigma_z' = \sigma_n'$) is 2MPa. If this hypothetical fold is assumed to begin to develop at a depth of 4km, with an average density of rock cover around 2.5gcm^{-3}, then the total vertical stress will be, σ_z = 100MPa, so that a fluid pressure of, $p = (\sigma_z - \sigma_z')$ = 98MPa must exist, that is $\lambda = p/\sigma_z$ = 0.98. Thus if a flexural slip fold is to be initiated under a cover of 4km or more, then the value of λ must exceed 0.95 even for modest values of L/a (even for a depth of 1km, then λ = 23/25MPa = 0.92).

Field observation of slickensides on activated bedding planes frequently shows them to be composed of layers of crystal fibres which have grown preferentially parallel to the direction of dilation (Fig.2.4.2.4). Such mineral fibres developed on flexurally sheared bedding planes show that often there is a significant component of movement normal to the beds, so that not only do the beds move over each other during folding, but they also separate slightly. Thus Price & Cosgrove concluded that, for such separation, $\lambda = p/\sigma_z$ = 1 with a resultant loss of cohesion along the bedding plane. It is therefore at the point in the deformational history where the sedimentary pile contains a significant number of bedding planes with no cohesion and virtually no resistance to frictional sliding as a result of fluid overpressuring, that unstable buckling due to bedding-parallel shear can most readily occur.

Using terminology analogous to production-related seismicity (section 2.4.1) "triggered" or "induced" bedding-parallel shear has also been recognised as a consequence of engineering activity. In civil engineering, stress release can occur by gradual squeezing. Whilst in one form of squeezing, the rock is either very soft or intensely fractured, so that it deforms like toothpaste in a ductile manner, in another, excavation releases locked-in stresses and allows horizontal beds to slide inward over one another like a deck of

cards (Franklin & Dusseault, 1989[118], pp.154-156). As illustrated schematically in Fig.2.4.2.5, the inward movement cannot be resisted by the weak bedding planes, and shear displacement can occur for distances as great as several hundred metres from the excavation. Whilst displacements can reach magnitudes of 200mm or more, displacements of 50mm are commonplace (Quigley *et al*, 1978[119]) evidence of bedding plane slip frequently manifesting itself as offset along blastholes in open cuts.

The effect of bedding-parallel shear slippage is of particular importance with regard to deformation of underground excavations. Jeremic (1980)[120] showed that in the Rocky Mountain coal belt of Western Canada, in flat and gently dipping seams, mine structures had deformation modes ranging from "individual" coal layer extrusion to "differential" coal layer extrusion. The extrusion deformation of coal structures in response to the removal of lateral confinement is facilitated by reduced strength of the coal, resulting from both the effects of previous orogenic movement and the inelastic behaviour of most coal bands during and after mining. The different types of deformation may be defined in terms of the frequency of orogenic shear planes, coal seam thickness, and the proportion and number of soft and hard coal bands. The extrusion of individual coal layers occurs due to their differing elastic properties. Jeremic argued that the mechanics of such extrusion could be explained by frictional effects between hard and soft coal bands: (i) the integral expansion of pillars is resisted by hard coal layers which have a higher Young's modulus and a lower Poisson's ratio and thereby set up forces opposing the expansion of softer layers; (ii) the initiation of shearing motion in soft layers depends on the magnitude of cohesion and frictional resistance between bands which in turn is influenced by interlocking surface irregularities; (iii) when shearing motion starts the amount of horizontal movement will be controlled by the elastic properties of hard layers and by the magnitude of the shearing force generated along stratification planes. Whilst extrusion of individual layers is relatively unimportant in extracting coal from short-term structures such as longwall faces, for semi-permanent and permanent structures such as pillars, extrusion of individual layers is of paramount importance because surfaces are exposed for significant periods of time. Due to progressive extrusion of soft layers,

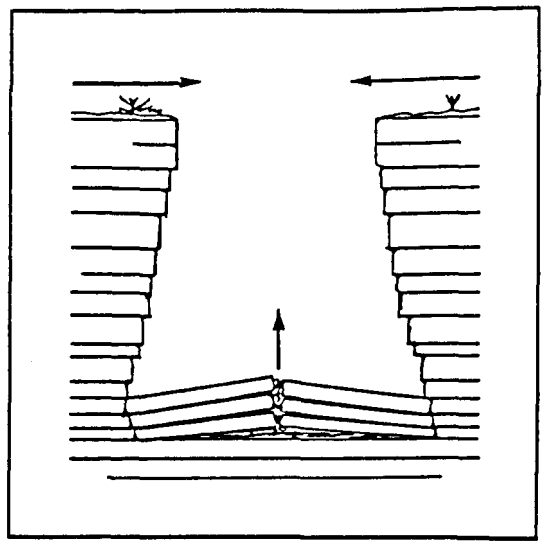

Fig.2.4.2.5 Bedding slip "squeezing" in the walls of an excavation with associated upward heave and buckling in the invert, after Franklin & Dusseault [118].

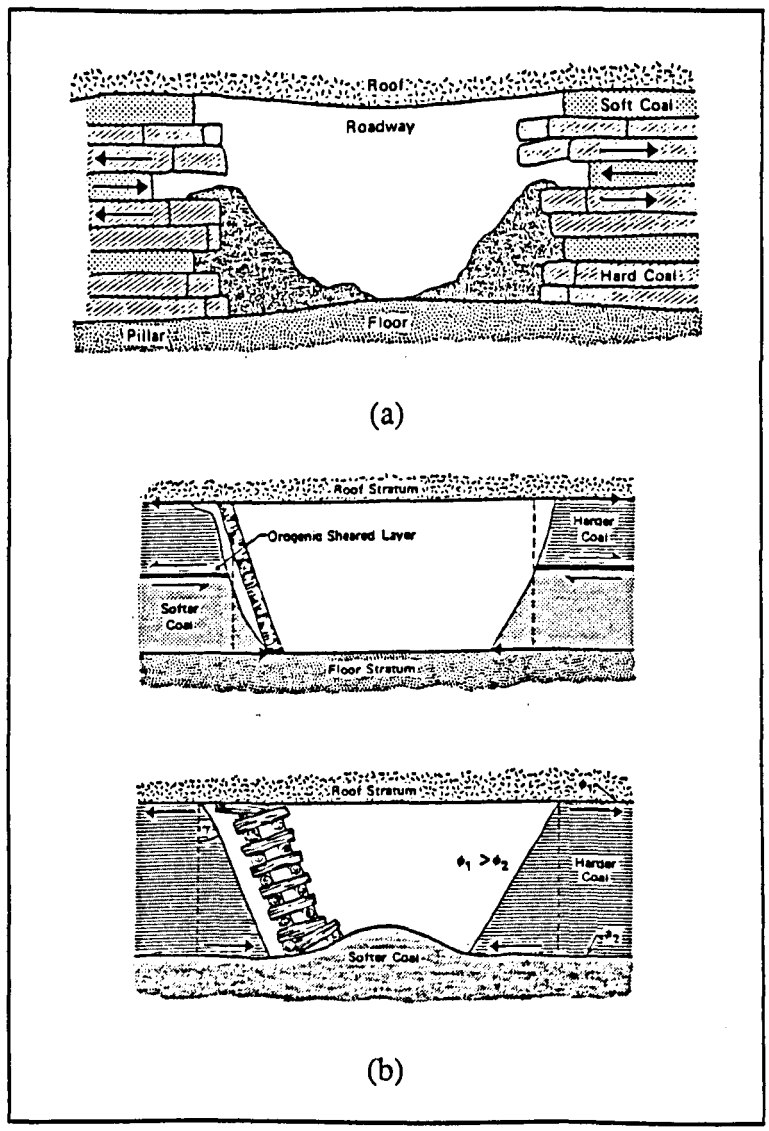

Fig.2.4.2.6 (a) Profile along rib faces showing progressive extrusion of indivdual soft layers. (b) Differential shearing of pillars, after Jeremic [120].

unsupported fragments of hard coal layers in the outer zone of pillars have a tendency to break and fall into roadways as shown in Fig.2.4.2.6(a). The mechanics of extrusion deformation by differential shearing, which was particularly well-exhibited in thick coal seams, is also governed by frictional effects between stratification planes, as shown in Fig.2.4.2.6(b). Here the differential deformation results from differential shear resistance at the top and bottom of the seam, where, for example, there may be a high magnitude of constraint between the top coal slice and a massive sandstone of high elastic modulus and a moderate amount of restraint between the bottom coal slice and the inelastic floor stratum, or vice versa.

To quantify shearing deformation of mine structures, shear strength characteristics of different petrographic coal units and of mudstone partings were tested under direct shear laboratory conditions using constant normal load control. For all three coal types tested the peak friction angle of coal bedding planes was constant at about 34°, whereas the apparent cohesion varied appreciably from 0.35-1.2MPa, hard coal and brittle coal having a greater cohesion than fibrous coal. As the great majority of sheared bedding planes are vitrinite (brittle) bands, however, cohesion is of lesser importance in determining mine stability because it resists only the initial shearing stress, the main strength component being residual frictional resistance. The residual friction angle was found to be 27° with zero cohesion. Direct shear testing of carbonaceous and shaley parting planes showed these stratification contacts to have only residual strength, with an average friction angle of 28° and zero cohesion, similar to the residual shear behaviour of coal bedding planes. In conclusion, Jeremic noted that mine stability is greatly controlled by the shearing characteristics between individual bands with differing petrographic characteristics within coal seams, shear displacement along stratification planes being mobilised by the redistribution of excess overburden pressure in the mine structure, as well as by frictional effects between individual layers of different mechanical properties. Thus Jeremic noted that the "classical" approach for excavation design in coal seams using the uniaxial compressive strength of coal is of lesser significance in the Rocky Mountain belt as the shear strength of coal seams is lower than in other coal regions of the world, with

shearing stresses along stratification planes in the former governing the mechanics of deformation and failure in mine structures.

Osterwald & Dunrud (1965)[121], based on a six year study investigating relationships between geological features and coalmine "bumps" (violent coal rib failures) at Sunnyside, Utah, noted that the bumps are spatially and genetically related to structural and stratigraphic features, with some bumps being directly related to stress accumulation along faults, either from tectonism or as a result of mining. Importantly, frictional properties of bedding planes between coal and roof rock, and between some rock units within the roof, were considered to directly influence the deformation of coal ribs, and hence the incidence of bumps. These frictional properties were related to the lithology of the roof rocks, as well as to the sedimentary structures within the rocks. Commonly a sequence consisting of 10cm of carbonaceous siltstone, about 20cm of rider coal and about 60cm of massive siltstone or sandstone overlies the main seam, this sequence causing difficult roof conditions in the mines, difficult mining conditions and, directly or indirectly, many bumps.

Early in the investigation it was observed that the deformation of coal mine workings at Sunnyside, of which bumps are a part, was dependent on the type of roof rock overlying the coal. Coal was considered to move into openings more easily beneath argillaceous roof rocks than beneath sandstone or siltstone, presumably because friction is less beneath argillaceous rocks (although no laboratory friction results were reported!) thus allowing stress in the ribs to be easily relieved by many small bumps. In contrast, massive sandstone or siltstone units in the roof may form a rigid plate, thereby placing increased stress components on the ribs. If the ribs are strong or are strongly supported, then such massive units in the roof may fail in shear and cave under the large horizontal stress components in these competent stress risers (Fig.2.4.2.7). Interrelated roof caves and rib bumps were observed wherein massive roof siltstones caved under horizontal compression along curved shear failure surfaces that flatten in dip downwards. Later, violent rib failures (bumps) took place along curved shear failure surfaces (described as "cymoidal" fractures) that increased in dip downwards. Similarly floor heaves and rib

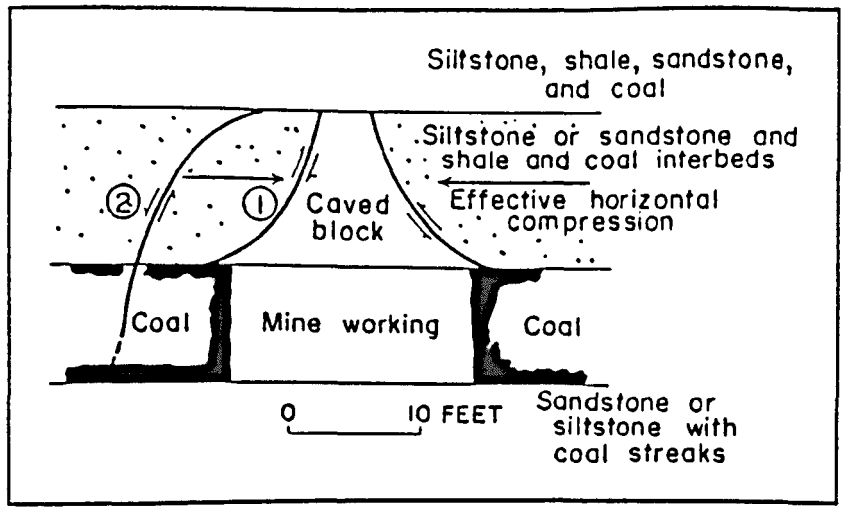

Fig.2.4.2.7 Shear failure (1) of massive roof rock under inferred horizontal compression, followed by violent shear failure along "cymoidal" fractures (2) that increase in dip downwards, after Osterwald & Dunrud [121].

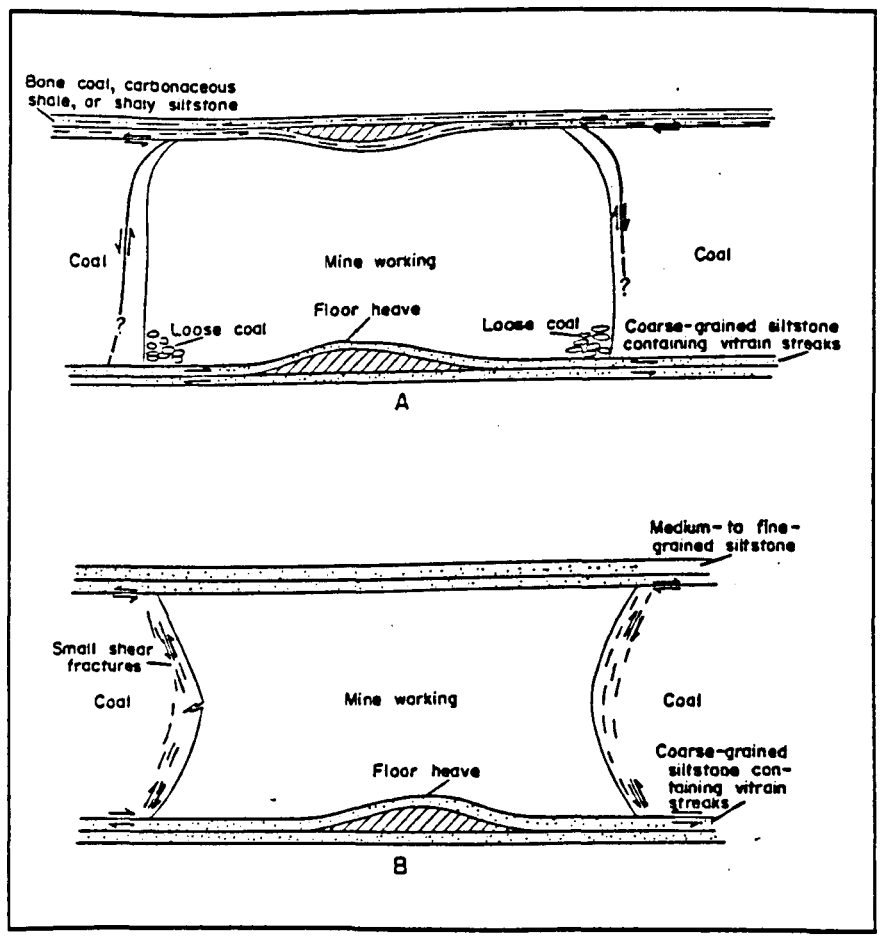

Fig.2.4.2.8 Relation of common types of rib failures to lithology of roof rocks, Utah. (a) "Cymoidal" fractures in rib where coal is free to slip beneath the roof. (b) Bulged and buckled ribs where coal adheres to roof, after Osterwald & Dunrud [121].

bumps that were probably interrelated were observed. Ribs in the Sunnyside mines commonly fail in one of two ways. Where coal is free to slip beneath the roof, "cymoidal" shear fractures form within the ribs, and where coal adheres to the roof, the ribs bulge and buckle (see Fig.2.4.2.8). Most bumps result from failure along "cymoidal' fractures, but loose coal is thrown down from some bulged ribs during bumps. Commonly one rib will fail along "cymoidal" shear fractures whereas the opposite rib will fail by bulging and buckling, implying that coal is free to slip beneath the roof in one direction, but not in the other. Osterwald & Dunrud considered this probably to be the result of original sedimentary features in the bedding surfaces, such as ripple marks, channel fills, load casts, crossbeds and slump structures, which impart pronounced but variable differences to the frictional properties of the slip surfaces in different directions.

Smart (1991)[122] contends that deformation, not just of coal sequences, but of all tabular deposits, is controlled by "dominant parting planes" (DPP's) particularly with regard to the release of strain energy around an excavation. A DPP is here defined as, "a laterally extensive but thin natural feature parallel to bedding which allows both relative normal motion (separation) and importantly parallel motion (shear) between adjacent strata." The argument is that, even at moderate depth, DPP's controlled by sedimentology will be activated in shear ahead of excavations such as longwall coalfaces, due to the release of horizontal stresses in the strata. This shearing action creates striations in a layer of frictional wear debris on the partings, which tend to point towards the approaching excavation and the associated release of horizontal stress. Importantly, Smart used finite element modelling to study the process of strata deformation in the vicinity of a gateroad and longwall coalface, finding a significant reduction in strain energy when shear was permitted along DPP's, compared with an equivalent model in which the same bedding planes were pinned. Thus DPP's were considered to represent an energetically favourable strata deformation mechanism. Considering the models to be 1m thick sections, a 4.8MJ reduction in strain energy was associated with the treatment of DPP's as frictional interfaces.

Whilst the above summary highlights the importance of bedding-parallel shear as a natural mechanism for the accommodation of tectonic strain, particularly under conditions of high fluid overpressure, and emphasises the role of bedding-parallel shear as a means of stress release associated with civil and mining engineering excavations, the main point in question is whether or not it occurs in the hydrocarbon reservoir environment in association with stress perturbations resulting from production. The best evidence for such slip on bedding planes lies in the generation of shallow focus earthquakes at Wilmington oil field in Long Beach, California, associated with fluid extraction, as discussed in section 2.4.1. Here six earthquakes (M2.4 to 3.3) were generated by bedding plane shear at depths of 470 to 520m (Kovach[102]). The significance of this phenomenon with regard to its potential effect on production operations is readily assessed from consideration of the results at Wilmington, where tens to hundreds of wells were sheared off over several square kilometres. As far as the author is aware, no incidences of induced earthquakes due to bedding-parallel slip resulting from fluid injection operations have been reported in the literature, which is perhaps surprising considering the role of fluid overpressure with regard to theories of tectonic thrusting and flexural slip folding.

Important corroborative evidence for bedding-parallel slip resulting from fluid withdrawal is provided by unpublished finite element modelling of a producing wellbore conducted within the Department of Petroleum Engineering, Heriot-Watt University, by Mr.P.W.H.Olden (pers. comm.). The model represented an idealised producing oil reservoir horizon, and was constructed using the ANSYS program, from 130 solid elements and 88 frictional interface elements in an axisymmetric formulation, the wellbore taken to be along the y-(vertical) axis. The model represented a 50m thick central producing horizon, with respectively, 50m and 30m of stratified rock mass above and below it, each containing frictionless bedding planes at regular 10m-spaced intervals. The model was assumed to be composed of a single rock type with elastic deformation and failure strength properties indicative of a moderately weak sandstone. An important feature of this model was the coefficient of thermal expansion used for the material,

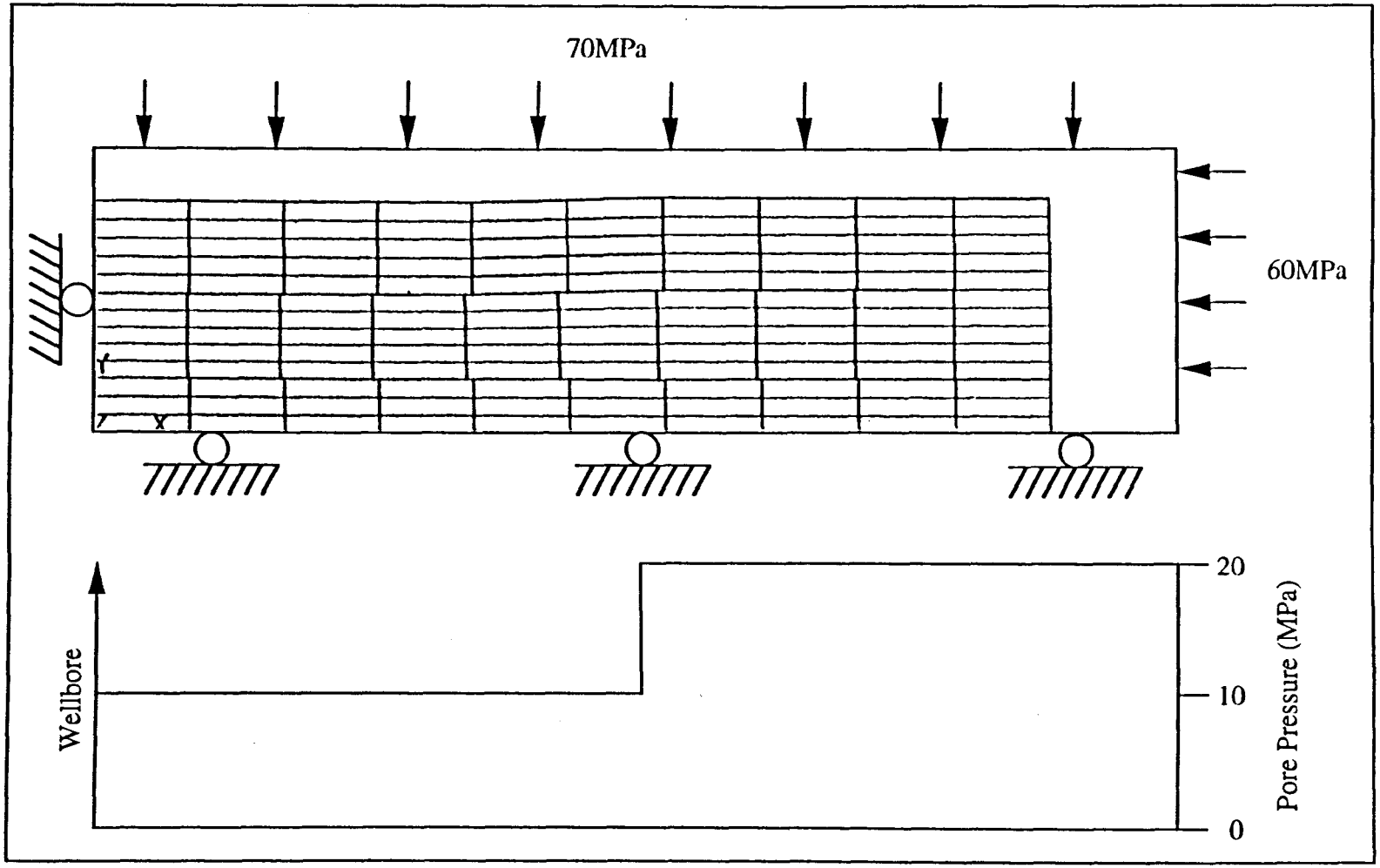

Fig.2.4.2.9 F.E. model of a producing oil reservoir indicating induced bedding-parallel shear slippage.

which enabled the effect of pore pressure to be simulated through analogy with thermal strain. By using a coefficient of thermal expansion, α, expressed by:

$$\alpha = \frac{(1-2\nu)}{E}\left(1-\frac{K_b}{K_s}\right) \quad \ldots\ldots\ldots \quad 2.4.2.2$$

where E is Young's modulus, ν is Poisson's ratio and K_b and K_s are the bulk moduli of the rock and the rock matrix respectively. Assuming $(1-K_b/K_s) = 1$, pore pressures are simply input by using element temperatures (Warren & Smith, 1985[123]). For remote stresses and boundary conditions as shown in Fig.2.4.2.9, a transient of 10MPa in the initial ubiquitous pore pressure of 20MPa throughout the stratigraphy was modelled (shown in detail in Fig.2.4.2.9) to simulate fluid withdrawal. The finite element mesh of Fig.2.4.2.9 represents a displacement plot, however relative displacements have been magnified for the purposes of clarity. The immediately noticeable point is that interlayer slip has occurred above and below the producing horizon to accommodate strain associated with fluid withdrawal, with a maximum of about 0.1m displacement occurring near the centre of the model. A complementary plot of horizontal stress distribution in the sequence of beds overlying the producing horizon shows that the net effect is for tensile stresses to be induced in the convex side of the sequence, and compressive stresses on the concave side. Relative subsidence from wellbore to outer edge of the model, associated with fluid withdrawal, is of the order of 45mm.

3. DIRECT SHEAR EXPERIMENTATION: RIG DESIGN AND RESULTS

3.1 INTRODUCTION

Current rock mechanics "philosophy" regards the rockmass as a composite material consisting of two principal components: interbedded lithologies (intact rock types) characterised by porosity, mineralogy, grain texture, degree of microcracking etc. and discontinuities characterised by population statistics (size distribution and 3-D orientation) mode of genesis, roughness, infilling etc. The global mechanical behaviour of a typical hydrocarbon reservoir rockmass (stratified, transected by discontinuities) is governed by its deformability and strength characteristics. Natau (1990)[124] suggests that these characteristics in the simplest sense can be described by an elasto-plastic constitutive relation determined by a global Young's modulus, E_g, a global Poissons ratio, ν_g, a global friction angle, ϕ_g, and a global cohesion, c_g, (Fig.3.1.1). These global characteristics in turn are determined by the behaviour and interaction of the rockmass's individual components. The stress-strain behaviour of the intact rock is determined by the Young's modulus, E_i, and Poissons ratio, ν_i, of each lithology, whilst strength criteria can be expressed using an internal friction angle, ϕ_i, and a cohesion, c_i. Standard uniaxial and triaxial tests for estimating these intact rock parameters are conducted within compression rigs. The mechanical properties of the discontinuities are also dependent on the properties of the intact host rock itself. Constitutive laws for discontinuities consist of descriptions of the discontinuity deformability (normal and shear stiffnesses, k_n and k_s) and strength criteria (discontinuity friction angle, ϕ_d, and cohesion, c_d). These parameters are estimated experimentally using a direct shear rig. Direct shear testing should therefore be perceived as being of equal importance with the more conventional uniaxial and triaxial compression tests, in determining rockmass deformability and strength parameters.

3.2 DIRECT SHEAR RIG DESIGN

The Heriot-Watt servo-hydraulic direct shear rig was conceived as an essential addition to the existing rock mechanics experimental facility (centred around a 100T stiff compression machine as described in Chapter 4) to enable the testing of rock

ROCKMASS: ϕ_g, c_g, E_g, ν_g

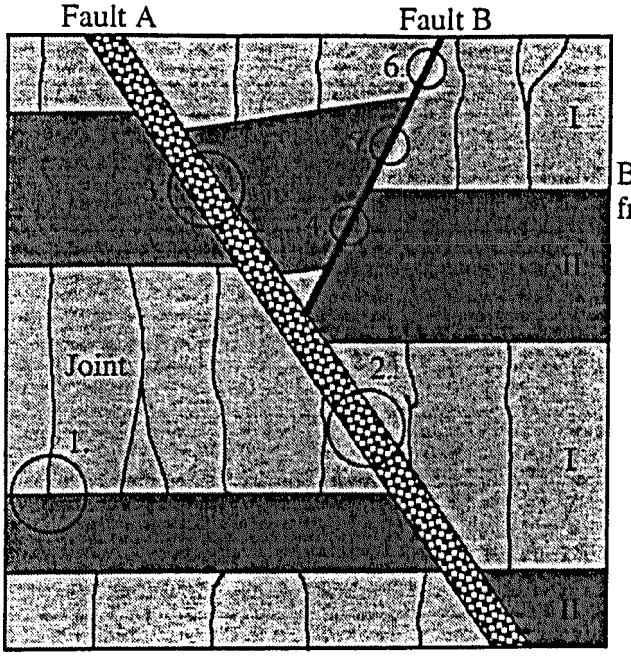

"Global" deformability of rockmass (composite material) governed by behaviour of its components and their interaction.

COMPONENTS:

1. lithology I: ϕ_o^I, c_o^I, E_o^I, ν_o^I
   lithology II: ϕ_o^{II}, c_o^{II}, E_o^{II}, ν_o^{II}
   joint in I: ϕ_j^I, c_j^I, kn_j^I, ks_j^I
   bedding plane: $\phi_{bp}^{I/II}$, $c_{bp}^{I/II}$, $kn_{bp}^{I/II}$, $ks_{bp}^{I/II}$
2. fault A in I: ϕ_{fA}^I, c_{fA}^I, kn_{fA}^I, ks_{fA}^I
3. fault A in II: ϕ_{fA}^{II}, c_{fA}^{II}, kn_{fA}^{II}, ks_{fA}^{II}
4. fault B in II: ϕ_{fB}^{II}, c_{fB}^{II}, kn_{fB}^{II}, ks_{fB}^{II}
5. fault B in I/II: $\phi_{fB}^{I/II}$, $c_{fB}^{I/II}$, $kn_{fB}^{I/II}$, $ks_{fB}^{I/II}$
6. fault B in I: ϕ_{fB}^I, c_{fB}^I, kn_{fB}^I, ks_{fB}^I

Fig.3.1.1 Schematic model of an interbedded rockmass with discontinuities, consisting of two lithologies, two faults, a joint set and bedding-planes (see text for details). Modified from Natau (1990)[124].

discontinuities. The direct shear rig was fabricated by RDP - Howden Ltd. of Leamington Spa, U.K., to a customer-specified design, allowing specimen shearing under either controlled normal stress or controlled normal displacement modes, depending on the likely *in situ* boundary conditions. Details of the rig design with preliminary results can be found in Smart & Crawford (1990)[125]. Fig.3.2.1 shows an end view of the rig, parallel to the direction of shearing. The frame consists of two side plates of flame-cut sheet steel 47mm thick, with a fixed base and adjustable top beam on which a 500kN hydraulic linear actuator with a vertical stroke of 200mm is mounted, to provide vertical normal reaction. The vertical actuator piston rod is machined with a location spigot and a matrix of drilled holes for the attachment of an upper shear box. Specimen sliding displacement is achieved by means of a unique design of shear table, which utilises a linear hydrostatic bearing to provide effectively frictionless motion, even when acted on by the 500kN normal compressive load. This hydrostatic base table has a surface area of 600mm x 600mm and a maximum sliding movement of 100mm. The table has a matrix of drilled holes for the attachment of a lower shear box. Specimen shearing is achieved by relative horizontal displacement of the lower shear box fixed to the base table, with respect to a stationary upper shear box, attached to the piston head of the vertical ram. The upper shear box is held immobile during slip of the lower, by means of a heavy steel roller bolted to the frame of the direct shear rig, which reacts against four flanges on the upper shear box, ensuring no lateral displacement. The vertical piston rod and flanged upper shear box, hydrostatic table and attached lower shear box, shear rig reaction frame and restraining roller are all visible in Fig.3.2.1.

Fig.3.2.2 shows a side view of the rig, perpendicular to the direction of shearing. The top beam may be adjusted vertically through six fixed elevations at 150mm intervals using external lifting gear, and bolted in position, enabling a maximum clearance of 630mm to be generated between the actuator piston head and the shear table. Sliding displacement is generated by two horizontal, opposing 500kN linear actuators with strokes of 100mm, each ram acting only in push. The vertical actuator, opposing horizontal actuators and crosshead locating bolt-holes are all evident in Fig.3.2.2.

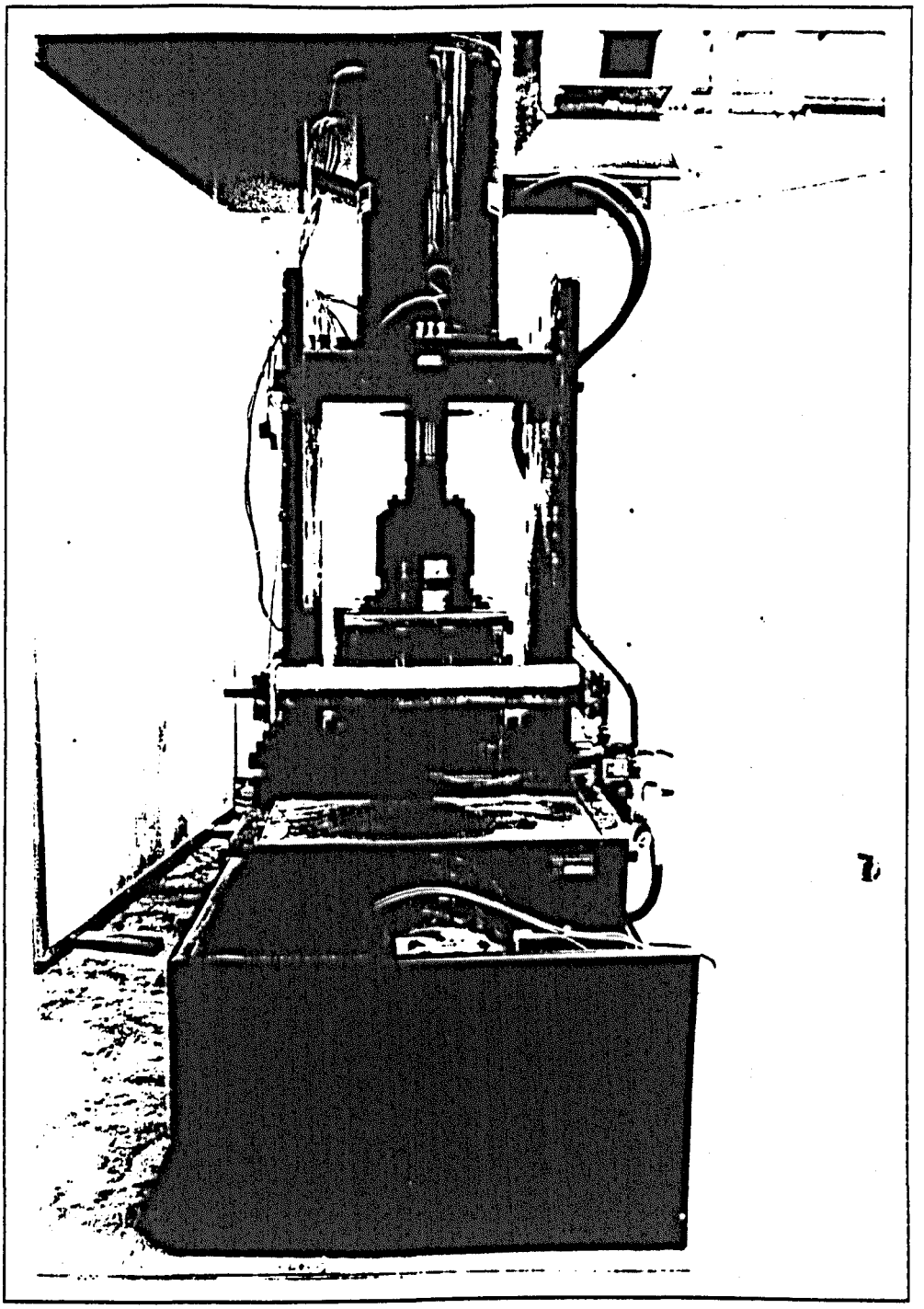

Fig.3.2.1 End view of the direct shear rig parallel to the direction of sliding.

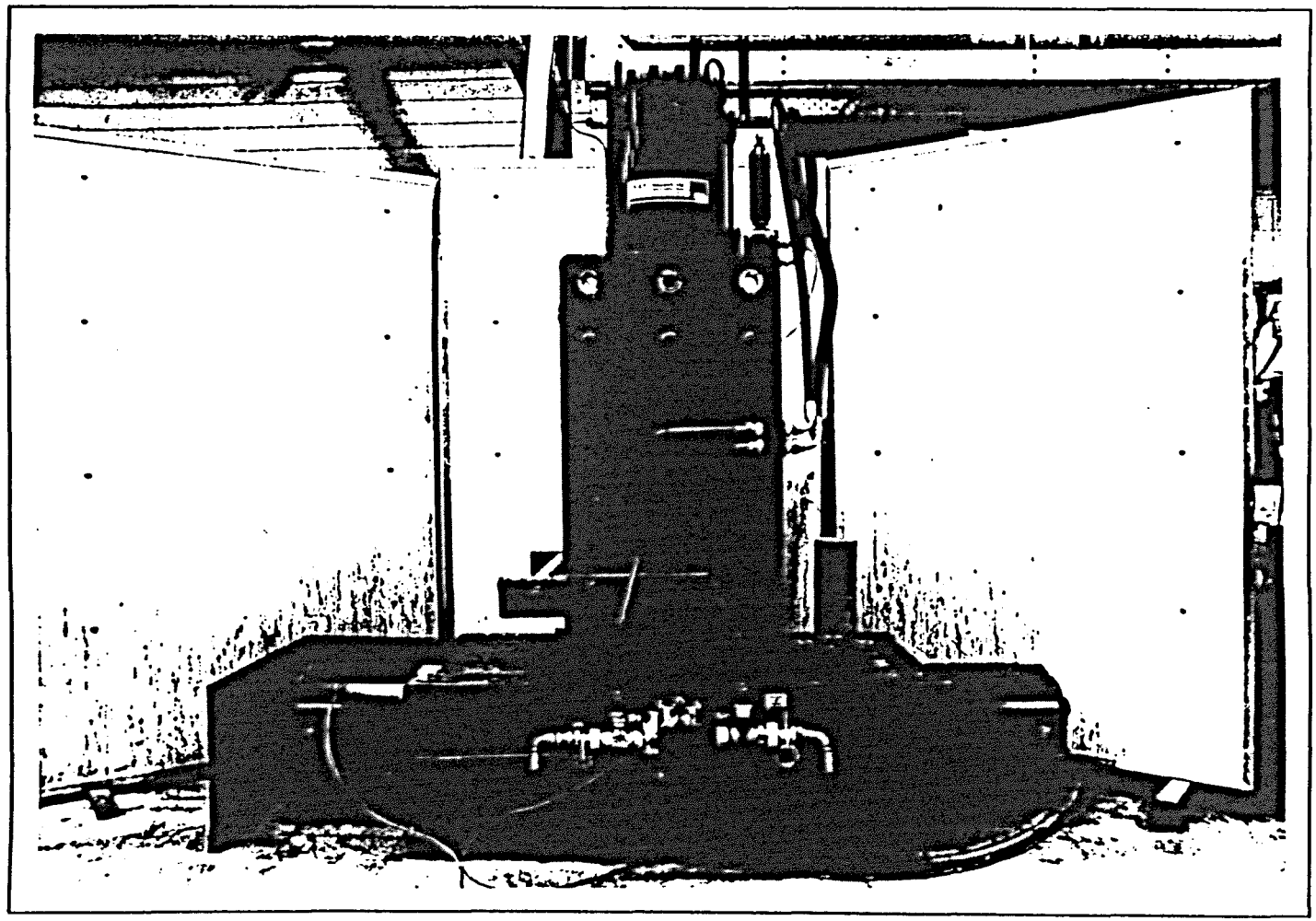

Fig.3.2.2 Side view of the direct shear rig perpendicular to the direction of sliding.

Fig.3.2.3 shows a scaled schematic of the direct shear rig (both front and back elevations perpendicular to the direction of shearing) detailing the hydraulic supply and control systems. A constant pressure oil supply for the vertical and horizontal actuator servo systems is provided by a mobile hydraulic power pack with a maximum system pressure of 30MPa (4300psi). This power pack also supplies the 100T compression rig and pressure intensifier for triaxial testing. The shear table linear hydrostatic bearing is fed from a separate mobile hydraulic power pack which supplies a maximum system pressure of up to 20MPa (3000psi), and scavenges the spent oil. The bearing action is created by feeding hydraulic oil through four orifices on the underside of the shear table. The 20MPa system pressure is dissipated in a 0.05mm gap between the rims of the orifices and a lower bearing plate. The linear actuator providing vertical thrust is an unequal area, double acting unit capable of producing greater compressive than tensile forces. It is suitable for operation under closed loop control with displacement or pressure as the controlling parameter. A servo-valve manifold block, high pressure accumulator, displacement and pressure transducers are fitted as standard. An internal LVDT provides measurement of piston travel for normal displacement control, whilst a pressure transducer in the hydraulic feed line enables the actuator to be operated under the alternative condition of normal load control. The vertical ram is controlled from an RDP-Howden System 2000 Command Module, a control console also used to direct the compression rig and confining pressure facilities. This unit theoretically allows any parameter conditioned to a 0 - 10V scale to control the vertical actuator, for example a load cell could provide an alternative means of normal load measurement (shown dotted in Fig.3.2.3) although for the tests described here, only closed loop pressure transducer control was utilised. Although both axial load and confining pressure can be controlled simultaneously using the System 2000, triaxial and direct shear tests cannot be performed at the same time, so that servo-valve and transducer connections to the control console have to be swapped around depending on which test is to be conducted. The pair of single acting (push-only) horizontal actuators mounted either side of the hydrostatic shear table are controlled separately from the vertical ram. LVDT's allow measurement of horizontal displacement, whilst pressure transducers in the hydraulic feed-lines enable measurement of shear loads. A bench console provides control of the horizontal actuators. This

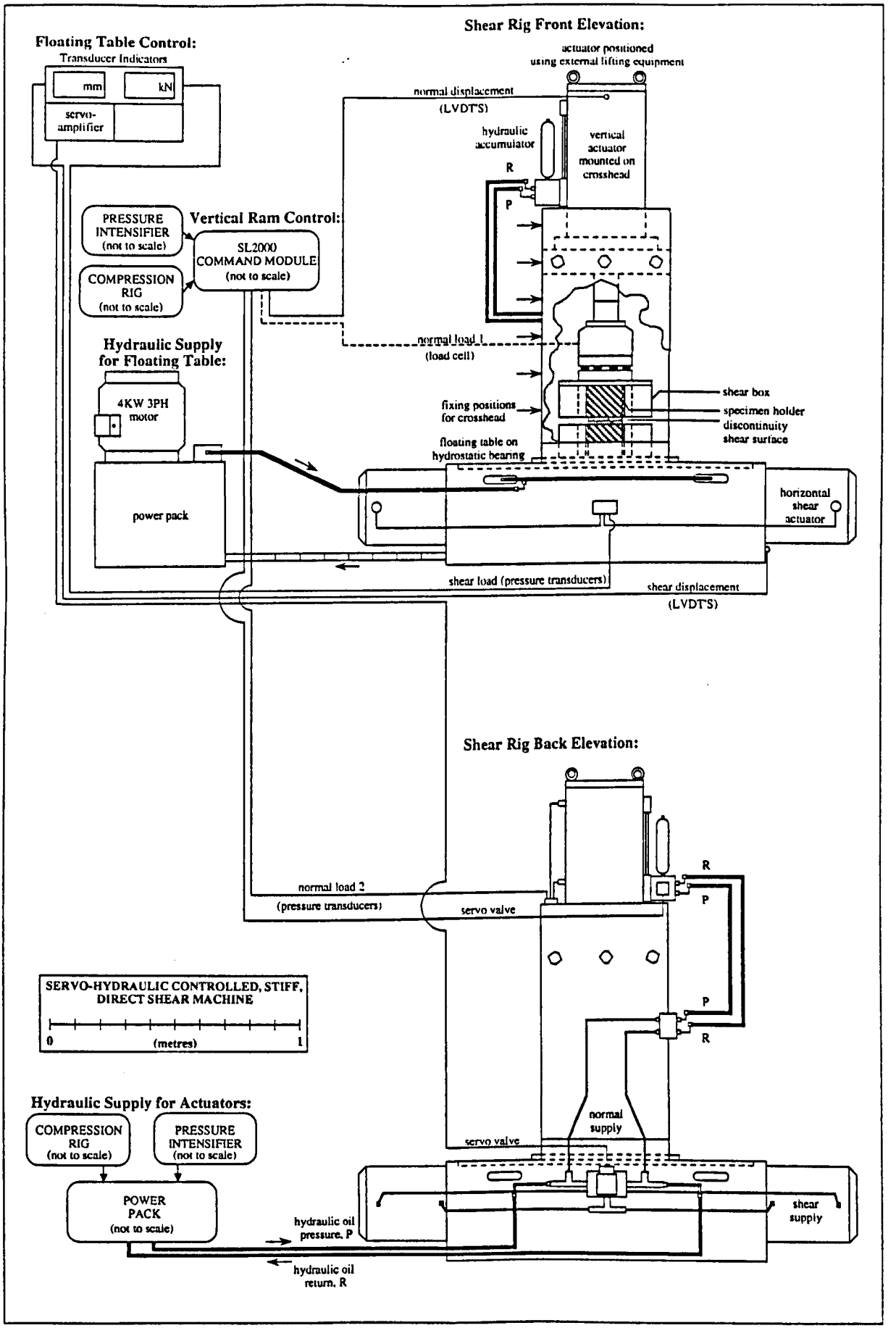

Fig.3.2.3 Scaled schematic of the direct shear rig, showing details of the control system and hydraulics.

comprises a servo amplifier to supply the drive current for the servo-valve, and a dual amplifier/monitor unit with transducer indicators giving digital displays in mm and kN respectively. Hardcopy data from tests performed under constant normal displacement conditions is provided in the form of continuous line traces of normal load, shear load and normal displacement against shear displacement, recorded on a multi-channel, moving-paper chart-recorder.

3.3 TEST SPECIMENS AND EXPERIMENTAL METHODOLOGY

To facilitate initial appraisal of direct shear rig performance, the frictional strengths of a dozen cylindrical test specimens sourced from a wide range of sedimentary rock types were measured, all under constant normal displacement conditions. The main variable in the experimental programme was therefore lithology. Cylindrical test specimens were produced by coring large (typically 100kg) blocks obtained from quarrying and open cast mining operations. The diameter of the core samples (around 4.5" or 118mm) is directly equivalent to a standard size of reservoir whole core routinely taken when retrieving core from exploration and production wells. Brief lithological descriptions of the twelve specimens tested in direct shear are given below: three were red medium-grained aeolian sandstones, specifically quartz arenites consisting of predominantly quartz grains and some potassium feldspar, with significant haematite cement coating the grains (specimens #3, #5 and #6); two were dark grey, highly fissile mudrocks (specimens #8 and #9) specimen #8 possessing some minor silty laminae, specimen #9 appearing homogeneous and predominantly composed of clay-grade material; three were planar laminated, highly heterolithic siltstones (specimens #11, #12 and #14) consisting of dark-grey/black carbonaceous, laminated siltstone with profuse plant debris, containing variable numbers of up to cm-thick bands of white fine-grained quartz arenite sandstone; four were grey, highly heterolithic, inter-banded sandstones and siltstones (specimens S1, S2, S3 and S4) consisting of thickly laminated fine sandstone and siltstone layers with varying clay contents, showing signs of significant soft sediment deformation resulting in undulose and non-planar bedding. Individual core specimen identification numbers are given in the brackets following the above lithological descriptions.

From the above, it is evident that the direct shear specimens fall broadly into four distinct rock types: the red medium sandstones #3, #5 and #6; the dark-grey fissile mudrocks #8 and #9; the black carbonaceous siltstones #11, #12 and #14; the grey heterolithic siltstones S1, S2, S3 and S4. Whilst the red sandstone specimens appear broadly homogeneous on the core specimen scale, with only faint traces of a planar cross-lamination so that between-sample variation is low, specimens from the remaining three lithological groups show higher degrees of sedimentological heterogeneity, and thus higher between-sample variation for each rock type. Both mudrock specimens show strong fissility on shaley partings perpendicular to their long axes, however between-sample variation is moderate and due primarily to the existence of silty laminae in #8 not seen in #9, the latter being almost 100% claystone. The black carbonaceous siltstones also show moderate discrepancies in between-sample sedimentology due to bands of variable thickness, white, fine-grained sandstone being present with different frequency in each specimen. However, greatest between-sample lithological variability is shown by the grey inter-banded sandstones/siltstones, where their heterolithic nature combined with varying degrees of chaotic bed disruption due to soft sediment deformation, has resulted in widely different quartz, feldspar, clay and muscovite percentage mineral contents. X-ray diffraction analyses of >500micron-sized fault gouge fractions, obtained by sieving shear debris sampled from the sliding surfaces of each of the post-test direct shear specimens, provide approximate quantification of initial specimen mineralogy's. Such XRD-derived percentage mineral contents from specimens #3, #5, #8, #9, #12, #14, S1, S2, S3 and S4 are presented in Chapter 6.

To mount a cylindrical specimen in the direct shear rig, upper and lower core holders (steel hollow cylindrical sheaths bolted to the rock core) are fitted to the specimen so that a 10mm gap is left between them to accommodate the shear plane. The specimen with its core holders is then positioned in the lower shear box, and the upper shear box carefully lowered over it until flush with the specimen top surface. The core holders are then bolted securely into the shear boxes. Whilst the core holders used are machined specifically to fit specimens 118mm (4.5") in diameter, the shear boxes could accommodate core up to about 200mm (8") with suitably sized core holders. Due to the depth of the shear boxes,

core samples must be some 300mm in length, necessitating the capping of some undersized specimens with quick-setting, high-strength concrete. To aid in the capping process, split moulds were constructed.

An interesting indirect consequence of the difference in lithology shown by the test specimens was reflected in the nature of the discontinuity introduced into each prior to shearing. Each specimen was initially "notched" using a hammer and chisel at the desired location for the intended shear plane, secured in the shear boxes as described above, leaving a 10mm gap containing the notch between the upper and lower shear boxes, and then "popped" in tension using the normal load actuator to pull apart the specimen halves. The discontinuity introduced into the red sandstones by this means proved to be a rough planar tensile fracture that had propagated from the circumferential notch with no lithological control. In contrast, discontinuities induced in the fissile mudstone specimens corresponded to smooth, fissile shaley partings. The carbonaceous siltstones also produced discontinuities within the notched region controlled by sedimentary lamination, being largely carbonaceous and micaceous bedding parallel partings. The grey heterolithic sandstones/siltstones tended to produce concavo-convex tensile fractures, partially associated with clay-rich laminae within the vicinity of the notched region, but also cross-cutting sandier bands. The chaotic nature of the bedding due to soft sediment deformation meant that the discontinuities were more undulose than those in the other lithologies, with between-sample variation in discontinuity surface roughness being much greater in specimens S1, S2, S3 and S4. Specimen surface roughness appeared to be fairly constant within the red sandstone, fissile mudstone and carbonaceous siltstone rock types.

To conduct a direct shear test, following the creation of a discontinuity in tension as described above, the specimen halves were re-mated with the pre-shear discontinuity protruding, respectively, some 5mm below and above the upper and lower core holders. A normal stress of around 1.0MPa (minimum 0.7MPa for #9, maximum 2.7MPa for #3) was then applied across the discontinuity, prior to shearing the upper and lower specimen halves relative to each other on this plane. Horizontal displacement of the lower specimen

half (contained within the shear box bolted to the "frictionless" shear table with linear hydrostatic bearing) was achieved through activation of a single horizontal actuator operated in push only, controlled manually from a bench console (see section 4.2). Horizontal actuator displacement was varied manually from the servo-amplifier mounted in the bench console, via an input level control knob (a high-resolution potentiometer). Most specimens were sheared for a total displacement of about 20mm, although the discontinuity planes in specimens S1, S2 and S3 experienced slip of 23, 24 and 25mm respectively. The frictional strength of the twelve specimens tested under constant normal displacement (never exceeding about 0.1mm) shearing mode, was measured from hardcopy plots of variation in normal load and shear load with increasing shear displacement, produced by each of the direct shear test runs. A summary of the direct shear specimen lithologies and pre-shear discontinuity descriptions are given in Table 3.3.1, as well as the pre-shear normal stress magnitudes and total shear displacements applied to each of the samples.

3.4 EXPERIMENTAL RESULTS

3.4.1 Sliding Surface Morphology

Whilst graphical output as described above provides invaluable data for quantifying the effects of lithology on rock friction, and for calculating shear strength envelopes for frictional sliding in constant normal displacement shearing mode, "post mortem" examination of the test specimen sliding surfaces provides equally valuable qualitative information on deformation associated with the slip event. Through such study, structural features observed for laboratory sliding under known stresses and boundary conditions can be contrasted with those observed on natural tectonic shear discontinuities including sub-seismic sealing faults, granulation seams, bedding-parallel frictional interfaces etc. from which, at best, only measurements of shear strain and displacement vectors, and inferences with regard to palaeostress magnitudes and directions can generally be drawn. Thus laboratory investigations utilising direct shear experimentation have sought to re-examine fault-related brittle structures as seen in the field (see for example Gamond, 1983[126] and Petit, 1988[127]).

Direct Shear Specimen I.D.	Geological Age	Lithological Description	Nature of Pre-Shear Discontinuity	Pre-Shear Normal Stress (MPa)	Total Shear Displacement (mm)
#3	Permian	red sandstone	tensile fracture	2.7	20
#5	"	"	"	2.2	21
#6	"	"	"	1.1	20
#8	Carboniferous	fissile mudstone	fissile shaley partings	0.8	20
#9	"	"	"	0.7	20
#11	"	carbonaceous laminated siltstone	carbonaceous/ micaceous laminae	1.0	19
#12	"	"	"	0.9	19
#14	"	"	"	1.0	19
S1	"	heterolithic sandstone/ siltstone	undulose bedding-plane controlled	1.0	23
S2	"	"	"	0.8	24
S3	"	"	"	1.2	25
S4	"	"	"	2.1	20

Table 3.3.1 Specimen lithologies, pre-shear discontinuity descriptions and test variables for direct shear experimental programme.

Colour plates showing the lower and upper sliding surfaces of the twelve direct shear specimens, taken post-testing, are presented in Appendix I. These photographs were taken under oblique lighting, illuminating the surfaces from right to left, that is approximately perpendicular to the direction of sliding, in order to highlight surface roughness and topography. Arrows shown in each figure indicate the displacement direction of the lower sliding surface (identified as the "BOT" sample) and the upper sliding surface (identified as the "TOP" sample) as shown. Each specimen has been separated into lower and upper halves about the shear plane so that, as photographed, the tops of the lower and upper sliding surfaces were originally in contact, as were the right-hand-side of the BOT-surface and the left-hand-side of the TOP-surface. In this orientation, as illustrated, it is informative to envisage the TOP-half being held rigid and stationary in its shear box, whilst the BOT-half was displaced horizontally, with the resultant shear couple as indicated.

From Appendix I the most striking feature that is immediately apparent on inspection, is that all surfaces, to a greater or lesser extent, are liberally covered in sliding-induced frictional wear debris. This shear debris can be considered as representing "genuine" fault gouge, that is comminuted rock fragments liberated from the actual experimental sliding surfaces due to the shearing action, as opposed to "artificial" fault gouge so often used in laboratory experiments. The latter commonly consists of a layer of glass beads, clay particles, crushed silica, or sampled natural fault gouge, placed between rigid rock or steel platens which are subsequently sheared, so deforming the artificial gouge layer. One principal advantage of conducting the direct shear testing programme under constant normal displacement conditions, has been that shear debris production has been maximised (due to total suppression of dilatancy in favour of asperity shear) by comparison with expected production under shearing modes of constant normal stress or stiffness. This has produced relatively large masses of shear debris, from a range of rock types deformed under known boundary conditions, for analysis. Results from small particle statistical analyses of these debris distributions, as well as correlations with measured frictional strength parameters of the various sliding surfaces, are presented in Chapter 6. In this section, qualitative descriptions of the various features observed on

sliding surfaces will be given, and an attempt made to characterise the different surface morphologies that have evolved, in terms of lithological controls.

All the structural features observed on the sliding surfaces, regardless of the test lithology, were attributed to brittle fracture and mechanical abrasion during frictional sliding. The red sandstone specimens #3, #5 and #6 are shown in Fig.AI.1, Fig.AI.2 and Fig.AI.3 respectively. All three samples show white patches of ground quartz grains, easily discernible against the red background of the iron oxide-stained initial tensile failure surfaces. These isolated patches of localised grain-size reduction show variable areal extent, but always incomplete coverage of the sliding surfaces. Intuitively, the surface distribution of the sheared patches and the location of the peak contact asperities will be highly correlated. These regions of fault gouge are strongly striated with slip-parallel linear features also recorded from natural fault surfaces, where they are recognised as being the result of "asperity ploughing", "debris streaking" and "erosional sheltering" (Means, 1987)[128].

A second feature immediately apparent on the surface of the red sandstone shear planes, takes the form of a planar structure showing a distinct resemblance to "slickensides" so often noted from faults in the field (for a definition see Fleuty, 1975)[129]. It has long been known that these striations and step structures can be used for the determination of the direction of movement along a fault, and prior to 1958 it was generally assumed that the step-like protuberances faced in the direction of movement of the overriding surface (Billings, 1954, p.149)[130]. However Paterson (1958)[131] published a photograph of steps developed on a shear surface formed during a triaxial test on Wombeyan marble which clearly showed that the steps opposed the movement of the overriding surface. Paterson concluded that movement directions along fault planes should not be determined only from the attitude of the steps on the plane, but from other geological features as well. All the slickensteps observed on both the BOT- and TOP- shear surfaces of red sandstone specimens #3, #5 and #6 appeared to be incongruous, that is they faced against the movement of the overriding block. Currently, two theories have been proposed to account for this common facing direction. Gay (1970)[132], from experimental double shear testing

and microscopic observation, suggested a mechanism for the formation of "accretion steps" whereby the steps are bounded by two sets of tension cracks, one parallel to the maximum compressive stress and the other perpendicular to the shear plane. On parting the shear plane, these steps are plucked out of the host rock and adhere to the opposite side of the shear plane. Alternatively, Lindstrom (1974)[133] proposed that such steps form by the partial disintegration of temporarily coherent clumps of cohesive fault gouge dragged along the shear surface.

The upper and lower sliding surfaces produced by the fissile mudrock direct shear specimens #8 and #9 (Fig.AI.4 and Fig.AI.5 respectively) appear dramatically different to those from the red sandstones as described above. As opposed to discrete, localised patches of comminuted debris representing shear of contact asperities in the latter rock type, the BOT- and TOP-surfaces of the mudrocks are almost 100% covered by debris. Whereas the red sandstones yielded predominantly shear products in the form of "rock flour" consisting of white patches of mechanically crushed constituent quartz grains, the mudrocks generated a much greater fraction of broken rock fragments, including cm-sized particles, due to the presence of a pre-test foliation. Many strongly laminated sedimentary mudrocks respond to the induced transverse strains resulting from predominantly uniaxial vertical loading on burial, by deforming in a "quasi-plastic" manner (Gramberg, 1989, p.44)[134]. This phenomenon is readily observable in shales at the free boundaries of underground excavations associated with coal mining, where they tend to "flow" to fill the void. Such deformation results in the formation of highly polished, smooth, anastamosing slip surfaces, imparting a fissility to the mudrock which is characteristically friable, often crumbling on these serrated shear surfaces. Both specimens #8 and #9 showed this characteristic polished and serrated fabric, oriented approximately perpendicular to their long axes. On testing in direct shear, this fabric was reactivated, generating often sigmoidally-shaped, cm-sized lithological fragments bounded on all sides by these polished slip planes, such fragments being progressively comminuted on further shear displacement, but also being liberated over the entire sliding event. Minor striae were observed in small clumps of fine-grained gouge resulting from

the experimental shear conditions. Pre-existing polished slip planes are particularly evident on the #9 TOP-surface (Specimen #9 being almost 100% claystone).

Fig.AI.6, Fig.AI.7 and Fig.AI.8 show the sliding surfaces from carbonaceous siltstones #11, #12 and #14 respectively. It is evident that frictional sliding has proceeded with much less comminution than in the case of the mudrock samples, and that gouge formation has not been so obviously confined to asperity contacts as found for the red sandstones. Both sliding surface morphology and low shear debris production are interpreted as being facets of the initial test lithology. The planar nature of the BOT- and TOP-shear surfaces reflect the sedimentary lamination, this low roughness also contributing to the minimal amounts of debris. Slickensides, slickenlines and slickensteps are nevertheless very well defined in the compacted, fine-grained gouge fraction. With the black siltstone laminae being rich in "low friction" organic-carbon and mica components, it is not surprising that all the shear planes formed within these horizons. However the arcuate white bands visible in Fig.AI.7 delineate where a more competent, 4mm-thick sandstone band has been "pulled-apart" in tension, due to the shear couple across "easy slip" horizons lying immediately above and below it. Interestingly, this has resulted in a step within the sandstone band which faces in the direction of movement of the overriding surface, that is in the opposite direction to the observed slickensteps on both the BOT- and TOP-surfaces.

The sliding surfaces generated by the grey heterolithic sandstone/siltstone direct shear specimens S1, S2, S3 and S4 (given in Fig.AI.9, Fig.AI.10, Fig.AI.11 and Fig.AI.12 respectively) each produced large quantities of comminuted constituent mineral grains and also of lithological fragments, and in this respect therefore combined features of both the red sandtones and of the fissile mudrocks. Whether because of the initially "cup-and-cone" nature of the induced tensile failure surface prior to shear testing, or because of differential compaction of the chaotic bedding resulting from soft-sediment deformation, sliding surface morphologies suggest that minor relative rotation of the sample halves has occurred during shearing, which has the effect of inducing inhomogeneous stress/strain distributions within the specimens. This is reflected particularly in Fig.AI.9, in which

separate semi-circular areas of zero frictional lineations and of intense striae coverage, are evident on both the BOT- and TOP-sliding surfaces. This is consistent with the rear of the specimen opening in tension and the front of the specimen being subjected to more confined conditions, due to relative rotation of the specimen halves. Schematic cross-sections showing the forms of macroscopic specimen deformation occurring for the four different lithologies tested under direct shear, are illustrated in Fig.3.4.1.1. A photomicrograph taken of the BOT-sliding surface of red sandstone specimen #3, and showing slickensides, slickenlines and slickensteps, is presented in Fig.3.4.1.2.

3.4.2 Force-Displacement Curves

Following Byerlee (1978)[135] consider any typical friction experiment in which a rider of mass m is free to slide on a rigid flat, as shown in Fig.3.4.2.1(a). The tangential force required to move the rider is applied through a spring AB by moving the point B slowly to the right at a velocity v. Fig.3.4.2.1(b) shows the graph obtained by plotting the force in the spring as a function of the displacement of point B, and over which several distinct regions are discernible. From O to C, initial elastic increase in force is evident, until the point C where the curve departs from a straight line. The departure over the region C to D indicates that there is either nonelastic deformation of the rider (or of the flat), or that there is relative displacement between the rider and flat. On reaching the maximum at point D, the rider may suddenly slip forward, resulting in the force in the spring immediately dropping to the point E, from which the force will again rise until sudden slip takes place once more at point F. This sudden jerky type of movement is known as stick-slip. Alternatively, movement between the rider and flat may occur smoothly, in which case the force-displacement curve will be continuous, as shown schematically by the dotted line from D to G. This alternative movement mode to stick-slip behaviour is termed stable sliding. Byerlee refers to the force at the points C, D and G as the initial, maximum and residual friction respectively. Not surprisingly, Byerlee pointed out that confusion has arisen in the published literature, due to the practice adopted amongst many investigators of simply tabulating the coefficient of friction μ, without clearly stating whether it is the initial, maximum or residual friction that was measured. Obviously, if μ is not a constant but depends on the normal stress, then a table of

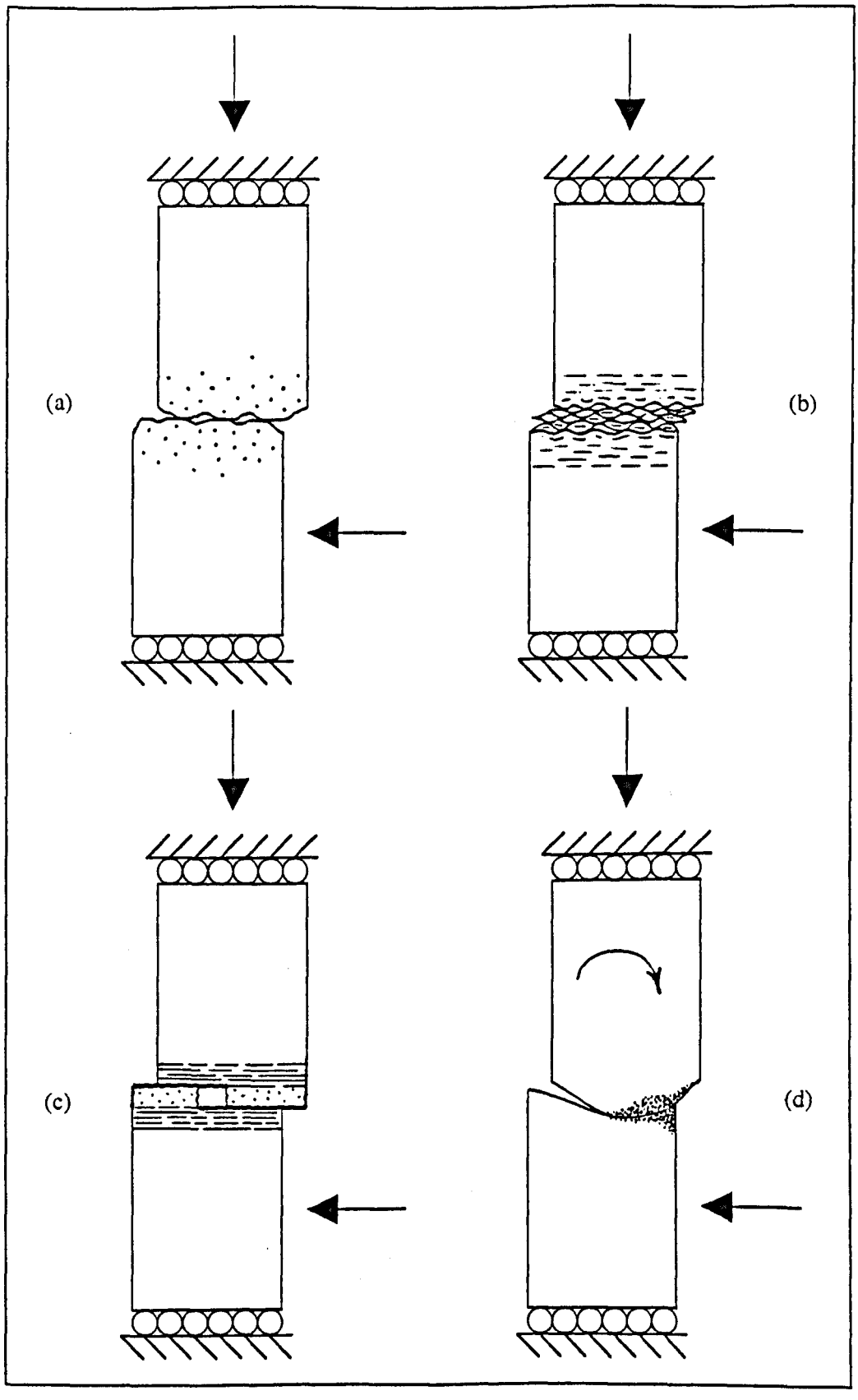

Fig.3.4.1.1 Schematic cross-sections illustrating macroscopic specimen deformation on direct shear of (a) red sandstone (b) fissile mudrock (c) carbonaceous siltstone and (d) heterolithic sandstone/siltstone test lithologies.

1000 microns

Direct shear specimen #3, lower (BOT) sliding surface, ≈ ×11
displacement sense from top to bottom.

Fig.3.4.1.2 Photomicrograph of laboratory direct shear specimen showing slickensides, slickenlines and slickensteps.

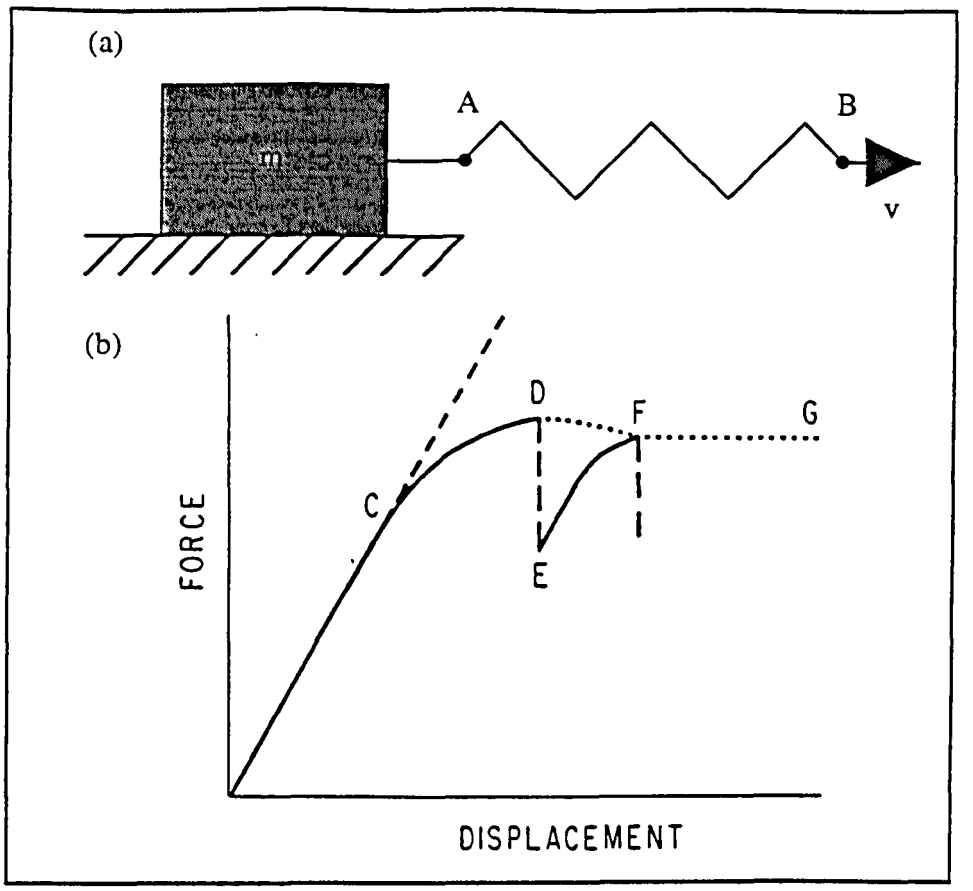

Fig.3.4.2.1 Schematic diagrams of (a) a typical friction experiment and (b) typical frictional force as a function of rider displacement results (Byerlee[135]).

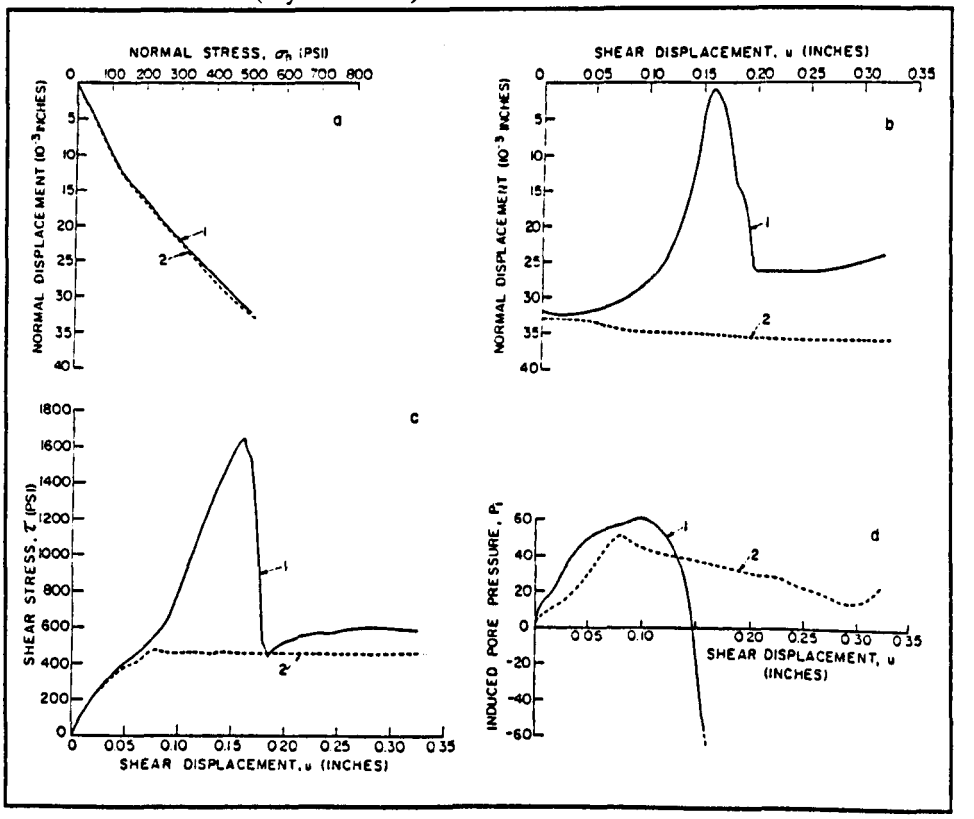

Fig.3.4.2.2 Undrained direct shear test results with (1) intact and (2) fractured samples of Lyons sandstone (Goodman & Ohnishi[136]).

frictional coefficients is of little value if the normal stress at which it was measured is not also given. According to Byerlee, the best way of avoiding confusion when quoting friction results would be to publish the force-displacement curves for all the experiments, however due to the impracticalities associated with this prohibitive amount of data, plots of shear stress against normal stress for each experiment, coupled with a clear statement relating whether the data refers to initial, maximum or residual friction would serve to minimise any potential ambiguity.

Direct shear testing yields the necessary relationships between stresses τ and σ_n and displacements Δs and Δn to characterise the discontinuity deformability and strength properties. Whilst it is usual to conduct a direct shear test under constant normal stress, so that dilation is possible as the surfaces ride over asperities, such a test yields too low a shear strength for frictional sliding under constrained conditions. Direct shear test results for an intact specimen (1) and a specimen with an initially open discontinuity oriented in the plane of shear (2) are presented in Fig.3.4.2.2, from a test conducted by Goodman & Ohnishi (1973)[136] on a sandstone specimen sheared at constant normal pressure. However, with one of the advantages of the direct shear test over the triaxial compression test being the ability to specify and control the normal load boundary condition, servo-feedback enables no-displacement or controlled stiffness conditions to be achieved in the direction of applied normal load. The range of discontinuity-normal loading conditions can best be represented by assuming that the deformability of the surrounding rock mass is modelled by a spring with normal stiffness $K = d\sigma_n/dn$ where $d\sigma_n$ and dn are the changes in discontinuity normal stress and displacement respectively (Saeb & Amadei, 1990)[137]. Thus stiffness K varies between zero for a discontinuity under constant normal stress, and infinity if the rockmass is very stiff for which no change in discontinuity normal displacement is allowed.

Following Goodman (1976)[138] discontinuity thickening (dilatancy) or thinning (contractancy) can be measured directly if the normal load is very soft as shown in Fig.3.4.2.3(a). If the normal load is stiff as in Fig.3.4.2.3(b) a tendency for dilatancy will be determined by monitoring the change in the normal load during shear. It is usual to

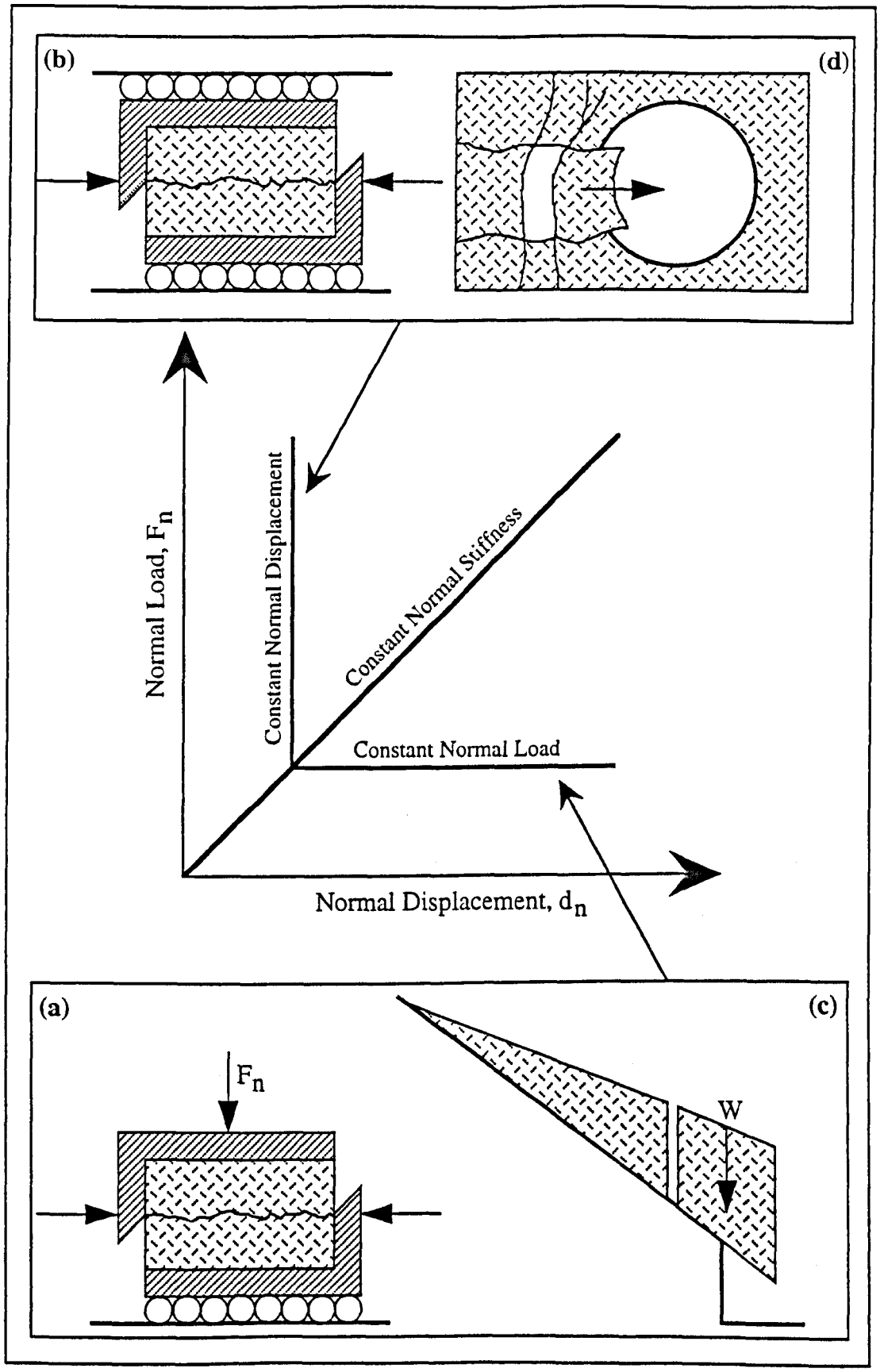

Fig.3.4.2.3 Controlled normal stress, (a) & (c), and controlled normal displacement, (b) & (d), direct shearing modes (Goodman [138]).

conduct a direct shear test so that the normal stress remains constant during shear. This corresponds to sliding of a free block on a slope as in Fig.3.4.2.3(c). However, such a test yields too low a shear strength for sliding of blocks constrained between parallel dilatant joints, as for example in an underground opening, shown in Fig.3.4.2.3(d), or in the middle of a rockface. A no-displacement or controlled stiffness condition in the normal load direction, which can be maintained by servo or manual feedback control, is the correct type of shear test for such design situations. The results of a normal displacement controlled shear test will depend not only on the stiffness of the normal load member, but upon the stiffness of the wall rock so the data require processing to scale to any given field case. One of the advantages of the direct shear test over the triaxial test is the greater ease in specifying and controlling the normal load boundary condition.

One of the very few experimental direct shear rigs capable of applying the constant normal stiffness (CNS) technique is described in Lam & Johnston (1982)[139] and Johnston *et al* (1987)[140]. The rig was commissioned specifically to simulate side resistance development of piles socketed into rock, under such boundary conditions. Test specimens consisted of an upper concrete specimen half and a lower "artificial mudstone" specimen half, the latter cast from mudstone powder, cement, water and accelerator with an artificial sawtooth interface geometry. Four identifiable regions of behaviour were recognised in the development of full shear resistance. Fig.3.4.2.4(a) shows diagrammatically the idealised general variations in shear stress, normal stress and dilation with shear displacement which would be expected from an interface test on regular triangular asperities conducted in the CNS equipment for an initial normal stress. As the shear stress is increased from zero (point A) there will be virtually no displacement (only minor deflections due to interface compressibility) until the frictional resistance to asperity sliding (due to second order wavelength asperities) is overcome at point B. When this occurs, dilation, and therefore normal stress, will increase. The shear stress often shows a slight decrease to point C as the cohesive bond is destroyed. However, on continued sliding displacement, because of the increase in normal stress, the shear stress will also increase until a peak shear stress is attained at point D. This point represents the onset of asperity failure and shearing and where, depending on the

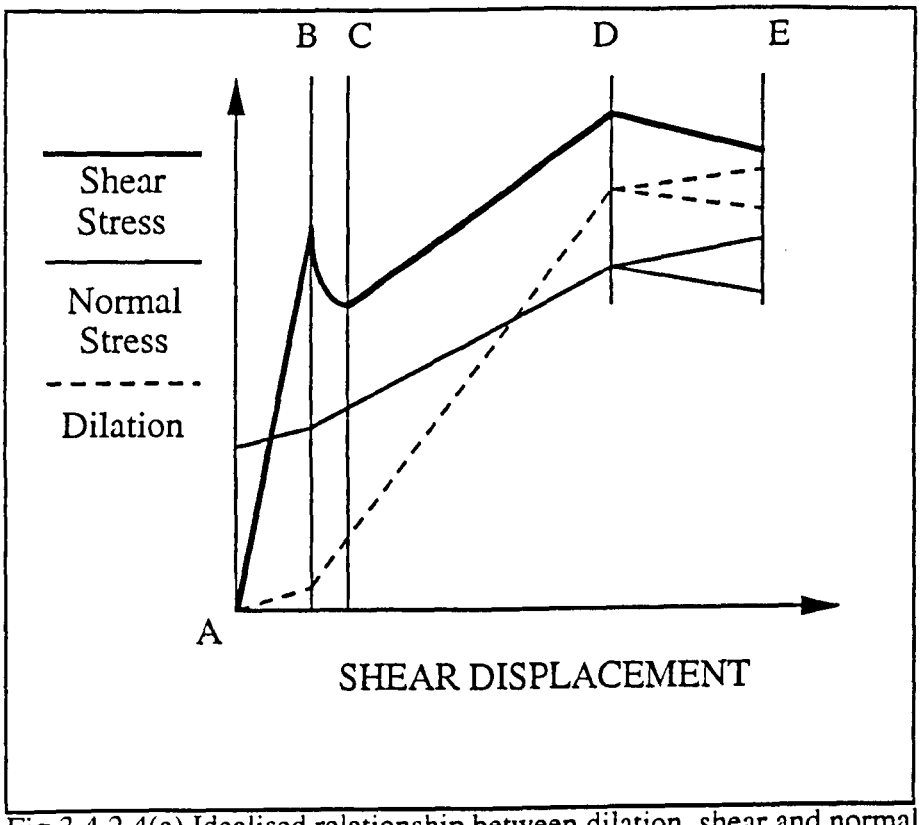

Fig.3.4.2.4(a) Idealised relationship between dilation, shear and normal stress with shear displacement for CNS conditions (Lam &Johnston[139]).

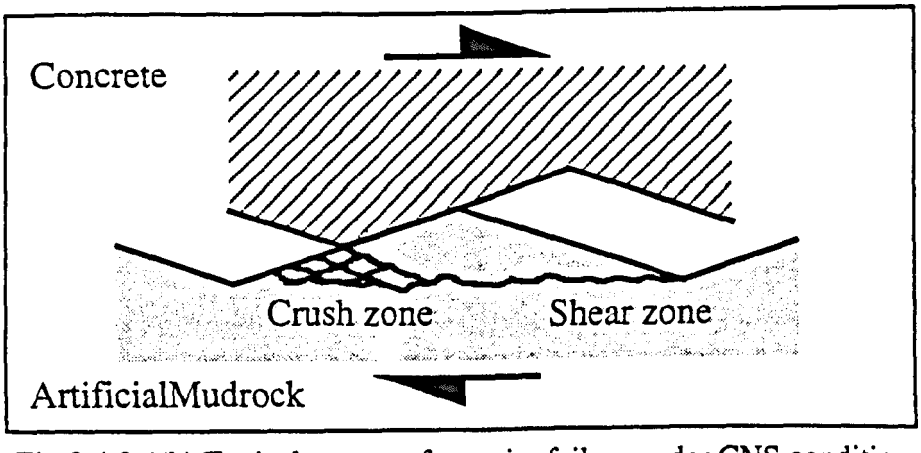

Fig.3.4.2.4(b) Typical pattern of asperity failure under CNS conditions (Lam & Johnston[139]).

inclination of the shear plane, dilation and normal stress become effectively constant. For continued shear displacement, the shear stress may decrease to the point E as the strength of the rock on the shear plane approaches its residual condition. A schematic of a typical asperity after failure has been initiated is shown in Fig.3.4.2.4(b). Whilst the mudstone above the shear plane is relatively intact, that portion roughly below the tip of the concrete asperity has been so crushed as to resemble a granular material. It was observed that the extent of the crushed-zone was smaller with the higher stiffness tests, but that the degree of granulation appeared much greater than with those tests conducted under lesser stiffness conditions. With asperity sliding producing dilation and thus a linear increase in normal and shear stresses (C to D), this movement was observed to produce tension cracks and some crushing within asperities, thereby reducing the shear resistance (failure strength) of the asperities. It would appear therefore that shearing through the asperities takes place when the sliding resistance exceeds the shearing resistance, but that shearing resistance changes progressively as sliding takes place. Failure shear stress was found to increase with increasing normal stiffness. The result of asperity shearing through the weakened asperities was to induce rapid reduction in shear stress (D to E) but with the normal stress remaining relatively constant.

The laboratory direct shear tests conducted as part of this thesis work were performed under constant normal displacement (CND) conditions, with the main variable being that of lithology (red sandstones, fissile mudrocks, carbonaceous siltstones and heterolithic sandstones/siltstones as described in section 3.3 all being tested). The imposition of effectively infinite normal stiffness and thus almost zero normal displacement, resulted in asperity failure and shear debris production probably far in excess of that reported above for a CNS shearing mode. As such, direct shear testing in a CND mode represents an ideal means of studying the process of shear debris production. Test conditions including pre-shear applied normal stress magnitudes and total shear displacements are given in Table 3.3.1. Whilst pre-and post-shear sliding surface roughnesses were not directly quantified, all initial discontinuities were induced under tension and proved to be significantly influenced by existing planar sedimentary fabrics (if any) so that variation in the degree of pre-test roughness was most likely insignificant for specimens of the same

lithology, but probably high from rock type to rock type. The greatest unavoidable between-sample variable for test specimens sourced from the same rock type, was probably sliding velocity, which may have varied by up to a factor of two in the most extreme case, as a result of manual control of horizontal actuator displacement.

Force-displacement curves for the direct shear (CND) test programme are given in Fig.3.4.2.5 to Fig.3.4.2.8. Force-displacement curves for red sandstone specimens #3, #5 and #6 are presented in Fig.3.4.2.5(a) to (c) respectively. Maximum shear and normal loads for #5 are more than twice those of #3 and #6, despite the lithology being broadly homogeneous on a specimen-scale, and the pre-shear normal load for #5 being intermediate between that of #3 and #6. This could be a result of specimen #5 possessing a rougher sliding surface, as it appears to have produced the greatest amounts of large fragment-sized wear products (Fig.AI.2). Specimens #3 and #5 show several complementary peaks in their shear and normal load profiles, followed by sudden stress drops, such jerky fluctuations as particularly exemplified by #3, probably representing dynamic failure of relatively large-wavelength asperities. Specimen #6, which shows gradual increases in both shear and normal load to broad plateau's, is seen to produce a post-test sliding surface morphology characterised by minimal damage confined to small isolated patches of crushed grains, corresponding to areas of asperity contact. Small-scale jerky fluctuations in the shear load profile for #6 are interpreted as stick-slip oscillations, which are often associated in the literature (see Jaeger & Cook[8] p61) with frictional sliding on relatively smoother shear planes. The fissile mudrock specimens #8 and #9 record markedly different load-displacement curves (Fig.3.4.2.6(a) and (b) respectively) to those of the red sandstones. Both specimens exhibit synchronous peak normal and shear loads, occurring at exactly the same sliding displacement. Specimen #8 shows shear and normal load profiles which are almost symmetrical, with the pre-peak and post-peak parts of each curve being almost mirror images about the peaks. However #9 exhibits load-displacement curves reminiscent of red sandstone #3, with pre-peak variations suggestive of asperity failure. Carbonaceous siltstones #11, #12 and #14 (Fig.3.4.2.7(a) to (c) respectively) all show similar load-displacement profiles characterised by broadly linear increases in normal and shear loads with sliding displacement up to peak values,

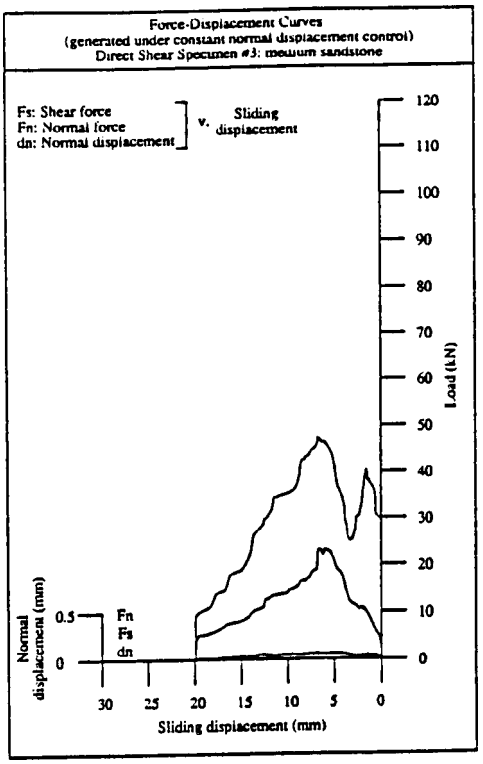

(a)

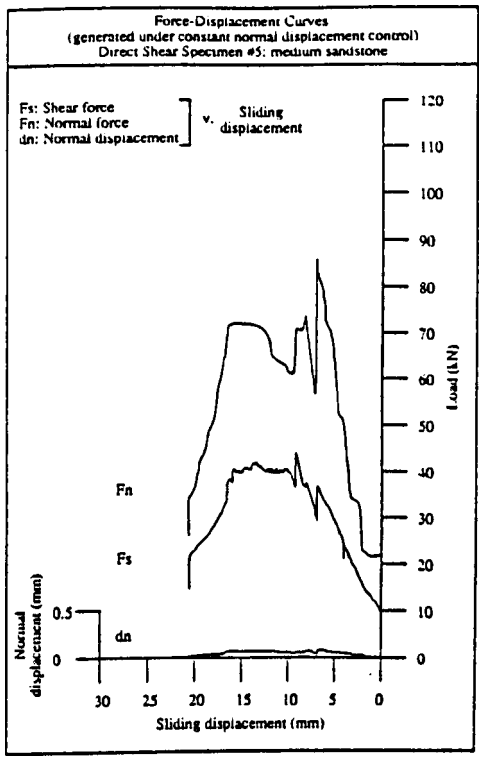

(b)

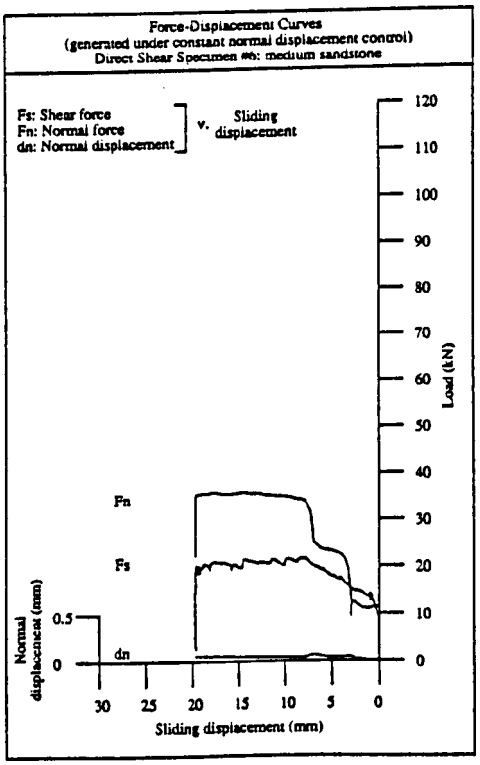

(c)

Fig.3.4.2.5 Load-displacement curves for direct shear specimens #3, #5 & #6.

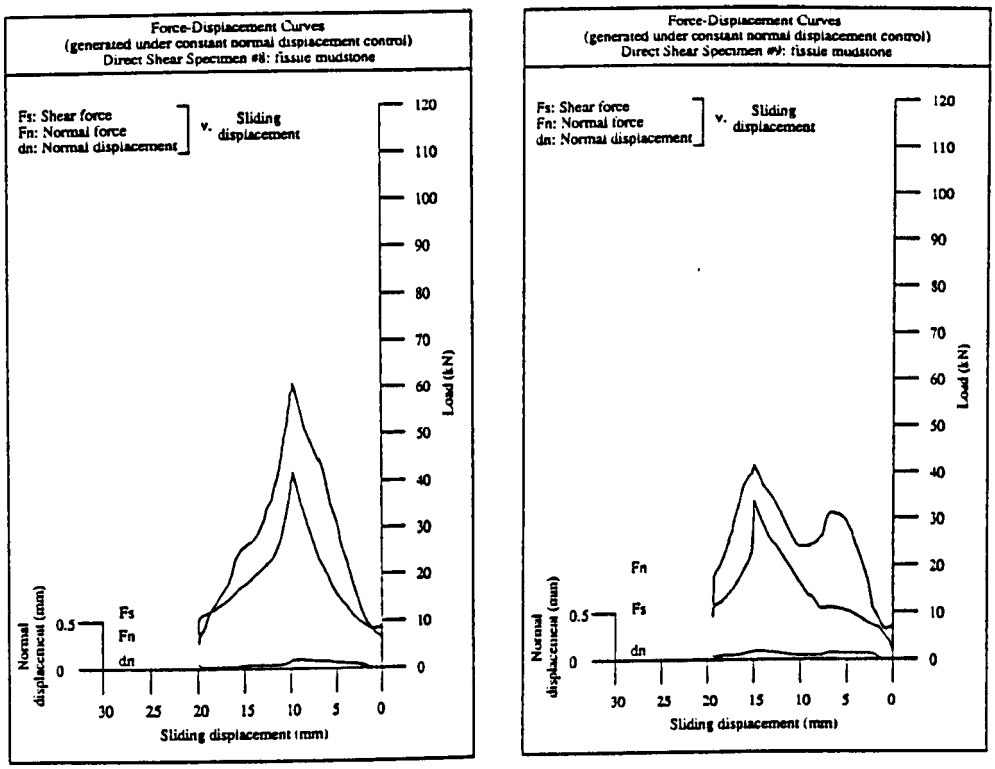

Fig.3.4.2.6 Load-displacement curves for direct shear specimens #8 & #9.

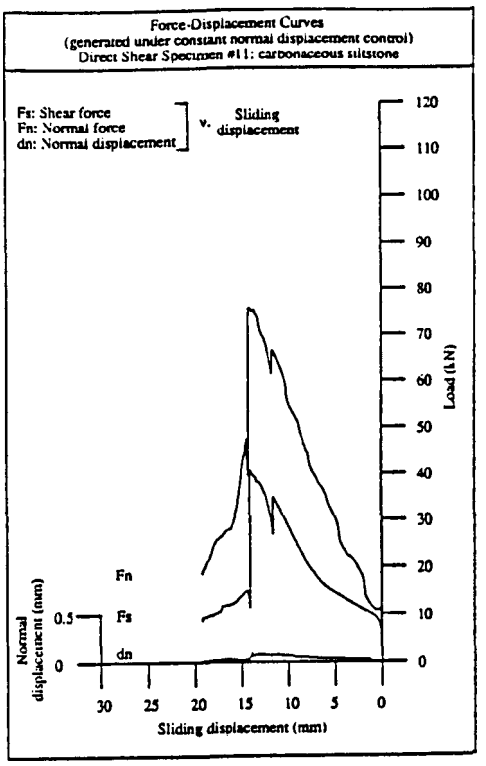

(a)

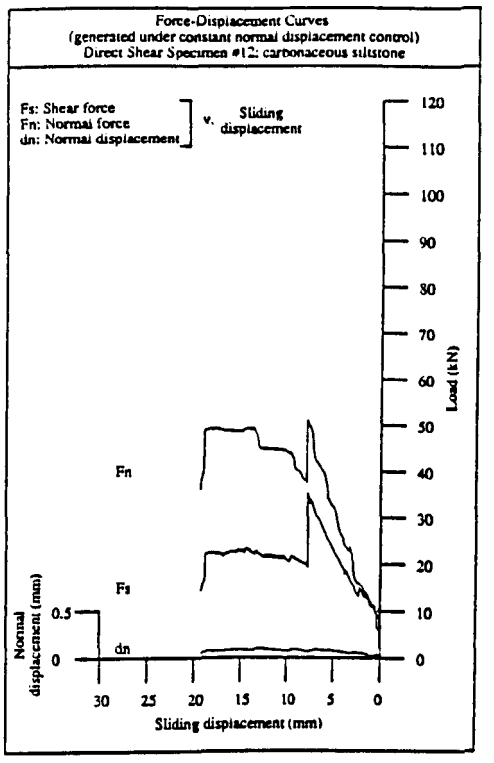

(b)

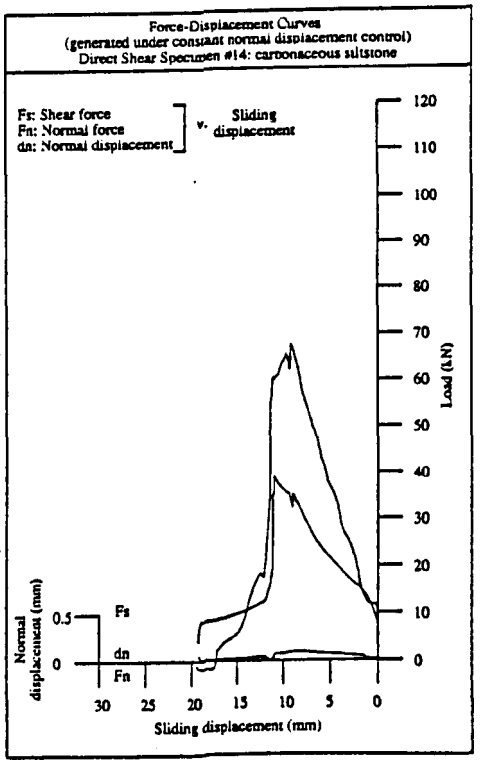

(c)

Fig.3.4.2.7 Load-displacement curves for direct shear specimens #11, #12 & #14.

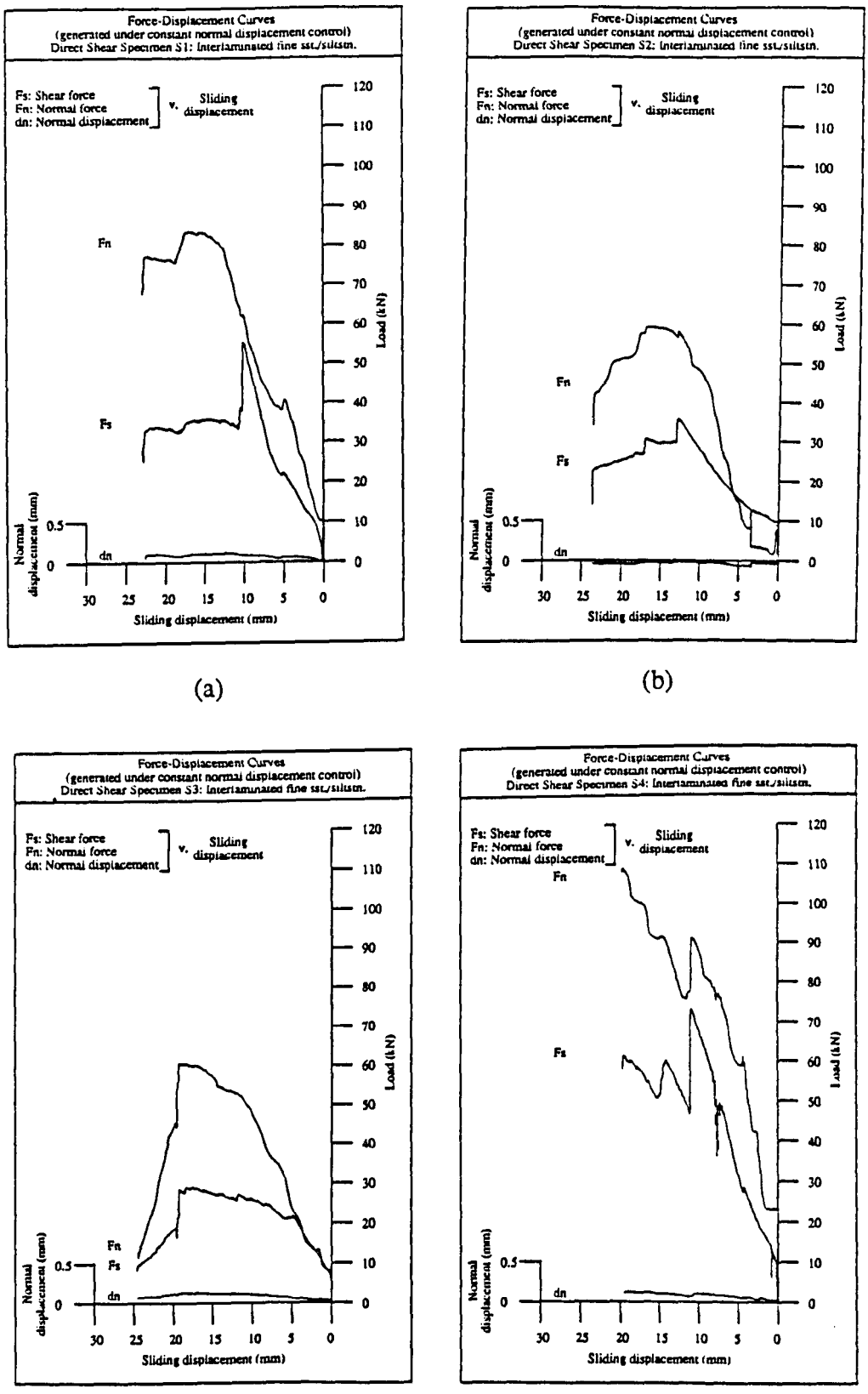

Fig.3.4.2.8 Load-displacement curves for direct shear specimens S1, S2, S3 & S4.

followed by sudden, large magnitude vertical drops which may well signify the failure of more competent laminae through "pulling-apart" in tension. Finally, heterolithic specimens S1, S2, S3 and S4 (Fig.3.4.2.8(a) to (d) respectively) show a wide range in force-displacement curves, reflecting presumably the wider variability in their percentage mineral composition and discontinuity surface roughness. Relatively larger variation in normal displacement (up to around 0.2mm) than recorded for the other lithologies may well reflect rotation of the upper specimen half as illustrated in Fig.3.4.1.1(d).

3.4.3 Theoretical Analysis of Contact Area Variation With Sliding Displacement

In order to convert the normal and shear load profiles as presented above, into variations in normal and shear stress magnitude with shear displacement, it is necessary to know the discontinuity sliding surface area across and along which, respectively, the normal and shear stresses have acted. Whilst, to a first order approximation, the cross-sectional area of the cylindrical specimen might suffice, such an assumption ignores variation in upper and lower specimen half contact area with sliding displacement, and thus tends to underestimate stress magnitudes. Ideally, variation in asperity contact area with slip is required, however this is difficult to evaluate experimentally without unloading the specimen, and is even more complex for specimens generating a large volume of comminuted rock debris. Instead, a theoretical analysis was undertaken to determine the area of overlap of two circles (representing the upper and lower direct shear specimen halves) with varying centre displacement. Consider the geometry depicted in Fig.3.4.3.1 in which a circle of equation $x^2 + y^2 = r^2$ with centre O on the origin, has suffered a translation in the x-direction to a new position with centre X. This translation, s, is equivalent to sliding displacement. No displacement is experienced in the y-direction. The Cartesian-coordinates of the points indicated in Fig.3.4.3.1 are thus: O(0, 0); 1(s-r, 0); 2(s/2, 0); 3(r, 0) and 4(s, 0). With the point of contact between the two circumferences being given by $y=(r^2 - x^2)^{1/2}dx$, the shaded area as shown in Fig.3.4.3.1 and representing one-quarter of the total area of overlap is given by:

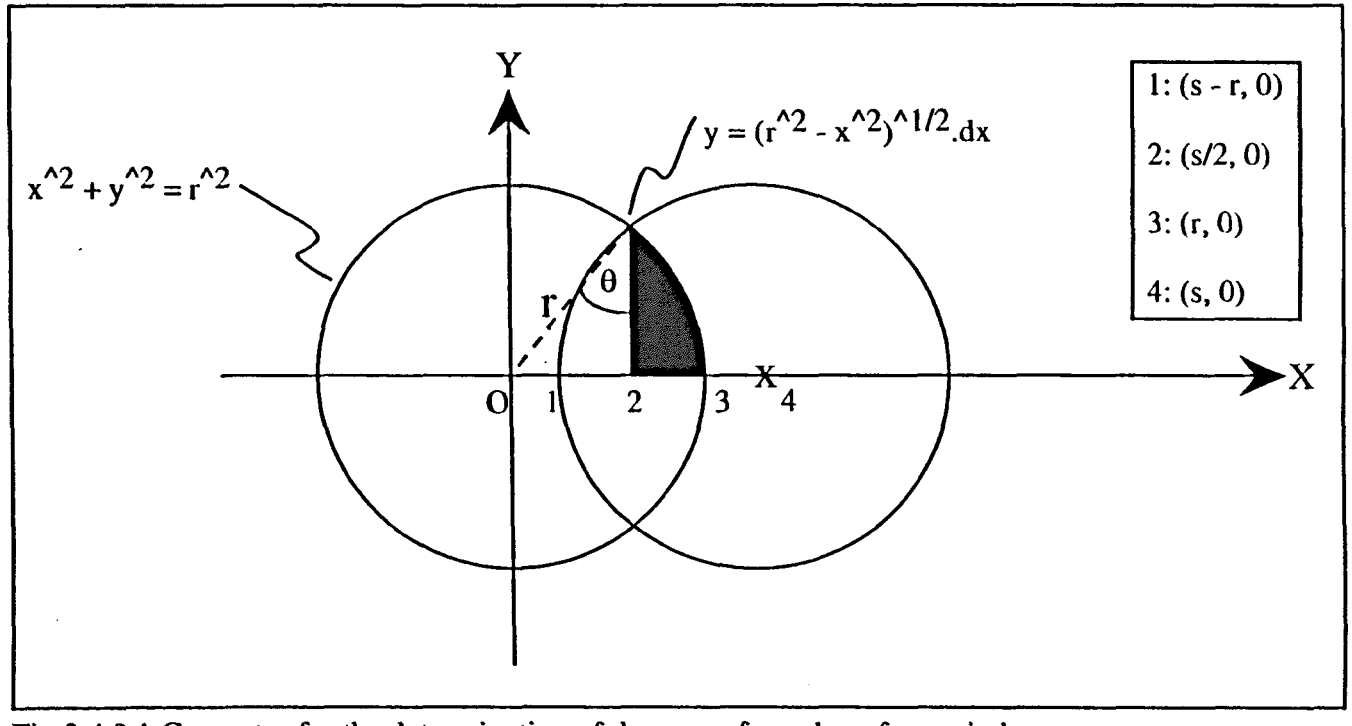

Fig.3.4.3.1 Geometry for the determination of the area of overlap of two circles with varying centre displacement.

$$A/4 = \int_{s/2}^{r} \sqrt{r^2 - x^2}.dx \quad \ldots\ldots\ldots \quad \text{Eqn.3.4.3.1}$$

utilising the standard integral:

$$\int \sqrt{u^2 - x^2}.dx = \frac{x}{2}\sqrt{u^2 - x^2} + \frac{u^2}{2}\sin^{-1}\frac{x}{u} + C \quad \ldots\ldots\ldots \quad \text{Eqn.3.4.3.2}$$

and substituting $\theta = \sin^{-1}x/r = \sin^{-1}s/2r$ gives:

$$A/4 = \left[\frac{x}{2}\sqrt{r^2 - x^2} + \frac{r^2}{2}\sin^{-1}\frac{x}{r}\right]_{s/2}^{r}$$

$$= \frac{r^2}{2}\left[\frac{\pi}{2} - \sin^{-1}\left(\frac{s}{2r}\right) - \frac{s}{2r}\sqrt{1 - \left(\frac{s}{2r}\right)^2}\right] \quad \ldots\ldots\ldots \quad \text{Eqn.3.4.3.3}$$

$\therefore$ the contact area of overlap of two circular sliding surfaces, A, is:

$$= 2r^2\left[\frac{\pi}{2} - \sin^{-1}\left(\frac{s}{2r}\right) - \frac{s}{2r}\sqrt{1 - \left(\frac{s}{2r}\right)^2}\right] \quad \ldots\ldots\ldots \quad \text{Eqn.3.4.3.4}$$

$\therefore$ if $A = \pi r^2.f(\phi)$ where $\phi = s/2r$:

$$f(\phi) = 1 - \frac{2}{\pi}\sin^{-1}(\phi) - \frac{2\phi}{\pi}\sqrt{1 - \phi^2} \quad \ldots\ldots\ldots \quad \text{Eqn.3.4.3.5}$$

when s = 0, that is for complete overlap $\phi = 0$ and $f(\phi) = 1$ $A = \pi r^2$, and when s = 2r, that is for zero overlap $\phi = 1$ and $f(\phi) = 0$ $A = 0$.

Thus by using Eqn.3.4.3.4, slip-dependent contact areas can be calculated for more accurate quantification of stress magnitudes from measured shear and normal load profiles. For a shear displacement of 20mm, as routinely applied to the majority of the direct shear specimens described here, contact area has decreased to around 78% of that corresponding to zero offset.

3.4.4 Stress - displacement curves

Utilising the theoretical variation in contact area with shear displacement relationship presented in section 3.4.3, the load versus displacement plots given in section 3.4.2 were converted to stress versus sliding profiles. Individual load values were manually read at 1mm shear displacement increments, directly from the shear and normal load plots for the twelve direct shear specimens. These values were then entered into a Microsoft® Excel spreadsheet and divided by the appropriate "slip-corrected" contact areas. Thus the normal and shear stress versus sliding displacement plots were generated, as presented in Fig.3.4.4.1 (red sandstones) Fig.3.4.4.2 (fissile mudrocks) Fig.3.4.4.3 (carbonaceous siltstones) and Fig.3.4.4.4 (heterolithics). These plots also present stress profiles calculated using a contact area equivalent to the specimen cross-sectional area (initial diameter of core = 118mm ≡ 10936mm^2) thus ignoring any variation with shearing. From comparison of the constant and variable contact area stress profiles, it is readily apparent that consideration of a sliding surface area which changes with shear displacement, produces markedly different results from those generated under the assumption of constant contact area.

3.5 EMPIRICAL EXPRESSIONS FOR FRICTIONAL STRENGTH

In defining Amonton's[141] law (see for example Jaeger & Cook[8] pp.53-54) suppose that two bodies with an approximately plane surface of contact of apparent area A are pressed together by force W normal to the plane of contact, and the shear force F parallel to the

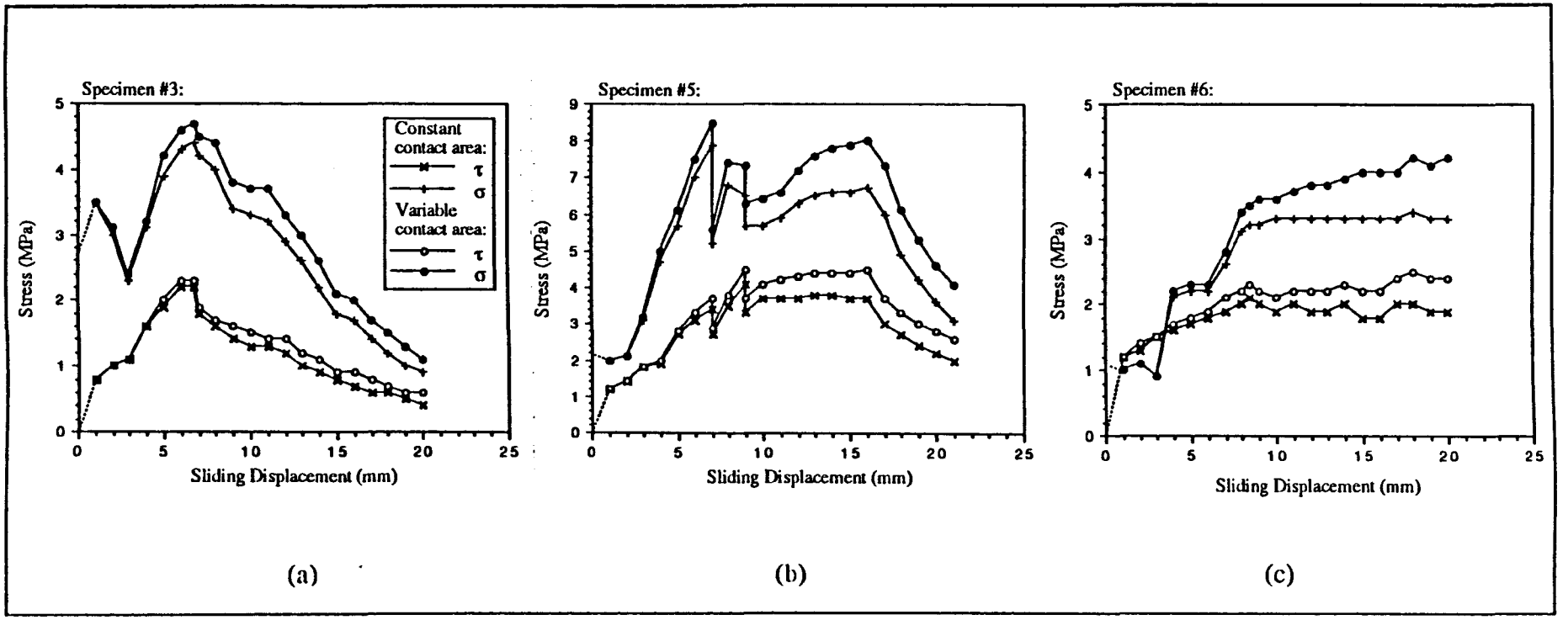

Fig.3.4.4.1 Displacement-stress plots for direct shear specimens #3, #5 & #6

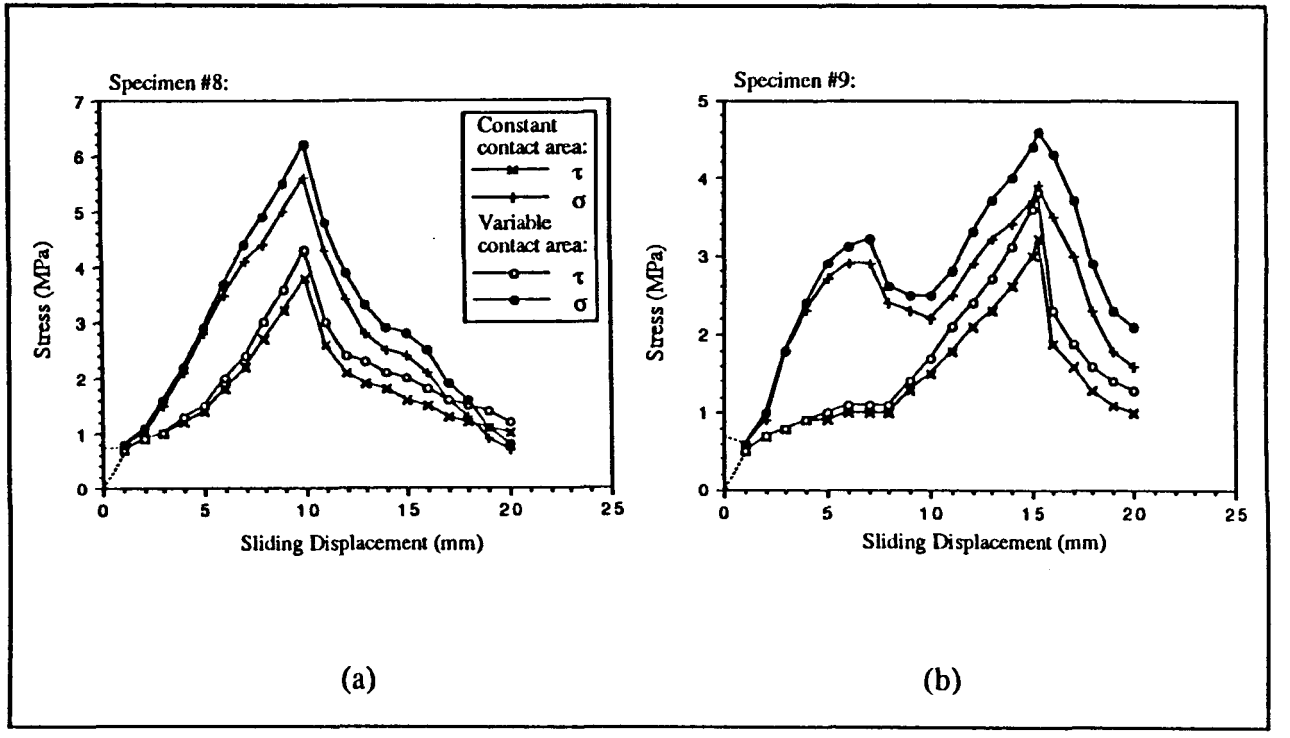

Fig.3.4.4.2 Displacement-stress plots for direct shear specimens #8 & #9

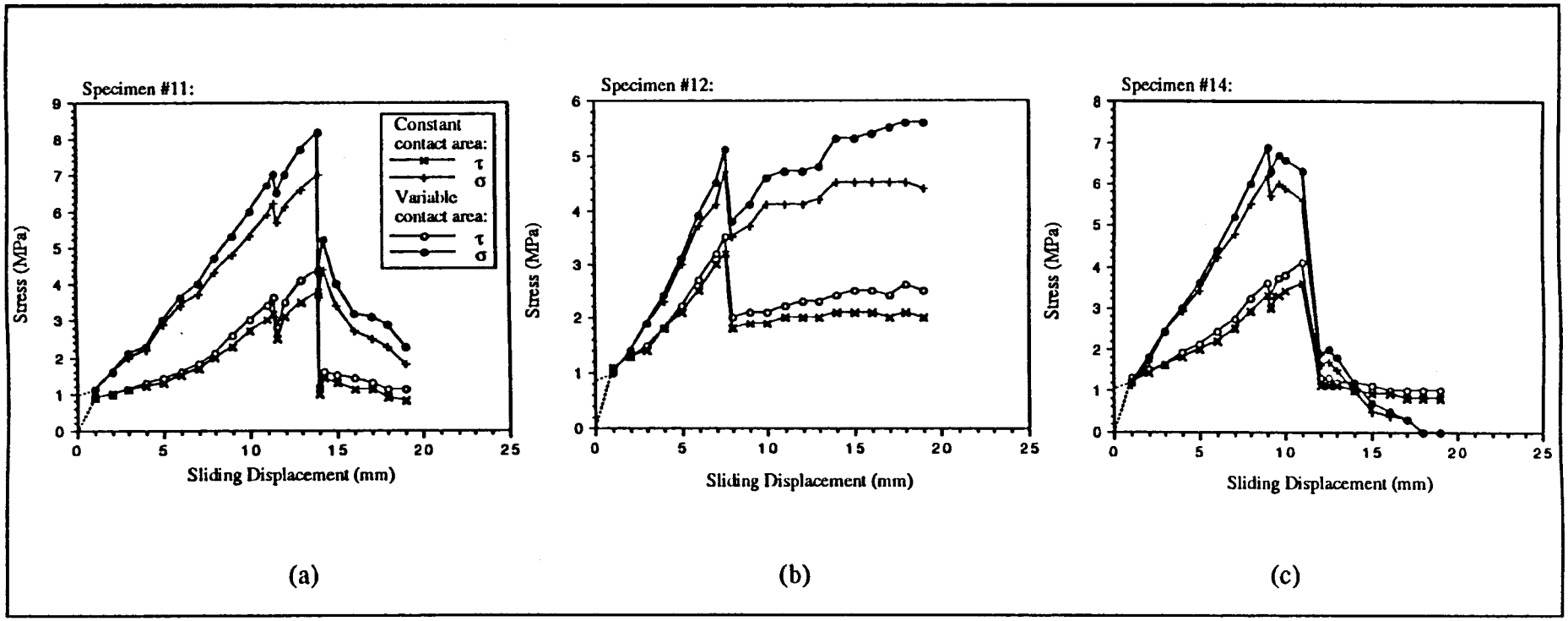

Fig.3.4.4.3 Displacement-stress plots for direct shear specimens #11, #12 & #14

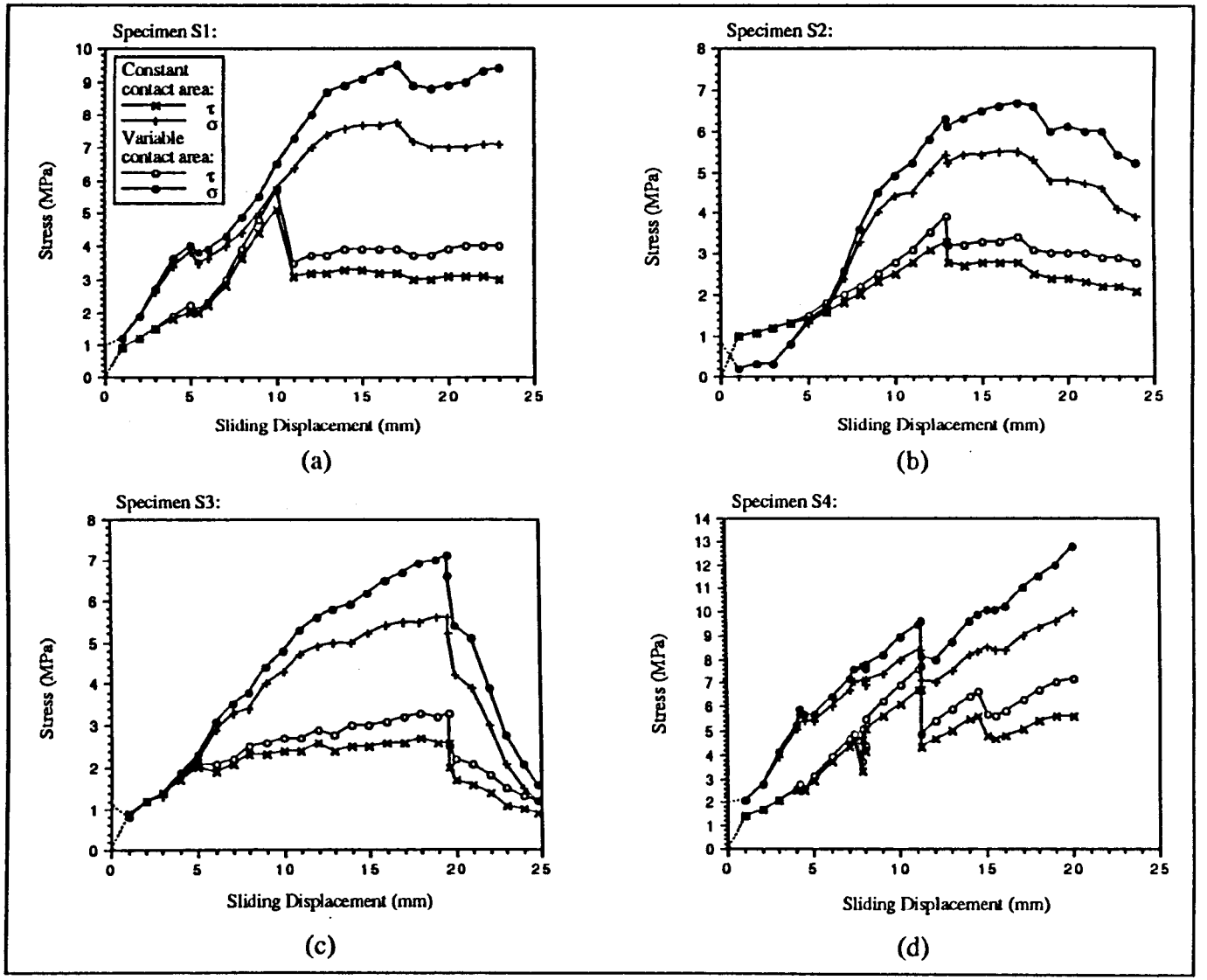

Fig.3.4.4.4 Displacement-stress plots for direct shear specimens S1, S2, S3 & S4

surface of contact necessary to initiate sliding on it is measured. The relationship between F and W is thus expressed as:

$$F = \mu^*.W \quad \ldots\ldots\ldots \quad \text{Eqn.3.5.1}$$

where μ^* is called the coefficient of friction and is dependent on the nature of the materials and the finish and state of the surfaces in contact. This relation is known as Amonton's law, in which division of Eqn.3.5.1 by A yields:

$$\tau = \mu^*.\sigma \quad \ldots\ldots\ldots \quad \text{Eqn.3.5.2}$$

where σ is the normal stress across the surfaces in contact and τ the shear stress necessary to initiate sliding. It is important to note that an asterisk superscript is here employed specifically to indicate a frictional coefficient defined as the ratio of τ to σ, that is by Amonton's law as given in Eqn.3.5.2, and should not be confused with various other frictional constants (also designated by μ, but without the asterisk superscript) associated with different criteria for sliding. Jaeger & Cook make the important acknowledgement that understanding of frictional phenomena is derived largely from the work of Bowden and his co-workers based on the study of metals, Bowden and Tabor (1950)[142], (1964)[143]. The adhesion theory of friction proposed by Bowden, Moore and Tabor (1943)[144] to explain the frictional resistance developed between metal surfaces, postulates that the very great adhesive forces at asperity contacts result in cold welding at these junctions, so that the frictional resistance developed is equal to the product of the real area of contact and the shear strength of the metal junctions. Indeed, at these junctions the contact appears to be so intimate that the metals became welded together, with the initiation of sliding requiring the shearing through of these welded contacts. This theory leads to the relationship described by Eqn.3.5.2, and thus Amonton's law is qualitatively explained. However, the situation is probably more complex in reality than that described by the above theory, for example a large number of asperities will exhibit a

wide range of contact loads, so that deformation at some may be elastic whilst others may be deforming plastically. Archard (1958)[145] has discussed such details of the frictional sliding process more completely, and concluded that the law of friction was perhaps best expressed by the power relationship:

$$F = \mu . W^m \quad \ldots\ldots\ldots \quad \text{Eqn.3.5.3}$$

where 2/3 m 1. The specific case of m=2/3 corresponds to purely elastic deformation in which the area of contact is proportional to $w^{2/3}$.

Whilst the above defined adhesion theory of friction, with much of it having been checked empirically, appears admissible for sliding of metallic interfaces, it is of doubtful validity for rocks and minerals, because most minerals tend to fail by brittle fracture rather than by plastic flow, and the welding postulated for metals may not hold for minerals. The concept of contact at a limited number of asperities does, however, remain valid for geomaterials, although as yet no adequate theory of their behaviour has been forwarded. Initial study along such lines was instigated by Byerlee (1967)[146] who proposed a simple theory of friction based on tensile brittle fracture, as a more realistic alternative to the classic adhesion theory developed for metals. In Byerlee's model the surfaces were assumed to touch at the peaks of asperities, and sliding to occur when the asperities failed by brittle fracture. The frictional coefficient, μ^*, was defined as the ratio of the shear force required to cause sliding to the applied normal force across the surfaces. For the postulation of brittle asperity failure rather than plastic shear, the characterising brittle failure criterion was taken as low tensile strength, thus it was assumed that the stress to produce brittle fracture in tension was much less than the stress to produce plastic shear. Byerlee investigated a unique relation between the forces required to break off the tips of the asperities, by analysing certain ideal asperity shapes. Using a truncated cone as an asperity model, and assuming it to fail in tension, Byerlee deduced that Amonton's law should hold for such a geometry, with a small value of μ^* of the order of 0.1. For experiments approximating closely to this ideal brittle friction

model, μ^* was found to be very close to 0.1, even for materials such as quartz and calcite with widely differing strengths. The character of wear particles produced during sliding and the way in which μ^* was seen to depend on normal load, roughness and environment all tended to support Byerlee's model of friction based on brittle fracture of asperities as opposed to one involving plastic shear deformation. Byerlee attributed the fact that higher values are commonly measured to the interlocking of asperities. As well as small-scale tensile failure of asperities, the extended shear discontinuities that occur in rockmasses including hydrocarbon reservoirs show irregular surface roughness, so that the effects of asperity ploughing and inclined sliding may be expected to occur. In Table 3.5.1 a summary of empirical and theoretical frictional strength criteria for rock discontinuities, as compiled from the rock mechanical literature, is presented. No derivation or discussion of individual criteria are given here, as these can be gained from the appropriate references. However, what is immediately apparent from Table 3.5.1, is the wide range of empirically derived constants utilised by the various criteria.

The resistance to sliding at an interface is usually expressed in terms of a coefficient of friction, μ^*, defined as the ratio of the shear force to normal force which is necessary either to initiate sliding (the coefficient of "static", "stationary" or "starting" friction) or to maintain continuing sliding (the coefficient of "dynamic", "kinetic" or "sliding" friction). This coefficient μ^*, as defined by Amonton's law (Eqn.3.5.2) was designated the "variable" coefficient of friction by Jaeger (1959)[147], whilst Donath *et al* (1972)[157] referred to it as the "idealised" coefficient of friction. Paterson[9] noted that even under given conditions, unique values cannot in general be given for the coefficients of friction, especially of dynamic friction, because of change in the frictional resistance with the amount of sliding. This change occurs because, in most studies on rock friction, two relatively large surfaces are moved over each other by amounts that are usually much less than the linear dimensions of the surfaces, and the average normal stresses are such that considerable wear or surface damage occurs during the sliding, affecting the resistance to further sliding. It is clear that both the evolving sliding surface morphology and the progressive production of fragmented rock debris play integral roles in determining the

SOURCE:	FORM:	DESCRIPTION:
Amontons (1699)[141]	$\tau = \mu^* . \sigma$	μ^* independent of σ and A, linear law
Jaeger (1959)[147]	$\tau = c + \mu . \sigma$	empirical linear "Coulomb-type" law
Bowden & Tabor (1950)[142]	$\tau = \mu_o . \sigma, \quad \sigma < c/(\mu_o - \mu_1)$ $\tau = c + \mu_1 . \sigma, \quad \sigma > c/(\mu_o - \mu_1)$	bilinear envelope
Patton (1966)[148]	$\tau = \sigma . \tan(\phi + i)$, dilation $\tau = c + \mu . \sigma$, shearing	bilinear envelope
Jaeger (1971)[149]	$\tau = a[1 - \exp(-b\sigma)] + \mu\sigma$	continuous curvature equivalent bilinear law
Byerlee (1975)[150]	$\tau = 0.85\sigma, \quad 0 < \sigma > 2\text{kbar}$ $\tau = 0.5 + 0.6\sigma, \quad \sigma > 2\text{kbar}$	"constancy of friction" hypothesis, linear law
Archard (1958)[145] Maurer (1965)[151] Murrell (1965)[22] Hobbs (1970)[152] Denby & Scoble (1984)[153]	$\tau = k . \sigma^m$	theoretical power law for metals[145], demonstrated empirically for rock[22, 151-153]
Jaeger (1971)[149]	$(\tau/C_o) = k . (\sigma/C_o)^m + (\tau_s/C_o)$	dimensionless power law
Lundborg (1968)[154]	$\tau = \tau_o + \mu\sigma/[1 + \mu\sigma/(\tau_i - \tau_o)]$	empirical non-linear law
Ladanyi & Archambault (1970)[155]	$\tau = \dfrac{\sigma(1-\alpha_s)(\dot{\gamma}+\mu) + \alpha_s \eta C_o [(m-1)/n](1 + n\sigma/\eta C_o)^{1/2}}{1-(1-\alpha_s)\dot{\gamma}\mu}$	curvilinear semi-empirical law
Barton & Choubey (1977)[156]	$\tau_{peak} = \sigma \tan\{JRC . \log_{10}[(\sigma_1 - \sigma_3)/\sigma] + \phi_b\}$	empirical non-linear law

Table 3.5.1 Frictional Strength Criteria (see individual references for derivations and definitions of parameters.)

frictional properties of a particular interface. Typical values of μ^* for various minerals and rocks have been collated by Jaeger & Cook[8] (p.59) representing the results of a number of measurements by various workers utilising different forms of testing machine. Further values are given by Ohnaka (1975)[158] and by Barton and Choubey (1977)[156]. The range is from about 0.2 to 0.8. No clear dependence on rock type is apparent, since the variations between the results of different workers on a given rock type tend to be comparable to the differences between assorted lithologies reported by a given worker. Whilst these values for rocks serve as a rough guide for a variety of conditions, the values for a given lithology are subject to influence by a wide variety of factors including normal stress and stiffness, surface conditions, moisture and pore pressure, temperature and sliding rate. Summaries of the relative effects of each of these variables on residual sliding and frictional strength are provided in Paterson[9], together with comprehensive references.

All experiments on friction make a number of measurements of τ in Eqn.3.5.2 for a given pair of sliding surfaces (shear discontinuity or frictional interface) at various values of σ. Amonton's law, that the coefficient of friction is independent of normal force and of the macroscopic area of contact, is obeyed to a rough approximation, but careful measurements show that the coefficient of friction tends to become smaller as the normal stress is increased (Maurer[151]; Raleigh & Paterson (1965)[159]; Byerlee (1967)[160], (1968)[161]; Hoskins *et al* (1968)[162]; Handin (1969)[163]; Abey & Heard (1973)[164]; Edmond & Murrell (1973)[165]; Olsson (1974)[166]; Jaeger & Cook[8] p.60). This approach was used by Bowden & Tabor[142] and by Maurer[151] who plotted $\mu^*=\tau/\sigma$ as a function of σ. Maurer, using a double shear test machine, observed μ^* to decrease from about 1.8 to 0.8 as the contact pressure was increased from 1000 psi (6.9 Mpa) to the compressive strength of the rocks. Byerlee[160,161] commented that this phenomenon of variable friction decreasing with increasing normal stress was not clearly understood, and indeed regarded it as being a phenomenon exclusive to the high confining pressure regime. Handin & Stearns (1964)[167] suggested that the decrease in μ^* for dolomite at high confining pressure occurred because the sliding surfaces became smoother. Raleigh & Paterson[159]

proposed that the decrease in μ^* for peridotite occurred because of increase in plasticity of the minerals with high confining pressure, however Maurer's[151] results serve to show that extremely brittle materials, such as granite, also exhibit this same decrease in μ^* with increasing σ.

The above non-linearity has led to various types of expressions being used for the relationship between τ and σ. Two such expressions discussed below are $\tau=\mu_o\sigma^m$ and $\tau=S_o+\mu_s\sigma$, where μ_o, m, μ_s and S_o are empirical constants. As opposed to Eqn.3.5.2, for a better fit to experimental results, Eqn.3.5.3 suggests the law:

$$\tau = \mu_o.\sigma^m \quad \ldots\ldots\ldots \quad \text{Eqn.3.5.4}$$

Archard[145] has provided theoretical justification for such a power law relationship, where μ_o is a constant and $2/3<m<1$. Jaeger[147] was the first to use the linear law:

$$\tau = S_o + \mu_s.\sigma \quad \ldots\ldots\ldots \quad \text{Eqn.3.5.5}$$

and found good agreement with experiment, particularly at low stresses, for artificially filled discontinuities where cut surfaces with coatings of plaster were used to simulate filled joints. Hoskins *et al* [162] used a double shear rig to study the friction of 12 inch-square (929cm^2) rock surfaces, and found that plotting τ versus σ, for a diverse range of lithologies, gave very good straight line fits. The intercept, S_o, was described as a "cohesion" or "inherent shear strength" of the contact surfaces, and the slope as a coefficient of sliding friction. Tabulated values of S_o and μ_s from a wide range of rock types as tested by Hoskins *et al* are given in Table 3.5.2. This law has the great mathematical advantage of being linear and has the same form as the Coulomb failure criterion for intact rock fracture strength, and as the expression used in soil mechanics. Appropriate modifications to Eqn.3.5.5 to accomodate pore pressure, p, based on the effective stress concept, gives $\tau = S_o + \mu_s.(\sigma-p)$. Whilst Murrell[22] interprets his friction

Rock Type	Surface Roughness (μin.)	μ_s	S_o (MPa)
Granite	180 ± 20	0.64	0.30
Gabbro	Rough	0.66	0.38
Trachyte	300 - 350	0.58	0.45
Trachyte	Rough	0.68	0.41
Wet Trachyte	300 - 350	0.56	0.41
Sandstone	Rough	0.51	0.28
Wet Sandstone	Rough	0.61	0.31
Sandstone on Trachyte	Rough	0.57	0.28
Wombeyan Marble	200	0.75	1.10

Table 3.5.2 Coefficient of sliding friction, μ_s, and inherent cohesion, S_o, for rough rock surfaces tested in a double shear rig (Hoskins *et al* [162]).

results on sandstone in terms of a power law, giving $\tau = 2.1(\sigma)^{0.89}$, Hoskins *et al* [162] point out that, in fact, his results for σ<20,000psi (137.9MPa) may equally well be represented by $\tau = 500+0.70\sigma$(psi). However, the frequently observed rapid decrease in μ^* with increasing σ, as described above, would be the case if τ and σ were connected by either the power law or the linear law of Eqn.3.5.4 and 3.5.5 respectively. In order to give the coefficient of friction a meaning derivable from any given friction law, Olsson[166] defined it as the derivative of the curve representing the sliding criterion. This may be written as:

$$\mu' = d\tau/d\sigma \quad \ldots\ldots\ldots \quad \text{Eqn.3.5.6}$$

Eqn.3.5.6 applied to the linear friction law leads to the same coefficient of friction, μ_s, however, when applied to a sliding criterion with the form of a power law, $\mu'=d\tau/d\sigma=km\sigma^{m-1}$ where k and m are constants, whereas for the same frictional power law the variable coefficient of friction is given by $\mu^* = \tau/\sigma = k\sigma^{m-1}$.

3.5.1 Maximum Friction Plots

From the load versus sliding displacement profiles (section 3.4.2) it is apparent that each of the samples deformed under direct shear, irrespective of lithology, produced a shear load curve with a distinct peak, corresponding to a maximum value required to maintain sliding under constant normal displacement conditions. It is also apparent that this shear load peak does not always correspond to an equivalent peak in the normal load curve (see samples #5, #14 and S1 in particular). Amonton's law was applied to this peak shear condition and a variable coefficient of friction, μ^*, calculated for each test, by dividing the peak shear load value by the corresponding normal load value, measured at the same sliding displacement. The resulting variable coefficient of friction will be referred to as the maximum friction coefficient, $\mu^* = \mu_{max}$. Alternatively, this coefficient can be presented as a friction angle, ϕ_{max}, using the relation $\mu_{max} = \tan.\phi_{max}$. A summary of maximum friction data is given in Table 3.5.1.1.

Direct Shear Specimen I.D.	Peak Shear Load (kN)	Normal Load (kN)	Slip (mm)	μ^*_{max}	ϕ_{max} (^{o})	Constant Contact Area:		Variable Contact Area:	
						τ (MPa)	σ (MPa)	τ (MPa)	σ (MPa)
#3	23.7	47.0	6.0	0.50	27	2.2	4.3	2.3	4.6
#5	44.4	71.6	9.0	0.62	32	4.1	6.5	4.5	7.3
#6	22.6	34.8	8.4	0.65	33	2.1	3.2	2.3	3.5
#8	41.8	60.7	10.0	0.69	35	3.8	5.6	4.3	6.2
#9	34.6	42.4	15.3	0.82	39	3.2	3.9	3.8	4.6
#11	41.1	76.3	14.0	0.54	28	3.8	7.0	4.4	8.2
#12	35.4	51.4	7.6	0.69	35	3.2	4.7	3.5	5.1
#14	39.4	61.2	11.0	0.64	33	3.6	5.6	4.1	6.3
S1	56.0	63.6	10.0	0.88	41	5.1	5.8	5.7	6.5
S2	36.5	58.8	13.0	0.62	32	3.3	5.4	3.9	6.3
S3	29.4	60.6	18.0	0.49	26	2.7	5.5	3.3	6.9
S4	73.8	92.0	11.2	0.80	39	6.7	8.4	7.7	9.6

Table 3.5.1.1 Maximum friction data for direct shear tests under constant normal displacement control.

Following Byerlee[135], peak shear stress and corresponding normal stress (calculated using both constant and slip-dependent variable contact areas) data is presented as maximum friction plots in Fig.3.5.1.1. Byerlee's relationship $\tau = 0.85\sigma$ (see Table 3.5.1) representing the shear stress required to cause sliding under normal stresses up to 200MPa is also shown for the purposes of comparison. This relation was derived as a linear best-fit to intermediate pressure ($\leq$100MPa) maximum friction data. At low normal stresses ($\leq$5MPa) more in keeping with those generated during this direct shear study, Byerlee's maximum friction data, derived from a compilation of published results sourced from the civil engineering field, showed a wide scatter about $\tau = 0.85\sigma$. This large variation was interpreted as being due to the strong dependence of friction on surface roughness at low normal stresses. From Fig.3.5.1.1, however, it is apparent that the direct shear specimen maximum friction data plots consistently below Byerlee's low normal stress relation. This implies that the direct shear specimens were relatively weak in comparison to the average from Byerlee's compilation. Interestingly, the direct shear maximum friction data would be better represented by Byerlee's high normal stress (200MPa<σ<2000MPa) straight line relationship, $\tau=0.5+0.6\sigma$. This could reflect the constant normal displacement shearing mode, and resultant total suppression of dilatancy, under which all the direct shear tests were conducted. Byerlee's low and high normal stress linear friction laws doubtless reflect the different physical mechanisms involved in the sliding process operative within these low and high pressure ranges. Specifically, at low pressure the surfaces are free to move with respect to one another by lifting over asperities, whilst at high pressure this effect is suppressed and sliding is achieved through asperity shear. Perhaps the direct shear data fits the high pressure frictional relationship more closely because the mechanism of asperity shearing is wholly dominant, even although the normal stress magnitude never exceeds 10MPa? This would highlight an important omission with regard to Byerlee's interpretation, which fails to consider the influence of discontinuity normal stiffness on the initial, maximum and residual friction. Obviously the direct shear data set is at present too small to comment further. Fig.3.5.1.1 shows no evidence of clustering of data into specific lithological fields, in accord with the observation of Byerlee that, "rock type has little or no effect on friction."

Peak Shear Stress (MPa)

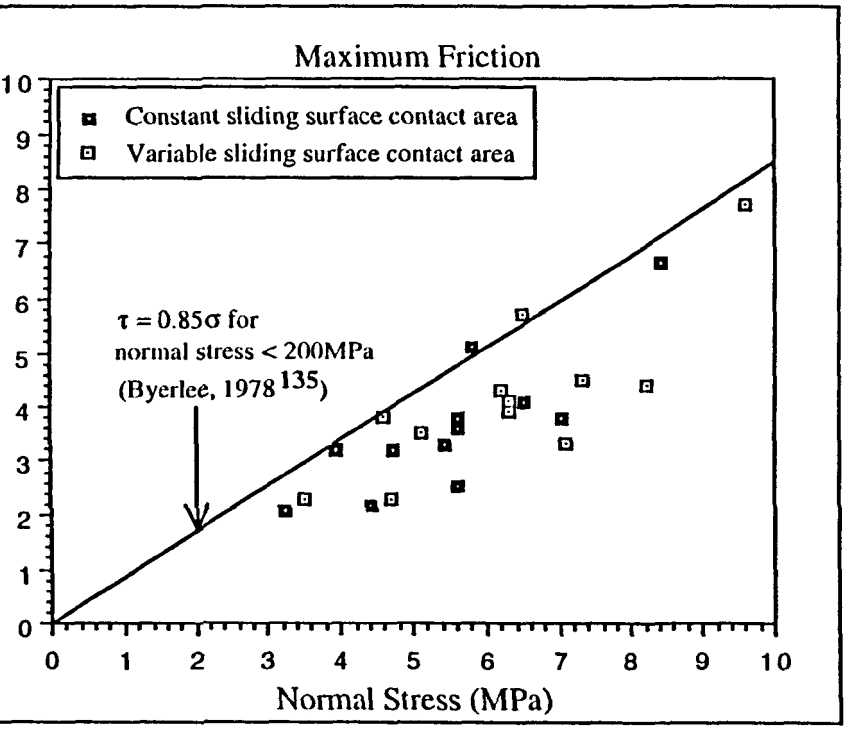

Fig.3.5.1.1 Maximum friction plot for direct shear data.

3.5.2 Variable Friction Plots

To assess the validity of Amonton's law, plots of variable friction versus normal stress have been constructed for the four lithologies tested in direct shear. These μ^* versus σ plots are presented in Fig.3.5.2.1. In addition to rock type, the variable friction data has been further subdivided into pre-peak and post-peak data sets, where "peak" refers to the maximum shear load magnitude on the load-displacement profiles. It should be appreciated that the shear load maximum giving rise to the "maximum friction" data discussed in section 3.5.1 need not necessarily correspond to the greatest magnitude value of variable friction coefficient. From Fig.3.5.2.1, for the red sandstone direct shear specimens, it is apparent that the pre-peak variable friction shows a rapid decrease from initially high values at low normal stress, to values oscillating around an average value of about 0.5. The wide range of magnitudes exhibited by the pre-peak data (1.7 to 0.2) is in direct contrast to the post-peak data, which lies between 0.6 and 0.4 inclusive, throughout the entire range of normal stress. The mudrocks provide variable friction pre- and post-peak values which decrease from 0.9 to 0.3 and from 1.5 to 0.5 respectively. The carbonaceous siltstones provide variable friction pre- and post-peak values which decrease from 1.1 to 0.4 and from 3.1 to 0.3 respectively. The heterolithics provide variable friction pre- peak values which decrease from 4.6 to 0.5 and post-peak values which lie between 0.7 and 0.4 inclusively. From these results it is evident that only the red sandstone and the heterolithics post-peak data shows an "unvarying" variable friction coefficient with increasing normal stress, constant enough to suggest that Amonton's law is applicable. All four rock types tested show either pre- or post-peak μ^* well in excess of unity at low normal stress magnitudes. From the variable friction versus normal stress plots of Fig.3.5.2.1, it is concluded that Amonton's law is at best only very weakly adhered to, and should probably be considered invalid for the rock types tested in direct shear under constant normal displacement conditions. This observed non-linearity depicted in Fig.3.5.2.1 indicates that an alternative relationship between τ and σ, other than that described by Amonton's law (Eqn.3.5.2) should be sought.

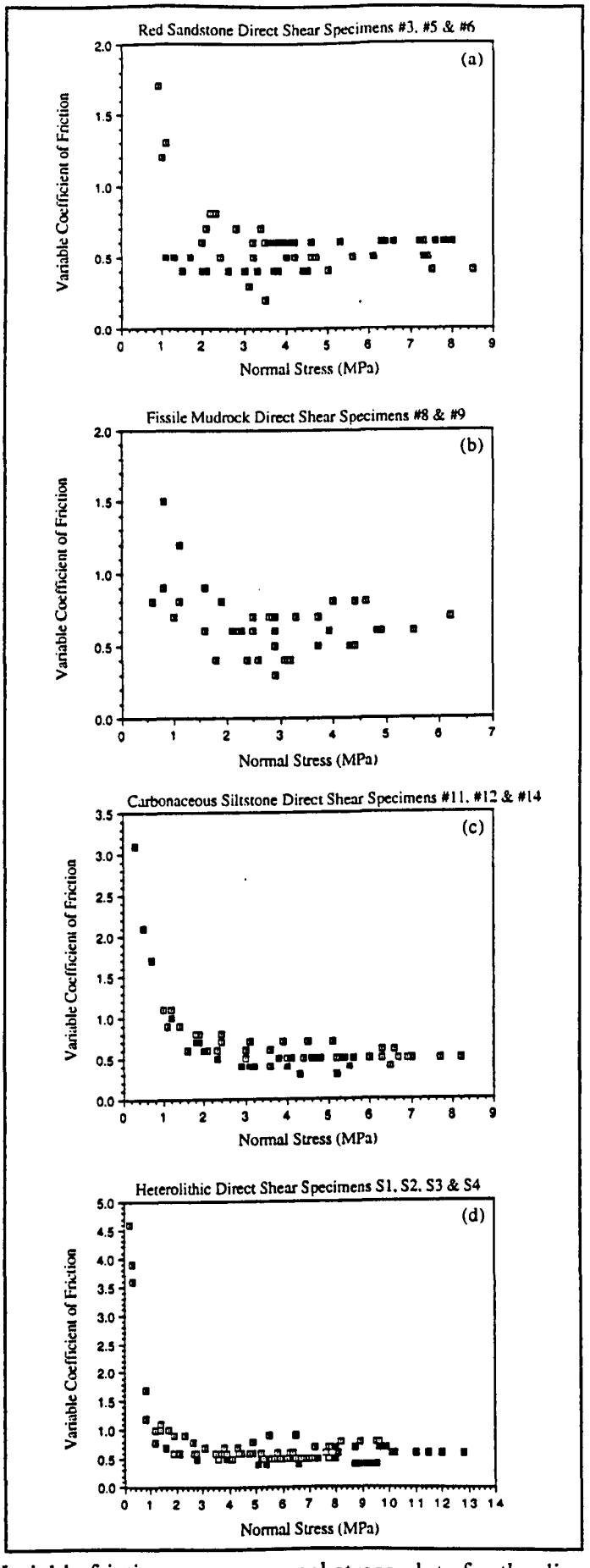

Fig.3.5.2.1 Variable friction versus normal stress plots for the direct shear test data (open squares: pre-peak data; closed squares: post-peak data).

3.5.3 Shear Stress - Normal Stress Plots

For further analysis of the direct shear data, division into pre-peak (including maximum friction) and post-peak (for additional frictional sliding following peak shear stress) data sets has been maintained, and shear stress versus normal stress plots constructed for both constant and variable sliding surface contact areas. Graphical representations for the red sandstones, fissile mudrocks, carbonaceous siltstones and heterolithics are given in Fig.3.5.3.1, Fig.3.5.3.2, Fig.3.5.3.3 and Fig.3.5.3.4 respectively.

For the red sandstones, pre-peak data appears quite "noisy", although approximately linear correlations are just discernible. Deviations are associated with pre-peak stress drops in either normal or shear stress, probably resulting from asperity shear prior to the formation of a through-going, pervasive slip surface. Post-peak data shows stronger linear relationships for all three red sandstone specimens, although sample #6 is strongly influenced by the choice of contact area. For the assumption of a constant, slip-independent, sliding surface contact area, equal to the cross-sectional area of the cylindrical specimen, all post-peak (σ, τ) data points group around the maximum friction value, μ_{max}, so that no slope can be defined to the data spread from which to evaluate μ_s (see Eqn.3.5.5). However, by using a variable, slip-dependent, sliding surface contact area (area decreasing with increasing slip) the post-peak data inherits a positive gradient, with associated moderate linear regression coefficient. An immediate difference becomes apparent between the red sandstone and fissile mudrock data when plotted in σ versus τ stress space, in that for the latter rock type, both specimens show pre-peak data with a strongly concave upwards trend. For sample #8, this trend is best described by an exponential relationship of the form, y = A.10^Bx (or logy = logA + Bx). Although sample #9 pre-peak data also exhibits this exponential relationship overall, it is complicated by a linear deviation, again probably associated with pre-peak asperity shear. Exponential regression for sample #8 gives $\tau = 0.60*10^{0.14\sigma}$, with r^2 = 0.994, for the assumption of variable contact area. Post-peak data for the fissile mudrocks is strongly linear with high regression coefficients. The carbonaceous siltstone specimens #11, #12 and #14 all show broadly exponentially correlated pre-peak data, and linearly correlated post-peak data. Sample #11 pre-peak data conforms to $\tau = 0.69*10^{0.10\sigma}$, with r^2 =

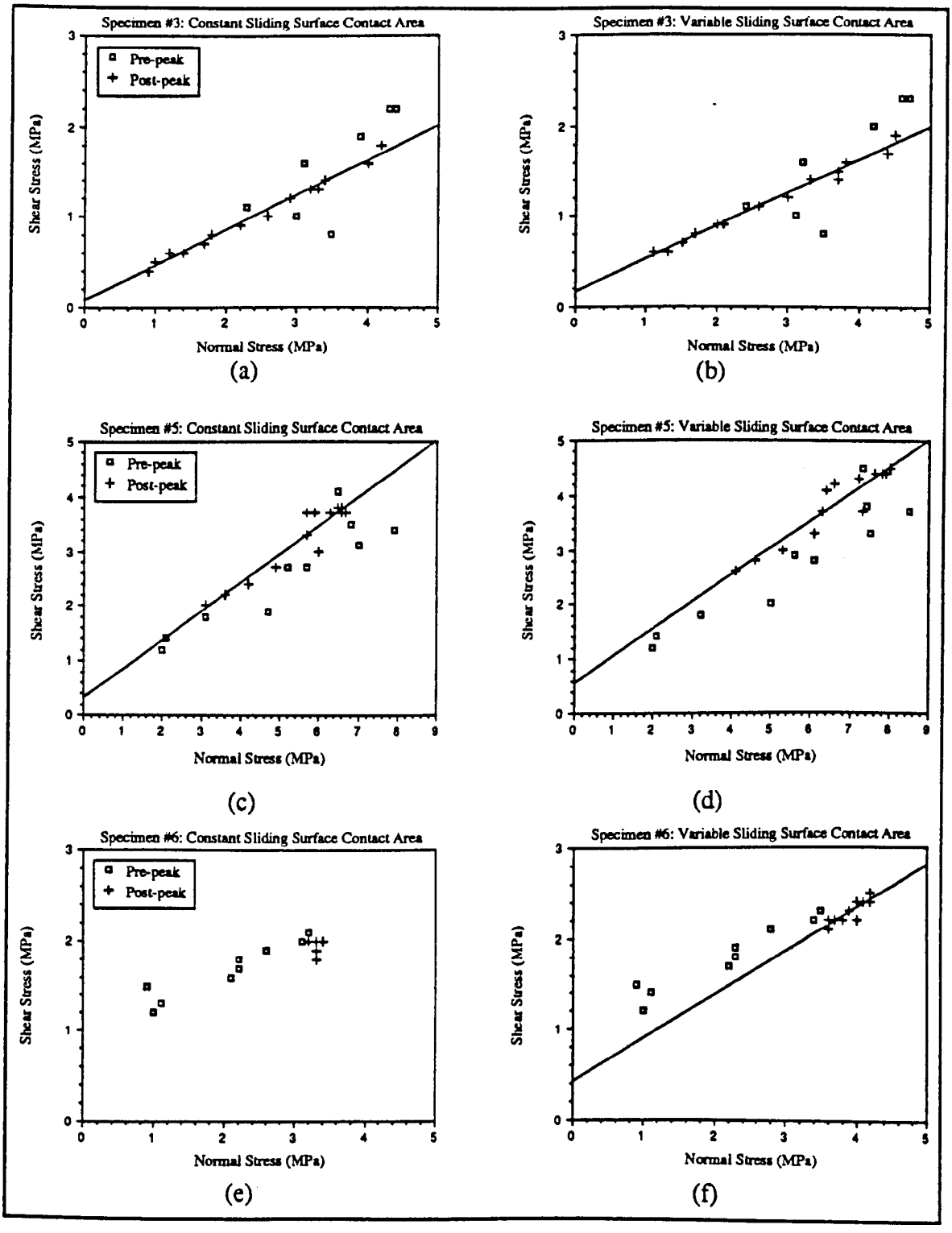

Fig.3.5.3.1 Frictional strength envelopes for direct shear specimens #3, #5 & #6

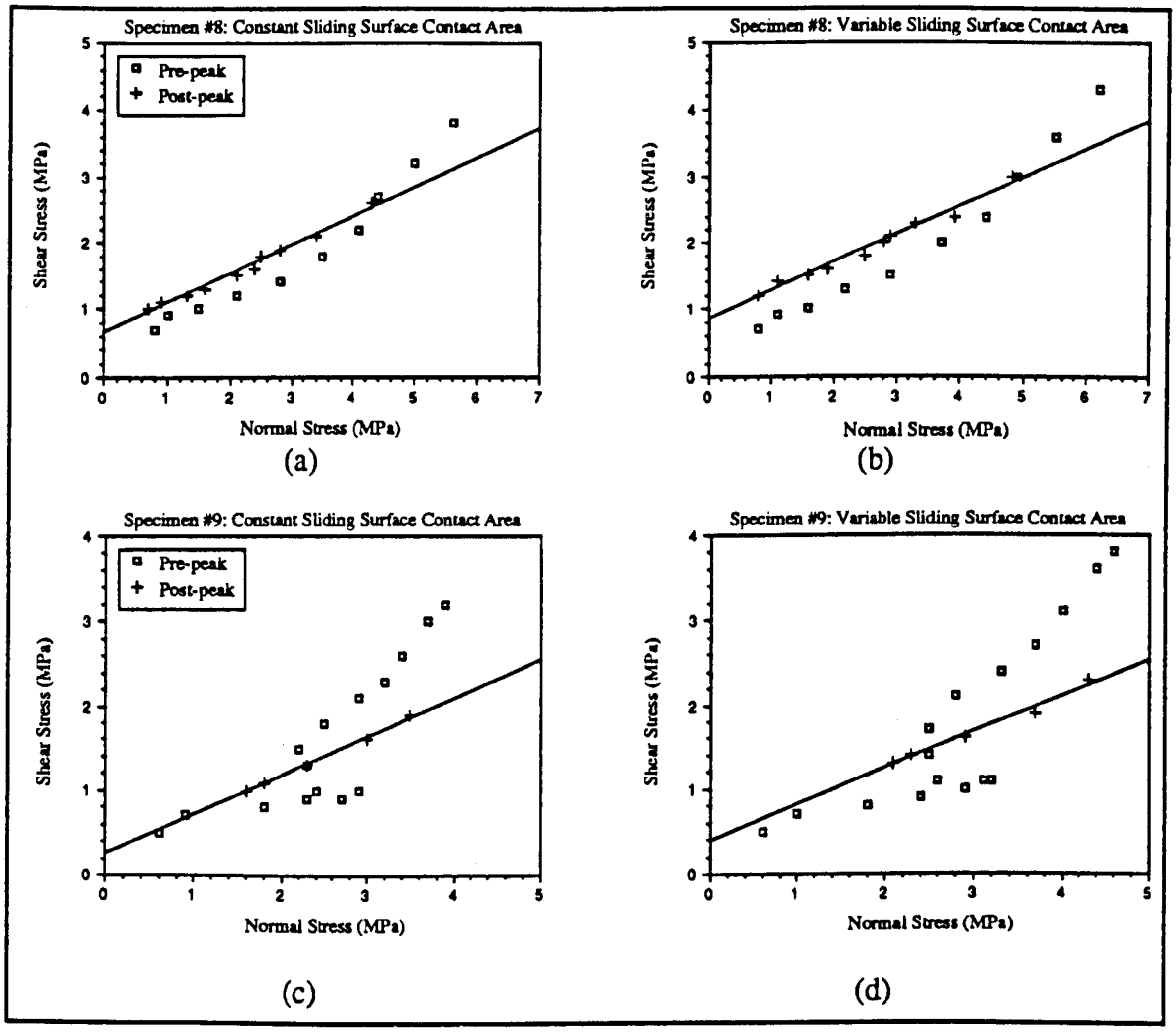

Fig.3.5.3.2 Frictional strength envelopes for direct shear specimens #8 & #9

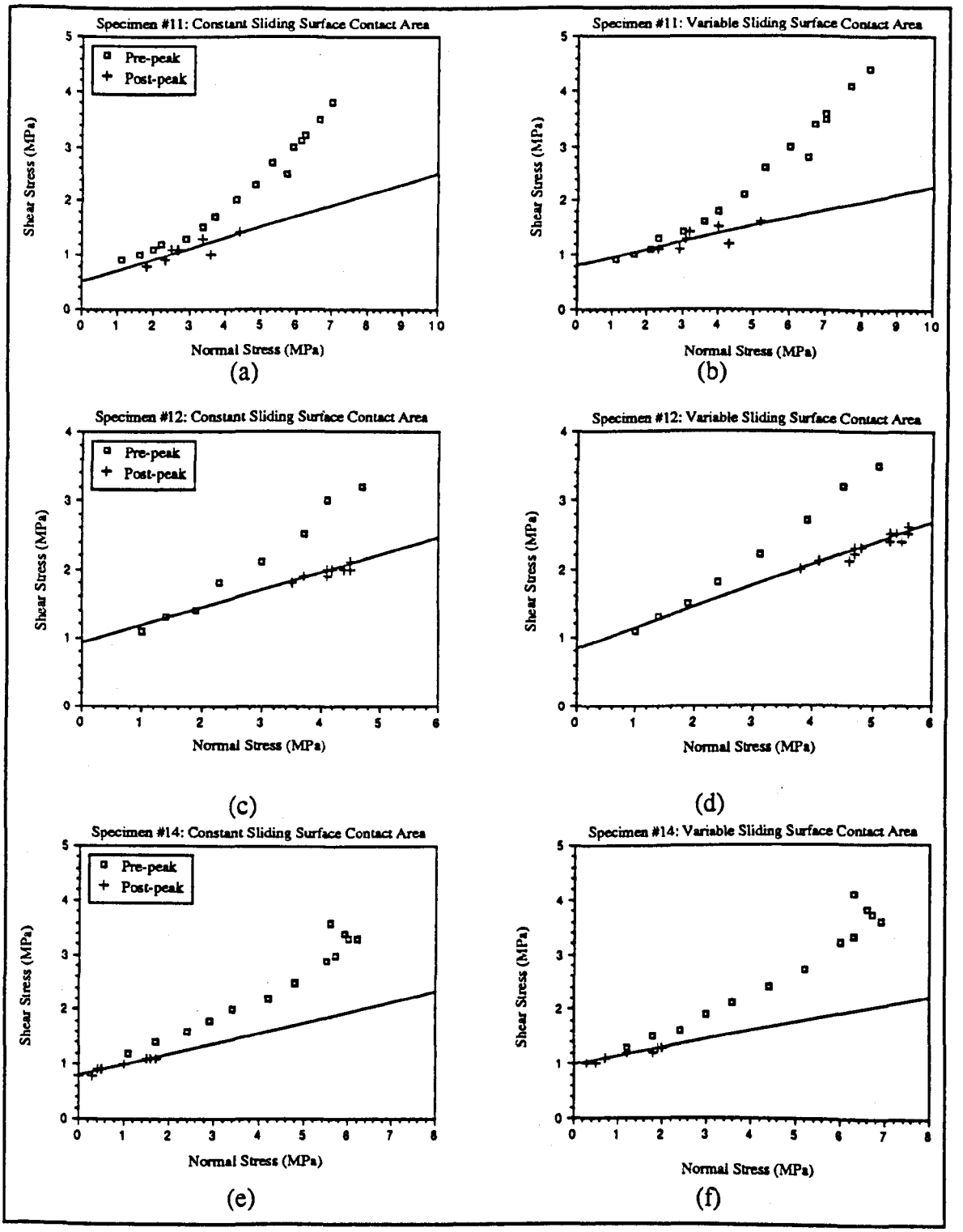

Fig.3.5.3.3 Frictional strength envelopes for direct shear specimens #11, #12 & #14

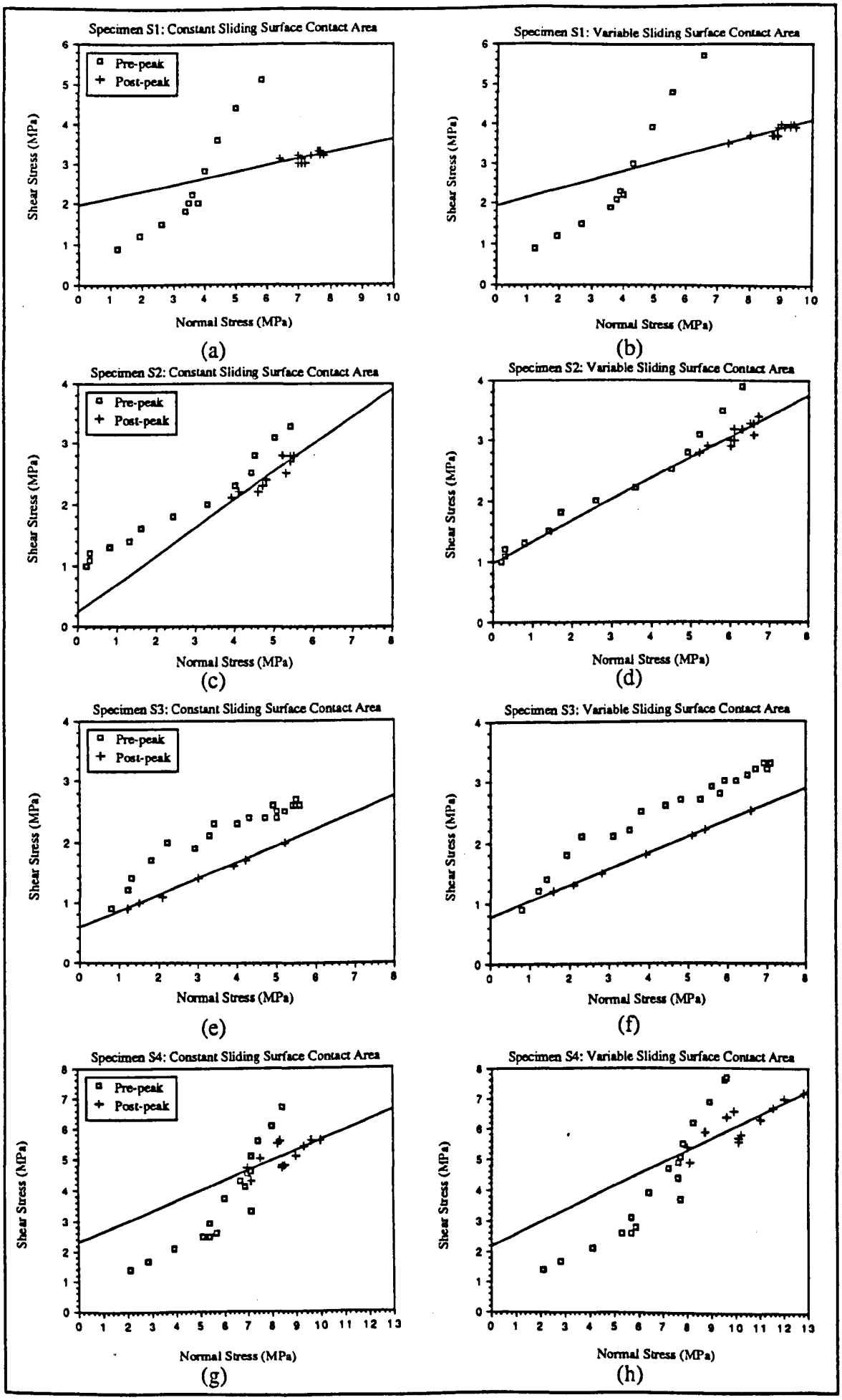

Fig.3.5.3.4 Frictional strength envelopes for direct shear specimens S1, S2, S3 & S4

0.995, for the assumption of variable contact area. The heterolithic specimens, with the exception of sample S3, all show broadly exponentially correlated pre-peak data, and linearly correlated post-peak data. Sample S1 pre-peak data has the form $\tau = 0.56*10^{0.16\sigma}$, with $r^2 = 0.975$, for the assumption of variable contact area. However, sample S3 shows a strong concave downwards trend between increasing σ and τ inconsistent with an exponential relationship. Instead, it is best represented by a logarithmic relationship of the form, $y = A + B\log x$, with $\tau = 1.06 + 2.45*\log\sigma$, $r^2 = 0.978$, for the assumption of variable contact area. This pre-peak data logarithmic relationship might reflect relative rotation between upper and lower specimen halves. Post-peak data for S1 is, however, still linear, with a regression coefficient of 1.00. In fact, independent of rock type, all specimens tested in direct shear under constant normal displacement conditions, showed linear relationships between σ and τ for frictional sliding subsequent to the attainment of maximum friction conditions.

Tabulated values of frictional sliding constants μ_s (slopes) and S_o (intercepts) are given in Table 3.5.3.1. The slopes and intercepts were calculated for "best fit" straight lines, determined using linear regression analysis based on the principle of least squares, as outlined in Barford (1987)[168] together with standard errors for each slope and intercept, $S_n(\mu_s)$ and $S_n(S_o)$ respectively. From Table 3.5.3.1 it is apparent that the choice of either a constant or a variable sliding surface contact area has a marked effect on the magnitude of the frictional sliding constants, μ_s and S_o. With regard to friction angles, ϕ_s (where $\phi_s = \tan^{-1}\mu_s$) this is evident in up to 7° difference between calculated constants. However, this difference resulting from whether a constant or a variable contact area is chosen, is small compared with the difference between maximum friction angles, ϕ_{max}, (see Table 3.5.1.1) and sliding friction angles, ϕ_s, which can be in excess of 30° (specimen S1). Inherent shear strength, S_o, of the post-peak sliding surfaces, was also found to be moderately dependent on the choice of a constant or a variable contact area. Magnitudes ranged from a few tenths of a MPa (specimen #3) to over 2MPa (specimen S4). Finally, in accord with the observation made for maximum friction, no obvious correlation was evident between rock type and the magnitude of either of the post-peak frictional sliding constants, μ_s or S_o.

I.D.	N	Constant Sliding Surface Contact Area:						Variable Sliding Surface Contact Area:					
		μ_s	$S_n(\mu_s)$	ϕ_s	S_o	$S_n(S_o)$	r	μ_s	$S_n(\mu_s)$	ϕ_s	S_o	$S_n(S_o)$	r
#3	14	0.39	0.01	21	0.07	0.04	0.99	0.36	0.01	20	0.16	0.04	0.99
#5	13	0.53	0.05	28	0.30	0.29	0.95	0.50	0.05	27	0.54	0.36	0.94
#6	12	≈0.6	-----	33	-----	-----	-----	0.48	0.11	26	0.42	0.43	0.82
#8	10	0.44	0.02	24	0.64	0.05	0.99	0.43	0.02	23	0.83	0.06	0.99
#9	5	0.46	0.02	25	0.26	0.04	1.00	0.43	0.03	23	0.38	0.11	0.99
#11	7	0.20	0.06	11	0.50	0.18	0.83	0.15	0.06	9	0.79	0.22	0.74
#12	12	0.25	0.04	14	0.93	0.17	0.90	0.30	0.03	17	0.82	0.17	0.94
#14	9	0.19	0.01	11	0.80	0.01	0.98	0.15	0.01	9	0.98	0.02	0.96
S1	13	0.16	0.06	9	1.96	0.46	0.62	0.21	0.04	12	1.93	0.37	0.84
S2	12	0.46	0.06	25	0.24	0.30	0.92	0.35	0.06	19	0.95	0.39	0.86
S3	7	0.27	0.01	15	0.57	0.02	1.00	0.26	0.00	15	0.76	0.01	1.00
S4	12	0.33	0.11	18	2.29	0.90	0.70	0.39	0.08	21	2.13	0.80	0.85

Table 3.5.3.1 Frictional sliding constants for direct shear data.

N: Number of data points

μ_s: Coefficient of sliding friction (slope)

$S_n(\mu_s)$: Standard error of slope

S_o: Inherent cohesion of contact surface (intercept)

$S_n(S_o)$: Standard error of intercept

r: Coefficient of correlation

3.6 DISCUSSION

From the above considerations of shear stress versus normal stress relations and frictional strength criteria, with respect to slip in direct shear under constant normal displacement conditions, it is evident that the frictional sliding mechanism can be envisaged as a two-stage process. Initially, for sliding displacements up to and including that associated with peak shear stress (maximum friction) conditions, such pre-peak data shows exponential increase in τ with increasing σ for the majority of samples tested. Exceptions include the red sandstone specimens which show poorly correlated linear σ versus τ relationships, indicative perhaps of an incipient lithological dependency. Heterolithic specimen S3 exhibits a logarithmic relationship between pre-peak (τ, σ) data, which may reflect relative rotation between the upper and lower sample halves. Pre-peak data is further complicated by linear deviations from the gross σ versus τ relationship, associated with pre-peak stress drops in the shear and normal stress versus sliding displacement profiles, resulting from localised asperity shear. Fissile mudrock specimen #9 illustrates this phenomenon particularly clearly, where a stress drop primarily in the normal stress versus sliding displacement profile has resulted in a prominent linear deviation from the overall exponentially correlated pre-peak data. In direct contrast to the pre-peak data discussed above, post-peak (τ, σ) points define robust straight line relationships for all twelve specimens tested in the constant normal displacement shearing mode. In physical terms, the maximum friction point is thus interpreted as representing peak shear strength of the sliding discontinuity, immediately prior to pervasive breaching of the interlocking asperity system (usually associated with a significant, and frequently audible dynamic stress drop as illustrated by specimens #5, #8, #9, #11, #12, #14, S1, S2, S3 & S4) followed by frictional sliding on the newly created and pervasive shear plane. Post-mortem examination reveals this plane to be composed of frictionally comminuted shear debris (analogous to natural fault gouge) which frequently shows steps and slip-parallel striae (analogous to slickensides and related features as observed on natural fault surfaces). Thus true "residual" strength when shearing under constant normal displacement conditions is perhaps best described by the constants μ_s and S_o as defined in Eqn.3.5.5.

Corroboration of the above experimental observations relating to the development of shear strength for a frictional discontinuity undergoing constant normal displacement shearing, can be found in Gerrard (1986)[169]. By the application of appropriate theoretical constraints pertaining to "shear failure" of rock discontinuities, Gerrard was able to assess various empirical relations and to develop formulations for strength and dilatancy. In his analysis, the rock discontinuity was imagined as consisting of an array of contacts, as a means of establishing a basis for mechanical properties determination, its shear strength being inferred to consist of both "fracture" and "friction" components. At these contacts deformation was considered to occur by a combination of elastic, crushing, sliding and ploughing processes. In general, during shear failure of a rock discontinuity, all of these processes were considered to be operative, with sliding and ploughing being dominant. Due to the range of contact orientations, Gerrard proposed that their shear behaviour ranged from sliding to heavy ploughing, the shear strength of each contact thus being envisaged as consisting of a component required for "fracturing" and a component required for "sliding" (usually inclined to the plane of the discontinuity). Through summation, these shear strength components for an individual contact would be reflected in the corresponding components for the rock discontinuity as a whole, as expressed in Gerrard's following general failure criterion:

$$F = 0 = (\tau - a - \sigma\mu_i)/\sigma_r \quad \text{.....} \quad \text{Eqn.3.6.1}$$

- F: failure criterion
- τ, σ: shear and normal stresses
- σ_r: reference stress
- a: component of shear strength due to fracturing
- μ_i: effective coefficient of friction for inclined sliding

Jaeger & Cook[8] showed that the effective coefficient of friction for inclined sliding is given by:

$$\mu_i = (\mu + g)/(1 - \mu g) \quad \text{.....} \quad \text{Eqn.3.6.2}$$

$$\mu_i = \tan\phi_i = \tan(\phi + \psi) \quad \text{.....} \quad \text{Eqn.3.6.3}$$

μ: effective coefficient of friction for sliding without dilation = $\tan\phi$

g: gradient of the dilation at failure = $\tan\psi$

Gerrard proposed that the factors affecting the shear strength of a rock discontinuity can be identified by considering the terms involved in Eqn.3.6.1, Eqn.3.6.2 and Eqn.3.6.3. The component of shear strength due to fracturing alone, a, will depend on the hardness and toughness of the asperities and on their average height and radius. It will also depend on the normal stress and will tend to zero as $\sigma \rightarrow 0$. The effective coefficient of friction for sliding without dilation, μ, will vary between two extreme conditions. One of these will be the case of minimal damage of the asperities, this being applicable to the case when the normal stress, σ, is relatively low and the asperities have enhanced strength due to the combined effects of favourable surface topography and hardness/toughness. The appropriate coefficient of friction for this condition will be that for sliding of smooth surfaces of the rock material, μ_{smooth}. The other extreme will occur when extensive fracturing of the asperities is induced during shear failure of the rock discontinuity. This condition is associated with relatively high normal stress and/or relatively weak asperities due to unfavourable surface topography and hardness/toughness. It appears that two coefficients of friction are relevant. The first, μ_{peak}, relates to the process of actually creating the fractures through the asperities, while the second, $\mu_{residual}$, relates to the sliding over the resultant freshly fractured surfaces and debris. For this condition of extensive fracturing, μ_{peak} will be associated with peak strength whilst $\mu_{residual}$ will be associated with the residual strength. Gerrard's analysis assumes that, for a given rock discontinuity, μ_{smooth}, μ_{peak}, and $\mu_{residual}$ can have different values. Thus there appears to be a direct analogy between Gerrard's peak and residual coefficients, μ_{peak} and $\mu_{residual}$ for sliding without dilatancy, and the empirically derived frictional coefficients, μ_{max} and μ_s respectively, tabulated from this direct shear experimental study.

4. COUPLED PERMEABILITY-MICROSEISMICS MEASUREMENT DURING TRIAXIAL COMPRESSION TESTING: EQUIPMENT DEVELOPMENT

4.1 INTRODUCTION

In a review of the various laboratory apparatus used for shear testing of rock discontinuities (see summary Table 4.1.1) the important point is made that each possesses distinct experimental advantages, as well as certain limitations, necessitating careful matching of experimental requirements with equipment strengths. Whilst the direct shear machine allows testing of relatively large shear surface areas under known boundary conditions, ideal for fundamental frictional strength studies, to investigate the effects of faulting on fluid flow under realistic reservoir stress magnitudes, the discontinuity triaxial compression test is better suited, due to technical difficulties involved in confining direct shear specimens, and in adequately sealing the sliding interface for fluid flow studies. In contrast, the triaxial method offers a facility for breaking cylindrical rock specimens in shear under differential axial and radial stresses, whilst simultaneously monitoring (albeit discontinuously) transient core plug permeability allied with changing stress states ranging from hydrostatic to those operative during post-peak frictional sliding conditions. The limitations of the triaxial test system are that: only axial stress and confining pressure (σ_1 and σ_3) as opposed to shear and normal stresses are directly controllable; geometric constraints make only very small sliding displacements (of the order of a couple of mm's maximum) achievable; induced fault orientation is oblique to the specimen long axis and thus oblique to the direction of fluid flow associated with permeability measurement.

The system used to investigate laboratory induced faulting in core specimens essentially consists of three individual components, stress application, permeability measurement and microseismic monitoring. This system, and the interconnection of its individual components, is illustrated schematically in Fig.4.1.1. Each core plug is subjected to realistic *in situ* reservoir stress magnitudes, and ultimately to differential stresses resulting in shear failure, using a 100T stiff servo-hydraulic compression rig and "Hoek/Franklin-type" 10 000psi-rated confining pressure cell combination (the triaxial

CAPABILITIES:	LABORATORY SHEAR TESTING APPARATUS:					
	TRIAXIAL COMPRESSION	DIRECT SHEAR	BIAXIAL SHEAR	DOUBLE SHEAR:		RING SHEAR
				CONFINED	UNCONFINED	
Can control applied normal stress		×		×	×	
Can accept core plugs	×	×		×		
Can test large sliding surfaces		×	×		×	
Can test confined specimens	×			×		
Can apply large shear displacements		×				×
Can accomodate k measurement	×	×				×
Can test over constant contact area		×	×		×	×

Table 4.1.1 A qualitative comparison of the capabilities of laboratory shear testing apparatus.

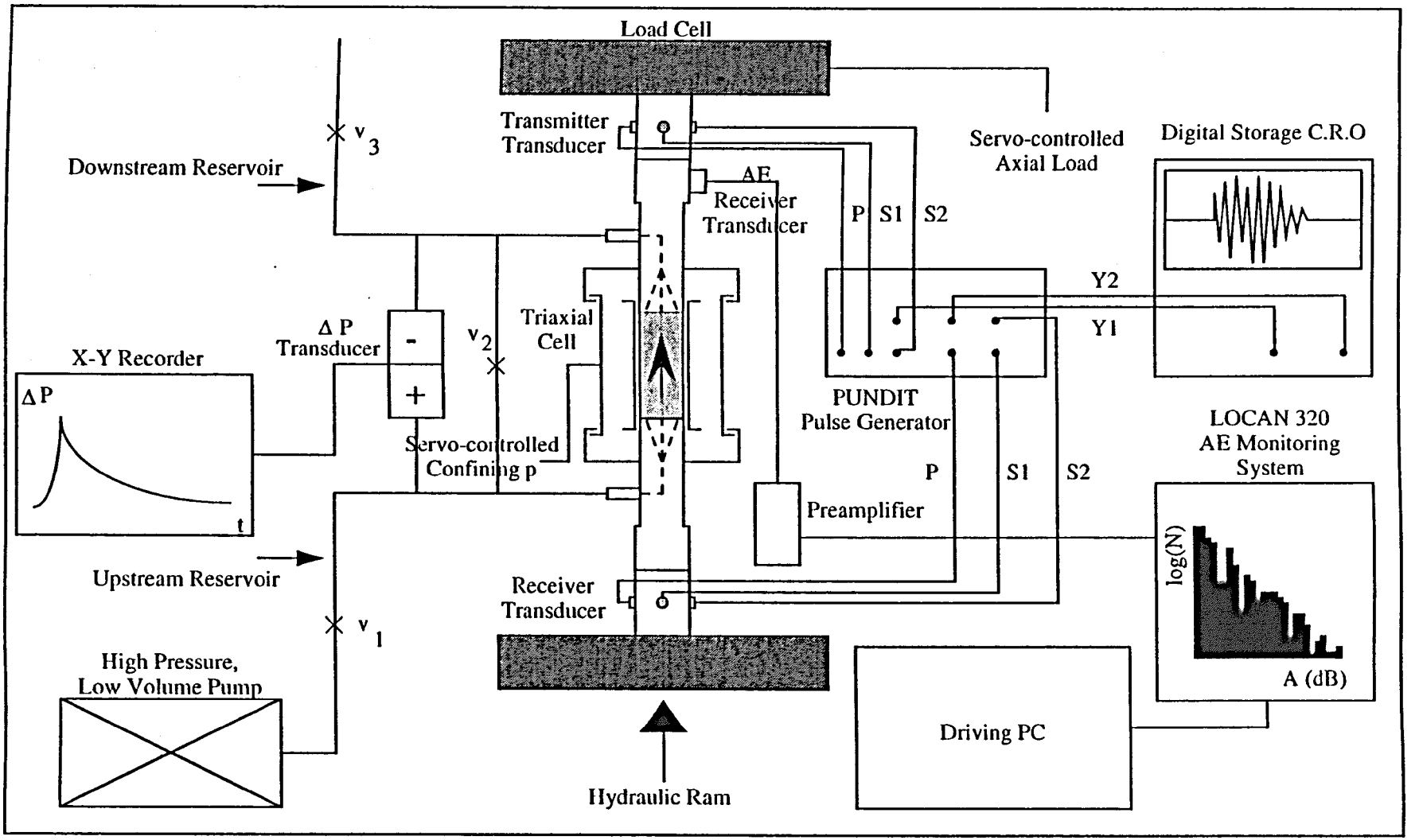

Fig.4.1.1 Schematic representation of coupled permeability - microseismics experimental testing facility, peripheral to the triaxial compression configuration.

compression setup). This system forms the "backbone" of the rock mechanics research facility. Envisaging the "in situ" rockmass as an anisotropic and heterogeneous assemblage of intact/microcracked rock elements separated by planar discontinuities (joints, faults and bedding planes) the triaxial setup enables the deformability, strength and fluid flow characteristics of core plugs (representing intact blocks) to be characterised, complementing discontinuity deformability and strength parameters as measured using the direct shear rig. By such means, important constitutive stress-strain relations and permeability data is generated which can be incorporated directly into numerical reservoir simulation. Whilst fault sealing is currently assessed using the triaxial compression method to induce shear fracturing, it is however hoped that further equipment development will allow the permeability/transmissibility of frictional interfaces tested under direct shear conditions to be achieved.

Linked to the triaxial compression system is a coupled permeability-microseismic facility which allows measured changes in pemeability resulting from controlled variation in the applied triaxial stress field, to be related to microstructural deformation processes occurring within the core specimen (including elastic pore closure, inelastic grain-boundary sliding, axial microcracking etc). The permeameter system basically comprises a high pressure low volume pump, differential pressure transducer, x-y-t plotter assembly, enabling either steady-state or transient pulse-decay absolute liquid permeability measurements to be conducted using a variety of pore fluids including refined mineral oils, distilled water, brines and artificial seawaters of varying composition. The microseismics system incorporates both passive (acoustic emission, AE) monitoring and active (artificial compressional- and orthogonally polarised shear-wave) techniques. In Fig.4.1.1 the active transmitting and receiving transducers are shown mounted respectively above and below the rock specimen loading platens, whilst the AE transducer is shown mounted on the end of a waveguide which pierces the body of the confining pressure cell. For this present study only passive AE monitoring was conducted to assess microstructural evolution. Both the permeability and microseismic systems are mounted on separate trolleys for manoeuvrability, so that they can be positioned by the compression rig when required, as shown in Fig.4.1.2.

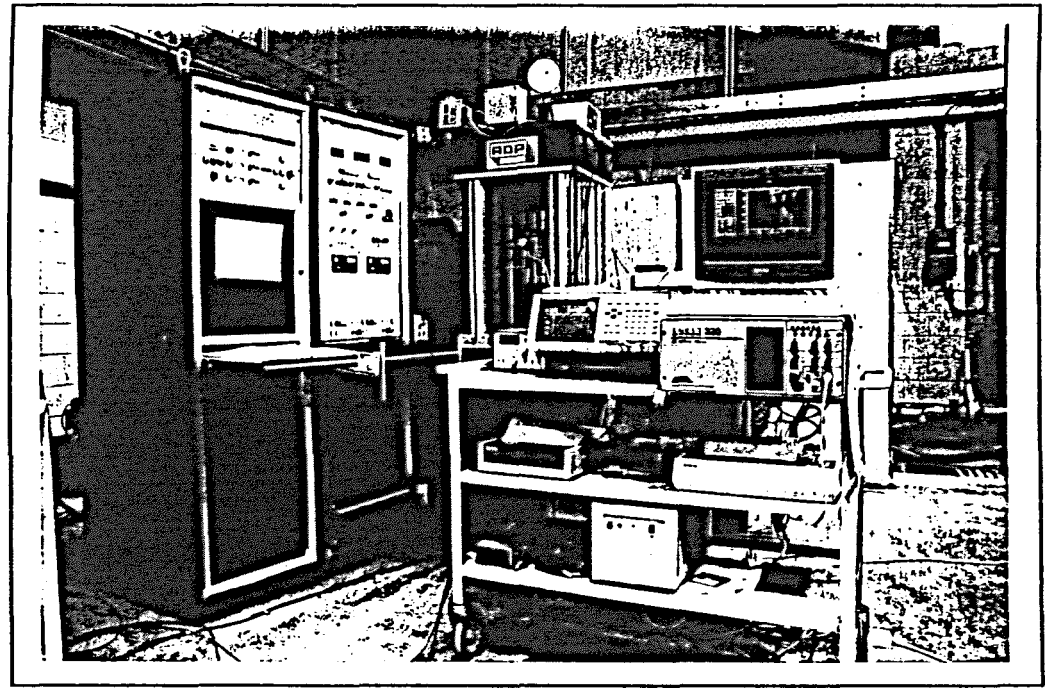

Fig.4.1.2 Overview of the triaxial compression system showing the microseismics trolley positioned in front of the stiff testing rig (the permeability trolley is obscured to the rear). Note the system control unit on the L.H.S., and the Hoek-cell with waveguide sitting within the compression frame.

In the following chapter, details of the triaxial compression system, and of the coupled permeability-microseismics facility are outlined. Information on the stiff compression rig was obtained primarily from the RDP-Howden Customer Instruction and Maintenance Manual (1984)[170]. Specifics relating to the pulse-decay permeability technique were found from McMeekin (1991)[171] and Smart *et al* (1992)[172]. Acoustic emission system description and operating procedures were sourced from the LOCAN-320 User's Manual (1988)[173]. Also, as a useful additional reference dealing with general instrumentation and control theory, Haslam *et al* (1991)[174] proved invaluable.

4.2 STRESS APPLICATION

The simplest and most commonly used procedure for achieving a triaxial state of stress in a laboratory test is to superimpose a hydrostatic pressure and a uniaxial stress. Such a test is usually referred to simply as a "triaxial test" following the nomenclature of soil mechanics (of course the test is only a special case of triaxial stress in which the intermediate principal stress is always equal to one or other of the extreme principal stresses, but the term is widely used without qualification to refer to these conditions). Since, in these tests, cylindrical specimens are subjected to simple compression or extension in the presence of a superposed hydrostatic pressure, the state of stress in the specimen ideally consists of two equal principal stresses normal to the compression or extension axis and a third principal stress parallel to it. Adopting the convention common in geologic and rock mechanics literature that compressive stress is positive, and designating the greatest, intermediate and least principal stresses σ_1, σ_2 and σ_3 respectively, the applied stress in a triaxial compression test is as shown in Fig.4.2.1. The two equal stresses have the same magnitude as the superposed hydrostatic pressure, whilst the third principal stress departs from it. The superposed hydrostatic pressure is called the confining pressure since it is the pressure in the medium surrounding the specimen (note that this is not the same as the mean/nondeviatoric stress in the specimen, which is equal to $1/3(\sigma_1 + 2\sigma_3)$ in the triaxial compression test). The amount by which the axial stress departs from the confining pressure is called the differential stress and is commonly designated by $\sigma_1 - \sigma_3$.

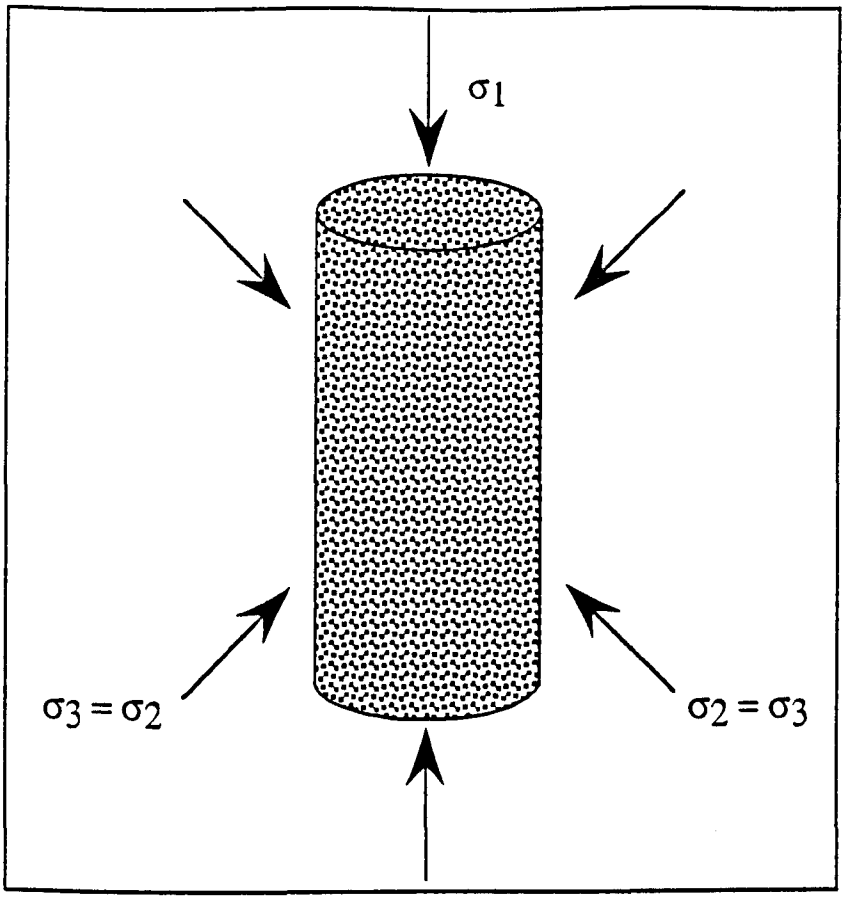

Fig.4.2.1. Applied stress convention in the triaxial compression test.

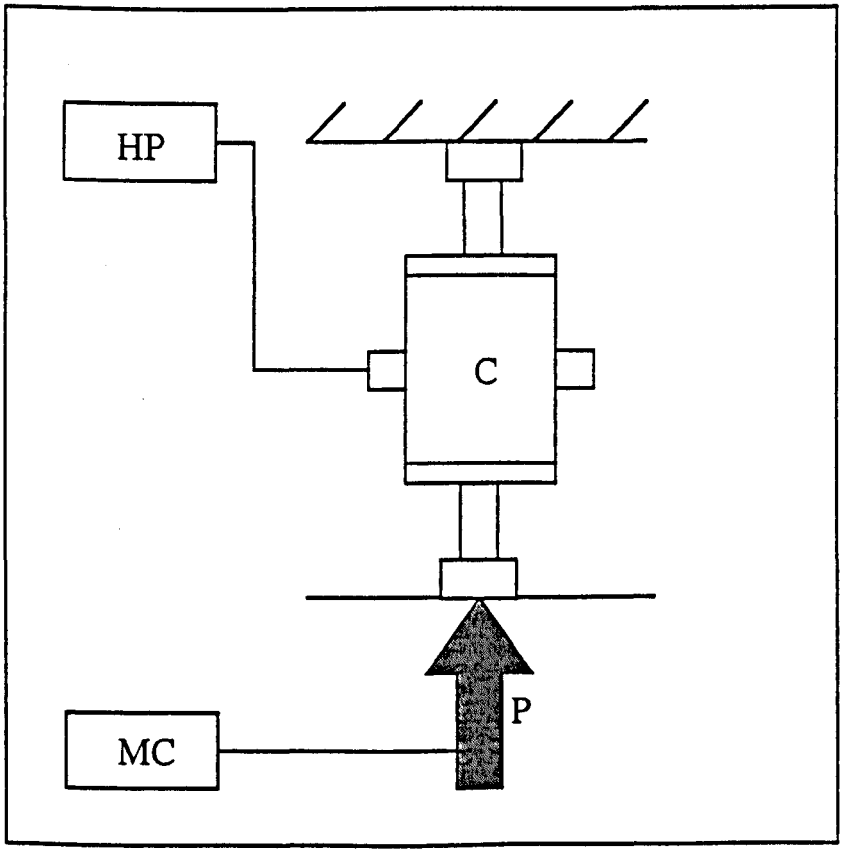

Fig.4.2.2. Block diagram of triaxial test arrangement showing:- P: compression rig; MC: control unit; C: triaxial cell; HP: equipment for generating and controlling confining pressure. (Vogler & Kovari[175])

For the application of nonhydrostatic triaxial stress states, the ability to apply an axial stress to the specimen independent of the radial confining pressure is fundamental. In such conventional triaxial testing of core plugs, a uniform radial stress is usually applied hydraulically to the curved surface of the rock cylinder, whilst simultaneously the prepared flat and parallel specimen ends are loaded axially through spherical seats and platens. In terms of equipment used, radial pressurisation or confinement is usually achieved through a pressure vessel in which hydraulic fluid at pressure, p, acts on a synthetic rubber membrane sheathing the sample. Axial load is generated parallel to the specimen long axis via a stiff, servo-hydraulic compression machine. In this manner, axial loading over the specimen cross-sectional area results in an axial stress, σ_a, wholly independent of p. Two admissible stress field conditions are thus within the limitations of conventional triaxial testing, resulting from independent control of σ_a and p:

(i) triaxial compression, where $\sigma_a = \sigma_1 > \sigma_2 = \sigma_3 = p$

(ii) triaxial extension, in which $\sigma_1 = \sigma_2 = p > \sigma_3 = \sigma_a$

Thus apparatus for achieving triaxial stress states on cylindrical rock specimens, essentially consists of three components as indicated schematically in Fig.4.2.2: a loading device for applying, controlling and measuring axial load, a triaxial cell for applying confining pressure to the curved specimen surface, and equipment for generating and measuring the confining pressure (Vogler & Kovari, 1977[175]).

Before the peak of the load-deformation curve is reached, work must always be done on the combined specimen-machine system in bringing about an increment of deformation in the specimen. The system is therefore, in this case, inherently stable mechanically. However, beyond the peak, because potential energy is released from the machine as the load decreases, it is possible that the work needed for further deformation of the specimen can be fully provided from within the specimen-machine system, so that the deformation process can continue spontaneously and uncontrollably, preventing the load-bearing capacity of the specimen from being readily assessed as a function of the deformation, and leading rapidly to destruction of the specimen. This situation is normal with the

brittle failure of a rock specimen in a conventional "soft" testing machine, especially a machine with hydraulic loading. This problem is comprehensively discussed in rock mechanics textbooks and will not be further reviewed here (for a more detailed discussion see: Paterson, 1978[9], p.138-141; Jaeger and Cook, 1979[8], p.177-183; Goodman[95], p.76-78). To study the complete progression of the failure process beyond peak load, two experimental approaches have been made to overcome the limitation just described. One is to use a "stiff" testing machine, and the other to use a suitably servo-controlled machine. With regard to the former approach, the complete load-deformation curve can be followed at will if the stiffness of the machine corresponds to a slope that is steeper than the most steeply descending part of the load-displacement curve of the specimen. The most obvious step is therefore to use a machine of massive construction, although loading of elastic elements in parallel with the specimen, and use of mercury as a hydraulic fluid have also been tried. With respect to the latter experimental approach, in the servo-control of a testing machine for post-failure studies, positive steps are taken to unload the specimen when less load is required for its further deformation, without relying on the stiffness of the machine. Normally the load control is achieved by programming the machine to follow a prescribed displacement sequence, so that if the displacement at the specimen begins to run ahead of the prescribed course, the servo-control reduces the load being applied by the machine, usually by extracting oil from the loading ram.

The mainstay of the stress application apparatus for achieving triaxial loading of cylindrical rock specimens, is a stiff (>2500 kN/mm) servo-hydraulic compression rig for applying axial loads up to 1000kN over the prepared flat and parallel core plug ends. The compression machine comprises a four column fixed crosshead straining frame incorporating a double acting unequal area actuator with integral displacement transducer. Specimens are tested between this piston rod and a strain gauged load cell attached to the fixed crosshead. The basics of the compression rig's servo-control system are described below. Closed-loop control of a conventional hydraulic system is achieved by obtaining an electrical feedback signal, V_f, from a transducer tightly coupled to the mechanical parameter to be controlled, e.g. load displacement or strain. This signal is

compared with the command signal, V_c, and the error signal, $V_e=V_c-V_f$, is amplified to drive the mechanical system to the commanded condition. The principles of operation of a basic closed loop electro-hydraulic servo system are outlined in Fig.4.2.3. The following numbers in square brackets refer to specific components as illustrated. Pressurised oil from a hydraulic power pack [1] is fed via an electro-hydraulic servovalve [2] to a double acting linear actuator [3] causing movement of the piston resulting in the specimen [4] being loaded. Load, displacement and strain transducers [5, 6 & 7] may be used in the system with their respective amplifiers [8, 9 & 10] producing voltage signals proportional to the individual parameters. These are connected via a control console [11] to the servo-amplifier [12]. This unit compares the "command" from a signal generator [13] with the selected control parameter and drives the servovalve with the amplified error signal. This results in any difference between the "command" and "actual" signals being corrected.

Radial specimen confinement is achieved using a confining pressure intensifier and pressure vessel system. The pressure intensifier is a high response servo-hydraulic unit for controlling the confining pressure of the triaxial cell. The intensifier operates at pressures up to 110MPa over an 80cc volume change from a 30MPa external hydraulic power supply (also supplying the compression and direct shear rigs) controlled by an electro-hydraulic servovalve operating under closed loop control with pressure or volume as the feedback parameter. A strain gauged pressure transducer measures the output pressure whilst an internal transducer senses the change in volume over the entire operating range. Volume change measurement is accomplished by a displacement transducer connected to the intensifier piston. The triaxial cell used in this study was of a design known as the "Hoek-type", named after one of the inventors (Hoek and Franklin, 1968[176]; Franklin and Hoek, 1970[177]) and comprises: a cell body into which the specimen may be placed in order to apply the confining pressure, this body having an air bleeder-hole and a connection for a hydraulic line; threaded end-caps for ease of deformed specimen removal from the cell; a flexible jacket (usually synthetic rubber) to prevent the hydraulic fluid from entering the specimen. The Hoek-cell is rated to a maximum operating pressure of 10 000psi (68.9MPa) and was of a size suitable for 1.5"-

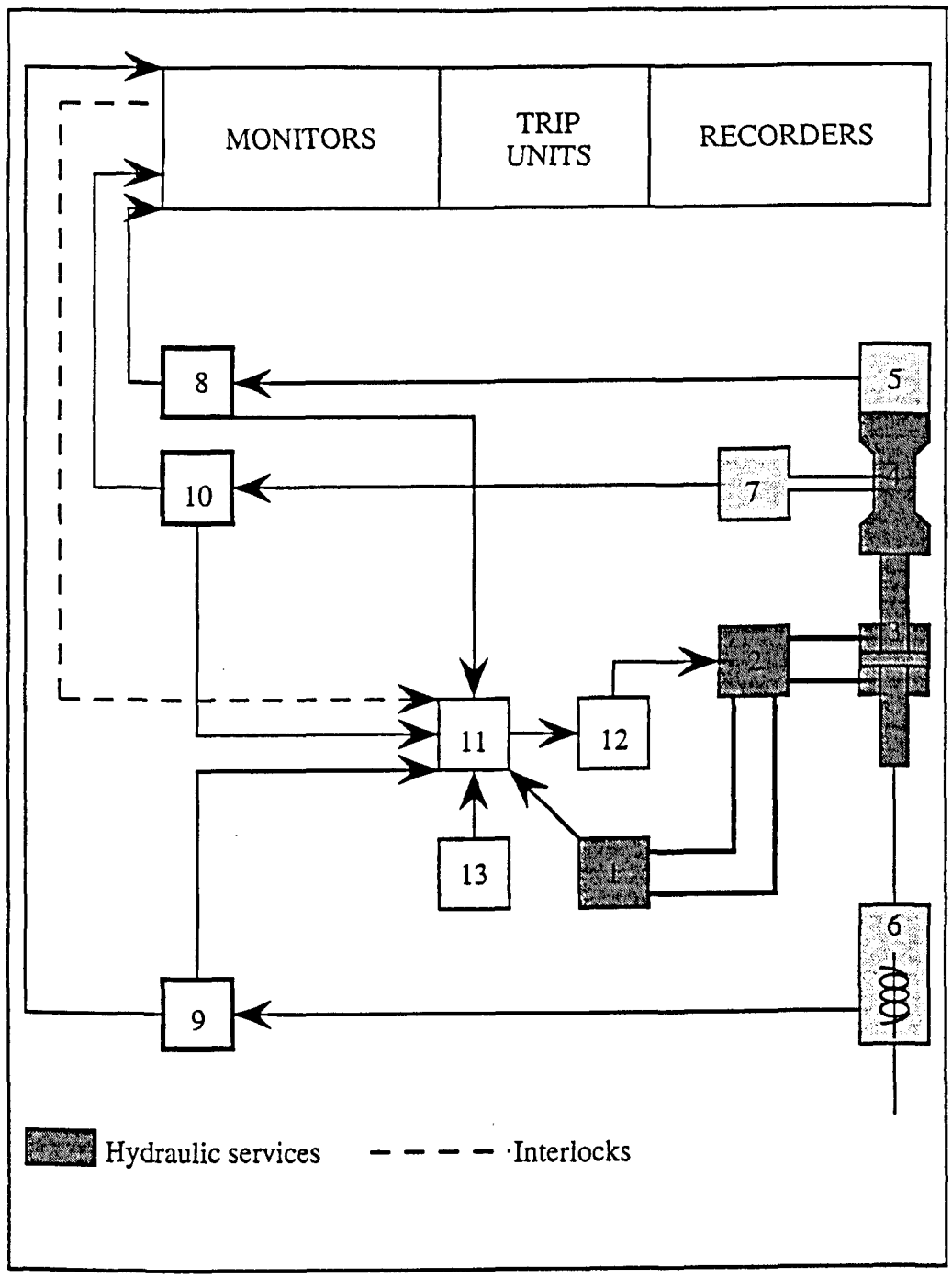

Fig. 4.2.3 Principles of operation of the basic closed loop electro-hydraulic servo system (see text for discussion).

(38.1mm-) diameter specimens. For coupled permeability-microseismics experimentation, the body of the standard Hoek-type triaxial cell as described above, has been modified to accept a waveguide, in order to facilitate optimum coupling between the acoustic emission sensor and the stressed rock sample. ISRM recommended procedures for triaxial compression testing, which discuss equipment specifications, can be found in Vogler and Kovari[175].

4.3 PERMEABILITY MEASUREMENT

Permeability measurements are some of the most essential performed on core plugs from recovered reservoir whole core. They represent important input data for accurate reservoir characterisation and reserves estimation, and aid in the selection of recovery processes. However, routine plug permeabilities are normally measured at lower stress magnitudes than those operative in the reservoir environment, and further, the applied laboratory stress field is invariably hydrostatic. Given the complex nature of the *in situ* rock stress field, and the relative sensitivity of measured plug permeability to the laboratory applied stresses, routine core analysis data should be treated with caution. Holt (1990)[1878] provides both a summary of previous stress-dependent permeability measurements conducted under hydrostatic conditions, and presents permeability reduction data induced by non-hydrostatic stress fields.

4.3.1 The Pulse-Decay Permeability Method

Whilst previous studies of permeability sensitivity to applied stress, utilising the permeameter system components described below, made use of steady state conditions to evaluate changing fluid flow potential, for this experimental programme in which test specimens will be subjected to high differential stresses resulting ultimately in post-peak dynamic instability and macroscopic shear failure, a "pseudo-pulse decay" method was preferentially employed in recognition thatlow permeability magnitudes would be encountered in cores subjected to high differential stress states and that large quantities of fines would be generated by frictional sliding

Thus a pulse-decay measurement method was chosen in preference to the more routine steady state permeability arrangement, in order to access lower permeabilities, and to minimise the migration of fines during testing. A literature review of various published pulse-decay methods was conducted by McMeekin[171] as part of an M.Eng. project. The development of pulse decay methods appears to have been driven by the realisation that the conventional (steady-state flow) method is not adequate for low permeability test specimens (k<1mD). For any arbitrary, desired, constant flow rate, relatively low sample permeability manifests itself in a resultant relatively large pressure drop across the specimen, necessitating a long test duration to achieve an equilibrium pressure differential. Also, for relatively high constant flow rates, pressure differentials can be very large, resulting in turbulent flow within the specimen. Brace *et al* (1968)[179] introduced a transient flow method to measure the permeability of Westerly granite specimens. Their experimental arrangement consisted of a cylindrical specimen connected to two fluid reservoirs. At the commencement of testing, the fluid pressure in the upstream reservoir is suddenly increased, so that as the pressure decays fluid flows from the upstream reservoir, through the sample, to the downstream reservoir. Sample permeability was calculated by Brace *et al* from the observed pressure decay in the upstream reservoir, given by the equation:

$$(p_i - p_1) = \Delta p[(v_2 / v_1)+v_2]\exp^{\wedge}-\alpha t \quad \ldots\ldots\ldots \quad \text{Eqn.4.3.1.1}$$

p_i: initial pressure

p_1: final pressure

Δp: pressure pulse ($p_1 - p_i$)

v_1: upstream reservoir volume

v_2: downstream reservoir volume

α: $(kA / \mu\beta L).(1/v_1 + 1/v_2)$

t: real time

k: permeability

A: core specimen cross-sectional area

μ: fluid viscosity

β: fluid compressibility

L: specimen length

From the mathematical model for the transient pulse decay technique as originally formulated by Brace *et al* and re-stated by other investigators (based on Darcy's law and the one-dimensional diffusion equation) McMeekin compared three different analytical solutions for calculating permeability:

(i) determination of k from the pressure pulse peak value

(ii) determination of k using pressure decay early time data, plus upstream and downstream volumes

(iii) determination of k from pressure decay late time data and an upstream volume

However each solution has its own particular disadvantages, for example (i) involves extrapolation of the pressure-time curve to t = 0 seconds (ii) utilises early time data where boundary interference effects could be significant, also the mathematical solution requires that the sample porosity equals zero and (iii) requires discrete porosity values to calculate the permeability. McMeekin compared the three analytical solutions using parameters determined experimentally on tight North Sea reservoir gas sandstone core plugs. He concluded that:

(i) the transient pulse decay technique is well suited for the determination of effective oil permeabilities in low quality reservoir rocks

(ii) the late time analytical solution gives the most accurate values for permeability providing good quality data is recorded

(iii) use of the "zero-porosity" approximation can lead to substantial errors

Due to the disadvantages listed above which are associated with each of the three methods used for deriving permeability from the transient pulse decay technique, an alternative

"pseudo pulse decay method" was investigated, based on an integration of Darcy's equation over the duration of the pressure pulse decay. The analysis is taken from Smart *et al* [172]. Consider the experimental pseudo pulse decay arrangement as depicted schematically on the left-hand-side of Fig.4.1.1. The system is initially at equilibrium with a given pore pressure. A pressure pulse is then introduced into the upstream reservoir and allowed to decay through the test specimen against a constant pore pressure. For steady state flow, or at any instant during the decay of the pressure pulse, and provided that the pressure distribution across the core is linear:

$$(\Delta p/L) = (\mu/k).(1/A).Q \quad \ldots\ldots\ldots \quad \text{Eqn.4.3.1.2}$$

Δp: pressure drop across specimen

L: core specimen length

μ: fluid viscosity

k: specimen permeability

A: specimen cross-sectional area

Q: volumetric flow rate

However,

$$Q = C.d/dt\ \Delta p \quad \ldots\ldots\ldots \quad \text{Eqn.4.3.1.3}$$

C: constant relating rate of pressure decay in the upstream reservoir to the volume of outflowing fluid

Substituting Eqn.4.3.1.3 into Eqn.4.3.1.2, integrating with respect to time and rearranging thus gives:

$$k = \frac{\mu.C.L\left(\Delta P_{t_1} - \Delta P_{t_2}\right)}{A}\left(\frac{1}{\int_{t_1}^{t_2}\Delta P dt}\right) \quad \text{.....} \quad \text{Eqn.4.3.1.4}$$

Again, with reference to the system depicted in Fig.4.1.1, a pseudo pulse decay permeability measurement under a constant triaxial stress state is conducted as follows: with the core plug in direct contact with both the upstream and downstream reservoirs, prior to the application of a pressure pulse and with both valves v_1 and v_2 open, the pump is used to pressurise the entire system to some initial pressure; valve v_2 is then shut to generate an upstream pressure pulse around 0.2MPa (30psi) over the system pressure; with the pump switched off and v_1 shut to prevent leakage through the pump seals, pressure pulse decay across the sample is monitored via a differential pressure transducer. The x-y-t recorder is used to provide a hardcopy Δp-time decay curve, the integration of which (utilising a digital planimeter) gives $\int_{t_1}^{t_2}\Delta p dt$. The system compressibility constant, C, can be determined by measuring the Δp's created by injecting known volumes of fluid into the upstream reservoir, so that for a given core plug with known L and A (remembering that both dimensions vary with applied stress) containing a permeant of known μ, k can be readily calculated from Eqn.4.3.1.4.

4.4 MICROSEISMIC MONITORING

Direct microscopic observation of the development of microcracking during deformation is a very useful tool for studying micromechanisms, however except under very restricted circumstances (Zhao *et al,* 1993)[180] it is difficult to observe microcrack development as the rock sample is being deformed. To use scanning electron microscopy (SEM) or even simple optical microscopy, it is almost always necessary to stop the test and unload the sample in order to make the observation, and as the changes that occur in the microstructure during unloading and preparation for observation are not known. there is always some uncertainty as to whether what is being observed is actually the same

microstructure that was present when the specimen was under load. In addition, observational methods only view what is happening near a flat surface and obtaining a three-dimensional picture of the microcracking process is difficult. For these reasons, several indirect observational techniques have obvious attractions.

One of the most useful of the indirect fracture monitoring techniques is the recording of acoustic emissions (AE) the high frequency elastic vibrations emitted by, amongst other sources, a propagating crack. A short introduction on the use of the AE technique, as applied to the study of rock deformation is given below, drawn mainly from Costin (1989)[181]. The detection of microcracking in rock by acoustic emission was first reported by Obert (1942)[182] and Obert and Duval (1942)[183]. Since that time, the technique has been improved to the extent that it is now used to monitor the development of cracking during triaxial compression testing, constant stress (creep) testing, and cyclic loading of rock. In addition, acoustic sensors are used in mine safety applications to give early warning of failure in support structures. The exact source mechanism of the emissions is not known but believed to be due to the sudden advance of the crack tip resulting in a release of elastic energy in the form of acoustic waves. These emissions are detected by acoustic transducers in direct contact with the sample, and then electronically processed in any one of a variety of ways depending on what information is required. The most common method is simply to record the cumulative number of emissions. By plotting the number of emissions as a function of the stress or strain, the influence of microcracking on the deformation can be determined. Sometimes the energy contained in the emissions is calculated or the frequency content is analysed to try to determine the nature of the source. However, these results should be viewed with some caution since the frequency and energy content of the recorded signal depend somewhat on the transducer and electronics used, thus comparisons between the results of different investigators is not always possible. More recently, experimenters have been able to determine the source location of selected emissions using an array of detectors similar to a seismic network (Sondergeld and Estey, 1981)[184]. By plotting the location of emissions as the stress is applied to a rock sample, a three-dimensional picture of the development of microcracking can be generated. A final note of interest deals with what is usually

referred to as the Kaiser effect. It is known that during cyclic loading, the emissions are much reduced after the first cycle (Goodman, 1963)[185]. A similar effect has been noted for metals, where the source of the emissions is dislocation motion associated with plastic flow.

4.4.1 Acoustic Emission Characteristics

Acoustic emission (AE) testing is a powerful method for examining the behaviour of materials deforming under stress. AE can be defined as transient elastic waves generated by the rapid release of energy within a material. Materials can thus be envisaged as "talking" when they are in trouble, whilst AE monitoring equipment enables the operator to "listen" to these sounds, resulting from the various modes of active damage which are occurring in the stressed material, including crack growth. Small-scale damage is detectable long before failure, so that AE monitoring can be used as a non-destructive technique to find defects, for example during structural proof tests and plant operation. AE equipment is also adaptable to many forms of production quality-control testing, including weld monitoring and leak detection. AE also offers a unique capability for materials research in the laboratory, for example as utilised in this thesis work.

The conventional parameters used to describe an AE signal are illustrated in Fig.4.4.1.1 which shows a typical "burst type" emission signal. the phrase "burst type" refers to the transient, fast-rise/slow-decay nature of the signal. It is used in contrast with "continuous" emission signals from leaks or dislocation motion in metals. "Burst" is one of the oldest words in the AE vocabulary. The term "counts" (sometimes called ringdown counts or threshold crossing counts) refers to the number of times the AE signal crosses the threshold. This is a simple measure of signal size, since larger signals typically give more counts. Electronically this is a very easy measurement, and it was the first to come into widespread use. Summing the counts from all the detected emissions (accumulation) gives a convenient measure of the total emission from the specimen or structure. The term "amplitude" refers to the peak voltage attained by the AE waveform. This is an important parameter because it governs the detectability of the event (detection depends on the amplitude exceeding the equipment threshold). Like counts, amplitude is a useful

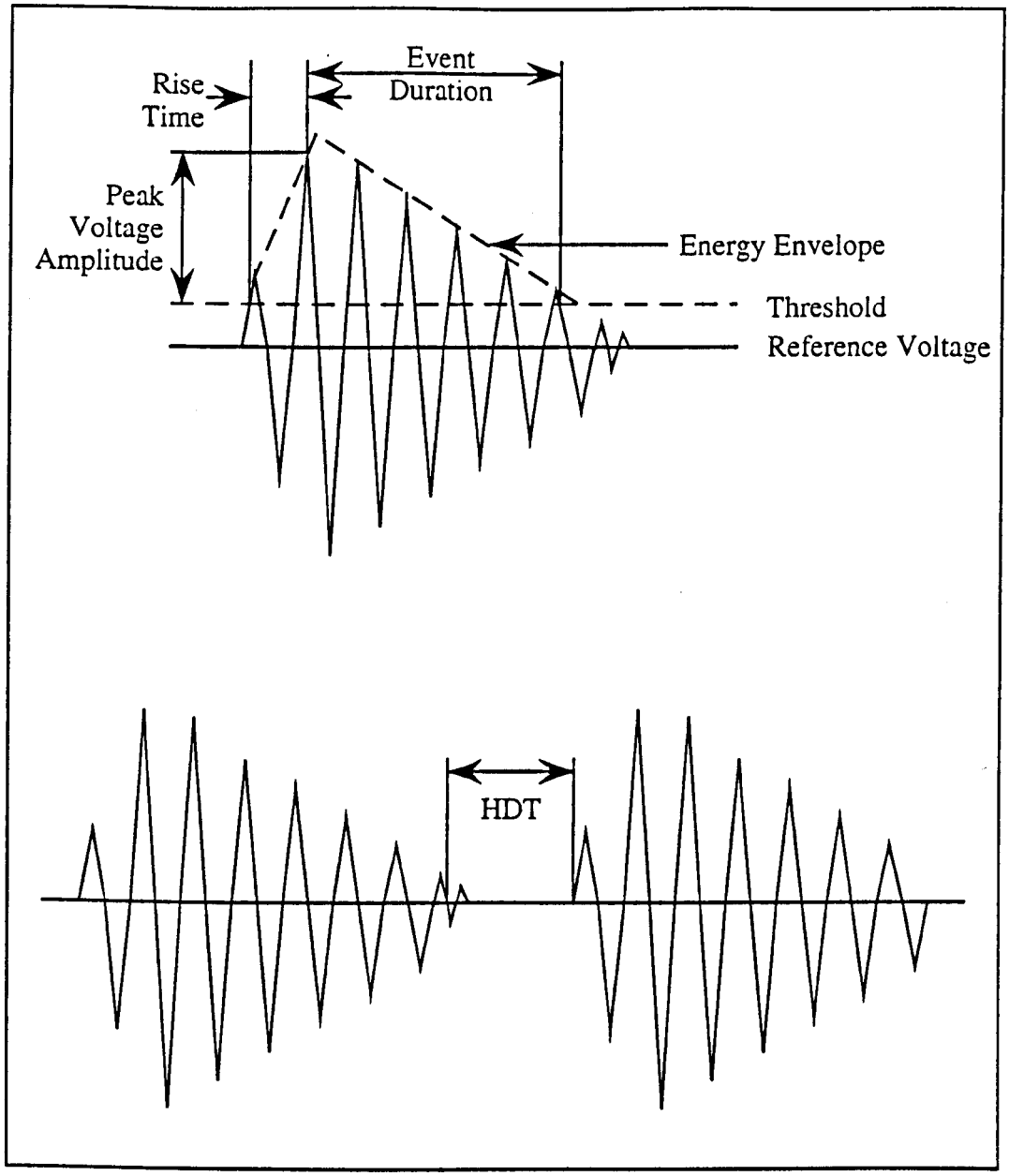

Fig.4.4.1.1. Conventional parameters used to describe an AE signal (seven counts, two counts-to-peak in example shown).

measure of signal size, and it is the appropriate variable to use for attenuation measurements. Amplitude is conventionally expressed in decibels relative to one microvolt at the sensor, the same scale that is used to specify threshold. This scale converts the wide range of observed signal voltages (from a few microvolts to hundreds of millivolts) into convenient numbers between 0 and 100:

Events with amplitudes <35dB are considered small

Events with amplitudes 35-55dB are considered medium-sized

Events with amplitudes 55-75dB are considered large

Events with amplitudes >75dB are considered very large

To accommodate the very wide dynamic range between the smallest and largest signals encountered in actual testing, amplitude measurements are often made through a logarithmic amplifier. This is placed in parallel with the linear amplifier that serves for the other measurements. "Energy counts" describes the measured area under the rectified signal envelope (also known as MARSE). This measurement requires relatively complex circuitry, but it has the advantage that it is responsive to both the height (amplitude) and width (duration) of the signal. As with ringdown counts, a convenient measure of the total AE from a structure can be obtained by summing (accumulating) the energy counts of the individual signals. The parameter "duration" refers to the time from the first to the last threshold crossing. This parameter is closely related to ringdown counts, but it is used more for discrimination that for the measurement of emission quantities. Signals from electromagnetic interference typically have very short durations, so this can be used to filter them out. The "risetime" is the time from the first threshold crossing to the signal peak. This parameter is useful for source discrimination and signal filtering. It can be used to filter out signals from electromagnetic interference which usually have very short risetimes. Also, it depends in a useful way on the distance wave propagation effects. So to selectively monitor a known defect right under the sensor, a filter can be set to eliminate acoustic signals coming from further away.

The term "sensitivity" refers to the ability of the system to detect small signals from the loaded structure. In part, this is determined by sensor spacing and sensor sensitivity, and in part by the controls set on the main equipment. The governing control is the "threshold", an operator-set voltage level against which the amplified AE signals are compared. When the AE signal exceeds this voltage threshold, a hit is recognised and the signal-measurement circuitry comes into play. With sensitivity decreasing with increasing threshold setting, in practice thresholds below 20dB are quite difficult to achieve due to electronic noise, whilst those in excess of 65dB are unattractive due to their very low sensitivity.

Maximum available sensitivity is, however, not always the ideal setting, as risk of picking up acoustical background noise is also raised. A typical recommended threshold for general purposes or unknown situations is 40dB. Lower sensitivity can be used when the background noise is exceptionally severe, or when it is known that the signals of interest are of large amplitude. Higher sensitivity can be used when the signals of interest are of low amplitude, or when dealing with high attenuation or large sensor spacing. In basic research into material deformation, where the operator is often seeking maximum information, a higher sensitivity may well be the more appropriate choice, whereas for practical non-destructive testing (NDT) the larger AE events are usually of greater significance with respect to structural integrity, so that a lower sensitivity may be better. System timing parameters enable the AE monitoring unit to determine when each signal has passed. The AE signal coming from the sensor is amplified, filtered and then presented to the measurement circuitry, which produces a digital description of each detected signal. The measurement process begins when the amplified and filtered signal first crosses the threshold, this first threshold crossing triggering assorted timers and opening gates etc., depending on the specifications of the particular AE monitoring system. When the signal has passed, however, the measurement circuitry must close out its operation, output the resulting hit description, and get ready for the next hit, so that a basic and necessary, non-trivial task, is to determine when the signal has passed. This is accomplished by means of a hit definition timer in the measurement circuitry. This timer is a "retriggerable one-shot" circuit. It is turned on (triggered) by the first threshold

crossing, and retriggered by each new threshold crossing. It turns off, terminating the measurement process, when the "hit definition time" (HDT) has expired without any more triggerings (threshold crossings). The HDT is selected by the operator before the test. When a suitable value is selected, each acoustic emission will produce a single hit description in a timely manner. If the HDT is set too low, the timer may expire in the middle of the signal, and the system will treat the next part of the signal as a separate event, producing invalid data. If the HDT is set too high, a separate event may be included along with the first in a single hit description, also resulting in invalid data. Whilst the function of the HDT is to enable the system to determine the end of the hit, close out the measurement process and store the measured attributes of the signal, the function of the "peak definition time" (PDT) is to enable determination of the time of the true peak of the AE waveform. For PDT, the main requirement is to avoid false measurements being made on a high-velocity, low-amplitude precursor, so that ideally, PDT should be set as short as possible. The function of "hit lockout time" (HLT) is to inhibit the measurement of reflections and late-arriving parts of the AE signal, so that data from wave arrivals can be acquired at a faster rate.

4.4.2 The LOCAN-320 AE Monitoring Unit

The LOCAN-320 is a computerised AE monitoring system supplied by the Physical Acoustics Corporation (PAC) that performs AE signal measurements and stores, displays and analyses the resulting data in real time. The AE signals from the loaded structure (confined rock specimen) are converted into electrical signals by the sensors, amplified to usable voltage levels by the preamplifiers and measured in two-channel computerised modules known as Independent Channel Controllers (ICC's). Each AE signal (hit) is described in terms of various measured parameters as outlined above. Other variables such as time of occurrence or load on the structure at the time the event occurred are also included in the hit description. Hit descriptions are stored in the output of the ICC until the system's main processor is ready to run them. The Standard LOCAN-320 system hardware design incorporates a modular architecture that contains an analogue interface and pre-processor bus organiser, as well as channel controller and parametric channel controller under the control of a multibus based microprocessor. The requirements of

high-speed data acquisition have been separated from the more complex requirements of analysis and display, with the result that substantially faster data acquisition, with more information about each event can be achieved. The dual bus structure separates tasks between processors, allowing the IBM-PC to process and present graphical displays, and the multibus to acquire and extract the appropriate features from the AE signals. The ICC is a single board, two channel AE computer which utilises the dual-bus architecture of the LOCAN-320 to communicate with the main processor. The ICC performs signal feature extraction, temporary hit buffering (>1000 hits) and front-end data filtering. The buffer data is immediately available to the host computer (80286) for processing and real-time graphics. The basic standard application software package supplied with every LOCAN-320 serves for setting up channel parameters, real-time graphics, conditioning alarms, filtering, testing, file handling, acquisition start and replay.

The most important single factor in successfully performing an AE application is the reliability of the AE sensor. As an AE sensor converts the mechanical energy carried by the elastic wave into an electrical signal, the sensor is more properly termed a transducer. The transducer most often used in AE applications is the piezoelectric transducer. This choice has been dictated by its inherently high sensitivity and relative ruggedness. The active element of a piezoelectric transducer is a thin disk of piezoelectric material (a material which can convert mechanical deformation into electrical voltage). This disk is metallized on both faces for electrical contact, and mounted in a metal cylinder to provide electromagnetic interference shielding. The piezoelectric ceramics commonly used in AE transducers are made of small crystals of titanates and zirconates which are mixed with other materials, moulded to the desired shape, and fired in a kiln. The ceramic material is then made piezoelectric by poling, which is the process of heating the material above its Curie temperature whilst under a strong electric field. To take advantage of the extreme sensitivity of the piezoelectric transducer, it must be attached to the material under observation in such a manner that the acoustic energy passes into the transducer with minimum loss at the transducer-material interface. The required intimate mechanical contact is achieved on flat surfaces by mechanical clamping using thin films of grease, oil or epoxy adhesive between the transducer and the material. In general, the problem of

coupling is much more severe for shear wave observation because the coupling medium must be sufficiently viscous to support the shear motion. For a compressional wave any fluid will act as a couplant. The AE waveform at the source is generally a simple, broadband step or pulse, however the detected signal is much more complex in form, being largely shaped by wave propagation effects between the source and the sensor.

Successful AE testing relies on being able to detect the signals of interest above the background noise. Sources of noise fall into two main categories, electrical and mechanical. Electrical noise sources include "white" noise generated at the front end of the amplifier, "ground loop" noise produced by improper electrical grounding of system and structure and electromagnetic interference from power switching circuits and other sources of e.m. radiation in the neighbourhood of the AE equipment. Mechanical noise sources include test machine noise, flow noise from pumps and valves and frictional noise from moving components. The function of the sensor is to convert the AE stress wave into an electrical signal for processing by the AE instrumentation. Most sensors are resonant types with resonant frequencies or frequency ranges specified by the manufacturer. Resonant sensors are more sensitive than non-resonant ("broadband" or "flat frequency response") types. Whilst most users would prefer a more sensitive sensor over a less sensitive one, sensor sensitivity depends on a variety of design variables including size, mechanical strength and temperature performance, so that sometimes there are design "trade-offs". Sensitivity is shown as a function of frequency, on the calibration curves supplied by the sensor manufacturers. Major efforts have been expended by the U.S. National Bureau of Standards and other agencies, to provide a technically solid basis for AE sensor calibration, and absolute reference standards are now available.

The present AE hardware setup, used to monitor rock core specimens subjected to varying triaxial stress systems, utilises only one active channel, with a single associated transducer sensor and external preamplifier. The sensor used is a relatively wide band transducer (model number WD, serial number 929) measuring 17.5mm in diameter. The associated calibration curve, as supplied by PAC, is shown in Fig.4.4.2.1. The transducer is used in conjunction with a PAC 1220A preamplifier. This preamplifier is a versatile

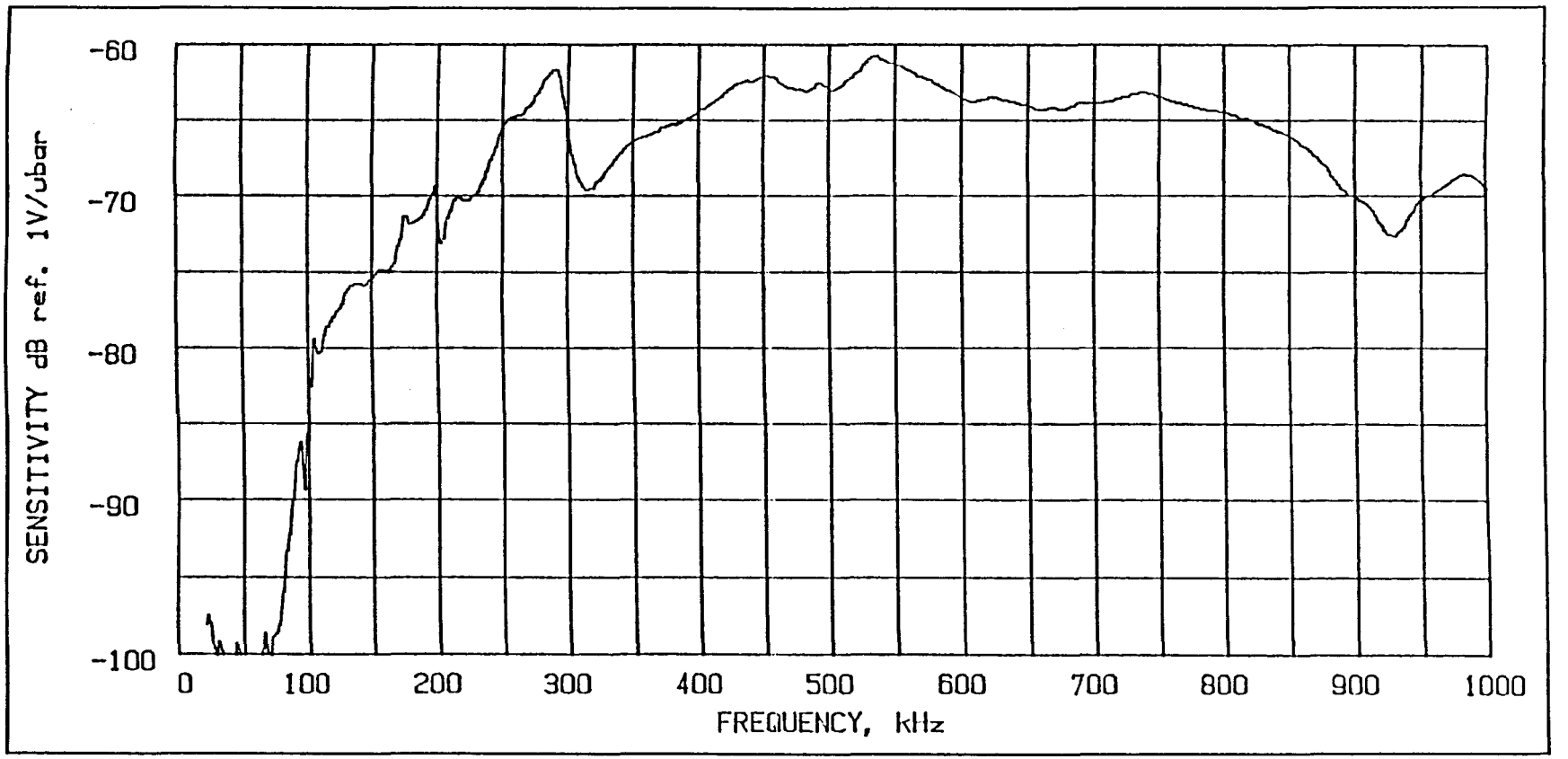

Fig.4.4.2.1. PAC-supplied calibration curve for the AE transducer used in this study.

one, allowing the user to select high pass, low pass or bandpass filters, single-ended or differential input, and either 40dB or 60dB gain. The 1220A output and power is supplied by a single conductor 50Ω coaxial cable with a BNC connector. The +28VDC operating voltage and signal run on the same line and are internally isolated in the preamplifier. As potential sources of noise were manifold, in association with coupled permeability-microseismics monitoring under triaxial stress, much effort was expended in trying to maximise the signal-to-noise ratio. Potential sources of noise included creaking in the confining pressure vessel, flow noise from hydraulic fluid pumps and valves, inertial dither on the servovalves, plant operating noise (as the compression rig is housed in a busy workshop), friction at platen/rock interfaces, as well as white noise and electromagnetic interference. Due to the dimensions of the transducer and the geometric limitations associated with the stress application equipment, a special waveguide was designed in order to direct AE from the stressed rock specimen to the sensing transducer. Initially the transducer was mounted on a machined flat on one of the loading platens, but this was found to produce too low a signal by comparison with the background noise level. A schematic diagram of the waveguide design is shown in Fig.4.4.2.2. The waveguide screws directly into the body of the confining pressure cell, without affecting its maximum pressure rating. An external thread allows the waveguide to screw into the cell, sealing with an O-ring, whilst an internally threaded waveguide rod measuring some 120mm in length is tightened by hand, prior to the application of confining pressure to the specimen. This forces a floating anvil or "shoe" into direct circumferential contact with the rock sample through the synthetic rubber jacketing sleeve. Confining fluid tracks up this internal thread and inflates a Shamban seal situated within an internally machined chamber. The AE transducer is located on the extreme end of the waveguide rod, furthest from the floating anvil, and is mechanically held in position by four locating screws. A thin layer of silicon vacuum grease was used as a viscous couplant between the transducer and the waveguide rod. A photograph of the Hoek-type confining pressure cell with waveguide and mounted AE transducer, all sitting within the stiff compression frame, is shown in Fig.4.4.2.3.

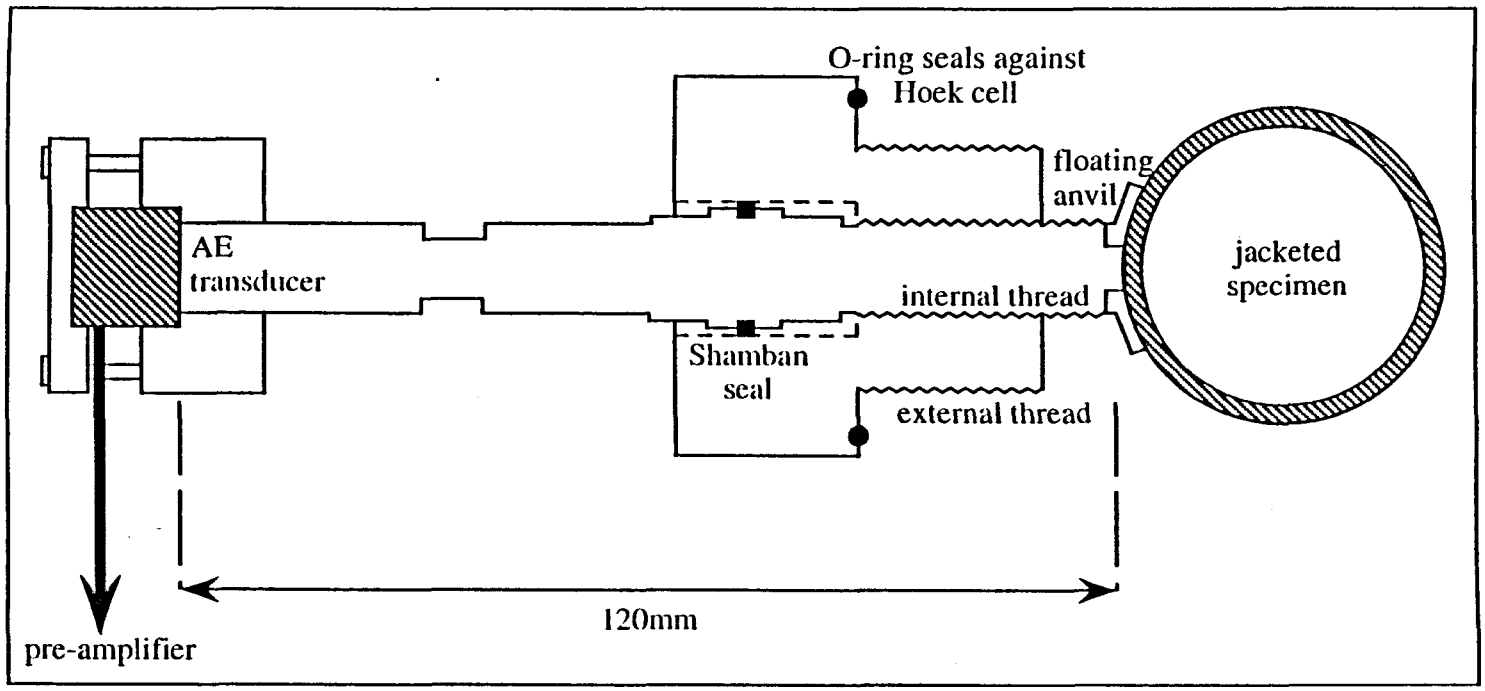

Fig.4.4.2.2. Scale drawing showing components of AE waveguide.

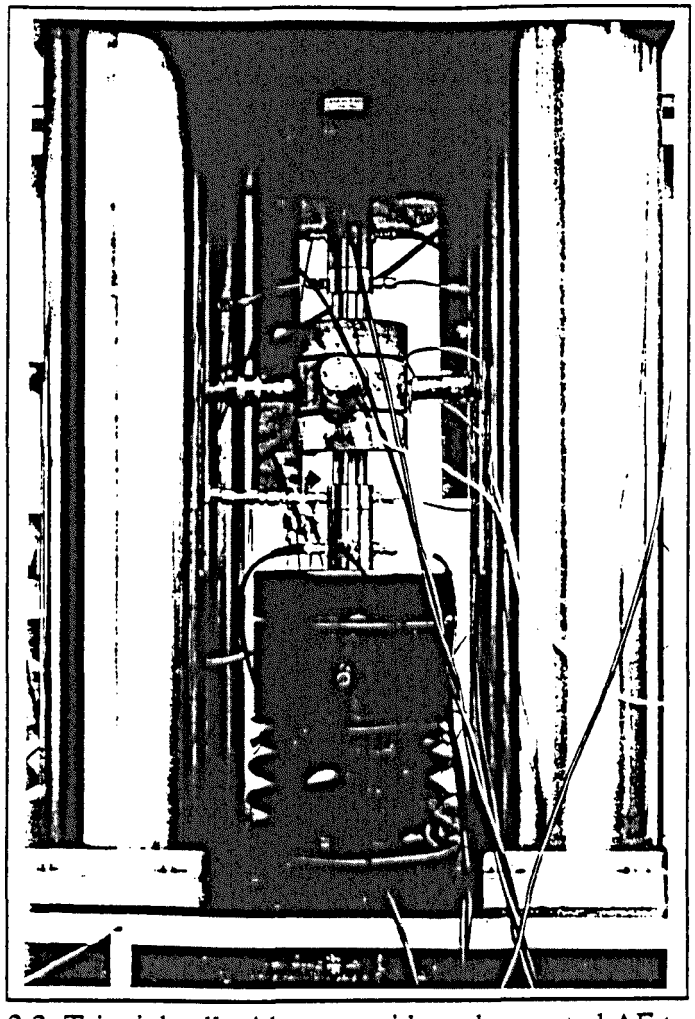

Fig.4.4.2.3. Triaxial cell with waveguide and mounted AE transducer, sitting within stiff compression rig.

5. COUPLED PERMEABILITY-MICROSEISMICS MEASUREMENT DURING TRIAXIAL COMPRESSION TESTING: RESULTS

5.1 INTRODUCTION

Using the triaxial compression system in combination with the coupled permeability-microseismics capability (equipment specifics as detailed in the previous chapter) the effects of an increasing magnitude of applied confining pressure (broadly equivalent *in situ* to a greater depth of burial) was assessed in terms of its observed influence on: fracture (peak failure) and friction (residual sliding) strengths; discrete transient permeability values; acoustic emission (AE) signatures. For initial confining pressures ranging from 1000psi or 6.9MPa to 9000psi or 62.1MPa (this chosen range reflecting the triaxial compression cell maximum operating pressure rating of 10,000psi or 68.9MPa) discrete triaxial failure tests were conducted on 1.5"-diameter cylindrical specimens of Clashach sandstone quartz arenite. AE monitoring over the resulting complete stress-strain curves thus provided information on progressive microcrack coalescence and strain localisation leading to fault formation and dynamic failure, interpreted in terms of existing damage mechanics theory. Further AE monitoring under various post-peak residual sliding stress conditions, also provided important additional information relating to the frictional sliding process and fault gouge formation. Four "pseudo" pulse decay permeability measurements were taken throughout each discrete failure test, at constant stress states corresponding to hydrostatic, immediate post-dynamic failure, post-residual sliding and post-re shearing under increased confining pressure conditions. Thus fault formation resulting from a wide range of differential stress magnitudes, and its effect on fluid flow was able to be examined. Also, the sealing potential of fault gouge bands generated by frictional sliding of these induced shear fractures under a variety of stress conditions was assessed. Of course, due to the geometrical constraints of the experimental facility, with the direction of fluid flow always being oblique to the induced fault plane, such permeability measurements represent the comparative influence of faulting and fault gouge formation on axial fluid flow, and do not represent the actual permeabilities of the shear bands themselves, such as, for example, a linear

flow cell measurement does for a proppant bed. "Post-mortem" particle sizing analyses of the fault gouge samples formed by these discrete discontinuity triaxial compression tests are reported in Chapter 6. There, emphasis is placed on the establishment of empirical relations between the size distributions of the different fault gouge samples, and their associated frictional strength and fluid flow characteristics as described in this chapter.

5.2 EXPERIMENTAL METHODOLOGY

Whilst in Chapter 3 the main objective was to investigate the effects of constant normal displacement boundary conditions on the direct shear response of a variety of lithologies, that is to study the influence of rock type on frictional strength, in the discontinuity triaxial compression tests described below, the primary variable under scrutiny was the magnitude of applied triaxial stress, so that ideally, initial pre-stress microstructure should be as constant as possible between test specimens. To this end, Clashach sandstone was chosen as being the most readily available reservoir sandstone analogue possessing this quality, that is being sufficiently homogeneous and isotropic on a quarried block scale so as to provide core plugs with a minimum of between-sample variation.

The Clashach sandstone is a commercially available Permo-Triassic sandstone sourced from a quarry in Elgin, Scotland. It is a pale-fawn, well-sorted, medium- to coarse-grained (0.5-1mm) quartz arenite with well-developed quartz overgrowths. X-ray diffraction (XRD) analysis shows quartz content ranging from 90 to 96%, K-feldspar constituting the remaining modal percent, and trace amounts of illite (Ngwenya *et al*, 1993)[186]. Occasional thin-sections also show very minor development of ferroan dolomite and kaolinite. Ngwenya also notes that permeability measurements conducted under hydrostatic conditions on different Clashach sandstone specimens proved variable, ranging from 200mD to 1D, the lower permeability samples in general showing a more reddish colour, suggestive of the observed variation being the result of pore-throat blockage by ferric compounds. Mineralogical, poroperm and rock mechanical parameters

determined from a programme of characterisation conducted on the Clashach sandstone core specimen source-block used for this suite of tests, are detailed in Table 5.2.1. Elastic constants were measured from uniaxial compression of 1.5"-diameter (38mm) strain-gauged core plugs, which were subsequently taken to failure to determine unconfined strengths. Tensile strengths were evaluated using the Brazilian disk indirect method. The theoretical and empirical failure criteria constants were determined using the multi-failure state triaxial method to generate ten Mohr circles from a single specimen at confining pressures ranging from 1000psi (6.9MPa) to 10 000psi (68.9MPa).

Due to the relatively complex nature of the experimental procedure, over twenty discrete triaxial tests were run with a success rate of 30%, before the maximum range of stress magnitudes was achieved. The main problems encountered were those of perforated triaxial cell liners due to excessive sliding displacements, poor AE coupling prior to the waveguide installation, and initial "teething" problems associated with proving of the pseudo pulse decay method, such as permeant leakage. The Clashach core plugs consisted of 1.5 inch-diameter (38mm) right circular cylinders 3.1 inches in length, giving a length-to-diameter ratio in excess of 2:1. Specimen ends were prepared flat and parallel to within ISRM specifications (Vogler & Kovari[175]) using a lathe as opposed to a lapping jig, in order to minimise damage and "skin effects" which would influence fluid flow.

The triaxial compression system with coupled permeability-microseismics facility used for this suite of tests, is as illustrated schematically in Fig.4.1.1. Starting from ambient atmospheric conditions, each specimen was taken to an initial pre-determined hydrostatic stress state by increasing both axial load and confining pressure in step. Axial load was then increased over constant confining pressure (thus $\sigma_a=\sigma_1$ and $p=\sigma_3$) under displacement control and at a constant displacement rate equivalent to a strain rate of $1.6\times10^{-5}s^{-1}$. Fig.5.2.1 illustrates schematically the experimental test programme that each specimen was subjected to, with of course the magnitude of the initial hydrostatic stress being the main variable under examination. From Fig.5.2.1 it is evident that whilst

Reservoir sandstone analogue	Source locality	Age	Lithology	Mineralogy	Helium Boyle's law porosity (%)	Nitrogen "klinkenberg" permeability (mD)	Young's modulus (GPa)	Poisson's ratio	Tensile strength (MPa)	Uniaxial compressive strength (MPa)	"best-fit" linear Mohr-Coulomb failure criterion constants:		Hoek-Brown empirical failure criterion constants:		
											cohesion (MPa)	internal friction angle (°)	m (s = 1)	A	B
CLASHACH	commercial quarry, Elgin, Scotland	Permo-Triassic	pale-fawn, medium-coarse grained, well-sorted subarkosic arenite	sub-rounded quartz (89%), fresh-altered K-feldspar (11%) secondary quartz overgrowths	13.9	142	11.3	0.24	7.6	105.8	53	34	7.28	0.83	0.661

Table 5.2.1 Geological, poroperm and rock mechanical characteristics of the Clashach test sandstone.

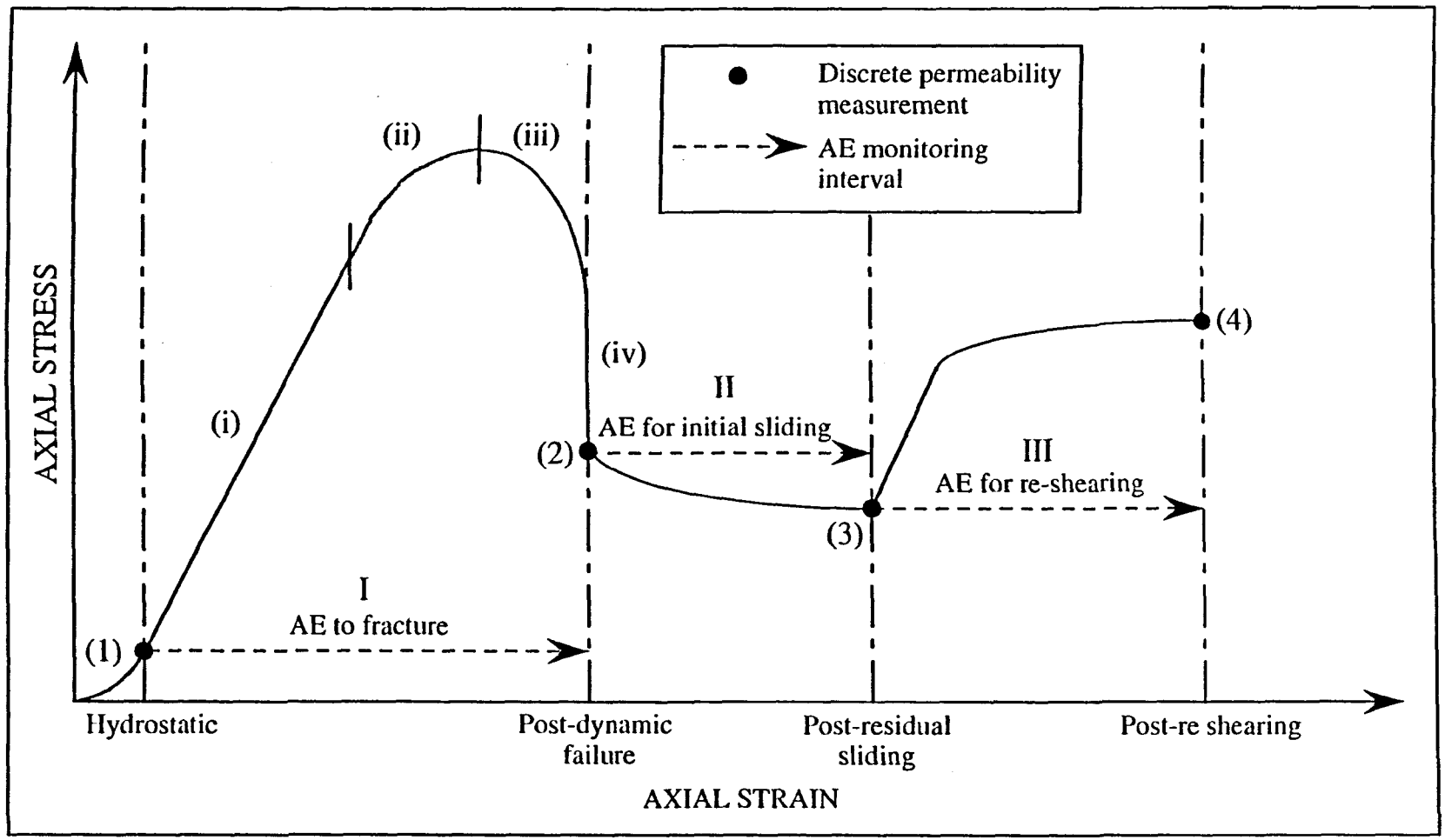

Fig.5.2.1. Schematic of experimental programme for triaxial compression testing (see text for details).

discrete permeability measurements were conducted under constant stress states, AE was monitored over conditions of changing stress associated with a constant applied strain rate. As noted in the introduction, four "pseudo" pulse decay permeability measurements were made throughout each discrete failure test, under constant stress conditions corresponding to: (1) hydrostatic; (2) immediate post-dynamic failure; (3) post-residual sliding; (4) post re-shearing under increased confining pressure conditions. The aim of such an experimental method was to assess the effects of fault formation, and of progressive dynamic fragmentation resulting in shear debris (fault gouge) generation, on axial plug flow occurring in the same rock type but at stresses corresponding to different depths in the Earth's crust. Also, it was hoped that the hydrostatic measurements would allow normalisation of those permeabilities recorded under post-faulting stress conditions, thus offering some means of compensating for between-sample variability and for elastic stress-sensitivity. Three different AE signatures were recorded under varying stress test conditions corresponding to: (I) taking the initially intact core specimen from hydrostatic stress, over its complete failure cycle, to a faulted state; (II) sliding the induced shear fracture for a pre-determined displacement to a residual strength state; (III) further sliding the faulted specimen under an altered stress state achieved by increasing the confining pressure by an arbitrary 1000psi (6.9MPa) thus re-shearing the fault under an artificially strengthened state. In summary, AE (I) was measured over varying stress conditions from that associated with permeability (1) to that associated with permeability (2), AE (II) from permeability (2) to permeability (3) and AE (III) from permeability (3) to permeability (4). The aim of the AE experimental procedure was to allow a comparison of acoustic properties (in constant-lithology systems but corresponding to different depths in the Earth's crust) during: (I) the nucleation phase of faulting; (II) initial sliding of the fault after quasi-static and dynamic slip-weakening followed by; (III) a longer-term recovery in frictional strength. The mechanical strengthening effect resulting from increasing the normal stress across the fault by increasing the confining pressure, mimics to some extent the quasi-static strength recovery which can occur in the Earth from combined physico-chemical processes over longer timescales and with a more reactive pore fluid, namely pressure

solution "crack-seal" (Ramsay, 1980[187]) and dilatancy hardening (Brace & Martin, 1968[188]). In Fig.5.2.1 AE (I) is further subdivided into: (i) a linear quasi-elastic phase; (ii) a strain hardening phase up to the peak strength of the material; (iii) a stable strain softening phase; (iv) dynamic stress drop. Phase (i) is termed "quasi-elastic" since, although axial stress and strain are related in a linear manner, local inelastic processes resulting in AE are also characteristic.

In total seven Clashach sandstone specimens were tested, with initial hydrostatic stress states ranging from 1000psi to 9000psi. For the "industry accepted" approximate overburden stress gradient of 1.0psi/ft (Skopec, 1991[189]) and assuming a uniform increase in overburden stress with depth, the limits of applied laboratory hydrostatic stress correspond to depths extending from 1000ft (0.3km) to 9000ft (2.7km). Table 5.2.2 lists the hydrostatic stress magnitudes, equivalent to the confining pressures applied during AE monitoring for stages (I) and (II), and the final confining pressures for AE stage (III) and for permeability (4) following a 1000psi (6.9MPa) increase. From Table 5.2.2 it is evident that five specimens were tested under initial confining pressures of 1000, 3000, 5000, 7000 and 9000psi whilst a further two duplicate specimens were also tested under 3000 and 9000psi pressures, to check data reproducibility.

5.3 STRENGTH RESULTS

Using the triaxial stress application system as described above, for the experimental methodology as described above, the effect of initial specimen confinement on strength measures was appraised. To this end, the main method of data recording was graphical generation of axial load versus axial displacement profiles on an x-y-t chart recorder, linked to a plotter drive unit within the servo-control system. From these curves any axial load could be converted to an equivalent axial stress by dividing by the specimen cross-sectional area, whilst the corresponding axial displacement could be converted to an axial strain by dividing the change in specimen length by its initial pre-deformation length and expressing the resultant in either microstrain or percent. Axial load-displacement profiles from the seven triaxial tests conducted are shown in Fig.5.3.1. The

Specimen I.D.	Confinement in phases I & II (psi) [MPa]	Confinement in phase III (psi) [MPa]
#15	(1000) [6.9]	(2000) [13.8]
#16	(5000) [34.5]	(6000) [41.4]
#18	(7000) [48.3]	(8000) [55.2]
#19	(3000) [20.7]	(4000) [27.6]
#20	(9000) [62.1]	(10 000) [68.9]
#21	(3000) [20.7]	(4000) [27.6]
#22	(9000) [62.1]	(10 000) [68.9]

Table 5.2.2 Initial confining pressures for dynamic failure and frictional-sliding, and final confining pressures for re-shearing.

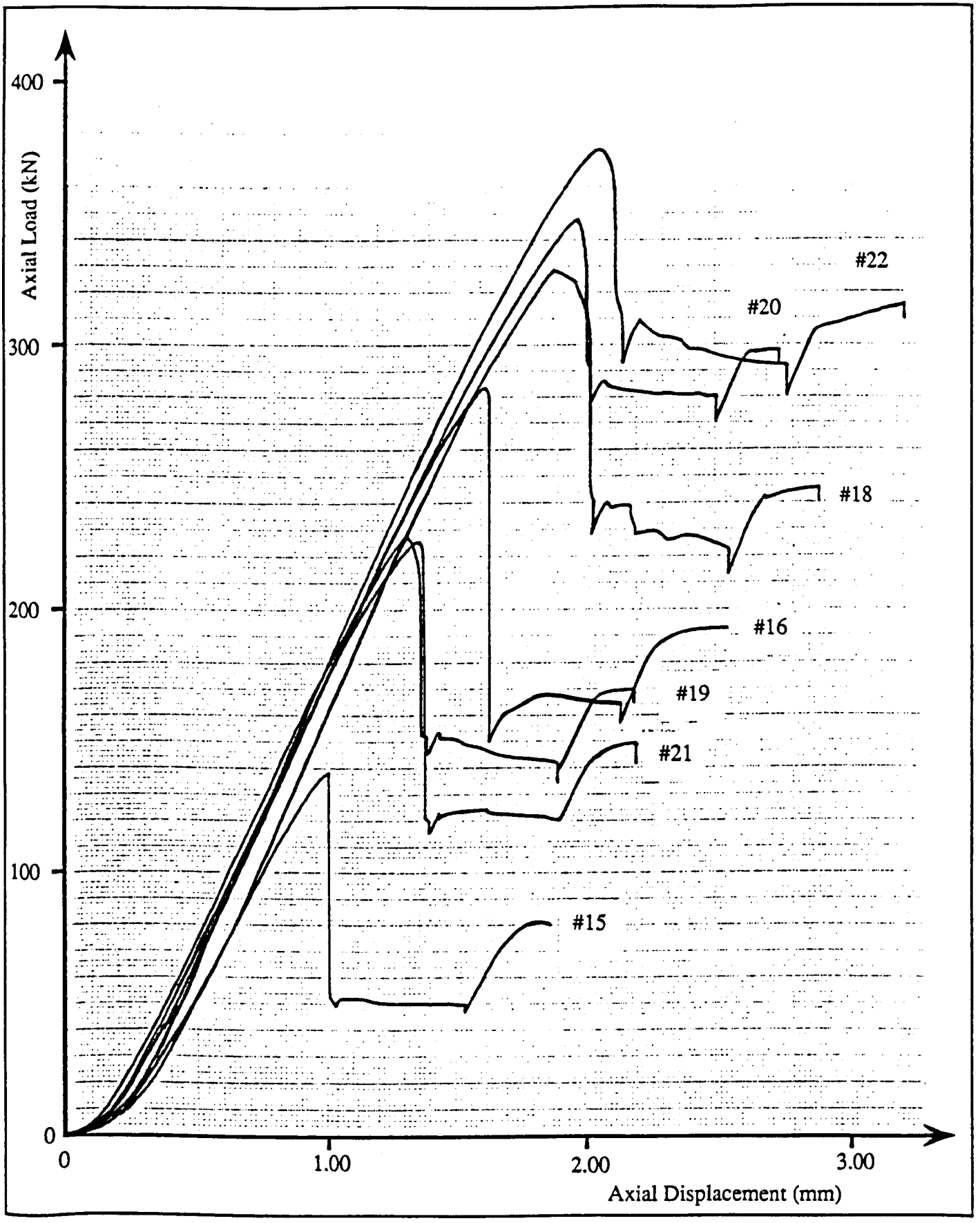

Fig.5.3.1 Axial load-displacement curves for seven Clashach sandstone specimens deformed under different confining pressures.

peak stress value recorded from these curves was taken as the fracture stress, that is the ultimate strength of the material under that particular confining pressure, $p=\sigma_3$. Residual strength for frictional sliding under the initial magnitude confining pressure was taken as the relatively constant value "plateau" part of the slip-weakening curve, whilst residual strength for re-shearing under increased confining pressure was taken as the plateau following asymptotic increase in axial stress resulting from fault strengthening due to increased σ_3.

Fig.5.3.2 shows a Mohr stress circle plot for the seven discrete failure tests performed on oil-saturated specimens under confining pressures ranging from 1000 to 9000psi. By comparison with the multi-failure state triaxial test conducted on an oven-dried Clashach specimen to define the strength measures given in Table 5.2.1, both cohesive strength and internal friction angle were found to decrease from 53MPa to 33MPa and from 34° to 32° respectively, with the addition of a pore fluid. The linear Coulomb envelope of the form $|\tau| = \tau_o + \sigma_n.\tan\phi$ (see Eqn.1.3.4) is shown in Fig.5.3.2, however the non-linear, concave downwards, normal versus shear stress Mohr envelope clearly implies that a curved relationship may be more appropriate. Accordingly, the procedure of Bland (1983[190]) was used to generate the parabolic plane Griffith failure criterion of the form $\tau^2 = 4\sigma_t.\sigma_n + 4\sigma_t^2$ where σ_t = tensile strength (Griffith[14],[17], see Eqn.1.3.17) from the principal stress data. According to Bland's analysis, a proposed form of Mohr's (1900[7]) failure criterion ($\tau = [a.\sigma_n + b]^n$; $a, b \geq 0$; $0 < n \leq 1$) is shown to reduce, under certain conditions, to several classical failure criteria, the failure envelopes of which can then be determined using the method of least squares. Using Bland's analysis, σ_t values were calculated from the experimentally determined principal stress data, so that from Eqn.1.3.17 Griffith failure envelopes could be generated for specific values of σ_n, as shown in Fig.5.3.2. Tensile strength, σ_t, was found to decrease from about 30MPa to 20MPa so that Griffith "cohesion" (shear stress intercept magnitude) is also seen to decrease from 61MPa to 40MPa with addition of the Shell Tellus pore fluid.

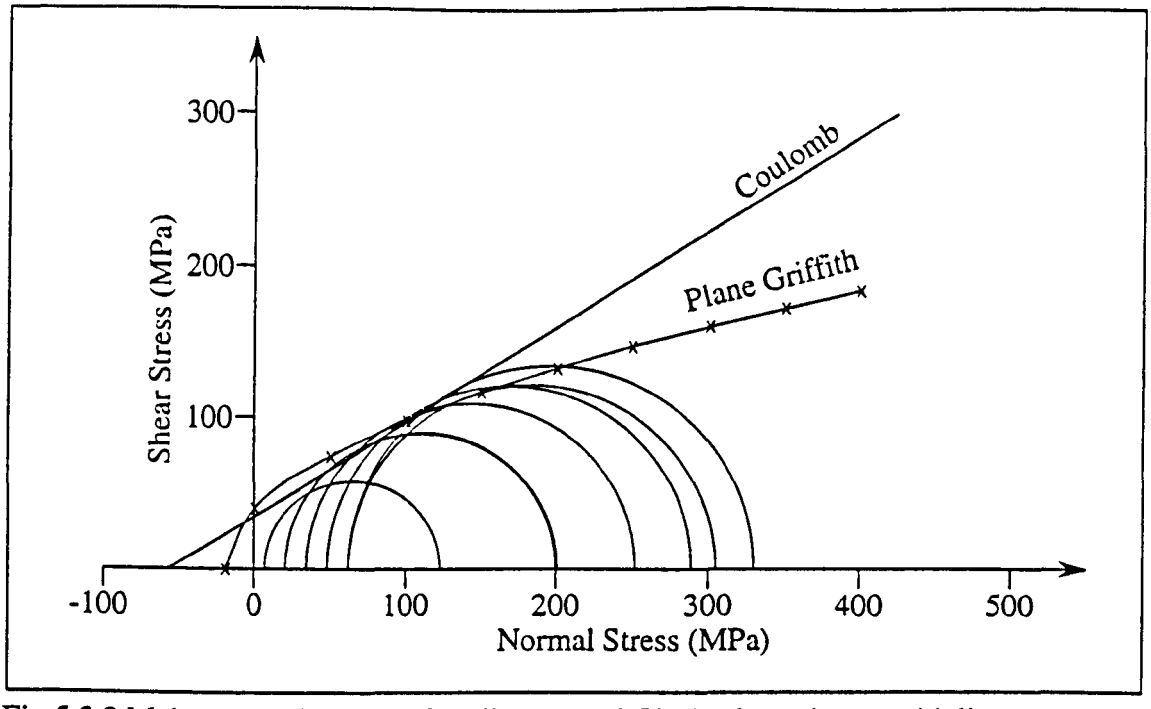

Fig.5.3.2 Mohr stress circle plot for oil-saturated Clashach sandstone with linear Coulomb and parabolic Griffith fracture strength envelopes.

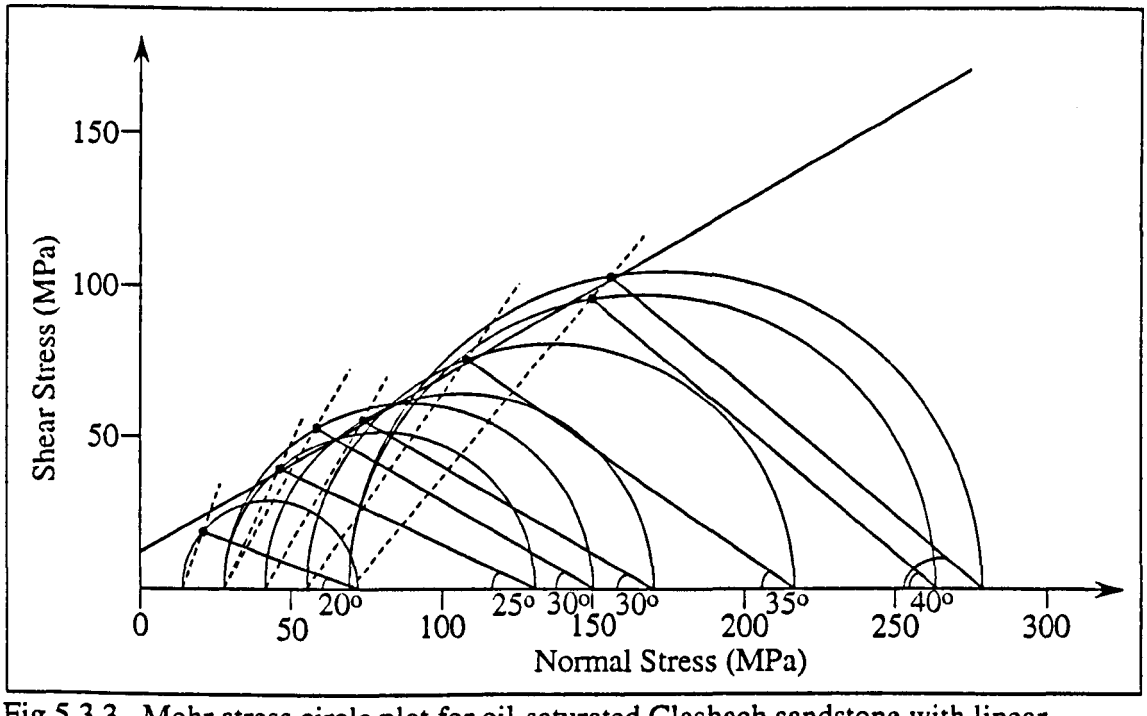

Fig.5.3.3 Mohr stress circle plot for oil-saturated Clashach sandstone with linear Coulomb-type frictional strength envelope for re-shearing.

Ruling out any mechanical effects associated with the pore fluid (pore pressure being equal to atmospheric conditions) the observed sharp drop in fracture strength associated with oil-saturation compared to dry conditions, may be a direct result of stress corrosion (see section 1.4) whereby hydrolytic weakening associated with residual aqueous fluids within pore space serves to weaken strained silicon-oxygen bonds at crack tips, thereby facilitating crack propagation at less than critical stress intensities. Therefore, despite the permeant (refined mineral oil) being chemically inert, stress corrosion may be an operative mechanism, allied to minor amounts of water retained in the specimens despite the best experimental oven-drying and vacuum oil-impregnation procedures. It has been widely observed, especially in quartz-rich rocks but also in limestone, that water, including even that adsorped from a humid atmosphere, has a specific weakening effect relative to behaviour after careful drying (see for example Rutter, 1972[191]). Alternatively, it is also feasible that the reduction in strength/hardness may be adsorption-induced, and thus attributable to a phenomenon known as the "Rehbinder effect" in recognition of Rehbinder's first observation (Rehbinder, 1928[192]). Ishido & Mizutani (1980[193]) found that the ζ-potential at the rock/aqueous solution interface (the ζ (zeta)-potential is an electric potential across the solid/liquid interface) had a strong effect on the uniaxial compressive strength of quartz diorite, strength reduction being largest around the zero ζ-potential, although they could offer no conclusion with regard to the actual mechanism responsible for the observed ζ-potential correlation.

In addition to fracture strength, friction strength was also analysed using a Mohr stress circle plot, however the resultant strength criterion is NOT an envelope to the series of Mohr circles, as failure is not free to develop in the most critical orientation but is constrained to occur along the fault at angle θ = fault^σ_1. The appropriate analysis follows that as outlined in Goodman[95], pages 160-163. Using this procedure, a focus is located on the right-hand-side of the Mohr stress circle at the point (σ_1, 0). The normal and shear stresses on the fault plane corresponding to the principal stresses at peak load are then found by drawing a line from this focus at an angle θ to the horizontal normal stress axis, to pierce the periphery of the Mohr stress circle (alternatively make an angle

θ with the vertical from a focus on the left-hand-side of the circle at the (σ_3, 0) point). Thus the series of discrete residual triaxial compression tests conducted on the seven oil-saturated Clashach samples at different normal stresses yield a series of (σ_n, τ) points through which a failure criterion can be drawn. Fig.5.3.3 shows a straight-line criteria constructed in such a manner for re-shearing conditions, generated using a linear regression analysis "best-fit" technique. By analogy with the linear Coulomb-type frictional strength criterion given in Eqn.3.5.5, little or no difference was evident between the initial residual sliding and the re-shearing under increased confining pressure envelopes (S_o = 11MPa as opposed to 12MPa and μ_s = 0.59 by comparison with 0.58 respectively). The magnitudes of these frictional constant values should be compared with those generated by direct shear testing under zero confinement and comparatively much lower axial stress conditions (Table 3.5.3.1). Thus it is apparent that, under triaxial compressive stress conditions, and despite shear fracture strength exhibiting a marked curved Mohr envelope, shear friction strength shows an equally pronounced tendency towards a linear Mohr envelope, just as found experimentally for the direct shear testing experimental programme, conducted on a variety of rock types.

Calculation of the variable coefficient of friction, $\mu^*=\tau/\sigma_n$, for the seven discrete triaxial stress states associated with residual sliding and re-shearing stress conditions, shows μ^* decreasing from about 1.0 to around 0.7 with increasing normal stress. Hence, again, and just as concluded from the direct shear testing programme, Amonton's law is shown to be invalid, probably due to frictional wear and surface damage affecting the resistance to further sliding. The empirically derived linear frictional strength criterion, with slope and intercept constants μ_s and S_o respectively, can be used to rationalise this inapplicability of Amonton's law as follows. By dividing the linear friction law of Eqn.3.5.5 throughout by σ_n to define the variable coefficient of friction, μ^*, as defined by Eqn.3.5.2, gives:

$$\mu^* = \tau/\sigma_n = \mu_s + S_o/\sigma_n \quad \text{.....} \quad \text{Eqn.5.3.1}$$

Whilst at very high normal stress the error introduced by neglecting the second term may be small, at low normal stress it can lead to considerable error.

Fault inclination, θ, is observed to increase systematically from 20° to 40° with increasing confining pressure, σ_3, as shown in Fig.5.3.4, and is reflected in a corresponding change in elliptical fault area with σ_3, fault area being determined from a surface trace using a digital planimeter (Fig.5.3.5). This θ versus σ_3 relationship, a well-known one in experimental rock mechanics, is readily understood through consideration of the form of the empirical fracture strength criterion exhibited by oil-saturated Clashach sandstone (see the discusson of shear fracturing in Paterson[9] pages 24-28). Consideration of the peak principal compression magnitudes to achieve fracturing under the range of specified confining pressures applied to the Clashach specimens, has shown that triaxial compression strength conforms to a curvilinear Griffith-type failure criterion as opposed to a linear Navier-Coulomb type relation between principal stresses at failure. Whilst frictional sliding strength is seen to conform to a linear Coulomb-type strength law, fault orientation is, however, determined by the form of the fracture envelope. As implied by the Mohr fracture theory (failure occurs on a given plane when τ and σ_n on it satisfy a relation $\tau = f\{\sigma_n\}$ where the function f is non-explicit) the shear failure surface is usually observed to have an orientation, θ, roughly equal to $(45-\phi/2)^\circ$ where $\tan\phi$ (equal to the "coefficient of internal friction" in the particular Coulomb case) is the slope of the Mohr envelope (see Eqn.1.3.10). Thus, as noted by Price & Cosgrove[26], pages 26-27 for a parabolic "concave-downwards" Griffith-type failure envelope, ϕ decreases and thus θ increases with increasing confining pressure, σ_3. This dependency of the plane of fracture inclination on the applied stress state has important consequences with respect to theoretical estimates of shear fracture permeability, and will be discussed further in section 5.4.2.

5.4 PERMEABILITY RESULTS

Four discrete pseudo pulse decay permeability measurements were recorded for each triaxial compression test corresponding to hydrostatic, fault nucleation, slip weakening

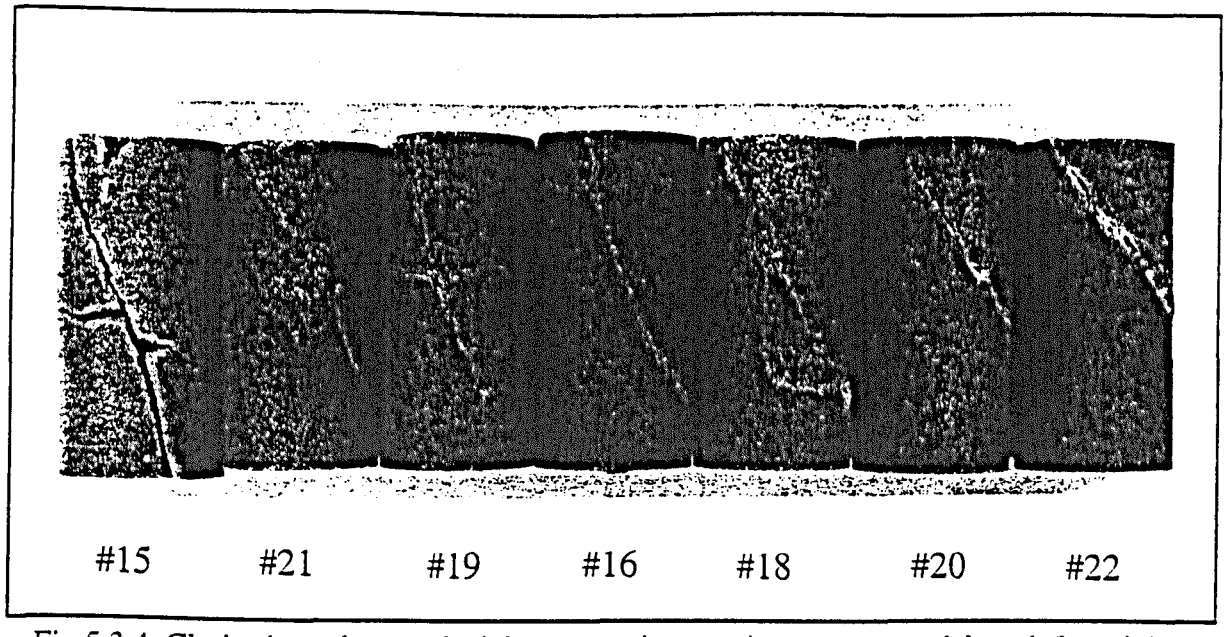

Fig.5.3.4. Clashach sandstone triaxial compression specimens, arranged from left to right in order of increasing confining pressure, to illustrate the attendant increase in fault angle.

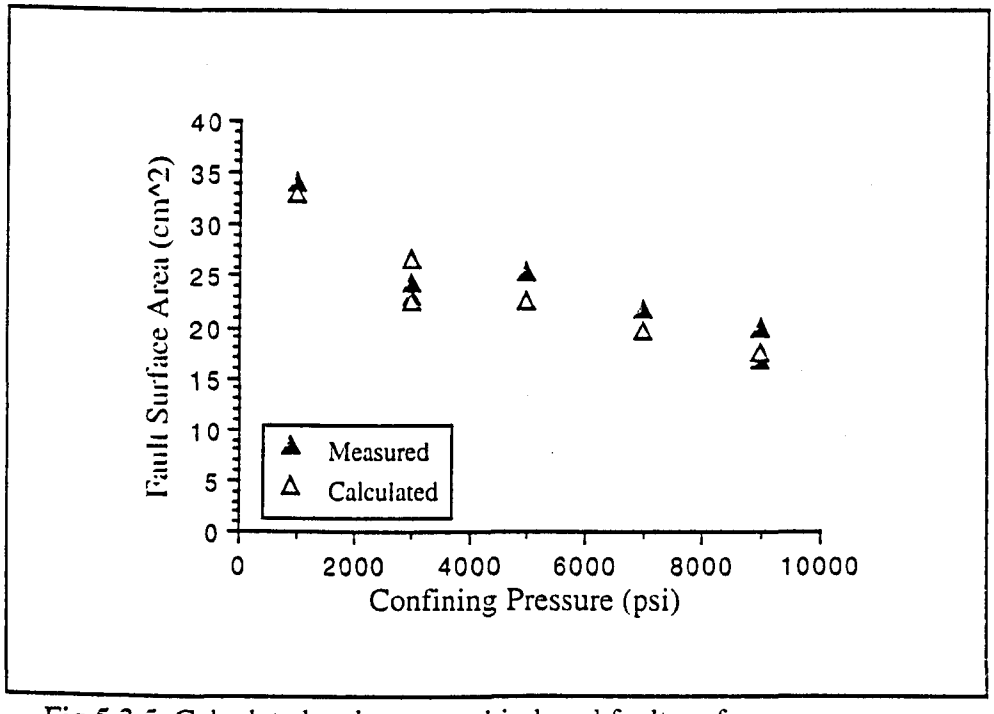

Fig.5.3.5. Calculated and measured induced fault surface areas versus confining pressure operative at macroscopic fracture.

and strength enhanced recovery stress states. Each was recorded under constant stress conditions achieved through servo-control of the confining pressure and by holding the axial load constant under displacement control. The permeability equipment configuration, experimental method and underlying physics are as outlined in section 4.3.1. Each Clashach core plug was tested under "drained" triaxial conditions, that is with an external pressure source connected continuously to the pore system of the rock with the aim of maintaining constancy of pore pressure by introducing or removing fluid. In the Clashach sandstone test programme the downstream end of each core plug was left open to the atmosphere, so that pore pressure was equivalent to a constant atmospheric pressure. Such drained conditions (rock specimen in continuous contact with the pore fluid reservoir, with permeability being sufficient to enable pore pressure to remain constant and uniform even on specimen deformation) are in direct contrast to "undrained" conditions, in which the specimen is saturated and then isolated from the pore fluid reservoir, so that changes in pore pressure will be induced by changes in porosity accompanying deformation. As noted in section 4.3.1, a metering pump was used to apply a pressure pulse of about 30psi to the upstream end of the core, at a constant flow rate equivalent to $0.15ccs^{-1}$. Transient pressure pulse decay across the sample was measured using a differential pressure transducer, whilst an x-y-t chart recorder provided simultaneous hardcopy of the Δp-time curve. Numerical integration of the pressure decay curve over the appropriate real time interval is achieved without defining its explicit function, by measuring the area under the hardcopy curve using a digital planimeter. The system compressibility constant, C, was determined experimentally to be $2.59 \times 10^{-11}\ m^3Pa^{-1}$, by measuring pressure change associated with injecting known volumes of permeant into the upstream reservoir. It should be noted that the value of C is dependent on the permeant used. Viscosity of the pore fluid, a refined mineral oil (Shell Tellus 15) was measured at room temperature, using a Brookfield dynamic viscometer, at 18×10^{-3}Pasecs (18cP). Specimen lengths and cross-sectional areas were measured using digital callipers, however only change in length was corrected on specimen deformation.

5.4.1 Permeability Data

Discrete, pulse-decay, axial permeability values, measured at hydrostatic and at post-dynamic failure stresses, are shown plotted against the appropriate measured axial microstrain in Fig.5.4.1.1(a). Four permeability values as discussed above, for each of the seven Clashach core plugs tested under differing confining pressures, are recorded in this plot. The same data is alternatively presented in Fig.5.4.1.1(b) in which post-fracturing permeability values are normalised as percentages with respect to the appropriate initial measurements taken under hydrostatic conditions, and plotted against percentage specimen shortening. From these graphs it is evident that. for all specimens, axial permeability progressively decreases from immediate fault formation to post-frictional sliding to post-re-shearing conditions. These decreases appear to be broadly non-linear. With regard to between-sample variation, reduction in absolute permeability magnitudes appears to increase with increasing confining pressure (a) however percentage permeability reductions (b) show a non-systematic variation with increasing confining pressure.

Obviously, before any analysis can be made pertaining to possible mechanisms of permeability reduction, it is vital to ascertain the magnitude of experimental uncertainty associated with the permeability calculation, as the pseudo-pulse decay method is a new one, and the number of specimens tested is statistically small. Only once the experimental error has been quantified with respect to the measured change in permeability, can the measured variation be confidently accepted as being physically meaningful. Accordingly, error analysis proceeded as follows, based on the method of combining component errors in overall system-accuracy calculations, as outlined in Doebelin (1975)[194]. The permeability measurement system can be considered as a chain of components, each being subject to individual inaccuracy. Thus from the permeability experiment, the results or measurements from several different instruments are used to compute the actual permeability quantity. How is the overall inaccuracy in the computed permeability value calculated from the individual component inaccuracies ? To answer

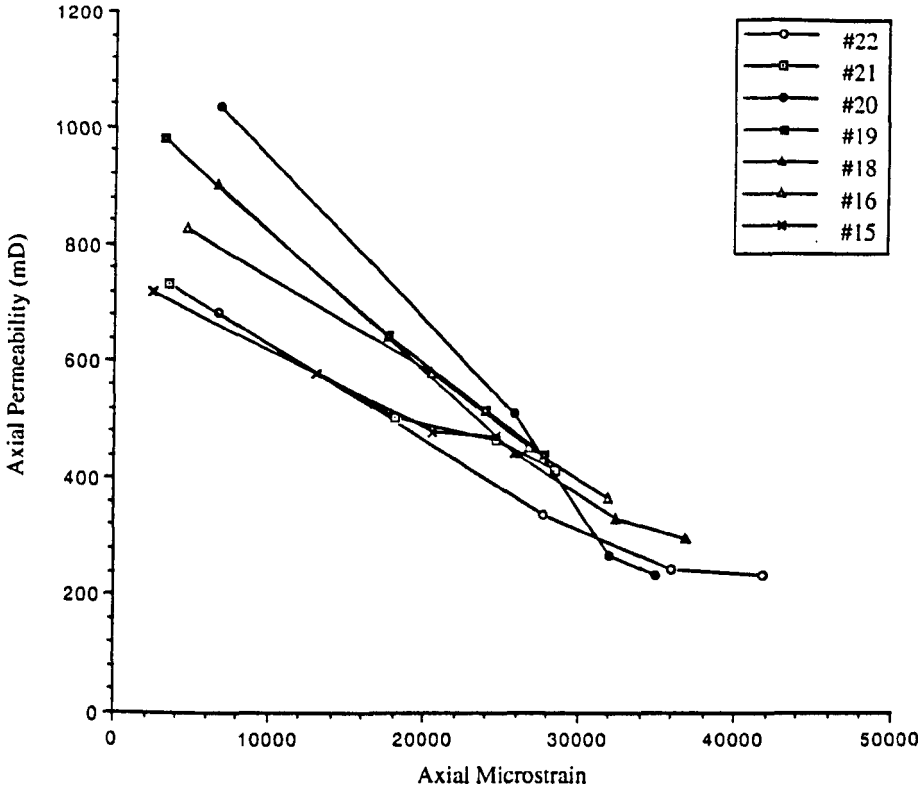

Fig.5.4.1.1(a) Axial permeability versus axial microstrain for Clashach triaxial tests

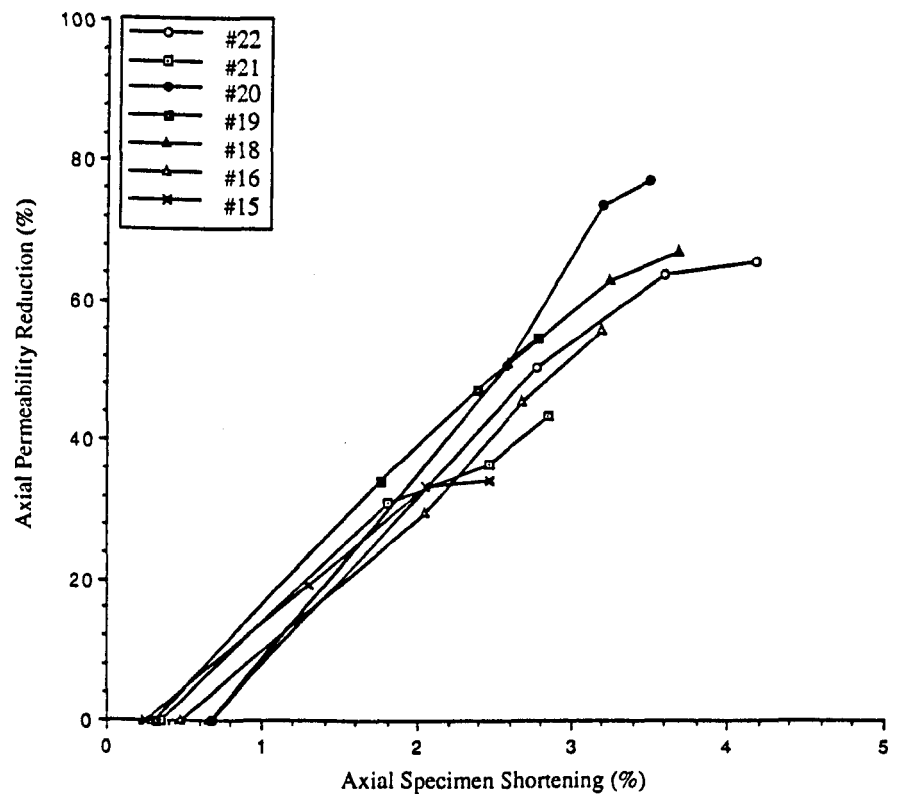

Fig.5.4.1.1(b) Percentage permeability reduction versus percentage specimen shortening for Clashach triaxial tests

this question, consider the problem of calculating a quantity N, where N is a known function of the n independent variables, $u_1, u_2, u_3, \ldots\ldots\ldots, u_n$:

$$N = f(u_1, u_2, u_3, \ldots\ldots\ldots, u_n) \quad \ldots\ldots\ldots \quad \text{Eqn.5.4.1.1}$$

From Eqn.4.3.1.4 the u's are the measured quantities (instrument or component outputs) u_C, u_μ, u_A, u_L, $u_{\Delta p}$ and u_x, and are in error by $\pm u_C$, $\pm u_\mu$, $\pm u_A$, $\pm u_L$, $\pm u_{\Delta p}$, $\pm u_x$ respectively, where C = system compressibility, μ = permeant viscosity, A = specimen cross-sectional area, L = specimen length, Δp = pressure drop across core in specific time interval $t_2 - t_1$, and $x = \int_{t_1}^{t_2} \Delta p dt$. These errors will cause an error ΔN in the computed result N, where N is the pseudo-pulse decay permeability, k. The Δu's can be considered as absolute limits on the errors, as statistical bounds or as uncertainties on which we are willing to give certain odds as including the actual error. However, the method of computing ΔN and the interpretation of its meaning are different depending on the nature of Δu. If the Δu's are considered as absolute limits on the individual errors, then to calculate absolute limits on the error in N requires:

$$N \pm \Delta N = f(u_1 \pm \Delta u_1, u_2 \pm \Delta u_2, u_3 \pm \Delta u_3, \ldots\ldots\ldots, u_n \pm \Delta u_n) \quad \ldots\ldots\ldots \quad \text{Eqn.5.4.1.2}$$

By subtracting N in Eqn.5.4.1.1 from $N \pm \Delta N$ in Eqn.5.4.1.2, $\pm \Delta N$ can be obtained. This procedure is, however, needlessly labour intensive, so that Doebelin recommends an approximate solution, valid for engineering purposes, which can be obtained through application of the Taylor series. Thus, the absolute error, E_a, can be obtained from:

$$E_a = \Delta N = \left|\Delta u_1 + \frac{\partial f}{\partial u_1}\right| + \left|\Delta u_2 + \frac{\partial f}{\partial u_2}\right| + \ldots\ldots\ldots + \left|\Delta u_n + \frac{\partial f}{\partial u_n}\right| \quad \ldots\ldots\ldots \quad \text{Eqn.5.4.1.3}$$

The absolute value signs are used because some of the partial derivatives might be negative, so that for a positive Δu, such a term would reduce the total error, which is obviously inadmissible. Since an error Δu is just as likely to be positive as negative, to estimate the maximum possible error the absolute-value sign must be used. The form of Eqn.5.4.1.3 is very useful, since it shows which variables (u's) exert the strongest influence on the accuracy of the overall result. For example, if $\partial f/du_3$ is large compared with the other partial derivatives, this means that a small Δu_3 can have a large effect on the total error, E_a. The relative or percentage error is given by:

$$E_r = \Delta N / N \times 100 = 100 E_a / N \quad \ldots\ldots\ldots \quad \text{Eqn.5.4.1.4}$$

The calculated result can therefore be expressed as either $N \pm E_a$ or $N \pm E_r\%$, interpreted by Doebelin to mean that, it is *certain* that this error will not be exceeded.

However, when the Δu's are not considered as absolute limits of error, but rather as statistical bounds or uncertainties, the formulas given above for calculating overall errors must be modified. Scarborough (1965)[195] shows that the proper method of combining such errors is according to the root-sum-square (rss) formula:

$$E_{a_{rss}} = \sqrt{\left(\Delta u_1 + \frac{\partial f}{\partial u_1}\right)^2 + \left(\Delta u_2 + \frac{\partial f}{\partial u_2}\right)^2 + \ldots\ldots\ldots + \left(\Delta u_n + \frac{\partial f}{\partial u_n}\right)^2} \quad \ldots\ldots\ldots \quad \text{Eqn.5.4.1.5}$$

Eqn.5.4.1.5 gives a smaller value of error than Eqn.5.4.1.3. Using this method of "adding in quadrature", the uncertainties associated with each of the component variables required for the calculation of permeability were evaluated. Uncertainties in the measured quantities were thus computed as, $u_C \pm 5\%$, $u_\mu \pm 1\%$, $u_A \pm 0.2\%$, $u_L \pm 0.1\%$, $u_{\Delta p} \pm 5\%$, $u_x \pm 7\%$. The relatively large uncertainties associated with the last two components are due to the fact that these measurements were scaled off the chart recorder hardcopy pulse-decay curve. Using the measured quantities and their associated

uncertainties, and solving the partial derivatives in Eqn.5.4.1.3 and Eqn.5.4.1.5 respectively, allows calculation of the absolute errors E_a and $E_{a(rss)}$ (or relative errors E_r and$E_{r(rss)}$ following Eqn.5.4.1.4) for each calculated permeability value. Thus choosing to consider the component errors as absolute errors gives $k \pm E_r = k \pm 18\%$, whilst assuming the individual errors to be uncertainties in the measurement of each component gives $k \pm E_{r(rss)} = k \pm 10\%$. Thus $E_{r(rss)}$ is significantly smaller than E_r. Following Doebelin[194], this is interpreted to mean that whilst the error is *possibly* as large as 18%, it is *probably* not larger than 10%. Tabulated permeability values and their associated errors, $E_{a(rss)}$, are given in Table 5.4.1.1, along with the applied stress conditions and sliding displacements at which each was measured. From this it is evident that sliding displacement, δ s (calculated from $\delta s = \delta l / \cos\beta$, where δl = axial displacement and β = fault^σ_1) remains fairly constant from test to test, whilst the main variable appears to be applied stress. In particular, striking linear relationships between axial permeabilities and resolved normal stresses across induced fault surfaces are obtained, as shown in Fig.5.4.1.2. The shear stress, τ, and normal stress, σ_n, may be computed from knowledge of the applied principal stresses σ_1 and σ_3, and of fault inclination with respect to the direction of maximum compression, θ = fault^σ_1, using the well-known biaxial stress equations (for example Byerlee[160]). In graph (a) initial permeabilities are plotted against the applied hydrostatic stress conditions whilst immediate post-faulting permeabilities are plotted against resolved normal stress magnitudes. Whilst in the former a wide scatter is evident (testament to the relatively stress-insensitive, high-porosity open microstructure of Clashach sandstone, for which increasing hydrostatic stress only results in elastic pore closure with little or no effect on connectivity) in the latter, the effect of shear fracture formation is evidently to immediately induce a normal stress-dependent permeability reduction. Graph (b) shows similar results for residual sliding and re-shearing under increased strength conditions, from which it is evident that, for each case, permeability shows a strong linear reduction with increasing normal stress, both relationships possessing high correlation coefficients. Whether the permeability-normal stress dependence is truly linear, or just a function of the small sample size is not known, so that the relationship may become non-linear at higher stress.

I.D.	Hydrostatic stress:		Post-dynamic failure:		Post-initial residual sliding:					Post-re-shearing under increased confinement:				
	k_{axial} (mD)	E_a (mD)	k_{axial} (mD)	E_a (mD)	k_{axial} (mD)	E_a (mD)	δ_s (mm)	τ (MPa)	σ_n (MPa)	k_{axial} (mD)	E_a (mD)	δ_s (mm)	τ (MPa)	σ_n (MPa)
#15	720	132	580	106	480	88	0.67	11.44	11.06	473	87	1.02	18.61	20.57
#16	829	152	583	107	453	83	0.59	48.19	62.32	366	67	1.06	55.94	73.69
#18	905	166	443	81	332	61	0.82	69.91	97.24	297	54	1.01	75.83	108.28
#19	983	180	647	118	520	95	0.66	45.37	46.89	445	81	1.00	53.12	58.26
#20	1037	190	512	94	272	50	0.72	91.39	138.76	235	43	1.03	95.87	149.32
#21	735	135	509	93	469	86	0.60	32.71	35.95	417	76	0.93	39.56	46.04
#22	685	125	340	62	247	45	0.95	91.44	138.80	234	43	1.55	103.35	155.60

Table 5.4.1.1. Tabulated permeability (k_{axial}) and associated absolute errors (E_a), stress states (τ, σ_n) and sliding displacements (δ_s) for the seven Clashach triaxial compression experiments.

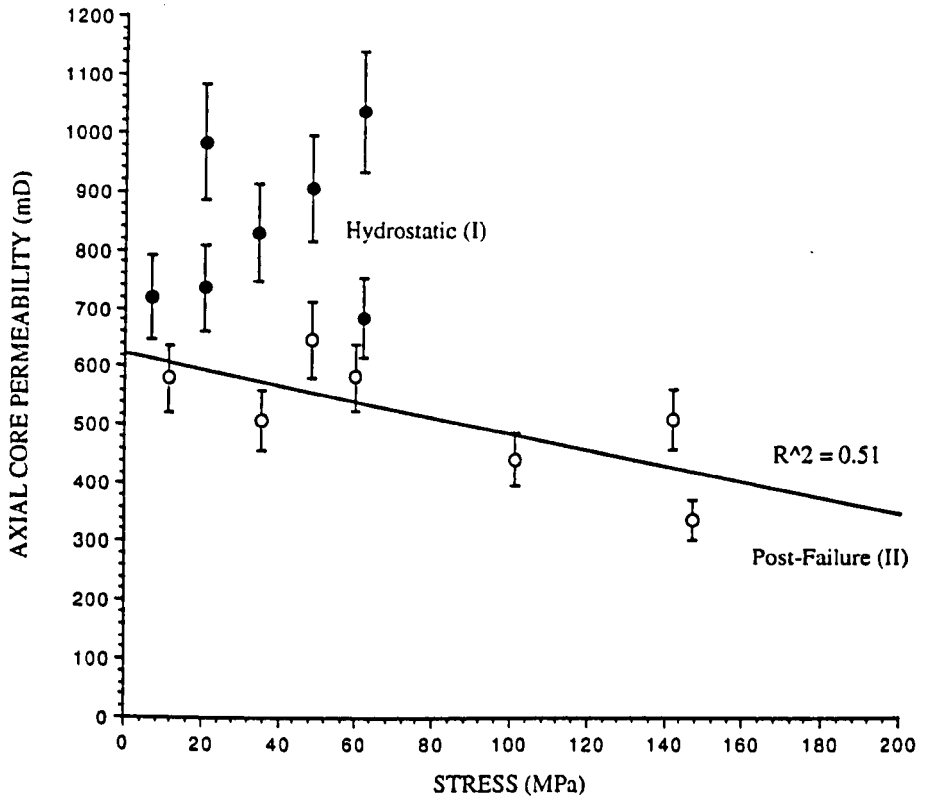

Fig.5.4.1.2(a) Axial permeability versus (I) hydrostatic stress and (II) resolved normal stress post-dynamic failure.

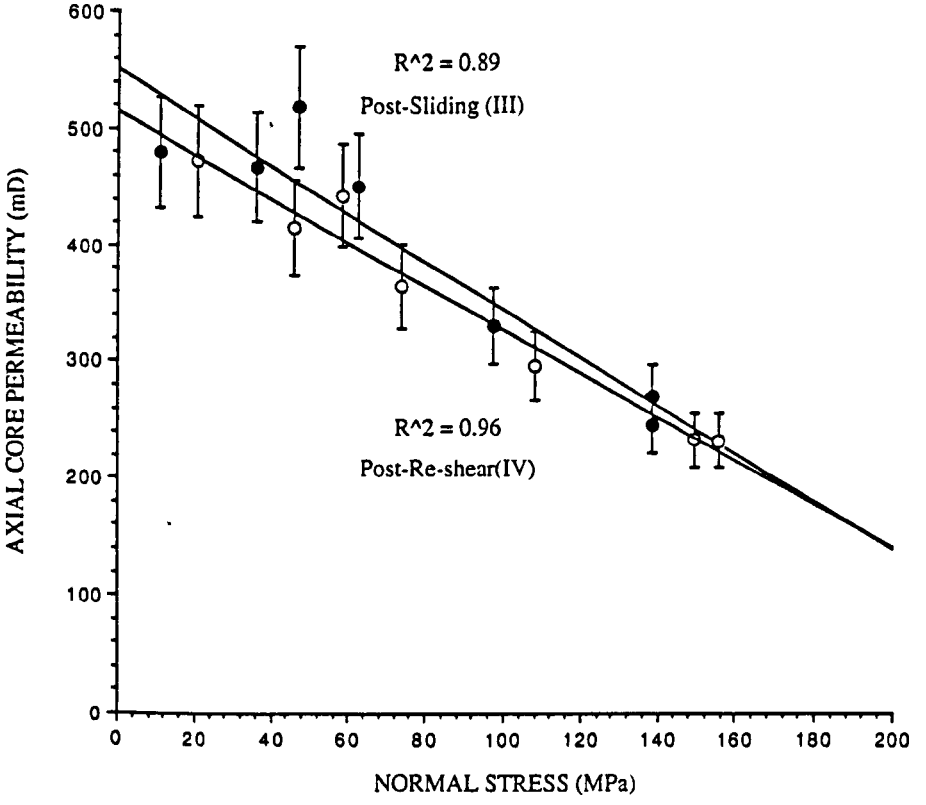

Fig.5.4.1.2(b) Axial permeability versus resolved normal stress (III) post-frictional sliding and (IV) post-re-shearing.

It is evident, however, that the effect of increased frictional sliding (post-dynamic failure with little or no shear displacement, to frictional sliding, to re-shearing conditions) in this test programme has been to progressively reduce permeability. Further, it is inferred that the associated generation of frictional wear debris (fault gouge) from the displaced fracture walls, has produced a granular shear band (in many respects morphologically similar to a natural granulation seam) oblique to the direction of fluid flow, which under increased stress (and being particularly susceptible to normal stress acting perpendicular to the fracture zone) has provided a normal stress-sensitive granular baffle responsible for the observed decrease in axial permeability measurements. In Chapter 6, this relationship will be further examined through particle-size analysis of the collected fault gouge samples, whilst in the discussion below, the potential of variable fault inclination to influence axial permeability measurements is also assessed.

5.4.2 Discussion

As noted in section 5.3, due to the non-linear failure envelope appropriate to Clashach sandstone, the angle θ = fault^σ_1 shows a steady increase with increasing σ_3. One important consequence of such a stress-dependent fault inclination already mentioned, is that induced fault area subsequently decreases in a remarkably linear fashion as σ_3 increases (Fig.5.3.5). Were the failure envelope truly linear as in the conventional Coulomb sense, then observed changes in axial permeability could positively be ascribed to either differences in applied stress, resultant slip displacements or microstructural alteration (or combinations of all three). However, this disparity in fracture inclination/elliptical area between test specimens in effect represents yet another test variable with the potential to have a systematic influence on axial permeability measurements over the core lengths. It is thus desirable to conduct a semi-quantitative analysis of the relative control that such a variation in fracture area might have on fluid flow, before commenting on permeability variation as a direct function of gouge evolution.

A very simple method for estimating the permeability of an inclined shear fracture induced under triaxial compression of a cylindrical specimen, from conventional axial permeability measurement conducted on the host core plug, is outlined below. This incorporates fracture plane area, and hence allows for between-specimen differences in induced fracture inclination. Two main, and rather limiting assumptions which tend to restrict application of the basic analysis are that:

(i) the permeability of the shear band is very much less than the permeability of the stressed rock-matrix forming the two specimen halves

(ii) the shear fracture conforms to a shear band geometry with finite and uniform thickness

The implication of condition (i) is that virtually all the pressure drop measured across the specimen is in fact occurring across the shear band:

$$k_{fault} << k_{core} \quad \text{.....} \quad \text{Eqn.5.4.2.1}$$

$$\therefore \Delta p_{fault} \approx \Delta p_{core} \text{ (measured)} \quad \text{.....} \quad \text{Eqn.5.4.2.2}$$

This experimental arrangement is shown in Fig.5.4.2.1, in which a constant pressure exists from the upstream-end of the core to the shear band, a pressure drop across the fault zone, and a lesser constant pressure to the downstream end of the core. From Eqn.4.3.1.4 for the pseudo-pulse decay permeability test, rearranging gives:

$$\Delta p_{core} = (k_{core}.A_{core}.\int_{t_1}^{t_2} \Delta p dt) / (C.\mu.L) \quad \text{.....} \quad \text{Eqn.5.4.2.3}$$

$$\Delta p_{fault} = (k_{fault}.A_{fault}.\int_{t_1}^{t_2} \Delta p dt) / (C.\mu.\varepsilon) \quad \text{.....} \quad \text{Eqn.5.4.2.4}$$

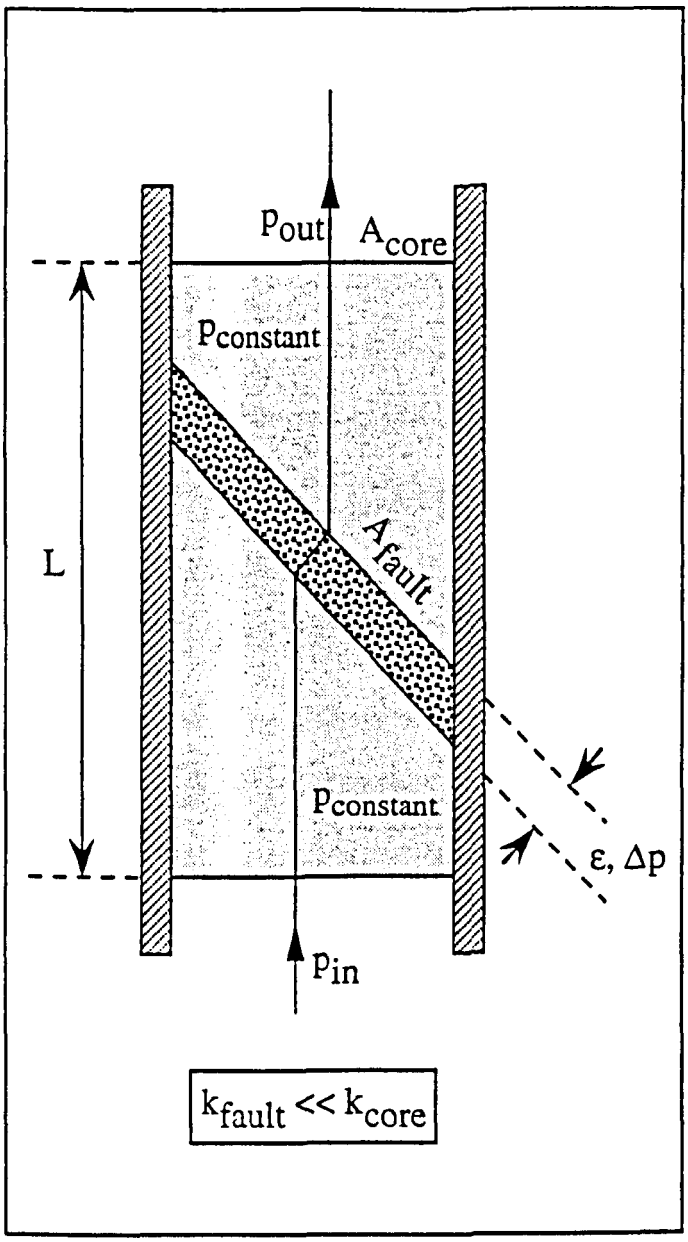

Fig.5.4.2.1. Schematic illustration of faulted core with shear band inclined to axial flow direction.

where the core possesses: permeability, k_{core}

cross-sectional area, A_{core}

length, L

the shear band possesses: permeability, k_{fault}

elliptical area, A_{fault}

thickness, ε

Substituting Eqn.5.4.2.3 and Eqn.5.4.2.4 into Eqn.5.4.2.2, rearranging and cancelling results in an expression for the measured axial permeability of the core specimen, in terms of the shear band permeability per unit thickness, multiplied by a geometrical factor which incorporates the fault surface area:

$$k_{core} = \left(\frac{L.A_{fault}}{A_{core}}\right).\left(\frac{k_{fault}}{\varepsilon}\right) \quad \text{.....} \quad \text{Eqn.5.4.2.5}$$

Obviously the most important insight gained from the above analysis is that measured $k_{core} = f(A_{fault}, k_{fault}, 1/\varepsilon)$ however, unfortunately, the experimental methodology adopted for this series of triaxial compression tests does not allow direct quantification of shear band permeability from measured plug permeability, as ε cannot be measured or calculated to any accuracy. Whilst ε could be estimated by thin-sectioning of resin impregnated specimens, this method was precluded by the desire, instead, to sample the non-indurated experimental fault gouge for particle-size analysis. However Eqn.5.4.2.5 does allow individual assessment of the influence of the geometric factor, "G", defined as $G = (L.A_{fault} / A_{core})$, on measured k_{core}, and to determine an order of magnitude value for k_{fault}. Fig.5.4.2.2(a) illustrates an inverse linear correlation between this geometric constant, G, and the resolved normal stress across each of the induced shear fractures. Error bars shown were calculated using the "method of adding in quadrature" as outlined above, with an estimated uncertainty in the measurement of fault inclination of $\pm 5^{o}$ due to the relative waviness of the fault surfaces. Fig.5.4.2.2(b) shows a linear

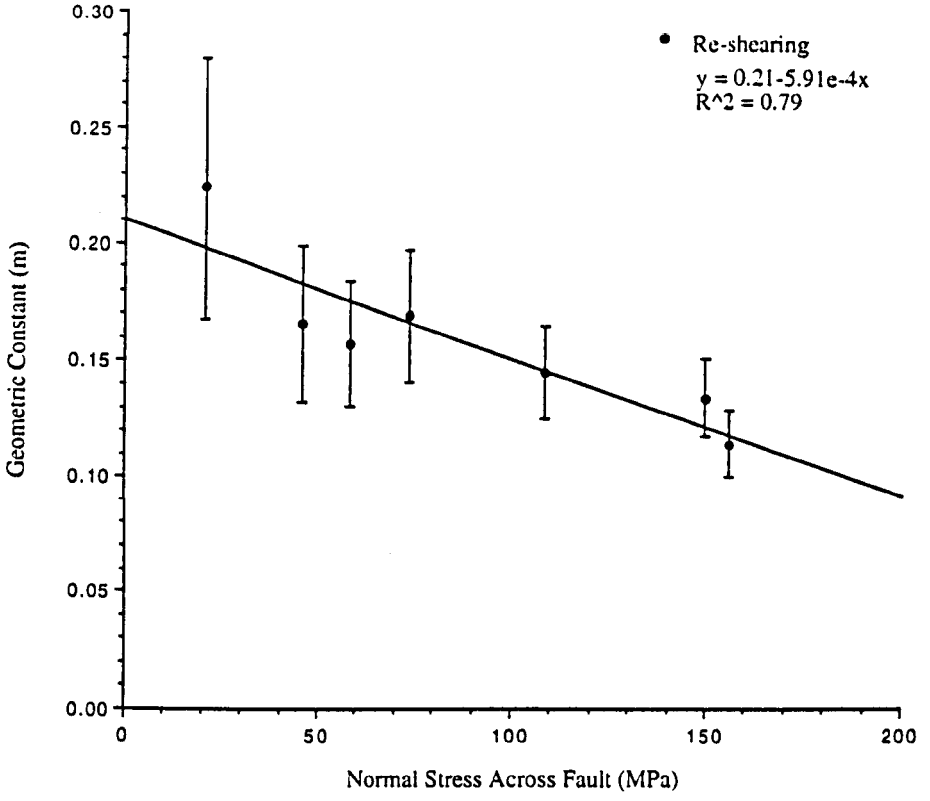

Fig.5.4.2.2(a) The influence of normal stress on the geometric constant "G" for Clashach triaxial specimens.

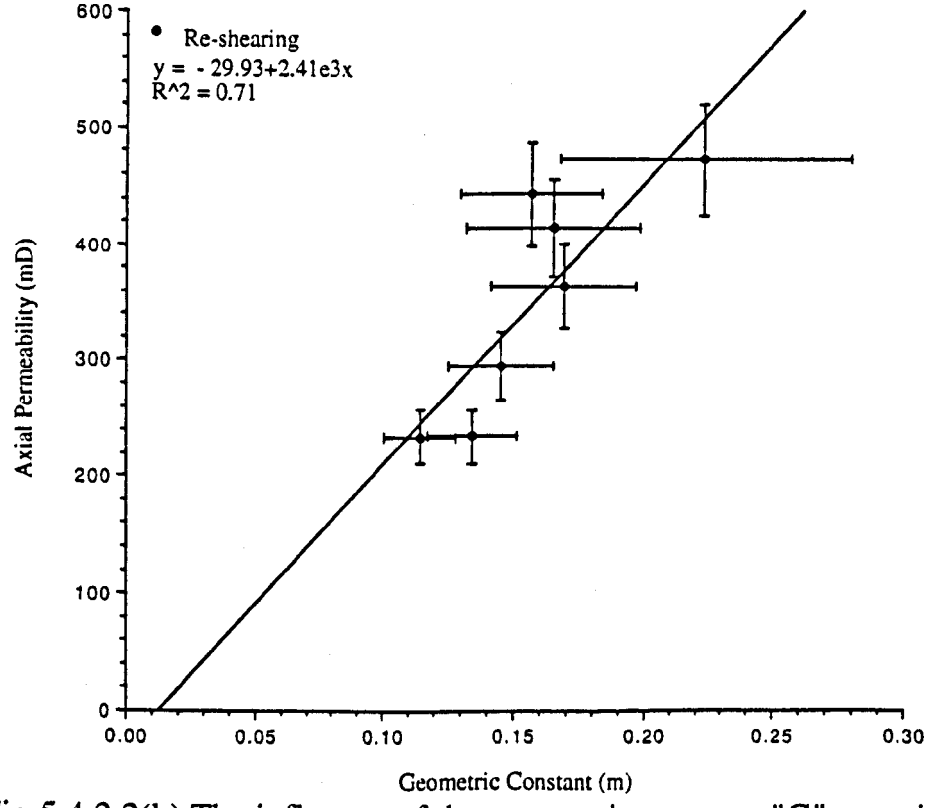

Fig.5.4.2.2(b) The influence of the geometric constant "G" on axial permeability for Clashach triaxial specimens.

relationship between the measured axial permeability, k_{core}, and the geometric constant, G. These empirically determined variations, $G \propto 1/\sigma_n$ and $k_{core} \propto G$, suggest that the observed inverse linear correlation's between measured axial plug permeabilities and resolved normal stress across the induced faults (see Fig.5.4.1.2) $k_{core} \propto \sigma_n$, are influenced by variable fault plane inclination, imparting a stress-dependency to the geometric constant, G. Thus it is apparent that the effect of a non-linear failure envelope on θ = fault^σ_1 is being reflected in the measured k_{core}. However, the lower correlation coefficient for the normal stress-dependency of G ($R^2 = 0.79$) compared with that for k_{core} ($R^2 = 0.96$) does suggest that an additional structural contribution to the axial permeability stress-sensitivity, perhaps due to fault gouge, also exists.

In the above analysis, only data relating to the process of re-shearing has been discussed, however it is believed that the same principle (that is the dependency of k_{core} on G) will also apply to post-dynamic failure and residual sliding conditions. The main difference between calculated G-values for these different conditions will lie in estimation of A_{fault}, which strictly speaking will vary with sliding displacement (similar to that given in section 3.4.3 for sliding circles, but for the contact area of overlapping ellipses with displaced centres). However, as the ratio of sliding displacement to semi-major axes length varies in the range of 1 to 3% for the triaxial compression specimens, this minor correction has been ignored, with A_{fault} being taken simply as that calculated from fault inclination, with no shear displacement correction. In Chapter 6, using plausible predictions of fault thickness (ε) variation with increasing confining pressure, estimates are made of k_{fault} for all seven specimens, and relationships explored between these values and resolved normal stress across the shear bands, variation in angular shear strain resulting from thickness and slip displacement differences, and variance between certain sampled fault gouge particle size distribution parameters.

5.5 MICROSEISMIC RESULTS

In this final section, acoustic emission data complimenting the strength and permeability results outlined above, will be reviewed. Prior to this, and in order to aid in digestion of

the AE results and their implications, brief summaries of both fractal set and damage mechanics theories are given in sections 5.5.1 and 5.5.2 respectively. Differential stress and natural AE were measured over three separate phases corresponding to fault nucleation (phase I), frictional sliding (phase II) and fault strengthening (re-shearing under increased confinement, phase III). The AE was interpreted using a mean field theory for damage evolution, in terms of temporal variation in seismic event rate, b-value and the inferred fractal dimension of the AE. Whilst results from the fault nucleation phase confirm other observations of damage evolution leading to failure reported in the literature (see below for pertinent references) AE monitoring for the frictional sliding stages II and III under triaxial compression, and subsequent interpretation of the collected data, represents new work which offers important insights into the physical processes involved. Prior to this study, the only reported incidence of AE monitoring during shearing of rock discontinuities, was that of Li & Nordlund (1990)[196] who reported characteristics of AE resulting from frictional sliding, of both artificial and natural sliding surfaces in granite and slate samples, under direct shear (unconfined, constant normal stress) conditions. Their test results indicated that the AE rate peaks coincided with the stress drops caused by fracturing of asperities during shear. When the discontinuity surface became smooth, the strength reached a residual value, the shear stress drops became larger and less frequent, and the AE count rate declined. The AE intensity was seen to depend on both the roughness and the compressive strength of the discontinuity surface. Ideally, perhaps what is required is a combination of the fractal damage mechanics theory used to evaluate the triaxial compression AE data recorded during this present study, with the experimental advantages of large fault surface area, known boundary conditions and significant slip displacements common to the direct shear method of Li & Nordlund.

5.5.1 Definition of a Fractal Set

Prior to a discussion of acoustic emission statistics and also before considering measured fault gouge distributions, it is considered pertinent to provide a brief outline of some of the more essential features underlying the theory of fractals. Mandelbrot (1967)[197]

introduced the concept of fractals. With regard to derivation of the term he noted that, "I coined the term "fractal" from the latin *fractus* which describes the geometry of a broken stone." The adjective "fractus" means irregular or broken. Mandelbrot introduced fractals within the context of scale invariance. The scale invariance of geological phenomena is easily understood when consideration is given to the fact that, without the inclusion of a suitable object of known dimensions to define the scale of observation, such as a hammer a coin or a person, it is often impossible to determine whether a photograph of a geological feature covers a scale appropriate to a thin-section or to a cliff face (mm's or km's). Without inclusion of an object with a characteristic dimension, the scale of the photograph cannot be determined. With recourse to the now classic example of the length of a rocky coastline obtained using a measuring rod with a specified length, due to scale invariance the length of the coastline increases as the length of the measuring rod decreases according to a power law. The power exponent determines the fractal dimension of the coastline, and it is noted that it is not possible to obtain a specific or unique value for the length of the coastline, owing to all the minor indentations down to a scale of mm's or less. Many phenomena relating to shear fracturing are scale invariant. including the frequency-size distributions of acoustic emissions, faults, earthquakes and shear debris (gouge). Thus the fractal dimension provides a powerful tool for describing scale invariant geometries. A fractal distribution requires that the number of objects larger than a specified size has a power-law dependence on the size. However, the empirical applicability of power-law statistics to geological phenomena was recognised long before the concept of fractals was conceived, an example being the Gutenberg-Richter relation for the frequency-magnitude statistics of earthquakes (Gutenberg & Richter, 1954)[198]. Power-laws are of course not the only statistical distributions to be applied to geological processes, other examples being the normal and log-normal distributions, although the power law is the only one not to include a characteristic length scale. Thus the power-law distribution must be applicable to scale-invariant phenomena. Whilst scale-invariance provides a rational basis for the applicability of the power law, fractal distribution, fractal concepts can also be applied to continuous distributions, an example being topography, where the fractal dimension is a

measure of the roughness of the features. Thus fractals are also capable of uniquely describing fault (or joint) surface morphologies for comparative purposes relating to strength and fluid flow studies. In the following section a definition of a fractal set is given, after Turcotte (1992)[199] pages 6-17.

Following Turcotte consider the definition of a fractal set according to:

$$N_n = C/r_n^D \quad \ldots\ldots\ldots \quad \text{Eqn.5.5.1.1}$$

where N_n is the number of objects (fragments) with a characteristic linear dimension r_n, C is a constant of proportionality and D is the fractal dimension. The fractal dimension can be an integer, in which case it is equivalent to a Euclidian dimension. The Euclidian dimension of a point is zero, of a line segment is one, of a square is two and of a cube is three. In general the fractal dimension is not an integer, but a fractional dimension. This is the origin of the term fractal, and its application to irregular (non-Euclidian) geometry is encapsulated in its derivation.

To illustrate why it is appropriate to refer to D as a fractional dimension, consider the line segment shown in Fig.5.5.1.1(a) which is divided into two parts so that $r_1 = 1/2$ and one part retained so that $N_1 = 1$. The remaining segment is then divided into two parts so that $r_2 = 1/4$ and again one segment retained so that $N_2 = 1$. In order to determine D, Eqn.5.5.1.1 can be rewritten in terms of logarithms to the base e as:

$$D = \text{In}(N_{n+1} / N_n) / \text{In}(r_n / r_{n+1}) \quad \ldots\ldots\ldots \quad \text{Eqn.5.5.1.2}$$

Thus for the example considered, $\text{In}(N_2/N_1) = \text{In}1 = 0$, $\text{In}(r_1/r_2) = \text{In}2$, and $D = 0$, the Euclidian dimension of a point. With reference to the examples (b) to (f) also shown in Fig.5.5.1.1: (b) a line segment is divided into three parts and one retained, $D = \text{In}1/\text{In}3 = 0$, the fractal dimension of a point; (c) a line segment is divided into two parts and both

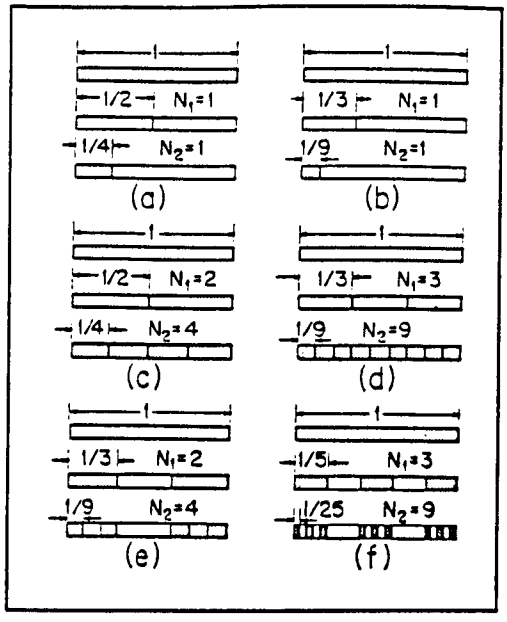

Fig.5.5.1.1 Cantor Dust

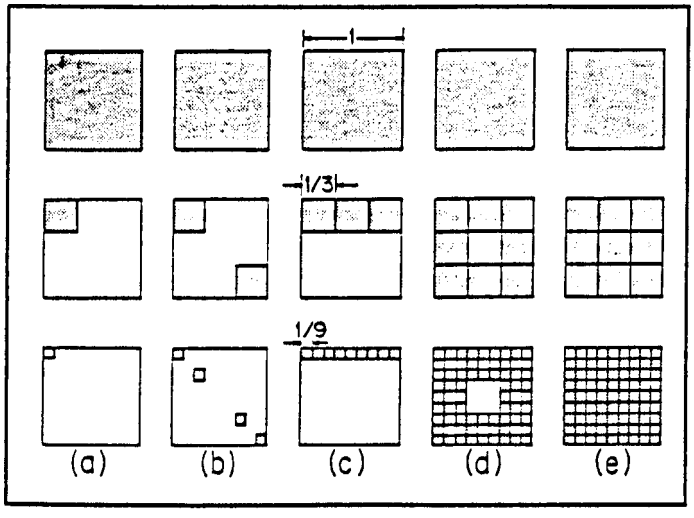

Fig.5.5.1.2 Sierpinski Carpet

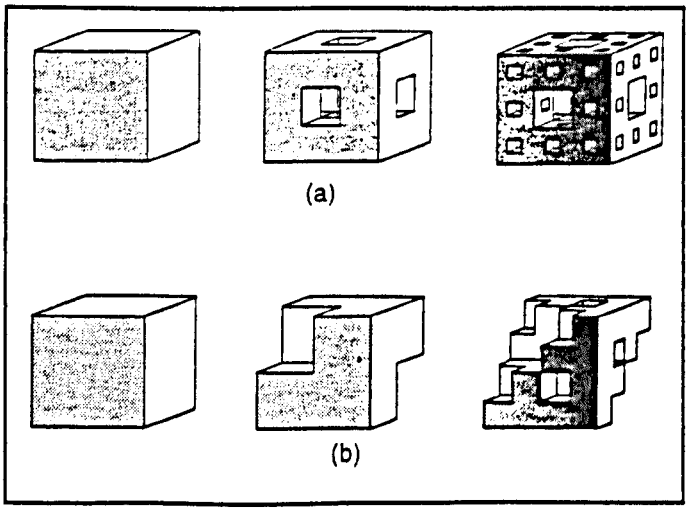

Fig.5.5.1.3 Mengor Sponge

Illustration of fractional dimensions, after Turcotte[199] (see text for details).

retained, D = In2/In2 = 1, the fractal dimension of a line; (d) a line segment is divided into three parts and all three are retained, D = In3/In3 = 1, the fractal dimension of a line; (e) a line segment is divided into three parts and two retained, D = In2/In3 = 0.6309, a non-integer fractal dimension: (f) a line segment is divided into five parts and three are retained, D = In3/In5 = 0.6826, a non-integer fractal dimension. For examples (a) and (b) the construction can be extended to higher and higher orders, but at each order n, $N_n = 1$, so that as the order approaches infinity the remaining line length approaches zero and it becomes a point. Thus the Euclidian dimension of a point , zero, is appropriate. In both cases (c) and (d) the fractal dimension is the Euclidian dimension of a line, appropriate because the remaining segment will be a line segment of unit length as the construction is repeated. However, in examples (e) and (f) the repeated process yields non-integer fractional dimensions between the limiting cases of zero and one, known as Cantor sets. Constructions can be devised to give any fractional dimension between 0 and 1 using the method illustrated. If n iterations are carried out (the nth iteration is referred to as order n) then the line length at the nth iteration, r_n, is related to the length at the first iteration, r_1, by $r_n/r_0 = (r_1/r_0)^n$, thus as $n \rightarrow \infty$, $r_n \rightarrow 0$. In this limit the Cantor set is known as a "dust", an infinite set of clustered points, and the repetitive iteration leading to it as "curdling". The scale invariance of the constructions in Fig.5.5.1.1 is readily apparent.

The fractal concepts applied to the line segment in Fig.5.5.1.1 are applied to a square in Fig.5.5.1.2. At order one the unit square is divided into nine equal-sized smaller squares with $r_1 = 1/3$. At order two the remaining squares are divided into nine smaller equal-sized squares with $r_2 = 1/9$. Five examples are given in Fig.5.5.1.2(a) to (e) in which various numbers of squares, N, are retained: (a) $N_1 = 1$, $N_2 = 1$, D = In1/In3 = 0; (b) $N_1 = 2$, $N_2 = 4$, D = In2/In3 = 0.6309; (c) $N_1 = 3$, $N_2 = 9$, D = In3/In3 = 1; (d) $N_1 = 8$, $N_2 = 64$, D = In8/In3 = 1.8928; (e) $N_1 = 9$, $N_2 = 81$, D = In9/In3 = 2. Construction (e) is known as a Sierpinski carpet. Iterative constructions can be devised to yield any fractal dimensions between 0 and 2 and again each construction is scale invariant.

These examples described above for one and two dimensions can be extended to three dimensions. two examples of which are illustrated in Fig.5.5.1.3(a) and (b): (a) at first order the unit cube is divided into 27 equal-sized smaller cubes with $r_1 = 1/3$, 20 cubes are retained so that $N_1 = 20$. At second order, $r_2 = 1/9$ and 400 out of 729 cubes are retained so that $N_2 = 400$, $D = \text{In}20/\text{In}3 = 2.727$; (b) at first order the unit cube is divided into 8 equal-sized smaller cubes with $r_1 = 1/2$, 6 cubes are retained so that $N_1 = 6$. At second order, $r_2 = 1/4$ and 36 out of 64 cubes are retained so that $N_2 = 36$, $D = \text{In}6/\text{In}2 = 2.585$. These constructions are known as Mengor sponges. Iterative constructions can be devised to yield any fractal dimension between 0 and 3, and again each construction is scale invariant. The Mengor sponge can be used as a model for flow in a porous media with a fractal distribution of porosity.

The statistical number-size distribution for a large number of objects can also be fractal. A specific example is rock fragments (gouge) where, in order for the distribution to be fractal, the number of objects N with a characteristic linear dimension greater than r is required to satisfy the relation:

$$N = C/r^{D} \quad \text{.....} \quad \text{Eqn.5.5.1.3}$$

It is often appropriate to use this cumulative relation rather than the set relation of Eqn.5.5.1.1. Eqn.5.5.1.3 is also appropriate for the frequency-size relation of earthquakes. As a statistical representation of a natural phenomenon, Eqn.5.5.1.3 will be only approximately applicable, with both upper and lower bounds to the range of applicability. Whilst the definition of fractal as fractional dimension is implicit in Fig.5.5.1.1 to Fig.5.5.1.3, the precise meaning of a measured fractal dimension may become less clear when dealing with statistical power-law relations. Some power-law distributions fall within the limits associated with fractional dimensions, that is $0 < D < 3$, whilst others do not, thus an important question is whether or not all power-law distributions that satisfy Eqn.5.5.1.1 or Eqn.5.5.1.3 are fractal. With regard to this question, Turcotte was of the opinion that they are fractal, that is all power-law

distributions fulfilling these criteria, but with D -values outwith the fractional dimension range, should be considered fractal, noting that, "such distributions are clearly scale invariant even if not directly associated with a fractal dimension."

5.5.2 Fractal Damage Mechanics

The concept of a single variable, or set of variables, used to describe the changing state of the microstructure of a material as it is deformed, is referred to as a damage theory. There are three basic elements to any damage theory: a definition of damage; an evolutionary equation for the damage; a constitutive equation relating the strains to the stresses and the damage. A simple damage theory for the uniaxial tensile loading of a brittle material is outlined by Costin[181] pages 196-198, and is cited as a simple example prior to discussion of the more complex problem of failure under compressional loading.

Main et al (1993)[200] proposed an idealised synoptic model of damage development in a heterogeneous brittle solid under compression. In it, test specimens or *in situ* "elements" of rock are considered to fail under compressional loading ultimately by the organised, unstable coalescence of microcracks which initially grow in tensile mode, nucleating first on the weakest elements in a polycrystalline matrix. Initially crack growth is stable and distributed throughout the sample, implying that the sites of incremental crack growth initially tend to avoid one another, testament to a kind of negative feedback process operating on the microscopic level. Thus crack growth is initially energetically favourable, but only for a small increment until the energy balance favours arrest or rupture. In the early stages of damage, crack growth is not continuous, and appears to stop when the stress has been locally relieved. Whilst a number of mechanisms were proposed by Main et al for such crack arrest, this same phenomenon can be described in terms of a reduction in the rate of subcritical crack growth as the local stress intensity decreases due to crack growth itself, controlled by a characteristic "domain" size which might represent a local aureole of stress relaxation surrounding the growing crack. Initially the crack is deemed to relieve the stress intensity within the domain and growth

is inhibited as the crack semi-length approaches the radius of the domain. Following Costin[181] the reduction of stress intensity factor, K, at the crack tip is described by:

$$K \propto S_r[(d - a)/d].(\pi a)^{1/2} \quad \ldots\ldots\ldots \quad \text{Eqn.5.5.2.1}$$

S_r: remote stress

d: radius of the "domain"

a: crack semi-length

This equation, although unlikely to be correct in detail, preserves the essential physical idea that under compression, growth of individual cracks occurs in a stable mode, and is unlikely to be the cause of dynamic failure. The stability of this quasi-static state of damage is due to the negative feedback between the increase in crack length and the stress intensity, represented by the term (d - a)/d. The stability of initial crack growth may also be due to, amongst others, the mechanism of dilatant hardening in the presence of a pore fluid (Brace & Martin[188]).

Once a critical crack density is attained, however, neighbouring cracks begin to interact and nucleate a larger scale shear or tensile crack through positive reinforcement of the stress field at the crack tip. The main feature of models looking at crack interaction leading to rock failure in compression (see for example Rudnicki & Kanamori, 1987[201]) is that the stress intensity at the tip of a crack is increased by the presence of a neighbour, as is the stress in the intervening non-cracked region. Thus for a critical crack density, crack interaction corresponds to a positive feedback in the crack's growth process, eventually leading to a runaway instability:

$$K \propto S_r[\text{ctan}(\pi a/2c)]^{1/2} \quad \ldots\ldots\ldots \quad \text{Eqn.5.5.2.2}$$

c: centre-to-centre distance between adjacent cracks

Eqn.5.5.2.1 and Eqn.5.5.2.1 show the effects of, respectively, the domain of stress intensity relaxation, d, and the domain of crack interaction, c, for the elements which are at the tips of growing cracks. Crack- crack interaction and linkage, whilst a strong contender as a possible mechanism for strain-softening, also occurs prior to attainment of peak strength. Such stable crack linkage does ultimately lead to the development of runaway instability as avalanches of such cracks are produced under increased dynamic, critical conditions, where positive feedback between an increment of crack growth and further growth dominates. A schematic illustration of the general transition from distributed damage to concentrated fault localisation under compression, due to the transition from local rules involving negative and positive feedback in crack growth (Eqn.5.5.2.1 and Eqn.5.5.2.2) is shown in Fig.5.5.2.1, taken from Main *et al* [200].

Meredith et al (1990)[202] used constitutive relations derived from observations of subcritical crack growth under tension, to develop a synoptic model for acoustic emission statistics during compressional failure. Summarising their approach, stress intensity (K) is a measure of the intensity of the concentrated stress field around a crack tip (see section 1.4) and depends on the length (c) of the crack responsible for crack extension as well as on the remotely applied stress. Lawn & Wilshaw (1975)[203] show that for tensile failure:

$$K = Y\sigma c^{1/2} \quad \ldots\ldots\ldots \quad \text{Eqn.5.5.2.3}$$

By comparison with Eqn.1.4.2, Y is a numerical factor dependent on the loading configuration and crack geometry. Empirically, the crack propagation (rupture) velocity, V, is found to be related to the stress intensity, $K=Y\sigma\sqrt{c}$ by Charles' (1958)[204] law:

$$V=V_o(K/K_o)^n \quad \ldots\ldots\ldots \quad \text{Eqn.5.5.2.4}$$

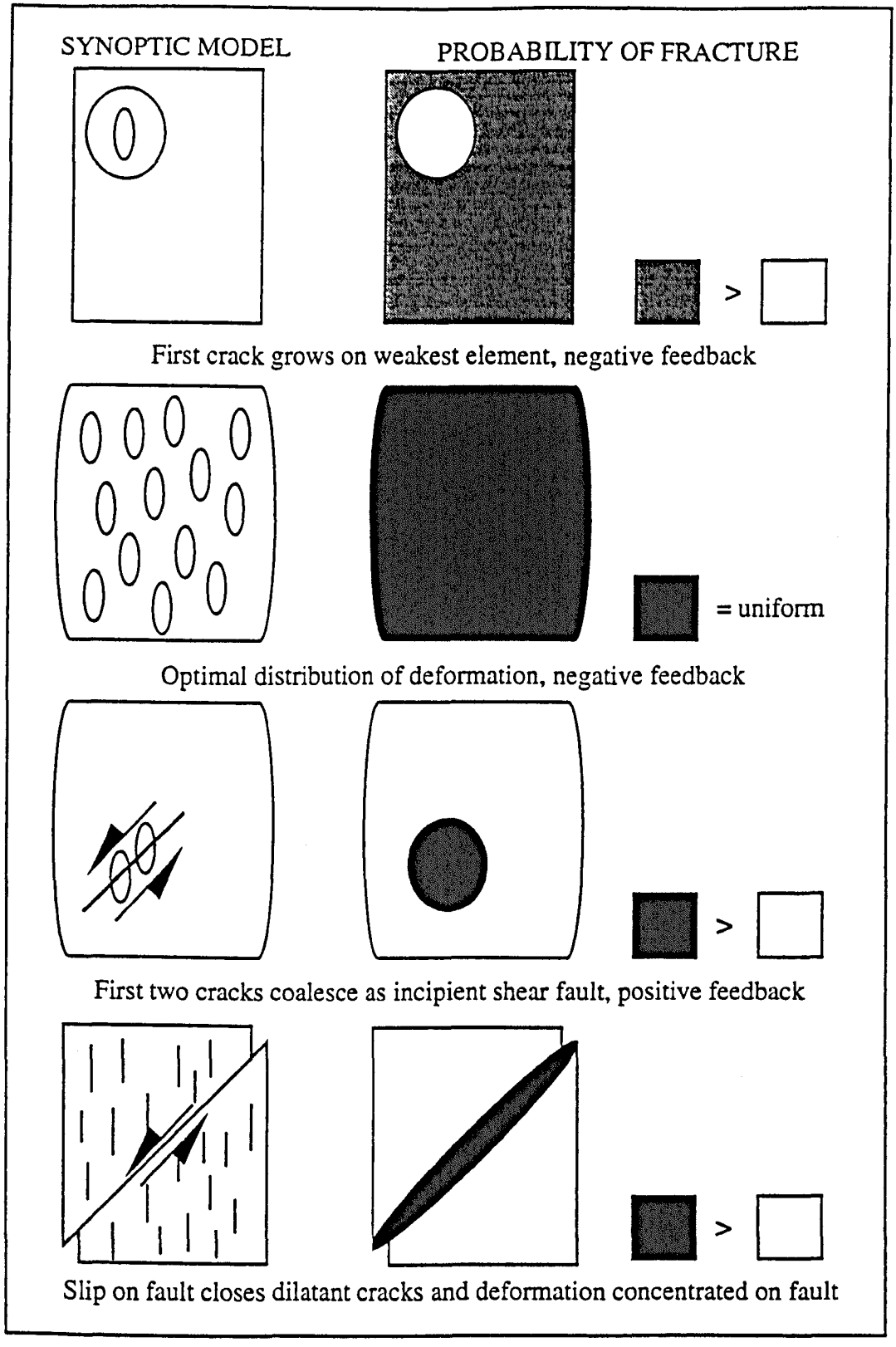

Fig.5.5.2.1. Idealised synoptic model of damage development in a heterogeneous brittle solid under compression, after Main *et al* [200] (see text for details).

The constants V_o and K_o depend on the pressure, temperature, rock type and chemical environment. K_o is a threshold stress intensity for subcritical crack growth below which no crack growth occurs, and is an upper bound for the occurrence of crack healing. The exponent n is known as the stress corrosion index. In general for polycrystalline rock typical of earhquake nucleation depths, $20<n<60$, so that the process of accelerating subcritical crack growth as represented by the power law of Eqn.5.5.2.4 is in fact extremely non-linear.

Although distributed damage is macroscopically stable and quasi-static, crack growth occurs by increments that may be dynamic enough to be recorded by acoustic emission (AE) monitoring. AE may be used to monitor the evolution of damage during subcritical crack growth experiments above a detection threshold magnitude, m_c. Meredith & Atkinson (1983)[205] showed that AE from tensile subcritical crack growth experiments showed the same frequency-magnitude distribution as earthquakes (the log-linear Gutenberg-Richter[198] relation):

$$\log N_c = a - b(m - m_c) \quad \text{.....} \quad \text{Eqn.5.5.2.5}$$

where N_c is the number of events of magnitude greater than or equal to m in a unit time interval, $N = N_c(m_c) = 10^a$ is the event rate for occurrence above a threshold magnitude m_c, and b is the seismic b-value.

Main & Meredith (1991)[206] assumed proportionality between: the number of acoustic events, N, and the total number of potentially active cracks, N_T, for a theoretical distribution of aligned, elliptical cracks

$$N = 10^a = \lambda N_T \quad \text{.....} \quad \text{Eqn.5.5.2.6}$$

The number of acoustic events, N, in a time interval, dt, is equal to the change in N_T in the same period, so that $N = dN_T/dt = \lambda N_T$. After integration it follows that $N_T = N_{T0}\exp(\lambda t)$, where N_{T0} is the total number of potentially active cracks at time t = 0, thus Eqn.5.5.2.6 predicts an exponential increase in event rate, N, controlled by the rate constant, λ, exactly as seen in the early stages of damage during compressional failure of intact rock specimens (Meredith *et al* [202]). This observation was considered strong indirect evidence of the proportionality between event rate and the total number of potentially active cracks in the early phase of rock failure in the laboratory.

Meredith & Atkinson[205] showed that the event rate, N, was also non-linearly related to the stress intensity by:

$$N = N_0(K/K_0)^{n'} \quad \text{.....} \quad \text{Eqn.5.5.2.7}$$

By comparison with Eqn.5.5.2.4, n' is referred to as the "effective stress corrosion index" since the exponents n and n' are found to be equal to within a few percent, for example in Fig.5.5.2.2 n = 29.0 and n' = 29.1. The event rate, N, and average crack extension velocity, V, are therefore strongly positively correlated in a non-linear fashion to the stress intensity, testifying to the non-linear nature of the constitutive laws governing crack growth.

Scholz (1968)[207] showed that the b-value is negatively correlated to a first order with the stress in laboratory experiments involving dilatant microcracking. To second order Fig.5.5.2.3 shows that the b-value is negatively correlated to the stress intensity, K, via an expression of the form, b=p-qK, where p and q are positive constants. Within the limits of experimental resolution, all crystalline rocks studied to date fall on the same curve for a given chemical environment when normalised by their critical stress intensity (fracture toughness) K_c for which p and q become:

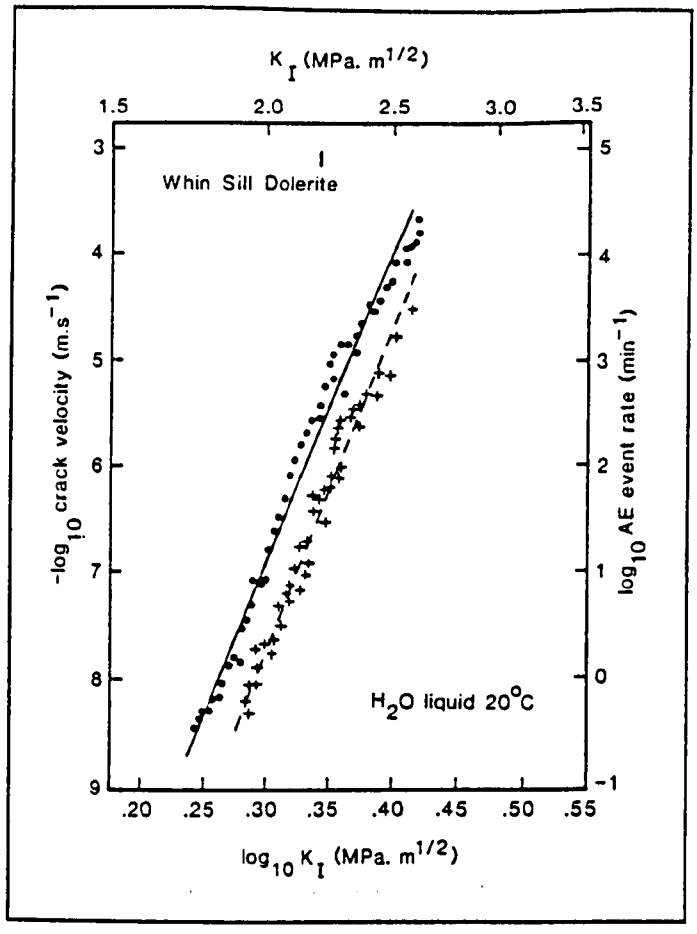

Fig.5.5.2.2 Dependence of crack velocity (dots) and event rate (crosses) on measured (Mode I) stress intensity K_I from double torsion tensile experiments carried out in water at room temperature, after Meredith & Atkinson[205].

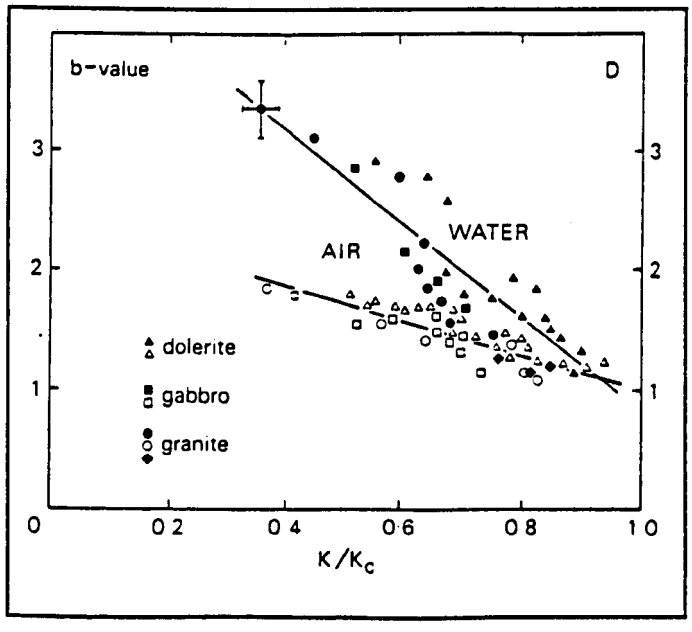

Fig.5.5.2.3 Variation in b-value(and inferred crack length distribution exponent *D*) with stress intensity and crack tip humidity, for a variety of crystalline rocks, after Meredith *et al*[202].

$$b = b_o - (b_o - b_c).[(K - K_o) / (K_c - K_o)] \quad \text{.....} \quad \text{Eqn.5.5.2.8}$$

As for Eqn.5.5.2.4 and Eqn.5.5.2.7, K_o is the threshold stress intensity for subcritical crack growth, below which crack healing takes place.

Meredith et al (1990)[202] used Eqn.5.5.2.8 to predict transients in the seismic b-value for a variety of stress histories during the compressional failure of intact laboratory specimens, ranging from nearly elastic brittle failure at low confining pressures to cataclastic flow at high confining pressure. Their semi-quantitative synoptic model is shown graphically in Fig.5.5.2.4. Good qualitative agreement between the general shape of the predicted and observed anomalies were thus regarded as being indicative of the fact that laws established for tensile failure were equally applicable to the compressional regime, although the values of the controlling constants may be different. Whilst stress intensity, K, was directly related to the seismic b-value via the constants p and q, the b-value was in turn related to the fractal dimension, *D*, through a relationship noted by several authors (for example, Aki, 1981[208]) in which the slope b of the log-linear frequency -magnitude distribution of earthquakes is consistent with a power law distribution of fault lengths of egative exponent, *D*, where:

$$D = 3b/C \quad \text{.....} \quad \text{Eqn.5.5.2.9}$$

With C representing a recording instrument-dependent scaling constant ranging from 1 to 3, for most intermediate earthquake studies C=1.5, so that D =2b. Eqn.5.5.2.9 has obtained recent experimental confirmation from direct measurement of crack length distributions and b-values under open tensile loading (Hatton, Main & Meredith, 1993[209]).

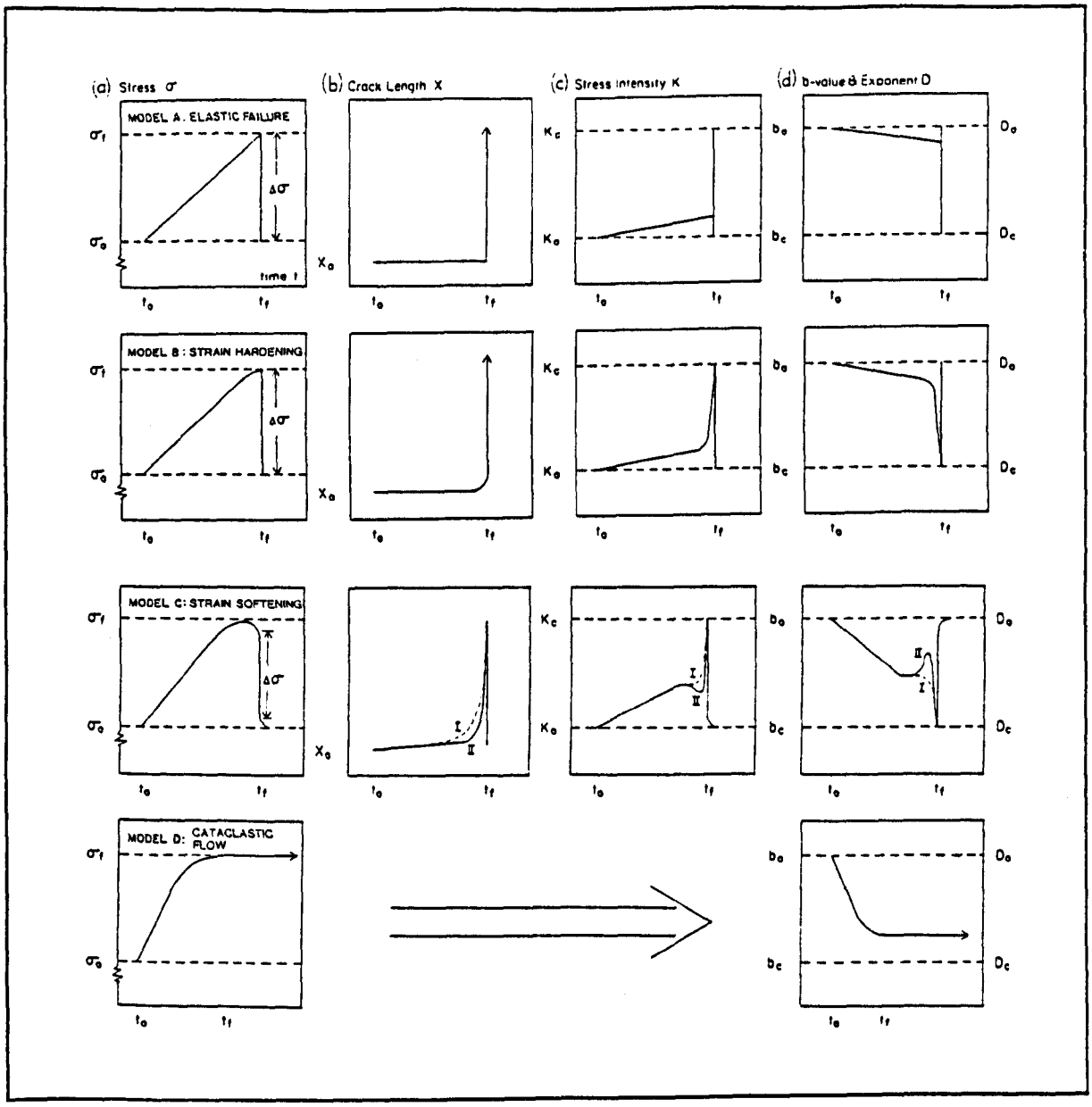

Fig.5.5.2.4 Synoptic model of the evolution of seismic b-values predicted by Fig.5.5.2.3, after Meredith *et al*[202] (see text for details).

5.5.3 Acoustic Emission Data

Passive microseismic (AE) monitoring for the triaxial compression test protocol as described in section 5.2 above, was achieved using the LOCAN 320 plus PAC preamplifier plus waveguide-mounted sensor system, as described fully in section 4.4 of the previous chapter on equipment development. Internal amplifier gain and threshold values were set at 20dB and 50dB respectively, in conjunction with a preamplifier gain setting of 40dB, following initial noise calibration testing utilising a steel "dummy" specimen. The relatively high threshold value was an unavoidable consequence of monitoring within a hydraulic pressure vessel. Also, the permeability measurement capability necessitates drilled platens to allow permeant circulation, thus precluding mounting of the sensor in the conventional manner inside the body of a load-bearing platen (see for example Meredith *et al*, 1990[202]) a waveguide being employed instead to contact the specimen through the rubber confining sleeve, with a resultant decrease in the signal-to-noise ratio. However, the dynamic range between this threshold and the maximum amplitude recorded during the experiments was found to be about 45dB or over two orders of magnitude. The LOCAN monitoring system was set up to log on Channel 1, the time of each recorded hit, the risetime, number of counts, energy, duration, amplitude, frequency and RMS of every event, and the axial load via a parametric channel. The voluminous logged AE binary data was converted to ASCII text files in line format on the LOCAN 320, and imported into Microsoft® Word using Apple® File Exchange. The word files were then transferred to Microsoft® Excel and the data column formatted. Excel is a standard spreadsheet package which offers the facility to perform specialised calculations and customised tasks by creating and storing macros (command scripts which tell the computer how to execute particular tasks). As part of a complementary M.Eng Thesis project, two macros were specially written to process the AE data in the form of calculated instantaneous seismic b-values and hence inferred exponent D-values over specified time intervals (Burnside, 1992[210]). All discrete data were sampled at 10second time intervals. A pre-processing macro removes unwanted logged data from the database, including columns containing the active channel number and the threshold value in dB, incomplete data rows in which no AE events were

recorded thus leaving only a time logged, and rows containing only alphanumerics (unwanted command information). Following this "clean-up" process the data is saved on disk as a "Macro1. output file" ready for calculations to be performed by the second macro. A post-processing macro converts the logged times from minutes to seconds, sets up column headings and formats for the final results table, counts the number of hits and sums their magnitudes in each specified time interval, performs the b-value calculation (see Eqn.5.5.3.1 below) for specified values of threshold, half bin-size and time interval and presents the results in tabulated format containing columns of the number of hits, their summed amplitudes, the calculated b-value and the average axial load for each discrete time period. This results table is then saved on disk as a "Macro2.output file". The post-processing macro used the maximum likliehood estimate (Aki, 1965[211]) to calculate the b-value, defined as:

$$b = 20.N.\log e / \Sigma(M_i) - N.M_{min} \quad \ldots\ldots\ldots \quad \text{Eqn.5.5.3.1}$$

N: total number of AE events

M_i: any measured event amplitude

M_{min}: lowest amplitude considered less half the amplitude interval = [threshold - 1/2.bin-size] dB = [50-0.5] dB in this case.

Thus $\Sigma(M_i)$ is the sum of all event amplitudes having amplitudes exceeding M_{min}. M_{min} is defined as half the amplitude interval length (0.5dB in this case) less than the lowest amplitude considered, N is the total number of events in the time interval considered, and the standard deviation of the calculated b-value, s, is given by $s=b/\sqrt{N}$.

The factor 20 in Eqn.5.5.3.1 is a function of the definition of the decibel amplitude scale:

$$1dB = 20.\log[A/A_o] \quad \ldots\ldots\ldots \quad \text{Eqn.5.5.3.2}$$

Here, A_o is an arbitrary reference AE amplitude, so that an order of magnitude change in amplitude, A, corresponds to 20dB. Thus the slope of a logN versus M plot must be multiplied by 20 to obtain the b-value. Macro1.output files represent prospective databases totalling some 39.346MB for the seven specimens tested. The Excel macros were run on an Apple® Macintosh® Quadra 900 computer, utilising version 7.01 of the operating system with a 400MB hard disk and 32MB of memory. A virtual memory capability allowed up to 100MB to be enabled. Using the tabulated Macro2.output files, double y-axis plots of differential stress and AE event rate, and of instantaneous seismic b-value/inferred fractal dimension (D =2b) versus time were produced for the dynamic failure, frictional sliding and re-shearing processes monitored for each specimen, as shown in Appendix II, Fig.AII.1 to Fig.AII.7. As an alternative means of presentation to the above temporal variation diagrams, the three processes were adjoined by plotting the above parameters against axial microstrain, as shown in Fig.AII.8 to Fig.AII.14.

The above mentioned AE results can be interpreted using the synoptic model first presented in Meredith *et al* (1990)[202] which predicts qualitative variations in b-value with time for different loading histories (models A, B, CI, CII and D) as depicted in Fig.5.5.2.4. This shows, schematically, predictions of the time dependence of D for a range of loading histories under microscopically brittle conditions and constant remote strain rate. Four variants of the proposed b-value anomaly model are depicted, associated with different stress histories and levels of stress concentration. Model A corresponds to ideal macroscopically brittle behaviour, with instantaneous crack acceleration from zero to near-sonic velocities at failure. The stress intensity is assumed proportional to the applied effective stress and square root of the dominant flaw and D is negatively correlated to K. Model B represents failure at peak strength following a period of strain hardening, and predicts a more gradual concave-downwards decrease in D to a critical value, D_c=1 at failure. Model C represents failure after periods of strain hardening followed by strain softening, with in this case, the variation in D depending on the mechanism of strain softening (see Meredith *et al* for a full explanation). If slip behind the accelerating crack front is responsible for the strain softening stress decrease (dashed

lines in Fig.5.5.2.4, model CI) then an inflexion or hiatus (respite) in K is predicted at peak stress, because local stress release by this mechanism results in greater concentration of stress at the growing crack tip. A similar inflexion in *D* is predicted following an initial convex-downward decrease. However, strain softening by stress release off the dominant crack, or by an increase in pore pressure, followed eventually by accelerating crack growth, results in two maxima in the stress intensity and two minima in D (solid lines in Fig.5.5.2.4, model CII). Finally, model D involves no stress drop and the mode of failure is quasi-static cataclastic flow, for which there is no stress concentration, K therefore being undefined. In the synoptic model illustrated, *D* was simply assumed to be negatively correlated to the stress, and tends towards a steady-state value somewhat above the critical level, D_c=1. Thus models A to D represent a gradation from purely elastic-brittle behaviour to macroscopically more ductile behaviour.

AE monitoring over stage I (see Fig.5.2.1) from hydrostatic to immediate post-dynamic failure stress conditions, will be addressed first, for the seven Clashach sandstone test specimens. This stage can be further subdivided into five substages including: (i) a convex downwards initial "settling-in" phase, in which slight non-parallelism between specimen ends is flattened under stress, and pre-existing cracks at a high angle to the direction of axial load application are closed; (ii) a linear quasi-elastic phase ("quasi-elastic" as local inelastic processes on the microscale leading to AE are also characteristic); (iii) a phase of strain hardening up to the ultimate/peak strength of the rock; (iv) a stable phase of strain softening which may or may not be long enough to be recorded; (v) a dynamic stress drop associated with macroscopic fault formation.

Time-varying, as opposed to cumulative results from the seven tests are presented in the form of the measured differential stress, $\sigma_1 - \sigma_3$, AE event rate, N (within a 10second time interval) and the corresponding seismic b-value. All parameters are alternatively presented against axial microstrain. Fig.AII.1 and Fig.AII.8 show the results from test #15 conducted under the least confining pressure (1000psi over dynamic failure) that is corresponding to the most brittle case macroscopically. Stage I can be subdivided into a

linear quasi-elastic phase of deformation followed by a strain hardening phase up to peak stress (ultimate strength) which is immediately succeeded by a marked stress drop indicating the end of phase I (fault nucleation). In this case it is inferred that the strain softening phase is simply too short to be recorded by the experimental apparatus. Thus the stress history shows strain hardening right up to dynamic failure, corresponding to model B behaviour. In phase I, the AE event rate, N, increases relatively slowly in the linear quasi-elastic phase, but accelerates markedly once strain hardening has commenced, consistent with dilatant microcrack growth. The b-value exhibits a slight initial increase (note that the error in measurement of b-values is inversely proportional to $\sqrt{N}$ so that variability in b-values is much greater during the relatively quiescent low stress phase of loading than during the dilatant phase when the AE rate is much increased) followed by a decline to a broad intermediate term minimum and subsequent peak over the strain hardening phase, both features NOT being predicted by model B, prior to a dramatic drop on dynamic failure to a second and lower minimum of 0.71. This observed inconsistency between model B stress history and model CII b-value signature may be the result of fluctuations in pore pressure which were not monitored (for observed double b-value minima under servo-controlled pore fluid volume see Sammonds *et al* 1992[212]). Alternatively, the stress history shows little strain hardening, with Clashach responding in an extremely brittle manner at this lowest confining pressure, and may reflect model A, elastic-brittle behaviour. In this case, the b-value profile could also be construed as reflecting model A behaviour, with a decrease to a first minimum, followed by a sharp jump to a near b_o magnitude value, followed by dramatic almost vertical (instantaneous) decrease on dynamic failure. Test #16 (Fig.AII.2 and Fig.AII.9) shows model B behaviour in both stress history and b-value signature. It differs from #15 in that the confining pressure is higher, and the event rate increases to higher values on dilatancy. The b-value exhibits monotonic decrease to a point within the strain hardening phase associated with "supra-exponential" increase in event rate, from which the b-value shows rapid reduction. On dynamic failure, the b-value drops to a single minimum of 0.69. Specimen #18 (Fig.AII.3 and Fig.AII.10) which although not deformed under the highest confining pressure, or displaying the greatest ultimate

strength, shows the most "ductile" rheology on a macroscopic scale, with post-peak strain-softening indicating model C behaviour. The AE event rate shows a relative decrease during the strain softening phase, implying an apparent seismic "quiescence". The b-value decreases to a broad minimum at about the onset of strain hardening, followed by a gradual increase to peak stress, from which it again decreases over the strain-softening phase to a second minimum on dynamic failure of 0.57, consistent with model CII behaviour. Test #19 (Fig.AII.4 and Fig.AII.11) also shows strain softening (although to a much lesser extent) despite more than a factor of two difference between the respective confining pressures of #18 and #19, however the latter's b-value profile resembles model CI more closely. The AE rate increases exponentially during the strain hardening phase leading to peak stress, but falls dramatically close to dynamic failure. A decreasing b-value associated with increasing linear elastic stress, levels out to a broad intermediate-term minimum from about the onset of strain hardening to peak strength, followed by a rapid decrease over the strain softening phase to a minimum of 0.67 on macroscopic faulting. Test #20 (Fig.AII.5 and Fig.AII.12) is much the same as test #18, although the strain softening phase is less well developed. On faulting the b-value drops to a second minimum of 0.54. Test #21 (Fig.AII.6 and Fig.AII.13) is much the same as test #16, with a b-value minimum on faulting of 0.76. Test #22 (Fig.AII.7 and Fig.AII.14) is similar to test #20, but with a higher b-value on dynamic failure of 0.65.

Thus, for the seven Clashach triaxial specimens monitored for AE, it is evident that in general, a transition in model variants from (possibly) model A (elastic-brittle) to model B (strain hardening) to model C (strain softening) is apparent with increasing confining pressure. Whilst this indicates a gradation to increasingly more macroscopically ductile behaviour with increasing confinement, at the applied pressure magnitudes used for this study no cataclastic flow was observed. Inconsistencies with this general observation, and between stress and b-value histories for individual specimens may reflect:

(i) inadequacies in the synoptic model (it is a mean field theory and assumes no crack-crack interaction)

(ii) too high a system threshold

(iii) unmonitored transients in pore fluid pressure;

(iv) recording system limitations (rate limit and event masking).

With regard to the latter shortcoming, rate limitation refers to the following. When the amplitude threshold has been exceeded, the desired parameters for the event are measured and the information stored in a queue, which is continuously scanned by the computer so that if data is present, it is immediately transferred to disk. However, a maximum transfer rate is associated with this process (usually a few hundreds of events per second) which fixes the rate of continuous AE recording. At continuous rates in excess of this maximum transfer rate, the buffer space available to accommodate the data queue fills up, since new data is added faster than the existing data is downloaded to disk. When the buffer is full so that no more events can be added to it, the system pauses, thus leading to gaps in the continuous AE data time series. Over high hit rate periods event masking can also occur. If a second event occurs before the amplitude of the coda of an earlier event has decayed below the trigger threshold, then the simple amplitude threshold logic used in the discriminator (the user-defined HDT as discussed in section 4.4.1) refuses to recognise the second event, instead logging both hits together as a single long duration event, thus leading to an underestimation of event number, and logging of events with anomalously small amplitude to duration ratios. Thus, Meredith *et al* recognised that quiescence may be a real or an instrumental phenomenon with a number of possible explanations:

(i) failure may be characterised by a small number of large-amplitude, long-duration events which could mask a large number of smaller events from the measuring instrument, resulting in an artificially low event rate

(ii) failure may be marked by a very large number of small events running into one another, and appearing to the instrument as a single, small-amplitude, long-duration event, again resulting in a low event rate

(iii) failure may only result in events with amplitudes lower than the detection threshold

Of these, Meredith *et al* felt it likely that explanation (ii) applied to laboratory results, whilst (iii) was pertinent to field observations.

After dynamic failure, all specimens continued to deform by shear sliding at an approximately constant stress, or with mild slip weakening, however interestingly, all showed constant b-value profiles despite distinct and pronounced fluctuations in event rate (it is important to note that the two minima in AE event rates at the end of phases I and II, evident in the event rate N versus strain diagrams of all specimens, are artefacts of the experimental procedure, in which stress was held constant and AE monitoring discontinued whilst permeability was measured). In particular, for specimen #18 (Fig.AII.3 and Fig.AII.10) over phase II, two large spikes in N are evident, but are not associated with significant fluctuations in the b-value. Once the confining pressure was increased further by an arbitrary 1000psi (6.9MPa) and AE monitoring continued over phase III, sliding stress was observed to increase asymptotically to a new constant plateau value, and the AE event rate also showed an increase with increasing stress, but again over a remarkably constant b-value profile. Thus for all test specimens over both frictional sliding phases II and III, the b-value magnitude remained in general between 0.8 and 1.0.

Compressive failure by shear faulting in the laboratory is preceded by a phase of tensile microcrack nucleation, growth and coalescence, and a fracture mechanics model of rock failure which includes a range of flaw sizes can be tested by seismic (AE) monitoring. The preceding AE results recorded to dynamic failure have been shown to conform with such a published[202, 213] fracture mechanics model of rock failure for a variety of styles of deformation (see Fig.5.5.2.4) this model predicting the time-dependence of the seismic b-value and of D up to and including failure. Critical coalescence of microcracks during dynamic failure (analogous to earthquake foreshocks) occurred when $D = 1$(b = 0.5); random processes (for example cataclastic flow although not seen in our experiments, and background seismicity) are associated with $D = 2$ (b = 1); positive

feedback (see Eqn.5.5.2.2) in the concentration of stress on the dominant flaw (for example during strain softening and shear localisation) occurred when $D < 2$ ($b < 1$); negative feedback (see Eqn.5.5.2.1) in stress concentration (for example during the early stages of dilatancy when a highly diffuse crack system is produced) occurred when $D > 2$ ($b > 1$). Thus these results confirm the idea that changes in the "instantaneous" value of the seismically inferred D (note that examination of the final structure of a deformed rock specimen yields a cumulative or time-integrated value of D) can be associated with positive or negative feedback in local stress concentration during deformation. Variation in the instantaneous D with deformation also surely must imply variation in the connectivity of the evolving microcrack system, which suggests that deformation-induced temporal variation in the b-value may mimic an associated variation in rock permeability.

5.5.4 Discussion

Equivalent AE results for Phase I initial fracture are discussed in terms of consistency with observations made on natural shear fracture systems by Main *et al* (1990)[213]. Here, the geometry of shear fault systems over a range of scales from fractions of a millimetre to hundreds of kilometres, but all characteristically dominated by one master, pervasive, through-going fault, are contrasted with frequency-length distributions of mapped faults showing evidence of Holocene activity in the contiguous US (data drawn from Shaw and Gartner, 1986[214]). From this it is evident that those systems with one dominant cross-cutting fault, when normalised to the length of the maximum through-going fault, show the same relative power law size distribution of subsidiary faults with a negative exponent of $D = 1$. Such a mapped fault distribution is perhaps best described mathematically by the Cantor set (see Fig.5.5.1.1) with an extension to 3D requiring a dominant fault plane with a cascade of smaller fault planes and an associated power law frequency distribution in area. In contrast, whilst the U.S. Holocene data still exhibits a power law over the scale range 10 - 200km, this system possesses a higher cumulative fractal dimension of $D = 1.76$, implying an overall fault assemblage where no single thorough-going dominant fault exists, deformation being accommodated by a more

distributed system of unconnected, relatively minor faults. Thus, with the maximum permissible value for D in a Euclidean volume being 3, when the whole volume is eventually filled by a cascade of ever smaller fractures, the expected range for the negative exponent of the power-law size distribution is $1 \leq D < 3$. Within this physical limitation, lower D represents a greater concentration of deformation on a few relatively large faults, and higher D a more diffuse system dominated by a greater proportion of relatively small faults. The fractal interpretation has also been widely validated by seismological studies of faults, for example the log-linear, Gutenberg-Richter, frequency-magnitude distribution (Eqn.5.5.2.5). Main *et al* [213] note that seismological investigations with a high degree of statistical significance have established a typical background value of $b \approx 1$ ($D \approx 2$) with in general b fluctuating between $0.5 \leq b < 1.5$ ($1 \leq D < 3$) and earthquake foreshocks occurring when $b \approx 0.5$ ($D \approx 1$). Such results are in very good agreement with the observations and predictions of the range of D derived from direct structural fault mapping but with the advantage of better resolution with depth for the smaller faults that do not break the surface.

These results for the cycle of fracture in the intact specimen (Phase I) conform to one of the models in Meredith *et al*, and confirm previous results obtained using the same technique on samples of Darley Dale sandstone saturated in water (Main *et al* [200]). Results for phase II (post-dynamic failure frictional sliding) are not discussed by Main *et al*, but in the Clashach experiments reported here, are characterised by a relatively constant sliding stress and b-value, despite pronounced fluctuations in event rate. These fluctuations, however, are much smaller than the overall variation in phase I where large fluctuations in stress, event rate and particularly the seismic b-value are observed. On increasing the confining pressure (phase III re-shearing on the strengthened fault) sliding stress increases asymptotically to a constant value with corresponding moderate increase in event rate, but little variation is observed in b-value. Thus it is apparent that once a fault has been formed, continued slip is accommodated under very stable conditions in almost all the tests, consistent with the system being maintained in a state of dynamic equilibrium near a critical point (I.G. Main, *pers comm*, 1993). Results from stages II

and III thus show all the "hallmarks" of a self-organised critical (SOC) phenomenon with relatively constant driving stress and b-value at constant strain rate, despite fluctuation in N, presumably as fault wall roughness and asperities are sheared.

AE data presented above, resulting from applied stress ranging from hydrostatic to that immediate post-dynamic failure, has been shown to represent experimental confirmation of existing fractal damage mechanics theory. These experimental results have been further analysed using a mean field theory for damage evolution which calculates a mean crack length <c> from the seismic event rate N and the b-value, and a mean energy release rate <G> from (σ_1 - σ_3) and <c> (Liakopoulou-Morris *et al*, 1994[215]) and will not be discussed any further here. Conversely, AE generated under post-peak slip weakening and re-shearing under increased confinement during this present study, provides new insight into the physical processes involved. Specifically, whilst in the nucleation stage of faulting, the scaling exponent b is associated with large fluctuations, in contrast the b-value remains almost constant at a value near unity in the sliding phase, even when the fault is mechanically strengthened. This stability in b, combined with a relatively constant sliding stress, implies that frictional sliding conforms to a self-organised critical (SOC) phenomenon, as discussed below.

A system is said to be in a state of SOC if it is maintained near a critical point (Bak *et al* 1988[216]). According to this concept a natural system is in a marginally stable state, and when perturbed from this state it will evolve naturally back to the state of marginal stability. In this critical state there is no longer a natural length scale so that fractal statistics are applicable. An illuminating overview of the "new" physics of critical point phenomena is given by Bruce & Wallace (1988)[217] and will not be discussed further here. The principles of self-organised criticality are also summarised in Turcotte[199] (Chapter 16) including an illustration using a simple cellular-automata model. The simplest physical model for SOC ("toy" example) is a sandpile (Bak *et al*, 1989[218]). Consider building a sandpile from scratch by adding particles randomly and very slowly. Grains of sand are randomly dropped on the pile until the slope of the pile reaches the

critical angle of repose. Additional grains then simply slide down this slope. This is however, not what is observed to happen. The sand pile never reaches the hypothetical critical state. As the critical state is approached additional sand grains trigger landslides of various sizes, with fractal frequency-size distribution. The sand pile is said to be in a state of SOC, with on average the number of sand grains added balancing the number that slide down and off the slope, but the actual number of grains in the pile fluctuates continuously. The behaviour of the sandpile has remarkable similarities to the seismicity associated with an active tectonic zone (Turcotte[199] pp.188). The addition of sand grains is analogous to the addition of stress caused by the relative displacement between the two fault walls, whilst the multiple landslides by which particles are lost from the pile is analogous to microseismicity in which some accumulated stress is transferred and some is lost.

Brittle deformation of rocks in the Earth's upper crustal levels is characterised by the formation, growth and organised coalescence of cracks into, ultimately, larger-scale faults on which deformation can be accommodated by frictional sliding at much lower stresses than those required to initiate shear failure in the intact state. The long-term evolution of such systems has been compared by Bak & Tang with the phenomenon of SOC where the system evolves to a state where the material is close to failure everywhere, but deformation is concentrated on the larger faults (see Sornette *et al*, 1990[219]). Liakopoulou-Morris *et al* [215] note that this state is characterised in the Earth by: a constant remote strain rate; a relatively constant remote driving stress, σ, where the local stress drop, $\Delta\sigma$, for individual earthquakes ($\approx$3MPa) is small compared to the breaking stress, σ_c ($\approx$100MPa); and a power law distribution earthquake source length with a universal negative exponent $D \approx 2$, usually corresponding to a seismic b-value of unity, and which remains relatively constant in space and time. Such phenomena are seen both in natural seismicity and in seismicity induced by mining, dam impoundment and pressure drawdown during hydrocarbon production. One of the problems of examining the relevance of SOC to deformation in the Earth's upper crust, is the difficulty of measuring the applied stresses. This problem can be overcome to some

extent in the laboratory where experimental conditions can be controlled, but where, for example, it is impossible with current technology to achieve strain rates as low as those applicable in the Earth (even for cases of induced seismicity where there is often a time delay of months or years to the onset of earthquakes). From the experiments reported here, in contrast to stage I, the results from stages II and III do show evidence of universal SOC, with relatively constant b and σ at constant strain rate, even though N may fluctuate as a particular asperity on the fresh fault surface is sheared off. This is fully consistent with recent treatment of faulting as a self-organised process which maintains the system in a universal critical state, implying a degree of order in the formation of fault gouge and continued shearing. Whilst it might be expected for the b-value to evolve with time as surfaces become worn and asperity shearing is replaced by frictional wear of debris as a slip mechanism, this was not observed for the Clashach test programme (admittedly involving only minor slip displacements) implying that roughening processes such as grain-plucking or "brecciation" are also taking place to balance the comminution of gouge which would tend to help smooth the contact surfaces. This has obvious implications for the long-term permeability of fault zones, and further, it is tentatively suggested that AE statistics may provide a suitable basis on which to build a micromechanical theory of rock friction.

6. ARTIFICIAL FAULT GOUGE GENERATED UNDER DIRECT SHEAR AND TRIAXIAL COMPRESSION CONDITIONS: RESULTS

6.1 INTRODUCTION

In general, there is not much difference between the fracture mechanics analysis of shear and tensile cracks (see section 1.4) however one major point of disparity is that, unlike tensile cracks, shear crack faces are not stress-free even if the surfaces have been well-slid. Following dynamic shear rupture, gross shear load does not drop to zero, but falls to a value commensurate with the residual frictional resistance of the plane of sliding. Importantly, this frictional work acts as an additional energy sink, reducing the amount of energy available to drive the crack tip. Energy dissipation associated with that part of the total energy budget expended in frictional traction behind the rupture front, occurs mainly by thermomechanical processes involving heat generation and grain comminution. The creation of new surface area in the form of frictional wear debris (fault gouge) is thus fundamental to fault mechanics, and can also readily be envisaged as a process with first order control on shear fracture fluid flow potential.

Artificial (experimentally created from laboratory testing) fault gouge samples generated by the direct shear and triaxial compression test programmes described in Chapters 3 and 5 respectively, are quantified in this Chapter 6, with regard to particle size distributions (see section 6.2) using both conventional sieving, as well as relatively new laser diffraction technology to access the sub-micron size range (section 6.3). In section 6.4 the influence of host lithology on resultant fault gouge distribution is studied, and correlation with frictional strength, measured in direct shear under constant normal displacement control, explored. In section 6.5, shear band (induced under triaxial compression) permeabilities are estimated from pulse decay axial core plug permeability measurements, and correlated with measured fault gouge distributions, shear band deformation and the applied stress state.

6.2 PARTICLE SIZE DISTRIBUTIONS

Particle size determinations are almost always undertaken in order to obtain information on the size characteristics of a very large number of particles, and as the particles are generally

not of the same size, information is required concerning both the average particle size and the distribution of sizes about this average. For particle size determination, the size of a large number of particles must be measured and the data arranged in such a way that the distribution of size is apparent. The first step in the arrangement of such data is the classification of the data in the form of a frequency distribution, readily represented by a histogram, with the abscissa representing the independent variable (size) and the ordinate the frequencies per class interval. If an infinite number of particles could be measured and the class intervals made to approach zero, a smooth curve would be generated so that the ordinate would represent a function of the particle size. The function corresponding to the curve is known as a distribution function. Particle size determinations of the experimental fault gouge samples produced by the direct shear and triaxial compression test programmes, have been analysed using three such distribution functions - the normal, log-normal and Rosin-Rammler functions, which are defined below. Definitions of these distribution functions with particular regard to small particle statistics are drawn from Cadle (1955)[220] and Herdan (1960)[221].

6.2.1 Normal

Undoubtedly the most familiar distribution function is the normal distribution. It is defined by the equation:

$$y = \frac{1}{\sigma_n \sqrt{2\pi}} \exp\left(-\frac{(x - \bar{x})^2}{2\sigma_n^2} \right) \quad \ldots\ldots\ldots \quad \text{Eqn.6.2.1.1}$$

- y: probability density
- x: particle diameter
- $\bar{x}$: arithmetic mean
- σ_n: number standard deviation

Herdan (page 80) considered materials showing a normal distribution of particle size to be relatively rare, being found chiefly amongst the particulate substances produced by

chemical processes like condensation and precipitation. Normal distributions are symmetrical about the arithmetic mean and thus have the property that the mode, median and mean are identical.

6.2.2 Log-Normal

The diameters of most types of particulate materials are not normally distributed, but instead have skewed distributions, which can be quite satisfactorily represented by the so-called log-normal distribution, in which the logarithms of particle size, rather than the sizes themselves, are normally distributed. The log-normal distribution is defined by the equation:

$$y = \frac{1}{\log\sigma_g\sqrt{2\pi}}\exp\left(-\frac{\left(\log x - \log x_g\right)^2}{2\log^2\sigma_g}\right) \quad \text{.....} \quad \text{Eqn.6.2.2.1}$$

x_g: geometric mean

σ_g: geometric standard deviation

Herdan (page 81) notes that if the dispersion is attained by comminution (milling, crushing or grinding) then the distribution appears to be governed very often by the log-normal law, with pulverised silica, granite, calcite, limestone, quartz, soda, ash, sodium bicarbonate, alumina and clay all being satisfactorily fitted by it.

6.2.3 Rosin-Rammler

Rosin & Rammler (1933)[222] developed a distribution function for broken coal which later was claimed to be applicable to cement, gypsum, magnesite, clay, dye-stuffs, quartz, flint, glass, ores and even to the distribution of droplets according to size obtained by various types of atomisers. Herdan[221] deemed it advisable to restrict use of the Rosin-Rammler law to distributions representing a greater departure from normality (greater skewness) than the log-normal law, and to distributions obtained by sieving analysis.

Following Rosin & Rammler[222], suppose that the distribution of a sample of broken coal is obtained by sieving. Calling the quantity (in percent) which passes the sieve, D (that is the weight percentage of particles smaller than the sieve opening, the percent undersize) and the quantity retained on the sieve, R (that is the percentage by weight of particles bigger than the sieve opening, the percent oversize or the residue) by plotting either D or R against particle size, x, a "fineness characteristic curve" is generated, D and R being connected for every sieve opening by the relation D + R = 100%. From probability considerations, Rosin & Rammler deduced that the weight distribution is governed by the law:

$$y = \frac{dG(x)}{dx} = 100nbx^{n-1}e^{-bx\wedge n} \quad \ldots\ldots\ldots \quad \text{Eqn.6.2.3.1}$$

G:total weight of particles in sample

In Eqn.6.2.3.1 "n" and "b" are constants, with, according to Herdan[221], b increasing with increasing fineness and thus being comparable to a measure of spread, and n being independent of fineness but characteristic of the substances.

Integrating Eqn.6.2.3.1 gives for the undersize weight distribution:

$$D = G(x) = 100(1 - e^{-bx\wedge n}) \quad \ldots\ldots\ldots \quad \text{Eqn.6.2.3.2}$$

Similarly, integrating Eqn.6.2.3.1 gives for the oversize, residual weight distribution:

$$R = 100 - G(x) = 100e^{-bx\wedge n} \quad \ldots\ldots\ldots \quad \text{Eqn.6.2.3.3}$$

Rosin & Rammler[222] claimed that the exponential equation given by Eqn.6.2.3.3 was, "a universal law of size distribution valid for all powders, irrespective of the nature of the material and the method of grinding." Bennett (1936)[223] provided a physical interpretation of the constants in the above Rosin-Rammler law. Bennett termed these constants the Rosin-Rammler "numbers" calling n the "distribution constant" and $\bar{x} = [1/(n\sqrt{b})]$ the "absolute size constant". For theoretically perfect grading so that all the particles are the same size, $n \rightarrow \infty$, for a material obeying the simple exponential law n = 1 with steady size reduction, whilst for more rapid size reduction, n < 1, characteristic of a "dusty" material. Thus the distribution constant, n, standing for the distribution of size, is a measure of the closeness of grading and fixes the distribution of particle size, the greater its value the more closely sized the material, the smaller its value the more dispersed the sizes. The absolute size constant, $\bar{x}$, measures the actual size of the material, large values meaning coarse material and small values fine material. As a note of caution, in the above discussion the absolute size constant, $\bar{x}$, is the inverse of the constant, b, defined in Eqn.6.2.3.1, and also should note be confused symbolically with the arithmetic mean, $\bar{x}$, of Eqn.6.2.1.1.

6.2.4 Graphical Representation of Data

There are numerous reasons for representing particle size distributions graphically, not least of which are the facts that graphs are much more concise than long tables of measurements, and present much more complete information than can be indicated by an average and some measure of the deviation. Cumulative curves can be described as curves which involve plotting the percentage of particles greater than (or less than) a given particle size against the particle size, so that the limiting values for the ordinate range from 0 to 100%. The ordinate can represent the percentage of total surface or of total weight instead of the percentage of the number of particles. Such curves have an advantage over histograms in that the class interval is eliminated, so that cumulative curves can be used to represent data which is classified into unequal class intervals, for example that obtained by means of sieving analysis. The usefulness of cumulative curves can be considerably increased by plotting them in such a way that straight lines result, accomplished by plotting the data on probability or log-probability paper.

Suppose that the percentage of the number of particles less than x in diameter, D_n, can be represented by an equation of the type $D_n = f_i(x)$, then a straight line is obtained by plotting D_n against $f_i(x)$. If the diameters of the particles are normally distributed, an expression in the form of $D_n = f_i(x)$ can be obtained by integrating Eqn.6.2.1.1. Whilst direct integration so as to express D_n as an explicit function of x is not possible, it can be evaluated from tables of probability integrals. Probability paper represents x on a linear scale and D_n on a probability scale such that a straight line is obtained when the integrated form of Eqn.6.2.1.1. is satisfied. Using the terms of the cumulative series (for number distributions the sums of observations or the percentage frequencies up to specified class intervals, for weight distributions the weight percent of particles less than or greater than a given size) percentages are plotted on a probability grid against the corresponding values of the variable. The cumulative values are plotted not against the class interval centres as are those of the frequency curve, but against the class interval limits. The straight line of the graph is some evidence, even though no strict mathematical proof, that the distribution is governed by the normal law. From such a graph, the mean and standard deviation can be readily obtained by drawing a horizontal line at the 50% point, the crossing point with the straight distribution line when projected onto the x-axis giving the arithmetic mean particle size. Furthermore, projecting the crossing points with the horizontals erected at the percentage points which correspond to a distance of once the standard deviation on either side of the mean, that is at either the 84% or the 16% point, approximately, on to the x-axis, the distance of either of these projections from the mean represents the standard deviation.

Just as most powders can be better represented by the log-normal frequency distribution than by the normal one, log-probability paper is generally more satisfactory. Log-probability paper is based on the integrated form of Eqn.6.2.2.1. If the distribution follows the log-normal law, to obtain a straight line graph connecting particle size with frequency of occurrence, a probability grid is used whose x-axis has a logarithmic scale. Statistical parameters of the log-distribution, its geometric mean and standard distribution, x_g and σ_g respectively, is as that described above for the arithmetic distribution. It is common to find

the experimental points at the upper and lower extremes of the distribution deviating considerably from the straight line.

Jensen (1991)[224] outlines a procedure for plotting probability plots on computers where statistical packages with this facility are not available. His procedure is as follows:

1. Order the N data (particle size or log particle size) points according to magnitude (either increasing or decreasing) so that $x_1 \leq x_2 \leq \ldots\ldots\ldots x_N$.
2. Assign a probability to each datum. A convenient formula is: $P(x_i)=(i-1/2)/N=R/100$.
3. Calculate the z_i (normal variable) value for each probability $P(x_i)$. This may be done using the rational approximation to the probability integral (Abramowitz & Stegun, 1965[225], page 933) given by:

$$z_i = t - \frac{2.30753 + 0.27061t}{1 + 0.99229t + 0.04481t^2} \quad \ldots\ldots\ldots \quad \text{Eqn.6.2.4.1}$$

where:

$$t = \sqrt{-2\ln\left[P(x_i)\right]} \quad \text{for } 0 < P(x_i) \leq 0.5 \quad \ldots\ldots\ldots \quad \text{Eqn.6.2.4.2}$$

$$t = \sqrt{-2\ln\left[1 - P(x_i)\right]} \quad \text{for } P(x_i) > 0.5 \quad \ldots\ldots\ldots \quad \text{Eqn.6.2.4.3}$$

For $P(x_i) > 0.5$, use Eqn.6.2.4.3 and $-z_i$ in Eqn.6.2.4.1.

4. Plot x_i versus z_i. The points will fall on a straight line if they come from a normally distributed population.

How far the points can deviate from a straight line will depend on the number of data. For 10-15 points the allowable variation can be large, whereas for 100-200 points the variation

about the line should be small. For these reasons a lot of data are required to distinguish between a normal and a log-normal distribution, and with increasing skewness the curvature on probability plots is more apparent.

Recalling the development of the Rosin-Rammler formula (section 6.2.3) for the mass of particles (residual weight distribution, R) whose diameter is greater than a stated size, x (Eqn.6.2.3.3) the distribution can be represented in iterated logarithmic form as a straight line. Taking logs to the base 10 of Eqn.6.2.3.3 gives:

$$\log R/100 = -bx^n.\log e \quad \ldots\ldots\ldots \quad \text{Eqn.6.2.4.4}$$

So that:

$$\log \log 100/R = \log b + \log \log e + n \log x \quad \ldots\ldots\ldots \quad \text{Eqn.6.2.4.5}$$

Eqn.6.2.4.5 represents a straight line relation between log log100/R and logx. If the series of corresponding values of these quantities plot approximately to a straight line, it would support the view that the Rosin-Rammler curve was a satisfactory description of the distribution in question. The slope of the line represents the quantity n, and substituting into Eqn.6.2.4.5 gives the constant = logb + log loge, and thus also b, so that from Eqn.6.2.3.3 it is possible to calculate R for any specified value of x. The practical value of a linear relationship of this type is that by means of sieving, a few determinations of corresponding values of R and x can be made, using preferably sieves whose openings are far apart in the scale, from which b and n can be obtained using the straight line relationship of Eqn.6.2.4.5, and by means of the exponential formula of Eqn.6.2.3.3 the distribution can easily be calculated for the whole range of particle size.

6.2.5 Fractal Fragmentation

If fragmentation due to the initiation and propagation of fractures, results in fragments with a wide range of sizes, and if natural scales are not associated with either the fragmented material or the fragmentation process, then it is to be expected that fractal distribution of number versus size might result. Excellent summaries of fractal concepts applied specifically to fragmentation theory can be found in Turcotte[199] (Chapter 3, pp.20-34) and in Korvin (1992[226], Chapter 3, pp.191-230) and will only be touched on this summary section. The cumulative frequency distribution of fragment size, according to the above, is generally approximated by one of the following functions: by an exponential distribution (for example Brown *et al* , 1983[227]) $N(r) \propto \exp[-(r/r_0)^{\alpha}]$, where N(r) is the number of fragments greater than r, and r_0 and α are constants; by a logarithmic-normal distribution (see section 6.2.2 above); and by the power-law (or "Pareto" or "hyperbolic") distribution, $N(>m) \propto Cm^{-b}]$ where N(>m) is the number of fragments with mass greater than m, and C and b are constants. Turcotte[199] shows that D = 3b, so that the power-law distribution is equivalent to the fractal distribution given by Eqn.5.5.1.3.

An alternative empirical correlation for the size-frequency distribution, is the "Weibull" distribution (Weibull, 1951[228]):

$$\frac{M(<r)}{M_o} = 1 - \exp\left[-\left(\frac{r}{r_o}\right)^{\nu}\right] \quad \text{.....} \quad \text{Eqn.6.2.5.1}$$

In Eqn.6.2.5.1, M(<r) is the cumulative mass of fragments with size less than r, M_o is the total mass of fragments and r_o and ν are constants. With M(>r)+M(<r) = M_o, it is possible to write:

$$\frac{M(>r)}{M_o} = \exp\left[-\left(\frac{r}{r_o}\right)^{\nu}\right] \quad \text{.....} \quad \text{Eqn.6.2.5.2}$$

Eqn.6.2.5.2 is just the Rosin-Rammler distribution law, so that the Weibull and Rosin-Rammler relations are entirely equivalent. In Eqn.6.2.5.2, the constants r_o and ν are entirely equivalent to the Rosin-Rammler constants, $\bar{x}$ and n respectively, as defined in Eqn.6.2.3.3. For $(r/r_o) \ll 1$, the Weibull Eqn.6.2.5.1 becomes approximately:

$$\frac{M(<r)}{M_o} = \left(\frac{r}{r_o}\right)^{\nu} \quad \text{.....} \quad \text{Eqn.6.2.5.3}$$

Thus, for the small fragments, the Weibull distribution reduces to a power-law relation. The power-law mass relation of Eqn.6.2.5.3 can be related to the "Korcak-type" fractal number relation, $N(r) \propto r^{-D}$ (Eqn.5.5.1.3) through the identity:

$$D = 3 - \nu \quad \text{.....} \quad \text{Eqn.6.2.5.4}$$

For the derivation of Eqn.6.5.2.4, see, for example, Turcotte[199] (p21-22).

Table 6.2.5.1., taken from Korvin[226] (Table 3.3, p204) and based on results from Hartmann (1969)[229] and Turcotte (1986[230], 1989[231]) lists more than twenty fractal dimensions quantified for a wide variety of fragmented objects, which all fall between 1.4 and 3.6. Whilst the values of fractal dimension are seen to vary considerably, most lie within the range $2<D<3$.

Sammis *et al* (1986)[232] and Sammis & Biegel (1989)[233] proposed a comminution model for fragmentation based on the hypothesis that direct contact between two fragments of near equal size during the fragmentation process will result in the break-up of one of the blocks, and that it is unlikely that small fragments will break large fragments or that large fragments will break small ones. Sammis *et al* 's[232] discrete model for fragmentation is illustrated in Fig.6.2.5.1. This fragmentation model is very similar to the 3-D Mengor sponge geometry shown in Fig.5.5.1.3, however although the geometry and fractal dimension are the same,

OBJECT	D [from $N(>r) \propto r^{-D}$]	REFERENCE
Projectile fragmentation of gabbro with steel	1.44	Lange *et al* (1984)
Projectile fragmentation of gabbro with lead	1.71	Lange *et al* (1984)
Meteorites (Prairie network)	1.86	McCrosky (1968)
Artificially crushed quartz	1.89	Hartmann (1969)
Plane of weakness model	1.97	Turcotte (1986)
Disaggregated gneiss	2.13	Hartmann (1969)
Disaggregated granite	2.22	Hartmann (1969)
0.2kt FLAT TOP I chemical explosion	2.48	Schoutens (1979)
61kt PILEDRIVER nuclear explosion	2.50	Schoutens (1979)
Broken Coal	2.50	Bennett (1936)
Interstellar grains	2.50	Mathis (1979)
Asteroids (theory)	2.51	Dohnanyi (1969)
Projectile fragmentation of basalt	2.56	Fujiwara (1977)
Sandy clays	2.61	Hartmann (1969)
Terrace sands & gravels	2.82	Hartmann (1969)
Pillar of strength model	2.84	Allegre *et al* (1982)
Glacial till	2.88	Hartmann (1969)
Stony meteorites	3.00	Hawkins (1960)
Asteroids	3.05	Donis & Sugden (1984)
Ash & pumice	3.54	Hartmann (1969)

Table 6.2.5.1 Fractal dimensions of a variety of fragmented objects (for full references cited above see Korvin[226]).

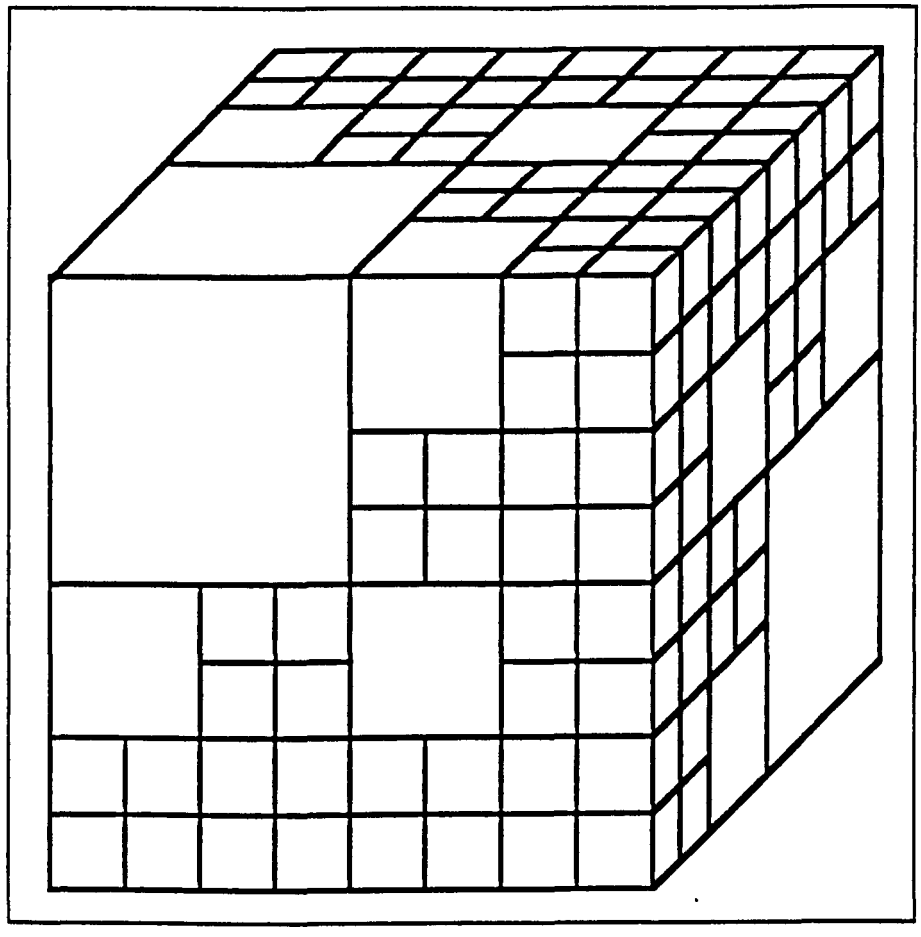

Fig.6.2.5.1 Self-similar gouge of cubic particles. Note that each time the particle size is halved, there are six times as many particles. Hence, the particle distribution follows a power law. The fractal dimension for this array is $D = \log 6/\log 2 = 2.58$ (after Sammis *et al* [232]).

the concepts of the two models are quite different - in the former the models are for porous configurations, whereas in the latter fragmentation is considered in which some blocks are retained at each scale, but others are fragmented. In Fig.6.2.5.1, two diagonally opposed blocks are retained at each scale, so that no two fragmented blocks of equal size are in direct contact with each other. For this array of cubes, each decrease in particle size by a factor of 1/2 corresponds to an increase in the number of particles by a factor of six, so that from Eqn.5.5.1.2, this gives a fractal dimension, D = (log6)/(log2) = 2.5850. Sammis *et al* (1987)[234] measured the particle-size distribution over the range 5microns to 4mm, of a natural fault gouge from the Lopez Canyon Fault in the San Gabriel Mountains of Southern California, using optical and electron microscopy, and found the fractal dimension to be 1.60±0.11 in 2-D cross-section, and thus 2.60±0.11 in an isotropic 3-D volume. However, Sammis*et al* [232] pointed out that when the cumulative volume fraction for this self-similar distribution is plotted on log-normal probability paper, it is evident that the finer fractions might be interpreted as log-normal (that is as a straight-line) thus making it impossible to distinguish, for this particular particle-size range, between a log-normal and a self-similar distribution.

6.3 EXPERIMENTAL SIZE DISTRIBUTION DETERMINATION

Grain-size distribution has been traditionally characterised in the hydrocarbon industry using sieve analysis, settling tube velocity measurements and thin-section grain-size analysis. However these methods are relatively time-consuming and do not permit detailed classification of the silt and clay size fractions. Accordingly, existing laser optics technology, initially developed for the powder industry, has been utilised to analyse the experimental fault gouge particle distributions. This laser technology offers a considerable extension to the common range of particle size measurement, size determination is rapid, and the data are reproducible. Laser sizing is readily adapted to distribution analysis of friable and unconsolidated sediments, and so is ideal for the experimental shear debris samples which are, unlike much natural gouge material, non-indurated (unhardened). As far as the author is aware, the only published example of the application of extended range particle size analysis using laser diffraction technology within the petroleum industry, is that of Griffin (1991)[17] who showed favourable comparison between laser optics data with

sieve analysis and settling tube analysis over traditional measurement ranges, with the clay size fraction comparing favourably with clay content determined by X-ray diffraction. Griffin highlighted the potential insights offered by such extended range data in well completion strategies (quantification of sand production and potentially mobile fines) sedimentology (determination of sediment uniformity) and log evaluation (determination of V_{shale} on cores).

As far as is known, the first published example of laser sizing technology being applied directly to fault gouge distributions, is that of Crawford *et al* (1994)[236] following from analysis of the direct shear experimental debris detailed in section 6.4 below. Laser sizing theory, equipment specifics and experimental methodology are described in section 6.3.2 below, whilst more common sieve analyses are used for comparative purposes (sieving technique outlined in section 6.3.1) to contrast with the broad range laser sizing results.

6.3.1 Sieving

Sieving is one of the simplest methods of determining particle size distributions, and is generally overlooked when carrying out fundamental research, which is unfortunate as it can be a very accurate technique. Sieving analysis applies to a range of grain sizes from very large grains (typically <1000microns) down to grains of about 0.05mm (50microns). With smaller grains the method cannot be applied, as it is impossible to produce sieve meshes fine enough for this purpose, and also due to the fact that for very small grains, the force of gravity is not great enough to overcome the resistance of grains to fall, resulting from grain adherence to one another and to the sieve cloth. Fortunately, the size of sieve screen openings have been standardised. Most sieves which are used for particle size determination have square openings, although circular, rectangular and even slit openings are available. In the USA the "Tyler" standard sieve series is used, based on the size of openings in wire cloth having 200 openings per linear inch (200-mesh). In the Tyler series, the openings of successive sieves are at the fixed ratio of $\sqrt{2}$, so that the areas of the openings of each sieve are double those of the next finer sieve. The British Standards Institution in 1932 adopted a sieve series known as the British Standard Sieve Series. The ration is the same as for the Tyler series, and the openings are nearly the same (the slight

differences being due to differences between U.S. and British wire). The sieve size openings of the Tyler and B.S. series are compared in Table 6.3.1.1 (those used in the present study being marked with an asterisk).

The sieving analysis relies on putting the substance concerned through a number of sieves of successively smaller mesh size, and determining the weight fraction which has passed each sieve, or which passes one sieve and is retained on the next smaller size. According to whether only the weight undersize (or weight oversize) fraction is determined, or the fraction passed and retained by two neighbouring sieves, the distribution of particle size is obtained in the form of either the weight cumulative or the weight frequency distribution. The errors specific to analysis by sieving arise out of the fact that the examination with regard to size is here performed simultaneously on a very great mass of particles, instead of individually as in the case of microscopic examination. Thus whether a particle will pass the sieve aperture depends not only on its dimensions in relation to those of the sieve aperture, but on many other factors including the size of the other particles and their quantity, whether it has free access to a given aperture and how it presents itself to the aperture, and the time of sieving during which such access may be gained, all such factors resulting in the particle only having a certain probability of passing the aperture in a given time.

6.3.2 Laser Sizing

The laser device used in the determinations on experimental fault gouge presented in this chapter is a Mastersizer high resolution 0.1-600microns particle size analyser supplied by ©Malvern Instruments Ltd, and the equipment design, capabilities and operating procedures detailed here are largely drawn from their Instruction Manual[237]. The system utilises composite laser light diffraction patterns produced by the dispersed particles to compute size distributions. Fig.6.3.2.1 is a schematic representation of the device. In essence, the laser light scattering sizer comprises a sample recirculating system which transports and presents the dispersed sample material to the measurement zone, an optical measurement unit that forms the basic particle size sensor, and a computer that manages the measurement and performs results analyses and presentation.

Tyler Series	Openings in (mm)	Nearest B.S.	Openings in (mm)
6-mesh	3.36	5-mesh	3.353
7-mesh	2.83	6-mesh	2.812
8-mesh	2.38	7-mesh	2.411
9-mesh	2.00	8-mesh	2.057
10-mesh	1.68	10-mesh	1.676
12-mesh	1.41	12-mesh	1.405
14-mesh	1.19	14-mesh	1.204
16-mesh	1.00	16-mesh	1.003
20-mesh	0.84	18-mesh	0.853
24-mesh	0.71	22-mesh	0.699
28-mesh	0.59	25-mesh	0.599
32-mesh	0.50	30-mesh *	0.500 *
35-mesh	0.42	36-mesh *	0.422 *
42-mesh	0.35	44-mesh	0.353
48-mesh	0.297	52-mesh *	0.295 *
60-mesh	0.250	60-mesh *	0.251 *
65-mesh	0.210	72-mesh	0.211
80-mesh	0.177	85-mesh	0.178
100-mesh	0.149	100-mesh *	0.152 *
115-mesh	0.125	120-mesh *	0.124 *
150-mesh	0.105	150-mesh *	0.104 *
170-mesh	0.088	170-mesh *	0.089 *
200-mesh	0.074	200-mesh	0.076
250-mesh	0.062	240-mesh	0.066
270-mesh	0.053	300-mesh	0.053
325-mesh	0.044	----------	----------
400-mesh	0.037	----------	----------

* Sieve sizes used in this present study.

Table 6.3.1.1 Comparison of U.S. Tyler and B.S. Sieve Series.

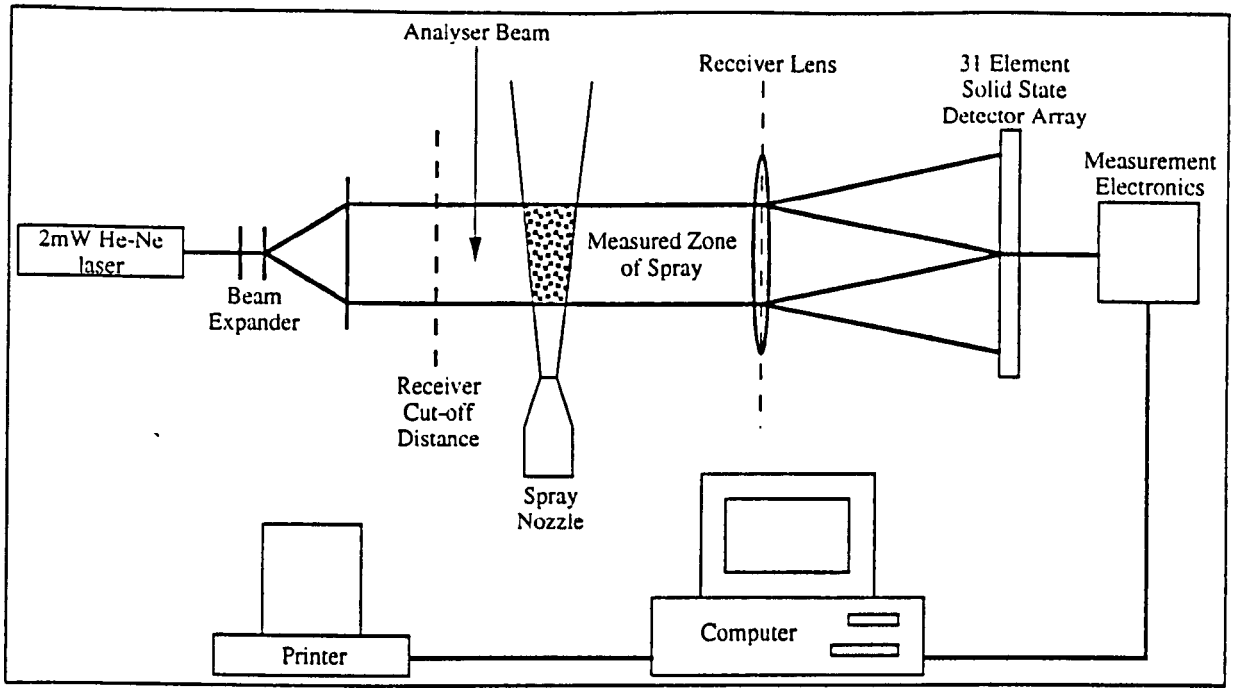

Fig.6.3.2.1 Schematic illustration of the optical configuration employed for laser particle sizing, comprising a sample recirculating system, an optics module and a microcomputer.

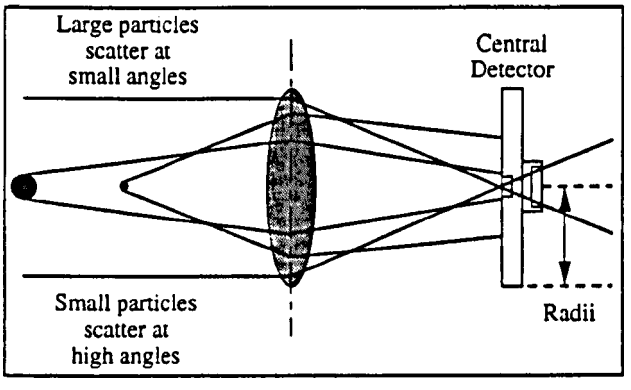

Fig.6.3.2.2 Properties of scattered light for large and small particles.

The Mastersizer has three standard user-defined size ranges: 600-1.2, 180-0.5 and 80-0.1μm. It cannot simultaneously cover the complete dynamic range in one measurement, so the total span is broken down into the above size ranges, each selected by fitting the appropriate receiver lens, of focal length 300mm, 100mm and 45mm respectively. The Mastersizer employs two forms of optical configuration to achieve its wide range. Whilst conventional Fourier optics are used for the two greater focal length lenses, the 45mm lens utilises a reverse Fourier optical configuration to minimise aberrations associated with large angle scattering detection (typically >10°) from small particles. When a particle scatters light, in this case sourced from a low-powered Helium-Neon laser it produces a unique light intensity characteristic with angle of observation. This light is scattered so that the measured energy on a detector has a peak at a favoured scattering angle which is related to the particle diameter. Large particles have peak energies in small angles of scatter and small particles *vice versa* (see Fig.6.3.2.2). In Mastersizer the range of detection has been extended up to in excess of 50° in order to measure sizes down to 0.1μm.

The conventional Fourier optical configuration is shown schematically in Fig.6.3.2.1. Laser light (2mW He-Ne laser of 633nm wavelength) is used to form a collimated and monochromatic beam known as the "analyser beam". Any particles present within the analyser beam, presented via thin optical presentation cells or by direct spraying through the measurement area, will scatter the laser light. The light scattered by the particles and the unscattered remainder are incident onto a receiver lens known as the "range lens", which operates as a Fourier transform lens, forming the far-field diffraction pattern of the scattered light at its focal plane, where a 31 element solid state detector in the form of a series of 31 concentric annular sectors, gathers the light over a range of solid angles of scatter. The range lens configuration has the beneficial property that, wherever the particle is in the analyser beam, its diffraction pattern is stationary and centred on the range lens optical axis, so that it does not matter that a particle is moving through the analyser beam, as its diffraction pattern remains stationary and centred on axis, just as it also does not matter where in the analyser beam the particle passes, as its diffraction pattern is always constant at any lens distance. In the reverse Fourier configuration the order of the components is altered, although in principle the measurement made is the same, the need

for the new configuration arising from the necessity to measure scattering at much higher angles than is feasible using the conventional method. Despite the modified optics, the diffraction pattern received by the detector still remains stationary and coaxial within the laser axis, regardless of particle movement.

The Malvern Mastersizer allows 3 particle size ranges with an overall span of 6000:1 to be accessed through choice of the range lens and optical configuration, necessitating the use of different optical theories to model the scattering. For scattering angles of 0.01-15° corresponding to a size range of 2μm and upwards, the scattering angle is largely independent of the optical properties of the material and the medium of suspension, and is caused by the diffraction of light around the particle. Light that couples into the particle is absorbed in all common cases and can be ignored, the "Fraunhofer" scattering theory (which assumes the particles scatter light like discs of the same diameter) proving adequate for modelling, without any requirements with regard to the powders' optical properties. However, for a detection range which has been extended up to >50° in order to measure down to 0.1μm, the scattering from such small particles at such high angles becomes heavily dependent on the optical properties of the material, necessitating use of the "Mie" theory model of light scattering. Mie theory is an exact solution to the Maxwell's equations for the case of a spherical particle, providing a complete description of the light scattering from optically homogeneous spheres, and requires assumptions regarding the optical nature of the particles. The optical constants that determine the scattering behaviour can be reduced to two, the differential refractive index between dispersant and particle, and the particle absorption, which can be set in the Mastersizer software using a four character code. The Fraunhofer scattering model is fully encompassed by the Mie theory, and fully agrees with it in the applicable range.

The time-averaged diffraction pattern shape is a convolution of the contributions of all of the particles of the composite sample. Signals from the measurment windows are econvolved into a multi-channnel histogram of the particle size distribution by a complex algorithm. The algorithms used to calculate particle size distribution from composite diffraction patterns are manufacturer dependent and proprietary, however from

relationships in Weiss & Frock (1976)[238] it is evident that the angle through which the light is diffracted is inversely related to particle size, and the diffracted light intensity is directly related to particle quantity. Thus it is possible for the computer to predict the scattering signal that would be received from a wide range of materials at a given size. It formulates a table that characterises how a unit volume of material, of a range of sizes throughout the working range, scatters light. Using this theoretical data the computer deduces the volume size distribution that gives rise to the observed scattering characteristics, by a process of constrained least squares fitting of the theoretical scattering characteristics to the observed data. This best fit result can either be obtained with no assumed form of size distribution (model independent) allowing the characterisation of multi-modal distributions with high resolution, or else the analysis can be constrained to three known forms of volume distribution, the normal, log-normal or Rosin-Rammler. The derivation of the result, the size distribution, V_i, can be related to the scattering data, D_i, using the matrix equation:

$$D_j = U_{i,j} . V_i \quad \text{.....} \quad \text{Eqn.6.3.2.1}$$

where i is the index of size bands, j is the index of detector elements, and $U_{i,j}$ describes how particles in size band i scatter light to detector element j, thus describing how a known distribution of particle sizes will scatter light. Whilst the required result is the size distribution responsible for producing the measured light energy pattern, the light scattering matrix $U_{i,j}$ cannot be inverted, so instead the Mastersizer software converts the result to a volume distribution, giving V_i as the relative volume of material contained in size band i. To start the analysis a volume distribution is estimated based on the measured light energy data and a new light energy distribution is calculated using Eqn.6.3.2.1. The residual difference is calculated as:

$$\text{Residual} = 100\frac{\sqrt{\Sigma(D_j - L_j)^2}}{\Sigma D_j} \quad \text{.....} \quad \text{Eqn.6.3.2.2}$$

where D_j is the measured data and L_j the data calculated from the estimated volume distribution. The difference between L_j and D_j is used to correct the initial solution and a new set of values for L_j are calculated. This iterative process is continued until the residual reaches a minimum. The two parameter analysis models use a similar analysis technique as the model independent option, however they constrain the volume distribution to have a single peak which can be completely specified by two parameters of a characterising equation, describing the position of the peak on the size scale and the width of the distribution. Whilst the natural result of the Mastersizer is a volume distribution, this can be transformed to other distribution functions in terms of surface area, length or number, based on:

$$X_i = V_i.d_i\text{^}T\text{-}3 \quad \ldots\ldots\ldots \quad \text{Eqn.6.3.2.3}$$

where X_i is the transformed distribution, V_i the volume in size band i, d_i the mean diameter of size band i, and T an integer equal to 3 for volume, 2 for surface, 1 for length, and 0 for number distributions.

6.4 DIRECT SHEAR RESULTS

Fault gouge distributions experimentally generated by the direct shear testing programme were analysed using both conventional sieving and novel laser diffraction technology particle sizing techniques. The same sampling procedure was followed for all twelve specimens. Following shearing, the displaced upper (TOP) and lower (BOT) sliding surfaces were separated and an arbitrary circular sampling area isolated on both surfaces, using a section of copper pipe with cross-sectional area of $7cm^2$ (representing 6.5% of the total sliding surface area). Collateral sampling areas were chosen on upper and lower sliding surfaces so that corresponding shear debris samples were isolated, together representing the total fault gouge over 6.5% of the total slip surface. Large shear debris fragments were carefully removed from the sampling area using tweezers, whilst the powder fraction was recovered through use of a vacuum suction technique. These TOP and

BOT samples were then sieved individually in a mechanical sieve shaker for 15 minutes, using a sieve stack consisting of B.S. 30-, 36-, 52-, 60-, 100-, 120-, 150- and 170-mesh sieves, with nominal openings of 0.500, 0.422, 0.295, 0.251, 0.152, 0.124, 0.104 and 0.089mm respectively (see Table 6.3.1.1) . Following fault gouge sampling for sieving purposes, the entire remaining mass of debris from both the upper and lower sliding surfaces was gently removed by soft brushing, both specimens were combined, and the entire weight sieved into >500μ and <500μ fractions, the latter size interval being used as sample material for the laser particle sizer. Table 6.4.1 summarises the recovered fault gouge weights.

In order to assess the influence of sedimentary lithology on frictional strength, and on small particle statistical characteristics of the induced shear debris distributions, quantitative X-ray diffraction (XRD) studies were conducted on the >500micron-sized gouge fractions, by Dr. B.T. Ngwenya of Edinburgh University. The results, presented as percentage mineral content, are given in Table 6.4.2.

6.4.1 Sieving Results

Particle size distributions by sieving (cumulative weight % versus nominal sieve opening) were analysed using the normal, log-normal and Rosin-Rammler distribution functions as defined in sections 6.2.1, 6.2.2 and 6.2.3 respectively. Graphical representations of each law were produced according to the methods outlined in section 6.2.4, and a summary of derived data from these distributions is given in Table 6.4.1.1.

Use was made of the equality between the harmonic mean of the weight distribution, ${}_{w}d_{h}$, and the volume-surface mean particle size, d_{vs} (Herdan[221], p35) to compute an estimate of the specific surface area, S_w, of the shear-induced powders:

$$1/{}_{w}d_{h} = 1/G.\Sigma(g_i/x_i) = 1/d_{vs} \quad \text{.....} \quad \text{Eqn.6.4.1.1}$$

G: Total sample weight

I.D.	TOTAL MASS (g)	SIEVING		LASER SIZING		TOTAL >/< (%)
		TOP (g)	BOT (g)	>500μ (g)	<500μ (g)	
#3	12.1383	.1620	.4010	1.9264	9.6005	19.6
#5	28.045	.2455	.6550	5.3806	21.7178	24.0
#6	10.1869	.9855	.4525	.8827	7.7682	10.4
#8	70.7464	8.7164	2.0554	50.9709	8.9759	579.5
#9	78.6001	2.1351	4.7989	60.8810	10.7399	561.4
#11	2.5936	.0241	.1924	1.5873	.7712	204.0
#12	6.5211	.0740	.5230	3.9666	1.9272	199.8
#14	10.566	.0384	.5020	8.0816	1.9209	419.1
S1	54.5417	.3966	1.1126	44.1834	8.7938	484.5
S2	12.0125	.2623	.3563	8.1363	3.2404	233.2
S3	20.1718	.8779	.8696	14.0183	4.3803	308.9
S4	35.9045	.6917	.1635	26.5377	8.4975	295.9

Table 6.4.1 Recovered experimental direct shear fault gouge weights.

I.D.	XRD % Mineral Content:-			
	Quartz	K-Feldspar	Clays	Mica
#3	94.5	5.5	0	0
#5	82.5	17.5	0	0
#6	-----	-----	-----	-----
#8	15.1	38.8	46.1	0
#9	0	0	100	0
#11	-----	-----	-----	-----
#12	76.4	4.6	14.5	4.6
#14	65.4	8.7	22.1	3.8
S1	44.9	5.7	38.7	5.7
S2	44.5	4.1	45.5	5.9
S3	24.4	0	70.7	4.9
S4	45.1	0	45.5	9.4

Table 6.4.2 Direct shear specimen percentage mineral contents.

I.D.	Weight Distribution			Normal Distribution			Log-Normal Distribution			Rosin-Rammler Distribution		
(1)	(2) Mass (g)	(3) d_{vs} (μ)	(4) S_w (cm^2/g)	(5) $\bar{x}$ (μ)	(6) σ_{n-1} (μ)	(7) R^2	(8) x_g (μ)	(9) σ_g (μ)	(10) R^2	(11) n	(12) $\bar{x}$ (μ)	(13) R^2
#3 TOP	0.1620	219	103	314	158	0.980	273	1.93	0.990	2.03	355	0.998
#3 BOT	0.4010	164	138	238	146	0.972	198	1.83	0.992	1.87	268	0.991
#5 TOP	0.2455	142	159	198	150	0.927	168	1.85	0.994	1.72	230	0.976
#5 BOT	0.6550	164	138	220	120	0.995	184	1.67	0.970	2.05	247	0.996
#6 TOP	0.9855	198	114	264	115	0.979	221	1.63	0.991	2.53	290	0.989
#6 BOT	0.4525	153	148	220	144	0.943	184	1.81	0.995	1.86	249	0.977
#8 TOP	8.7164	428	53	1031	428	0.954	5236	5.87	0.999	1.25	3067	0.997
#8 BOT	2.0554	304	74	649	361	0.949	1080	4.43	0.999	1.15	1158	0.995
#9 TOP	2.1351	392	58	916	485	0.920	3709	6.06	0.994	1.14	2610	0.987
#9 BOT	4.7989	372	61	824	391	0.957	2241	5.05	0.999	1.20	1852	0.997
#11 TOP	0.0241	174	130	333	297	0.878	290	3.28	0.978	1.09	419	0.953
#11 BOT	0.1924	290	78	645	365	0.932	1050	4.44	0.996	1.14	1131	0.986
#12 TOP	0.0740	207	109	371	252	0.936	342	2.81	0.997	1.33	458	0.983
#12 BOT	0.5230	275	82	580	348	0.939	807	4.17	0.996	1.14	942	0.987
#14 TOP	0.0384	215	105	394	264	0.867	370	2.87	0.973	1.36	482	0.943
#14 BOT	0.5020	360	63	850	424	0.910	2371	5.59	0.989	1.12	1972	0.977
S1 TOP	0.3966	216	105	485	373	0.908	539	4.54	0.988	0.96	740	0.973
S1 BOT	1.1126	274	83	664	423	0.942	1141	5.67	0.998	0.94	1331	0.993
S2 TOP	0.2623	235	96	326	275	0.907	515	3.59	0.989	1.17	659	0.973
S2 BOT	0.3563	174	130	474	315	0.977	286	3.16	0.995	1.09	418	0.999
S3 TOP	0.8696	232	98	549	400	0.931	706	5.13	0.996	0.92	938	0.990
S3 BOT	0.8779	299	76	858	535	0.919	2474	8.81	0.993	0.80	2553	0.986
S4 TOP	0.1635	104	218	118	174	0.988	119	2.09	0.987	1.21	162	0.998
S4 BOT	0.6917	162	140	333	345	0.953	293	4.16	0.999	0.88	459	0.995

(1) "TOP"=upper sliding surface; "BOT"=lower sliding surface.
(2) Total shear debris mass collected from 7cm^2 sample area = 6.5% of total slip surface area.
(3) Harmonic mean of the weight distribution ≡ volume-surface mean diameter, $_wd_h \equiv d_{vs}$.
(4) For spherical particles with $\rho = 2.65 gcm^{-3}$, the specific surface area by weight, $S_w = 6/\rho . {}_wd_h^{-1}$.
(5) Arithmetic mean.
(6) Population standard deviation.
(7) Critical coefficient (R^2) for linear regression of the normal distribution.
(8) Geometric mean.
(9) Geometric standard deviation.
(10) Critical coefficient (R^2) for logarithmic regression of the log-normal distribution.
(11) Distribution constant.
(12) Absolute size constant.
(13) Critical coefficient (R^2) for logarithmic regression of the Rosin-Rammler distribution.

Table 6.4.1.1. Direct shear fault gouge distribution characteristics by sieving.

g_i: Weight of particles in class interval i

x_i: particle size

The quantity which is used for characterising the surface extension of a bed of powder is the specific area, that is the surface area per ml of the packing (volume surface, S_v) or the surface area per g of the powder (weight surface, S_w) the relation between which is given by $S_w = S_v/\rho$, where ρ is the density of the powder phase. For the specific surface calculated from a weight distribution obtained, for instance, by sieving (Herdan, p193):

$$S_w = \alpha_s/\alpha_v.1/\rho.d_{vs} = 6/\rho(w_1/x_1 + w_2/x_2 + w_3/x_3.....) \quad ..... \quad \text{Eqn.6.4.1.2}$$

α_s/α_v: volume shape factor / surface shape factor

$w_1, w_2, w_3...$: weight fractions or % per g of sample

$x_1, x_2, x_3...$: mean particle sizes of the corresponding size intervals

The ratio α_s/α_v is the factor of proportionality which turns the reciprocal of the volume-surface mean diameter into the specific surface of a bed of particles. For the cube and the sphere, $\alpha_s/\alpha_v = 6$ whilst for other shapes the ratio is >6, for example crushed quartz gives a ratio of 11. As an approximation Eqn.6.4.1.2 calculates the sum of partial surfaces, one for each size interval. In Table 6.4.1.1 the mean-volume surface diameter, and an estimate of the specific surface area (assuming spherical particles and a single mineral-phase density of 2.65gcm^-3, equivalent to that of quartz) for both TOP and BOT weight distributions is given.

For the assumption that each of the weight distributions obtained by sieving follows one of the standard forms described in section 6.2 above, the arithmetic mean and standard deviation characterising the normal distribution, the geometric mean and geometric standard deviation characterising the log-normal distribution, and the distribution and absolute size constants defining the Rosin-Rammler law, are also quoted in Table 6.4.1.1. Accepting

that the straight line of the graph is some evidence, even though no strict mathematical proof, that the distribution is governed by the normal, log-normal or Rosin-Rammler laws, critical coefficients, R^2 (where R = correlation coefficient) are tabulated in Table 6.4.1.1 for regression fits to the three distribution functions. Visual inspection of the plots shows a systematic curvature to all of the normal distributions, which also possess the lowest of the critical coefficients, suggesting that this is not a valid law for particle size distributions obtained by direct shear. Visual inspection of the log-normal and power-law distributions show much closer approximations to linearity (although some are still visibly curved, for example the Rosin-Rammler plots of specimens #11, #12 and #14 due to their strongly skewed nature) however, no conclusion can be drawn regarding the relative superiority of the log-normal to the power law distribution, especially considering the few data points (8) and the small spread in particle size (<1 order of magnitude). There is a tendency for those specimens with high clay content to produce high-magnitude geometric means (σ_g) and absolute size constants ($\bar{x}$), reflecting the large residual weights contained within the >500micron fractions. For these specimens, such values are consistent with the mm-sized fragments observed on the 500micron pan.

Modest trends were evident between the Rosin-Rammler constants (averaged for both upper "TOP" and lower "BOT" sliding surface samples) and percentage mineral content, as shown in Fig.6.4.1.1(a) and (b) for n and $\bar{x}$ values respectively. The distribution constant (n) exhibits a gross non-linear increase with increasing quartz content, and a non-linear decrease with increasing clay content, suggesting that grading becomes closer with increasing quartz content, and more dispersed (dustier) with increasing clay content. The absolute size constant ($\bar{x}$) shows a gross linear increase with increasing clay content, and a linear decrease with increasing clay content, suggesting that the gouge material is becoming coarser with increasing clay content, and finer with increasing quartz content.

Grady & Kipp (1987)[239] proposed that growing evidence from a wide variety of different fragmentation methods, whilst far from being complete or systematic, did tend to suggest that the broad range in size of the distribution constant, n, might be related, at least in part, to the type or method of fragmentation. Several different fragmentation processes are listed

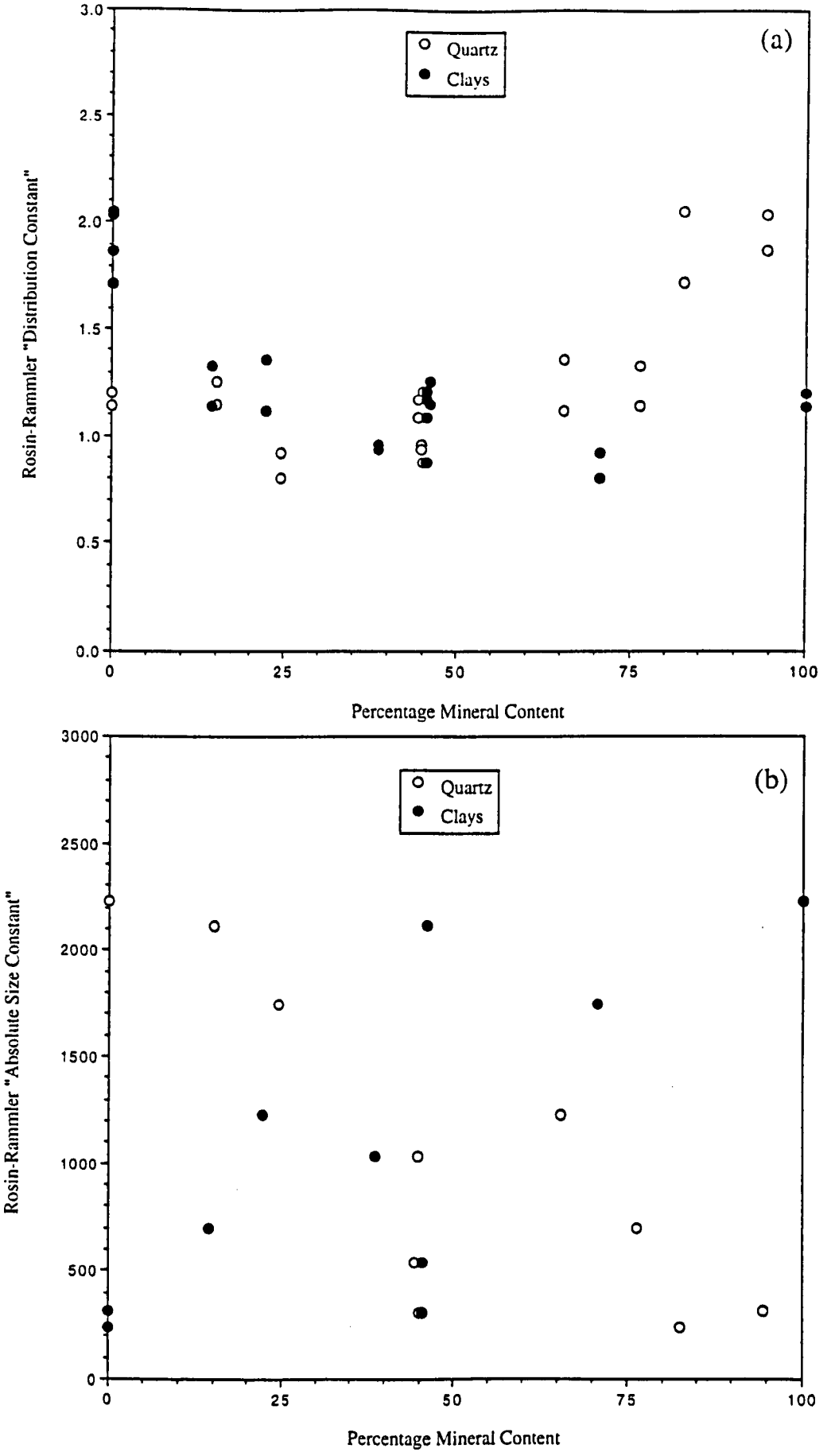

Fig.6.4.1.1 Influence of lithology on averaged (a) distribution and (b) absolute size Rosin-Rammler constants, of sieved direct shear debris.

in Table 6.4.1.2, in order of decreasing n. From the above list, Grady & Kipp suggested that single tensile fragmentation leads to fragment size distributions with large values of n, whereas in contrast, fragmentation with significant shearing and continued comminution leads to lower values. In Fig. 6.4.1.1(a), average distribution constants, n, from the relatively large-size fraction sieving analyses, are plotted against percentage mineral content, determined by XRD of the multilithologic direct shear specimens. From this, it is evident that the distribution constant increases from $n \approx 1$ to $n \approx 2$ with increasing quartz content, and decreases with increasing clay content. As the method of fragmentation has been the same for all rock types, direct shear testing under constant normal displacement control, this observed variation in distribution constant therefore probably reflects material property differences. It is therefore suggested that a tentative explanation for this observed trend can be found through considering the micromechanics of the deformation. For the high quartz content sandstones with grain-supported "ball-bearing like" structures, macroscopic shearing will on the microscale be transmitted as stress-concentrations at the point-to-point quartz grain contacts, resulting in predominantly tensile splitting as shown schematically in Fig.6.4.1.2(a). By contrast, due to the foliated nature of the clay-rich lithologies, macroscopic shearing may activate this fabric, resulting in foliation shearing, illustrated schematically in Fig.6.4.1.2(b) as observed in natural argillaceous fault gouge (Rutter *et al*, 1986[240]) . Thus the mechanisms of strain accommodation on the microscale can be construed as being determined by initial rock microstructure, the relative amounts of resultant shearing fragmentation to tensile cracking being reflected in the resultant debris distributions. However, the data is not of sufficient quality to distinguish between a bimodal population of quartz-rich sandstones and clay-rich heterolithics, or whether there is continuous gradation between the distribution constant and clay content, reflecting relative amounts of shear to tensile comminution on the microscale.

6.4.2 Malvern Results

Whilst sieving studies as described above benefit from being widely-applied, speedy and accurate, they only allow access to particle sizes just under 0.1mm, so that complementary laser diffraction techniques are of particular interest in admitting ingress to sub-micron particles, with detectable size ranging over 3.5 orders of magnitude. Such ©Malvern

Process	Distribution constant, n	Reference
Theoretical upper limit	6	Grady & Kipp (1985)
Fragmenting bomb casings	4 - 5	Weimar & Rogers (1979)
Direct impact fragmentation	2 - 3	Shockey *et al* (1974)
Hopkinson bar tests (sunstantial torsional shear)	1.2 - 1.8	Grady *et al* (1981)
Ball milling (multiple comminution)	0.6 - 1	Rosin & Rammler (1933)

Table 6.4.1.2 Behaviour of the distribution parameter, n, for various fragmentation methods (for full references cited above see Grady & Kipp[239]).

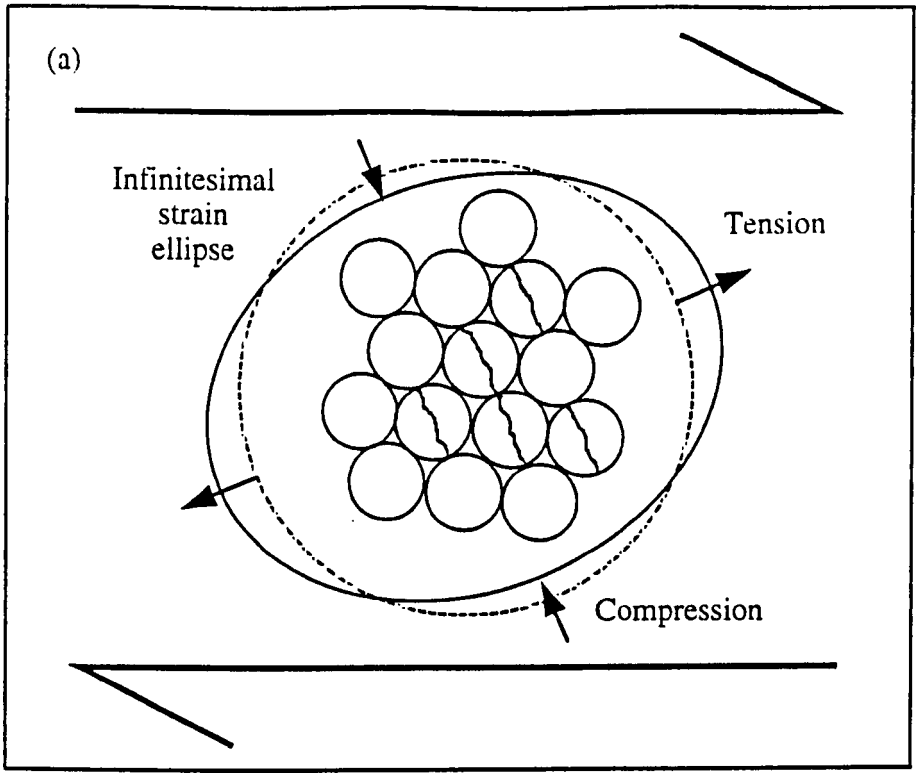

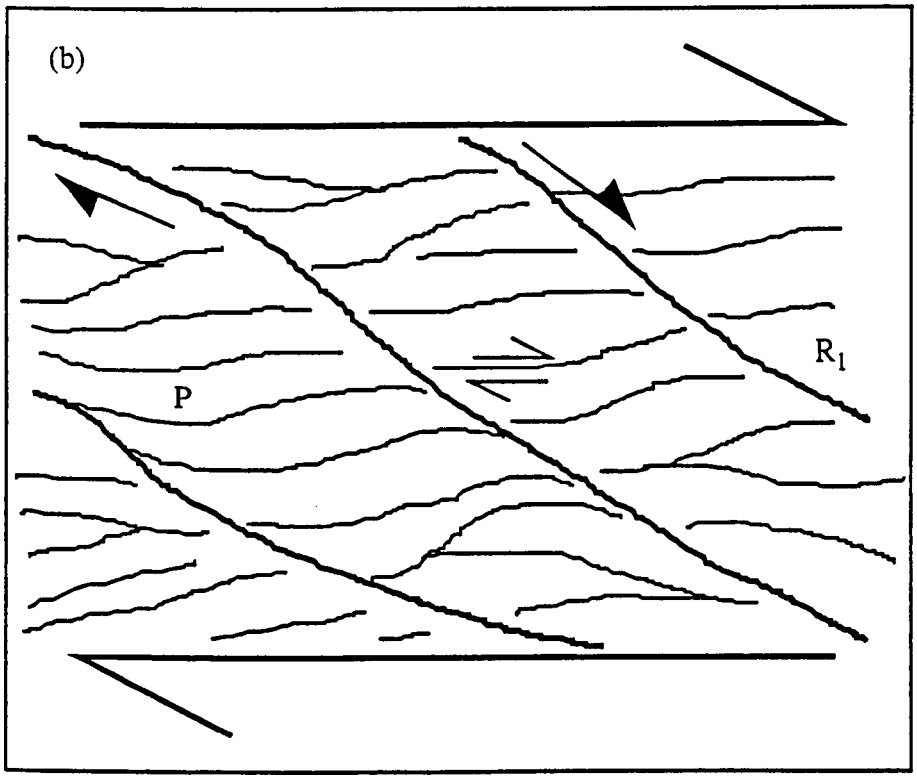

Fig.6.4.1.2 Schematic representation of the micromechanics of fault gouge comminution associated with macroscopic shearing of (a) quartzose granular and (b) phyllosilicate-rich rocks. In (a) macroscopic shearing leads to predominantly tensile microcracking at grain-impingement stress concentrations. In (b) foliation shearing leads to sliding on pre-existing platy P-foliation and the development of secondary Riedel, R_1-shears.

Mastersizer studies utilised the <500micron-sized fraction detailed in Table 6.4.1, suspended in distilled water as a supporting medium. The optical model employed by the Mastersizer to compute volume distributions was customised by entering the optical constants of the sample material and supporting medium, all direct shear powder samples being treated as quartz, with a refractive index of 1.54. Also, for specific surface area (per g of sample) calculations, all sample materials were assigned the specific gravity of quartz = 2.65. Thus despite the polyminerallic nature of the direct shear specimens, with clay contents ranging up to 100% (#9) operating restrictions forced the Mastersizer to regard all experimental fault gouge powders as volume distributions of quartz spheres. Independent powder samples from each direct shear specimen (BOT and TOP combined) were analysed using the 300mm- and 45mm-range lenses, giving particle sizes extending from 600 to 1.2microns and 80 to 0.1microns respectively. The analysis mode was set to model independent, in which no assumption is made about the form of the result with regard to its distribution.

Resultant cumulative weight oversize (%) versus particle size data was analysed using the log-normal and Rosin-Rammler laws, and represented graphically as given in Fig.6.4.2.1 (red sandstones), Fig.6.4.2.2 (fissile mudstones), Fig.6.4.2.3 (carbonaceous siltstones) and Fig.6.4.2.4 (heterolithics) using the methods outlined in section 6.2.4. This Mastersizer data is complemented by superimposition of the sieving data detailed in section 6.4.1, for the purposes of comparison. With the exception of the fissile mudstone results, good correlation is shown between the 300mm range lens data and sieving results. Geometric means and standard deviations for the log-normal curves are given in Table 6.4.2.1, as well as distribution and absolute size constants characterising the Rosin-Rammler plots. Due to the sigmoidal nature of some of these power-law distributions (especially the fissile mudstones) straight line logarithmic regression fits were calculated for the central portion of each curve, the particle size range of these fits also being given in Table 6.4.2.1. The distribution constants, n, were converted to inferred fractal dimensions, D, using the linear relation, $D = 3 - n$ (Eqn.6.2.5.4).

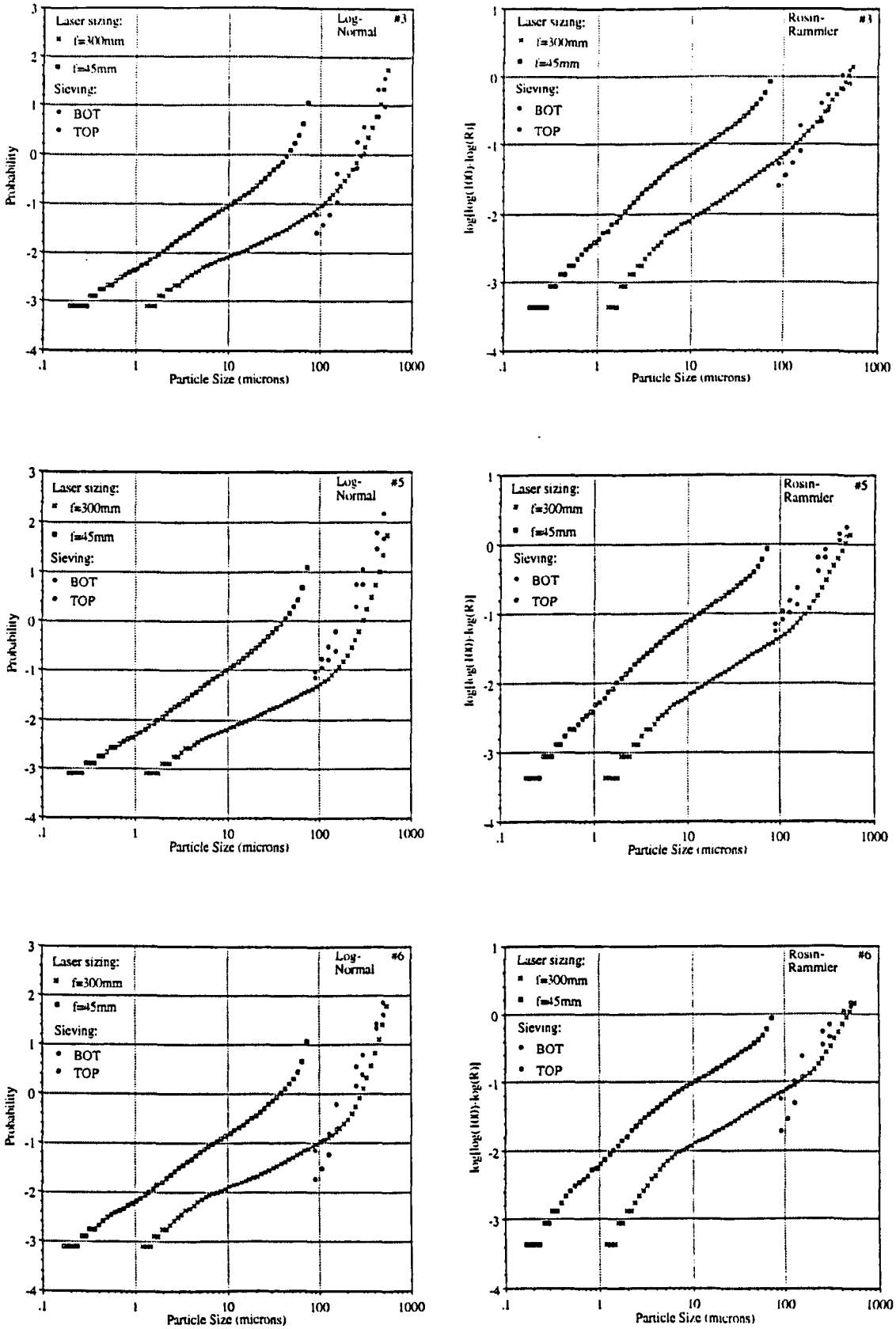

Fig.6.4.2.1 Distribution functions for red sandstones #3, #5 & #6.

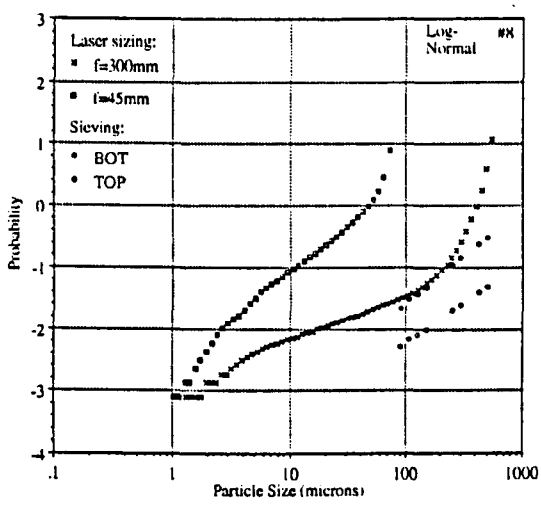

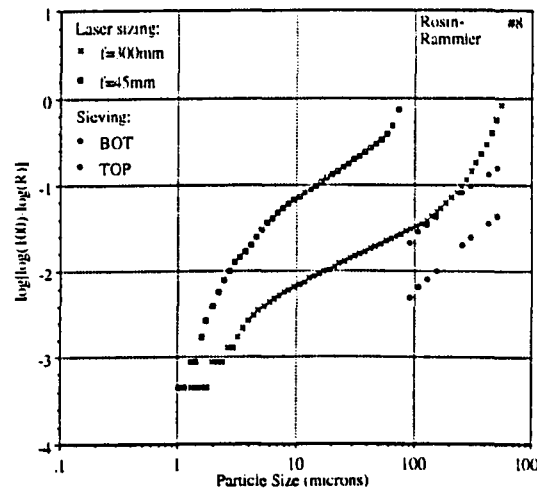

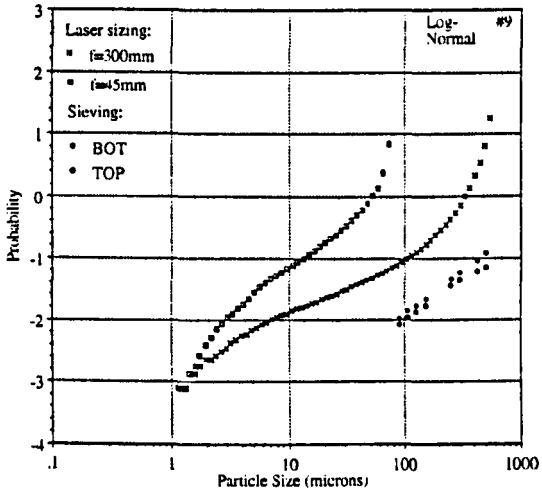

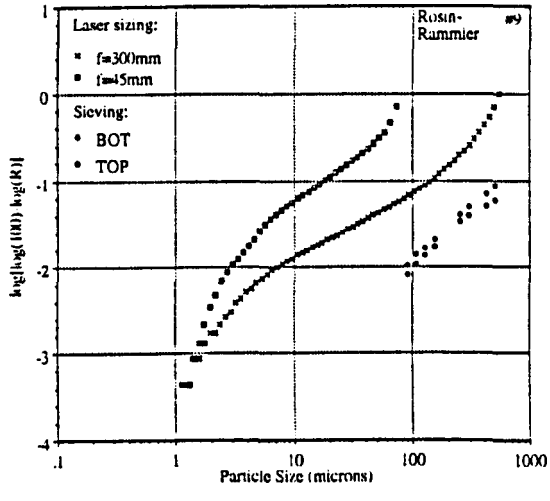

Fig.6.4.2.2 Distribution functions for fissile mudstones #8 & #9.

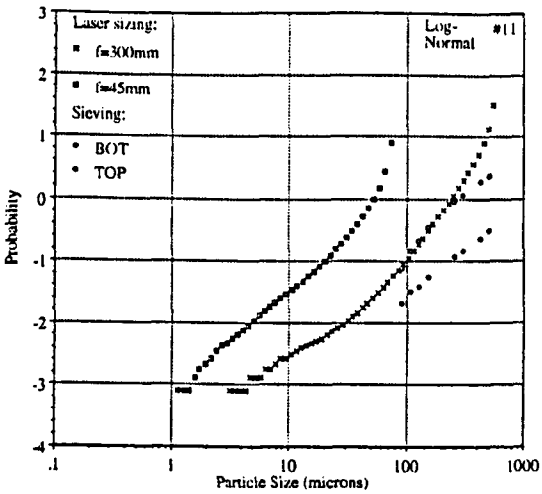

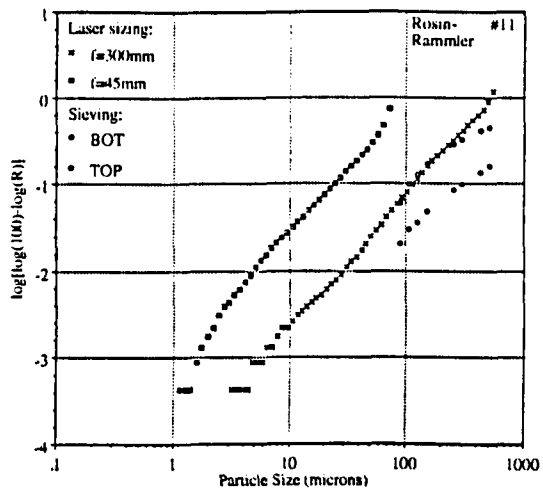

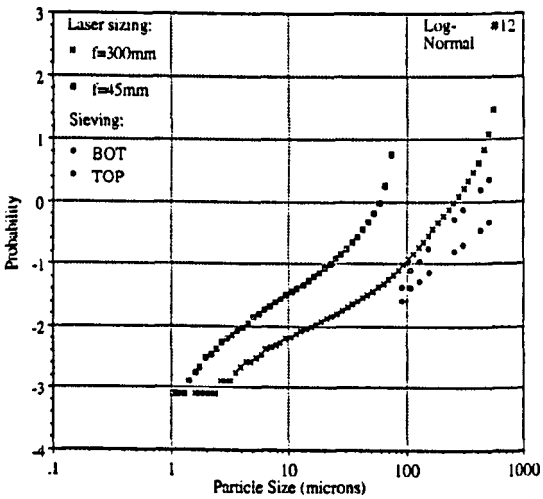

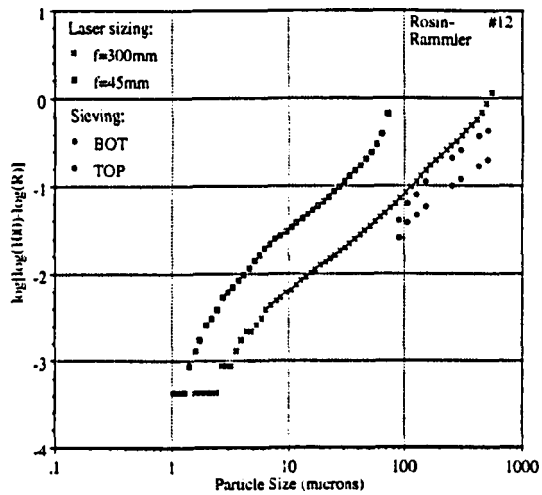

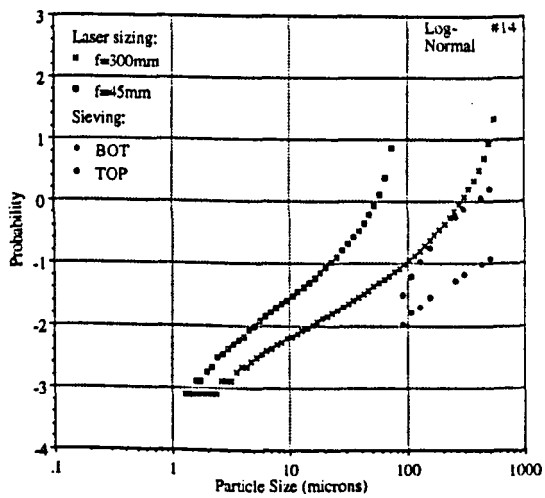

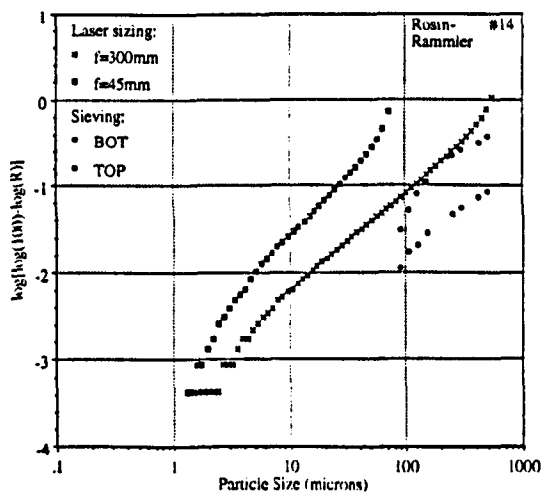

Fig.6.4.2.3 Distribution functions for carbonaceous siltstones #11, #12 & #14.

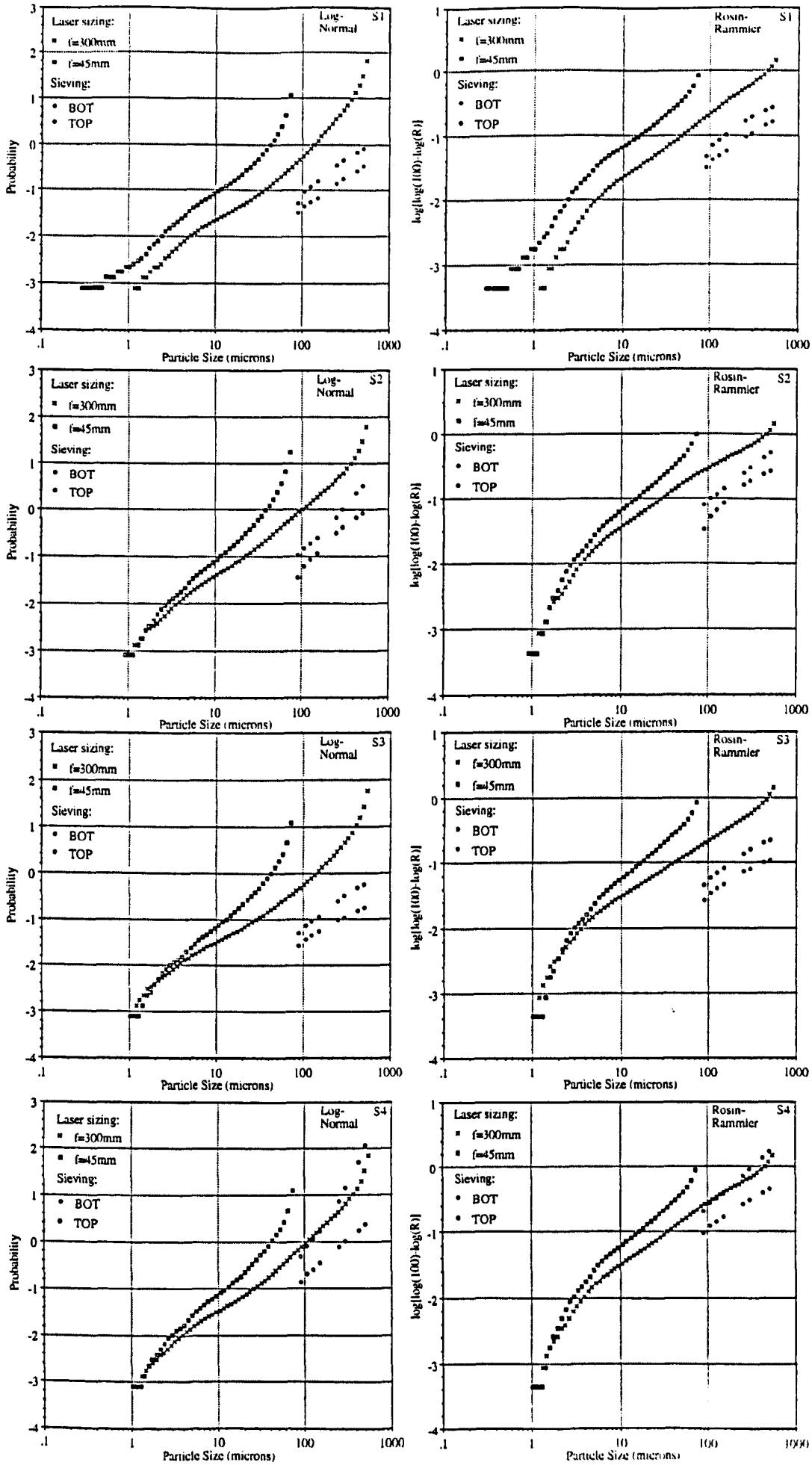

Fig.6.4.2.4 Distribution functions for heterolithics S1, S2, S3 & S4.

I.D.	f=300mm range lens, 1.2<x<600μ							f=45mm range lens, 0.1<x<80μ						
	x_g (μ)	σ_g (μ)	n	α (°)	*D*	$\bar{x}$ (μ)	$\alpha/\bar{x}$	x_g (μ)	σ_g (μ)	n	α (°)	*D*	$\bar{x}$ (μ)	$\alpha/\bar{x}$
#3	304	5.11	0.88	41.4	2.12	926	.045	46	5.16	0.93	42.9	2.07	70.8	.61
#5	415	5.41	0.85	40.4	2.15	1383	.029	41	5.00	0.99	44.7	2.01	58.6	.76
#6	295	5.54	0.80	38.7	2.20	865	.045	35	5.13	0.87	41.0	2.13	57.4	.71
#8	1069	7.98	0.69	34.6	2.31	4054	.009	41	3.51	0.95	43.5	2.05	71.2	.61
#9	425	6.81	0.74	36.5	2.26	1131	.032	46	3.61	0.97	44.1	2.03	80.7	.55
#11	251	3.40	1.54	57.0	1.46	318	.179	56	3.35	1.37	53.9	1.63	72.6	.74
#12	278	4.46	1.05	46.4	1.95	565	.082	68	3.83	1.09	47.5	1.91	111	.43
#14	310	4.69	1.12	48.2	1.88	431	.112	61	3.37	1.33	53.1	1.67	82.6	.64
S1	116	4.27	1.00	45.0	2.00	204	.221	43	4.24	1.05	46.4	1.95	60.4	.77
S2	88	4.50	0.95	43.5	2.05	140	.311	34	3.19	1.15	49.0	1.85	53.8	.91
S3	114	5.02	0.87	41.0	2.13	210	.195	38	3.26	1.16	49.2	1.84	58.5	.84
S4	92	4.39	0.92	42.6	2.08	173	.246	37	3.25	1.12	48.2	1.88	58.6	.82

Table 6.4.2.1 Particle size distribution constants derived from laser sizing, for direct shear-generated fault gouge.

With the possible exception of specimen S1, visual observation of the strongly sigmoidal expression of the log-normal probability plots, suggests that this function does not have wide application for the direct shear gouge distributions (it should be noted however that both the natural and experimental fault gouge distributions described by Engelder (1974)[69] as being log-normal over much more restricted particle size ranges determined from sieving, also showed similar sigmoidal profiles). In general, the deviation of each graph from the straight line indicates a corresponding deviation of the particle size distribution from normality. The slope of the curve is a measure of particle sorting, sorting deteriorating with decreasing slope. Using this method, Engelder found the sorting of experimental quartz fault gouge deformed under triaxial compression, to decrease both with increasing confining pressure and with increasing shear displacement. A general trend is apparent amongst the quartz-rich/clay-poor sample plots generated by the 300mm-range lens (#3, #5, #6, #11, #12, #14, S1) for initially steep slopes down to particle sizes of around 100microns, parallel to the sieve data, followed by shallower slopes which remain linear down to the lowest limits of the measuring range. Such convex downwards curves represent a change in sorting at about the 0.1mm particle size, which may reflect relatively well-sorted initial grains which have not been fragmented, contained within a fine-grained matrix of comminuted debris representing steady-state size reduction down to the limits of particle size resolution. In contrast, the clay-rich/quartz-poor samples (#8, #9, S2, S3, S4) exhibit strongly sigmoidal curves, which reflect initial decrease in sorting, followed by an increase in sorting down to around 1micron, representing the lower limit of particle size. The fact that both the 300mm- and 45mm-range lens data converge at this lower limit of around 1micron, strongly suggests that the argillaceous samples achieve a minimum comminution limit. This observation indicates that the comminution efficiency of the clay-rich specimens is reduced at small particle size, compared to that of the quartz-rich specimens, which may reflect the nature of the inter-particle stress concentrations for the different mineral phases. This could well be due to the relative shape factors of the clay and quartz fractions, however it is also possible that plastic deformation, as opposed to fracturing and increase in new surface area, may be occurring in the clay phase. Interestingly, Mackenzie & Milne (1953)[241] showed that the X-ray diffraction pattern of muscovite becomes more diffuse as industrial grinding proceeds until, after 8hours, no

sharp pattern remains. After further grinding the pattern reappears but has a different form to the original, suggesting the possibility of recrystallisation.

The power-law (fractal) distribution curves for the direct shear debris samples, show fairly robust approximations to linearity for the quartz-rich specimens, over the entire measurement range, however, as observed for the log-normal plots, specimens with clay contents >50% (#8, #9, S2, S3, S4) show sigmoidal trends with both the laser-sized distributions converging at around 1micron. For the purposes of comparison, straight-line logarithmic regression fits were constructed for the linear mid-sections of all 12 direct shear power-law distributions, in order to determine fractal dimensions for the fault gouge samples. Whilst scale-invariance is inherent in the definition of a fractal or fractional dimension, "natural" as opposed to "mathematical" fractals do possess finite upper and lower fractal limits above and below which this scale invariance breaks down. The direct shear fractal dimension magnitudes are given in Table 6.4.2.1. From this, it is evident that the magnitude of D lies in the range $1.5<D<2.4$ and $1.7<D<2.2$ for f=300mm and f=45mm respectively, both limits lying within the range of published magnitudes for a diverse range of fractal fragment-size distributions (see for example Table 6.2.5.1).

6.4.3 Frictional Strength Correlations and Surface Energy Considerations

For the direct shear experimental programme, in which shearing was conducted under constant normal displacement conditions conducive to maximum gouge production (post-maximum frictional slip occurring wholly upon a substrate of comminuted shear debris) it is obviously of interest to investigate any relations between the nature of the fragmented wear products, and the frictional strength of the sliding interfaces. Whilst no correlation was found between either of the parameters describing the log-normal distribution (x_g and σ_g in Table 6.4.2.1) and the frictional strength parameters (μ^*_{max} in Table 3.5.1.1, μ_s and S_o for constant and variable contact areas in Table 3.5.3.1) presumably due to the poor applicability of this distribution function, correlation was indeed evident between fractal dimension, D, as listed in Table 6.4.2.1, and μ_s. Whilst correlation between μ_s, and D -values from the 300mm-range lens was evident, better correlation was shown with the 45mm data, illustrated in Fig.6.4.3.1. From this plot it is evident that the magnitude of the

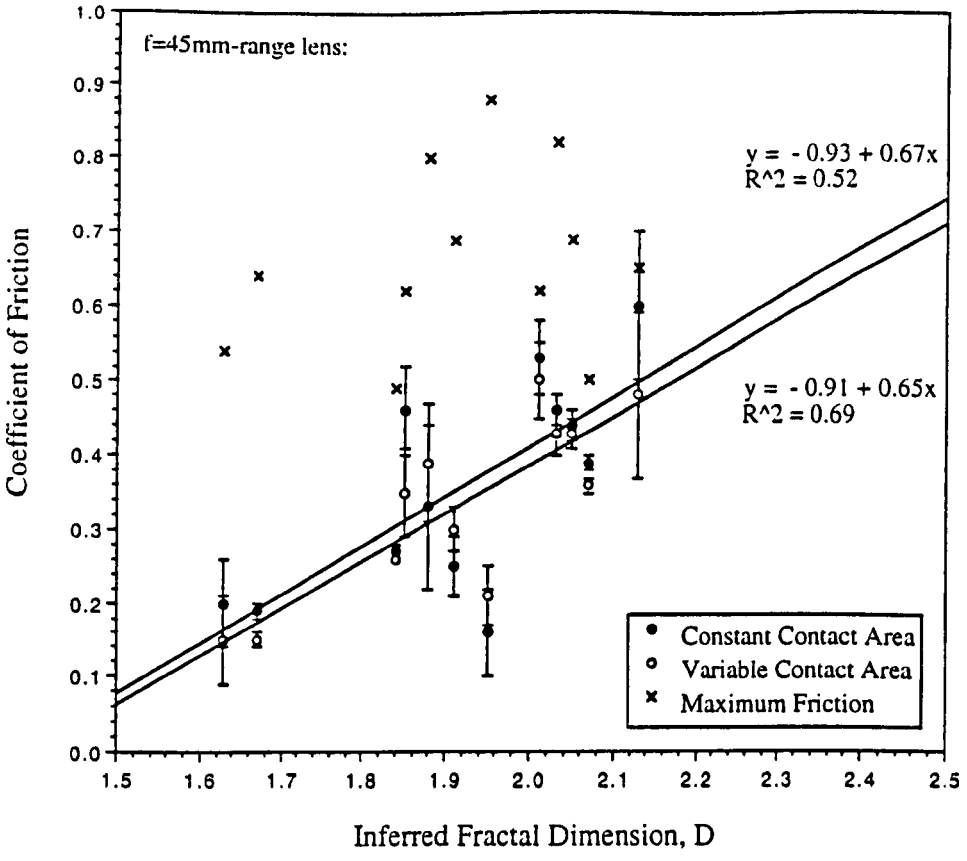

Fig.6.4.3.1 Empirical correlation between macroscopic frictional strength and induced shear debris distribution, from direct shear experimentation.

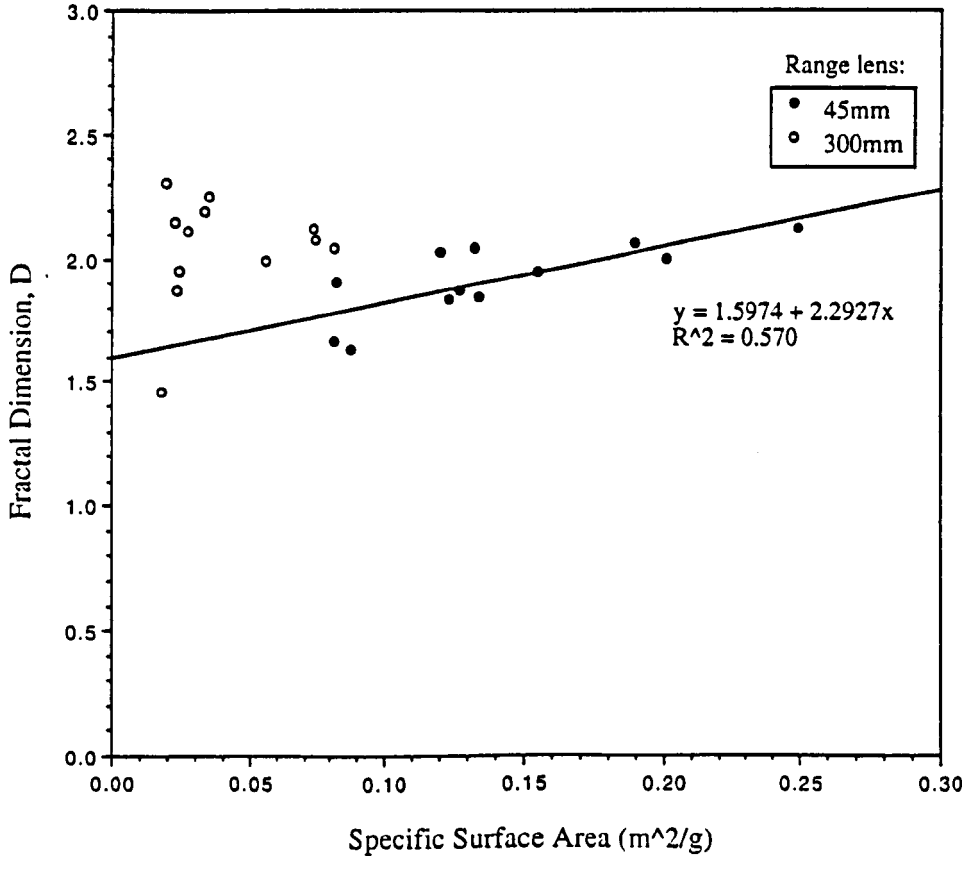

Fig.6.4.3.2 Empirical correlation between specific surface area and fractal dimension of induced shear debris distributions, from direct shear experimentation.

maximum friction is independent of the fractal dimension of the induced gouge, which is to be expected if μ^*_{max} represents maximum interlocking of asperities, prior to pervasive shearing of roughness and frictional sliding upon a comminuted substrate.

As higher values of *D* indicate higher numbers of small fragments relative to larger fragments than in populations with lower fractal dimensions, and as surface area varies inversely with particle size (see Eqn.6.4.1.2), intuitively it follows that higher *D* indicates greater surface area. This relation is borne out between the empirically determined correlation between specific surface area, S_w, calculated for the 45mm-range lens data using Eqn.6.4.1.2, and the fractal dimension, *D*, as given in Fig.6.4.3.2. No correlation is evident between *D* and S_w as determined from the 300mm-range lens data, although it is pointed out that maximum surface area determination is generated from the smallest particle size measurements, as shown by Table 6.4.3.1, which lists volume-surface mean particle sizes and weight specific surfaces for the two laser measurement ranges. The coefficient of sliding friction, μ_s, also correlates with the model independent, volume-surface mean particle size determinations of specific surface area, as shown in Fig.6.4.3.3.

Olgaard & Brace (1983)[242] studied quartz fault gouge from two mining-induced seismic shear fractures, in order to determine that portion of the total strain energy released during an earthquake that is allocated to the creation of new surface area (fault gouge). They noted that the three principal sinks for the strain energy released during faulting are heat, seismic waves and microstructural defects formed during crushing (as new surface area is the principal defect produced at shallow crustal levels, this "defect" energy is mostly surface energy). Olgaard & Brace estimated the surface area energy, W_A, that is the amount of energy consumed in creating new surfaces, using the relation:

$$W_A = S_W.\rho.\gamma \quad \text{.....} \quad \text{Eqn.6.4.3.1}$$

W_A: energy density, the energy per unit volume (Jm^-3)

S_W: specific surface area per gram of powder (m^2kg^-1)

I.D.	f=300mm range lens 1.2<x<600μ		f=45mm range lens 0.1<x<80μ		Shear Fracture Energy G_{IIc} (Jm^{-2})	
	d_{vs} (μ)	S_W (m^2/g)	d_{vs} (μ)	S_W (m^2/g)	CONSTANT AREA	VARIABLE AREA
#3	83	.0274	12	.1891	8254	7659
#5	102	.0221	11	.2008	14965	15106
#6	69	.0330	9	.2487	-----	-----
#8	115	.0196	17	.1319	7569	8729
#9	65	.0346	19	.1202	2677	2795
#11	128	.0177	26	.0874	1489	1135
#12	96	.0236	25	.0891	-----	-----
#14	97	.0234	27	.0826	2278	2215
S1	41	.0555	15	.1543	-----	-----
S2	28	.0810	17	.1340	4620	3544
S3	31	.0731	18	.1231	2390	2830
S4	30	.0744	18	.1271	-----	-----

Table 6.4.3.1 Volume-surface mean particle size and weight specific surface area for laser-sized distributions charactersied by the 300mm- and 45mm-range lenses, as well as shear fracture energies for both constant and variable macroscopic sliding surface contact area, for those samples that exhibited slip-weakening.

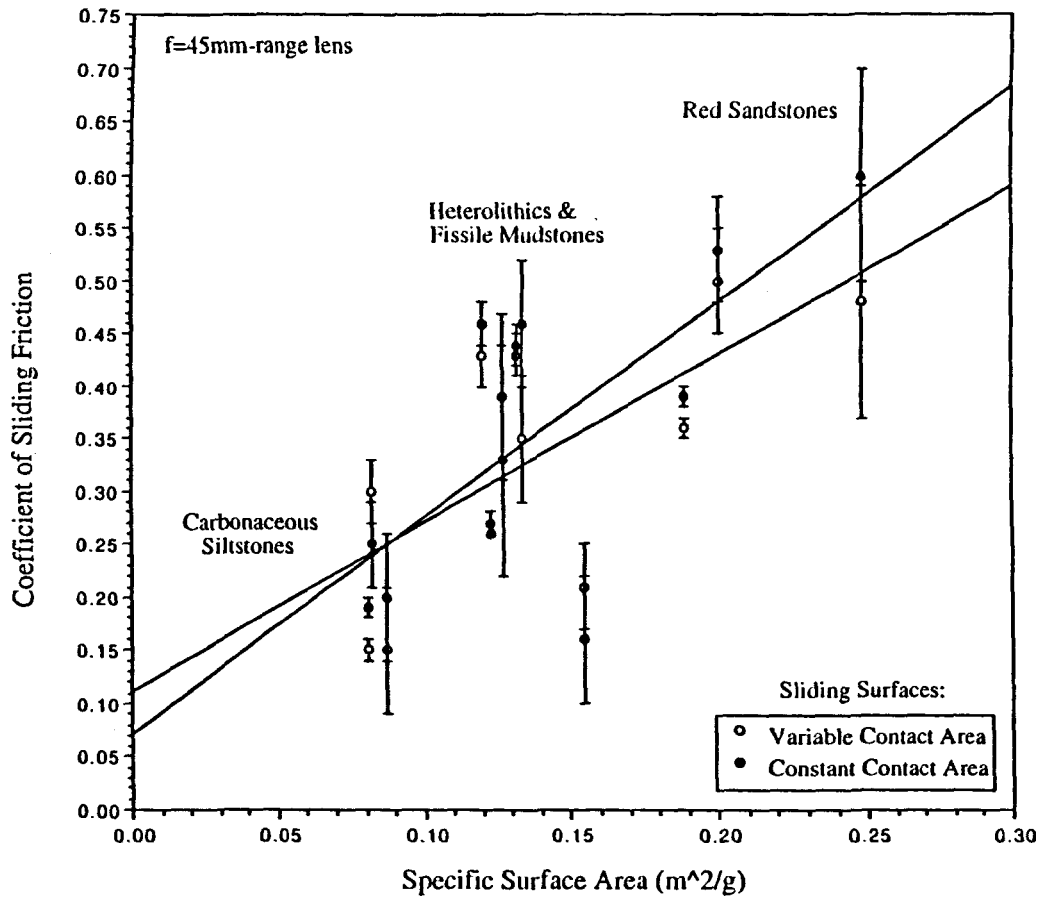

Fig.6.4.3.3 Empirical correlation between induced fault gouge specific surface area, and macroscopic frictional strength.

ρ: density of the single mineral phase (kgm^-3)

γ: specific surface energy of single crystal determined in tension (Jm^-2)

For quartz fault gouge with S_W=2.0m^2/g, γ=0.7J/m^2 and ρ=2.65$\times$10^{3}kg/m^3, Olgaard & Brace calculated W_A=3.7$\times$10^{6}J/m^3. They then compared this value for W_A with the total energy released during an earthquake, E_T:

$$E_A/E_T = (W_A.A.u)/E_T \quad \text{.....} \quad \text{Eqn.6.4.3.2}$$

A: area of fault plane

u: width of fault gouge zone

From Brune (1968)[243], $E_T = A.d.\bar{\sigma}$ where d is the average fault displacement, and $\bar{\sigma}$ is the average stress on the fault. Thus for typical mine values of A, u, d and $\bar{\sigma}$, they calculated that E_A/E_T = 1 - 9%, that is the surface energy is of the same order of magnitude as the seismic energy, with heat thus representing the principal energy sink. This is in agreement with Engelder *et al* (1975)[244] for experimental sliding under triaxial compression of pre-cut Tennessee sandstone on an artificial layer of quartz fault gouge, who likewise found the increase in surface energy to be a negligible fraction of the total work done (≈0.1%).

From Eqn.6.4.3.1, it is evident that the energy density varies directly with the specific surface area, suggesting that, possibly, the positive linear correlation of frictional strength with both S_W and *D*, may reflect an increase in frictional resistance associated with an increase in the energy required to create new surface area. However, Eqn.6.4.3.1 also highlights the fact that a reasonable estimate of W_A depends heavily upon the accuracy of the measurement of S_W. Olgaard & Brace[242] used a combination of scanning and transmission electron microscopy, X-ray sedimentation and gas adsorption to measure S_W, and to study particle size and shape in the submicron-size region. Unfortunately, however, the laser-sizing method, whilst able to measure over a wide particle-size range, assumes a

shape factor of 6 for theoretically spherical particles, so that S_w may be underestimated by up to an order of magnitude. Thus an inability to quantify shape factor and its variation with mineralogy, combined with a lack of knowledge of potential digression from XRD-quantified percentage mineral content with particle size, precludes any estimation of energy density, W_A, for the direct shear polymineralllic gouge samples, using the method outlined above.

Instead of a direct estimate of the surface energy per unit volume of gouge, W_A, the "shear fracture energy" (see section 1.4) is estimated following an integration scheme proposed by Rice (1980)[245] in which he suggested that the shear fracture energy, or critical energy release rate under mode II loading, G_{IIc}, can be evaluated by performing an appropriate integration under the post-failure stress-displacement curve. Physically this quantity G_{IIc} (Jm^-2) represents the energy flux for "breakdown" processes at a crack tip, and is the crucial parameter that constrains the energetics at the crack tip. This crack extension force or strain energy release rate, G_{IIc}, is the loss of energy per unit area of new crack sliding area formed during an increment of crack extension. The relevant results of Rice have been succinctly reviewed by both Wong (1982)[246] and Li[31], so that only the briefest details will be summarised here. The slip-weakening model (Fig.6.4.3.4) considers an earthquake fault as a shear crack with a peak shear strength, τ^p. Relative slip initiates when the shear stress, τ, reaches τ^p, and the strength degrades from τ^p to a constant residual frictional strength, τ^f, as the slip, δ_s, increases to a critical value, δ_s^*. Consequently, there is a breakdown zone at the shear crack tip of dimension, w, and with distribution of τ and δ_s as shown on the left-hand-side of Fig.6.4.3.4. Rice[245], applying the J-integral and assuming that w is small compared to the overall crack size, was able to derive a criterion analogous to the critical energy release rate criterion in LEFM. The shear fracture energy or critical energy release rate in mode II is then given by:

$$G_{IIc} = \int_0^{\delta_s^*} \left[\tau(\delta_s) - \tau^f\right].d(\delta_s) \quad \text{.....} \quad \text{Eqn.6.4.3.3}$$

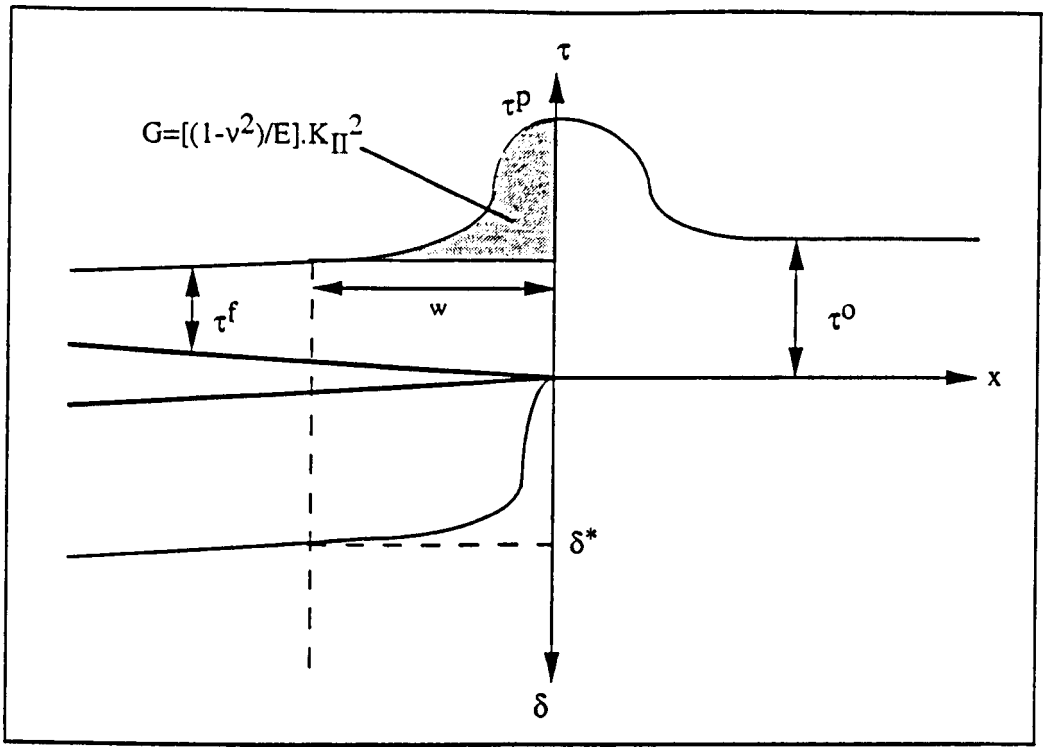

Fig.6.4.3.4 Stress and slip distributions near a crack tip with a breakdown zone in which the deformation behaviour is governed by the slip-weakening relation (Li[31]).

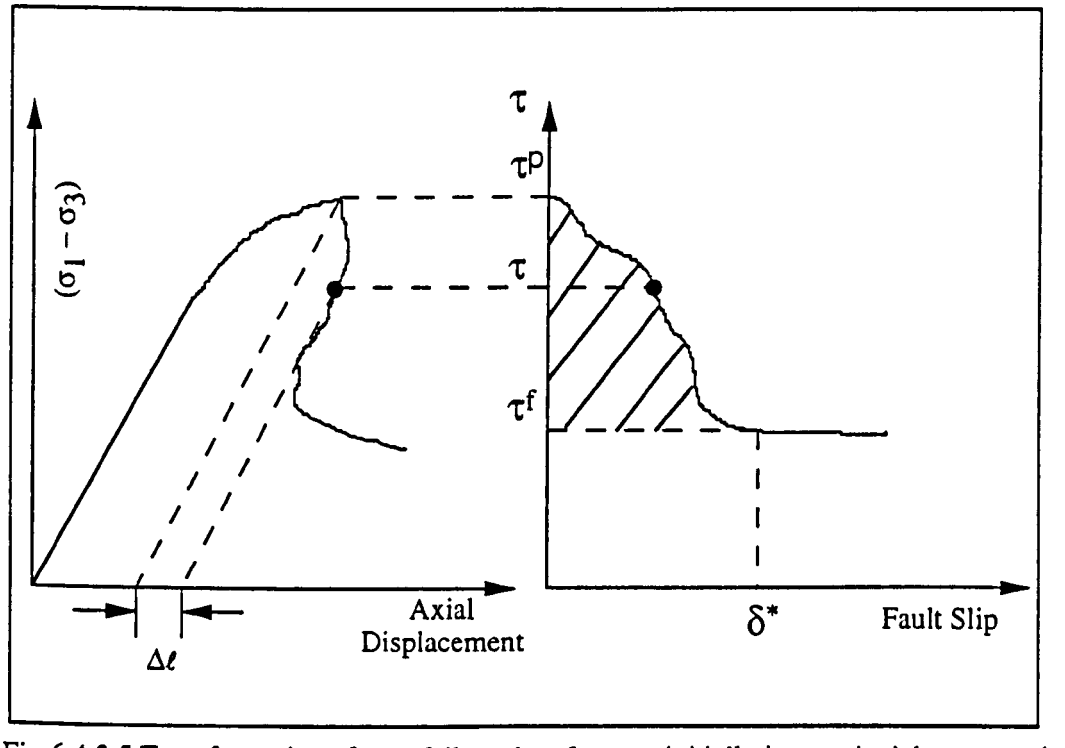

Fig.6.4.3.5 Transformation of post-failure data from an initially intact triaxial compression test to infer the shear stress versus relative slip relation used in the slip-weakening model (Rice[245]).

A graphical representation of this relation is shown in Fig.6.4.3.5, where G_{IIc} is simply the hatched area under the shear stress versus shear displacement curve. Li[31] notes that Eqn.6.4.3.3. may be interpreted as follows: the excess energy flux (above doing frictional work) made available balances the energy absorption in the breakdown process for slip zone extension. Eqn.6.4.3.3, with the left-hand-side interpreted as a crack driving force and the right-hand-side interpreted as a fracture resistance, then affords a criterion for propagation of the slip zone. Note that G_{IIc} does not include any contribution from the residual shear stress, since τ^f is explicitly subtracted from the integrand.

Using the integration scheme outlined above, an estimate of the G_{IIc} magnitude for the direct shear samples that showed post-peak strength, slip-weakening response, was simply obtained by quantifying the area under their post-maximum friction shear stress versus shear displacement curves (see Fig.3.4.4.1, Fig.3.4.4.2, Fig.3.4.4.3 and Fig.3.4.4.4) using a digital planimeter. In total, only 8 samples showed this slip-weakening behaviour (#3, #5, #8, #9, #11, #14, S2 & S3) and estimates of the shear fracture energies for both constant and variable sliding surface contact areas, are give in Table 6.4.3.1. From such data, it is evident that G_{IIc} ranges from about 0.1 to 1.5×10^4 Jm^{-2}. Rice (1984)[247] recognised that the values of peak and residual stress, τ^p and τ^f, are affected by the normal stress acting across the fault, and suggested a correction for triaxial compression data based on Mohr circle analysis. A similar scheme for reducing raw triaxial data to that corresponding to constant normal stress was detailed by Wong(1986)[248], who found that the constant stress correction reduces the uncorrected value of G_{IIc} by approximately a factor of two. This approximate scheme was utilised by Wong to determine the expected slip-weakening behaviour, under constant normal stress conditions, from the post-failure deformation data of triaxial compression tests, and as such its application to the constant normal displacement, low-normal stress, direct shear configuration is not immediately apparent . Consequently, the shear fracture energy values quoted in Table 6.4.3.1 are not adjusted for constant normal-stress conditions, and as such thus represent maximum values.

As described above, Wong[246] estimated G_{IIc} for the formation of the shear fracture using a method suggested by Rice[247], in which the work done in shear during the stress breakdown (Stage IV, see Fig.1.5.1 and Fig.1.5.2) is calculated. For Westerly granite, Wong estimated $G_{IIc} \approx 10^4 Jm^{-2}$, which is one to two orders of magnitude greater than an estimate he made, based on surface energy created in Mode I during the formation of the brecciated zone. The latter Mode I surface energy estimate was obtained from the density of stress-induced cracks produced during dilatancy (from a SEM survey) and by multiplying this by Mode I fracture energies of single crystals and rocks, an estimate of the total surface energy involved in microcracking was obtained, which compared satisfactorily with the work done against the inelastic component of the strains. The values of G_{IIc} estimated from triaxial compression tests are much higher than measured values of Mode I G_{Ic} for rocks (typically $>10^2\times$ higher) which Scholz[16] (p23-25) contends is in part due to the greater degree of brecciation involved in creating the shear zone, but probably mostly due to frictional work, as their is a large compressive stress present across the shear zone. Laboratory observations from triaxial rock compression tests indicate a complex breakdown process in the localised shear band in the post-peak regime. This breakdown process may involve buckling of slender columns in grains segmented by microcrack arrays, kinking in plate-shaped grains and rotation and crushing of joint blocks as seen under SEM (Evans & Wong, 1985[249]). On a large-scale, direct shear testing of rock joints indicates shearing off and crushing of asperities in jointed rock masses, the micromechanics being sensitive to the normal stress applied across the joint (Coulson, 1972[251]). Li[31] (pp.390-391) tables published values of G_{IIc} from triaxial tests on a variety of initially intact rock types (quartzite, gabbro and granites) which for minimum principal stresses varying from 14 to 400MPa, lie in the range 0.3 to $5.1\times10^4 Jm^{-2}$. Apart from triaxial tests, slip-weakening fracture parameters have also been reported by Okubo & Dieterich (1984)[251] based on biaxial tests of large-scale 2m long simulated faults. At a normal stress of 0.6-4MPa, they found that G_{IIc} varied from $0.1\text{-}2.4 Jm^{-2}$ for Sierra White granite with prepared surface roughness of 0.2 and 80microns.

A comparison of published G_{IIc} magnitudes detailed above, with those from the direct shear experimental programme given in Table 6.4.3.1 shows that the triaxial compression shear fracture energies are around the same size as those associated with frictional sliding under constant normal displacement conditions, even although the former were conducted under confining pressure, at considerably higher normal stresses. This highlights the importance of boundary conditions with regard to the frictional sliding mechanism. high stress triaxial tests under effectively zero stiffness conditions (the confining pressure cell controlling on constant normal stress) resulting in G_{IIc} values equivalent in magnitude to those resulting from direct shear at normal stresses <10MPa, but under maximum normal stiffness conditions conducive to greatest asperity fracturing and comminution. Thus it is possible that *in situ* boundary conditions may provide an answer to the discrepancy between the maximum laboratory measured values of shear fracture energy ($\approx 10^4 Jm^{\wedge}-2$) and those field estimates of G_{IIc} for natural faults from seismological data (see a summary in Wong[246]) which place the fracture energy typically from 10^6 to $10^8 Jm^{-2}$. Whilst Rice's[245] integration scheme provides shear fracture energy values closer to seismologically inferred values than laboratory measurements obtained in tension (with however a maximum discrepancy of three orders of magnitude still being unaccounted for) the results presented here are supportive of the idea that concurrence between field and laboratory G_{IIc} magnitudes may require the latter to be conducted, not only under realistic triaxial stress states, but also under realistic constant normal stiffness boundary conditions as well.

In Fig.6.4.3.6 and Fig.6.4.3.7, direct shear-induced fault gouge specific surface area and fractal dimension respectively, are plotted as functions of maximum (not corrected for any normal stress dependency) shear fracture energy. Such moderate direct linear correlations suggest that increasing G_{IIc} is associated with increasing surface area energy, W_A (see Eqn.6.4.3.1) that is the amount of energy consumed in creating new surfaces. This implies that the energy to create fault gouge and the energy expended in sliding the post-peak strength shear fracture under constant normal displacement conditions are directly related, with the former probably representing a significant (although as yet unquantifiable) proportion of the total energy dissipation in the process zone. In Fig.6.4.3.8, a moderate

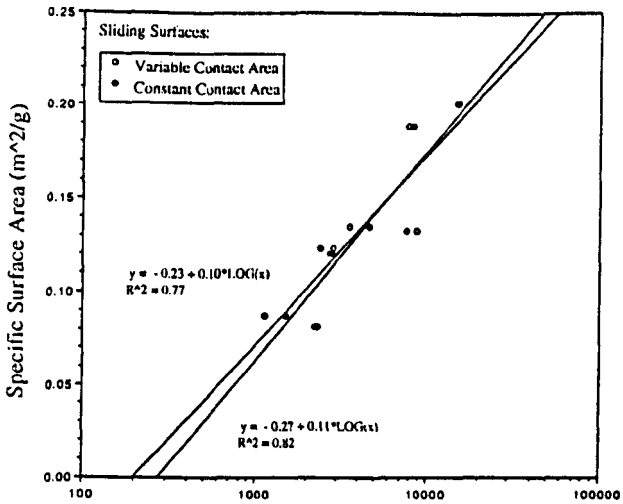

Fig.6.4.3.6 Empirical correlation between G_{IIc} and S_W.

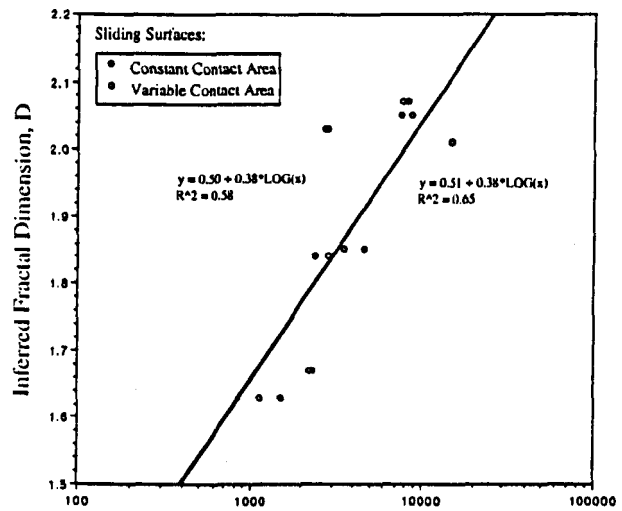

Fig.6.4.3.7 Empirical correlation between G_{IIc} and D.

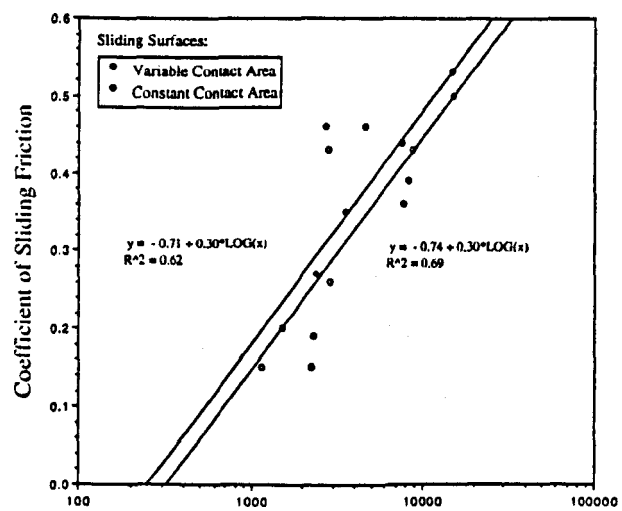

Fig.6.4.3.8 Empirical correlation between G_{IIc} and μ_s.

linear-positive relationship is evident between a measure of frictional resistance, the coefficient of sliding friction, μ_s, and the shear fracture energy, G_{IIc}. Interestingly, no such relationship is evident between lithology (as represented by XRD percentage mineral content) and the frictional coefficient. The empirical relation demonstrated between μ_s and G_{IIc} may in part reflect the fact that G_{IIc} is a "global parameter", incorporating the influence of both local asperity strength and degree of surface roughness (both presumably being lithology-dependent). The above experimental observation on gouge generation and fault strength highlight the important relationship between shear debris comminution (defined by S_W or D) as a strain energy sink, and resistance to sliding quantified in terms of either a frictional coefficient, μ_s, of a macroscopic strength law, or as an energy release rate, G_{IIc}, from fracture mechanics theory. Whilst in the above section, relations between residual strength and the nature of derived fault gouge have been explored for lithologically diverse rock types, in the following section the influence of fault gouge derived from an identical host rock lithology, but generated under a wide range of triaxial stress magnitudes, will be addressed specifically with regard to possible controls on fluid flow potential.

6.5 TRIAXIAL COMPRESSION DEBRIS

In section 5.4.1, pseudo pulse-decay permeability measurements, made on faulted Clashach core plugs under triaxially compressive stress states, were presented, along with associated relative error magnitudes, $E_{r(rss)}$, of 10%, calculated using the method of "adding in quadrature". Such data for re-shearing under increased confining pressure conditions, shows a strong linear negative correlation with resolved normal stress across the individual shear bands. However, as noted in section 5.3, due to the non-linear failure/rupture envelope determined for Clashach sandstone, the angle θ = fault^σ_1 shows a steady increase with increasing σ_3, resulting in a remarkably linear reduction in induced fault area with increasing σ_3, which will also be reflected in the experimentally observed stress-sensitive plug permeability relationship. Accordingly, in section 5.4.2 a semi-quantitative method for estimating the permeability of individual shear bands from core plug permeability measurements is presented, based on the assumption (valid for high porosity sandstones) that $k_{fault} << k_{core}$:

$$k_{fault} = (k_{core}/G).\varepsilon \quad \text{.....} \quad \text{Eqn.6.5.1}$$

$$G = (L.A_{fault})/A_{core} \quad \text{.....} \quad \text{Eqn.6.5.2}$$

k_{core}: measured core plug permeability

A_{core}: core plug cross-sectional area

L: core plug length

k_{fault}: shear band permeability

A_{fault}: shear band elliptical area

ε: shear band thickness

In Eqn.6.5.1 above, the geometric constant "G" (defined in Eqn.6.5.2) directly incorporates shear band elliptical area, so that any potential variability in fluid flow potential due to stress dependent shear band inclination, is directly incorporated in the estimate of k_{fault}. It is also evident from Eqn.6.5.1 that fault thickness is a first order variable with regard to shear band permeability estimation. Accordingly, in section 6.5.1 below, details of additional experimentation designed to elucidate the effect of stress on fault thickness in Clashach sandstone is presented, from which subsequent estimates of shear band permeability are based. In this section, shear band permeability magnitudes for specimens #15 to #22 are presented, and the influence of normal stress and angular shear strain on fault sealing potential explored. In section 6.5.2 results from laser particle sizing of the induced shear debris samples are presented in terms of the two-parameter Rosin-Rammler law, and in 6.5.3 correlation between characteristics describing the fault gouge distributions and estimated shear band permeability is examined.

6.5.1 Shear Band Permeability Estimation

As fault gouge induced by frictional slip of Clashach specimens #15, #16, #18, #19, #20, #21 and #22 was removed for laser particle sizing, no quantitative estimation of shear band thickness could be made with any accuracy, so that, instead, two additional, identical specimens (#23R and #24R) were subjected to the same stress paths, at initial confining

pressures of 1000psi (6.9MPa) and 9000psi (62.1MPa) respectively, representing the minimum and maximum triaxial stress states imposed on the specimens in which permeability was measured. Axial stress versus axial microstrain plots for both specimens are presented in Fig.6.5.1.1. Specimens #23R and #24R (also saturated with Shell Tellus mineral oil under drained conditions with the downstream end open to atmosphere) following removal from the pressure vessel, were then washed in acetone to remove the oil pore fluid, dried, and injected with a low viscosity epoxy resin. Thin-sections were prepared from these resin impregnated specimens, so that the plane of the section was taken perpendicular to the strike of the induced fault plane. From such sections, the observation was made that specimen #23R, sheared at a relatively low normal stress magnitude, produced a relatively thick shear band compared with specimen #24R, sheared under a seven times greater normal stress level. Details of stress levels for re-shearing conditions, post-peak sliding displacements and measured shear band thicknesses for specimens #23R and #24R, are given in Table 6.5.1.1. The thickness of the shear band granulated zone approximately perpendicular to the bounding wall rock was measured from thin-section under 25× magnification, at regular 0.2mm intervals along the fault zone. This was achieved by drawing chords on a captured video image of the thin-section, in NIH Image 1.54, a public domain image processing and analysis program for the Macintosh®.

Thin-section photomicrographs of shear bands from specimens #23R and #24R are shown in Fig.6.5.1.2. From Fig.6.5.1.2(a) of #23R, mean shear band thickness was measured at 1.00mm with a population standard deviation of 0.31mm. This shear band, displaced under conditions of low normal stress, exhibits relatively rough bounding wall-rock surfaces (reflected in the high thickness standard deviation) and shows numerous intact quartz grains "floating" within the gouge zone of cataclastically comminuted debris, indicating that both grain-boundary sliding and intra-granular fracturing contributed to the cataclastic deformation mechanism. From Fig.6.5.1.2(b) of #24R, mean shear band thickness was measured at 0.31mm with a population standard deviation of 0.13mm, that is at higher normal stress levels fault thickness has been suppressed to around a third of that observed at low stress levels. The shear band formed within specimen #24R appears highly localised, with smooth, planar and sub-parallel wall-rock surfaces, bounding a

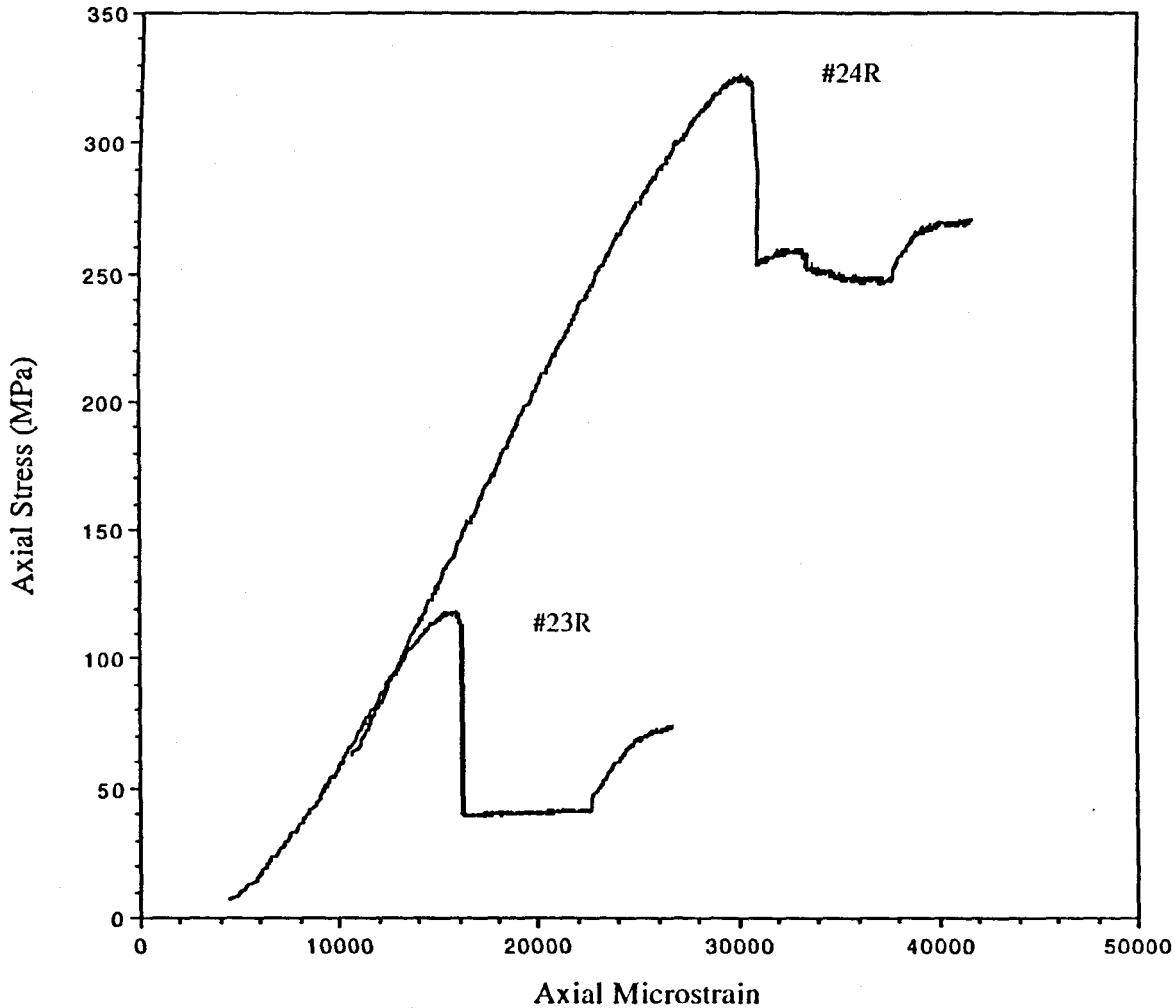

Fig.6.5.1.1 Axial stress versus strain plots for Clashach specimens #23R and #24R used in the determination of shear band thickness.

I.D.	Confinement MPa(psi)		Initial Sliding MPa		Re-shearing MPa		$\Delta\ell_{axial}$	Fault^σ_1	δ_s	ε	γ	Ψ^o
	Initial	Final	τ	σ_n	τ	σ_n	mm	θ^o	mm	mm		
#23R	6.9 (1000)	13.8 (2000)	9.4	10.3	16.5	19.8	0.81	20	0.86	1.00±.31	0.86	40.7
#24R	62.1 (9000)	68.9 (10000)	77.8	127.3	83.8	139.2	0.81	40	1.06	0.31±.13	3.42	73.7

Table 6.5.1.1 Experimental details for shear band thickness calibration specimens #23R and #24R.

Specimen I.D.	τ (MPa)	σ_n (MPa)	θ (^{o})	δ_s (mm)	ε (mm)	Ψ' (^{o})	k_{core}(A) (mD)	k_{core}(D) (mD)	k_{fault}(D) (mD)	$\frac{k_{fault}(D)}{k_{core}(A)}$ (%)
#15	18.6	20.6	20	1.02	1.18	41	720	473	2.49	0.35
#16	55.9	73.7	30	1.06	0.81	53	828	365	2.16	0.26
#18	75.8	108.3	35	1.23	0.62	63	903	296	1.27	0.14
#19	53.1	58.3	30	1.01	0.88	49	982	444	2.50	0.26
#20	95.9	149.3	40	1.03	0.21	78	1036	235	0.43	0.04
#21	39.6	46.0	25	0.92	0.89	46	734	415	2.23	0.30
#22	103.4	155.6	40	1.56	0.25	81	684	234	0.51	0.08

Table 6.5.1.2 Stress, strain and permeability values for shear bands induced under triaxial compression.

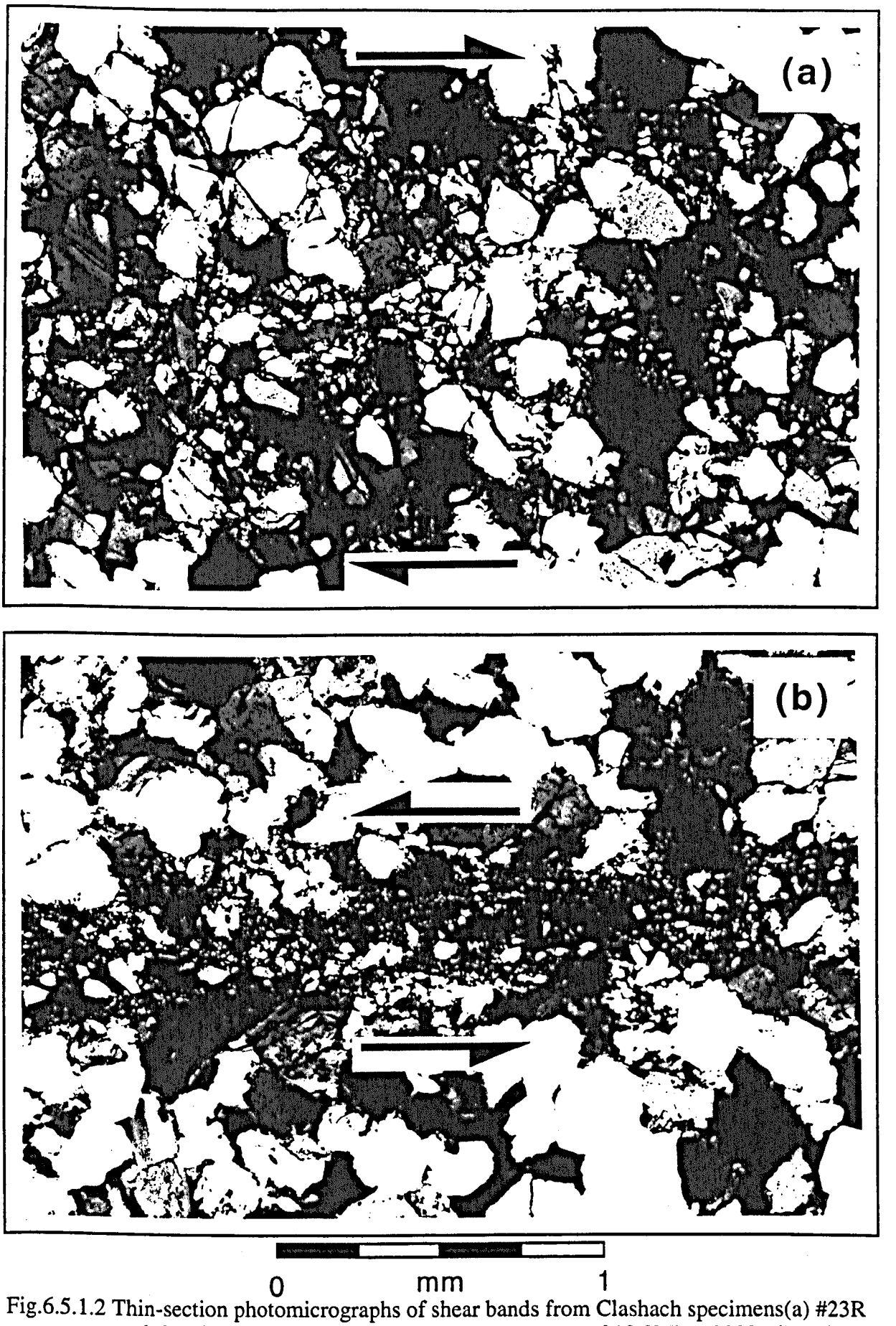

Fig.6.5.1.2 Thin-section photomicrographs of shear bands from Clashach specimens(a) #23R and (b) #24R re-sheared under confining pressures of 13.8MPa (2000psi) and 68.9MPa (10000psi) respectively.

gouge zone composed of highly comminuted grain-fragments in which intra-granular cracking has exclusively dominated the cataclastic process. Such observations are supported by those of Tullis & Yund (1992)[252] on the effects of increasing confining pressure (at temperatures <300°C) on the nature of faulting in feldspar (Bushveld anorthosite) aggregates. Tullis & Yund noted that at lower pressures the gouge zone was wider, which they attributed to its development from more irregular surfaces which break off more material as they slide, whilst at higher pressures the faults were sharp and smooth from the start, so that they could slide with less gouge development. Interestingly, a related aspect recognised by Tullis & Yund was that a wider range of fragment sizes developed in gouge formed at low pressures, compared with ubiquitously fine-grained fragment development at high pressure.

Archard (1953)[253] proposed a theory of wear (surface damage and erosion resulting from frictional sliding) which, although quantitatively describing the main properties of the process, is not specific about the mechanism by which wear particles are removed from the surface (adhesive wear or abrasive wear) and hence finds general application. Based on this model, Scholz (1987)[254] developed an expression for the gouge thickness to slip ratio (ε/d_s) in terms of the constant applied normal stress, σ_n, a dimensionless parameter called the "wear coefficient", k, and an unspecified hardness parameter, h:

$$(\varepsilon/d_s) = (k \,.\sigma_n) \,/\, (3h\,) \quad \ldots\ldots\ldots \quad \text{Eqn.6.5.1.1}$$

Scholz's law thus predicts a direct linear correlation between shear band thickness (normalised by slip) and normal stress, with a slope of (k /3h). Using the same value of h, Scholz predicted k = 0.3 for sandstone and k = 0.075 for granite, that is a wear rate for sandstone 3 to 4 times that of granite. Scholz pointed out that the above estimates appear inconsistent with the model, as both rock types are silica rich, however he did note that the model assumes a solid substrate, whereas some grain-plucking must occur during wear, so that differences in the grain-boundary strength of the two rocks should also be considered. The above wear law is obviously inconsistent with observations of thickness versus normal

stress relations for Clashach sandstone, and with the observations of Tullis & Yund[252], which both support an inverse linear correlation, however Scholz[16] notes that the wear law of Eqn.6.5.1.1 is for the case of steady-state wear, whereas a "complete" wear curve (see Scholz, Fig.2.14, page 71) also contains an early "running-in" phase, in which high initial wear rates decay exponentially with sliding until a steady-state rate is finally achieved. A possible explanation for running-in wear is that the starting surfaces have greater roughness than that which would be present in equilibrium with the sliding conditions, and so have an initially high wear rate that is proportional to this excess roughness. Thus the observed thickness-normal stress relation for Clashach sandstone may be at odds with that described by Eqn.6.5.1.1 due to the fact that the above wear law is for the assumption of a solid substrate, it is for the case of steady-state wear only, and also it neglects any change in porosity of the gouge zone.

In order to estimate the shear band thicknesses of Clashach specimens #15 to #22, from upper (specimen #23R, low normal stress) and lower (specimen #24R, high normal stress) limiting thickness determinations derived from thin-section measurements, (ε/d_s)-values for #23R and #24R were plotted against the resolved normal stress magnitudes recorded for re-shearing conditions under confining pressures of 13.8MPa (2000psi) and 68.9MPa (10, 000psi) respectively. The simplest case of a linear negative correlation between (ε/d_s) and σ_n was assumed, so that laying off of the known σ_n-magnitudes for specimens #15 to #22 (see Fig.6.5.1.3) yielded corresponding (ε/d_s)-values from which thickness estimates could be derived by multiplying by the measured slip displacement. As a point of interest, it should be noted that a quick estimate of fault thickness could be gained post-testing without the need for thin-section calibration, through X-ray photography, although this facility was not available at the time for analysis of the Clashach specimens. Thickness/slip ratios can also be expressed in terms of shear strain, $\gamma = d_s/\varepsilon$, and angular shear strain, $\Psi = \tan^{-1}\gamma$. Tabulated values of shear and normal stress magnitudes for re-shearing, slip displacements, estimated shear band thicknesses and resultant angular shear strains are presented in Table 6.5.1.2. Estimates of shear band permeability can thus be made by substituting measured core plug permeability values, geometric constants and estimated

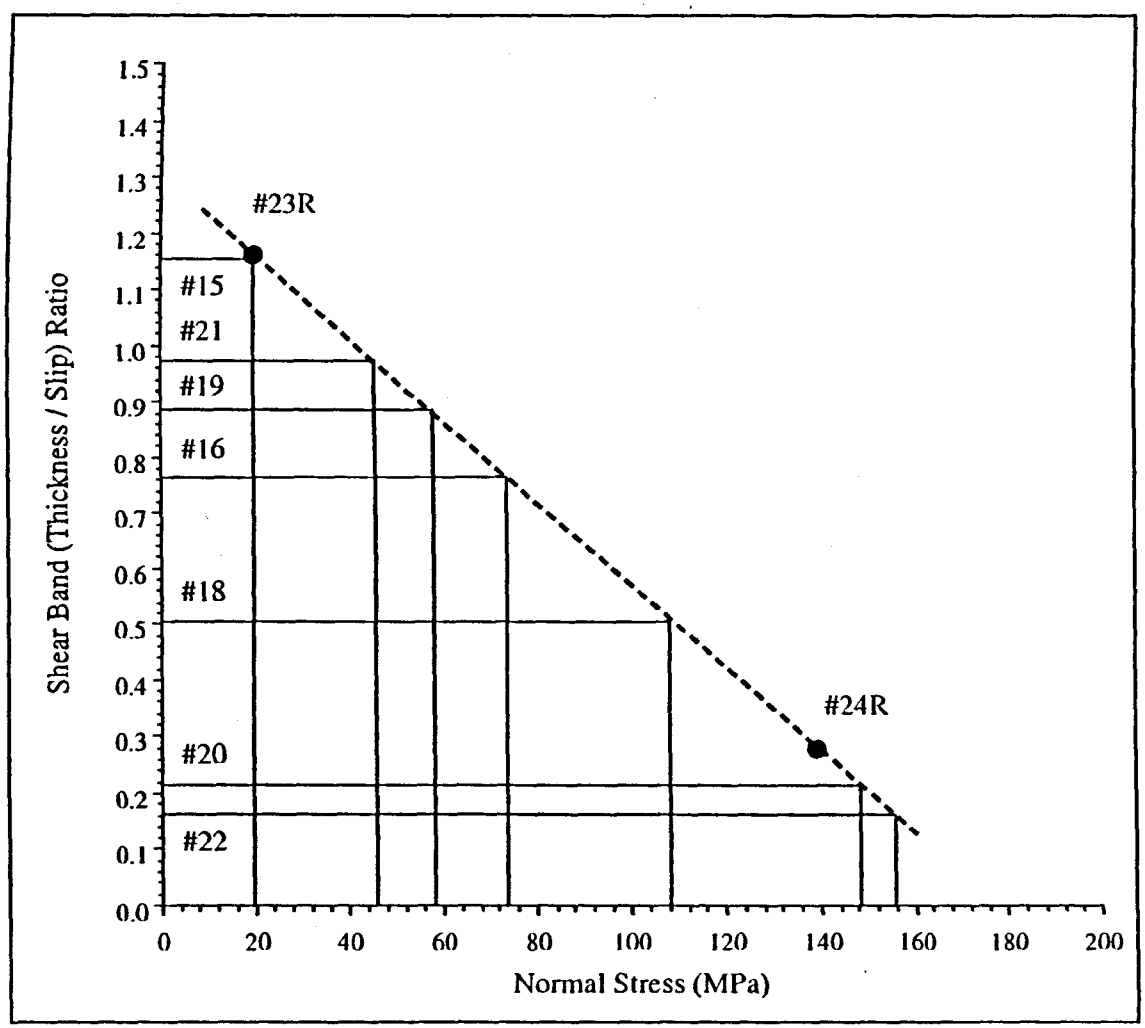

Fig.6.5.1.3 Shear band thickness/slip ratios (ε/δ_s) versus resolved normal stress across the shear plane.

thicknesses into Eqn.6.5.1. An indication of fault sealing potential which encompasses any initial between-sample variations due to microstructural dissimilarities between specimens, can be gained by normalising each estimate of fault permeability by the permeability values measured under initial hydrostatic stress conditions. Shear band permeability estimates and fault sealing potentials (expressed as percentages of hydrostatic permeabilities) are also given in Table 6.5.1.2.

From Table 6.5.1.2 it is evident that percentage fault sealing potential ranges from 0.35% at low stress to 0.04% at high stress, representing a 2.5 to 3.5 order of magnitude permeability reduction due to cataclasis alone (as the pore fluids were chemically inert, both hydrolytic weakening and pressure solution are inferred to have been absent). Such magnitudes are in agreement with outcrop minipermeameter measurements reported by Antonellini & Aydin (1994)[255] on granulation seams in the Navajo and Entrada sandstones of the Arches National Park, Utah, where, on average, a permeability three orders of magnitude less than the host rock was quantified. Antonellini & Aydin contended that the "intensity of cataclasis" and the clay content controlled the amount of permeability reduction as measured perpendicular to the band, however the minipermeameter method (see for example Goggin *et al*, 1988[256]) is conducted under zero-stress conditions so that extrapolation of measured magnitudes to reservoir conditions is necessarily tenuous. In contrast, the Clashach triaxial compression measurements, conducted under stress states associated with shear slippage, show an order of magnitude dependency on applied stress, as illustrated in Fig.6.5.1.4 where both estimated shear band permeability (a) and sealing potential (b) are plotted against normal stress resolved across the fault, giving robust linear negative correlations. The effect of the main experimental variable, confining pressure, was also evident in first order control on both fault inclination relative to the direction of the maximum principal stress, and on shear band thickness, as discussed above. Whilst any potential influence on permeability of the former additional variable is fully contained within the geometric constant defined by Eqn.6.5.1.2, the effect of a stress-sensitive shear band thickness is reflected in a wide between-specimen variability in angular shear strain, Ψ. Thus both estimated shear band permeability (a) and sealing potential (b) also show a strong linear negative correlation with Ψ, as illustrated in Fig.6.5.1.5. In section 6.5.2

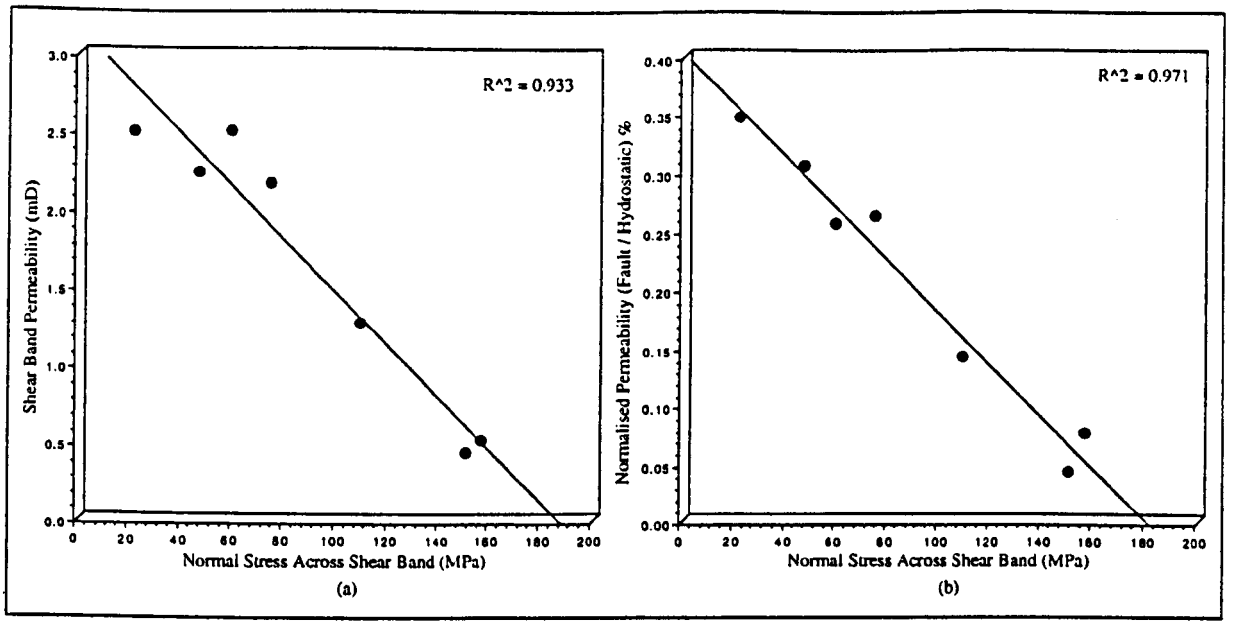

Fig.6.5.1.4 Influence of resolved normal stress on (a) estimated shear band permeability and (b) sealing potential defined as shear band permeability as a percentage of permeability at hydrostatic stress.

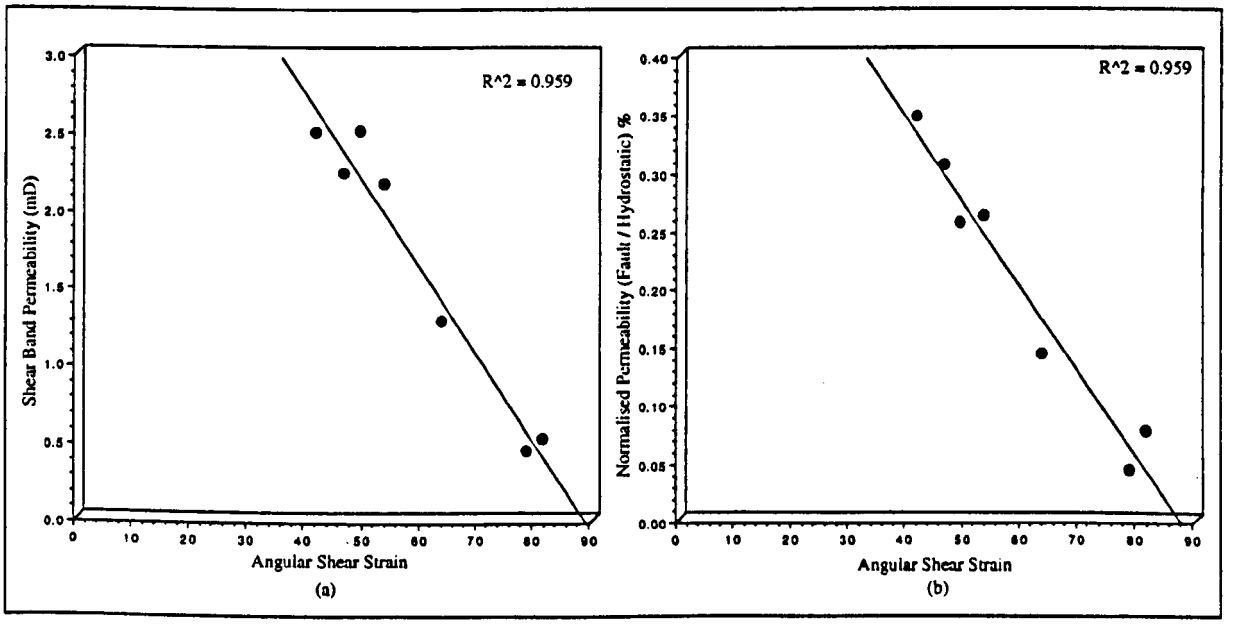

Fig.6.5.1.4 Influence of angular shear strain on (a) estimated shear band permeability and (b) sealing potential defined as shear band permeability as a percentage of permeability at hydrostatic stress.

below, the results from laser particle sizing of shear debris recovered from the Clashach specimens is reported, whilst in section 6.5.3 the "intensity of cataclasis" is quantified in terms of the Rosin-Rammler constants defining the gouge distributions, and related to the shear band permeability estimates.

6.5.2 Malvern Results

Fault gouge samples from the seven Clashach sandstone specimens #15 to #22 were carefully brushed from the intact specimen halves, and prepared by washing in acetone to remove excess oil pore fluid, agitating in a sonic bath with distilled water and finally by oven drying at 100°C for 24hours. The prepared samples were then sieved into >500 and <500micron fractions, the latter being used for laser particle sizing, suspended in distilled water as a supporting medium. The optical model employed by the Mastersizer to compute volume distributions was customised by entering the optical constants of the sample material and supporting medium, all the Clashach samples being treated as quartz, with a refractive index of 1.54. Also, for specific surface area (per g of sample) calculations, all sample materials were assigned the specific gravity of quartz = 2.65. This approximation of the fault gouge powders as volume distributions of quartz spheres was thus more realistic for these Clashach samples than for the direct shear suite, as Clashach sandstone is a quartz arenite with approximately 90% quartz and no clay fraction. Independent powder samples from each triaxial compression specimen were analysed using the 300mm- and 45mm-range lenses, giving particle sizes extending from 600 to 1.2microns and 80 to 0.1microns respectively. Unlike the direct shear specimen study, in which the analysis mode was set to model independent with no assumptions made about the form of the result with regard to its distribution, for the Clashach suite the Rosin-Rammler two-parameter analysis model was selected, constraining the volume distribution to have a single peak completely identified by the two parameters X (describing the position of the peak on the size scale) and N (describing the width of the distribution) as detailed in section 6.3.

Rewriting the Rosin-Rammler law for the oversize, residual weight distribution (Eqn.6.2.3.3) in terms of the absolute size constant, $\bar{x}$, gives:

$$R = 100e^{-\left(\frac{x}{\bar{x}}\right)^n} \quad \text{.....} \quad \text{Eqn.6.5.2.1}$$

For n = 1, the peak of the particle size weight distribution curve is theoretically at R=100e^-1 = 100/e = 36.8%, so that if we denote the mode of the distribution curve by $\bar{x}$, then Eqn.6.5.2.1 becomes, for n = 1 and b = $1/\bar{x}$, R = 36.8%. The sieve opening $\bar{x}$ corresponding to R = 36.8% is conveniently used as a characteristic of the degree of comminution of the material (Bennett[223]), and since the slope of the straight line on the Rosin-Rammler graph depends upon the range of particle size, the ratio of the angle α (n = tanα) and the mode $\bar{x}$ epitomises very effectively the distribution curve as regards both mode and range of particle size. The quantity ($\alpha/\bar{x}$) therefore represents a quasi "coefficient of variation" enabling direct comparison of the degree of dispersion (slope of the line) in samples from different materials which may possess different modes (position of the line).

Graphical representation of the Mastersizer Rosin-Rammler particle size distribution analyses are given in Fig.6.5.2.1(a) and (b), for f=300mm and f=45mm respectively. Tabulated constants n, α, b, $\bar{x}$ and ($\alpha/\bar{x}$) are presented in Table 6.5.2.1. The most obvious feature of the Rosin-Rammler plots is their extreme linearity, in marked contrast to those of the model independent volume distributions for the direct shear specimens, when plotted in the same Rosin-Rammler format. This linearity exhibited by the Clashach specimens is therefore attributed to the selection of the two-parameter analysis mode, although it is stressed that this is not unequivocal, as many other contrasts existed between the two test suites (in particular the mode of testing and associated boundary conditions) so that no further comparisons will be drawn between the direct shear and triaxial compression results.

From the particle size distribution plots and tabulated Rosin-Rammler constants, it is evident that the 300mm-range lens data shows a relatively wide spread in actual particle

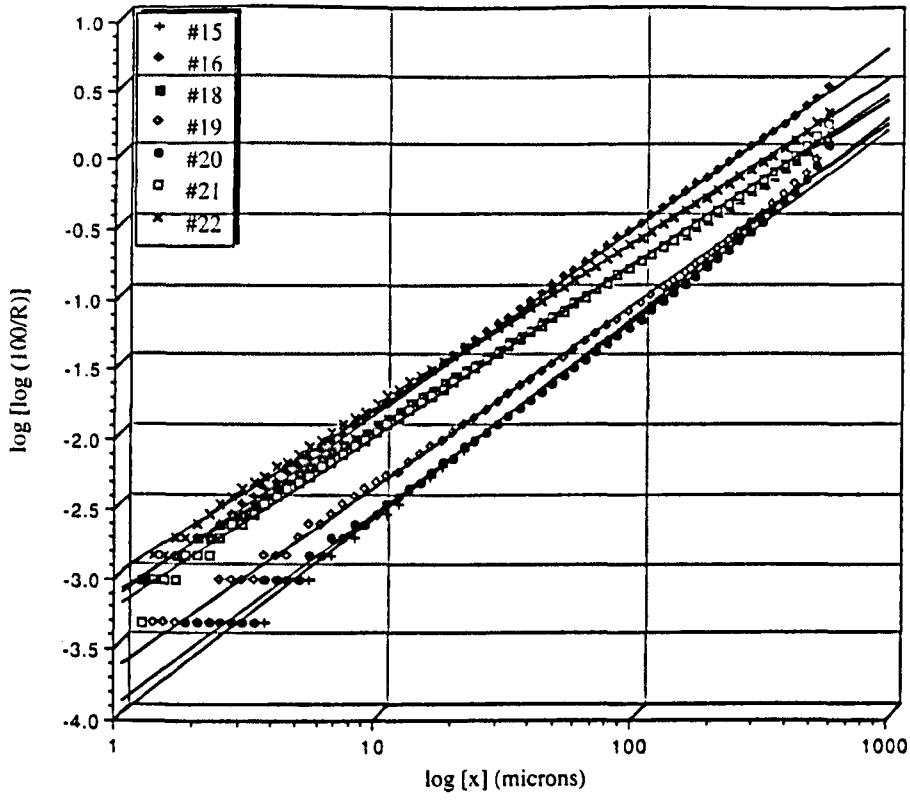

(a)

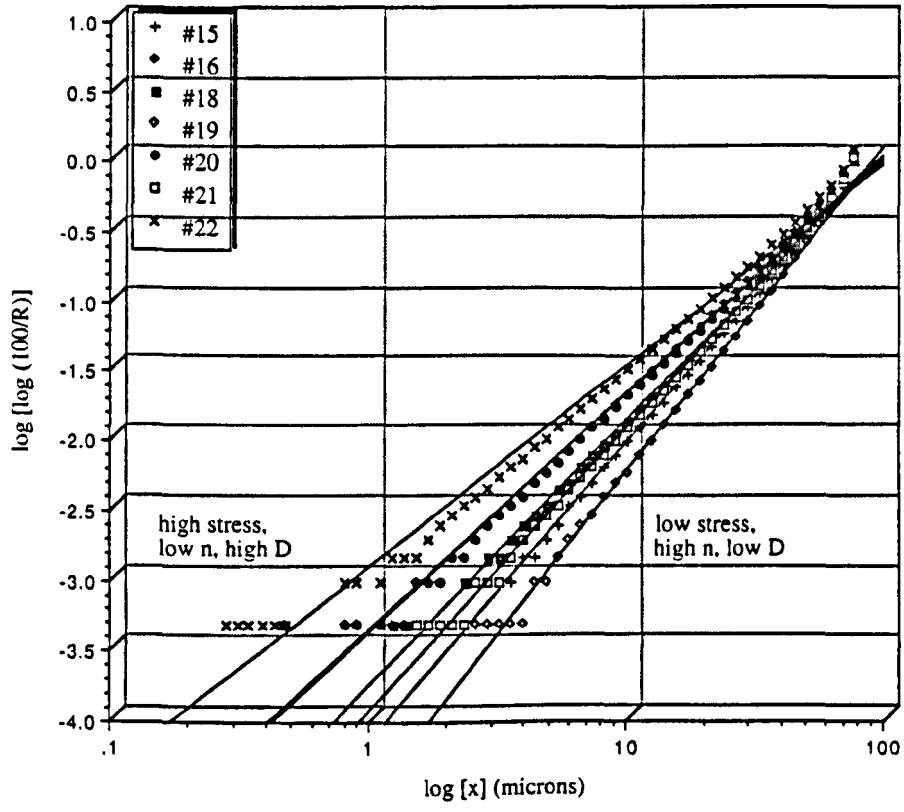

(b)

Fig.6.5.2.1 Straight-line graphical representations of the Rosin-Rammler function for laser-sized fault gouge distributions: (a) 300mm-range lens giving 500-1.2 μ particle size range; (b) 45mm-range lens giving 80-0.1 μ particle size range.

Specimen I.D.	n	$\alpha(^{o})$	b	$\bar{x}(\mu m)$	$(\alpha/\bar{x})$
f=300mm-range lens 1.2<x<600μm:					
#15	1.43	55	2.29e-4	347	0.16
#16	1.32	53	1.62e-3	130	0.41
#18	1.18	50	1.74e-3	219	0.23
#19	1.30	52	5.12e-4	341	0.15
#20	1.38	54	2.81e-4	381	0.14
#21	1.23	51	1.36e-3	213	0.24
#22	1.19	50	2.39e-3	163	0.31
f=45mm-range lens 0.1<x<80μm:					
#15	2.12	65	1.76e-4	59	1.09
#16	1.70	60	1.03e-3	57	1.04
#18	1.89	62	4.25e-4	61	1.03
#19	2.32	67	7.16e-5	62	1.08
#20	1.68	59	1.04e-3	60	0.98
#21	2.01	64	2.87e-4	58	1.10
#22	1.44	55	2.87e-3	58	0.96

Table 6.5.2.1 Tabulated Rosin-Rammler constants for laser-sized gouge distributions.

size, as denoted by the position of each line, with $\bar{x}$ ranging from 130microns to 380microns, whilst the between-specimen distribution of particle size remains relatively constant, with $n \approx 1.3 \pm 0.1$. In direct contrast, however, the 45mm-range lens data shows relative uniformity in absolute particle size, $\bar{x} \approx 59 \pm 2$, whilst the relative distribution of particle size between Clashach samples, denoted by the slope of each line, shows n ranging from 1.4 to 2.3. Thus the relatively large size range data (1.2<x<600microns) implies a wide diversity in the coarseness of the fault gouge from sample to sample, with however all samples showing the same closeness of grading, whereas the relatively small size range data (0.1<x<80microns) implies a similar degree of fineness for all samples but a spread in their individual size reduction characteristic.

In Fig.6.5.2.2, the "coefficient of variation", $(\alpha/\bar{x})$ for both the 300mm- and 45mm-range lens data is plotted against (a) normal stress resolved across each shear band, σ_n, and (b) the total angular shear strain, Ψ, imposed on each shear band. Strong linear negative correlations are evident between $(\alpha/\bar{x})$ measured on the 45mm-range lens, and both variables σ_n and Ψ, with critical coefficients, R^2 of 0.933 and 0.948 respectively. No such correlations were evident for the 300mm-range lens data. This correlation for $(\alpha/\bar{x})$ determined on particle size ranging from 80-0.1microns as opposed to the lack of correlation shown by $(\alpha/\bar{x})$ determined on particle size ranging from 600-1.2microns, may be attributed to the fact that the lower size range represents 100% cataclastic products, whereas the larger size range includes both remnant intact grains as well as comminuted grains. It is evident that for the 45mm-range lens, $(\alpha/\bar{x})$ represents the inverse of "cataclastic intensity" ($\bar{x}$ approximately constant, α decreasing with increasing rate of size reduction) so that the lower the value of the ratio $(\alpha/\bar{x})$, the more intense the cataclasis.

Marone & Scholz (1989)[257] investigated the comminution of simulated fault gouge (Ottawa sand with >99% quartz) under triaxial compression, between rough steel surfaces at 45° to the axis of a cylindrical sample. They found that the fractal dimension, D of the gouge increased from D =1.6 with increasing shear strain to Ψ-values of about 52° to 56°, then levelled off to an asymptotic value of $\approx D$ =2.8 thereafter (the greater the magnitude of

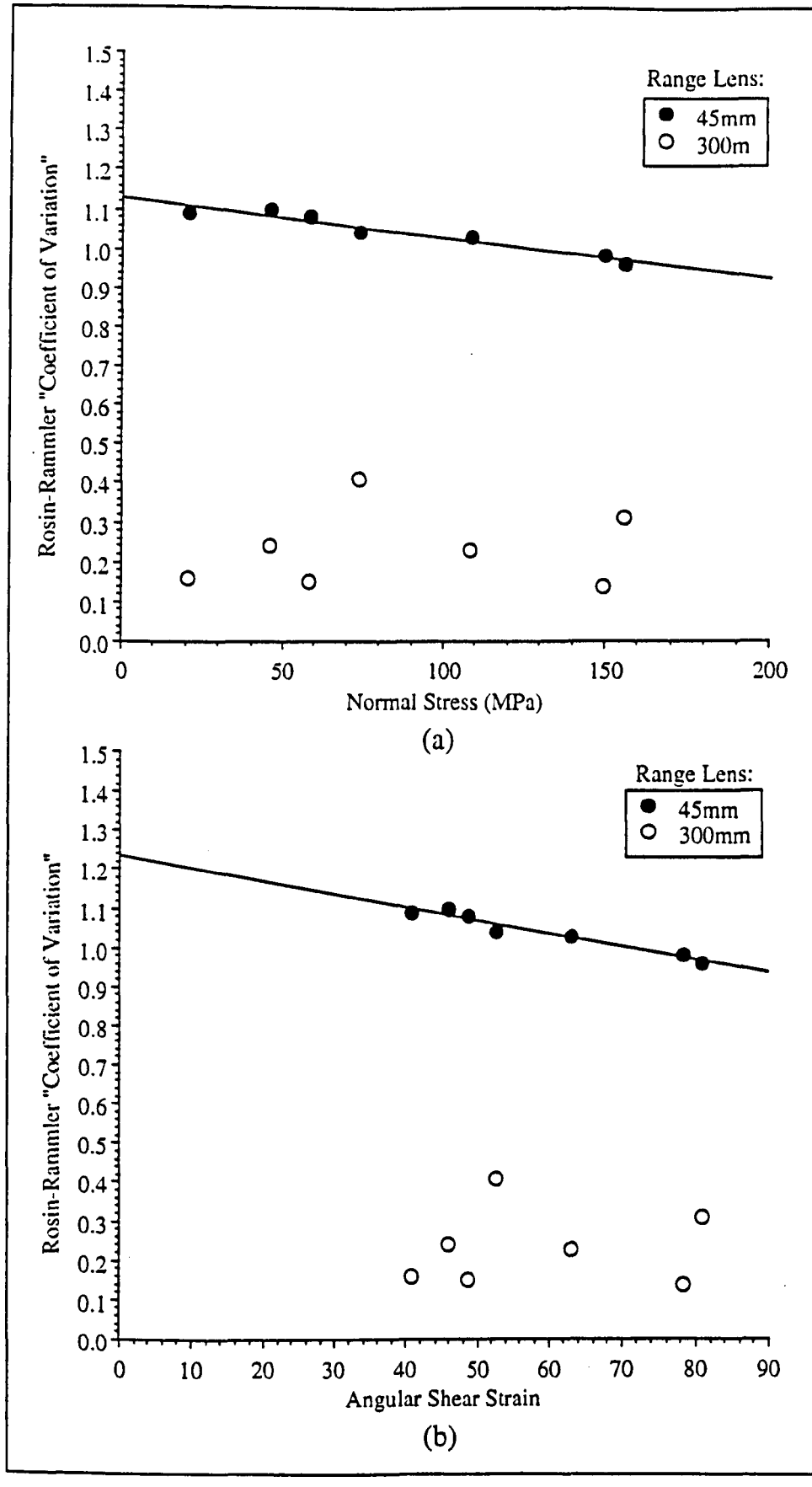

Fig.6.5.2.2 Clashach fault gouge "Coefficient of Variation" ($\alpha/\bar{\tau}$) versus (a) resolved normal stress and (b) angular shear strain.

D, the greater the number of small fragments relative to large fragments). Marone & Scholz's observation of D increasing with increasing Ψ supports the idea that in fact shear strain represents the primary control on comminution, as all their layer shearing was conducted at a constant effective normal stress of 100MPa. However, Sammis *et al* [232] found that collected samples of natural fault gouge material from the San Andreas fault zone showed a linear decrease in mean particle size with increasing confining pressure (depth) which they attributed to a suppression of microfracture extension and subsequent decrease in the spacing of axial microfractures with increasing confinement, leading to smaller particles being produced from denser microfractures at higher pressure. Whilst, with regard to the Clashach tests, the relative influence of a variable normal stress on frictional comminution cannot be separated from that of shear strain, the above related studies tend to suggest that both variables will have a complementary, mutually additive, control on cataclastic intensity.

Use of the Rosin-Rammler two-parameter model forces a relationship between the volume present in each sizeband on the analysis. This two-parameter analysis model uses an analysis technique to constrain the volume distribution to have a single peak which can be completely specified by two parameters of the characterising equation, X ($\equiv \bar{x}$) describing the position of the peak on the size scale, and N ($\equiv$n) describing the width of the distribution. The objective of the two-parameter analysis is to produce a result for which the residual is a minimum, however if the size distribution is not well represented by the two-parameter model, a local minima may be found some distance from the true minima. for example, assuming a value of X has been found which, if altered by a small amount, would lead to an increase in the residual, the analysis algorithm takes this to be the best fit and stops the calculation, however what it cannot predict is that moving the X value by a large amount may lead to an even lower residual. Thus it is possible that the residual for the 300mm-range lens calculated light energy distribution fit to the measured data may not be the true residual minimum, but a local one, resulting from a poor fit of the Rosin-Rammler model to the size distribution. For Clashach sandstone, the particle size range measured by the 300mm-range lens could include significant contributions from unfractured remnant grains for gouge developed at relatively low stress levels, whilst the size range accessed by

the 45mm-range lens will consist entirely of subgrain-sized cataclastic products resulting from intra-grain fracturing. Thus for the 300mm-range lens, lack of correlation between $(\alpha/\bar{x})$ and applied stress or resultant strain may reflect selection of the wrong residual minima due to poor description of the size distribution by the Rosin-Rammler law, due to associated intact grains producing a degree of bimodality to the low-stress gouge distributions.

6.5.3 Sealing Potential Correlation

In section 6.5.2 above, it is noted that the Malvern 45mm-range lens data shows relative uniformity in absolute particle size, $\bar{x} \approx 59 \pm 2$, whilst the relative distribution of particle size between Clashach samples, denoted by the slope of each line, shows n ranging from 1.4 to 2.3. A very robust linear negative correlation was proved between the "coefficient of variation" $(\alpha/\bar{x})$ and both σ_n and Ψ. As discussed in section 6.5.2 (with $(\alpha/\bar{x})$ providing an ideal measure of the "intensity of cataclasis" the magnitude of $(\alpha/\bar{x})$ was shown to decrease as the degree of comminution increased, however the important question is what effect does the intensity of cataclasis have on shear band permeability? In Fig.6.5.3.1 estimated shear band permeability (a) and percentage fault sealing (b) that is shear band permeability normalised to that measured at hydrostatic stress, are plotted against $(\alpha/\bar{x})$. From these relations it is evident that shear band fluid flow potential decreases with increasing cataclasis (linear positive correlation between permeability or sealing potential and $(\alpha/\bar{x})$, degree of cataclasis varying inversely with $(\alpha/\bar{x})$). Thus the more intensely comminuted the experimental fault gouge, the better the shear band cataclastic seal.

For the measurement of permeability and indirectly of the specific surface area of powder beds, Kozeny's (1927)[258] equation for the velocity of infiltration of a fluid percolating through porous packings of solid particles has advantages over Darcy's law in that it analyses the permeability constant, k, in terms of its constituent factors. The proportionality constant, k, which according to Darcy's law is a specific property of the material and independent of the viscosity of the fluid and the pressure difference, is expressed as a function of the porosity, ϕ, the pore shape and length $(c.l_s/l_w)$ and the specific surface area,

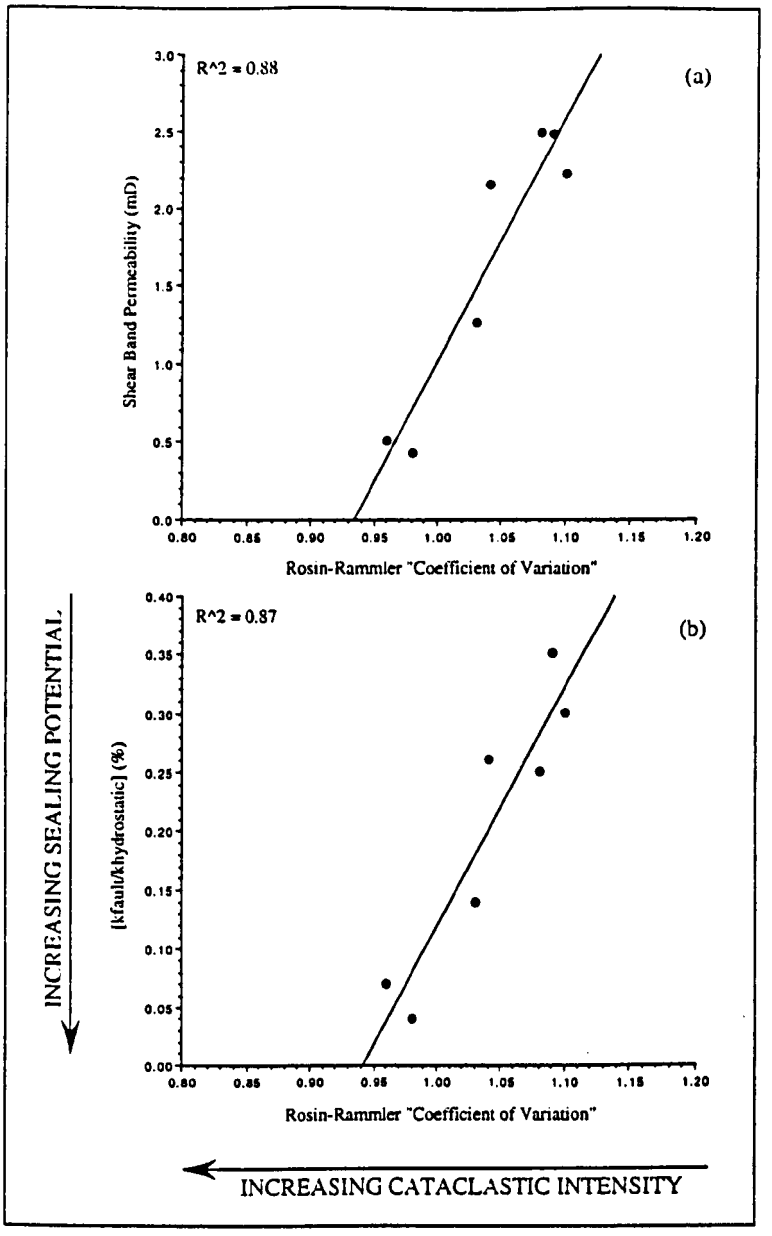

Fig.6.5.3.1 Empirical correlation between the Rosin-Rammler "Coefficient of Variation" of induced shear debris distributions and (a) estimated shear band permeability and (b) shear band permeability normalised to permeability quantified under initial hydrostatic stress states.

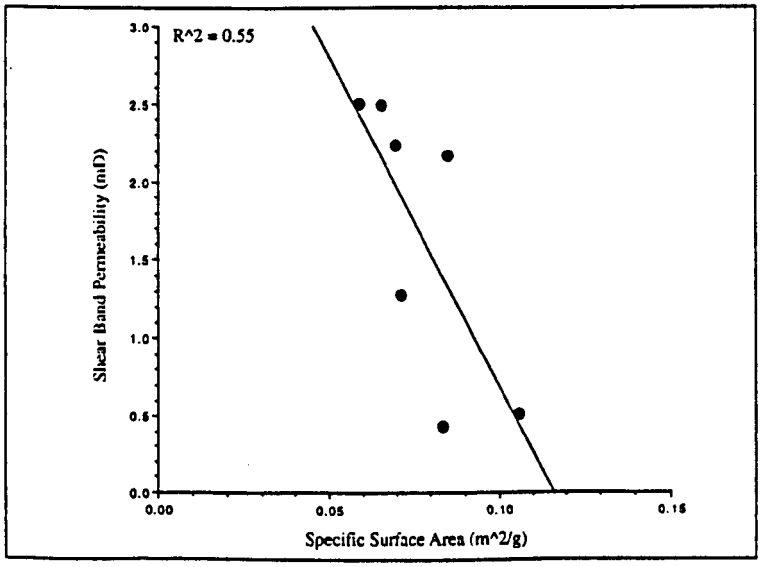

Fig.6.5.3.2 Estimated shear band permeability correlation with fault gouge specific surface area.

Sv (surface area per volume of packing). Assuming spherical particles, the expression for permeability is written as:

$$k = (c.l_s/l_w)\frac{\phi^3}{(1-\phi)^2}.\frac{1}{S_v{}^2} \quad \text{.....} \quad \text{Eqn.6.5.3.1}$$

This relation and its various equivalent forms is known as the Carman-Kozeny equation (see for example the discussion in Gueguen & Palciauskas, 1994[259], pp.126-133) and can be expressed by saying that the permeability constant is proportional to the shape and length of the pores, to a function of the porosity (that is of the total amount of pores as a fraction of the total volume of the packing) and inversely proportional to the square of the specific surface area of the particles forming the walls of those pores. This relation between the permeability of a powder bed and the various parameters given in Eqn.6.5.3.1 can be used to gain insight into the empirically demonstrated dependence of estimated shear band permeability on the degree of fault gouge cataclasis.

Marone & Scholz[257] note that porosity reduction within granular materials can be accommodated through either an increase in packing (a better fit between particles and thus decreased void space) or by a change in particle size distribution (sorting). For less sorted material the range of particle sizes is larger, so that smaller particles can fit between larger ones, thus reducing pore space. From the laser particle sizing studies, the intensity of cataclasis of Clashach sandstone was found quantifiable through the "coefficient of variation" parameter, $(\alpha/\bar{x})$ varying inversely with the degree of comminution. Whilst the absolute size constant, $\bar{x}$, was found unchanging for all test specimens (porosity being independent of size anyway) the slope α was found to decrease systematically with increasing normal stress and angular shear strain, implying more rapid size reduction leading to "dustier" powders with more dispersed size ranges. As distributions with greater size ranges possess "poorer" sorting it is thus intuitive that porosity must be decreasing with increasing cataclastic intensity, changes in sorting occurring via particle-size reduction and comminution. Thus the relationship of Fig.6.5.3.1 may well reflect the permeability

versus porosity relationship of Eqn.6.5.3.1 with fluid flow potential increasing with improved sorting. Also, it is possible that increased normal stress across the shear band may have the added effect of increasing compaction within the gouge zone, hence promoting grain-packing in addition to sorting as a mechanism for porosity reduction.

In Fig.6.5.3.2, shear band permeability is plotted as a function of the specific weight surface area, $S_w = S_v/\rho$, calculated from the harmonic mean of the weight distribution - volume surface diameter equivalency. A linear negative trend is evident, indicating that, as well as the presumed decrease in porosity with increasing comminution, increasing fault gouge specific area also decreases shear band permeability, as predicted by Eqn.6.5.3.1. It is also likely that tortuosity (defined as the ratio of real to apparent path length through which the fluid flows, l_w/l_s) will also increase with increasing cataclasis, with an attendant inverse effect on permeability magnitude.

7. EXPERIMENTAL CONCLUSIONS AND FURTHERANCE OF WORK

7.1 CONCLUSIONS

7.1.1 Direct Shear Experimentation

(i) A servo-hydraulic direct shear rig has successfully been used to shear whole core (118mm-diameter) rock specimens of diverse sedimentary lithology under constant normal displacement (CND) control, analogous to "ultra-stiff" wall-rock *in situ* boundary conditions.

(ii) Consequences of the CND experimental boundary conditions include maximum suppression of discontinuity-normal displacement and maximum production of frictional wear debris (fault gouge).

(iii) Macroscopic specimen deformation under CND conditions was observed to be markedly lithology-dependent. Four rock types were tested, including Permian red sandstone and Carboniferous fissile mudstone, carbonaceous siltstone and heterolithics, and exhibited widely different discontinuity deformation modes with regard to sliding surface morphology and shear debris production.

(iv) All CND direct shear specimens showed sliding surface structures analogous to those observed on natural faults and used as kinematic indicators (shear sense criteria). Specifically, well-developed slickensides, slickenlines and slickensteps were apparent, the latter being observed to face against the movement direction of the overriding block, in agreement with current structural geological interpretation.

(v) Force-displacement curves for CND-shear showed sudden distinct stress drops which were interpreted as being due to asperity shear.

(vi) Theoretical analysis of contact area variation with sliding displacement was undertaken, based geometrically on the area of overlap of two circles with divergent centre displacement. Incorporation of slip-dependent contact area into shear and normal stress magnitude calculations from measured loads was shown to have a first order influence on stress versus sliding displacement profiles, by comparison with those based on the assumption of constant contact area.

(vii) Each CND specimen showed a distinct peak in its shear load versus displacement profile which was used to define a maximum friction coefficient, μ_{max}, equal to the peak shear stress divided by the corresponding normal stress. Direct shear maximum friction data consistently plotted below Byerlee's low normal stress (σ_n<200MPa) frictional strength relationship, $\tau=0.85\sigma_n$, and was better represented by the high normal stress relationship, $\tau = 0.5+0.6\sigma_n$. This may reflect the suppression of dilatancy under CND conditions, where asperity shear is wholly dominant, and highlights discontinuity stiffness as an important omission with regard to Byerlee's hypothesis.

(viii) The variable friction coefficient, $\mu^*=\tau/\sigma_n$ was seen to decrease with increasing normal stress due to surface wear associated with CND shearing, indicating that Amonton's law as defined above is invalid for the various rock types tested under the experimental direct shear configuration.

(ix) In shear stress versus normal stress space, all lithologies exhibited the same overall attributes irrespective of lithology, namely a non-linear (generally exponential) increase in pre-peak strength data to maximum friction, μ_{max}, followed by post-peak data which exhibits a robust linear trend determined by a slope (designated the coefficient of sliding friction, μ_s) and an intercept (designated the inherent cohesion of the contact surfaces, S_o).

(x) From empirical observations detailed in (ix) above, direct shearing of sedimentary rocks under CND boundary conditions is thus envisaged as a two stage process associated with pre- and post-maximum friction deformation modes: In physical terms maximum friction represents peak shear strength of the macroscopic discontinuity, immediately prior to through-going breaching of the interlocking asperity system, followed by "residual" frictional sliding on a newly-created pervasive shear plane with a substrate of frictional wear debris. Thus for CND boundary conditions it appears that two coefficients of friction are relevant: the first, μ_{max}, relates to the process of actually creating the slip surface through the interlocking asperities, whilst the second, μ_s, relates to slip on the resultant pervasive, freshly fractured shear plane and associated wear products.

7.1.2 Triaxial Compression Experimentation

(i) A combined microseismics monitoring and liquid permeability measurement facility has successfully been coupled to a conventional rock mechanical triaxial compression system. Thus shear bands (morphologically similar to natural "granulation seams") induced under confining pressures equivalent to overburden depths ranging from 0.3km to 3km, have been studied with regard to synchronous measurement of acoustic emissions associated with post-failure frictional sliding deformation, and fault sealing potential associated with cataclasis.

(ii) The test reservoir sandstone analogue (Permo-Triassic Clashach sandstone, a coarse-grained subarkosic arenite with approximately 90% quartz and 10% feldspar) exhibits a curvilinear fracture strength envelope, better represented by the parabolic Griffith law than the linear Mohr-Coulomb criterion. Physically, this manifests itself in a stress-sensitive fault inclination, with the angle θ, between the shear band and the direction of maximum compressive stress increasing frrom 20^{o} to 40^{o} with increasing confining pressure.

(iii) Discrete, pulse-decay liquid (refined mineral oil) permeabilities have been measured at stress states corresponding to hydrostatic, post-dynamic failure, post-frictional sliding and post-re-shearing following artificial mechanical strengthening conditions, under a drained environment with pore pressure being equal to atmospheric. Experimental relative error on each individual permeability measurement was calculated to be probably not larger than $\pm 10\%$.

(iv) Axial permeability measurements showed no systematic correlation with hydrostatic stress magnitude. This was interpreted as being due to the fact that, for the relatively porous and strong Clashach sandstone, increasing hydrostatic stress led to quasi-elastic decrease in pore diameter, with however no lowering of pore space connectivity.

(v) In contrast, post-macroscopic shear failure, axial permeability showed a pronounced linear decrease in magnitude with increasing normal stress resolved across the shear band. The overall permeability drop with increasing stress, and the correlation coefficient of the linear fit, both increased with increasing shear displacement, that is from immediate post-failure to post-re-shear conditions. For

the latter situation, axial permeability decreased 100% with increasing resolved normal stress.

(vi) For the initial high-permeability Clashach sandstone (at hydrostatic stress, of the order of 1Darcy) for which the assumption of shear band permeability being very much less than that of the stressed rock matrix is valid (implying that virtually all of the measured pressure drop across the specimen actually occurs across the shear band) a simple empirical expression is derived which equates the measured core plug permeability to the product of a geometric constant (defined below) the shear band permeability, and the inverse of the shear band thickness.

(vii) With the geometric constant as described in (vi) above and defined as the product of core length, fault plane area and the inverse of the core plug cross-sectional area, also showing a linear decrease with increasing resolved normal stress (due to fault inclination stress sensitivity as defined in conclusion (ii) above) it is evident that shear band permeability dependence on the applied stress state cannot be inferred from axial permeability correlations alone.

(viii) Three-stage acoustic emission (AE) monitoring has allowed temporal variation in event rate, seismic b-value and inferred fractal dimension, D, to be determined for transient triaxial stresses increasing from hydrostatic to immediate post-dynamic failure conditions, for frictional sliding and for re-shearing on mechanical strengthening. This was achieved using a novel waveguide designed specifically for coupling a receiver transducer with rock core confined within a conventional Hoek-type hydraulic pressure vessel.

(ix) For stress histories involving triaxial loading from hydrostatic conditions to those associated with compressional failure in macroscopic shear, AE activity was seen to conform to an existing semi-quantitative, synoptic fractal damage mechanics model for brittle failure of intact laboratory specimens. Over the complete stress-strain curve, this model predicts transients in the seismic b-value and thus an "instantaneous" fractal dimension (D =2b). Fractal dimension was observed to range in magnitude from D >2 (b>1) associated with quasi-elastic loading to D =1 (b=0.5) at dynamic failure, corroborating the idea of rock failure in compression by shear faulting, being preceded by a phase of tensile microcrack nucleation,

growth and coalescence, associated with positive (D <2) or negative (D >2) feedback in local stress concentration during deformation.

(x) AE generated under conditions of post-peak slip-weakening, gave time-varying seismically inferred D -values of remarkably constant magnitude ≈ 2, characteristic of random processes (for example cataclastic flow) despite large spikes in event rate inferred to be the result of asperity shearing . On mechanical strengthening through a transient increase in confinement, this D -value remained unchanged, in direct contrast to the large fluctuations observed during the nucleation stage of faulting. This stability in the power law scaling exponent, combined with a relatively constant driving stress at constant strain rate, implies that frictional sliding conforms to a self-organised critical (SOC) phenomenon, consistent with recent treatment of crustal faulting, and suggests that fault-wall roughening processes are occurring synchronously with gouge comminution.

7.1.3 Experimental Fault Gouge Analyses

(i) Empirical correlations were demonstrated between the Rosin-Rammler constants of the relatively large-sized direct shear debris distributions quantified by sieving analysis, and percentage mineral content of the host multilithologic specimens. In particular, the distribution constant relation (n decreasing with increasing clay content) was interpreted to be a result of the influence of rock type on strain accommodation at the microscale, with the relative amounts of shearing fragmentation to tensile cracking being reflected in the resultant debris distributions.

(ii) Laser particle sizing techniques were successfully applied to both experimental direct shear and triaxial compression frictional wear products, over particle size ranges of 600-1.2 and 80-0.1microns, depending on the experimental configuration and optical model employed. In general, good correlation was evident between the sieving and laser sizing results over the appropriate size range.

(iii) With the slope of the log-normal curve providing an indication of particle sorting, a general trend was evident for the quartz-rich/clay-poor samples where a change

in sorting was evident at around 0.1mm particle size, which may reflect a gouge microstructure composed of relatively well-sorted, intact remnant grains within a fine-grained, comminuted matrix representing steady-state size reduction down to the limits of size resolution. In contrast, the clay-rich/quartz-poor samples exhibit strongly sigmoidal curves and a minimum comminution limit of about 1micron. This observation indicates that the comminution efficiency of the clay-rich specimens is reduced at small particle size, compared to that of the quartz-rich specimens, which may reflect the nature of the inter-particle stress concentrations for the different mineral phases.

(iv) Fault gouge fractal dimensions were generated from the linear portions of the Rosin-Rammler plots, utilising the relation D =3-n. The magnitude of D was found to be $1.5<D<2.4$ and $1.7<D<2.2$ for the 600-1.2 and 80-0.1micron size ranges respectively, in keeping with the range of published magnitudes for diverse fragmentation phenomena.

(v) A moderate empirical correlation was demonstrated between fault gouge fractal dimension and the coefficient of sliding friction, reflecting the direct relation between fractal dimension and specific surface area (surface area per unit mass of powder) as higher D -values indicate a higher number of small relative to large fragments. Linear positive correlation between specific surface area and the coefficient of sliding friction (also empirically demonstrated) may reflect an increase in frictional resistance associated with an increase in the energy required to create new surface area.

(vi) Shear fracture energies, G_{IIc}, were estimated for those direct shear experiments in which slip-weakening behaviour was evident, of magnitude $G_{IIc} = 0.1\text{-}1.5 \times 10^4 Jm^{-2}$. Constant normal displacement direct shear testing gives G_{IIc}-values four orders of magnitude greater than published biaxial tests under controlled constant normal stresses of equivalent measure, and of the same order of magnitude as triaxial compression tests conducted under considerably higher normal stresses, due to the greater degree of brecciation resulting from direct shear under maximum normal stiffness conditions, despite associated normal stresses <10MPa. Thus it is possible that *in situ* boundary conditions may provide an

answer to the discrepancy between the maximum laboratory measured values of shear fracture energy and field estimates for natural faults from seismological data.

(vii) Logarithmic positive empirical correlations have been demonstrated between shear fracture energy and both fault gouge specific surface area and fractal dimension, implying that increasing fracture resistance is associated with an increase in comminution (surface energy) as a proportion of the total energy dissipation process behind the rupture front. A logarithmic positive empirical correlation is also evident between the shear fracture energy and the coefficient of sliding friction.

(viii) From resin-impregnated thin-section photomicrographs of Clashach sandstone faulted triaxial specimens, shear band thickness and wall-rock roughness were both observed to decrease with increasing resolved normal stress, in direct contrast to an existing steady-state wear law developed for non-porous substrates with the assumption of zero fault gouge porosity change with compaction. At low normal stress magnitudes, both grain-boundary sliding and intra-granular fracturing contribute to the cataclastic deformation, whereas at high normal stresses, the latter mechanism dominates the cataclastic process.

(ix) For the assumption of a linear decrease in thickness:slip ratio with increasing normal stress (calibrated from thin-section measurement of two control specimens) Clashach sandstone experimentally induced shear bands were calculated to have absolute permeabilities ranging from approximately 2.5mD down to 0.5mD with increasing normal stress and angular shear strain. Normalised to permeability measured on the intact sample under hydrostatic stress conditions, these shear band permeability magnitudes equate to a "fault sealing potential" ranging from 0.35 to 0.04%. Thus computed permeability reductions range from 2.5 to 3.5 orders of magnitude, with shear band sealing exhibiting an order of magnitude increase with increasing normal stress and angular shear strain imposed on the gouge zone.

(x) Laser particle sizing was used to define the peak (relative fineness) and width of distribution (closeness of grading) of the fault gouge samples generated by the

above mentioned shear bands, through application of the exponential Rosin-Rammler distribution function, which was able to quantify "cataclastic intensity" via a "coefficient of variation" statistical parameter. The Rosin-Rammler coefficient of variation showed linear decrease (implying increasing cataclastic intensity) with increasing normal stress and angular shear strain, and a robust linear correlation with fault sealing potential was demonstrated, indicating that the effectiveness of cataclastic sealing as a fluid baffle decreases as the degree of fault gouge comminution decreases.

(xi) This empirical relation demonstrated between fault seal and degree of cataclasis can be rationalised through consideration of the Kozeny-Carman relation, which analyses permeability in terms of its constituent parameters of, porosity, surface area and tortuosity. An empirical linear negative correlation between estimated shear band permeability and fault gouge specific surface area was proven, as predicted by the Kozeny-Carman relation

7.2 FURTHER WORK

7.2.1 Direct Shear Experimentation

(i) Equipment development should concentrate on the provision of confining pressure for the direct shear specimens, so that comparison can be made between shear under constant normal stress and displacement boundary conditions at reservoir stress magnitudes. A coupled pore pressure and permeameter system would enable fault seal potential to be directly measured under stress histories associated with production.

(ii) AE monitoring of the direct shear programme would enable fractal damage mechanics to be applied to greater sliding displacement events. AE statistics could be used to provide a suitable basis on which to build a micromechanical theory of rock friction, and to assess the influence of boundary conditions on frictional sliding.

7.2.2 Triaxial Compression Experimentation

(i) Post-mortem analysis of sandstone specimens sheared under triaxial compression conditions, involving small particle statistics combined with wall-rock surface roughness measurement, would allow a frictional wear law relating thickness, wear loss, stress and displacement to be developed for porous reservoir rock.

(ii) The addition of finite pore pressures would enable investigation of the influence of effective stresses and degrees of overpressurisation on cataclastic seal integrity and on fault gouge statistics.

7.2.3 Experimental Fault Gouge Analyses

(i) As well as aiding in the understanding of fault-sealing by cataclasis, the ability to quantify comminution products through laser particle sizing and small particle statistics has great potential in the hydrocarbon industry, including study of the "crush" characteristics of proppant used to wedge open hydraulic fractures, and the problem of sand production from producing wells, where local shear stresses have exceeded rock strength in the vicinity of the wellbore.

(ii) The strain energy expended in creating new surface area (fault gouge) should be quantified under constant normal displacement boundary conditions and expressed as a percentage of the total work done in sliding. This value can then be contrasted with that obtained from constant normal stress tests.

REFERENCES

CHAPTER 1

[1] Rutter, E.H. 1986. On the nomenclature of mode of failure transitions in rocks. *Tectonophysics* Vol. 122. pp.381-387.

[2] Knipe, R.J. 1989. Deformation mechanisms - recognition from natural tectonites. *J. Struct. Geol.* Vol. 1. No. 2. pp.127-146.

[3] Maltman, A. 1984. On the term "soft sediment" deformation. *J. Struct. Geol.* Vol. 6. pp.589-592.

[4] Wang, C.H. 1986. Internal structure of fault zones. *Pure & Appl. Geophys.* Vol. 124. pp.373.

[5] Knipe, R.J. 1986. Microstructural evolution of vein arrays preserved in D.S.D.P. cores from Japan Trench Leg 57. In: *Structural Fabrics In D.S.D.P. Cores from Forearcs.* Moore, J.M. (Ed.) *Mem. Geol. Soc. Am.* 166. pp.75-88.

[6] Coulomb, C.A. 1773. Sur une application des règles de Maximis et Minimis a quelques problèmes de statique relatifs à l'Architecture. *Acad. Roy. des Sciences Memoires de math. et de physique par divers savans.* Vol. 7. pp.343-382.

[7] Mohr, O. 1900. Welche Umstande bedingen die Elastizitatsgrenze und den Bruch eines Materials? *Z. Ver. dt. Ing.* Vol. 44. pp.1524-1530; 1572-1577.

[8] Jaeger, J.C. & Cook, N.G.W. 1979. *Fundamentals of Rock Mechanics* . (3rd. Edn.) Chapman & Hall. London. 593pages.

[9] Paterson, M.S. 1978. *Experimental Rock Deformation - The Brittle Field.* Springer Verlag. Berlin. 254p.

[10] Mohr, O. 1914. *Abhandlungen aus dem Gebiete der technische Mechanik* (2nd. Edn.) Ernst und Sohn, Berlin.

[11] Griggs, D.T. & Handin, J. 1960. Observations on fracture and an hypothesis of earthquakes. In: *Rock Deformation, Geol. Soc. Am. Mem.* Vol. 79. pp.39-104.

[12] Anderson, E.M. 1951. *The Dynamics of Faulting and Dyke Formation with Applications to Britain.* (2nd. Edn.) Oliver & Boyd. Edinburgh.

[13] Sibson, R.H. 1973. Interaction between temperature and pore-fluid pressure during earthquake faulting - a mechanism for partial or total stress relief. *Nature Phys. Sci.* Vol. 243. pp.66-88.

[14] Griffith, A.A. 1920. The phenomena of rupture and flow in solids. *Phil. Trans. R. Soc.* Ser. A. Vol. 221. pp.163-198.

[15] Sneddon, I.N. 1946. The distribution of stress in the neighbourhood of a crack in an elastic solid. *Proc. R. Soc., London*. Vol. 187 A. pp.229-260.

[16] Scholz, C.H. 1990. *The Mechanics of Earthquakes and Faulting.* Cambridge University Press. Cambridge. 439pages.

[17] Griffith, A.A. 1924. The Theory of Rupture. In: *Proc. 1st. Int. Congr. Appl. Mech.* Biezeno, C.B. & Burgers, J.M. (ed.'s) Delft. Tech. Boekhandel en Drukkerij. J. Waltman Jr. pp.54-63.

[18] Brace, W.F. & Bombolakis, E.G. 1963. A note on brittle crack growth in compression. *J. Geophys. Res.* Vol. 68. pp.3709-3713.

[19] Orowan, E. & Nog, The N., 1949. Fracture and Strength of Solids. *Rep. Prog. Phys.* Vol.12. pp.185-232.

[20] Murrell, S.A.F. 1958. The strength of coal under triaxial compression. In: *Mechanical Properties of Non-metallic Brittle Materials.* Walton, W.H. (ed.) Buterworths. London. pp.123-145.

[21] Murrell, S.A.F. 1963. A criterion for brittle fracture of rocks and concrete under triaxial stress, and the effect of pore pressure on the criterion. In: Fairhurst, C. (ed.) *Rock Mechanics.* Proc. 5th. Symp. Rock Mech. Pergamon Press. N.Y. pp.563-577.

[22] Murrell, S.A.F. 1965. The effect of triaxial stress systems on the strength of rocks at atmospheric temperatures. *Geophys. J. Roy. Astr. Soc.* Vol.10. pp.231-281.

[23] McLintock, F.A. & Walsh, J.B. 1962. Friction on Griffith cracks in rocks under pressure. In: *Proc. 4th. U.S. Nat. Congr. Appl. Mech.* Vol. II. Am. Soc. Mech. Eng. N.Y. pp.1015-1021.

[24] Murrell, S.A.F. & Digby, P.J. 1970. The theory of brittle fracture initiation under triaxial stress conditions. I. *Geophys. J. Roy. Astr. Soc.* Vol.19. pp.309-334; II. ibid. pp.499-512.

[25] Brace, W.F. 1960. An extension of the Griffith theory of fracture to rocks. *J. Geophys. Res.* Vol.65. pp.3477-3480.

[26] Price, N.J. & Cosgrove, J.W. 1990. *Analysis of Geological Structures* Cambridge University Press. 502pages.

[27] Irwin, G.R. 1958. Fracture In: Flugge, S. (ed.) *Handbuch der Physik* Vol.VI. Elastizitat und Plastizitat. Springer-Verlag. Berlin. pp.551-590.

[28] Atkinson, B.K. 1987. Introduction to fracture mechanics and its geophysical applications. In: Atkinson, B.K. (ed.) *Fracture Mechanics of Rock* Academic Press. London. pp.1-26.

[29] Irwin, G.R. & de Wit, R. 1983. *J. Testing & Evaluation.* Vol.11. pp.56-65.

[30] ISRM Suggested Methods for Determining the Fracture Toughness of Rock. 1988. Ouchterlony, F. (Co-ordinator). *Int. J. Rock Mech. Min. Sci. & Geomech. Abstr.* Vol.25. No.2 pp.71-96.

[31] Li, V.C. 1987. Mechanics of shear rupture applied to earthquake zones. In: Atkinson, B.K. (ed.) *Fracture Mechanics of Rock* Academic Press. London. pp.351-428.

[32] Santarelli, F.J. & Brown, E.T. 1989. Failure of three sedimentary rocks in triaxial and hollow cylinder compression tests. *Int. J. Rock Mech. Min. Sci. & Geomech. Abstr.* Vol.26. No.5 pp.401-413.

[33] Hallbauer, D.K., Wagner, H., & Cook, N.G.W. 1973. Some observations concerning the microscopic and mechanical behaviour of quartzite specimens in stiff, triaxial compression tests. *Int. J. Rock Mech. Min. Sci. & Geomech. Abstr.* Vol.10. pp.713-726.

[34] Brace, W.F. 1964. Brittle fracture of rocks. In: Judd, W.R. (ed.) *State of Stress In the Earth's Crust* Elsevier. N.Y. pp.111-174.

[35] Brace, W.F., Paulding, B.W. & Scholz, C.H. 1966. Dilatancy in the fracture of crystalline rocks. *J. Geophys. Res.* Vol.71. pp.3939-3953.

[36] Bieniawski, Z.T. 1967. Mechanism of brittle fracture of rock. Part I. Theory of the fracture process; Part II. Experimental studies; Part III. Fracture in tension and under long-term loading. *Int. J. Rock Mech. Min. Sci.* Vol.4. pp.395-430.

[37] Walsh, J.B. 1965. The effect of cracks on the uniaxial elastic compression of rocks. *J. Geophys. Res.* Vol. 70. pp.399-411.

[38] Sobolev, G., Spetzler, H. & Salov, B. 1978. Precursors to failure in rocks while undergoing anelastic deformations. *J. Geophys. Res.* Vol.83. pp.1775-1784.

[39] Hadizadeh, J. & Rutter, E.H. 1983. The low temperature brittle-ductile transition in a quartzite and the occurrence of cataclastic flow in nature. *Geologische Rundschau* Vol.72. No.2. pp.493-509.

[40] Cox, S.J.D. & Scholz, C.H. 1988. On the formation and growth of faults: an experimental study. *J. Struct. Geol.* Vol.10. No.4. pp.413-430.

CHAPTER 2

[41] Aguilera, A. 1980. *Naturally Fractured Reservoirs* . Petroleum Publishing Co. Tulsa, Oklahoma.

[42] Heath, A.E., Walsh, J.J., & Watterson, J. 1994. Estimation of the effects of sub-seismic sealing faults on effective permeabilities in sandstone reservoirs. In: Aasen, J.O., Berg, E., Buller, A.T., Hjelmeland, O., Holt, R.M., Kleppe, J. & Torsaeter, O. (ed.'s) *North Sea Oil & Gas Reservoirs - III*. Norwegian Institute of Technology (NTH). Kluwer Academic Publishers. Dordrecht. pp.173-183.

[43] Childs, C., Walsh, J.J. & Watterson, J. 1990. A method for estimation of the density of fault displacements below the limits of seismic resolution in reservoir formations. In: Buller, A.T., Berg, E., Hjelmeland, O., Kleppe, J., Torsaeter, O. & Aasen, J.O. (ed.'s) *North Sea Oil & Gas Reservoirs - II*. Graham & Trotman. London. pp.309-318.

[44] Heffer, K.J. & Bevan, T.G. 1990. Scaling relationships in natural fractures - data, theory and applications. SPE 20981. *Proc. EUROPEC '90* The Hague. Netherlands. pp.367-376.

[45] Yielding, G., Walsh, J.J. & Watterson, J. 1992. The prediction of small-scale faulting in reservoirs. *First Break* Vol.10. pp.449-460.

[46] Walsh, J.J., Watterson, J, & Yielding, G. 1994. Determination and interpretation of fault size populations: procedures and problems. In: Aasen, J.O., Berg, E., Buller, A.T., Hjelmeland, O., Holt, R.M., Kleppe, J. & Torsaeter, O. (ed.'s) *North Sea Oil & Gas Reservoirs - III*. Norwegian Institute of Technology (NTH). Kluwer Academic Publishers. Dordrecht. pp.141-155.

[47] Knott, S.D. 1993. Fault seal analysis in the North Sea. *Bull. Am. Assoc. Pet. Geol.* Vol.77. No.5. pp.778-792.

[48] Marrett, R. & Allmendinger, R.W. 1991. Estimates of strain due to brittle faulting: sampling of fault populations. *J. Struct. Geol.* Vol.13. No.6. pp.735-738.

[49] Allegre, C.J., Le Mouel, J.L. & Provosi, A. 1982. Scaling rules in rock fracture and possible implications for earthquake prediction. *Nature* Vol.297. pp.47-49.

[50] Haldorsen, H.H. & Lake, L.W. 1984. A new approach to shale management in field-scale models. *J. Soc. Pet. Eng.* pp.447-457.

[51] Begg, S.H. & King, P.R. 1985. Modelling the effects of shales on reservoir performance: calculation of effective vertical permeability. *SPE 13539*.

[52] Holden, L., Hoiberg, J. & Lia, O. 1990. An estimator for the effective permeability. In: Guerillo, D. & Guillon, O. (ed.'s) *2nd. Eur. Conf. On the Mathematics of Oil Recovery*. Editions Technip. Paris. pp.287-290.

[53] Knipe, R.J. 1992. Faulting processes and fault seal. In: Larsen, R.M., Brekke, H., Larsen, B.T. & Talleras, E. (ed.'s) *Structural and Tectonic Modelling and its Application to Petroleum Geology*. Norwegian Petroleum Society (NPF) Special Publication 1. Elsevier. Amsterdam. pp.325-342.

[54] Hubbert, M.K. 1953. Entrapment of petroleum under hydrodynamic conditions. *Bull. Am. Assoc. Pet. Geol.* Vol. 37. pp.1954-2026.

[55] Watts, N.L. 1987. Theoretical aspects of cap-rock and fault seals for single and two-phase hydrocarbon columns. *Mar. Pet. Geol.* Vol.4. pp.274-307.

[56] Berg, R.R. 1975. Capillary pressure in stratigraphic traps. *Bull. Am. Assoc. Pet. Geol.* Vol. 59. pp.939-956.

[57] Sibson, R.H. 1981. Fluid flow accompanying faulting: field evidence and models. In: Simpson, D.W. & Richards, P.G. (ed.'s) *Earthquake Prediction: An International Review.* Am. Geophys. Union. M. Ewing Ser. Vol. 4. pp.593-603.

[58] Sibson, R.H. 1990. Conditions of fault-valve behaviour. In: Knipe, R.J. & Rutter, E.H. (ed.'s) *Deformation Mechanisms, Rheology and Tectonics*.. Geological Society Special Publication No. 54. London. pp.15-28.

[59] Burley, S.D., Mullis, J. & Matter, A. 1989. Timing diagenesis in the Tartan Reservoir (UK North Sea): constraints from combined cathodoluminescence microscopy and fluid inclusion studies. *Mar. Pet. Geol.* Vol. 6. No. 2. pp.98-120.

[60] Sibson, R.H. 1985. Stopping of earthquake ruptures at dilation fault jogs. *Nature* Vol. 316. pp.248-251.

[61] Sibson, R.H. 1986. Brecciation processes in fault zones - inferences from earthquake rupturing. *Pur. Appl. Geophysics.* Vol. 124. pp.159-175.

[62] Smith, D.A. 1980. Sealing and non-sealing faults in the Louisiana Gulf Coast Basin. *Bull. Am. Assoc. Pet. Geol.* Vol. 64. pp.145-172.

[63] Weber, K.J., Mandl, G., Pilaar, W.F., Lehner, F. & Precious, R.G. 1978. The role of faults in hydrocarbon migration and trapping in Nigerian growth fault structures. *SPE Proc. 10th Annual Offshore Technology Conference.* Vol. 4. pp.2643-2653.

[64] Lindsay, N.G., Murphy, F.C., Walsh, J.J. & Watterson, J. 1993. Outcrop studies of shale smears on fault surfaces. In: Flint, S.S. & Bryant, I.D. (ed.'s) The Geological Modelling of Hydrocarbon Reservoirs and Outcrop Analogues. *Spec. Publ. Int. Assoc. of Sedimentologists*. Vol. 15. pp.113-124.

[65] Ramsay, J.G. 1980. Shear zone geometry: a review. *J. Struct. Geol.* Vol. 2. pp.83-89.

[66] Ramsay, J.G. & Huber, M.I. 1983. *The Techniques of Modern Structural Geology Vol. I: Strain Analysis.* Academic Press Inc. London. 307pages.

[67] Barnett, J.A.M., Mortimer, J., Rippon, J.H., Walsh, J.J., & Watterson, J. 1987. Displacement geometry in the volume containing a single normal fault. *Bull. Am. Assoc. Pet. Geol.* Vol. 71. pp.925-937.

[68] Mandl, G., de Jong, L.N.J. & Maltha, A. 1977. Shear zones in granular material. *Rock Mechanics* Vol. 9. pp.95-144.

[69] Engelder, J.T. 1974. Cataclasis and the generation of fault gouge. *Geological Society of America Bulletin*. Vol. 85. pp.1515-1522.

[70] Aydin, A. 1978. Small faults formed as deformation bands in sandstone. *Pure Appl. Geophys.* Vol. 116. pp.913-930.

[71] Pittman, E.D. 1981. Effect of fault-related granulation on porosity and permeability of quartz sandstones; Simpson Group (Ordovician), Oklahoma. *Bull. Am. Assoc. Pet. Geol.* Vol. 65. pp.2381-2387.

[72] Jamison, W.R. & Stearns, D.W. 1982. Tectonic deformation of Wingate Sandstone, Colorado National Monument. *Bull. Am. Assoc. Pet. Geol.* Vol. 66. pp.2584-2608.

[73] Blenkinsop, T.G. & Rutter, E.H. 1986. Cataclastic deformation of quartz in the Moine thrust zone. *J. Struct. Geol.* Vol. 8. No. 6. pp.669-681.

[74] Underhill, J.R. & Woodcock, N.H. 1987. Faulting mechanisms in high-porosity sandstones; New Red Sandstone, Arran, Scotland. In: Jones, M.E. & Preston, R.M. (ed.'s) *Deformation of Sediments and Sedimentary Rocks.* Geological Society Special Publication No. 29. pp.91-105.

[75] Kulander, B.R., Dean, S.L. & Ward, B.J. 1990. *Fractured Core Analysis: Interpretation, Logging, and Use of Natural and Induced Fractures In Core.* Am. Assoc. Pet. Geol. Methods In Exploration Series No. 8. 88pages.

[76] Aydin, A. & Johnson, A.M. 1978. Development of faults as zones of deformation bands in sandstone. *Pure Appl. Geophys.* Vol. 116. pp.931-942.

[77] Aydin, A. & Reches, Z. 1982. The number and orientation of fault sets in the field and in experiments. *Geology* Vol. 10. pp.107-112.

[78] Fowles, J. & Burley, S. Textural and permeability characteristics of faulted, high porosity sandstones. *Mar. Pet. Geol.* Vol. 11. No. 5. pp.608-623.

[79] Lambe, T.W. & Whitman, R.V. 1969. *Soil Mechanics* John Wiley. N.Y.

[80] Aydin, A. & Johnson, A.M. 1983. Analysis of faulting in porous sandstones. *J. Struct. Geol.* Vol. 5. No. 1. pp.19-31.

[81] Rice, J.R. 1975. On the stability of dilatant hardening for saturated rock masses. *J. Geophys. Res.* Vol. 80. pp.1531-1536.

[82] Rudnicki, J.W. & Rice, J.R. 1975. Conditions for the localization of deformation in pressure-sensitive dilatant materials. *J. Mech. Phys. Solids.* Vol. 23. pp.371-394.

[83] Cleary, M.P. & Rudnicki, J.W. 1976. The initiation and propagation of dilatant rupture zones in geologic materials. *J. Appl. Mech.* Vol. 16. pp.13-30.

[84] Cleary, M.P. 1976. Continuously distributed dislocation model for shear-bands in softening materials. *Int. J. Numer. Meth. Engng.* Vol. 10. pp.679-702.

[85] Rudnicki, J.W. 1977. The inception of faulting in a rock mass with a weakened zone.*J. Geophys. Res.* Vol. 82. pp.844-854.

[86] Rice, J.R. 1979. Theory of precursory processes in the inception of earthquake rupture. *Beitr. Geophys.* Vol. 88. pp.91-127.

[87] Eshelby, J.D. 1957. The determination of the elastic field of an ellipsoidal inclusion, and related problems. *Proc. R. Soc. Lond.* Vol. 241 A. pp.376-396.

[88] Vardoulakis, I.G., Goldscheider, M. & Gudehus, G. 1978. Formation of shear bands in sand bodies as a bifurcation problem. *Int. J. Numer. Anal. Meth. Geomech.* Vol. 2. pp.99-128.

[89] Harper, T.R. & Moftah, I. 1985. Skin effect and completions options in the Ras Budran Reservoir. *SPE 13708.* Middle East Oil Technical Conference and Exhibition. Bahrain. pp.211-219.

[90] Nelson, R.A. 1985. Geologic analysis of naturally fractured reservoirs. In: *Petroleum Geology Engineering* Vol. I. Gulf Publishing Co. 320pages.

[91] Simpson, D.W. 1986. Triggered earthquakes. *Ann. Rev. Earth Planet Sci.* Vol. 14. pp.21-42.

[92] Marrow, P.C. 1989. Seismic monitoring in the North Sea. *British Geological Survey Report No. WL/88/25C* to the Department of Energy. HMSO.

[93] Raleigh, C.B., Healy, J.H. & Bredehoeft, J.D. 1972. Faulting and crustal stress at Rangely, Colorado. In: Heard, H.C., Borg, I.Y., Carter, N.L. and Raleigh, C.B. (ed.'s) *Flow and Fracture of Rocks (Griggs Volume).* American Geophysical Union Geohysical Monograph No. 16. pp.275-284.

[94] Raleigh, C.B., Healy, J.H. & Bredehoeft, J.D. 1976. An experiment in earthquake control at Rangely, Colorado. *Science* Vol. 191. pp.1230-1237.

[95] Goodman, R.E. 1989. *Introduction to Rock Mechanics* 2nd. Edn. John Wiley & Sons. N.Y. 562pages.

[96] Healy, J.H., Rubey, W.W., Griggs, D.T. & Raleigh, C.B. 1968. The Denver earthquakes. *Science*. Vol. 161. pp.1301-1310.

[97] Davis, S.D. & Pennington, W.D. 1989. Induced seismic deformation in the Codgell oil field of west Texas. *Bul. Seism. Soc. Am*. Vol. 79. No. 5. pp.1477-1494.

[98] Hubbert, M.K. & Rubey, W.W. 1959. Role of fluid pressure in overthrust faulting. I. Mechanics of fluid-filled porous solids and its application to overthrust faulting. *Geological Society of America Bulletin* . Vol. 70. No. 2. pp.115-206.

[99] Byerlee, J.D. & Brace, W.F. 1972. Fault stability and pore pressure. *Bul. Seism. Soc. Am*.. Vol. 62. pp.657-660.

[100] Yerkes, R.F. & Castle, R.O. 1976. Seismicity and faulting attributable to fluid extraction. *Eng. Geol.* Vol. 10. pp.151-167.

[101] Segall, P. 1989. Earthquakes triggered by fluid extraction. *Geology* Vol. 17. pp.942-946.

[102] Kovach, R.L. 1974. Source mechanisms for Wilmington oil field, California, subsidence earthquakes. *Bul. Seism. Soc. Am*.. Vol. 64. No. 3. pp.699-711.

[103] Pratt, W.E. & Johnson, D.W. 1926. Local subsidence of the Goose Creek oil field. *Jour. Geol.* Vol. 34. No. 1. pp.577-590.

[104] Howard, J.H. 1968. Recent deformation at Buena Vista Hills, California. *Am. Jour. Sci.* Vol. 266. pp.737-757.

[105] Wetmiller, R.J. 1986. Earthquakes near Rock Mountain House, Alberta, and their relationship to gas production. *Can. J. Earth. Sci.* Vol. 23. pp.172-181.

[106] Grasso, J.R. & Wittlinger, G. 1989. Ten years of seismic monitoring over a gas field area. *Bull. Seism. Soc. Am.* Vol. 80. pp.450-473.

[107] Feigner, B. & Grasso, J.R. 1990. Seismicity induced by gas production: I. Correlation of focal mechanisms and dome structure. *Pure Appl. Geophys.* Vol. 134. No. 3. pp.405-426.

[108] Grasso, J.R. & Feigner, B. 1990.Seismicity induced by gas production: II. Lithology correlated events, induced stresses and deformation. *Pure Appl. Geophys.* Vol. 134. No. 3. pp.427-450.

[109] Segall, P. 1985. Stress and subsidence resulting from subsurface fluid withdrawal in the epicentral region of the 1983 Coalinga earthquake. *J. Geophys. Res.* Vol. 90. No. B8. pp.6801-6816

[110] Biot, M.A. 1941. General theory of 3-dimensional consolidation. *J. Appl. Phys.* Vol. 12. pp.155-164.

[111] Rice, J.R. & Cleary, M.P. 1976. Some basic stress diffusion solutions for fluid-saturated elastic porous media with compressible constituents. *Rev. Geophys. & Space Phys.* Vol. 14. pp.1230-1237.

[112] Geertsma, J. 1973. Land subsidence above compacting oil and gas reservoirs. *J. Pet. Tech.* Vol. 25. pp.734-744.

[113] Moelle, K.H.R. & Chappell, B.A. 1985. The effect of anisotropies in the formation process of joint systems in sedimentary rocks. *Proc. Int. Symp. On Fundamentals of Rock Joints.* pp.35-45.

[114] Ramsay, J.G. & Huber, M.I. 1987.*The Techniques of Modern Structural Geology Vol. II: Folds and Fractures.* Academic Press Inc. London. 391pages.

[115] Ramsay, J.G. 1974. Development of chevron folds. *Bull. Geol. Soc. Am.* Vol. 85. pp.1741-1754.

[116] Tanner, P.W.G. 1989. The flexural-slip mechanism. *J. Struct. Geol.* Vol. 11. No. 6. pp.635-655.

[117] Krahn, J. & Morgenstern, N.R. 1979. The ultimate frictional resistance of rock discontinuities. *Int. J. Rock Mech. Min. Sci. & Geomech. Abstr.* Vol. 16. pp.127-133.

[118] Franklin, J.A. & Dusseault, M.B. 1989. *Rock Engineering.* McGraw Hill Publ. Co. N.Y. 600pages.

[119] Quigley, R.M., Thompson, C.D. & Fedorkiw, J.P. 1978. A pictorial case history of lateral rock creep in an open cut in the Niagara escarpment rocks at Hamilton, Ontario. *Can. Geotech. J.* Vol. 15. No. 1. pp.128-133.

[120] Jeremic, M.L. 1980. Influence of shear deformation structures in coal on selecting methods of mining. *Rock Mechanics.* Vol. 13. pp.23-38.

[121] Osterwald, F.W. & Dunrud, C.R. 1965. Geology applied to the study of coal mine bumps at Sunnyside, Utah. *AIME Trans.* Vol. 232. pp.168-174.

[122] Smart, B.G.D. 1992. Controls exerted by dominant parting planes over the deformation of tabular deposits. In: Kidybinski, A. & Dubinski, J. (ed.'s) *Effects of Geomechanics On Mine Design*. A.A. Balkema. Rotterdam.

[123] Warren, T.M. & Smith, M.B. 1985. Bottomhole stress factors affecting drilling rate at depth. *J. Pet. Tech.* Vol. 37. pp.1523-1533.

CHAPTER 3

[124] Natau, O. 1990. Scale effects in the determination of the deformability and strength of rock masses. In *Scale Effects In Rock Masses.* Pinto da Cunha (ed.) Balkema, Rotterdam. pp.77-88.

[125] Smart, B.G.D. & Crawford, B.R. 1990. An investigation of shear debris comminution as a mechanism of strain energy release for frictional sliding on dominant parting planes. In *Proc. ISRM Int. Symp. On Static and Dynamic Considerations In Rock Eng*. Swaziland. Brummer, R. (ed.) Balkema, Rotterdam. pp.389-400.

[126] Gamond, J.F. 1983. Displacement features associated with fault zones: a comparison between observed examples and experimental models. *J. Struct. Geol.* 5(1) pp.33-45.

[127] Petit, J.-P. 1988. Normal stress dependent rupture morphology in direct shear tests on sandstone with applications to some natural fault surface features. *Int. J. Rock Mech. Min. Sci. & Geomech. Abstr.* 25(6) pp.411-419.

[128] Means, W.D. 1987. A newly recognised type of slickenside striation. *J. Struct. Geol.* 9(5/6) pp.585-590.

[129] Fleuty, M.J. 1975. Slickensides and slickenlines. *Geol. Mag.* 112(3) pp.319-322.

[130] Billings, M.P. 1954. *Structural Geology.* Prentice-Hall Inc. New Jersey. 514p.

[131] Paterson, M.S. 1958. Experimental deformation and faulting in Wombeyan marble. *Geol. Soc. America. Bull.* 69. pp.465-476.

[132] Gay, N.C. 1970. The formation of step structures on slickensided shear surfaces. *J. Geol.* 78. pp.523-532.

[133] Lindstrom, M. 1974. Steps facing against the slip direction: a model. *Geol. Mag.* 111(1) pp.71-74.

[134] Gramberg, J. 1989. *A Non-Conventional View on Rock Mechanics and Fracture Mechanics.* A.A. Balkema. Rotterdam. 250p.

[135] Byerlee, J.D. 1978. Friction of rocks. *Pure & Appl. Geophys.* . 116. pp.615-626.

[136] Goodman, R.E. & Ohnishi, Y. 1973. Undrained shear testing of jointed rock. *Rock Mechanics* . 5 (3). pp.129-149.

[137] Saeb, S. & Amadei, B. 1990. Modelling joint response under constant or variable normal stiffness boundary conditions. *Int. J. Rock Mech. Min. Sci. & Geomech. Abstr.* 27(3). pp.367-371.

[138] Goodman, R.E. 1976. *Methods of Geological Engineering In Discontinuous Rocks*. West Publishing Co. St. Paul.

[139] Lam, T.S.K. & Johnston, I.W. 1982. A constant normal stiffness direct shear machine. *Proc. 7th. SE Asian Geotechnical Conf*. Hong Kong. pp.805-820.

[140] Johnston, I.W., Lam, T.S.K., & Williams, A.F. 1987. Constant normal stiffness direct shear testing for socketed pile design in weak rock. *Geotechnique* 37(1). pp.83-89.

[141] Amontons, M. 1699. De la resistance causee dans les machines. *Histoire de l'Academie Royale des Sciences.* Annee MDCXCIX. Amsterdam. pp.259-282.

[142] Bowden, F.P. & Tabor, D. 1950. *The Friction and Lubrication of Solids, Vol.I.* Clarendon Press, Oxford. 337p.

[143] Bowden, F.P. & Tabor, D. 1964. *The Friction and Lubrication of Solids, Vol.II.* Clarendon Press, Oxford. 544p.

[144] Bowden, F.P., Moore, A.J.W. & Tabor, D. 1943. The ploughing and adhesion of sliding metals. *J. Appl. Phys.* 14. pp.80-91.

[145] Archard, J.F. 1958. Elastic deformation and the laws of friction. *Proc. Royal Soc., London.* A243. pp.190-205.

[146] Byerlee, J.D. 1967. Theory of friction based on brittle fracture. *J. Appl. Phys.* 38(7). pp.2928-2934.

[147] Jaeger, J.C. 1959. The frictional properties of joints in rock. *Pure & Appl. Geophys.* 43. pp.148-158.

[148] Patton, F.D. 1966. Multiple modes of shear failure in rock. *Proc. 1st. Cong. Int. Soc. Rock Mech.* Lisbon. 1. pp.509-513.

[149] Jaeger, J.C. 1971. Friction of rocks and stability of rock slopes. Eleventh Rankine Lecture. *Geotechnique.* 21(2). pp.97-134.

[150] Byerlee, J.D. 1975. The fracture strength and frictional strength of Weber sandstone. *Int. J. Rock Mech. Min. Sci. & Geomech. Abstr.* 12. pp.1-4.

[151] Maurer, W.C. 1965. Shear failure of rock under compression. 1965. *J. Soc. Pet. Engrs* . 234. pp.167-176.

[152] Hobbs, D.W. 1970. The behaviour of broken rock under triaxial compression. *Int. J. Rock Mech. Min. Sci.* 7. pp.125-148.

[153] Denby, B. & Scoble, M.J. 1984. Quantification of power law indices for discontinuity shear strength prediction. *Proc. 25th. U.S. Symp. Rock Mech.* Denver. IIA. pp.233-240.

[154] Lundborg, N. 1968. Strength of rock-like materials. *Int. J. Rock Mech. Min. Sci.* 5. pp.427-454.

[155] Ladanyi, B. & Archambault, G.A. 1970. Simulation of shear behaviour of a jointed rock mass. *Proc. 11th. U.S. Symp. Rock Mech.* Am. Inst. Min. Eng. New York. pp.105-125.

[156] Barton, N. & Choubey, V. 1977. The shear strength of rock joints in theory and practice. *Rock Mechanics* 10. pp.1-54.

[157] Donath, F.A., Fruth, L.S. & Olsson, W.A. 1972. Experimental study of frictional properties of faults. In, *New Horizons In Rock Mechanics.* Hardy, H.R. & Stefanko, R. (eds.) Proc. 14th. Symp. Rock Mech., Penn. State Univ., Am. Soc. Civ. Eng. N.Y. pp.189-222.

[158] Ohnaka, M. 1975. Frictional characteristics of typical rocks. *J. Phys. Earth.* 23. pp.87-112.

[159] Raleigh, C.B. & Paterson, M.S. 1965. Experimental deformation of serpentinite and its tectonic implications. *J. Geophys. Res.* 70. pp.3965-3985.

[160] Byerlee, J.D. 1967. Frictional characteristics of granite under high confining pressure. *J. Geophys. Res.* 72. pp.3639-3648.

[161] Byerlee, J.D. 1968. Brittle-ductile transition in rocks. *J. Geophys. Res.* 73. pp.4741-4750.

[162] Hoskins, E.R., Jaeger, J.C. & Rosengren, K.J. 1968. A medium-scale direct friction experiment. *Int. J. Rock Mech. Min. Sci.* 5. pp.143-154.

[163] Handin, J. 1969. On the Coulomb-Mohr failure criterion. *J. Geophys. Res.* 74. pp.5343-5348.

[164] Abey, A.E. & Heard, H.C. 1973. Frictional characteristics of granite and granite/serpentine to high pressures. *EOS Trans. Am. Geophys. Union.* 54. pp.464.

[165] Edmond, O. & Murrell, S.A.F. 1973. Experimental observations on rock fracture at pressures up to 7kbar and the implications for earthquake faulting. *Tectonophysics*. 16. pp.161-182.

[166] Olsson, W.A. 1974. Effects of temperature, pressure and displacement rate on the frictional characteristics of a limestone. *Int. J. Rock Mech. Min. Sci. & Geomech. Abstr.* 11. pp.267-278.

[167] Handin, J. & Stearns, D.W. 1964. Sliding friction of rock. *Trans. Am. Geophys. Un.* 45. pp.103.

[168] Barford, N.C. 1987. *Experimental Measurements: Precision, Error and Truth.* (2nd. Edn.) John Wiley & Sons. Chichester. 159p.

[169] Gerrard, C. 1986. Shear failure of rock joints: Appropriate constraints for empirical relations. *Int. J. Rock Mech. Min. Sci. & Geomech. Abstr.* 23(6). pp.421-429.

CHAPTER 4

[170] Anon. 1984. *System 2000 Servo-Hydraulic Testing Machine Handbook: Instruction and Maintenance Manual.* RDP-Howden Ltd. Leamington Spa, U.K.

[171] McMeekin, C.E. 1991. *Evaluation of Pulse Decay Permeability Measurement using Analytical Solutions and Experimental Data for Low Permeability Core Samples at Simulated Reservoir Stresses.* M.Eng. Project Report. Department of Petroleum Engineering, Heriot-Watt University, Edinburgh. 40pages.

[172] Smart, B.G.D., Crawford, B.R., Main, I.G., Shimmield, G.B., Elphick, S.C. & Ngwenya, B.T. 1992. *The Effects of Combined Changes In Pore Fluid Chemistry and Stress State on Reservoir Permeability.* PSTI Core Research Programme Report Number 92/5. 63pages.

[173] *LOCAN AT POST User's Manual.* (Version 1.00). 1988. Physical Acoustics Corporation. Princeton, N.J.

[174] Haslam, J.A., Summers, G.R. & Williams, D. 1991. *Engineering Instrumentation and Control.*, Edward Arnold, London. 312pages.

[175] Vogler, U.W. & Kovari, K. 1977. Suggested Methods for Determining the Strength of Rock Materials in Triaxial Compression. In: *Rock*

Characterisation Testing and Monitoring ISRM Suggested Methods. Brown. E.T. (ed.) 1981. Pergamon Press, Oxford. pp.129-140.

[176] Hoek, E. & Franklin, J.A. 1968. A simple triaxial cell for field and laboratory testing of rock. *Inst. Min. Metall.*, London, Section A, 77. pp.22-26.

[177] Franklin, J.A. & Hoek, E. 1970. Developments in triaxial testing equipment. *Rock Mechanics* . 2. pp.223-228.

[178] Holt, R. 1990. Permeability reduction induced by a nonhydrostatic stress field. *SPE Formation Evaluation* pp.444-448.

[179] Brace, W.F., Walsh, J.B. & Frangos, W.T. 1968. Permeability of granite under high pressure. *J.Geophy. Res.* 63(7). pp.1225-2236.

[180] Zhao, Y., Huang, J. & Wang, R. 1993. Real-time SEM observations of the microfracturing process in rock during a compression test. *Int. J. Rock Mech. Min. Sci. & Geomech. Abstr.* 30(6). pp.643-652.

[181] Costin, L.S. 1987. Time-Dependent Deformation and Failure. In: Atkinson, B.K. (ed.) *Fracture Mechanics of Rock* Academic Press. London. pp.167-215.

[182] Obert, L. 1941. Use of subaudible noises for the prediction of rock bursts. *U.S.Bur. Mines Rept. 3555*.

[183] Obert, L. & Duvall, W. 1942. Use of subaudible noises for the prediction of rockbursts: Part II. *U.S.Bur. Mines Rept. 3654*..

[184] Sondergeld, C.W. & Estey, L.H. 1981. Acoustic emission study of microfracturing during the cyclic loading of Westerly granite.*J.Geophys. Res.* 86. pp.2915-2924.

[185] Goodman, R.E. 1963. Subaudible noise during compression of rocks. *Geo. Soc. Am. Bull.* 74. pp.487-490.

CHAPTER 5

[186] Ngwenya, B.T., Shimmield, G.B. & Elphick, S.C. 1993. A novel approach to testing core samples at reservoir conditions. *Society of Core Analysts Paper Number SCA 9325*. Houston, Texas.

[187] Ramsay, J.G. 1980. The crack-seal mechanism of rock deformation. *Nature.* 284. pp.135-139.

[188] Brace, W.F. & Martin, R.J. 1968. A test of the law of effective stress for crystalline rocks of low porosity. *Int. J. Rock Mech. Min. Sci.* 5. pp.415-426.

[189] Skopec, R. 1991. In-situ stress evaluation in core analysis. *SCA9103. 5th. Ann. Tech. Conf. Soc. Core Analysts.* Dallas.

[190] Bland, J.A. 1983. Fitting failure envelopes by the method of least squares. *Quarterly J. Eng. Geol.* 16(2).pp.143-147.

[191] Rutter, E.H. 1972. The effects of strain-rate changes on the strength and ductility of Solenhofen limestone at low temperatures and confining pressures. *Int. J. Rock Mech. Min. Sci.* 9. pp.183-189.

[192] Rehbinder, P.A. 1928. Effect of surface energy changes on cohesion, hardness and other properties of crystals. In: *Proc. VIth. Physics Congress*. State Press Moscow. pp.29.

[193] Ishido, T. & Mizutani, H. 1980. Relationship betweeen fracture strength of rocks and ζ-potential. *Tectonophysics*. 67.pp.13-23.

[194] Doebelin, E.O. 1975. *Measurement Systems (Application and Design).* McGraw-Hill Kogakusha Ltd. Tokyo. 772pages.

[195] Scarborough, J.B. 1955. *Numerical Mathematical Analysis*. 3rd. Edn. The Johns Hopkins Press. Baltimore.

[196] Li, C. & Nordlund, E. 1990. Characteristics of acoustic emisssions during shearing of rock joints. In: Barton, N. & Stephansson, O. (Ed.'s) *Rock Joints*. Balkema. Rotterdam. pp.251-258.

[197] Mandelbrot, B.B. 1967. How long is the coast of Britain? Statistical self-similarity and fractional dimension. *Science*. 156. pp.636-638.

[198] Gutenberg, B. & Richter, C.F. 1954. *Seismicity of the Earth and Associated Phenomenon*. 2nd. Edition. Princeton University Press. Princeton.

[199] Turcotte, D.L. 1992. *Fractals and Chaos In Geology and Geophysics.* Cambridge University Press. Cambridge. 221pages.

[200] Main, I.G., Sammonds, P.R. & Meredith, P.G. 1993. Application of a modified Griffith criterion to the evolution of fractal damage during compressional rock failure. *Geophys. J. Int.* 115.pp.367-380.

[201] Rudnicki, J.W. & Kanamori, H. 1987. Effect of fault interaction on moment, stress drop and strain energy return. *J. Geophys. Res.* 86.pp1785-1793.

[202] Meredith, P.G., Main, I.G. & Jones, C. 1990. Temporal variations in seismicity during quasi-static and dynamic rock failure. *Tectonophysics*. 175.pp.249-268.

[203] Lawn, B.R. & Wilshaw, T.R. 1975. *Fracture of Brittle Solids.* Cambridge University Press. Cambridge. 204pages.

[204] Charles, R.J. 1958. Static fatigue of glass. *J. Appl. Phys.* 29.pp.1549-1560.

[205] Meredith, P.G. & Atkinson, B.K. 1983. Stress corrosion and acoustic emission during tensile crack propagation in Whin Sill dolerite and other basic rocks. *Geophys. J. R. astr. Soc*. 75.pp.1-21.

[206] Main, I.G. & Meredith, P.G. 1991. Stress corrosion constitutive laws as a possible mechanism of intermediate-term and short-term seismic quiescence.*Geophys. J. Int.* 107.pp.363-372.

[207] Scholz, C.H. 1968. The frequency-magnitude relation of microfracturing in rock and its relation to earthquakes. *Bull. Seismol. Soc. Am.* 58.pp.399-315.

[208] Aki, K. 1981. A probabilistic synthesis of precursory phenomena. In: Simpson, D.W. & Richards, P.G. (Ed.'s) *Earthquake Prediction-An International Review.* Am. Geophys. Union, Maurice Ewing Ser. 4, Washington, D.C. pp.566-574.

[209] Hatton, C.G., Main, I.G. & Meredith, P.G. 1993. A comparison of seismic and structural measurements of scaling exponents during tensile subcritical crack growth. *J Struct. Geol.* 15(12).pp.1485-1495.

[210] Burnside. C. 1992. *Analysis of the Mechanics of Microfracturing In Rock Through the Application of Fractal Geometry to Thin-Sections and Acoustic Emission Data.* M.Eng. Thesis Project. Dept. of Petroleum Eng. Heriot-Watt University.

[211] Aki, K. 1965. Maximum likliehood estimates of b in the formula logN=a-bm and its confidence limits. *Bull. Earthquake Res. Inst.* Tokyo Univ. 43.pp.237-239.

[212] Sammonds, P.R., Meredith P.G. & Main, I.G. 1992. Role of pore fluids in the generation of seismic precursors to shear fracture. *Nature*. 359.pp.228-230.

[213] Main, I.G. Meredith, P.G., Sammonds, P.R. & Jones, C. 1990. Influence of fractal flaw distributions on rock deformation in the brittle field. In: Knipe, R.J. & Rutter, E.H. (Ed.'s) Deformation Mechanisms, Rheology and Tectonics. *Spec. Publ. Geol. Soc. Lond.* 54.pp.81-96.

[214] Shaw, H.R. & Gartner, A.E. 1986. On the graphical interpretation of palaeoseismic data. *U.S. Geol. Surv. Open-file Rep. 86-394*.

[215] Liakopoulou-Morris, F., Main, I.G., Crawford, B.R. & Smart, B.G.D. 1994. Microseismic properties of a homogeneous sandstone during fault nucleation and frictional sliding. *Geophysical Journal International*. 119. pp.219-230.

[216] Bak, P., Tang, C. & Weisenfeld, K. 1988. Self-organised criticality. *Phys. Rev.* A38. pp.364-374.

[217] Bruce, A. & Wallace, D. 1988. Critical point phenomena: universal physics at large length scales. In: Davies, P. (Ed.) *The New Physics.* Cambridge University Press. pp.236-267.

[218] Bak, P., Tang, C. & Weisenfeld, K. 1989. Scale invariant spatial and temporal fluctuations in complex systems. In: Stanley, H.E. & Ostrowsky, N. (Ed.'s). *Random Fluctuations and Pattern Growth: Experiments and Models.* Proc. NATO Advanced Study Institute. Kluwer Academic Publishers. pp.329-335.

[219] Sornette, D., Davy, P. & Sornette, A. 1990. A structuration of the lithosphere in plate tectonics as a self-organised critical phenomenon. *J.Geophys. Res.* 95(B11) pp.17353-17361.

CHAPTER 6

[220] Cadle, R.D. 1955. *Particle Size Determination.* Interscience Publishers Inc. NY. 303pages

[221] Herdan, G. 1960. *Small Particle Statistics.* (2nd. Edn.). Butterworths. London. 418pages.

[222] Rosin, P. & Rammler, E. 1933. The laws governing the fineness of powdered coal. *J. Inst. Fuel.* 7. pp.29-36.

[223] Bennett. J.G. 1936. Broken coal. *J. Inst. Fuel.* 10. pp.105-119.

[224] Jensen, J. 1991. *Introduction to Statistics for Reservoir Characterisation.* (MEng Course Notes) Dept. of Petroleum Eng. Heriot-Watt University.

[225] Abramowitz, M. and Stegun, I. A. 1965. *Handbook of Mathematical Functions.* New York. Dover Publications Inc. 1046pages.

[226] Korvin, G. 1992. *Fractal Models In the Earth Sciences.* Elsevier. Amsterdam. 396pages.

[227] Brown, W.K., Karp, R.R. & Grady, D.E. 1983. Fragmentation of the universe. *Astrophys. Space. Sci.* 94. pp.401-412.

[228] Weibull, W. 1951. A statistical distribution function of wide applicability. *J. Appl. Mech.* 18. pp.293-297.

[229] Hartmann, W.K. 1969. Terrestrial, lunar and interplanetary rock fragmentation. *Icarus.* 10. pp.201-213.

[230] Turcotte, D.L. 1986. Fractals and fragmentation. *J. Geophys. R.* 91(B2) pp.1921-1926.

[231] Turcotte, D.L. 1989. Fractals in geology and geophysics. *Pure & Appl. Geophys.* 131. pp.171-196.

[232] Sammis, C.G., Osborne, R.H., Anderson, J.L., Banerdt, M. & White, P. 1986. Self-similar cataclasis in the formation of fault gouge. *Pure & Appl. Geophys.* 124. pp.53-78.

[233] Sammis, C.G. & Biegel, R.L. 1989. Fractals, fault gouge & friction.*Pure & Appl. Geophys.* 131. pp.255-271.

[234] Sammis, C.G., King, G. & Biegel, R.L. 1987. The kinematics of gouge deformation. *Pure & Appl. Geophys.* 125. pp.777-812.

[235] Griffin, E.J. 1991. Extended range particle size distribution using laser diffraction technology: A perspective. *Soc. Core Analysts Conf. Paper No. SCA9126.* Dallas.

[236] Crawford. B.R., Smart, B.G.D. & Ngwenya, B.T. 1994. Relationship between frictional strength and fault gouge generation from direct shear testing under constant normal displacement control. *Proceedings of the SPE/ISRM Rock Mechanics In Petroleum Engineering - EUROCK '94* Delft, 29-31 August, 121-129, A.A.Balkema, Rotterdam.

[237] *Mastersizer Instruction Manual*. 1989. Malvern Instruments Ltd. Malvern, Worcester.

[238] Weiss, E.L. & Frock, H.N. 1976. Particle size control using light-scattering technology. *Powder Technology* pp.287-293.

[239] Grady, D.E. & Kipp, M.E. 1987. Dynamic rock fragmentation. In: Atkinson, B.K. (ed.) *Fracture Mechanics of Rock* Academic Press. London. pp.429-475.

[240] Rutter, E.H., Maddock, R.H., Hall, S.H. & White, S.H. 1986. Comparative microstructures of natural and experimentally produced clay-bearing fault gouges. *Pure & Appl. Geophys.* 124(1/2).pp.3-30.

[241] Mackenzie, R.C. & Milne, A.A. 1953. *Miner. Mag.* 30.pp.178.

[242] Olgaard, D.L. & Brace, W.F. 1983. The microstructure of gouge from a mining-induced seismic shear zone. *Int. J. Rock Mech. Min. Sci. & Geomech Abstr.* 20(1).pp.11-19.

[243] Brune, J.N. 1968. Seismic moment, seismicity and rate of slip along major fault zones. *J. Geophys. R.* 73.pp.777-784.

[244] Engelder, J.T. Logan, J.M. & Handin, J. 1975. The sliding characteristics of sandstone on quartz fault gouge. *Pure & Appl. Geophys.* 113.pp.69-86.

[245] Rice, J.R. 1980. The mechanics of earthquake rupture. In: Dziewonski, A.M. *et al* (Ed.'s) *Physics of the Earth's Interior*. pp.555-649.

[246] Wong, T-F. 1982. The shear fracture energy of Westerly granite from post-failure behaviour. *J. Geophys. R.* 87.pp.990-1000.

[247] Rice, J.R. 1984. Shear instability in relation to the constitutive description of fault slip. In: Gay, N.C. & Wainright, E.H. *Rockbursts and Seismicity In Mines*. S. Afr. Inst. Min. Metal. Johannesburg. pp.57-62.

[248] Wong, T-F. 1986. On the normal stress dependence of the shear fracture energy. In: Das, S. & Boatwright, J. *Earthquake Source Mechanics.* Am. Geophysics Union. Maurice Ewing Series 6. Washington DC. pp.1-11.

[249] Evans, B. & Wong, T-F. 1985. Shear localization in rocks induced by tectonic deformation. In: Bazant, Z. (Ed.) *Mechanics of Geomaterials.* John Wiley & Sons. Ltd. pp.189-210.

[250] Coulson, J.H. 1972. Shear strength of flat surfaces in rock. In: *Stability of Rock Slopes.* Proc. 13th. U.S. Symp. Rock Mech. Illinois. pp.77-105.

[251] Okubo, P.G. & Dieterich, J.H. 1984. Effects of physical fault properties on frictional instabilities produced on simulated faults. *J. Geophys. R.* 89(B7).pp.5817-5827.

[252] Tullis & Yund. 1992. The brittle-ductile transition in feldspar aggregates: an experimental study. In: Evans, B. & Wong, T.-F. (Ed.s) *Fault Mechanics and Transport Properties of Rocks* pp.89-117, Academic Press, London.

[253] Archard, J.F. 1953. Contact and rubbing of flat surfaces. *J. Appl. Phys.* 24.pp.981-988.

[254] Scholz, C.H. 1987. Wear and gouge formation in brittle faulting. *Geology.* 15.pp.493-495.

[255] Antonellini & Aydin. 1994. Effect of faulting on fluid flow in porous sandstones: petrophysical properties. *Am. Assoc. Pet. Geol.* 78.pp.355-377.

[256] Goggin, D.J., Thrasher, R.L. & Lake, L.W. 1988. A theoretical and experimental analysis of minipermeameter response including gas slippage and high velocity flow effects. *In Situ.* 12.pp.79-116.

[257] Marone, C. & Scholz, C.H. 1989. Particle-size distribution and microstructures within simulated fault gouge. *J. Struct. Geol.* 11(7).pp.799-814.

[258] Kozeny, J. 1927. Ueber kapillare Leitung des Wassers in Boden. *Sitz. Ber. Akad. Wiss. Wien, Mathem.-Naturwiss. Abt.* 136. pp271.

[259] Gueguen, Y. & Palciauskas, V. 1994. *Introduction to the Physics of Rocks.* Princeton University Press. New Jersey. 294pages.

APPENDIX I

Multilithologic direct shear specimen sliding surface morphologies:

- **Fig.AI.1 - A1.3: Red sandstones #3, #5, & #6.**
- **Fig.AI.4 - A1.5: Fissile mudstones #8, & #9.**
- **Fig.AI.6 - A1.8: Carbonaceous siltstones #11, #12 & #14.**
- **Fig.AI.9 - A1.12: Heterolithics S1, S2, S3 & S4.**

Direct Shear Specimen #3: Red medium-grained sandstone

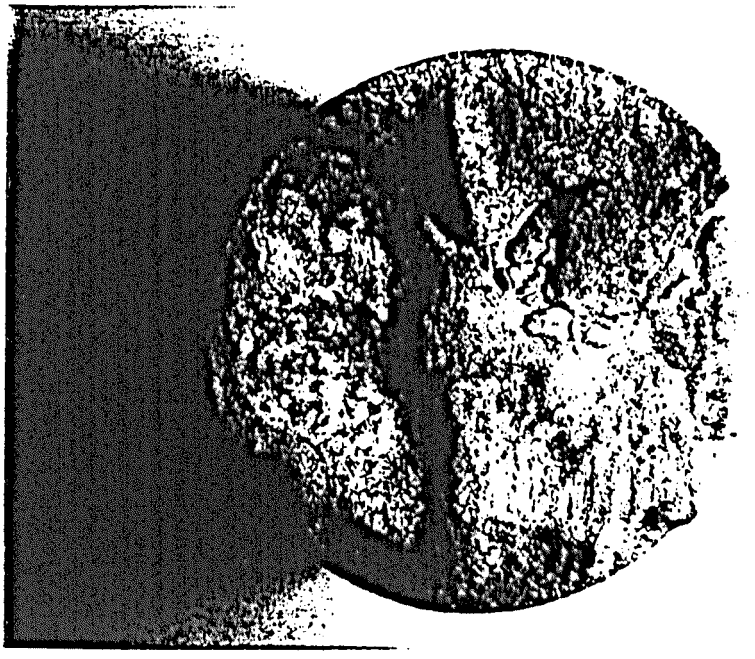

Lower sliding surface #3BOT (above)

BOT TOP

Upper sliding surface #3TOP (below)

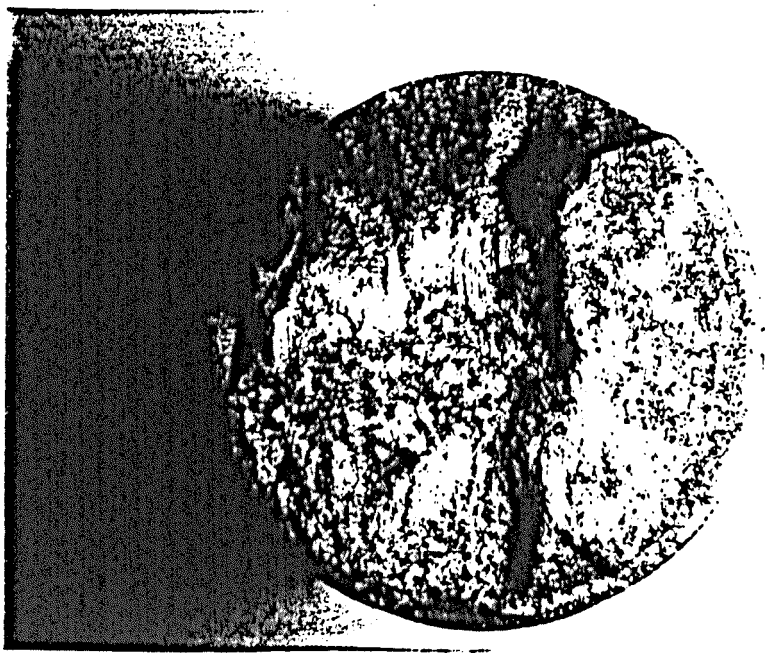

Fig.AI.1

Direct Shear Specimen #5: Red medium-grained sandstone

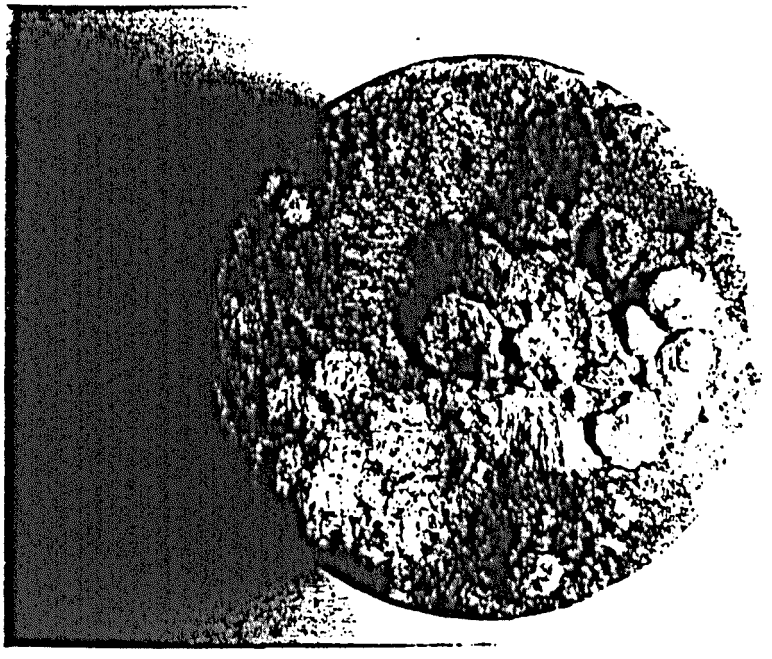

Lower sliding surface #5BOT (above)

BOT TOP

Upper sliding surface #5TOP (below)

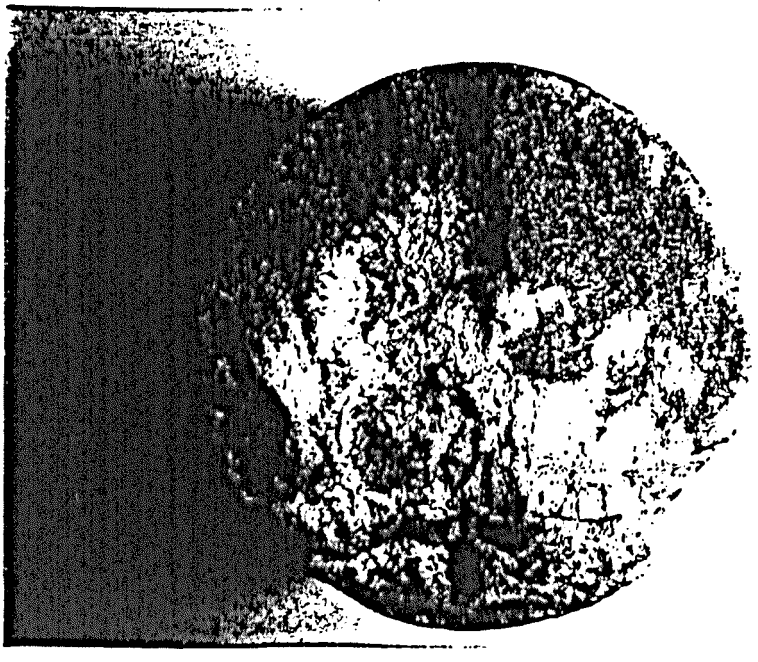

Fig.AI.2

Direct Shear Specimen #6: Red medium-grained sandstone

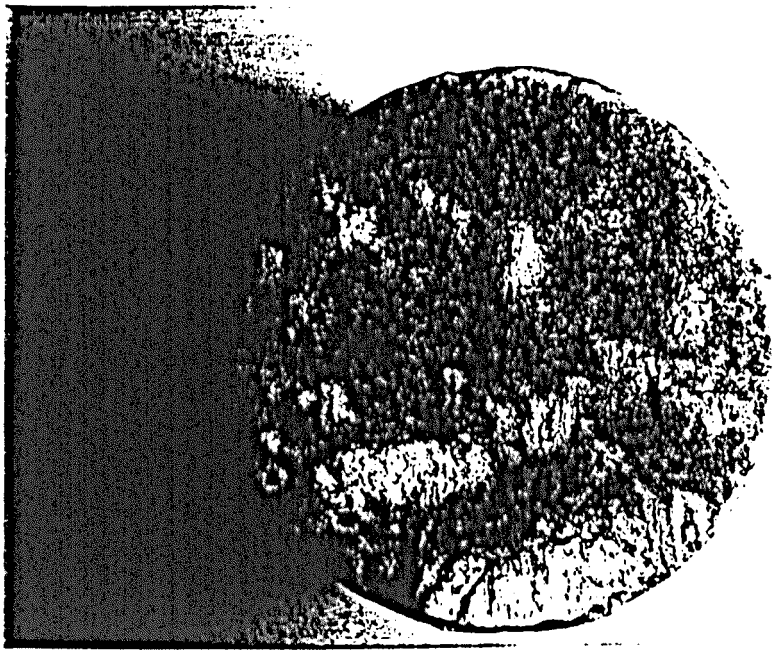

Lower sliding surface #6BOT (above)

BOT TOP

Upper sliding surface #6TOP (below)

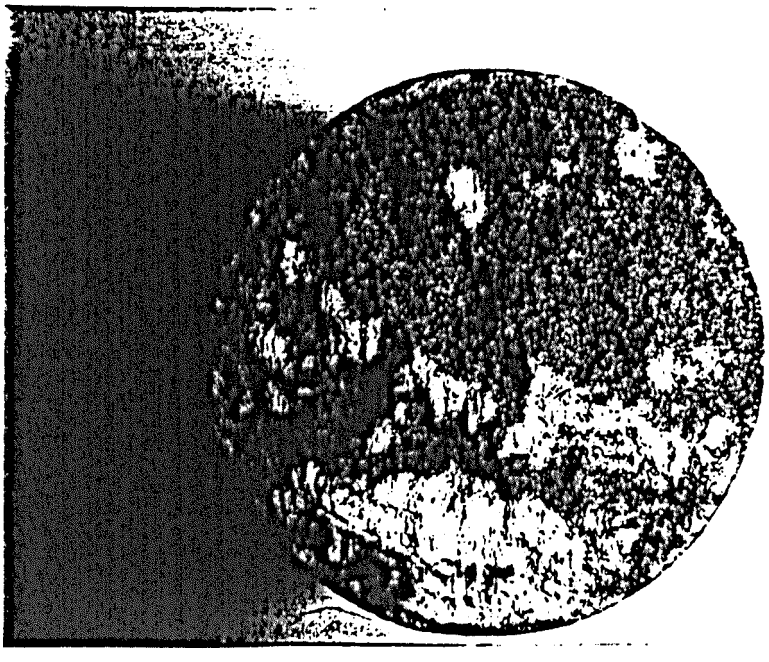

Fig.AI.3

Direct Shear Specimen #8: Dark-grey fissile mudstone

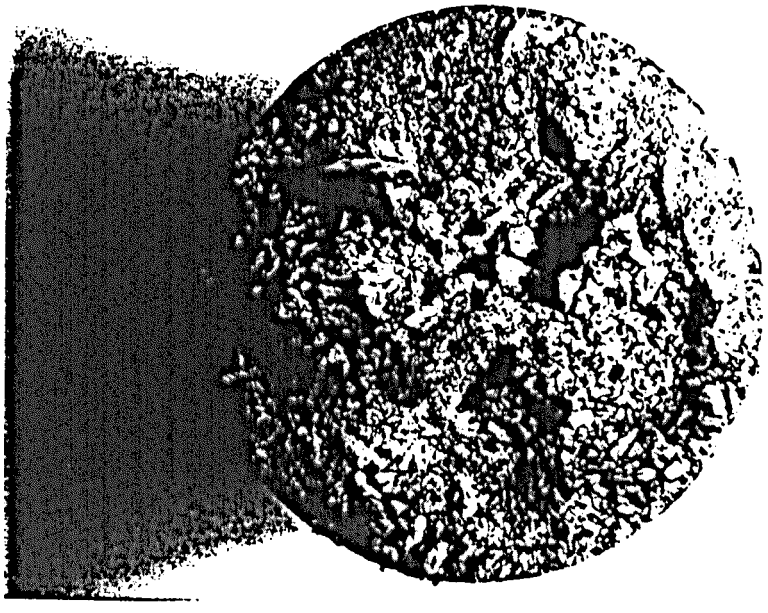

Lower sliding surface #8BOT (above)

BOT TOP

Upper sliding surface #8TOP (below)

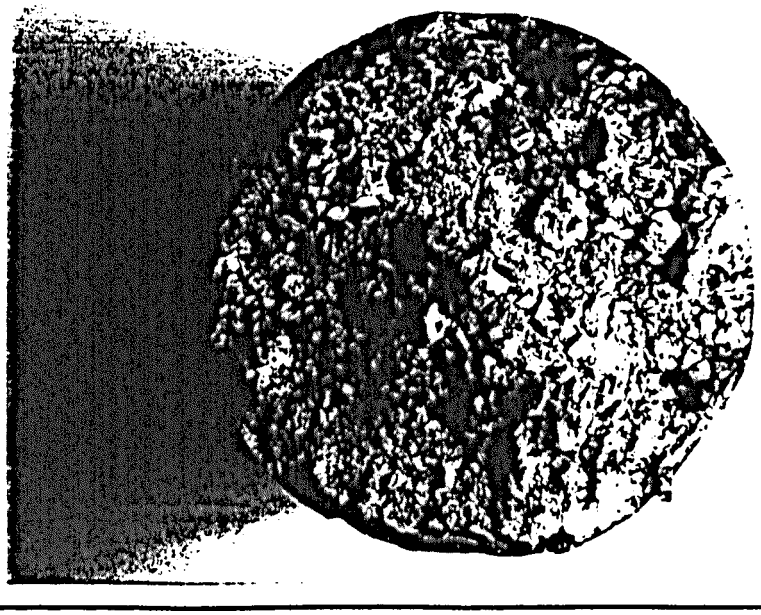

Fig.AI.4

Direct Shear Specimen #9: Dark-grey fissile mudstone

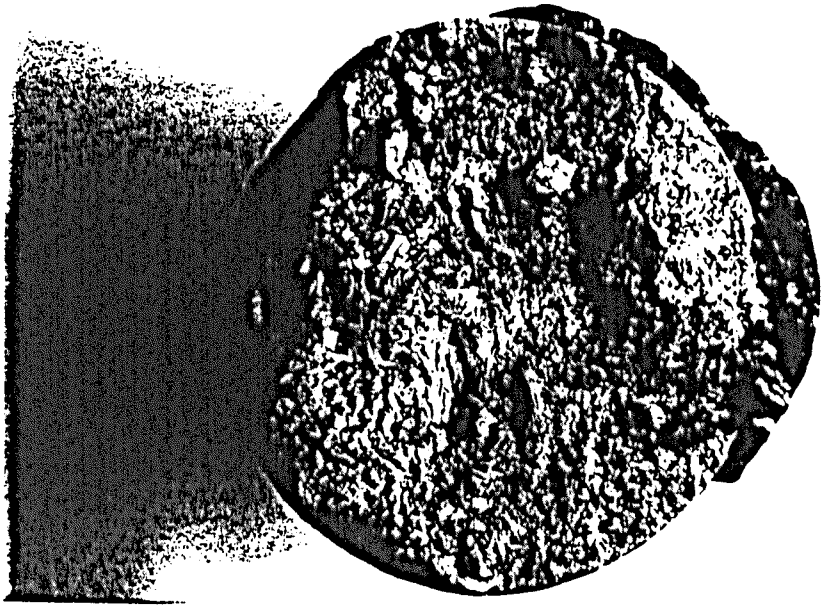

Lower sliding surface #9BOT (above)

BOT TOP

Upper sliding surface #9TOP (below)

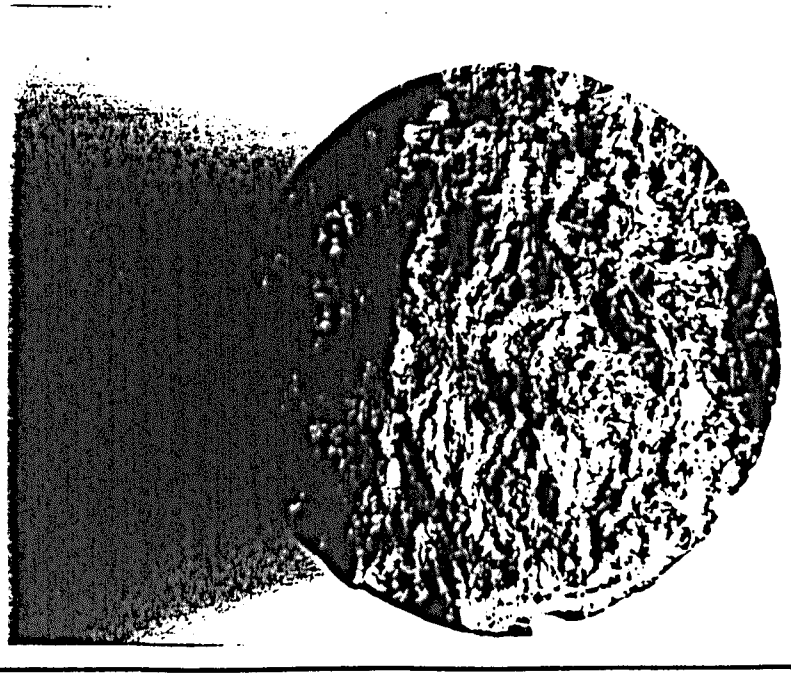

Fig.AI.5

Direct Shear Specimen #11: Dark-grey carbonaceous laminated siltstone

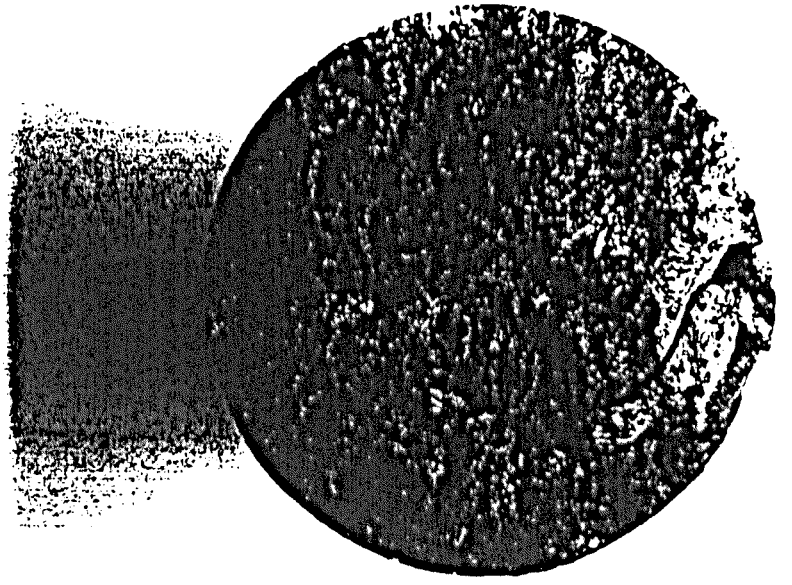

Lower sliding surface #11BOT (above)

BOT TOP

Upper sliding surface #11TOP (below)

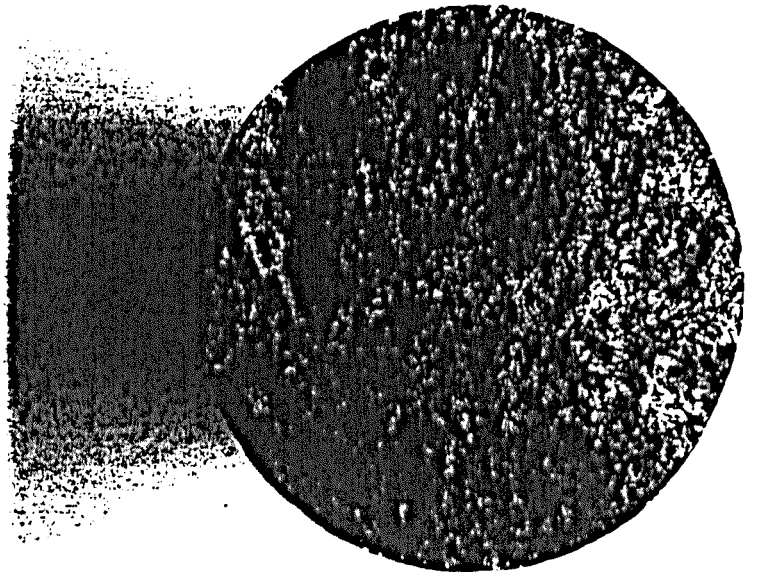

Fig.AI.6

Direct Shear Specimen #12: Dark-grey carbonaceous laminated siltstone

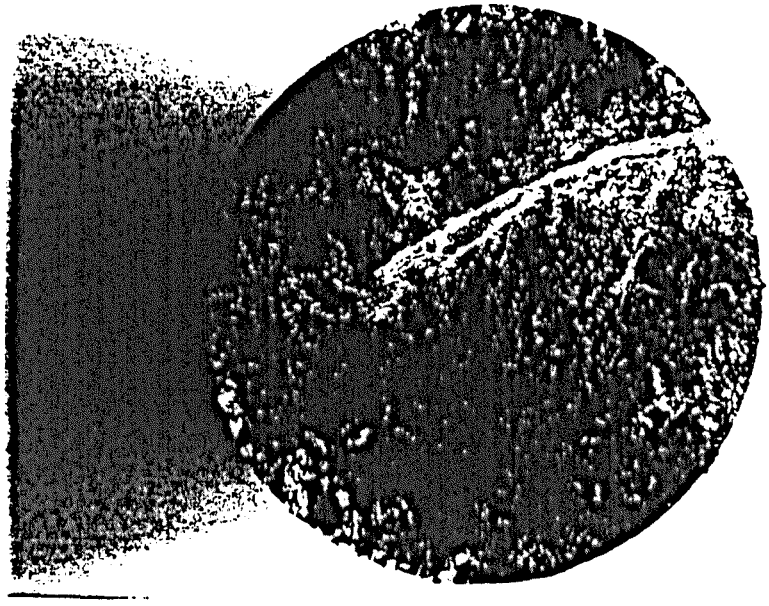

Lower sliding surface #12BOT (above)

BOT TOP

Upper sliding surface #12TOP (below)

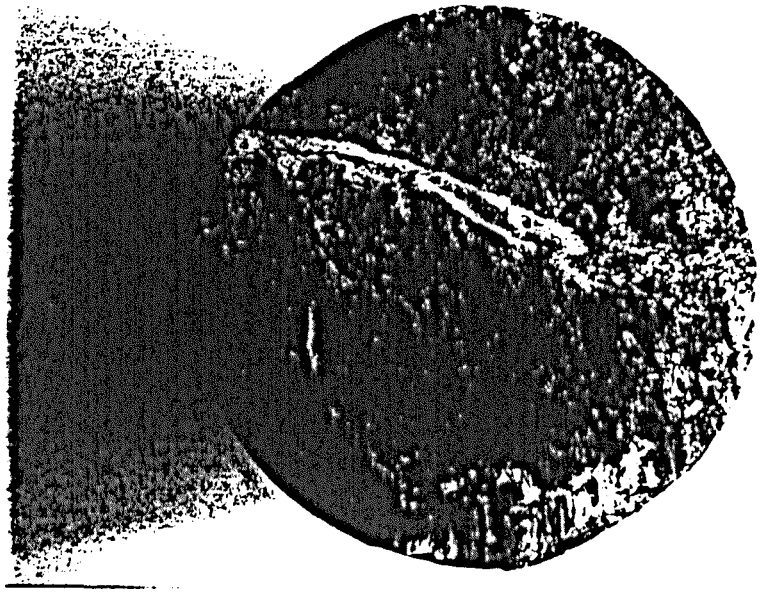

Fig.AI.7

Direct Shear Specimen #14: Dark-grey carbonaceous laminated siltstone

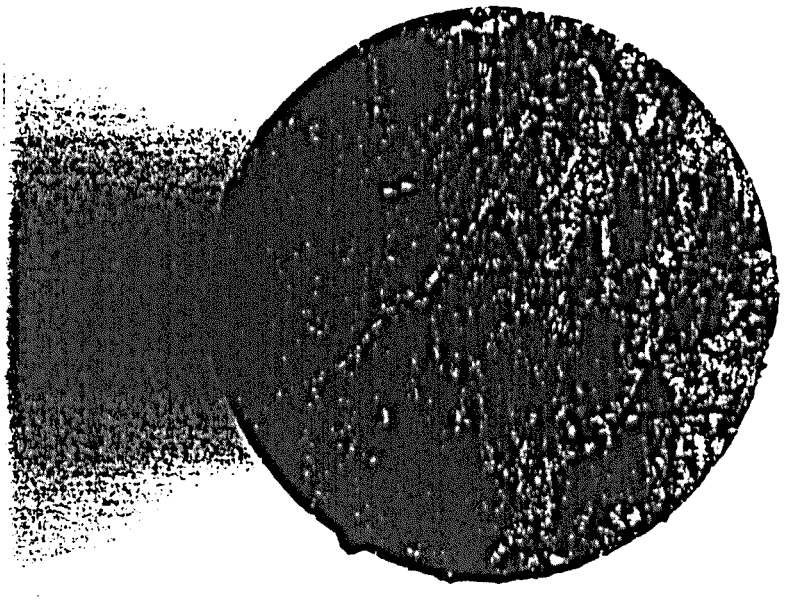

Lower sliding surface #14BOT (above)

BOT TOP

Upper sliding surface #14TOP (below)

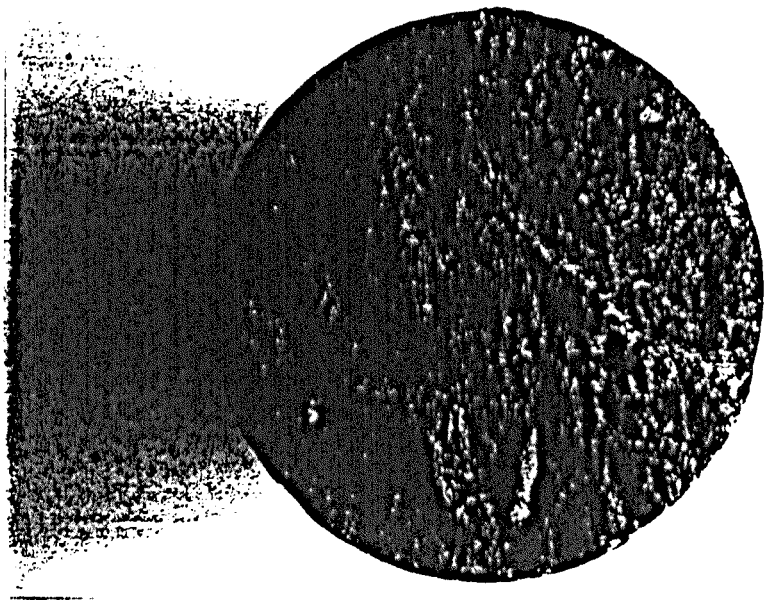

Fig.AI.8

Direct Shear Specimen S1: Grey interlaminated fine sandstone/siltstone

Lower sliding surface S1BOT (above)

BOT TOP

Upper sliding surface S1TOP (below)

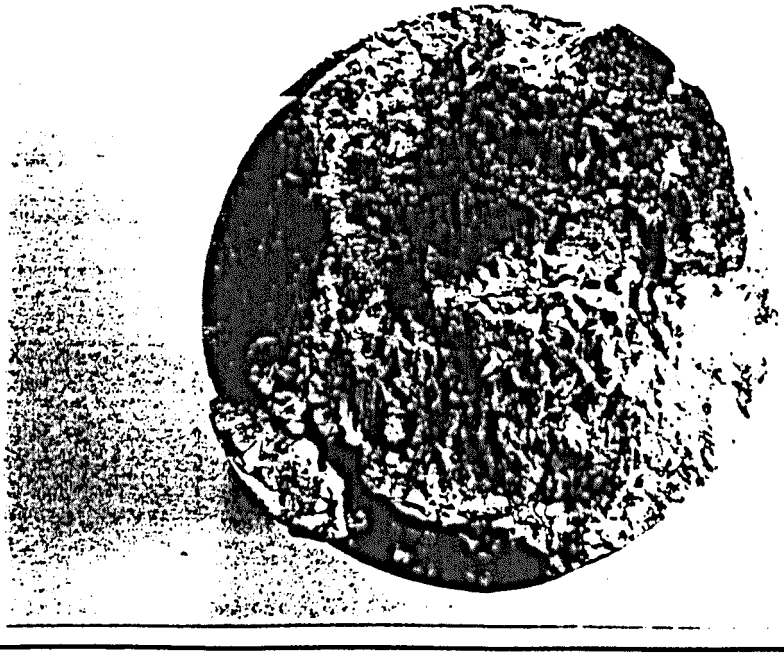

Fig.AI.9

Direct Shear Specimen S2: Grey interlaminated fine sandstone/siltstone

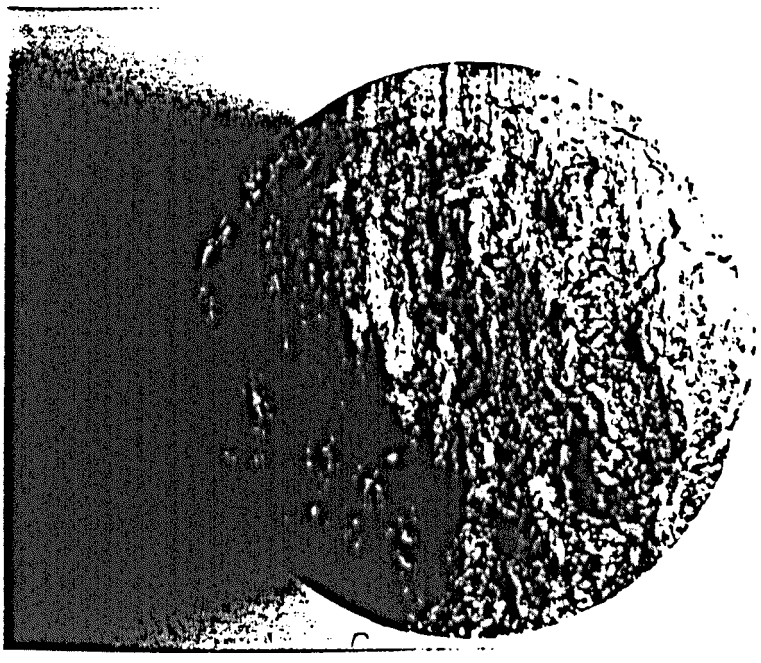

Lower sliding surface S2BOT (above)

BOT TOP

Upper sliding surface S2TOP (below)

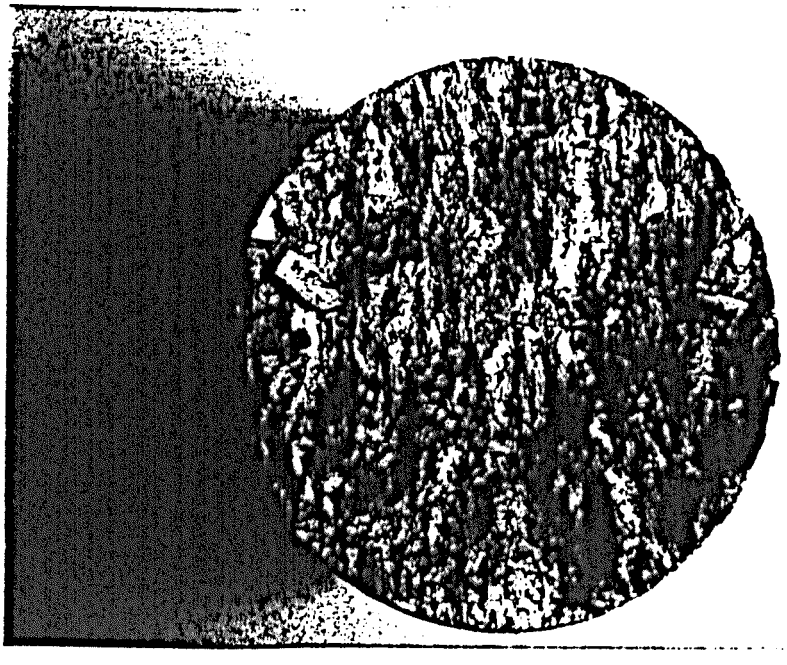

Fig.AI.10

Direct Shear Specimen S3: Grey interlaminated fine sandstone/siltstone

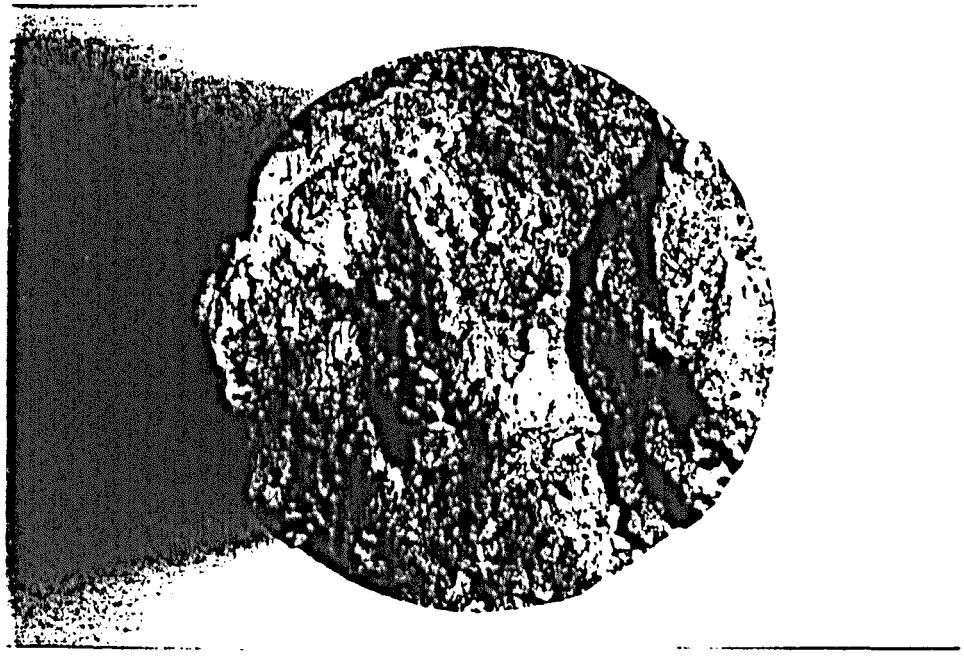

Lower sliding surface S3BOT (above)

BOT TOP

Upper sliding surface S3TOP (below)

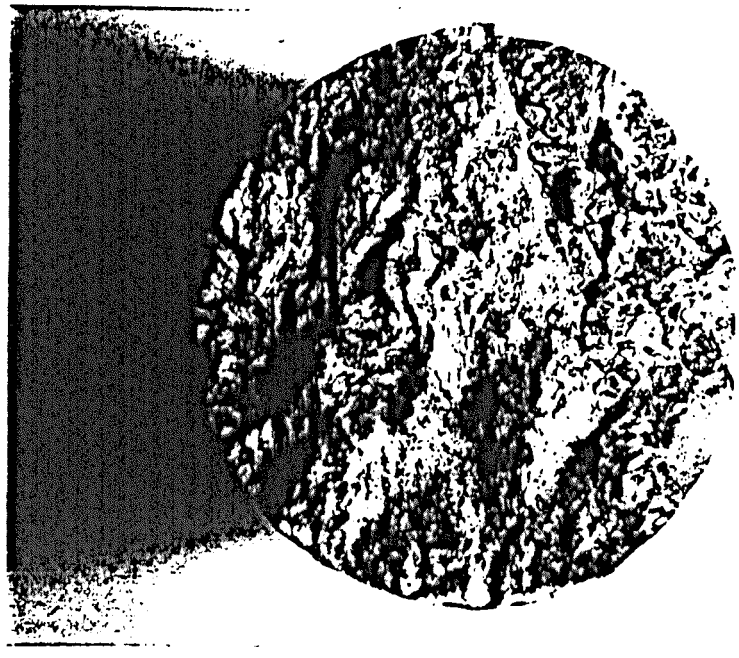

Fig.AI.11

Direct Shear Specimen S4: Grey interlaminated fine sandstone/siltstone

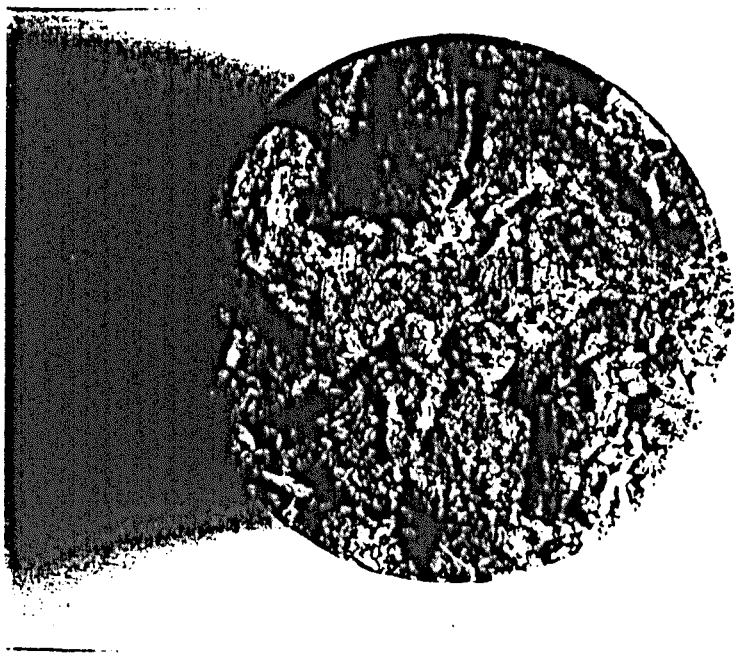

Lower sliding surface S4BOT (above)

BOT TOP

Upper sliding surface S4TOP (below)

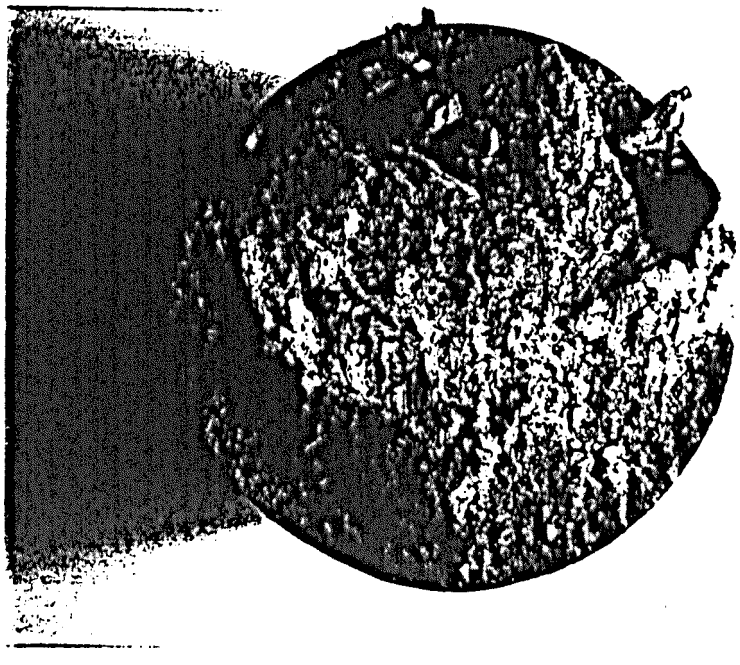

Fig.AI.12

APPENDIX II

Clashach sandstone triaxial compression specimens #15 - #22:

- **Fig.AII.1 - AII.7: Temporal variation in differential stress, AE event rate, seismic *b* -value and inferred fractal dimension**
- **Fig.AII.8 - AII.14: Differential stress, AE event rate, seismic*b* -value and inferred fractal dimension versus axial microstrain plots**

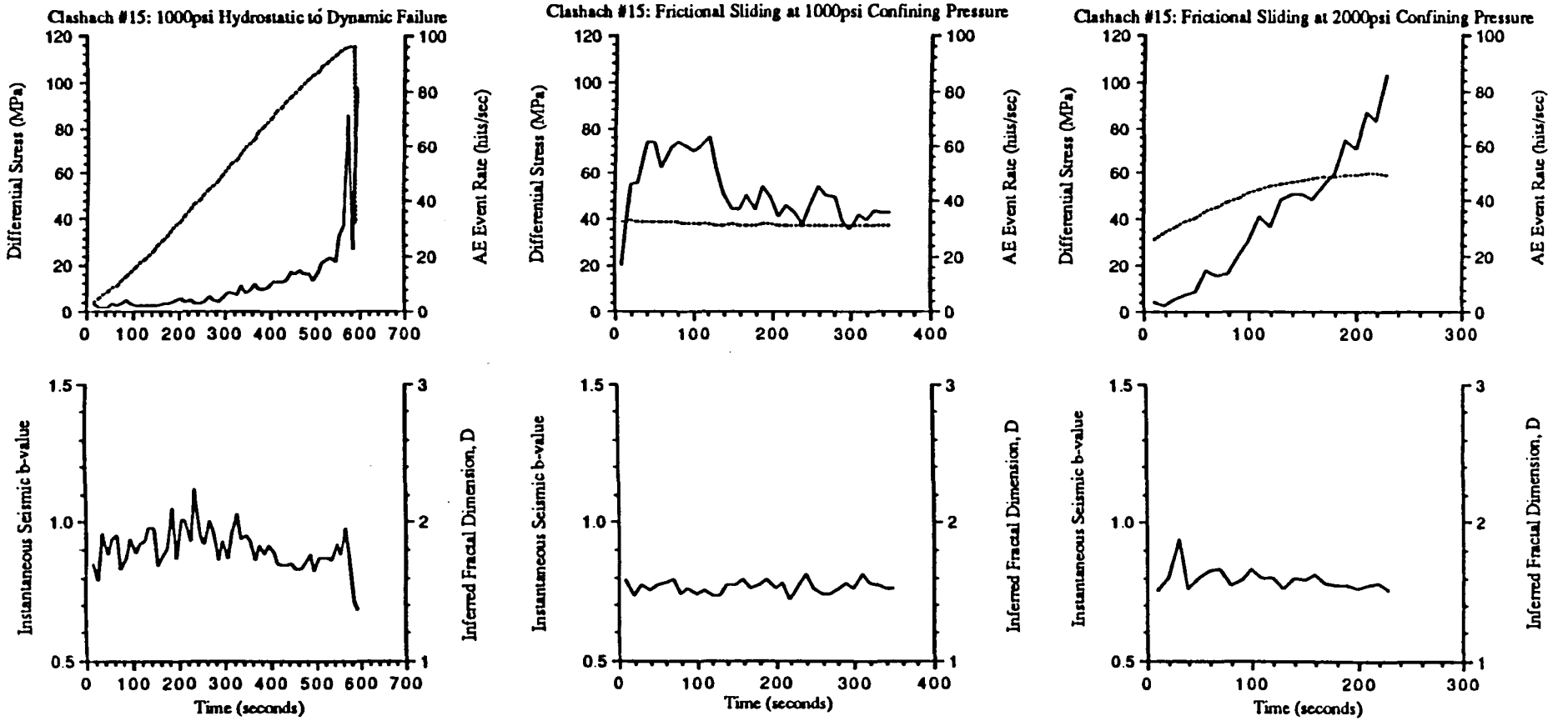
Clashach #15: 1000psi Hydrostatic to Dynamic Failure
Clashach #15: Frictional Sliding at 1000psi Confining Pressure
Clashach #15: Frictional Sliding at 2000psi Confining Pressure
Differential Stress (MPa)
AE Event Rate (hits/sec)
Instantaneous Seismic b-value
Inferred Fractal Dimension, D
Time (seconds)

Fig.AII.1

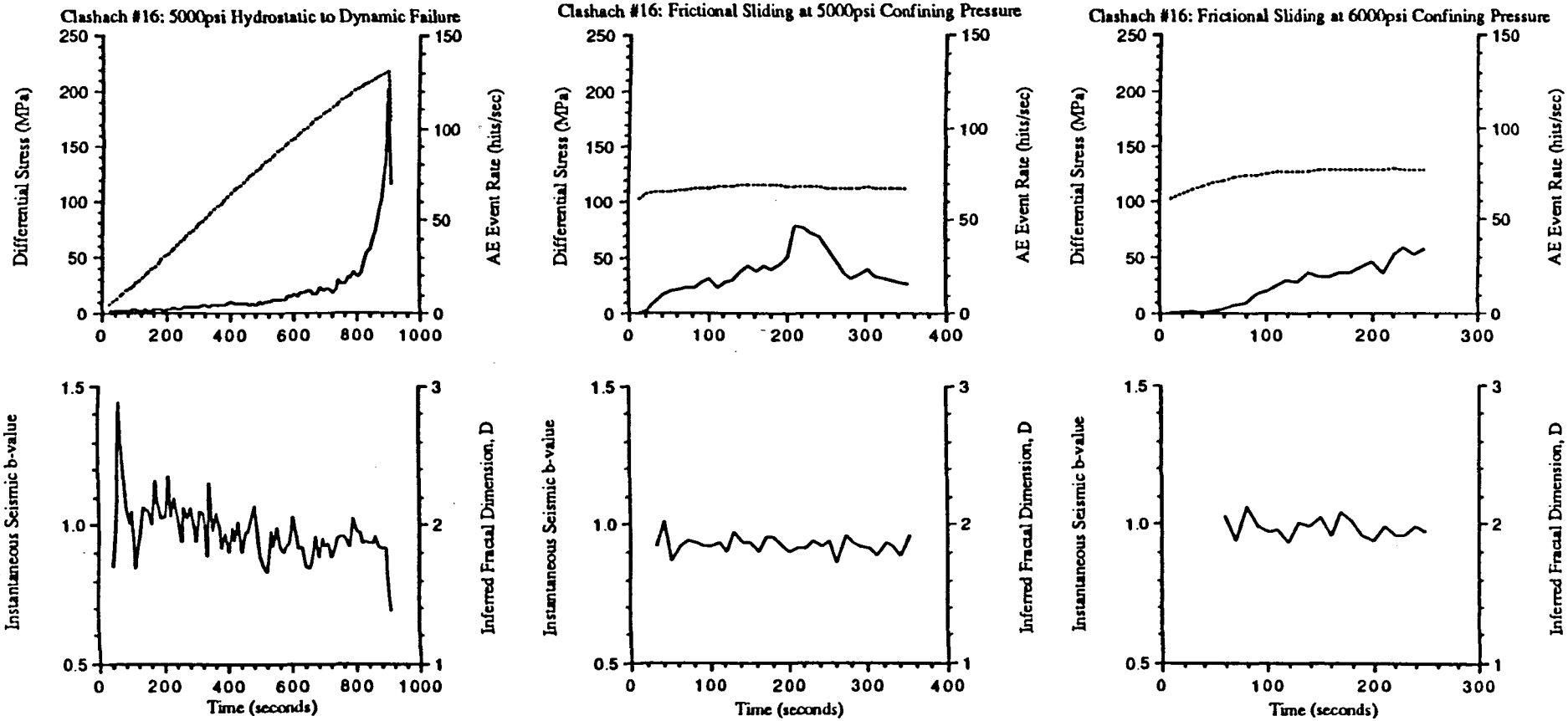
Clashach #16: 5000psi Hydrostatic to Dynamic Failure
Clashach #16: Frictional Sliding at 5000psi Confining Pressure
Clashach #16: Frictional Sliding at 6000psi Confining Pressure
Differential Stress (MPa)
AE Event Rate (hits/sec)
Instantaneous Seismic b-value
Inferred Fractal Dimension, D
Time (seconds)

Fig.AII.2

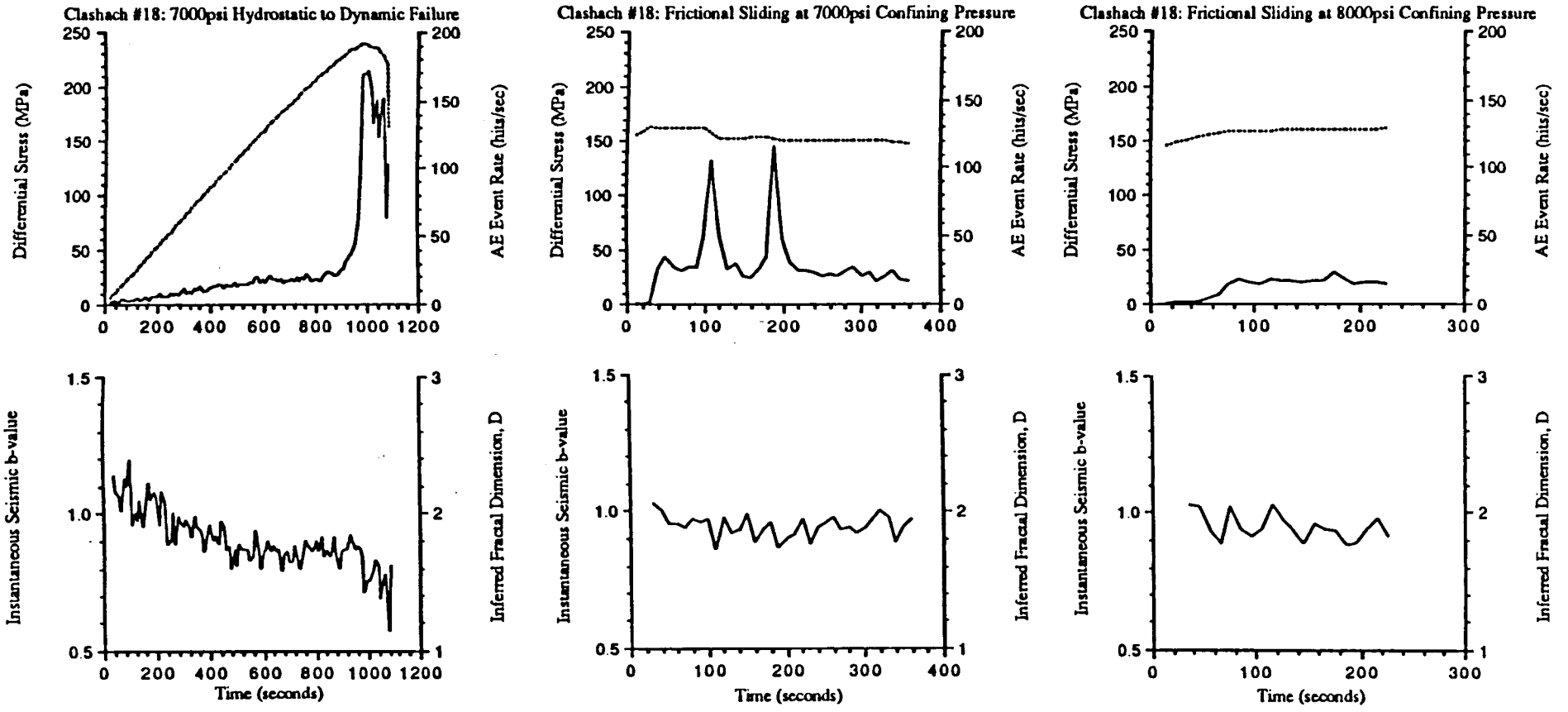
Clashach #18: 7000psi Hydrostatic to Dynamic Failure
Clashach #18: Frictional Sliding at 7000psi Confining Pressure
Clashach #18: Frictional Sliding at 8000psi Confining Pressure
Differential Stress (MPa)
AE Event Rate (hits/sec)
Instantaneous Seismic b-value
Inferred Fractal Dimension, D
Time (seconds)

Fig.AII.3

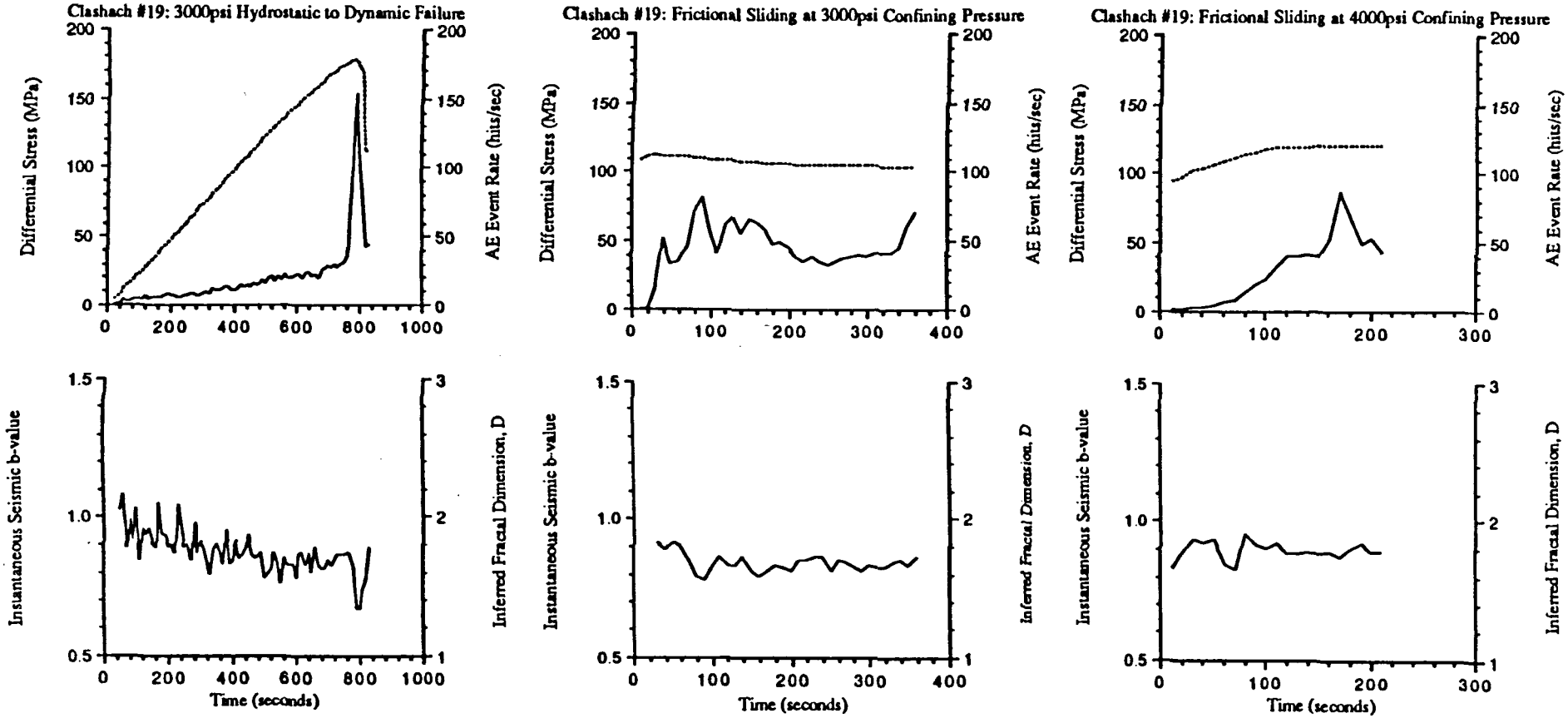
Clashach #19: 3000psi Hydrostatic to Dynamic Failure
Clashach #19: Frictional Sliding at 3000psi Confining Pressure
Clashach #19: Frictional Sliding at 4000psi Confining Pressure
Differential Stress (MPa)
AE Event Rate (hits/sec)
Instantaneous Seismic b-value
Inferred Fractal Dimension, D
Time (seconds)

Fig.AII.4

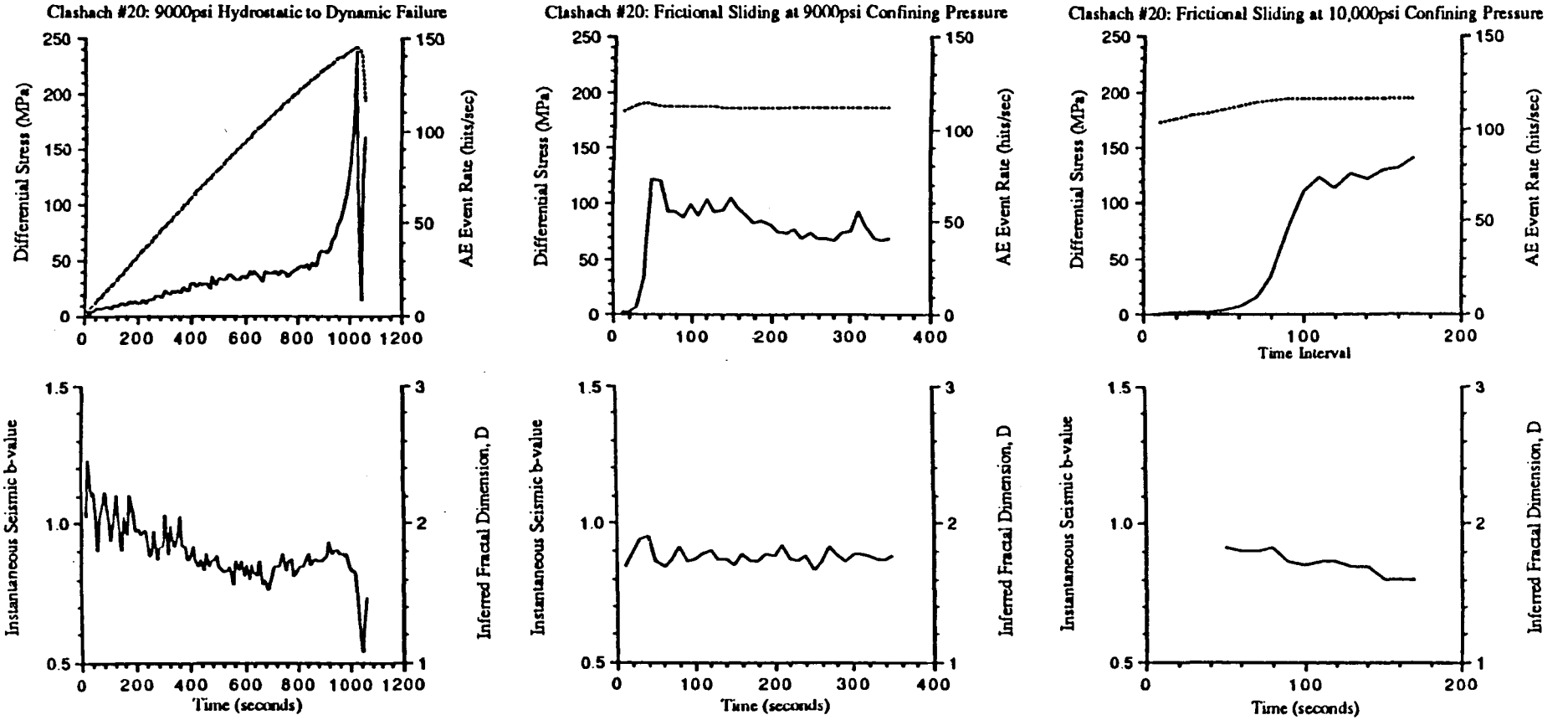
Clashach #20: 9000psi Hydrostatic to Dynamic Failure
Differential Stress (MPa)
AE Event Rate (hits/sec)
Instantaneous Seismic b-value
Inferred Fractal Dimension, D
Time (seconds)
Clashach #20: Frictional Sliding at 9000psi Confining Pressure
Differential Stress (MPa)
AE Event Rate (hits/sec)
Instantaneous Seismic b-value
Inferred Fractal Dimension, D
Time (seconds)
Clashach #20: Frictional Sliding at 10,000psi Confining Pressure
Differential Stress (MPa)
AE Event Rate (hits/sec)
Time Interval
Instantaneous Seismic b-value
Inferred Fractal Dimension, D
Time (seconds)

Fig.AII.5

Clashach #21: 3000psi Hydrostatic to Dynamic Failure
Differential Stress (MPa)
AE Event Rate (hits/sec)
Instantaneous Seismic b-value
Time (seconds)
Inferred Fractal Dimension, D
Clashach #21: Frictional Sliding at 3000psi Confining Pressure
Differential Stress (MPa)
AE Event Rate (hits/sec)
Instantaneous Seismic b-value
Time (seconds)
Inferred Fractal Dimension, D
Clashach #21: Frictional Sliding at 4000psi Confining Pressure
Differential Stress (MPa)
AE Event Rate (hits/sec)
Instantaneous Seismic b-value
Time (seconds)
Inferred Fractal Dimension, D

Fig.AII.6

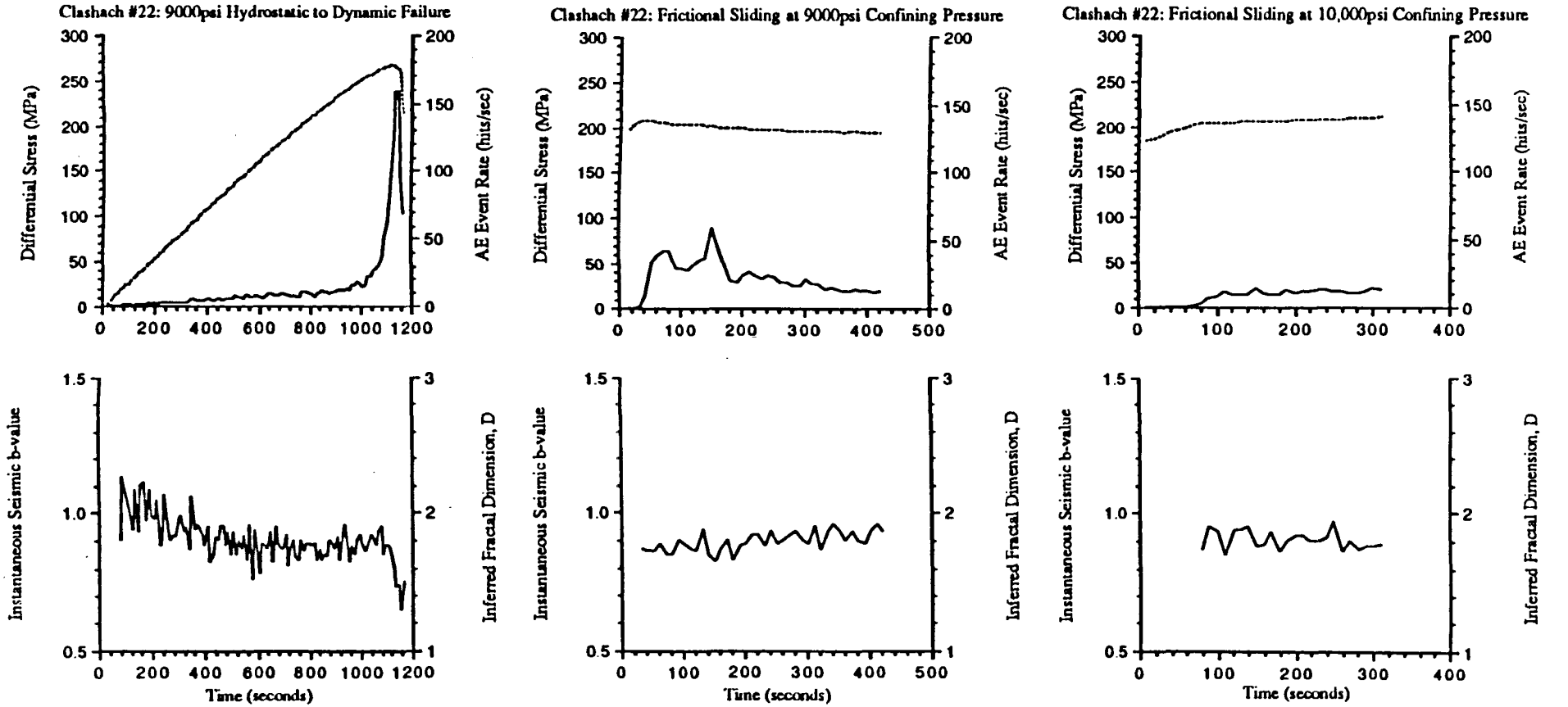
Clashach #22: 9000psi Hydrostatic to Dynamic Failure
Clashach #22: Frictional Sliding at 9000psi Confining Pressure
Clashach #22: Frictional Sliding at 10,000psi Confining Pressure
Differential Stress (MPa)
AE Event Rate (hits/sec)
Instantaneous Seismic b-value
Inferred Fractal Dimension, D
Time (seconds)

Fig.AII.7

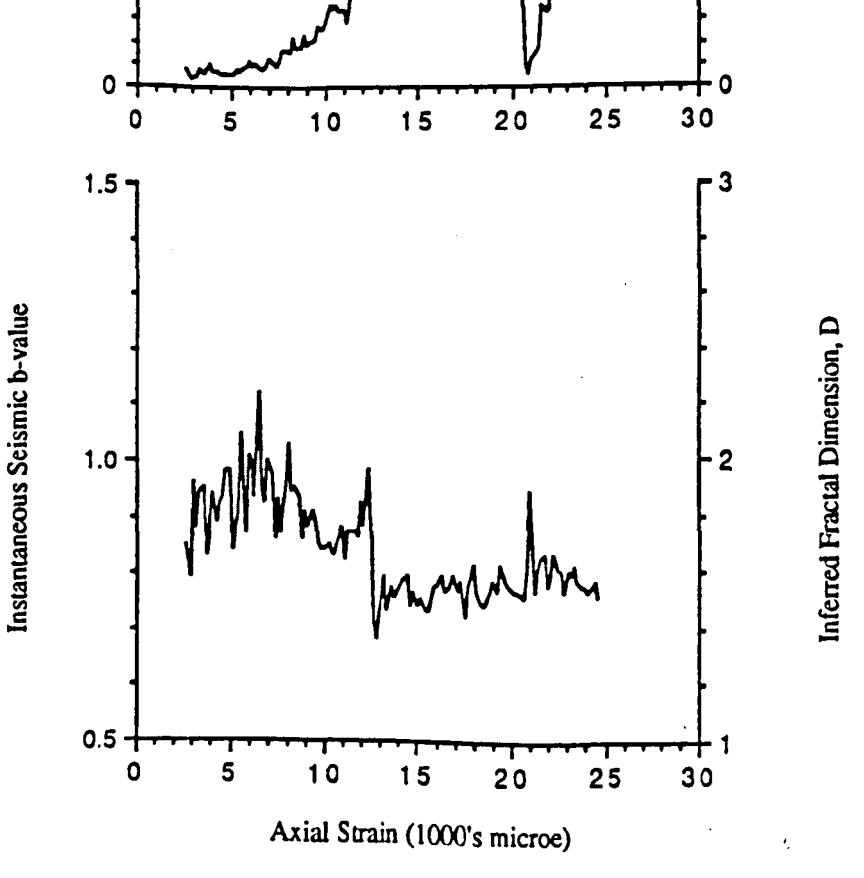
1.5
1.0
0.5
3
2
1
0
5
10
15
20
25
30
Instantaneous Seismic b-value
Inferred Fractal Dimension, D
Axial Strain (1000's microe)

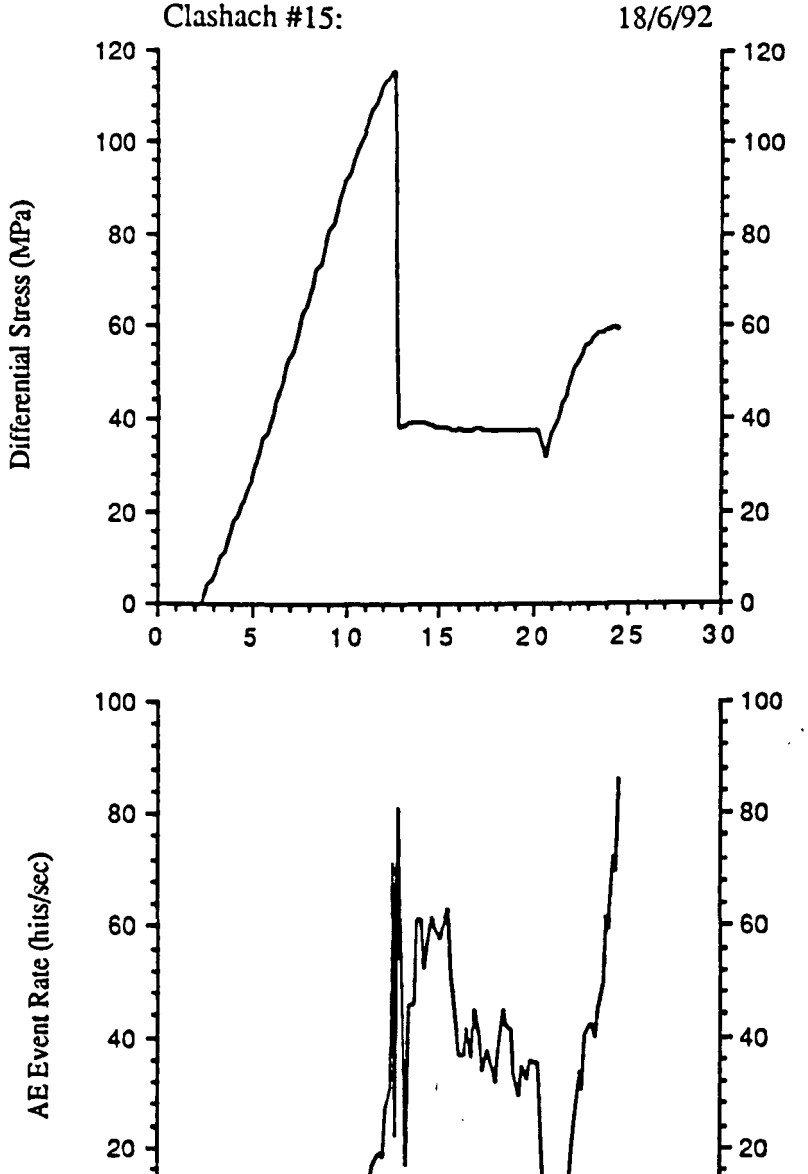
Clashach #15:
18/6/92
Differential Stress (MPa)
AE Event Rate (hits/sec)
0
20
40
60
80
100
120
0
5
10
15
20
25
30

Fig.AII.8

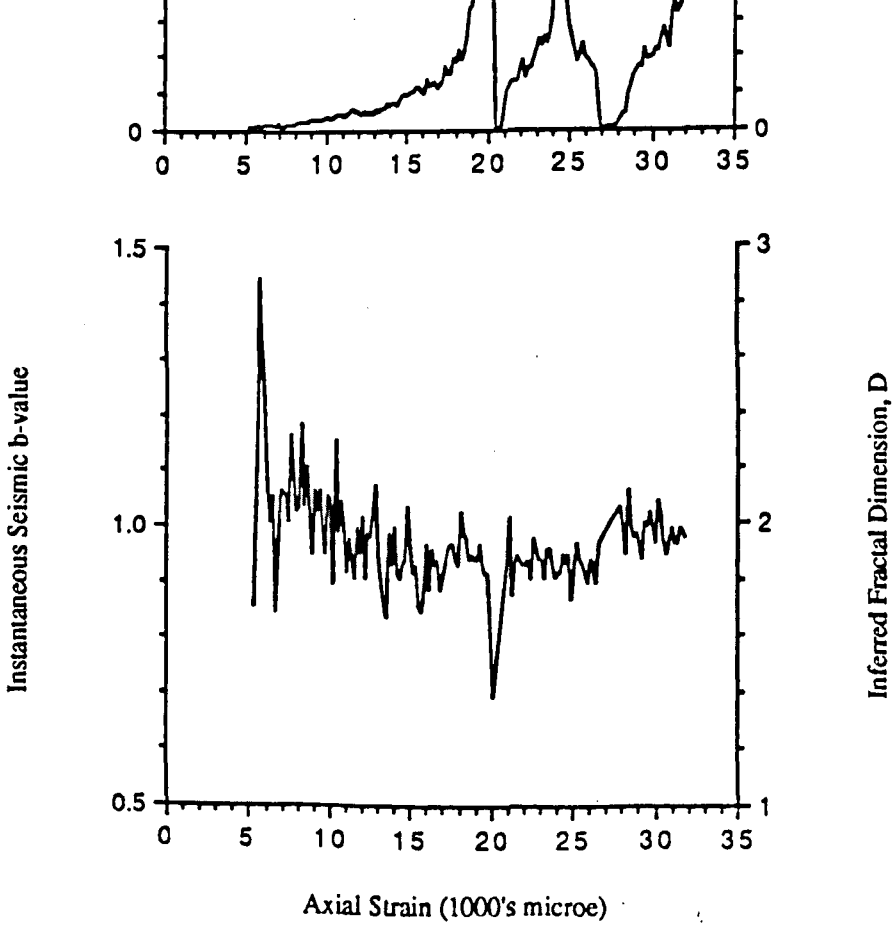
0
0
5
10
15
20
25
30
35
1.5
1.0
0.5
3
2
1
Instantaneous Seismic b-value
Inferred Fractal Dimension, D
Axial Strain (1000's microe)

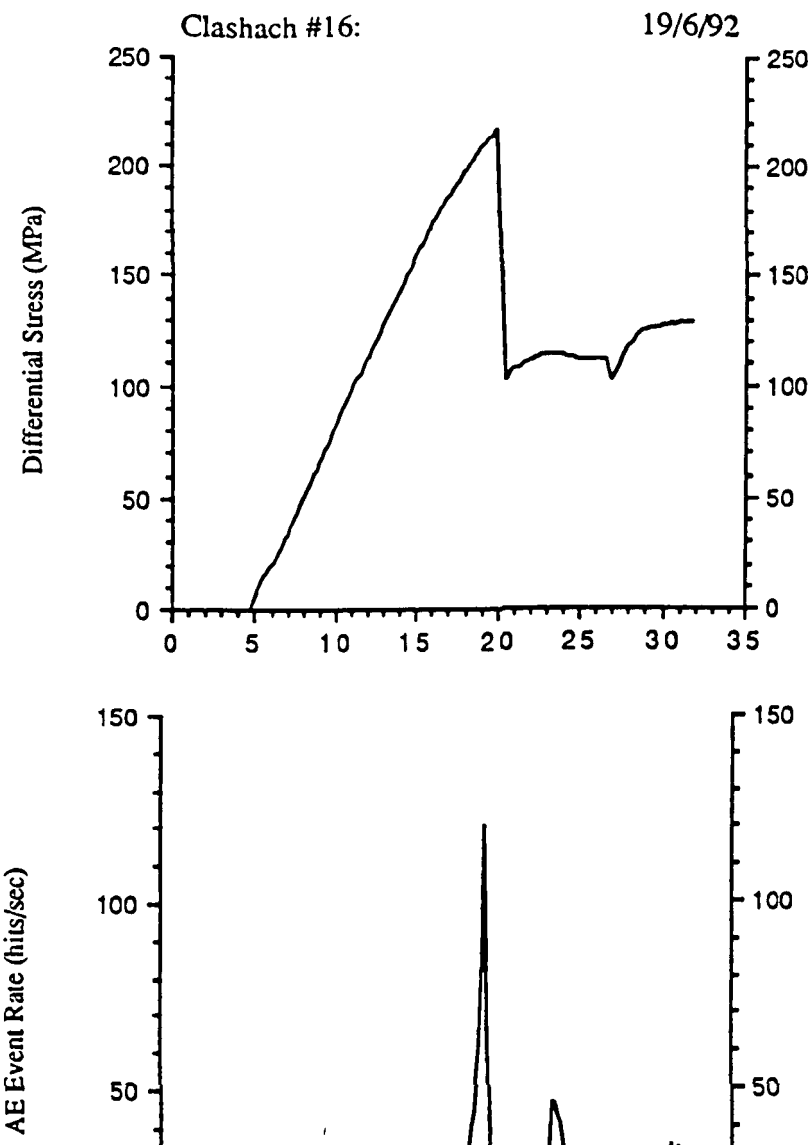
Clashach #16:
19/6/92
Differential Stress (MPa)
AE Event Rate (hits/sec)
250
200
150
100
50
0
0
5
10
15
20
25
30
35

Fig.AII.9

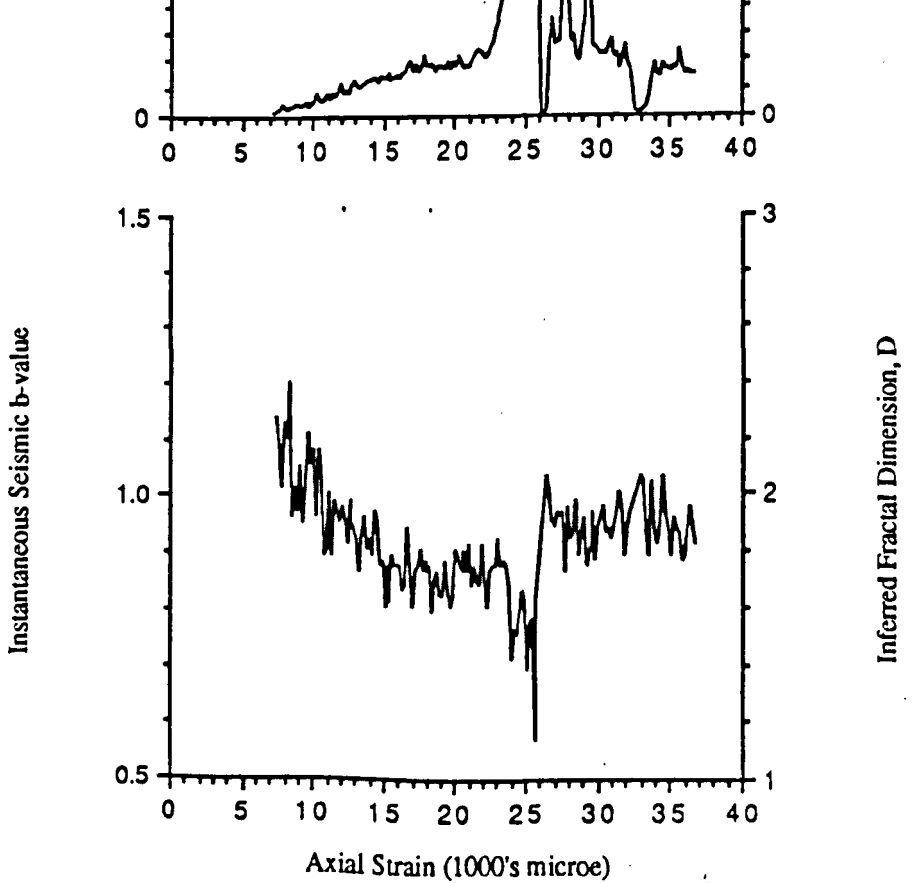
1.5
1.0
0.5
3
2
1
0
5
10
15
20
25
30
35
40
Instantaneous Seismic b-value
Inferred Fractal Dimension, D
Axial Strain (1000's microe)

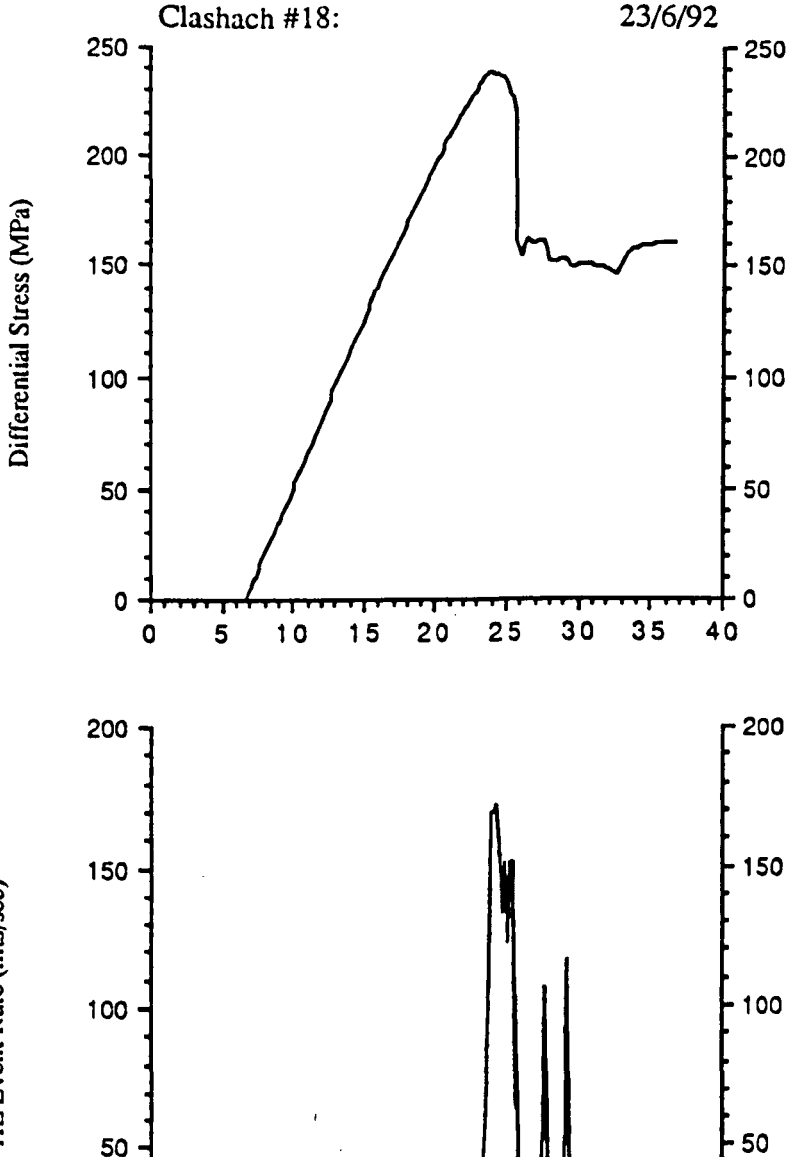
Clashach #18:
23/6/92
Differential Stress (MPa)
AE Event Rate (hits/sec)
0
50
100
150
200
250
0
5
10
15
20
25
30
35
40

Fig.AII.10

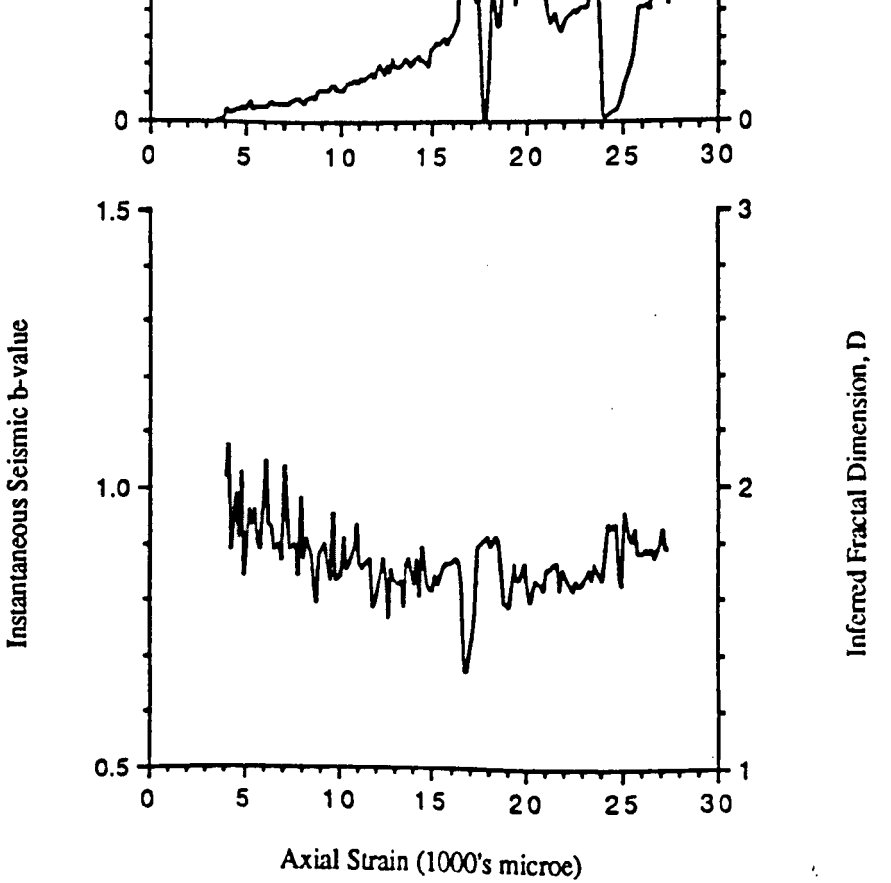
1.5
1.0
0.5
3
2
1
0
5
10
15
20
25
30
Instantaneous Seismic b-value
Inferred Fractal Dimension, D
Axial Strain (1000's microe)

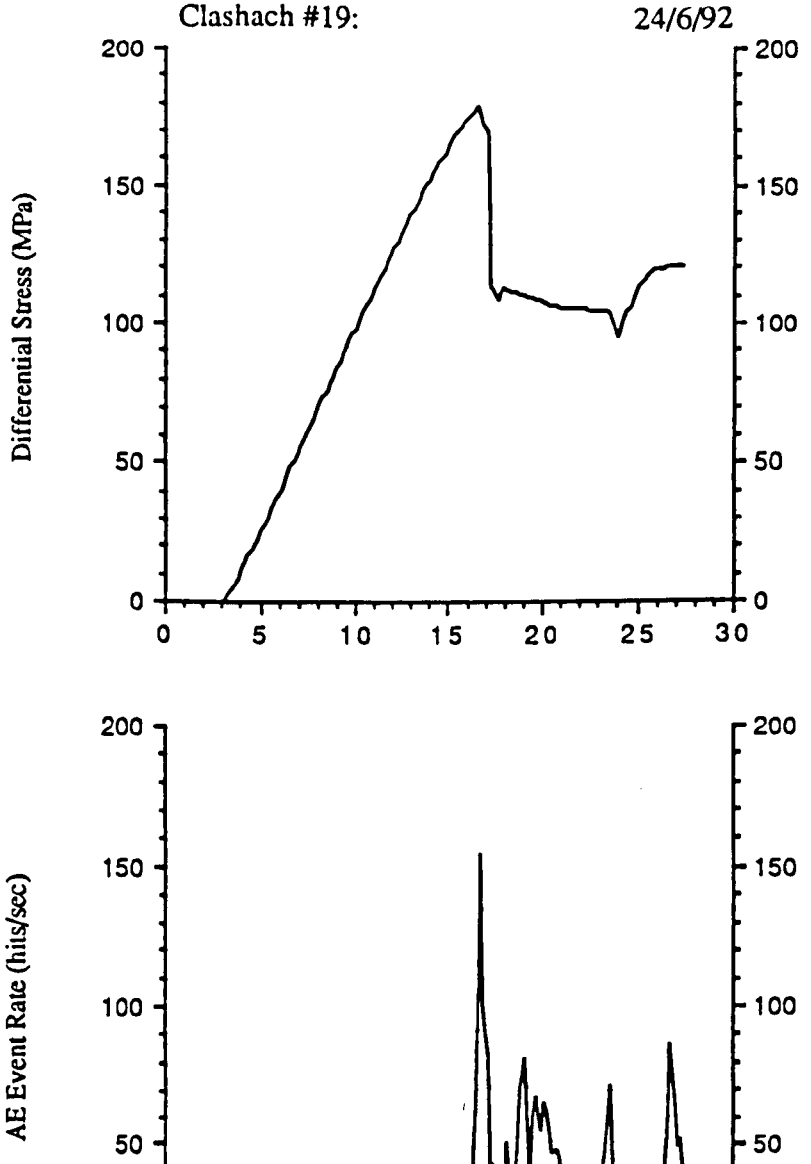
Clashach #19:
24/6/92
Differential Stress (MPa)
AE Event Rate (hits/sec)
0
50
100
150
200
0
5
10
15
20
25
30

Fig.AII.11

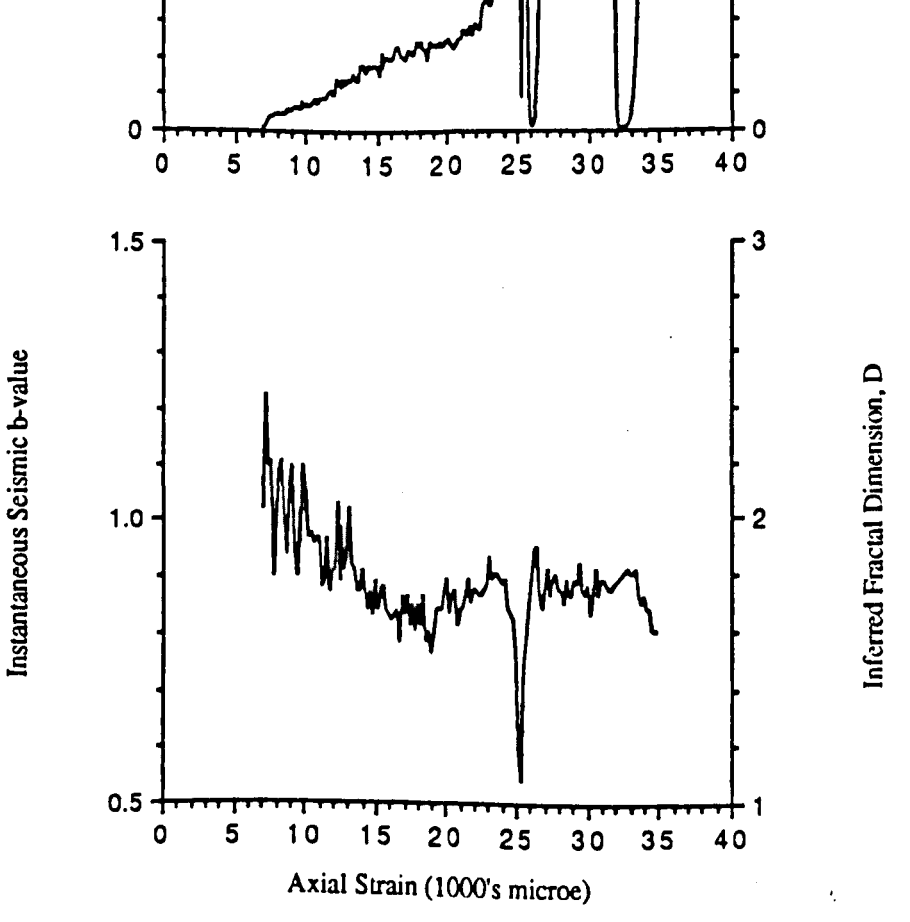
1.5
1.0
0.5
3
2
1
0
5
10
15
20
25
30
35
40
Instantaneous Seismic b-value
Inferred Fractal Dimension, D
Axial Strain (1000's microe)

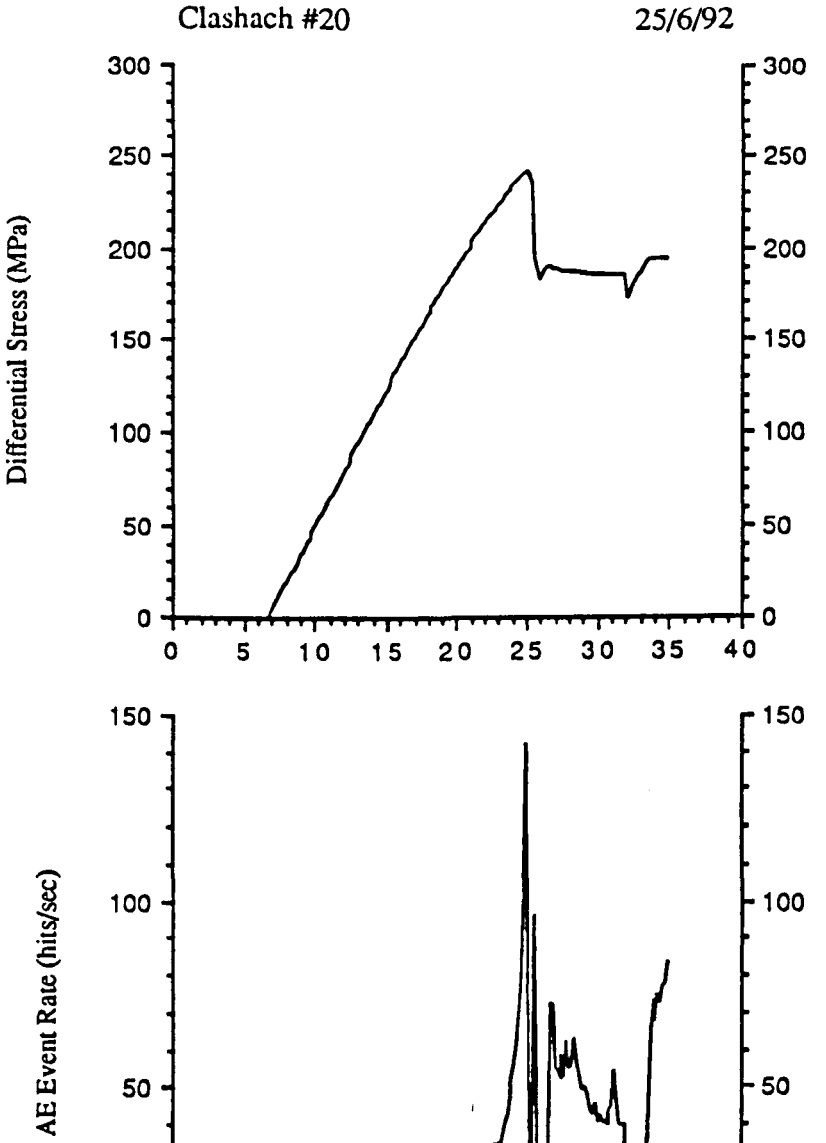
Clashach #20
25/6/92
Differential Stress (MPa)
AE Event Rate (hits/sec)
0
50
100
150
200
250
300
0
5
10
15
20
25
30
35
40

Fig.AII.12

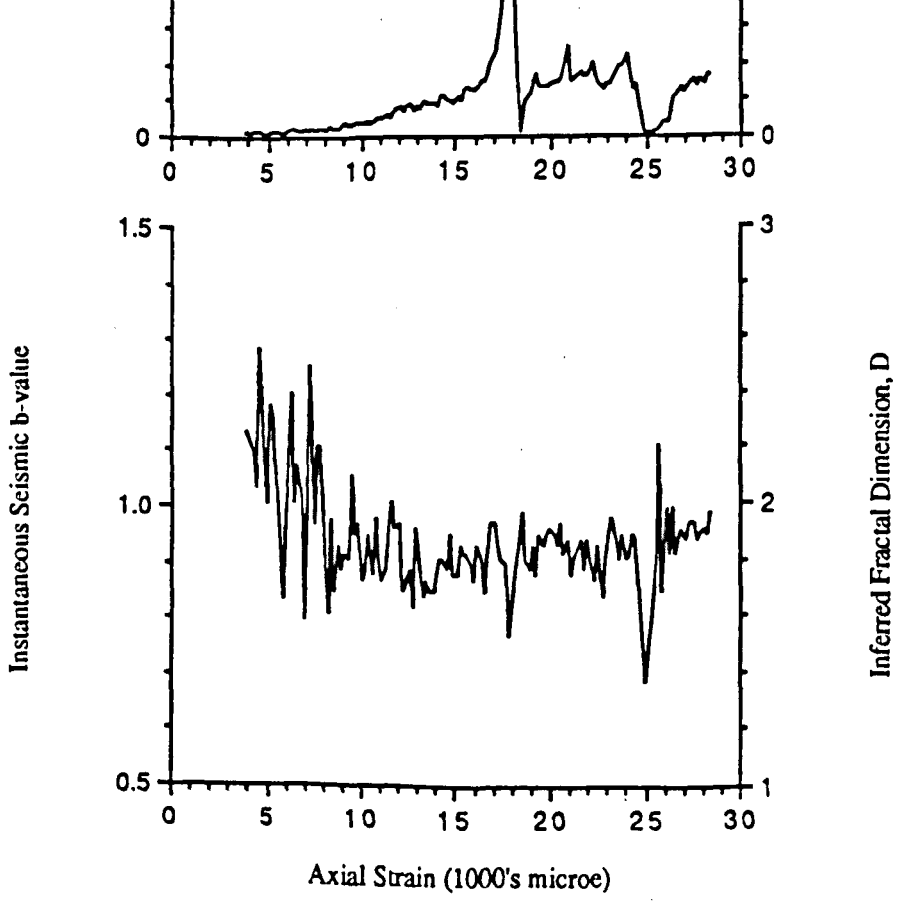
0
0
5
10
15
20
25
30
1.5
1.0
0.5
3
2
1
Instantaneous Seismic b-value
Inferred Fractal Dimension, D
Axial Strain (1000's microe)

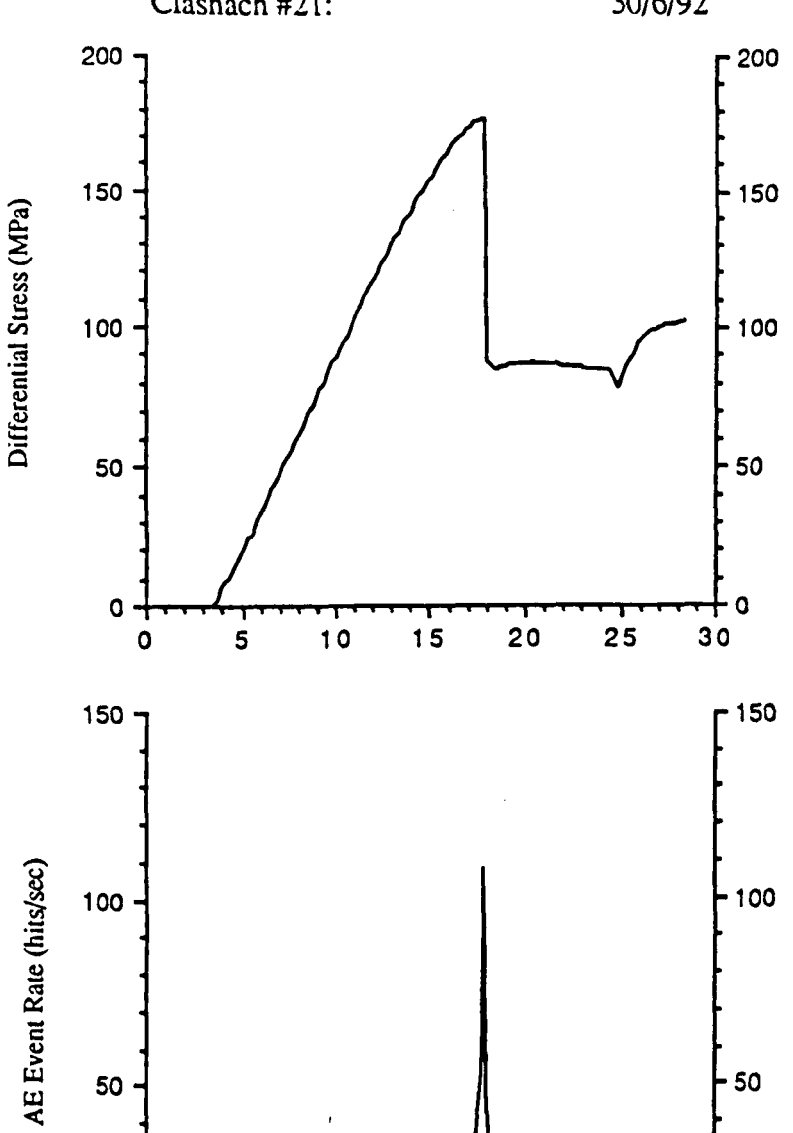
Clashach #21:
30/6/92
Differential Stress (MPa)
AE Event Rate (hits/sec)
0
50
100
150
200
0
5
10
15
20
25
30

Fig.AII.13